

Chapter 2

Carbon (Graphene/Graphite)

2.1 Structures

Carbon is the sixth element of the periodic table with the ground state level 3P_0 and electron configuration $1s^2 2s^2 2p^2$, which is hybridized to form sp^1 , sp^2 and sp^3 chemical bonds between atoms. The general oxidation states (numbers) of carbon in numerous inorganic compounds are (−4) (+4) and (+2); the radii of carbon are:

atomic (metallic, CN = 12)—0.091 nm,
atomic (van der Waals)—0.170 nm,
atomic (covalent)—various, see Table 2.1,
ionic (+4)—0.015 nm (CN = 4) or 0.016 nm (CN = 6);

its electronegativity is 2.55 in Pauling scale, or 2.50 in Allred–Rochow scale. The hybridized sp^n -bonding ($1 \leq n \leq 3$) differs considerably from common s - or p -bonds inherent to other chemical elements of the basic periods. The values of energy characteristics, in particular, specific bond energies (average bond energy per bond order) of carbon–carbon sp^n -bonds occupy a wide area of intermediate positions between those characteristics of s - and p -elements, depending substantially on the hybridisation type of bonding: $s > sp^3 > sp^2 > sp^1 > p$ (Table 2.1). The electron hybridization predetermines the ability of carbon atoms to arrange numerous compounds with other elements of the periodic table, but also the various allotropes, such as carbyne/carbyte, graphene/graphite and diamond (Table 2.2), which are structured with linear, planar and tetrahedral symmetry, coordination numbers of 2, 3 and 4 and the bond angles of 180° , 120° and 109.47° , respectively for sp^1 -, sp^2 - and sp^3 -hybridized forms. According to Mendeleev “none of the elements can compete with carbon in ability to form complex structures” [1, 540].

There has been a new wave of interest in carbon materials caused by the recent discoveries in the nanoscience [2, 9–14, 31, 42, 45–53], which has affected all science and engineering fields. Some points of view are developed in literature to classify carbon macro- and nanostructures. In this way, schemes based on hybridization characteristics were suggested by McEnaney [9], Heimann et al. [10],

Table 2.1 Comparative atomic bonding characteristics of *s*- and *p*-elements of the periodic table [2–9]

Outer electronic configuration	Bond type (examples)	Bond order	Specific bond enthalpy ^a , kJ mol ⁻¹	Bond length, nm	Covalent atomic radius, nm	Frequency, ^b cm ⁻¹	Force constant, ^b N/m
<i>s</i>	H–H	1	435	–	–	–	–
<i>sp</i> ³	Hydrogen molecule			0.074	0.030		
	C–C	1	369	–	–	997	3.5
	Diamond			0.154	–		
	<i>sp</i> ³ – <i>sp</i> ³ (6 peripheral atoms in total)			0.153 ^c	0.077		
	<i>sp</i> ³ – <i>sp</i> ² (5 peripheral atoms in total)			0.151 ^c	–		
	<i>sp</i> ³ – <i>sp</i> ¹ (4 peripheral atoms in total)			0.149 ^c	–		
	<i>sp</i> ² – <i>sp</i> ² (4 peripheral atoms in total)			0.146 ^c	0.073		
<i>sp</i> ² (aromatic)	<i>sp</i> ² – <i>sp</i> ¹ (3 peripheral atoms in total)			0.143 ^c	–		
	<i>sp</i> ¹ – <i>sp</i> ¹ (2 peripheral atoms in total)			0.138 ^c	0.069		
	C=C	1.5	345	–	–	–	–
	Graphene			0.142	0.071		
	Benzene (4 peripheral atoms in total)			0.140	–	1620	9.3
<i>sp</i> ²	C≡C	2	306	–	–		
	<i>sp</i> ² – <i>sp</i> ² (4 peripheral atoms in total)			0.134 ^c	0.067		
	<i>sp</i> ² – <i>sp</i> ¹ (3 peripheral atoms in total)			0.132 ^c	–		
	<i>sp</i> ¹ – <i>sp</i> ¹ (2 peripheral atoms in total)			0.128 ^c	0.064		
<i>sp</i> ¹	C≡C	3	279	–	–	2100	15.6
	Carbyne			0.128	–		
	<i>sp</i> ¹ – <i>sp</i> ¹ (2 peripheral atoms in total)			0.121 ^c	–		
	F–F	1	159	–	–	–	–
<i>p</i>	Fluorine molecule			0.141	0.071		

^a Average bond enthalpy per bond order^b From infrared absorption and combination scattering spectra data^c Average values

Table 2.2 Systematic classification of carbon nano- and macrostructures

Hybridisation types (proposed terms)	Existing (or predicted) structural forms of carbon			References	
	Nanostructures				
	Submolecular	Molecular (mesostructures)	Supramolecular		
$\sigma\text{-}sp^1 + 2\pi$ (carbyne general family)	Short polyyne and polycumulene chains	α - and β -Carbyne ^a (methine ^b)	Carbyne nanobundles Carbyne nanorings “Chain armour” structures	Carbyte ^c (carbolite, crystal forms of carbynes and their polytypes)	[9, 10, 15–20]
$(\sigma\text{-}sp^1 + 2\pi) - (\sigma\text{-}sp^2 + \pi)$ or $\sigma\text{-}sp^1 \text{ } ^{1 < n < 2} + (3-n)\pi$ (graphyne intermediate family) ^e	Nanographynes (?) Graphyne nanoribbons (?)	Graphynes Graphdiynes Graphynes-n Supergraphene	Bilayered graphyne Multi-layered graphynes (?)	α, β, γ -Graphyte ^d (various polytypes) Intermediate graphite (graphene) to carbyte (carbyne) transition phases (?)	[21–29, 53, 179, 187, 694]
$\sigma\text{-}sp^2 + \pi$ (graphene general family)	Nanographenes Graphene nanoribbons	Graphene	Bilayered graphene Multi-layered graphenes Expanded nano-platelets Nanofiber (nanowire, nanorods)	Graphite (H- and R-polymorphs/polytypes) Natural graphite Kish graphite Pyrolitic graphite Expanded (exfoliated) graphite Carbon (graphite) fiber Carbon (graphite) clothes, fabrics and prepregs (woven or non-woven)	[11, 30–44, 74–85, 136–138, 676, 694]
$(\sigma\text{-}sp^2 + \pi) - \sigma\text{-}sp^3$ or $\sigma\text{-}sp^2 \text{ } ^{2 < n < 3} + (3 - n)\pi$ (fullerene intermediate family) ^e	Nanoclusters of conjugated pentagon and hexagon cycles	Fullerenes (buckminsterfullerene C ₆₀ and other forms in C _{2n} series with $n = 10, 12, 13, 14, \dots$, e.g. C ₂₀ , C ₂₂ , C ₂₄ , C ₂₆ , C ₂₈ , C ₃₀ , C ₃₂ , C ₃₄ , C ₃₆ , C ₃₈ , C ₄₀ , C ₄₂ , C ₄₄ , C ₄₆ , C ₄₈ , C ₅₀ , C ₅₂ , C ₅₄ ,	Fullerene rings Fullerene nanotubes Fullerene nanowhiskers (fullerene nanofibers) Nanobeads (“pearl necklace” structures) Fullerene polymers	Fullerites (polymorph forms of fullerene molecular crystals and fullerene polymers) Nanotubular crystals (nanotube yarn) Nanotube lattices	[21, 42, 45–71, 75, 86–167, 649–652, 669–676, 682–688, 694–699]
					(continued)

(continued)

Table 2.2 (continued)

Hybridisation types (proposed terms)	Existing (or predicted) structural forms of carbon			References
	Nanostructures			
	Submolecular	Molecular (mesostructures)		
		Supramolecular	Macrostructures	
	C ₅₆ , C ₅₈ , C ₇₀ , C ₇₂ , C ₇₆ , C ₇₈ , C ₈₂ , C ₈₄ , C ₉₀ , C ₉₄ , C ₁₂₀ , C ₂₄₀ , C ₅₄₀ , C ₉₆₀ , etc.) Single-walled nanotubes (zigzag, arm-chair and intermediate chiral configurations) Capped (closed) single- walled nanotubes Defective single-walled nanotubes Nanotubes (nanoscrolls) with polygonal cross- sections Nanoscrolls (whiskers, “Swiss roll” structures) Nanobarrels Nanococones Nanodisks Nanobreadsticks Toroids (toroidal cages) Helical nanocoils (coiled cages) Squarographenes Glitter	Hyperfullerenes (multi- walled fullerenes, onion- like fullerenes, “Russian doll” structures) Fullerene intercalated graphite compounds Astralens Double-walled nanotubes Multi-walled nanotubes Capped (closed) multi- walled nanotubes Defective multi-walled nanotubes Nanohorn particles Megatubes Giant nanotubes Supertubes Nanotube bundles (ropes, strands) Nanofiber (nanowire, nanorods) Nanotube lattices Nanobuds Nanopeapods Nanofoams (glitter-like and defected graphene-like networks)	Haeckelites (pentaheptites, octites) Schwarzsites Soot Carbon black (channel black, thermal black, lamp black, acetylene black) Defected graphite (armchair prismatic edge dislocations) Defected graphite (zig-zag prismatic edge dislocations) Amorphous carbon Pyrolytic carbon Coke Charcoal Activated carbon Molecular-sieve carbon Carbon (amorphous) fiber Carbon (amorphous) clothes, fabrics, felts, prepregs Aerogel (cryogels, xerogels) Glassy (vitreous) carbon Glassy (vitreous) carbon foam Carbon bead powder (mesocarbon microbeads) Carbide derived carbon	

(continued)

Table 2.2 (continued)

Hybridisation types (proposed terms)	Existing (or predicted) structural forms of carbon			References
	Nanostructures			
	Macrostructures			
	Submolecular	Molecular (mesostructures)	Supramolecular	
σ - sp^3 (diamond general family)	Diamondoids Ultra-nanocrystalline (ultra-dispersed) particulate diamond	Nanocrystalline particulate diamond	Ortho-graphite-diamond hybrids	Diamond-like carbon films n-diamond (or γ -carbon, shock-compressed graphite phase) i-carbon (shock-compressed graphite phase) Intermediate graphite-to-diamond transition phases Diamond (3C-diamond) single crystal (or polycrystalline) Lonsdaleite (hexagonal diamond, H- and R-polytypes) Hexagonite (cold compressed nanotubes) Diamond D ₅ Lonsdaleite L ₅ Octacarbon (supercubane, prismane, BC8, ?)
		Diamond nanorods	Para-graphite-diamond hybrids	
		Diamond nanotubes	Hexagonite (based on barrelene fragment molecules)	
		Diamond nanowhiskers	Aggregated diamond nanorods (hyperdiamond)	
		Diamond nanocylinders	Diamond nanofiber (filaments)	
		Diamond nanocones	Ultra-nanocrystalline diamond films	
		Diamond nanoplatelets	Polycrystalline diamond nanopowder	
			Carbide derived diamond-structured carbon	

^a Despite many publications on various carbyne types, the existence of this allotrope has not been universally accepted [73]
^b According to IUPAC recommendation, the term “methine” has to replace “carbyne”, as the latter one is used to term an organic radical
^c The term “carbyte” is suggested for carbyne crystal forms by analogy with “graphene-graphite” and “fullerene-fullerite” correlations
^d The term “graphyte” is suggested for graphyne crystal forms by analogy with “graphene-graphite” and “fullerene-fullerite” correlations
^e σ - sp^m and σ - sp^n indicate intermediate carbon forms with a non-integer degree of carbon bond hybridization

Inagaki [11], Belenkov [12], Shenderova et al. [13, 78] and Falcao and Wudl [14]. The systematic classification of all the experimentally confirmed and theoretically predicted carbon structures, which is given in Table 2.2, is based mainly on the relative values of the specific bond energies of sp^n -hybridized carbons as well as carbon phase transformation diagram (see Sect. 2.2). This approach, employing within the overall hierarchy of classified carbon structures from submolecular to macroscopic scales, in accordance to the bonding energy criteria, allows marking out among the variety of carbon structures three general families (with integer degree of hybridisation index n):

carbyne general family ($n = 1$), including sp^1 -hybridized ($\sigma-sp^1 + 2\pi$) carbons from nanostructured carbyne to its macrostructural crystalline form “carbyte” (the existence of carbyne (or carbolite) has not been universally accepted; the proposed term for a macrostructural form is given on the basis of analogy with graphene–graphite and fullerene–fullerite correlations);

graphene general family ($n = 2$), including sp^2 -hybridized ($\sigma-sp^2 + \pi$) carbons from nanostructured graphene to macrostructural crystalline graphite with its polytypic (hexagonal and rhombohedral) forms;

diamond general family ($n = 3$), including sp^3 -hybridized ($\sigma-sp^3$) carbons from various nanostructured diamonds to macrostructural crystalline diamond with its polytypic (cubic and hexagonal) forms.

and two intermediate (or transitional) families (with non-integer degree of hybridisation index n):

graphyne intermediate family ($1 < n < 2$), including $sp^{1<n<2}$ -hybridized ($\sigma-sp^{1<n<2} + (3 - n)\pi$) carbons from nanostructured graphyne (analogue of graphene modified by triple bonds) to macrostructural “graphyte” with various polytypes, which are characterized by the intermediate between carbyne and graphene hybridisation type (currently, hypothetical structures calculated and predicted only theoretically; the proposed term for a macrostructural form is given on the basis of analogy with graphene–graphite and fullerene–fullerite correlations);

fullerene intermediate family ($2 < n < 3$), including $sp^{2<n<3}$ -hybridized ($\sigma-sp^{2<n<3} + (3 - n)\pi$) carbons from numerous species of nanostructured fullerenes and hyperfullerenes, single-walled and multi-walled nanotubes, nanoscrolls, nanobarrels, nanocones and other nanostructures to macrostructural forms, such as fullerites, nanotubular crystals, hypothetical structures of haeckelites and schwarzites, as well as plenty of carbon/carbonaceous products, such as soot, carbon black, so-called “amorphous” carbon, pyrolytic carbon, coke, charcoal, activated carbon, molecular-sieve carbons, glassy carbon, carbide derived carbons, intermediate graphite-to-diamond transition phases, diamond-like carbon films and others, which are characterized by the intermediate between graphene and diamond hybridisation type (mainly, the fullerene family structures can be considered as distorted graphene related structures, where deviation from planarity is occurred because of the partial heptagons and/or pentagons substitution for hexagons in graphene networks; special measures

Table 2.3 Characteristic and structural features of allotropic, polymorphic and polytypic carbon forms

Form	Character	Structure parameters (at ambient conditions)	Density, g cm ⁻³	Thermal stability	References
<i>Carbyne Family</i> ^a					
α -Carbyne (methine)	1D carbon polymer with polyyne bonding (—C \equiv C—) _n	Max. length 3.6–4.8 nm, with larger length—degenerate into β -carbyne polycumulene chains (predicted theoretically)	—	Extremely unstable	[9–10, 15–20]
β -Carbyne (methine)	1D carbon polymer with polycumulene bonding (≡C=C≡) _n	Chains length 50–250 nm stabilized by impurities and formation of covalent bonds between chains, C–C bond length—0.128 nm (predicted theoretically)	—	Unstable	[9–10, 15–20]
Carbyne nanobundles	Aggregates of various aligned 1D carbon polymers	—	—	—	[9, 11, 16–17]
Carbyne nanorings	Hypothetical 1D and 2D structures (calculated by molecular mechanics and <i>ab initio</i> methods)	Various structures (predicted theoretically)	—	—	[19]
“Chain armour” structures	Hypothetical 3D complex structures of carbyne nanorings (calculated by molecular mechanics and <i>ab initio</i> methods)	Various structures (predicted theoretically)	—	—	[19]
Carbyte	Molecular crystal of β -carbyne arranged in hexagonal bundles	Crystal structure—trigonal (rhombohedral), space group— <i>P3m1</i> , lattice parameters: $a = b = c = 0.3580$ nm, $\alpha = \beta = \gamma = 118.5^\circ$, $Z' = 1$ (calculated by molecular mechanics methods)	1.36 ^b	Unstable (predicted)	[20]
Carbyte (carbolite) ^d	Molecular crystal of carbyne chains (C–C bond length—0.133 nm) arranged in hexagonal bundles	Crystal structure—hexagonal, lattice parameters: $a = 1.193$ nm, $c = 1.062$ nm; interchain distance—0.344 nm (XRD)	1.46	—	[18]
<i>Graphyne Family</i>					
Graphynes (α -graphynes)	Hypothetical flat monolayers of atoms packed into 2D polyhexagonal lattices (basic blocks predicted for graphyne family materials)	C–C bond length—0.1421 nm, C–C (in phenyl rings) bond length—0.1428 nm, C \equiv C bond length—0.1202 nm (calculated by modified neglect of differential overlap (MNDO) quantum chemical method)	—	Stable (predicted)	[22, 53, 694]

(continued)

Table 2.3 (continued)

Form	Character	Structure parameters (at ambient conditions)	Density, g cm ⁻³	Thermal stability	References
Graphidynes (β - and γ -graphynes)	Hypothetical flat monolayers of atoms packed into 2D polyhexagonal lattices, where hexagons are linked through $(-C\equiv C-)$ units	—	—	—	[53, 694]
Graphynes-n	Hypothetical flat monolayers of atoms packed into 2D polyhexagonal lattices, where hexagons are linked by polyyne bonding $(-C\equiv C-)_n$	—	—	—	[53, 694]
Supergraphene	Hypothetical flat monolayers of atoms packed into distorted 2D hexagonal lattices, where 2/3 of all bonds are replaced by carbyne-like bonding	—	—	—	[694]
6,6,6-Graphyte (polytype with next-nearest layers eclipsed, like in graphite)	Graphynes AB-stacked into 3D structures	Crystal structure—monoclinic, space group— Pm , lattice parameters: $a = b = 0.686$ nm, $c = 0.672$ nm, $\gamma = 120^\circ$, $Z = 24$ (calculated by MNDO quantum chemical method)	1.75	Stable at high temp. (predicted)	[22]
6,6,6-Graphyte (polytype with next-nearest-neighbour layers related by a centre of symmetry)	Graphynes ABC-stacked into 3D structures	Crystal structure—triclinic, space group— $P(-1)$, lattice parameters: $a = b = 0.686$ nm, $c = 0.760$ nm, $\alpha = 76.5^\circ$, $\beta = 117.9^\circ$, $\gamma = 120^\circ$, $Z = 24$ (calculated by MNDO quantum chemical method)	1.75	Stable at high temp. (predicted)	[22]
Intermediate graphene-to-carbyne (graphite-to-carbyne) transition phases <i>Graphene Family</i> Nanographenes	? 2D flat hexagonal carbon atoms ring network with open edges	—	—	At ultra-high temp. and pressures (predicted)	[9, 28, 179, 187]
Graphene nanoribbons	2D thin strips of graphene or unrolled single-walled carbon nanotubes	Average diameter <10 nm Width is less than 50 nm and lengths—below 500 nm	—	—	[30] [30, 74]

(continued)

Table 2.3 (continued)

Form	Character	Structure parameters (at ambient conditions)	Density, g cm ⁻³	Thermal stability	References
Graphene	Flat monolayer of atoms tightly packed into a 2D hexagonal lattice (basic block for all graphene family materials)	C–C bond length—0.142 nm	–	At higher temp. unstable with respect to scrolling	[31–38, 75, 694]
2H-Graphite (α -carbon, α -Graphite)	Graphenes AB-stacked into 3D structures (main graphite polytype)	Crystal structure—hexagonal, space group— $P6_3/mmc$, lattice parameters: $a = 0.2464$ nm, $c = 0.6711$ nm, $Z = 4$, interlayer spacing—0.3356 nm (neutron diffraction, XRD)	2.267	Stable, sublimates at ultra-high temp., binding energy—7.99 eV atom ⁻¹	[41–43, 76, 676]
1H-Graphite	α -Graphite polytype with A-over-A-stacked graphenes (hypothetical)	–	–	–	[10]
10H-Graphite	α -Graphite polytype	–	–	–	[10]
12H-Graphite	α -Graphite polytype	–	–	–	[10]
3R-Graphite (β -Graphite)	Graphenes ABC-stacked into 3D structures	Crystal structure—trigonal (rhombohedral), space group— $R(-3)m$, lattice parameters: $a = b = c = 0.3635$ nm, $\alpha = \beta = \gamma = 39.49^\circ$, $Z = 2$ (in hexagonal setting: $a = 0.2456$ nm, $c = 1.0039$ nm, XRD)	2.267	Completely transforms to 2H-graphite (α -graphite) at temp. 1300–2100 °C	[44, 77]
6R-Graphite	β -Graphite polytype	–	–	–	[10]
Natural graphite	Powdered aggregates composed from α - and β -graphites with β -phase content 7.5–15 %	–	2.20–2.25	–	[42–44]
Kish graphite	Graphite quasi-single crystals	–	–	Stable at high temp.	[11]
Pyrolytic graphite	Highly oriented aggregates of graphenes with some covalent bonding between graphene sheets	Composed from crystallites with deviation from perfect parallel order less than 1 % and apparent size perpendicular to the graphene planes L_c —up to 50–500 nm	2.10–2.25	Stable, sublimates at ultra-high temp.	[10, 42, 136]
Expanded nano-platelets	Nanoparticles consist of small stacks of graphene	Thickness—1–25 nm, other linear sizes—ranging from 0.1 to 100 μ m, increased spacing between graphene layers	–	–	[79–81]
Expanded (exfoliated) graphite	Aggregates of graphene prepared by decomposition of intercalated graphite compounds	Increased spacing between graphene layers	10 ⁻³ –10 ⁻¹ (powd.) 0.7–1.3 (packed)	Stable, sublimates at ultra-high temp.	[11, 82–83]

(continued)

Table 2.3 (continued)

Form	Character	Structure parameters (at ambient conditions)	Density, g cm ⁻³	Thermal stability	References
Carbon (graphite) fiber	Bundle of graphitic filaments with prevailing alignment of graphene sheets parallel to the fiber axis, needle-shaped voids between crystallites and sheets essentially parallel to the surface	Diameter of filaments—5–8 μm, apparent crystallite thickness L _c —6 nm and sizes L _a —15–50 nm, 2H-graphite lattice parameters: $a = 0.246$ nm, $c = 0.671$ – 0.687 nm, length-to-diameter ratio >100	1.5–2.2	Stable, sublimates at ultra-high temp.	[8, 42, 84–85, 127, 136–137]
Carbon (graphite) clothes, fabrics and prepreps (woven or non-woven)	(2, 2.5, 3,...n) D-components made from carbon (graphite) fiber	Variety of structures	–	Stable, sublimates at ultra-high temp.	[8, 84, 136–137]
Fullerene Family					
Fullerene C ₆₀ (buckminsterfullerene)	Spherical molecule with polyhedral form containing 60 atoms (most abundant)	Truncated icosahedron made of 20 hexagons and 12 pentagons (ratio of pentagon/hexagon rings—0.6) with an atom at the vertices of each polygon and a bond along each polygon edge, each atom is covalently bonded to three others, nucleus-to-nucleus diameter—0.714 nm, C–C bond lengths: between two hexagons—0.1391 nm and between a hexagon and a pentagon—0.1455 nm, pyramidalization angle (obtained from π -orbital axis vector analysis)—11.6°	–	Destruction temp. of molecule (in gas phase) >2700 °C	[42, 52, 68, 78, 86–88]
Fullerene C ₇₀	Spherical molecule with polyhedral form containing 70 atoms	Polyhedron made of 25 hexagons and 12 pentagons (ratio of pentagon/hexagon rings—0.48) with an atom at the vertices of each polygon and a bond along each polygon edge, each atom is covalently bonded to three others, molecule sizes: full height (distance between 2 pentagons in mutually opposite polar areas)—0.780 nm and diameter of equator circle via atomic nuclei—0.694 nm, 8 types of C–C bonds with lengths from 0.137 to 0.147 nm, pyramidalization angle—10.7°	–	Destruction temp. of molecules (in gas phase) >2700 °C	[42, 52, 68, 86–88]

(continued)

Table 2.3 (continued)

Form	Character	Structure parameters (at ambient conditions)	Density, g cm ⁻³	Thermal stability	References
Fullerene C ₃₂	Spherical molecule with polyhedral form containing 32 atoms	Polyhedron made of hexagons and pentagons (ratio of pentagon/hexagon rings—2)	—	—	[51–52, 68, 78, 86–88]
Fullerene C ₂₈	Spherical molecule with polyhedral form containing 28 atoms	Polyhedron made of hexagons and pentagons (ratio of pentagon/hexagon rings—3)	—	—	[51–52, 68, 78, 86–88]
Fullerene C ₂₀	Spherical molecule with polyhedral form containing 20 atoms	Polyhedron made of pentagons (ratio of pentagon/hexagon rings—∞)	—	—	[51–52, 68, 78, 86–88]
Fullerenes in C _{2n} -series (buckyballs, carbon cages)	Variety of spherical molecules with polyhedral forms containing 2 <i>n</i> (<i>n</i> = 10, 12, 13, 14, 15...) atoms	Various polyhedral structures with pyramidalization angles in the range of 0° (graphene, <i>sp</i> ² -bonding) to 19.5° (diamond, <i>sp</i> ³ -bonding)	—	—	[42, 51–52, 58, 68, 78, 86–88]
Fullerene rings	Variety of C _{2n} -polymerized 2D ring-based structures	... E.g., (C ₆₀) _n -rings with number of members <i>n</i> = 3–8	—	Stable (predicted)	[106]
Fullerene nanotubes	Tubular thin fiber composed of C _{2n} molecules or their derivatives	E.g., C ₆₀ - or C ₇₀ -, or C ₆₀ -C ₇₀ -two-component nanotubes with diameter of ~0.24–1.5 μm and length of ~5–60 μm; crystal structure—hexagonal in solvated forms and cubic (face-centred) after losing the contained solvent molecules	—	Stable, decompose in air at temp. >415 °C	[651–652]
Fullerene nanowhiskers (fullerene nanofibers)	Single crystalline nanofibers composed of C _{2n} molecules with non-tubular morphologies	E.g., C ₆₀ - or C ₇₀ -nanowhiskers (needle-like crystals) with diameter from 80 nm up to ~1 μm and length from ~1–10 μm up to ~1–10 mm; crystal structure—hexagonal in solvated forms and cubic (face-centred) after losing the contained solvent molecules	—	Stable, decompose in air at temp. >450 °C	[649–650, 652]
Nanobeads (“pearl necklace” structures)	Quasi-1D-structures based on fullerenes, in particular, small fullerenes C _{2n} (2 <i>n</i> < 60)	Participation of ordinary, double, ternary, etc. chains of carbon atoms bonding vertices, edges and faces of neighbouring fullerenes	—	—	[53]
Fullerene polymers	Variety of C _{2n} -polymerized structures such as dimers, trimers, ..., 1D chains and 2D lattices	E.g., (C ₆₀) _n 2D orthorhombic, tetragonal and hexagonal (rhombohedral) lattices are bonded by the combination of parallel double bonds on adjacent molecules with intermolecular spacing reduced	—	Stable, decompose in air at temp. >470 °C	[55, 90, 91, 652]

(continued)

Table 2.3 (continued)

Form	Character	Structure parameters (at ambient conditions)	Density, g cm ⁻³	Thermal stability	References
Fullerites C ₆₀	Molecular crystals of C ₆₀ fullerenes and/or C ₆₀ fullerene polymers or 3D C ₆₀ fullerene polymers	Crystal structure—cubic (simple), space group— <i>P6₃/-3</i> , lattice parameter: <i>a</i> = 1.404 nm, <i>Z</i> = 240 (neutron diffraction)	1.729	Stable at lower temp.	[92]
		Crystal structure—cubic (face-centred), space group— <i>Fm₃-3m</i> , lattice parameter: <i>a</i> = 1.416 nm, <i>Z</i> = 240 (XRD)	1.686	Stable, melting point >280 °C, sublimates at 530 C ^{oe}	[93]
		Crystal structure—cubic (face-centred), space group— <i>Fm₃-3</i> , lattice parameter: <i>a</i> = 1.426 nm, <i>Z</i> = 240 (electron diffraction)	1.651	Stable, melting point >280 °C, sublimates at 530 C ^{oe}	[94]
		Crystal structure—orthorhombic (tetragonal), space group— <i>Ihmm</i> , lattice parameter: <i>a</i> = 0.909 nm, <i>c</i> = 1.495 nm, <i>Z</i> = 120 (calculated)	1.938	Stable under high pressures	[95]
		Crystal structure—orthorhombic (tetragonal), space group— <i>Ihmm</i> , lattice parameter: <i>a</i> = 0.9026 nm, <i>b</i> = 0.9083 nm, <i>c</i> = 1.5077 nm, <i>Z</i> = 120 (XRD)	1.937	—	[96]
Fullerites C ₇₀	Molecular crystals of C ₇₀ fullerenes and/or C ₇₀ fullerene polymers or 3D C ₆₀ fullerene polymers	Crystal structure—trigonal (rhombohedral), space group— <i>R₃-3m</i> , lattice parameters: <i>a</i> = 0.9175 nm, <i>c</i> = 2.4568 nm, <i>Z</i> = 180 (XRD)	2.005	—	[97]
		Crystal structure—tetragonal, space group— <i>P4₂/hmc</i> , lattice parameter: <i>a</i> = 0.9064 nm, <i>c</i> = 1.5039 nm, <i>Z</i> = 120 (XRD)	1.938	—	[98]
		Crystal structure—orthorhombic, space group— <i>Pnma</i> , lattice parameter: <i>a</i> = 1.0016 nm, <i>b</i> = 1.7349 nm, <i>c</i> = 1.853 nm, <i>Z</i> = 280 (XRD)	1.734	Stable at lower temp.	[99]
		Crystal structure—orthorhombic, space group— <i>Cmcm</i> , lattice parameter: <i>a</i> = 1.7303 nm, <i>b</i> = 0.9990 nm, <i>c</i> = 1.7924 nm, <i>Z</i> = 280 (XRD)	1.802	Stable at lower temp.	[100]

(continued)

Table 2.3 (continued)

Form	Character	Structure parameters (at ambient conditions)	Density, g cm ⁻³	Thermal stability	References
Fullerites C ₂₈	Molecular crystals of C ₂₈ fullerenes and/or C ₃₈ fullerene polymers or 3D C ₂₈ fullerene polymers, including lattices similar to diamond and lonsdaleite (so-called hyperdiamonds and hyperlonsdaleites)	–	1.10 (hyperdiamond)	–	[697]
Self-intercalated fullerites C ₂₈	Hypothetical 3D C ₂₈ fullerene network formed on the basis of hyperdiamonds, when two similar lattices inserted into one another	–	2.18	–	[697]
Fullerite C ₂₀	Molecular crystals of C ₂₀ fullerenes and/or C ₃₀ fullerene polymers or 3D C ₂₀ fullerene polymers	Crystal structure—cubic (body-centred), space group— <i>Im</i> ($\bar{3}$), lattice parameter: $a = 0.6897$ nm, $Z = 40$ (calculated by density-functional-based tight-binding (DFTB) method)	2.431	–	[101]
Fullerites C _{2n}	Molecular crystals of C _{2n} fullerenes and/or C _{2n} fullerene polymers or 3D C _{2n} fullerene polymers	Variety of different structures	–	–	[50, 91, 101]
Hyperfullerenes (multi-walled fullerenes, onion-like fullerenes, buckyonions or “Russian doll” structures)	Spherical nanoparticles based on multiple atomic layers surrounding an initial fullerene core	E.g., C ₆₀ @C ₂₄₀ , C ₆₀ @C ₂₄₀ @C ₅₄₀ , C ₆₀ @C ₂₄₀ @C ₅₄₀ @C ₁₅₀₀ ,..., outer diameter—from 10 nm to 1 μ m, inner diameter for C ₆₀ —0.7–1.0 nm, interlayer spacing for C ₆₀ @C ₂₄₀ —0.3524 nm (calculated)	–	–	[50, 68, 78]
Astrallens	Polyhedral multi-shell fullerene-like nanoparticles consist of large defect-free flat graphitic faces connected by defective edge regions presumably pentagon-like structured	Particles average size ~ 40 nm and its graphitic faces sizes ~ 15 nm (stacking of 20–50 graphene sheets with interlayer spacing ~ 0.340 nm)	2.1–2.3	–	[57]
Fullerene intercalated graphite compounds	Graphene/C ₆₀ (or C ₇₀), (C ₆₀) _n -clusters/graphene systems, where the surface contacts between fullerene “quasi-spheres” and graphene sheets are reduced to “point-like contacts”	For C ₆₀ intercalated graphite compound—interlayer spacing ~ 1.3 nm (TEM), for (C ₆₀) ₁₄ -cluster graphite compound the formation of 2 parallel 7-fullerene monolayers for 2.2–2.7 nm spacing is predicted theoretically	–	–	[698–699]

(continued)

Table 2.3 (continued)

Form	Character	Structure parameters (at ambient conditions)	Density, g cm ⁻³	Thermal stability	References
Single-walled nanotubes (buckytubes, SWCNT)	Cylindrical tube-like molecules with atoms tightly packed into a 2D hexagonal lattice	Molecular diameter—0.43–100 nm (typical—1–10 nm), length: typical—from 50 nm to 1 µm and max—up to centimetre scale, max. length-to-diameter ratio—up to 1.32 × 10 ⁸ :1	—	Stable at ultra-high temp.	[58–59, 68, 78, 104–106]
SWCNT capped (closed)	Cylindrical tube-like molecules with atoms tightly packed into a 2D hexagonal lattice with the ends capped by hemispheres of the fullerene structures	—	—	—	[58, 105]
Defective SWCNT	Cylindrical tube-like molecules with the defects in 2D hexagonal lattices (bent and toroidal tube-like structures)	Variety of different forms	—	—	[111]
Double-walled nanotubes (DWCNT)	Assemblies of two concentric cylindrical tube-like molecules with atoms tightly packed into a 2D hexagonal lattice	Outer molecule diameter—3–5 nm, interlayer (intertube) spacing—~0.39 nm	—	—	[58]
Multi-walled nanotubes (MWCNT)	Assemblies of several (up to 50 and even more) concentric cylindrical tube-like molecules with atoms tightly packed into a 2D hexagonal lattices	Outer molecule diameter—from 2.5 to 80 nm (the diameter of thinnest armchair (2,2)-type nanotube inside a multi-walled nanotube—0.3 nm), length (typical)—from 10 nm to 1 µm, interlayer (intertube) spacing—about 0.34 nm	—	Stable at ultra-high temp.	[58, 68, 78, 103–105]
MWCNT capped (closed)	Assemblies of concentric cylindrical tube-like molecules with atoms tightly packed into a 2D hexagonal lattice with the ends capped by hemispheres of the fullerene structures	—	—	—	[58]
Defective MWCNT	Assemblies of concentric cylindrical tube-like molecules with the defects in 2D hexagonal lattices (bent and L-, Y- and T-branched and helical multi-layered tube-like and bamboo-like structures)	Variety of forms, containing either topological (pentagon-heptagon) defects or structural (discontinuous or cone-shaped walls or bamboo structures)	—	—	[111]

(continued)

Table 2.3 (continued)

Form	Character	Structure parameters (at ambient conditions)	Density, g cm ⁻³	Thermal stability	References
Nanotubes (nanoscrolls) with polygonal cross-sections	1D needle-like molecules or assemblies of these molecules (with non-symmetric 2D hexagonal lattice fringes) shaped as twisted polygons	Outermost diameter of 10–50 nm, while the internal channel diameter varies in the range of 2–10 nm	–	–	[105, 145–147]
Nanobarrels	Imperfect cylindrical nanotubes with barrel-like forms	–	–	–	[53, 71]
Nanohorn particles	Spherical aggregates of capped SWCNTs	With average diameter—80–100 nm (each individual tube with diameter—2–3 nm and cap cone angle of 120°)	–	–	[113–114]
Megatubes	Self-assembled structures formed by branched nanotubes	Exceeding 5 μm in diameter	–	Stable	[89]
Giant nanotubes	Self-assembled knitted structures formed by nanotubes	With average sizes 5 μm in diameter and 100 μm in length	–	Stable	[63]
Supertubes	Hypothetical cylindrical structures built of single-walled nanotube fragments with Y-junctions	–	–	–	[53]
Nanotube bundles (ropes, strands)	Tightly packed aggregates of various aligned SWCNTs or MWCNTs	E.g., a typical bundle of SWCNTs with diameter range from 10 to 20 nm and length—between 10 μm and 1 mm (typical—10–100 μm) consist of 10 to 500 nanotubes, bundles (ropes, strands) are far longer than any individual tube in them	1.3–1.4 (in ropes)	Stable at ultra-high temp.	[78, 104–105, 108]
Nanotube lattices	2D ordered aggregates of various aligned single- or multi-walled nanotubes	Gap between the tubes (with average diameter 1.4 nm)—0.315 nm	–	–	[58, 110]
Nanotubular crystals (nanotube yarn)	Polycrystalline aggregates of various spun nanotube bundles	Length—up to 30 cm	–	Stable at ultra-high temp.	[104–105, 109]
Nanococones	Conical molecules with atoms tightly packed into a 2D polygonal (hexagonal and pentagonal) lattice	Dimensions—up to 1 μm, height and base diameter are of the same order of magnitude, the preferred values of apex angles are approximately 19°, 39°, 60°, 84° and 113°	–	–	[115–118]
Nanodisks	Hypothetical non-spherical (discoidal) molecules formed by cross-linking graphene layers, containing from 44 to 296 atoms	Diameters—from 0.675 nm to 1.952 nm and heights—from 0.307 nm to 0.472 nm (calculated by MM+ molecular mechanics and Hückel semiempirical methods)	–	–	[21]

(continued)

Table 2.3 (continued)

Form	Character	Structure parameters (at ambient conditions)	Density, g cm ⁻³	Thermal stability	References
Nanobreadsticks	Hypothetical non-spherical (discoidal-tubular) molecules formed by cross-linking graphene layers, adopting different conformations (similar to those in nanotubes) and containing from 148 to 248 atoms	Widths—from 1.078 nm to 1.156 nm, thicknesses—from 0.347 nm to 0.359 nm and lengths—from 1.536 nm to 2.621 nm (calculated by MM+ molecular mechanics and Hückel semiempirical methods)	—	—	[21]
Toroids (toroidal cages)	Giant ring tubular molecules with atoms tightly packed into a 2D hexagonal lattice or 2D hexagonal lattice with inserted pentagons and heptagons into the structures	E.g., series of molecules from C ₁₂₀ to C ₁₉₂₀ with 10 pentagons and 10 heptagons inserted within the each structure and approximate sizes: outer radii from 0.6 nm to 2.5 nm, inner and transverse radii from 0.25 nm to 1 nm (calculated by molecular dynamics method)	—	Stable	[53, 119–121, 125]
Helical nanocoils (coiled cages)	Giant tubular helical molecules with atoms tightly packed into a 2D hexagonal lattice or 2D hexagonal lattice with inserted pentagons and heptagons into the structures	E.g., derivatives of toroids with similar dimensions (calculated by molecular dynamics method)	—	Stable	[125]
Haackelones, haeckelites (pentaheptites, octites)	Hypothetical structures of hexagonal lattice distorted by the equal number of inserted pentagons and heptagons in order to compensate negative and positive curvatures, containing sometimes octagons	—	—	—	[53, 126, 694–696]
Schwarzones, schwarzites	Hypothetical negative curvature structures of hexagonal lattice distorted by the inserted heptagons	Various (predicted)	1.0–1.3 (calc.)	Stable (predicted)	[53, 126]
Squaragraphenes	Hypothetical structures formed by distorted hexagons and regular squares or by undistorted hexagons and rhombuses	—	—	—	[694]

(continued)

Table 2.3 (continued)

Form	Character	Structure parameters (at ambient conditions)	Density, g cm ⁻³	Thermal stability	References
Nanobuds	Combined (0D + 1D) molecules of fullerenes covalently attached to the outer sidewalls of underlying nanotubes	Two types of fullerene-nanotube bonding: sp^2 - and sp^3 -hybridized	–	–	[61]
Nanopeapods	Combined (0D + 1D) molecules of fullerenes encapsulated inside nanotubes C_{2n} @SWCNT (e.g. C_{60} , C_{70} , C_{80} , C_{84})	Orientation of the fullerenes with strong anisotropy is controllable by changing the nanotube radius (on the basis of density-functional theory (DFT) calculations)	–	Stable to 800 °C, at higher temp. transform to bilayered nanotubes	[53, 62]
Nanoscrolls (whiskers, “Swiss roll” structures)	Cylindrical molecules of graphene sheets rolled into scrolls	Molecular dimensions: outermost diameter—up to 80 nm, innermost diameter—1–4 nm, length—0.5–10 μ m	–	Stable at ultra-high temp.	[60, 68, 75, 123–124]
Nanofiber (nanowire, nanorods)	Cylindrical nanostructures with graphene layers arranged as stacked plates, cones and other configurations	Diameter—less than 0.5 μ m, length—up to 1 cm	–	Stable at ultra-high temp.	[68, 91, 127–135]
Nanof foam	Low-density (nanoporous) assembly of graphene clusters (nanoplatelets) with negative curvature bonded with each other by sp^2 -hybridized atoms and strung together in a loose 3D network	Dimensions of graphene clusters with inclusions of heptagons among the regular hexagonal lattice—about 6 nm (\sim 4000 atoms)	Very low, up to 0.002–0.010	Stable	[53, 64, 122, 676]
Defected graphite (armchair prismatic edge dislocations)	Distorted graphite structure characterized by formation of wrinkled unbonded graphene layers (well-defined cavities and expansion of interlayer spacing due to the bends of layers)	Structure built from sp^2 -hybridized atoms with max. separation between the flat and curled graphene layers— \sim 0.68 nm and min. separation— \sim 0.32 nm; the bent layers perform as spacers in the AA-stacked graphite with spacing of \sim 1 nm	1.62	Very stable with binding energy—7.94 eV atom ⁻¹	[676]
Defected graphite (zigzag prismatic edge dislocations)	Distorted graphite structure characterized by the local interconnection of neighboring graphene layers by sp^3 -hybridized atoms (reorientation of graphene layers and formation of connected double layers with cavities and loops)	Structure formed by the graphitic stripes connected by sp^3 -hybridized atoms with sp^3 - sp^2 bond length—0.1491 nm; the cavities have a max. height of 0.67 nm, each double layer is repeated with \sim 1 nm distance and min. distance between two graphitic fragments—0.33 nm	1.62	Very stable with binding energy—7.88 eV atom ⁻¹	[676]

(continued)

Table 2.3 (continued)

Form	Character	Structure parameters (at ambient conditions)	Density, g cm ⁻³	Thermal stability	References
Glitter	Hypothetical 3D structure (3,4-connected atomic net) forming 3D network of interconnected channels constructed from a structural basis constituted by a 1,4-cyclohexadienoid motif (viewed as a plausible model of n-diamond, ?)	Crystal structure—tetragonal, space group— $P4_2/mmc$, lattice parameters: $a = b = 0.2560$ – 0.2564 nm, $c = 0.5925$ – 0.6064 nm, $Z = 6$ (trigonal sp^2 -hybridized atoms to tetrahedral sp^3 -hybridized atoms ratio—2:1, C–C bond length— 0.1510 – 0.1534 nm, C=C bond length— 0.1348 – 0.1350 nm, DFT and DFTB calculated)	3.00–3.12	Stability is similar to that of diamond (binding energy— 7.52 eV atom ⁻¹)	[673, 676]
Soot	Randomly formed spherical particulates with loose grape-like aggregates (various in origin and contamination), having dominant turbostratic order with graphenes stacked in the manner of roof tiles	Particles with common sizes 10–500 nm consist of small domains—up to 3 nm along the graphene sheets and 2 nm perpendicular to them, interlayer spacing—about 0.344 nm	1.85–2.18	Stable at ultra-high temp.	[42, 58, 136, 138]
Carbon black (channel black, thermal black, lamp black, acetylene black)	Partly crystallized or amorphous spherical particulates (colloids with various origin and contaminations)	Particles with common sizes—10–500 nm, high specific surface area (10 – 150 m ² /g) and low apparent density (0.01 – 0.1 g/cm ³)	2.04–2.18	Stable at ultra-high temp.	[42, 136, 138]
Amorphous carbon	Structures (including films, porous and contaminated materials) without long-range crystalline order, or having polycrystalline (nanocrystalline) areas distributed by various ways within an amorphous matrix	Deviation of interatomic distances (or interbonding angles) from the perfect graphite crystal is greater than 5 % in both a graphene plane and between graphene planes	1.8–2.1	Stable in some ranges of temp., transforms to crystalline materials	[42, 69, 78, 136, 138]
Pyrolytic carbon	Aggregates of graphenes with covalent bonding between graphene sheets	E.g., material deposited at low temp. composed from crystallites with average dimensions $L_a = 4$ nm, $L_c = 2$ nm and interlayer spacing—more than 0.344 nm	1.1–2.1	Stable, at ultra-high temp. transforms to highly ordered materials	[8, 43, 136]
Coke	Graphene containing products of hydrocarbons pyrolysis (partly contaminated)	Composed from crystallites with L_c —about 5 nm and interlayer spacing—more than 0.344 nm	1.7–2.2	Stable, at ultra-high temp. commonly transforms to highly ordered materials	[42–43, 136, 138–139]

(continued)

Table 2.3 (continued)

Form	Character	Structure parameters (at ambient conditions)	Density, g cm ⁻³	Thermal stability	References
Charcoal	Graphene containing biomorphous products of pyrolysis (porous, contaminated)	Similar to coke	1.5–2.0	Stable, at ultra-high temp. commonly transforms to highly ordered materials	[42, 136, 138]
Activated carbon	Nanoporous assemblies of defective graphene layers	Ratio of pentagons-to-hexagons in the atomic network (estimated by HRTEM for high temp. heat-treated material)—approximately 1:50, average pore diameter—1–5 nm and specific surface area—in the range of 300–2600 m ² g ⁻¹	1.4–1.7	Stable	[42, 58, 69, 136, 138, 140]
Molecular-sieve carbon	Nanoporous assemblies of roughly parallel graphene sheets with no 3D crystalline order	Disorientation angles of graphene sheets—up to several degrees, formed from packing imperfection pore structures, consist of relatively wide openings of 0.6–2.0 nm with small ultramicropores of 0.3–0.6 nm (bimodal pore distribution)	1.3–1.8	Stable	[69, 141–144]
Carbon (amorphous) fiber	Bundle of filaments without long-range crystalline order, or having polycrystalline (nanocrystalline) areas distributed by various ways within an amorphous matrix (2, 2.5, 3,...n)D-components made from carbon (amorphous) fiber prepregs	Various structures	1.4–1.8	Stable at high temp.	[8, 42, 84, 136–137]
Carbon (amorphous) clothes, fabrics, felts and prepregs	(2, 2.5, 3,...n)D-components made from carbon (amorphous) fiber	Various structures	–	Stable at high temp.	[8, 84, 136–137]
Aerogels (cryogels, xerogels)	Assemblies of nanoporous (microporous) spherical nanoparticles formed by defective graphene layers	Particles with diameter of 6–40 nm composed from crystallites with sizes: L _c of 0.6–0.9 nm and L _a of 2.5–4.5 nm, interparticulate mesopores with dimensions of 3–15 nm and interior micropores—0.7–1.5 nm, specific surface area—400–1400 m ² g ⁻¹	–	Stable at high temp.	[69, 70, 148–150]
Glassy (vitreous) carbon	3D random tough network of 2D hexagonal lattice ribbons tangled and joined with each other	Graphitic ribbon crystallites with dimensions—L _c of 1.5–3 nm and interlayer spacing—0.360–0.349 nm, total porosity—~30 % with pore diameters of 1 to 3.5 nm (most of the pore entrances—0.4–0.5 nm)	1.4–1.6	Stable at ultra-high temp.	[42, 151–153]

(continued)

Table 2.3 (continued)

Form	Character	Structure parameters (at ambient conditions)	Density, g cm ⁻³	Thermal stability	References
Glassy (vitreous) carbon foam	Cellular (highly porous) structures of 2D hexagonal lattice ribbons networks	Total porosity—97 %, specific surface area—1–2 m ² g ⁻¹	~0.05 (bulk), ~1.5 (strut)	Stable at high temp.	[42]
Carbon bead powder (mesocarbon micro-beads)	Spherical particles (contaminated by hydrogen) consist of quasi-graphene (planar aromatic compounds) sheets (lamellae) stacked in parallel array	Particle diameters of 1–80 μm, the sheets are arranged perpendicularly along one diameter of a sphere, but curved and normal to the surface with interlayer (interlamellar) spacing—0.346–0.348 nm	1.3–2.2	Stable	[154–156]
Carbide derived carbon	Tunable nanoporous carbons formed by chemically removing metallic or non-metallic elements from carbides and leaving a systematic array of pores	Variety of nanostructures with different parameters	–	–	[71, 157–165]
Diamond-like carbon	Amorphous or semi-crystalline films (partly contaminated by hydrogen) with no lattice long-range order	Broad range of structures (film thickness of 0.1–5 μm) composed of very small crystallites having either tetrahedral or planar threefold local atomic configuration	1.8–2.8	Metastable, convert to graphite at 250–400 °C	[13, 42]
Hexagonite (based on barrelene generating fragment molecules) ^f	Hypothetical 3D structure (3-, 4-connected network) with a large number of derivatives formed by the insertion of 1,4-dimethylene-2,5-cyclohexa-dieneoid organic spacers	Crystal structure—hexagonal, space group— <i>P6₃/mmm</i> , lattice parameters: <i>a</i> = 0.4772 nm, <i>c</i> = 0.4129 nm, <i>Z</i> = 10 (C–C bond length—0.1521 nm, C=C bond length—0.1326 nm, C–C–C trigonal angles—130°, C=C–C trigonal angles—115°, tetrahedral angles within the cage of barrelene substructures—103°, tetrahedral angles outside the cage of barrelene substructures—115°, calculated and optimized by a DFT algorithm)	2.449	–	[669–671]
Ortho-graphite-diamond hybrids	Hypothetical 3D structure (3-, 4-connected network) with graphene fragments connected with each other in perpendicular directions by <i>sp</i> ³ -bonding	–	–	–	[672]

(continued)

Table 2.3 (continued)

Form	Character	Structure parameters (at ambient conditions)	Density, g cm ⁻³	Thermal stability	References
Para-graphite-diamond hybrids	Hypothetical 3D structure (3-, 4-connected network) with graphene fragments connected with each other in parallel directions by <i>sp</i> ³ -bonding	–	–	–	[672]
Intermediate graphite-to-diamond transition phases	Hypothetical 3D structures as progressive intermediates in graphite-to-diamond phase transition	Crystal structure—orthorhombic, space group— <i>Cmmm</i> , lattice parameters: <i>a</i> = 0.4525 nm, <i>b</i> = 0.5334 nm, <i>c</i> = 0.5925 nm, <i>Z</i> = 16 (calculated by molecular mechanics methods)	2.222	Metastable	[166]
		Crystal structure—orthorhombic, space group— <i>Cmme</i> , lattice parameters: <i>a</i> = 0.4575 nm, <i>b</i> = 0.5304 nm, <i>c</i> = 0.5635 nm, <i>Z</i> = 16 (calculated by molecular mechanics methods)	2.334	Metastable	[166]
		Crystal structure—orthorhombic, space group— <i>Pbam</i> , lattice parameters: <i>a</i> = 0.4048 nm, <i>b</i> = 0.4885 nm, <i>c</i> = 0.6495 nm, <i>Z</i> = 16 (calculated by molecular mechanics methods)	2.484	Metastable	[166]
		Crystal structure—orthorhombic, space group— <i>Pcca</i> , lattice parameters: <i>a</i> = 0.4700 nm, <i>b</i> = 0.5978 nm, <i>c</i> = 0.4448 nm, <i>Z</i> = 16 (calculated by molecular mechanics methods)	2.554	Metastable	[166]
		Crystal structure—orthorhombic, space group— <i>Cmmm</i> , lattice parameters: <i>a</i> = 0.4870 nm, <i>b</i> = 0.5565 nm, <i>c</i> = 0.4406 nm, <i>Z</i> = 16 (calculated by molecular mechanics methods)	2.673	Metastable	[166]
		Crystal structure—orthorhombic, space group— <i>Cmme</i> , lattice parameters: <i>a</i> = 0.4964 nm, <i>b</i> = 0.5163 nm, <i>c</i> = 0.4387 nm, <i>Z</i> = 16 (calculated by molecular mechanics methods)	2.839	Metastable	[166]
		Crystal structure—orthorhombic, space group— <i>Pbam</i> , lattice parameters: <i>a</i> = 0.4127 nm, <i>b</i> = 0.4937 nm, <i>c</i> = 0.4819 nm, <i>Z</i> = 16 (calculated by molecular mechanics methods)	3.250	Metastable	[166]
		Crystal structure—cubic, space group— <i>Ia(-3)</i> , lattice parameters: <i>a</i> = 0.4591 nm, <i>Z</i> = 16 (calculated by molecular mechanics methods)	3.297	Metastable	[166]

(continued)

Table 2.3 (continued)

Form	Character	Structure parameters (at ambient conditions)	Density, g cm ⁻³	Thermal stability	References
i-carbon (shock-compressed graphite phase)	Nanocrystals in intermediate states between graphite and diamond (or glitter modification, ?)	Thin films or spherical particles with diameter of ~25 nm (crystal structure of glitter, ?)	—	—	[675, 682–685]
n-diamond (or γ -carbon, shock-compressed graphite phase)	Nanocrystals in intermediate states between graphite and diamond (or glitter modification, ?)	Crystal structure—cubic, space group— $Fm\bar{3}m$, or crystal structure of glitter, ?	—	—	[170, 674, 682, 684, 686–688]
n-diamond	Hypothetical 3D structure as an intermediate state between rhombohedral graphite and diamond	Crystal structure—trigonal (rhombohedral), space group— $R\bar{3}$, lattice parameters: $a = b = c = 0.35809$ nm, $Z = 8$ (calculated)	3.474	—	[167]
<i>Diamond Family</i>					
Diamondoids	Hydrogen-terminated molecules	Various shapes with sizes of 1–2 nm	—	—	[72, 677]
Ultra-nanocrystalline (ultra-dispersed)	3D tetrahedral atomic structure in substantially monocrystalline particles (often with multiple twins)	Range of primary particles sizes—2–20 nm, average (or typical) size—4–5 nm, minimal size—1.8 nm, specific surface area—300–400 m ² /g, crystal structure—cubic with lattice parameter: $a = 0.3573 \pm 0.0005$ nm	3.1–3.4	Stable in some ranges of temp., initial vacuum graphitization temp.—1100–1200 °C	[72, 78]
Ultra-nanocrystalline aggregated diamond	Agglomerates of 3D tetrahedral structured particles	Dimensions of agglomerates—from 40–50 nm to 0.1–1 mm	—	—	[72]
Nanocrystalline particulate diamond	3D tetrahedral atomic structure in monocrystalline particles	Range of smallest fraction sizes—0–50 nm with average size—ca. 25 nm, other fractions—0–100 nm (average size—~50 nm), 0–150 nm and up	—	More stable than graphite nanoparticles being in clusters with less than 10 ⁴ carbon atoms	[72, 78]
Nanocrystalline aggregated diamond	Polycrystalline agglomerates of 3D tetrahedral structured particles	Average grain size—~20 nm	—	—	[72]
Diamond nanorods	1D form of 3D tetrahedral atomic structure	Diameter of 5–200 nm, length—up to 1–10 μ m	—	—	[72, 78]
Aggregated diamond nanorods (hyperdiamond)	Assembly of interconnected diamond nanorods	Nanorods with diameters of 5–20 nm and lengths of ~1 μ m	3.526	—	[168–169]
Diamond nanotubes	1D form of 3D tetrahedral atomic structure	Diameter of 50–160 nm	—	—	[72]

(continued)

Table 2.3 (continued)

Form	Character	Structure parameters (at ambient conditions)	Density, g cm ⁻³	Thermal stability	References
Diamond nanowhiskers	1D form of 3D tetrahedral atomic structure	Diameter of 10–60 nm, length—~300 nm	—	—	[72]
Diamond nanocylinders	1D forms of nanodiamond with circular, triangular or squared cross-sections	Diameter—up to 600 nm, length—~5 nm	—	—	[72]
Diamond nanocoils	1D form of 3D tetrahedral atomic structure	Diameters at base—0.1–1 μm	—	—	[72]
Diamond nanofiber (filaments)	1D form of polycrystalline ultra-dispersed diamond	Diameter of 0.1–1 μm, length of 2–3 μm, average grain size <10 nm	—	—	[72, 78]
Diamond nanoplatelets	2D form of 3D tetrahedral atomic structure with triangular and parallelogram shapes	Thickness ranges from 20 to 70 nm and length—0.1–10 μm	—	—	[72]
Ultra-nanocrystalline diamond films	3D form of polycrystalline ultra-dispersed diamond with grain boundaries formed by <i>sp</i> ² -hybridized atoms	Average grain size—2–5 nm, grain boundaries width—0.2–0.4 nm	—	—	[72]
Polycrystalline diamond nanopowder	3D form of polycrystalline ultra-dispersed diamond	Grain sizes with bimodal distribution—1–4 nm and 10–160 nm	—	—	[72]
Carbide derived diamond-structured carbon	Wide variety of nanoporous diamond polypore structures formed by chemically removing non-metallic elements from carbides	Grain sizes—5–10 nm	—	—	[71–72, 78, 170–171]
Diamond (3C-diamond, β-carbon) single crystal (or polycrystalline)	Giant molecule with atoms tightly packed into a 3D tetrahedral lattice (or assemblies of grains with similar structure)	Crystal structure—cubic, space group— <i>Fd</i> (-3) <i>m</i> , lattice parameter: <i>a</i> = 0.35667 nm, <i>Z</i> = 8 (C-C bond length—0.1545 nm, XRD)	3.516	Thermodynamically unstable with respect to graphite with a negative free-energy change of 2.88 kJ mol ⁻¹ at standard conditions	[9, 42, 58, 172]
Lonsdaleite (2H-diamond, γ-carbon)	Diamond polypore	Crystal structure—hexagonal, space group— <i>P6₃/mmc</i> , lattice parameters: <i>a</i> = 0.25221 nm, <i>c</i> = 0.41186 nm, <i>Z</i> = 4 (XRD)	3.521	—	[42, 166, 172]
Lonsdaleite (4H-diamond)	Diamond polypore	Crystal structure—hexagonal, space group— <i>P6₃/mmc</i> , lattice parameters: <i>a</i> = 0.25221 nm, <i>c</i> = 0.82371 nm, <i>Z</i> = 8 (XRD)	3.521	—	[42, 166, 172]

(continued)

Table 2.3 (continued)

Form	Character	Structure parameters (at ambient conditions)	Density, g cm ⁻³	Thermal stability	References
Lonsdaleite (6H-diamond)	Diamond polytype	Crystal structure—hexagonal, space group— <i>P6₃/mmc</i> , lattice parameters: <i>a</i> = 0.25221 nm, <i>c</i> = 1.23557 nm, <i>Z</i> = 12 (XRD)	3.521	—	[42, 172]
Lonsdaleite (8H-diamond)	Diamond polytype	Crystal structure—hexagonal, space group— <i>P6₃/mmc</i> , lattice parameters: <i>a</i> = 0.25221 nm, <i>c</i> = 1.64743 nm, <i>Z</i> = 16 (XRD)	3.521	—	[10, 42, 172]
Lonsdaleite (10H-diamond)	Diamond polytype	—	—	—	[42]
Lonsdaleite (12H-diamond)	Diamond polytype	—	—	—	[10]
Lonsdaleite (16H-diamond)	Diamond polytype	—	—	—	[10]
Lonsdaleite (20H-diamond)	Diamond polytype	—	—	—	[10]
Lonsdaleite (15R-diamond)	Diamond polytype	Crystal structure—trigonal (rhombohedral), space group— <i>R$\bar{3}$2/m</i> , lattice parameters: <i>a</i> = 0.25221 nm, <i>c</i> = 3.08893 nm, <i>Z</i> = 30 (XRD)	3.521	—	[172]
Lonsdaleite (21R-diamond)	Diamond polytype	Crystal structure—trigonal (rhombohedral), space group— <i>R$\bar{3}$2/m</i> , lattice parameters: <i>a</i> = 0.25221 nm, <i>c</i> = 4.3245 nm, <i>Z</i> = 42 (XRD)	3.521	—	[172]
Hexagonite (cold compressed nanotubes) ^f	Super-hard phase	Crystal structure—hexagonal, space group— <i>P6₃/2c</i> , lattice parameters: <i>a</i> = 0.2496 nm, <i>c</i> = 0.4123 nm, <i>Z</i> = 4 (interlayer spacing—0.21 nm, C–C bond length—0.143 nm, electron diffraction, XRD) The ratio of pentagon/hexagon rings is going up to 9	3.65 (or 3.6 ± 0.2) ^g	Quenched from ~75 GPa, preserved at room conditions	[668]
Diamond D ₅	Hypothetical diamond-like networks consisting mostly of pentagon rings	The ratio of pentagon/hexagon rings is going up to 9	—	More stable than C ₆₀ (calculated)	[666–667]

(continued)

Table 2.3 (continued)

Form	Character	Structure parameters (at ambient conditions)	Density, g cm ⁻³	Thermal stability	References
Lonsdaleite L ₅	Hypothetical lonsdaleite-like networks consisting mostly of pentagon rings	The ratio of pentagon/hexagon rings is going up to 9	–	More stable than C ₆₀ (calculated)	[666–667]
Octacarbon (supercubane, High-temp. modification of diamond (?), prismane, BCS)		Crystal structure—cubic (body-centred), space group— <i>Im</i> ($\bar{3}$), lattice parameter: $a = 0.428$ nm, Z = 16 (electron diffraction and calculated by molecular mechanics methods)	4.1	Stable at ultra-high temp. and pressures	[166, 176–177, 187, 189]
		Crystal structure—cubic (body-centred), space group— <i>Ia</i> ($\bar{3}$), lattice parameter: $a = 0.4293$ nm, Z = 16 (calculated by molecular mechanics methods)	4.03	–	[166, 173–175, 187, 189]

^a Concerning the carbyne family, see notes *a–c* to Table 2.2
^b Calculated on the basis of data [20]
^c Number of formula units per lattice
^d Some other forms have been reported in literature [9]
^e Data available in literature are controversial [112]
^f Not to be confused with the inorganic mineral structure and some trademark names
^g Average (reduced) density due to possibly amorphous carbon on the grain boundaries

termed pyramidalization angle and/or curvature are used for evaluation of nonplanarity (deviation from graphene plane geometry) in fullerene family structures),

which differ in the sp^n -hybridisation ($1 \leq n \leq 3$) types of carbon structures.

The main structural characteristics, including crystal lattice parameters and densities, and relative thermal stabilities of the various carbon allotropic, polymorphic and polytypic forms, grouped under family headings within the overall hierarchy from submolecular to macrostructural scales, are summarized in Table 2.3.

2.2 Thermal Properties

2H-graphite (or α -graphite) is the most stable thermodynamically form of carbon under standard conditions, so its standard enthalpy of formation (at 298.15 K) $\Delta H_{f,298}^\circ$ is zero, similar to those characteristics for all other chemical elements. The generalized phase and transition diagram of carbon based on several main sources [28, 176–190, 535–538] is given in Fig. 2.1. In the region of moderate pressures, this variant of carbon phase diagram assumes the sequence of transformations with temperature (energy) increase from sp^3 (diamond) through sp^2 (graphite/graphene) to sp^1 (carbyte/carbyne), which is corresponding to the specific bond energy approach established for the carbon structures classification previously (see Sect. 2.1). The general thermodynamic properties of carbon (graphite) are summarized in Table 2.4.

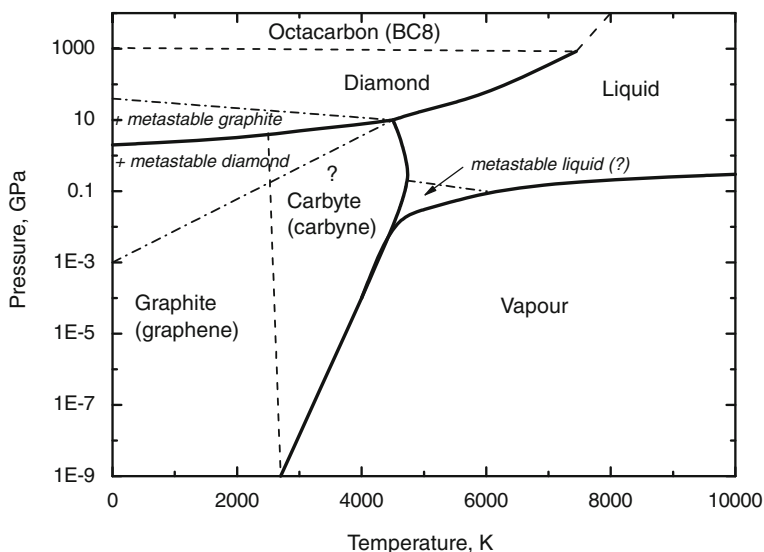


Fig. 2.1 The generalized phase and transformation diagram of carbon according to the several main sources [28, 176–190, 535–538]

Table 2.4 General thermodynamic properties of graphite

Characteristics	Symbol	Unit	Value	References
Standard molar entropy (at 298.15 K and 100 kPa)	S°_{298}	$\text{J mol}^{-1} \text{K}^{-1}$	5.74 5.697–5.743	[4] [42]
Molar enthalpy difference	$H_{298} - H_0$	kJ mol^{-1}	1.054	[540]
Standard molar heat capacity (at 298.15 K and 100 kPa)	$c^\circ_{p,298}$	$\text{J mol}^{-1} \text{K}^{-1}$	8.517 8.544 8.033–8.635	[4] [227] [42]
Specific heat capacity (at 298.15 K)	c	$\text{J kg}^{-1} \text{K}^{-1}$	690–719 651	[42] [138]
Molar enthalpy (heat) of melting	ΔH_m	kJ mol^{-1}	117 (for triple point) 146	[3–4] [138]
Specific enthalpy (heat) of melting		MJ kg^{-1}	12.2 10 (for melt. point)	[138] [180]
Molar enthalpy (heat) of vaporization	ΔH_v	MJ mol^{-1}	0.717 (for 298 K) 0.71	[6] [138]
Specific enthalpy (heat) of vaporization		MJ kg^{-1}	59.1	[138]
Sublimation point (at 0.1013 MPa)	T_{sub}	$\text{K (}^\circ\text{C)}$	4000 (3730) ^a 4100 (3825)	[42] [3]
Melting point (at 10 MPa) ^b	T_m	$\text{K (}^\circ\text{C)}$	4020 (3750) 4200 (3930)	[6, 138] [42]
Melting point (at 12 MPa) ^b			4160 \pm 50 (3890 \pm 50)	[186]
Melting point (at 10–100 MPa) ^b			4800 \pm 100 (4530 \pm 100)	[180]
Melting point (at 300 MPa) ^b			4750 (4480)	[138]
Boiling point	T_b	$\text{K (}^\circ\text{C)}$	4200 (3930) 4560 (4290) ^a	[6] [42]
Triple point (graphite-liquid-vapour) ^b	T_{tr}, p	$\text{K (}^\circ\text{C)}, \text{MPa}$	3800 (3530), 0.02 4000 (3730), 0.1 4200 (3930), 10 4500 (4230), 10 4760 (4490), 10,3	[28] [179] [42] [178] [3]
Triple point (graphite-diamond-liquid) ^b		$\text{K (}^\circ\text{C)}, \text{GPa}$	4100 (3830), 12.5 4250 (3980), 16.4 ^c 4300 (4030), 9.4 ^d 4500 (4230), 10	[6] [190] [188] [178]

(continued)

Table 2.4 (continued)

Characteristics	Symbol	Unit	Value	References
Triple point (diamond—octacarbon (BC8)—liquid) ^c		K (°C), GPa	7400 (7130), 850 ^f	[189]
Critical point ^g		K (°C), GPa	6810 (6540), 0.22	[911]

^a Estimated values (for practical application approximate values are recommended: total pressure of carbon over graphite surface at 3790 K (3520 °C) -0.1 MPa, mass vaporization rate of graphite at 3300 K (3030 °C) -10^{-2} kg m⁻² s⁻¹, linear vaporization rate of graphite at 3100 K (2830 °C) $\sim 10^{-6}$ m s⁻¹ [138])

^b The main divergences in the experimental results available in literature [178–186] are in the values of the true melting temperature and triple point of graphite in the range of 4000 or 5000 K

^c Determined using a semi-empirical long-range carbon bond-order potential partly based on *ab initio* data

^d Calculated within the framework of the statistical model

^e Melting point of carbon (diamond) at 12.4 GPa–4710 K (4440 °C)

^f Predicted from first-principles calculations based on density functional theory

^g Critical density— 0.64 g cm⁻³ [911]

For the molar heat capacity $c_p = f(T, K)$, J mol⁻¹ K⁻¹, the following relationship for the range of temperatures from 298 to 2500 K is recommended [227]:

$$c_p = 17.17 + (4.27 \times 10^{-3})T - (8.79 \times 10^5)T^{-2}. \quad (2.1)$$

The heat capacity of carbon (graphite) materials increases rapidly with temperature up to 1000 °C, where it levels off at approximately 2 kJ kg⁻¹ K⁻¹ with the subsequent increase beginning at 2800–3000 °C (Fig. 2.2). The important remark, which should be made in regard to the thermal behaviour of carbon at ultra-high temperatures, is connected with its vaporization (especially, in vacuum). At moderate pressures carbon (graphite) does not melt but sublimates very intensively with vaporization rate exceeding 0.01 kg m⁻² s⁻¹ when temperature reaches more than 3000 °C. The values of standard molar entropy S°_{298} , molar c_p and specific c heat capacities, enthalpies (heats) of melting and vaporization, molar and specific enthalpy differences $H_T - H_{298}$, vapour pressures and mass/linear vaporization rates are given in Addendum in comparison with other ultra-high temperature elements (refractory metals) in the wide ranges of temperatures.

All vector-defined thermal properties of carbon (graphite) reflect extremely high anisotropy inherent to graphite crystals. The properties can vary considerably depending on geometrical directions in carbon (graphite) structures. The main anisotropy coefficient

$$\zeta = a_{\text{para}}/a_{\text{perp}}, \quad (2.2)$$

where a_{para} , a_{perp} are, respectively, the values of a physical property in parallel and perpendicular directions to the graphene basal plane (or axis of symmetry), for thermal conductivity of quasi-single crystalline graphite material, such as highly oriented pyrolytic graphite, reaches up to 200.

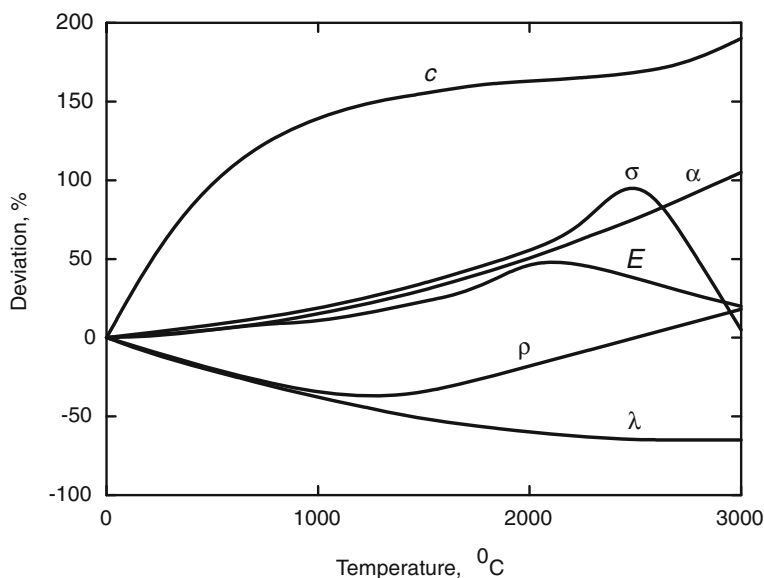


Fig. 2.2 Relative variations of some physical properties of common industrial graphite materials with temperature: c —heat capacity, α —thermal expansion, σ —mechanical strength, E —Young's modulus, ρ —electrical resistivity and λ —thermal conductivity (based on several sources [41–43, 136, 138, 194, 209, 223–224])

Around the hierarchy of graphene/graphite structures from nano- to macro-scales all the materials are characterized by highly anisotropic properties; e.g., carbon nanotubes are very good thermal conductors along the tube, but good insulators laterally to the tube axis (Table 2.5). Some kind of similar particularities are also common for the variety of carbon (graphite) products, including the graphite containing bulk materials, which are very different in structure and composition. The variation of thermal conductivity in the different directions of graphite crystals with temperature is shown in Fig. 2.3.

For bulk carbon (graphite) materials produced in industry, thermal conductivity depends strongly on the various defects of their structures. The values of thermal heat capacity and thermal conductivity of various carbon products: industrial graphitized carbon materials, pyrolitic (pyrographite) and vitreous (glass-like) carbons, thermally expanded (exfoliated) graphite materials and carbon (graphite) filaments in commercial carbon fibres are given in Tables 2.6, 2.7, 2.8, 2.9, 2.10.

Table 2.5 Some physical properties of graphitic nanostructured carbons and quasi-single crystalline graphite at room temperature

Nanostructure	Thermal conductivity, $\text{W m}^{-1} \text{K}^{-1}$	Electrical resistivity, $\Omega \text{ m}$	Young's modulus, TPa	Tensile strength, GPa	References
Graphene	4800–5300	$\sim 1 \times 10^{-8}$	0.67–0.91 ^a	130 ^a	[191, 197–200]
Single-walled nanotubes	3500 (axial direction), 1.5 (radial direction)	$\sim 3 \times 10^{-10}$ (for metal-like nanotubes, axial direction)	~ 1 (axial direction)	13–53 ^b , 94.5–126.2 ^a (axial direction)	[91, 195, 196, 201–204]
Multi-walled nanotubes (in axial direction)	~ 1500	$\sim 1 \times 10^{-9}$	0.27–0.95 ^a	11–150 ^a	[91, 205–206]
Nanoscrolls (whiskers, in axial direction)	~ 1300	–	0.7–0.8	3–20	[91, 208, 221]
Nanofiber (nanowire, in axial direction)	20–1300	$(0.6\text{--}1.4) \times 10^{-6}$	0.01–0.7	up to 4.5 ^b	[91, 130]
Quasi-single crystalline graphite (highly oriented pyrolytic graphite) ^{b,c}	~ 1500 (in basal plane) ~ 7.5 (perpendicular to basal plane)	3.85×10^{-7} (in basal plane) 5.2×10^{-5} (perpendicular to basal plane)	~ 1 (in basal plane)	~ 100 (in basal plane)	[91, 136, 209]

^a Theoretical prediction^b Experimental observation^c Linear coefficient of thermal expansion (20–200 °C): $(-1.1) \times 10^{-6}$ and $(25\text{--}27) \times 10^{-6} \text{ K}^{-1}$ (in basal plane and perpendicular to basal plane, respectively) [138, 209, 214]

The thermal expansion–contraction behaviour of carbon (graphite) is very complicated (Fig. 2.4). To take into account this aspect is a question of vital importance in the materials design for ultra-high temperature applications. The magnitudes of linear thermal expansion coefficients for various industrial carbon (graphite) products are also presented in Tables 2.6–2.10.

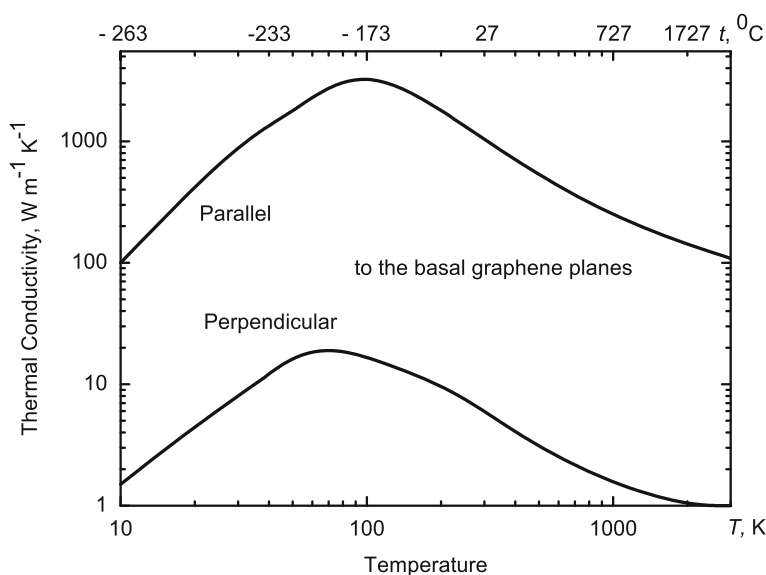


Fig. 2.3 Variation of the thermal conductivity in the different directions of graphite crystals with temperature [41–43, 138, 209]

For averaged highly oriented graphite and quasi-isotropic carbon (graphite), compared with other ultra-high temperature elements (refractory metals), the values of thermal conductivity and thermal expansion in the wide range of temperatures are summarized in Addendum.

2.3 Electro-Magnetic and Optical Properties

Together with thermal properties, electrical resistivity of carbon (graphite) materials and its property-temperature relationship are also extremely anisotropic and sensitive to the order/disorder of carbon atoms in graphitic materials structures. For well-ordered crystals (highly oriented pyrolytic graphite), the variations of specific electrical resistance in the general crystallographic directions and in the wide range of temperatures are presented in Fig. 2.5.

Indeed, the character of these plots differs essentially from the electrical resistivity—temperature relationships observed for the common graphite materials (see Fig. 2.2), which are far from the ideal structure. The values of electrical resistance of graphitic nanostructured carbons, various industrial graphitized carbon materials, pyrolytic (pyrographite) and vitreous (glass-like) carbons, thermally expanded (exfoliated) graphite materials and carbon (graphite) filaments in commercial carbon fibres are given in Tables 2.5–2.10.

Carbon (graphite) is highly diamagnetic with molar magnetic susceptibility χ_{mol} (SI) = $-75.4 \times 10^{-6} \text{ cm}^3 \text{ mol}^{-1}$ in parallel direction to the basal graphene planes

Table 2.6 Physical properties^a of industrial graphitized carbon materials [11, 42, 136, 138, 192–194, 209–211, 215, 222–225, 228, 230, 237, 539]

Trade mark or grade ^b	d , g cm ⁻³	P , %	c , kJ kg ⁻¹ K ⁻¹	λ , W m ⁻¹ K ⁻¹	α , 10 ⁻⁶ K ⁻¹	ρ , $\mu\Omega$ m	E^* , GPa	σ_t , MPa	σ_f , MPa	σ_c , MPa	K_{IC} , MPa m ^{1/2}
<i>Structural and electrode graphite materials (Union Carbide)</i>											
AGSR	1.53–1.58	23–28	–	130–180/–	1–2/–	7–10/–	10/6	10–14/–	15–20/–	22–30/22–30	–
	1.53–1.65	26–32	–	130–200/90–140	0.5–1.5/1.0–2.5	6.5–10/9–14	10/6	3–5/2–5	4–6/3–5	7–13/7–13	–
	1.58–1.64	26–32	–	130–180/90–130	1–2/1.5–3	7–10/10–14	10/6	3–5/2–5	5–8/4–7	9–15/7–15	–
	1.60–1.67	23–28	–	130–180/–	1–2.5/2.5–4	7–10/–	10/6	7–12/4–9	7–14/6–12	16–23/16–23	–
CS	1.60–1.70	23–28	–	130–180/–	1–2/–	7–10/–	10/6	9–13/–	12–18/–	25–33/25–33	–
	1.60–1.75	15–20	–	140–170/	1.5–3/2.7–4.5	7.5–9/9–12	14/8	–	15–20/–	45–55/–	–
				110–140							
	1.70–1.80	14–19	–	150–200/	1.5–3/2.7–4.5	6.5–8.5/	14/8	8–20/5–15	15–30/10–20	35–65/30–40	–
AIL	–	9	–	110–150		8.5–12					
				100/–	3.4/–	14/–	8.5/–	25/–	25/–	70/–	–
ATJ	1.69–1.76	9–13	–	120/100	2.3/3.4	11/14	7.7–8.4/	21/26–27	30/25	63–68/70–79	–
							11.3–11.8 ^a				
RVA	1.84–1.87	–	–	–	–	–	9.0–9.2/	16.5/	–	71.5/70.7	–
							13.1–13.9	21.9–23.3			
RVC	1.84–1.85	–	–	–	–	–	9.2–9.9/	10.3/	–	72.2/75.8	–
							12.1–12.6	16.4–16.5			
RVD	1.88–1.93	–	–	–	–	–	8.0–9.4/	19.6/	–	86.0/88.9	–
							14.6–16.1	27.0–27.9			
CFW	1.89–1.91	–	–	–	–	–	10.3–10.5/	11.9/	–	62.0/60.9	–
							11.0–11.4	13.2–13.4			
CFZ	1.92–1.93	–	–	–	–	–	9.9–10.6/	16.2/	–	80.0/83.8	–
							13.0–14.2	24.2–24.6			
CHQ	1.58–1.61	–	–	–	–	–	6.6/8.6–9.4	–/19.0–19.7	–	68.9/102.4	–
ZTA	1.94–1.96	–	–	–	–	–	4.6–4.9/	11.2/	–	101.3/57.9	–
							17.7–23.0	30.0–30.3			

(continued)

Table 2.6 (continued)

Trade mark or grade ^b	d , g cm ⁻³	P , %	c , kJ kg ⁻¹ K ⁻¹	λ , W m ⁻¹ K ⁻¹	α , 10 ⁻⁶ K ⁻¹	ρ , $\mu\Omega$ m	E^c , GPa	σ_t , MPa	σ_c , MPa	K_{IC} , MPa m ^{1/2}
<i>Carbonix[®] structural graphite materials (Groupe Carbone Lorraine)</i>										
6250	1.67	-	-	-	3.8/2.3 (100-600 °C)	12/7	-	-	27/45	-
2191	1.74-1.75	12	-	116	4.2 (20-1000 °C)	10.7-10.9	-	-	44	97
2020	1.77	9	-	81-85	4.3-4.5 (20-1000 °C)	15.5-18	-	-	33-45	66-99
2910	1.74	17	-	77	4.1 (20-1000 °C)	16	-	-	30	-
2114	1.80-1.81	10	-	104-116	5.0-5.3 (20-1000 °C)	12.4-12.95	-	-	52	114
2120	1.84	7	-	106	6.0 (20-1000 °C)	12.2	-	-	65	-
2123	1.84	8	-	112	5.5 (20-1000 °C)	11.4	-	-	58	-
2124	1.83	8	-	112	5.4-5.7 (20-1000 °C)	11.25	-	-	52	114
2318	1.86	6	-	81	5.7 (20-1000 °C)	16	-	-	76	-
2320	1.82	10	-	122	5.0 (20-1000 °C)	10.6	-	-	50	-
2333	1.86	6	-	81	6.0 (20-1000 °C)	16	-	-	76	167
2340	1.88	13	-	102	7.2 (20-1000 °C)	12.7	-	-	90	-
2450	1.86	8	-	85	4.3 (20-1000 °C)	15.5	-	-	45	-
2715	1.82	10	-	56	5.1-6.5 (20-1000 °C)	23	-	-	55	121
2720	1.80	10	-	60	5.0 (20-1000 °C)	21.6	-	-	53	117

(continued)

Table 2.6 (continued)

Trade mark or grade ^b	d , g cm ⁻³	P , %	c , kJ kg ⁻¹ K ⁻¹	λ , W m ⁻¹ K ⁻¹	α , 10 ⁻⁶ K ⁻¹	ρ , μΩ m	E^s , GPa	σ_t , MPa	σ_f , MPa	σ_c , MPa	K_{IC} , MPa m ^{1/2}
<i>Structural and electrode graphite materials (SGL Carbon Group)</i>											
MKS	1.73	16	—	—	—	10	10	—	18	45	—
MSY	1.78	13	—	190/120	2.5/3.5	7/11	12/7	12/7	24/14	45/40	—
	1.83	11	—	160/100	2/3.5	8/13	15/8	16/9	30/17	55/50	—
HLM	1.70–1.78	17–23	—	105–180	1.4–3.6 (20–200 °C)	9.4–12.4	7.4–10.2	—	15–18	37–44	—
MNC	1.80	14	—	130	1.5 (20–200 °C)	10	16	—	40	55–60	—
MNT	1.75	16	—	130	1.0 (20–200 °C)	10	15	—	20	28–30	—
R4340	1.72	15	—	90	2.9 (20–200 °C)	12	10.5	—	45	90	—
R4500	1.77	13	—	80	3.9 (20–200 °C)	14	10.5	—	50	120	—
R4550	1.83	10	—	100	4.0 (20–200 °C)	13	11.5	—	60	125	—
R4810	1.83	10	—	135	4.1 (20–200 °C)	10.5	10	—	50	105	—
R4820	1.82	10	—	125	4.2 (20–200 °C)	11.5	11	—	45	105	—
R6300	1.73	15	—	65	3.8 (20–200 °C)	17	10	—	40	90	—
R6340	1.72	15	—	90	4.0 (20–200 °C)	12	10.5	—	45	90	—
R6500	1.77	13	—	80	5.0 (20–200 °C)	14	10.5	—	50	120	—
R6510	1.83	10	—	90	5.1 (20–200 °C)	13	11.5	—	60	125	—
R6650	1.84	10	—	90	5.0 (20–200 °C)	14	12.5	—	65	150	—
R6710	1.88	10	—	100	5.8 (20–200 °C)	13	13.5	—	85	170	—
R6810	1.80	11	—	130	5.2 (20–200 °C)	10	10	—	45	100	—
R6830	1.82	9.5	—	130	5.0 (20–200 °C)	10	10	—	50	100	—
R8710	1.88	10	—	100	4.7 (20–200 °C)	13	13.5	—	85	170	—
<i>Structural and electrode graphite materials (Conradty)</i>											
CCF/XN	1.70–1.74	16–18	—	100–120	1.8–2.5	—	—	—	18–20	27–32	—
	1.72–1.76	14–16	—	100–120	1.8–2.5	—	—	—	20–25	30–40	—
	1.75–1.78	15	—	110–130	1.8–2.5	—	—	—	20–25	30–40	—
	1.76–1.80	15	—	120–130	2.2–2.6	—	—	—	40	60	—
B497XN	1.75	13	—	120	2.3	11	11.4	30	30	68	—
B650XN	1.82	14	—	80	4.5	13	—	—	60	105	—

(continued)

Table 2.6 (continued)

Trade mark or grade ^b	d , g cm ⁻³	P , %	c , kJ kg ⁻¹ K ⁻¹	λ , W m ⁻¹ K ⁻¹	α , 10 ⁻⁶ K ⁻¹	ρ , μΩ m	E^* , GPa	σ_t , MPa	σ_f , MPa	σ_c , MPa	K_{IC} , MPa m ^{1/2}
<i>Structural and electrode graphite materials (The Carbon/Graphite Group)</i>											
AI1RL	1.72	-	-	-	3.2 (100-600 °C)	16	-	-	28	-	-
AI4RL	1.82	-	-	-	5.7 (100-600 °C)	18	-	-	42	-	-
AI5RL	1.90	-	-	-	7 (100-600 °C)	20	-	-	77	-	-
<i>Structural and electrode graphite materials (Toshiba Ceramics)</i>											
IP40	1.7	-	-	-	3.8	12	-	-	30	-	-
NP60	1.8	-	-	-	4.5	14	-	-	45	-	-
<i>Structural and electrode graphite materials (Nihon Carbon)</i>											
EGM-63	1.78	-	-	-	4.8	15	-	-	38	-	-
EGM-74	1.82	-	-	-	4.8	14.5	-	-	40	-	-
<i>Structural and electrode graphite materials (Tokai Carbon)</i>											
G345	1.76	-	-	-	3.7	11	-	-	42	-	-
G548	1.85	-	-	-	4.5	12	-	-	70	-	-
<i>Electrode graphite materials (HTU Industrial)</i>											
Electrode RP	1.52-1.58	-	-	-	≤2.9/- (20-100 °C)	≤8.5/-	≤9.3/-	-	7.0-9.8	-	-
Electrode HD	≥1.60	-	-	-	≤2.7/- (20-100 °C)	7.0-7.5/-	≤10.0/-	-	≥10.0	-	-
Electrode HP	≥1.63	-	-	-	≤2.4/- (20-100 °C)	≤6.5/-	≤12.0/-	-	≥10.5	-	-
Electrode SHP	≥1.65	-	-	-	≤1.8/- (20-100 °C)	≤6.0/-	≤14.0/-	-	≥12.0	-	-
Electrode UHP	≥1.68	-	-	-	≤1.5/- (20-100 °C)	≤5.8/-	≤14.0/-	-	≥14.0	-	-
Nipple RP	1.63-1.72	-	-	-	2.7-2.8/- (20-100 °C)	7.5-8.2/-	13.7-14.0/-	-	13.0-15.0	-	-
Nipple HD	≥1.73	-	-	-	≤2.5/- (20-100 °C)	≤6.5/-	≤14.0/-	-	≥15.0	-	-

(continued)

Table 2.6 (continued)

Trade mark or grade ^b	d , g cm ⁻³	P , %	c , kJ kg ⁻¹ K ⁻¹	λ , W m ⁻¹ K ⁻¹	α , 10 ⁻⁶ K ⁻¹	ρ , μ Ω m	E^s , GPa	σ_b , MPa	σ_f , MPa	σ_c , MPa	K_{IC} , MPa m ^{1/2}
Nipple HP	≥1.73	-	-	-	≤2.2/- (20-100 °C)	≤5.5/-	≤16.0/-	-	≥18.0	-	-
Nipple SHP	≥1.74	-	-	-	≤1.6/- (20-100 °C)	≤5.0/-	≤18.0/-	-	≥19.0	-	-
Nipple UHP	≥1.77	-	-	-	1.4 (20-100 °C)	≤4.5/-	≤18.0/-	-	≥20.0	-	-
<i>Structural and electrode graphite materials ("Soyuzglerod"/"Uglerodprom")</i>											
PG-50	0.90-1.05	48-52	1.16 (0-1000 °C)	45/- (20 °C) 33/- (200 °C)	3.8/3.5 (20-100 °C)	37.2/- (20 °C)	1.66	3.4-4.4 /4.6-6.0 (20 °C)	6.5-8.0 /7.0-9.5 (20 °C)	11.0-12.0 /10.8-12.0 (20 °C)	-
			1.45 (0-1500 °C)	30/- (300 °C) 27/- (400 °C)	4.3/4.0 (20-500 °C)	32.2/- (200 °C)		5.6-7.5 /9.0-10.5 (2000 °C)		13.0-15.5 /13.5-15.0 (2000 °C)	
			1.6 (0-2000 °C)	26/- (500 °C) 24/- (600 °C)	5.2/4.8 (20-1000 °C)	30.5/- (300 °C)					
			1.69 (0-2500 °C)	23/- (700 °C) 20/- (1000 °C)	5.7/5.2 (20-1500 °C)	29.2/- (400 °C)		8.0-11.5 /12.0-17.0 (2500 °C)		13.5-20.0 /14.0-19.0 (2500 °C)	
			1.72 (0-2800 °C)	16/- (1200 °C) 12/- (1700 °C)	6.0/5.5 (20-2000 °C)	28.4/- (500 °C)		6.7-9.9 /9.5-10.5 (2800 °C)			
				11/- (2200 °C)	6.3/5.9 (20-2500 °C)	27.8/- (600 °C)					
						27.4/- (700 °C)					
						28.9/- (1200 °C)					
						33.2/- (1700 °C)					
						37.6/- (2200 °C)					
GÈ	1.52	24	-	-	-	7.6 (1000 °C)	-	-	-	24.5	-

(continued)

Table 2.6 (continued)

Trade mark or grade ^b	d , g cm ⁻³	P , %	c , kJ kg ⁻¹ K ⁻¹	λ , W m ⁻¹ K ⁻¹	α , 10 ⁻⁶ K ⁻¹	ρ , $\mu\Omega$ m	E^c , GPa	σ_t , MPa	σ_r , MPa	σ_c , MPa	K_{IC} , MPa m ^{1/2}			
MG	1.49–1.60	28	–	65/75 (20 °C)	4.5/3.3	22.6/19.0 (20 °C)	2.7–5.0	–/5–8 (20 °C)	13 (20 °C)	–/24.0–26.5 (20 °C)	–			
				49/60 (200 °C)	(20–100 °C)	14.5/16.5 (200 °C)		–/8–10 (1000 °C)		–/26 (1000 °C)				
				45/55 (300 °C)	(20–500 °C)	13.6/15.5 (300 °C)								
				42/51 (400 °C)		13.1/14.7 (400 °C)								
				38/48 (500 °C)	5.8/4.6	12.8/14.4 (500 °C)		–/8–11 (1500 °C)		–/29 (1500 °C)				
				36/44 (600 °C)	(20–1000 °C)	12.7/14.4 (700 °C)								
				34/41 (700 °C)	6.3/5.1	14.2/16.1 (1200 °C)				–/38 (2000 °C)				
				27/30 (1200 °C)	(20–1500 °C)	(1200 °C)								
				22/24 (1700 °C)	6.7/5.4	16.0/18.0 (1700 °C)								
				20/21 (2200 °C)	(20–2000 °C)	(1700 °C)								
MG-1	1.60–1.68	25	–		7.2/5.9	17.7/20.0 (2200 °C)								
					(20–2500 °C)	(2200 °C)								
				86/97 (20 °C)	4.5/3.3	14.8/12.3 (20 °C)	–	11.0–12.0 (20 °C)	–	34–47 (20 °C)	–			
				71/84 (200 °C)	(20–100 °C)	12.7/10.5 (200 °C)								
				66/78 (300 °C)	5.3/4.1	12.1/10.1 (300 °C)		11.5–12.5 (500 °C)		40.5 (500 °C)				
				60/73 (400 °C)	(20–500 °C)	11.8/9.8 (400 °C)								
				58/69 (500 °C)	5.8/4.6	11.6/9.7 (500 °C)		12.0–13.5 (1000 °C)		41.5–48.5 (1000 °C)				
				54/64 (600 °C)	(20–1000 °C)	11.4/9.5 (600 °C)								
				51/61 (700 °C)	6.3/5.1	12.3/10.5 (1200 °C)		13.5–15.5 (1500 °C)		50.5–53.0 (1500 °C)				
				42/48 (1200 °C)	(20–1500 °C)	(1200 °C)		15–20 (2000 °C)		51.5–61.5 (2000 °C)				
				36/41 (1700 °C)	6.7/5.4	13.9/12.0 (1700 °C)								
				32/36 (2200 °C)	(20–2000 °C)	(1700 °C)		28 (2500 °C)						
					7.2/5.9	15.6/13.5 (2200 °C)								
(continued)														
					(20–2500 °C)									
					6.7									
					(1000–2500 °C)									

Table 2.6 (continued)

Trade mark or grade ^b	d , g cm ⁻³	P , %	c , kJ kg ⁻¹ K ⁻¹	λ , W m ⁻¹ K ⁻¹	α , 10 ⁻⁶ K ⁻¹	ρ , $\mu\Omega$ m	E^c , GPa	σ_t , MPa	σ_r , MPa	σ_c , MPa	K_{IC} , MPa m ^{1/2}
PROG	1.60–1.70	24	1.63 (0–2500 °C)	120/- (20 °C) 75/47 (200 °C) 67/44 (300 °C) 61/41 (400 °C) 56/37 (500 °C) 51/34 (600 °C) 47/32 (700 °C) 37/23 (1200 °C) 32/21 (1700 °C) 28/20 (2200 °C)	3.5/4.7 (20–100 °C) 4.2/5.3 (20–500 °C) 4.8/5.9 (20–1000 °C) 5.2/6.4 (20–1500 °C) 5.6/6.6 (20–2000 °C) 5.9/6.9 (20–2500 °C)	10.5/- (20 °C) 8.3/13.0 (200 °C) 7.9/12.6 (300 °C) 7.7/12.2 (500 °C) 7.8/12.2 (600 °C) 7.9/12.4 (700 °C) 9.1/13.6 (1200 °C) 10.4/14.8 (1700 °C) 11.7/16.0 (2200 °C)	6.5–8.6 /5.5–6.0 (20 °C)	8.0–10.7 /4.5–7.2 (20 °C) 13.5–18.5 /6.0–13.5 (2000 °C) 17.0–28.5 /12.0–25.0 (2500 °C) 16.0–25.0 /8.0–12.1 (2800 °C)	10–19/10–15 (20 °C)	31–49/28–46 (20 °C) 40–68/35–61 (2000 °C) 62–71/60–69 (2500 °C)	–
EEG	1.55–1.80	–	1.38 (0–1000 °C) 1.92 (0–2500 °C)	–/102 (20 °C) 59/79 (200 °C) 56/73 (300 °C) 52/68 (400 °C) 50/64 (500 °C) 47/60 (600 °C) 44/56 (700 °C) 32/42 (1200 °C) 23/30 (1700 °C) 20/17 (2200 °C)	5.0/4.5 (20–100 °C) 5.6/5.2 (20–500 °C) 6.3/5.8 (20–1000 °C) 7.0/6.3 (20–1500 °C) 7.4/6.8 (20–2000 °C) 7.6/7.2 (20–2500 °C) –/6.5 (500–2500 °C)	–/14.1 (20 °C) 15.1/11.7 (200 °C) 14.2/11.0 (300 °C) 13.6/10.5 (400 °C) 13.2/10.3 (500 °C) 13.0/10.2 (700 °C) 13.5/10.6 (1200 °C) 15.0/12.8 (1700 °C) 16.6/13.3 (2200 °C)	–	–	76–93/64–75 (20 °C) 103.0–129.5 /95.0–103.0 (2000 °C)	–	

(continued)

Table 2.6 (continued)

Trade mark or grade ^b	d , g cm ⁻³	P , %	c , kJ kg ⁻¹ K ⁻¹	λ , W m ⁻¹ K ⁻¹	α , 10 ⁻⁶ K ⁻¹	ρ , $\mu\Omega$ m	E^a , GPa	σ_t , MPa	σ_f , MPa	σ_c , MPa	K_{IC} , MPa m ^{1/2}
GMZ	1.60–1.70	24	1.45	120/103 (20 °C)	3.7/4.1	9.6/11.3	6.4–6.6/4.8	8.8–9.0/	12.6/10.8	34–33/	–
			(0–1000 °C)	92/72 (200 °C)	(20–100 °C)	(20 °C)	(20 °C)	6.8–7.0		33–32	
			1.61	83/64 (300 °C)	4.5/4.8	7.8/9.7	7.6/5.4	(20 °C)			
			(0–2500 °C)	75/58 (400 °C)	(20–500 °C)	(200 °C)	(1000 °C)	10/7.5			
				68/52 (500 °C)	5.1/5.4	7.5/9.2		(1000 °C)			
				62/48 (600 °C)	(20–1000 °C)	(500 °C)		10/22			
				58/44 (700 °C)	5.5/6.1	7.8/9.5		(2000 °C)			
				39/32 (1200 °C)	(20–1500 °C)	(700 °C)		–/23.5			
				33/28 (1700 °C)	33/28 (1700 °C)	9.2/11.0		(2700 °C)			
				31–42/24–32	(20–2000 °C)	(1200 °C)					
Nuclear graphite materials ^b											
RBMK (RU)	1.68	–	–	103/89	3.8/4.2	10/13	6.5/5.0	7.6/6.0	19/14	34/33	0.37/0.33
EGP-6 (RU)	1.69	–	–	80/75	3.7/4.9	5.9/10.4	11.2/5.2	–	11.7/5.5	28/25	–
PPG (RU)	1.76	20	–	120	4.5	8	–	–	21.2	45	–

(continued)

Table 2.6 (continued)

Trade mark or grade ^b	d , g cm ⁻³	P , %	c , kJ kg ⁻¹ K ⁻¹	λ , W m ⁻¹ K ⁻¹	α , 10 ⁻⁶ K ⁻¹	ρ , μ m	E^c , GPa	σ_t , MPa	σ_p , MPa	σ_c , MPa	K_{IC} , MPa m ^{1/2}
VPG (RU)	1.84	-	-	160-192/115 (20 °C) 134/- (200 °C) 114/- (300 °C) 99/- (400 °C) 88/- (500 °C) 80/- (600 °C) 74/- (700 °C) 56/- (1200 °C) 45/- (1700 °C) 41/- (2300 °C)	3.7/4.1 (20-100 °C) 4.5/4.8 (20-500 °C) 5.1/5.4 (20-1000 °C) 5.5/6.1 (20-1500 °C) 5.8/6.3 (20-2000 °C) 6.1/6.7 (20-2500 °C)	7/8/10 (20 °C) 5.4/- (200 °C) 5.15/- (300 °C) 5.10/- (400 °C) 5.15/- (500 °C) 5.20/- (600 °C) 5.30/- (700 °C) 6.20/- (1200 °C) 7.20/- (1700 °C) 8.20/- (2200 °C)	12/9	16/8	35/20	60/58	1.2

(continued)

Table 2.6 (continued)

Trade mark or grade ^b	d , g cm ⁻³	P , %	c , kJ kg ⁻¹ K ⁻¹	λ , W m ⁻¹ K ⁻¹	α , 10 ⁻⁶ K ⁻¹	ρ , $\mu\Omega$ m	E^c , GPa	σ_t , MPa	σ_h , MPa	σ_c , MPa	K_{IC} , MPa m ^{1/2}
VPP (RU)	1.75–2.05	–	–	130/198 (20 °C) 106/143 (200 °C) 96/123 (300 °C) 87/110 (400 °C) 80/100 (500 °C) 72/90 (600 °C) 68/84 (700 °C) –/63 (1000 °C) 50/58 (1200 °C) 45/48 (1700 °C) 43/45 (2200 °C)	4.1/3.9 (20–100 °C) 4.8/4.6 (20–500 °C) 5.4/5.2 (20–1000 °C) 5.9/5.5 (20–1500 °C) 6.2/5.9 (20–2000 °C) 6.65/6.3 (20–2500 °C)	7.8/5.4 (20 °C) 7.0/4.5 (200 °C) 6.7/4.8 (500 °C) 7.8/6.3 (1200 °C) 9.0/7.4 (1700 °C) 10.0/8.3 (2200 °C)	8.6–8.8/9.1 (20 °C) 9.6/10.3 (20 °C) 12.3/12.8 (500 °C) 18/15 (1500 °C) 14.2/16.0 (2000 °C) 14.5/16.3 (2200 °C) 12.9/14.2 (2000 °C) (2500 °C)	14.5–15.0 (20 °C) 8.5–13.5 (20 °C) 14.5/12.0 (500 °C) 18/15 (1000 °C) 20–22/15 (1500 °C) 21–28/18 (2000 °C) 25/22 (2500 °C) 25.5–32.5/– (2800 °C) 22.5/– (3000 °C)	24–25/– (20 °C) 60/48 (500 °C) 63.5–73.5 /50.5 (1000 °C) 61–77/48 (1500 °C) 71.5–93.5 /58.5 (2000 °C)	60–69/41–65 (20 °C) 60/48 (500 °C) 63.5–73.5 /50.5 (1000 °C) 61–77/48 (1500 °C) 71.5–93.5 /58.5 (2000 °C)	–
MIG-1 (RU)	1.73	–	–	120	4.8 (250–500 °C)	11	7.9	16	24	55	–
MIG-2 (RU)	1.67	–	–	90	5.1 (250–500 °C)	13	–	35	70	75	–
ARV (RU)	1.60–1.76	17	–	87	4.5/3.3 (20–100 °C) 5.8/4.6 (20–1000 °C) 6.7/5.4 (20–2000 °C) 7.2/5.9 (20–2500 °C)	11	5.9–7.9	11/12	15–17	44–46	–

(continued)

Table 2.6 (continued)

Trade mark or grade ^b	d , g cm ⁻³	P , %	c , kJ kg ⁻¹ K ⁻¹	λ , W m ⁻¹ K ⁻¹	α , 10 ⁻⁶ K ⁻¹	ρ , μΩ m	E^c , GPa	σ_t , MPa	σ_p , MPa	σ_c , MPa	K_{IC} , MPa m ^{1/2}
ARVu (RU)	1.67–1.80	–	–	51/61	5.3/4.1 (250–500 °C)	16/13	6.8/7.8 (20 °C) 6.9/7.9 (500 °C) 7.5/8.9 (1000 °C) 9.2/10.7 (1500 °C) 10.7/12.1 (2000 °C) 10.6/12.0 (2500 °C) 9.7/11.2 (2200 °C) 8.8/10.7 (2700 °C)	14.5–15 (20 °C) 16 (1000 °C) 16.5 (1500 °C) 20 (2000 °C) 36 (2500 °C) 25.5 (2800 °C)	26–46	62 (20 °C) 60 (1000 °C) 63 (1500 °C) 84.5 (2000 °C)	–
GR-1 (RU)	1.73	–	–	86/90	5.2/5.4 (250–500 °C)	15/14	8–10	15/18	30/25	70/84	0.8
GR-280 (RU)	1.72	–	–	103/89	3.2/4.9 (250–500 °C)	–	6.5/5	7.6/6	–	34/24	–
GR2-125 (RU)	1.85	–	–	–	3.9/5.2 (250–500 °C)	–	12/8.5	15/8	–	59/59	–
AG-1500 (RU)	1.73–1.85	14–15	–	80/90	4.0/4.3 (25–500 °C)	9–12/13	8/10–13	–	41	73–60	–
KPG (RU)	1.80	–	–	140/140	6.8/6.8 (250–500 °C)	9/12/20/13	9.0/11	14	30/27	64	1.2/–
MPG (RU)	1.80	–	–	95/95	7.3/6.6 (250–500 °C)	11.7/10.7	11	32	55	100	1.1

(continued)

Table 2.6 (continued)

Trade mark or grade ^b	d , g cm ⁻³	P , %	c , kJ kg ⁻¹ K ⁻¹	λ , W m ⁻¹ K ⁻¹	α , 10 ⁻⁶ K ⁻¹	ρ , $\mu\Omega$ m	E^* , GPa	σ_n , MPa	σ_T , MPa	σ_c , MPa	K_{IC} , MPa m ^{1/2}
MPG-6 (RU)	1.72-1.85	-	-	95/- (20 °C) 75/- (200 °C) 70/- (300 °C) 66/- (400 °C) 62/- (500 °C) 58/- (600 °C) 55/- (700 °C) 48/- (1000 °C) 43/- (1200 °C) 37/- (1700 °C) 33/- (2200 °C)	6.6/6.0 (20-100 °C) 7.3/6.6 (20-500 °C) 7.9/7.2 (20-1000 °C) 8.5/7.7 (20-1500 °C) 8.8/8.1 (20-2000 °C) 9.15/8.8 (20-2500 °C)	14.2/- (20 °C) 11.2/- (200 °C) 10.4/- (300 °C) 9.9/- (400 °C) 9.7/- (500 °C) 9.5/- (600 °C) 9.4/- (700 °C) 9.5/- (1200 °C) 10.2/- (1700 °C) 11.2/- (2200 °C)	10.3-10.5 /10.3-10.5 (20 °C) 10.7/- (500 °C) 11.3/11.3 (1000 °C) 11.5/- (1500 °C) 10.9/- (2000 °C) 10.7/- (2200 °C) 9.9/- (2500 °C)	31.0-32.0 /33.5 (20 °C) 33.5/36.5 (1000 °C) 43.5/42.0 (2000 °C) 46.5/53.5 (2500 °C) 34.0/41.5 (2800 °C) 25.5/23.0 (3000 °C)	54/52-53 (20 °C)	96-100 /96-100 (20 °C) 109/106 (1000 °C) 119/124 (2000 °C)	-

(continued)

Table 2.6 (continued)

Trade mark or grade ^b	d , g cm ⁻³	P , %	c , kJ kg ⁻¹ K ⁻¹	λ , W m ⁻¹ K ⁻¹	α , 10 ⁻⁶ K ⁻¹	ρ , μ m	E^c , GPa	σ_t , MPa	σ_p , MPa	σ_c , MPa	K_{IC} , MPa m ^{1/2}
MPG-8 (RU)	1.75–1.85	–	–	87/122 (20 °C) 70/90 (200 °C) 64/83 (300 °C) 60/76 (400 °C) 55/70 (500 °C) 51/65 (600 °C) 47/61 (700 °C) 35/48 (1000 °C) 33/44 (1200 °C) 27/35 (1700 °C) 25/31 (2200 °C)	6.9/5.9 (20–100 °C) 7.6/6.6 (20–500 °C) 8.3/7.25 (20–1000 °C) 8.7/7.8 (20–1500 °C) 9.05/8.0 (20–2000 °C) 9.30/8.35 (20–2500 °C)	10.8/8.7 (100 °C) 9.8/8.2 (200 °C) 9.3/7.7 (300 °C) 9.1/7.5 (400 °C) 9.0/7.3 (500 °C) 9.1/7.4 (700 °C) 10.5/8.8 (1200 °C) 12.1/10.3 (1700 °C) 13.7/11.8 (2200 °C)	9.8/11.5 (20 °C) 10.2/11.9 (500 °C) 10.6/13.3 (1000 °C) 11.5/15.4 (1500 °C) 12.0/14.9 (2000 °C) 11.3/14.2 (2200 °C) 9.6/12.7 (2500 °C)	28.0/27.5 (20 °C) 28.5/31.5 (1000 °C) 32.5/36.0 (1500 °C) 37.5/41.5 (2000 °C) 45.0/60.5 (2500 °C) 48.0/48.5 (2800 °C) 30.0/26.5 (3000 °C) 18.5/24.0 (3200 °C)	35–60 (20 °C)	88.5/96.0 (20 °C) 92.0/98.5 (1000 °C) 88.5/93.5 (1500 °C) 97.0/102.5 (2000 °C)	–
SPP (RU)	1.56	–	–	80	5.8 (250–500 °C)	13.5	8.3	–	17	49	0.8
ER (RU)	1.60	–	–	50/170	5.9/1.2 (250–500 °C)	25/5.5	7.5/17.5	–	20/8	28/25	0.1/–
GSP-50 (RU)	1.72	–	–	86	5.8 (250–500 °C)	21	17	33	70	205	–
GSP-90 (RU)	1.79	–	–	90	5.5 (250–500 °C)	32	21	–	95	352	–
ChKG-3 (RU)	1.79–1.82	15–17	–	105–116	4.2–4.5 (250–500 °C)	10.3–12.0	8.9–10.0	–	21–30	53–62	–
ChKG-4 (RU)	1.82–1.83	15	–	118–137	4.1–4.3 (250–500 °C)	9.4–11.5	11.3	–	20–26	59–71	–

(continued)

Table 2.6 (continued)

Trade mark or grade ^b	d , g cm ⁻³	P , %	c , kJ kg ⁻¹ K ⁻¹	λ , W m ⁻¹ K ⁻¹	α , 10 ⁻⁶ K ⁻¹	ρ , μΩ m	E^c , GPa	σ_t , MPa	σ_p , MPa	σ_c , MPa	K_G , MPa m ^{1/2}
GRCh (RU)	1.77-1.89	9-19	-	113-217	3.6-5.0 (250-500 °C)	6-10	7.7-12.9	-	14.9-32.6	33-83	-
GRCh-G (RU)	1.82-1.89	13-16	-	133-165	4.1-4.5 (250-500 °C)	8.0	11.0	-	17.0-23.7	52-65	-
AGOT (US)	1.7	-	-	227/138	2.2/3.8 (250-500 °C)	-	10/8	10/9	16/13	41/41	-
TSCBF (US)	1.65	-	-	-	2.7/3.9 (250-500 °C)	14/20	16/8.6	-	-	-	-
TSX (US)	1.71	-	-	-	1.1/4.1 (250-500 °C)	6.0/12.6	11.4-14/ 3.8-6.3	-	25/7	38/37	-
CSF (US)	1.68	-	-	255/132	1.8/3.8 (250-500 °C)	4.5/7.7	11/5	-	17/14	52/46	-
H-327 (US)	1.78	-	-	150/140	1.3/3.1 (250-500 °C)	5.6/11	-4.5	13/8	21/15	32/28	0.64/-
H-451 (US)	1.76	-	-	135-150/ 125-135	3.6/4.6 (250-500 °C)	-	11-9/9.6-8	16-15/14-13	20-16/28-24	60-56/60-54	1.45/-
IG-11 (JP)	1.77	-	-	-	4.6 (250-500 °C)	11	-	-	40	-	-
IG-110 (JP)	1.75-1.78	-	-	124/128-138	(250-500 °C) 4.0-4.2/3.6-4.2 (250-500 °C)	11.5-10/-	9.4-10/10	25	39-34	80-71	0.78/-
ISO-88 (JP)	1.90	-	-	-	6.5 (250-500 °C)	15	-	-	95	-	-
PGA (UK)	1.68-1.74	-	-	140-200/109	1.3/3.3 (250-500 °C)	6	12/5.6	17-10/11-6	19-15/12-11	34-27/35-27	-
SM2-24 (UK)	1.7	-	-	-	-	-	8/8.5	12	19	47	-
IMI-24 (UK)	1.81	-	-	131	4.3 (250-500 °C)	-	11	27.5	23	70	-
Pitch-coke (UK/FR)	1.8	-	-	130/135	4.0/3.8 (250-500 °C)	-	13/10	25/17	32/26	70/63	-

(continued)

Table 2.6 (continued)

Trade mark or grade ^b	d , g cm ⁻³	P , %	c , kJ kg ⁻¹ K ⁻¹	λ , W m ⁻¹ K ⁻¹	α , 10 ⁻⁶ K ⁻¹	ρ , μΩ m	E^c , GPa	σ_t , MPa	σ_p , MPa	σ_c , MPa	K_{IC} , MPa m ^{1/2}
PPEA (<i>FR</i>)	1.85	-	-	140/130	5.0/5.3 (250–500 °C)	9/10	12/11	22/19	34/28	82/-	-
SLWXX (<i>FR</i>)	1.83	-	-	165/146	4.6/5.1 (250–500 °C)	7/9	11/10	20/16	24/21	64	1.3/-
DM332PU (<i>FR</i>)	1.81	-	-	117	4.6 (250–500 °C)	11	12	34	43	91	1.0
P3AN (<i>FR</i>)	1.68	-	-	-	2.5/3.9 (250–500 °C)	-	11/7.5	14/9.2	-	42/38	-
P3JHA2N (<i>FR</i>)	1.78	-	-	126	2.9/4.1 (250–500 °C)	10/16	11	16	-	-	-
ASR-1RS (<i>GE</i>)	1.78	-	-	125	4.7/4.9 (250–500 °C)	-	9.9/9.2	15/14	26/23	67/63	-
ATR-2E (<i>GE</i>)	1.8	-	-	179/163	4.4/4.9 (250–500 °C)	-	9.6/8.4	12.5	23/9	57/57	-

^a Physical properties; d —bulk density, P —porosity, c —specific heat capacity (averaged for the range of temperatures), λ —thermal conductivity, α —coefficient of thermal expansion, ρ —specific electrical resistivity, E —Young’s modulus, σ_t —Tensile, σ_p —flexural (bending) and σ_c —compressive strengths, K_{IC} —Fracture toughness (critical stress intensity factor); anisotropic properties a_i/a_j are given in parallel and perpendicular directions to the transversely isotropic symmetry axis of materials, respectively, so for quasi-isotropic materials average values $a_m = (a_i + 2a_j)/3$; values of properties given for the various temperatures or ranges of temperatures (different from the room temperature) are accompanied with special notations in brackets

^b Country of origin for trade marks or grades is given in brackets: *RU*—Russia, *US*—United States of America, *JP*—Japan, *UK*—United Kingdom, *FR*—France, *GE*—Germany

^c Indicated values of ranges include the results of measurements made by different methods

^d For tension loading: in parallel direction to the transversely isotropic symmetry axis initial static modulus and sonic modulus are 8.1 and 7.7 GPa, respectively, and in perpendicular directions to the axis initial static modulus and sonic modulus are 11.3–11.5 and 11.3–11.4 GPa, respectively (Poisson’s ratio values: $\nu_{12} = 0.10$, $\nu_{13} = 0.11$ and $\nu_{23} = 0.16$); for compression loading: in parallel and perpendicular directions to the transversely isotropic symmetry axis initial static moduli are 8.4 and 11.8 GPa, respectively

Table 2.7 General physical properties of pyrolytic carbon (graphite) materials^a

Property	Unit	T, °C	Direction to deposition plane		References
			perpendicular	parallel	
Density	g cm ⁻³	20	1.4–2.24		[138, 194, 208–209]
Specific heat capacity	kJ kg ⁻¹ K ⁻¹	20	0.962–1.00		[138, 194]
		250	1.25		
		500	1.55		
		750	1.8		
		1000	2.0		
		1500	2.05		
		2000	2.08		
Thermal conductivity	W m ⁻¹ K ⁻¹	20	1–6.5	190–1100	[42, 136, 138, 194, 209, 539]
		200	1.5–5.4	290–500	
		700	1.2–4.6	150–310	
		1200	0.96–3.9	120–210	
		1700	0.7–3.8	97–170	
		2200	0.5–2.0	70–140	
			15–25		
Coefficient of linear thermal expansion ^b	10 ⁻⁶ K ⁻¹	20–100	15–25	(–1.3)–(+1.0)	[42, 136, 138, 194, 209, 539]
		20–500	20–24	(–0.4)–(+2.1)	
		20–800	–	0.5–2.6	
		20–1000	22–25.5	0.7–1.1	
		20–1500	22–26.5	1.2–1.6	
		20–2000	24–26.5	1.2–1.9	
		20–2500	24–27	2	
Electrical resistivity	μΩ m	20	(0.25–10) × 10 ³	0.5–10	[42, 136, 138, 194, 208–209, 539]
		500	3.4 × 10 ³	2.6	
		700	(2.8–3.5) × 10 ³	2.5–2.7	
		1700	1.25 × 10 ³	3.5	
		2200	0.7 × 10 ³	4.0	
Young's modulus	GPa	20	3–11	7.5–41	[42, 138, 194, 207–208]
		600	–	10.3–28	
		1650	–	23.3–24.0	
		2200	–	18.5–20.6	
		2700	–	9.6–17.8	
Coulomb's (shear) modulus	GPa	20	–	14.5–15.5	[209]

(continued)

Table 2.7 (continued)

Property	Unit	T, °C	Direction to deposition plane		References
			perpendicular	parallel	
Tensile strength	MPa	20	4.8	21–170	[42, 138, 194, 207–209]
		1650	–	116–125	
		2200	–	152–188	
		2500	–	180–240	
		2800	–	316–415	
Flexural (bending) strength	MPa	20	80–250	10–20	[42, 136, 138, 194, 207–209]
		1000	180–206	–	
		2200	100–213	–	
Compressive strength		20	56–100	282–480	[208–209]
Hardness, Mohs HM		20	4.5	1.0	[194]

^a For isotropic pyrolytic carbon: density—2.1 g cm^{−3}, Young's modulus—28 GPa and flexural (bending) strength—350 MPa (at 25 °C) [42, 136]; for isotropic “pyroceramic” carbon: density—1.8–2.1 g cm^{−3}, specific electrical resistivity—12–18 μΩ m, Young's modulus—16–21 GPa, tensile strength—87–123 MPa, flexural (bending) strength—45–250 MPa, compressive strength—380–550 MPa (at 20 °C), coefficient of thermal expansion (20–500 °C)—(2.6–6.0) × 10^{−6} K^{−1}, thermal conductivity (1000–2000 °C)—14–17 W m^{−1} K^{−1} [207, 209]

^b Coefficient of volumetric thermal expansion, 10^{−6} K^{−1}—19–25 (20–100 °C), 21–26.5 (20–500 °C), 24–27 (20–1000 °C), 26–27.5 (20–1500 °C) and 28–29 (20–2000 °C) [539]

at room temperature [3, 539–540], the χ_{mol} versus temperature relationships for both main directions in the graphite crystals are shown in Fig. 2.6.

The general optical properties of carbon (graphite) for wavelength $\lambda = 0.620$ μm are following: index of refraction (single crystal)—2.6, index of absorptance (single crystal)—1.4, reflective index under normal incidence—0.24 (polished graphite) and 0.35 (cleaned single crystal surface) [6]. In visible-light spectrum the monochromatic emittance (spectral emissivity) ε_λ of graphite is near to that of a grey body and varies for $\lambda = 0.65$ μm from 0.77 (well-polished surfaces) to 0.95 (roughened surfaces). The integral emittance ε_T of graphite ranges from 0.6 to 0.9. The temperature variations for the both coefficients of emittance are linear:

$$\varepsilon = \varepsilon_0 \pm aT, \quad (2.3)$$

with the positive values of a for integral emittance ε_T and negative value—for spectral emittance ε_λ ($\lambda = 0.665$) [138]. The recommended values of electrical resistivity, magnetic susceptibility, integral and spectral emittances and thermoionic emission characteristics for carbon (graphite) materials are given in comparison with other ultra-high temperature elements (refractory metals) in Addendum.

2.4 Physico-Mechanical Properties

Hardness of carbon (graphite) materials ranges widely depending on their macro- and microstructures and bulk densities. To compare this property for the various graphitic products or with other ultra-high temperature materials is often

Table 2.8 General physical properties^a of common vitreous (glass-like) carbon materials [11, 42, 136, 207, 209, 539]

Trade mark or grade ^b	d_t g cm ⁻³	P_{ox} %	T_g °C	T_{gs} °C	Π_t cm ² s ⁻¹	λ_t W m ⁻¹ K ⁻¹	α_t 10 ⁻⁶ K ⁻¹	ρ_t μΩ m	E_t GPa	σ_{rt} MPa	σ_{cs} MPa	H
S-100 (<i>JP</i>)	1.45	–	1200	–	–	3.3–3.8	3.5 (20–200 °C)	45	20	98	–	120 ^c
GC-10 (<i>JP</i>)	1.47–1.51	0.2–0.4	1300	–	10 ⁻¹² –10 ⁻¹¹	3.5–4.7	2.2–3.2 (20–200 °C)	45–65	27–32	88–100	–	100–120 ^c
GC-20 (<i>JP</i>)	1.46–1.50	1–3	2000	–	10 ⁻¹² –10 ⁻¹¹	8.1–9.3	2.0–2.2 (20–1500 °C)	40–45	25–32	70–118	–	100–110 ^c
GC-30 (<i>JP</i>)	1.43–1.47	3–5	3000	–	10 ⁻⁹ –10 ⁻⁷	15.0–17.6	2.0–2.2 (20–1500 °C)	30–40	15–25	40–59	–	70–80 ^c
SU-1200 (<i>RU</i>)	1.45–1.55	0.2–1.3	1200	1000	–	–	3.5–4.0 (20–1500 °C)	45–50	28–31	70–100	–	–
SU-1300 (<i>RU</i>)	1.49–1.52	0.2–1.0	1300	1300	10 ⁻¹² –10 ⁻¹¹	3.7–4.1	4.4–5.1 (20–1500 °C)	45–50	25–30	107–127	–	30–33 ^d
SU-2000 (<i>RU</i>)	1.38–1.54	0.7–2.0	2000	2000	10 ⁻¹¹ –10 ⁻¹⁰	5.1–6.1 (20 °C)	2.3–2.4 (20–100 °C)	40–44 (20 °C)	27–30	130–160	–	20–23 ^d
						8.3 (500 °C)	2.7–2.9 (20–500 °C)	38 (300 °C)				
						9.0 (700 °C)	3.5–4.05 (20–1500 °C)	35 (500 °C)				
						10 (1200 °C)	(20–1500 °C)	27 (1200 °C)				
						11.5 (2200 °C)	5.0 (20–2500 °C)	20 (2200 °C)				
SU-2500 (<i>RU</i>)	1.44–1.50	1.5–2.5	2500	2500	10 ⁻¹⁰ –10 ⁻⁹	6.4–7.8 (20 °C)	2.3–2.4 (20–100 °C)	38–44 (20 °C)	25–30	70–100 (20 °C)	260 (20 °C)	18–20 ^d
						8.3 (500 °C)	2.7–2.9 (20–500 °C)	38 (300 °C)				
						9.0 (700 °C)	3.5–4.05 (20–1500 °C)	35 (500 °C)				
						10 (1200 °C)	(20–1500 °C)	27 (1200 °C)				
						11.5 (2200 °C)	5.0 (20–2500 °C)	20 (2200 °C)				

(continued)

Table 2.8 (continued)

Trade mark or grade ^b	d , g cm ⁻³	P_o , %	T_o , °C	T_s , °C	Π , cm ² s ⁻¹	λ , W m ⁻¹ K ⁻¹	α , 10 ⁻⁶ K ⁻¹	ρ , μΩ m	E , GPa	σ_f , MPa	σ_c , MPa	H
SU-3000 (RU)	1.06–1.27	1.8–2.2	3000	–	–	7.5	3.5–4.0 (20–1500 °C)	40–45	15–17	70–100	–	–
V10 (FR)	1.50–1.55	~0	–	–	–	–	3.2 (20–1500 °C)	55	28.5	100	–	–
V25 (FR)	1.50–1.55	~0	–	–	–	–	3.2 (20–1500 °C)	45	22	60–80	–	–
Sigradur (GE)	1.42	~0	2200	3000	10 ⁻⁹	6.3	2.6 (20–200 °C)	–	35	260	480	230 ^e
	1.54	~0	1100	1100	10 ⁻¹¹	4.6 (20 °C)	3.5 (20–200 °C)	45 (20 °C)	35	210	580	340 ^e
						11 (1000 °C)	4 (20–1000 °C)	30 (1000 °C)				

^a Physical properties: d —bulk density, P_o —open porosity, T_o —open porosity, T_s —final temperature of heat treatment, T_s —maximal service temperature, Π —gas permeability, λ —thermal conductivity, α —coefficient of thermal expansion, ρ —specific electrical resistivity, E —Young's modulus, σ_f —flexural (bending) and σ_c —compressive strengths, H —hardness; values of properties given for the various temperatures or ranges of temperatures (different from the room temperature) are accompanied with special notations in brackets

^b For trade marks or grades country of origin is given in brackets: JP—Japan, RU—Russia, FR—France, GE—Germany

^c Shore hardness

^d Microhardness, MPa

^e Vickers hardness HV₁

Table 2.9 General physical properties^a of common thermally expanded (exfoliated) graphite materials [212–213, 216]

Trade mark or grade ^b	d , g cm ⁻³	c , kJ kg ⁻¹ K ⁻¹	Π , cm ² s ⁻¹	λ , W m ⁻¹ K ⁻¹	α , 10 ⁻⁶ K ⁻¹	ρ , μΩ m	σ_t , MPa	β , 10 ⁻³ MPa ⁻¹	β' , %
Sigraflex Foil ^c (GE)	0.7–1.3	0.7	<5 × 10 ⁻⁵	4.8/155	~30/~1 (20–1000 °C)	≥650/~9	-/≥ 4 ^d	-	-
Grafoil (US)	1.1	-	-	5/140	-	-	-4.4–6.9	11/-	20/-
Grafleke (RU)	0.6–1.1	-	-	3–5/130–200	-	-	-3.5–7.0	10–11/-	10–20/-
Termografit (UA)	0.6–1.5	-	-	-/130–200	-	-	-5.0–6.0 ^e	6–13 ^f /-	12–30 ^f /-

^a Physical properties: d —bulk density, c —specific heat capacity, Π —gas permeability, λ —thermal conductivity, α —coefficient of thermal expansion, ρ —specific electrical resistivity, σ_t —tensile strength, β —compressibility (for loading pressure $P = 35$ MPa), β' —recoverability (for loading pressure $P = 35$ MPa); anisotropic properties a_i/a_j are given in parallel and perpendicular directions to the transversely isotropic symmetry axis of materials, respectively; values of properties given for the various temperatures or ranges of temperatures (different from the room temperature) are accompanied with special notations in brackets

^b For trade marks or grades country of origin is given in brackets: GE—Germany, US—United States of America, RU—Russia, UA—Ukraine

^c Physical properties are given for materials with bulk density $d = 1.0$ g cm⁻³ and ash content ≤0.15 %

^d Elongation at break ≥1 %

^e For materials with bulk density $d = 1.0$ g cm⁻³

^f For materials with bulk density $d = 1.2$ –1.5 g cm⁻³

Table 2.10 General physical properties^a of carbon (graphite) filaments in commercial carbon fibres [84, 136, 207, 217–221]

Trade mark and grade ^b	<i>D_f</i> , μm	<i>d_f</i> , g cm ^{−3}	<i>E_f</i> , GPa	<i>σ_t</i> , GPa	δ, %	<i>λ_f</i> , W m ^{−1} K ^{−1}	α, 10 ^{−6} K ^{−1}	ρ, μΩ m
<i>High-modulus (low strain to failure) PAN-based carbon fibres</i>								
BASF GY70 (GE)	8.0	1.96	520	1.9	0.3	175	–	6.5
Celion GY70 (US)	–	–	430–520	1.80–1.86	0.4	–	–	–
Kulon (RU)	–	1.90	400–600	2.0	0.4	–	–	–
Bestight HM45 (JP)	6.4	1.90	441	3.10	0.48	–	–	–
Modnor I (UK)	7.5–7.8	2.00	380–450	1.77–2.26	0.5	–	–	–
Torayca M50 (JP)	7.0	1.90–1.91	500	2.35–2.5	0.5	100	–0.7	9.5
Torayca M40A (JP)	6.0–7.0	1.78–1.84	340–450	2.0–2.5	0.5–0.6	–	–1.2	8–10
Grafil HMS (UK)	7.6	1.88	320–400	2.0–2.1	0.5–0.7	–	–	–
Hexcel HM-S (MagnaMite, US)	–	–	345	2.21	0.6	–	–	–
Bestight UM40 (JP)	6.6	1.83	392	2.55	0.65	–	–	–
Tenax HMA (GE)	6.75	1.77	358	3.00	0.7	–	–	–
Grafil HM (UK)	–	–	370	2.75	0.7	–	–	–
Torayca M40 ^c (JP)	6.5–7.0	1.81	392–400	2.40–2.74	0.6–0.75	45	–0.75	11
Torayca M60 ^c (JP)	4.7	1.94	585–588	3.80–3.82	0.7	–	–	–
Acif HM (UK)	6.6	1.86	335	2.20	0.75	–	–	–
Hexcel HMS4 (US)	8.0	1.80	360	2.3	0.8	–	–	–
Hexcel UHM (US)	–	1.87	441	3.45	0.8	–	–	–
Bestight HM35 (JP)	6.7	1.79	343	2.74	0.8	–	–	–
Torayca M50 ^c (JP)	5.0	1.88	475	4.12	0.8	–	–	–
Torayca M55 ^c (JP)	5.0	1.91	540	4.02	0.8	–	–	–
Torayca M46 ^c (JP)	5.0	1.84	436–450	4.20–4.21	1.0	–	–	–
Pyrofil HS40 (JP)	5.0	1.85	450	4.41	1.0	–	–	–
Pyrofil HR40 (JP)	6.0	1.82	390	4.41	1.1	–	–	–
Tenax UMS 2526 (GE)	4.8	1.78	395	4.56	1.1	–	–	–
Tenax UMS 3536 (GE)	4.7	1.81	435	4.50	1.1	–	–	–
Torayca M40 ^c (JP)	5.0	1.77	377–390	4.30–4.41	1.2	–	–	–
Pyrofil MS40 (JP)	6.0	1.77	345	4.61	1.3	–	–	–
Torayca M35J ^c (JP)	6.0	1.75	343	4.70	1.4	–	–	–
	4.7–7.8	1.75–2.00	320–600	1.45–4.7	0.4–1.4	–	–	–

(continued)

Table 2.10 (continued)

Trade mark and grade ^b	<i>D</i> , μm	<i>d</i> , g cm ⁻³	<i>E</i> , GPa	<i>σ_t</i> , GPa	<i>δ</i> , %	<i>λ</i> , W m ⁻¹ K ⁻¹	<i>α</i> , 10 ⁻⁶ K ⁻¹	<i>ρ</i> , μΩ m
<i>Intermediate-modulus (intermediate strain to failure) PAN-based carbon fibres</i>								
Avcarb HCB (US)	—	—	260	1.90	0.7	—	—	—
Elur (RU)	—	—	150	2.00	—	—	—	—
LU-2 (RU)	—	—	230	2.0–2.5	—	—	—	—
LU-3 (RU)	—	—	250	2.5–3.0	—	—	—	—
LU-4 (RU)	—	1.70	230	3.0–3.5	—	—	—	—
UKN-5000 (RU)	7.0–8.0	1.75	180–230	3.0–3.5	0.9	—	—	—
Grafil A (UK)	—	1.76	192	2.55	—	—	—	—
Grafil HTS (UK)	8.0	1.77	240	2.5–2.9	—	—	—	—
Avcarb HC (US)	—	—	207	2.07	—	—	—	—
SGL Technic C10 (UK)	—	—	180–240	≥2.00	—	—	—	—
SGL Technic C25 (UK)	—	—	215–240	≥2.50	1.05–1.40	—	—	—
Indecarf 25 (IN)	—	—	215–240	≥2.50	1.05–1.40	—	—	—
Torayca T300 (JP)	7.0	1.76	230–250	3.0–3.5	1.2–1.5	10	–0.6	18
Indecarf 30 (IN)	6.8	1.78	220–240	≥3.00	1.25–1.60	—	—	—
SGL Technic C30 (UK)	7.0	1.78	220–240	≥3.00	1.25–1.60	—	—	—
Apollo IM 43-600 (UK)	—	—	300	4.00	1.3	—	—	—
Acif IS (UK)	6.8	1.78	230	2.50	1.3	—	—	—
Koseca GP250 (KR)	6.8	1.80	220	2.80	1.3	—	—	—
Thornel T300 (US)	6.4–7.0	1.76	230–235	3.1–3.75	1.3–1.4	—	—	—
Acif HT (UK)	6.8	1.78	230	2.90	1.4	—	—	—
Koseca HS300 (KR)	6.8	1.80	230	3.30	1.4	—	—	—
Tenax IMS 3131 (GE)	6.4	1.76	295	4.12	1.4	—	—	—
Celion 1000 (US)	7.0–8.0	—	234	3.24	1.4	—	–0.7	15–16
Granit 40 (RU)	~7	1.76	~230	≤3.65	1.4	—	—	—
Hexcel IM6 (US)	5.0–5.2	1.76	276–280	4.4–5.6	1.4–2.0	—	—	—
Pyrofil MR35E (JP)	7.0	1.75	295	4.41	1.5	—	—	—
Pyrofil MR40 (JP)	6.0	1.76	295	4.41	1.5	—	—	—
Tenax HTA (GE)	7.0	1.77	238	3.95	1.5	—	—	—
Tenax HTS (GE)	7.0	1.77	238	4.30	1.5	—	—	—
Tenax STS (GE)	7.0	1.79	240	4.00	1.5	—	—	—

(continued)

Table 2.10 (continued)

Trade mark and grade ^b	<i>D</i> , μm	<i>d</i> , g cm ⁻³	<i>E</i> , GPa	<i>σ_b</i> , GPa	δ, %	λ, W m ⁻¹ K ⁻¹	α, 10 ⁻⁶ K ⁻¹	ρ, μΩ m
Besfight IM400 (JP)	6.4	1.75	295	4.31	1.5	—	—	—
Besfight HM30 (JP)	6.4	1.75	295	4.30	1.5	—	—	—
Acif XHT (UK)	6.8	1.78	230	3.30	1.55	—	—	—
Fortafil 506...509 (US)	7.0	1.80	217	3.45	1.59	—	—	—
Besfight HTA (JP)	7.0	1.77	235	3.92	1.6	—	—	—
Besfight STA (JP)	—	—	240	3.73	1.6	—	—	—
Panex 33 (US)	7.2	1.81	228	3.80	1.6	—	—	—
Fortafil 502...505, 510...513 (US)	6.0	1.80	231	3.80	1.64	—	—	—
Fortafil 555...556 (US)	6.2	1.80	231	3.80	1.65	—	—	—
	5.2–8.0	1.71–1.81	150–300	1.45–5.6	0.7–1.65	—	—	—
<i>High strain to failure PAN-based carbon fibres</i>								
Besfight ST1 (JP)	—	—	240	3.6	1.5	—	—	—
Hexcel AS4 (US)	7.0–8.0	1.78–1.81	227–235 ^f	3.6–4.3	1.5–1.9	7.2–16.0 ^e	—(1.2–1.7) ^b	15.3
BASF G40 (GE)	7.0	1.77	300	5.0	1.6	—	—	13
Besfight ST2 (JP)	—	—	240	4.08	1.7	—	—	—
Besfight IM500 (JP)	5.0	1.76	300	5.0	1.7	—	—	—
Thornel T650/35 (US)	6.8	1.77	255	4.28	1.7	—	—	—
Hexcel AS6 (US)	—	—	241	4.14	1.7	—	—	—
Torayca T400 (JP)	5.6–6.8	—	250–310	4.5–5.1	1.7–1.8	—	—	—
Hexcel IM4 (US)	6.7	1.78	276	4.80	1.74	—	—	—
Hexcel IM6 (US)	—	—	280	5.0	1.8	—	—	—
Besfight ST3 (JP)	—	—	240	4.32	1.8	—	—	—
Celcon ST (US)	—	—	235	4.34	1.8	—	—	—
Torayca T300J ^c (JP)	7.0	1.78	230	4.21	1.8	—	—	—
Torayca T400H ^c (JP)	7.0	1.80	250	4.41	1.8	—	—	—
Grafil 34-600...34-600WD (UK)	7.0	1.80	234	4.15	1.8	—	—	—
Pyrofil MR50 (JP)	6.0	1.80	290	5.40	1.8	—	—	—
Hexcel IM8 (US)	5.1	1.79–1.80	303–304	5.45–5.59	1.84	—	—	—
Hi-Carbonol (JP)	7.0	1.78	230	4.31	1.87	—	—	—
Hexcel IM7 (5000 Spec, US)	5.2	1.78–1.80	276–292	5.18–5.76	1.87–2.01	—	—	—
Hexcel AS4C (US)	6.9	1.78	231	4.35	1.88	—	—	—

(continued)

Table 2.10 (continued)

Trade mark and grade ^b	<i>D</i> , μm	<i>d</i> , g cm ⁻³	<i>E</i> , GPa	<i>σ_b</i> , GPa	δ, %	<i>λ</i> , W m ⁻¹ K ⁻¹	<i>α</i> , 10 ⁻⁶ K ⁻¹	<i>ρ</i> , μΩ m
Grafil 34-700 (UK)	7.0	1.80	234	4.50	1.9	—	—	—
Torayca M30S ^c (JP)	6.5	1.73	294	5.49	1.9	—	—	—
Torayca T600S ^c (JP)	—	1.79	230	4.31	1.9	—	—	—
Torayca T800 (JP)	5.1–7.0	1.81	250–300	5.0–5.7	1.9–2.0	15	–0.75	14
Torayca T800H ^c (JP)	5.0	1.81	290–294	5.49–5.60	1.9	—	—	—
Apollo HS 38-750 (UK)	—	—	260	5.00	1.9	—	—	—
Tenax IMS 5131 (GE)	5.0	1.80	290	5.60	1.9	—	—	—
Besfight ST3 (JP)	7.0	1.77	235	4.41	1.9	—	—	—
Pyrofil TR30S (JP)	7.0	1.79	235	4.41	1.9	—	—	—
Pyrofil TRH50 (JP)	7.0	1.80	255	4.90	1.9	—	—	—
Hexcel IMC (US)	5.4	1.80	290	5.52	1.90	—	—	—
Hexcel PV36/700 (US)	—	—	248	4.69	1.90	—	—	—
Hexcel PV42/800 (US)	5.4	1.80	290	5.52	1.90	—	—	—
Hexcel IMC (US)	—	1.80	290	5.52	1.90	—	—	—
Hexcel IM7C (US)	5.4	1.80	290	5.52	1.90	—	—	—
Hexcel AS4D (US)	6.7	1.79	245	4.69	1.92	—	—	—
Hexcel PV42/850 (US)	4.4	—	292	5.76	1.97	—	—	—
Hexcel IM7 (6000 Spec, US)	5.1	1.79	290	5.76	1.99	—	—	—
Pyrofil TR40 (JP)	7.0	1.80	235	4.70	2.0	—	—	—
Pyrofil TR50S (JP)	7.0	1.82	240	4.90	2.0	—	—	—
Tenax UTS (GE)	7.0	1.80	240	4.70	2.0	—	—	—
Hexcel IM9 (US)	4.4	1.80	290	6.07–6.14	2.10	—	—	—
Torayca T700S ^c (JP)	7.0	1.80	230	4.90	2.1	—	—	—
Torayca T700G ^c (JP)	—	1.80	240	4.90	2.1	—	—	—
Torayca T1000G ^c (JP)	5.0	1.80–1.82	294	6.37–7.06	2.2	—	—	—
Torayca T1000 (JP)	5.7	1.80–1.82	255–300	6.4–7.2	2.2–2.4	—	—	—
Coal tar and petroleum pitches based carbon fibres	4.4–7.0	1.73–1.82	230–310	3.6–7.2	1.5–2.4	—	—	—
Thornel P75 (US)	9.6–10.0	2.00	500–520	2.0–2.1	0.25–0.40	150	–1.4	7
Thornel P100S (US)	10	2.16	758	2.07	0.27	—	—	—
Thornel P120S (US)	10	2.17	827	2.24	0.29	—	—	—

(continued)

Table 2.10 (continued)

Trade mark and grade ^b	<i>D</i> , μm	<i>d</i> , g cm ⁻³	<i>E</i> , GPa	<i>σ_b</i> , GPa	δ, %	<i>λ</i> , W m ⁻¹ K ⁻¹	<i>α</i> , 10 ⁻⁶ K ⁻¹	<i>ρ</i> , μΩ m
Thornel P120 (US)	9.6–10.6	2.10–2.17	820–827	2.20–2.41	0.29–0.30	640	–1.6	–
Thornel K1100X, K1000X (US)	10	2.20	965	3.10	0.30	1100	–1.6	–
Thornel P100 (US)	8.8–10.0	2.16–2.20	690–760	2.2–2.4	0.30–0.35	300–520	–(1.4–1.6)	2.5–3.0
Diallead K139 (JP)	10	2.14	735	2.75	0.37	–	–	–
Granoc XN85A ^d (JP)	8.5	2.17	830	3.63	0.4	–	–	–
Granoc YS90A ^e (JP)	7	2.19	880	3.63	0.4	–	–	–
Diallead K137 (JP)	–	2.12	637	2.65	0.42	–	–	–
Carbonic HM70 (JP)	10	2.18	686	2.94	0.43	–	–	–
Diallead K135 (JP)	–	2.10	539	2.55	0.47	–	–	–
Thornel P55S (US)	10	2.00	379	1.90	0.50	–	–	–
Thornel P55 (US)	8.7–10.0	2.00	380	1.90–2.10	0.50–0.55	100	–1.3	7.5–8.5
Thornel P100HTS (US)	10	2.17	724	3.62	0.50	–	–	–
Granoc XN70A ^d (JP)	10	2.16	720	3.63	0.5	–	–	–
Granoc XN80A ^d (JP)	10	2.17	785	3.63	0.5	–	–	–
Granoc YS70A ^e (JP)	7	2.16	720	3.63	0.5	–	–	–
Granoc YS70 ^e (JP)	7	2.14	690	3.53	0.5	–	–	–
Granoc YS80 ^e (JP)	7	2.15	785	3.53	0.5	–	–	–
Carbonic HM60 (JP)	10	2.17	588	2.94	0.50	–	–	–
Forca FT700 (JP)	10	2.16	700	3.30	0.5	–	–	–
Diallead K133 (JP)	–	2.08	441	2.35	0.53	–	–	–
Carbonic HM50 (JP)	10	2.16	490	2.75	0.56	–	–	–
Forca FT500 (JP)	10	2.14	500	3.00	0.6	–	–	–
Granoc YS60 ^e (JP)	7	2.12	590	3.53	0.6	–	–	–
Donacarbo (JP)	9	2.10	500	3.00	0.6	–	–	–
Granoc XN50A ^d (JP)	10	2.14	520	3.83	0.7	–	–	–
Granoc YS50A ^e (JP)	7	2.14	520	3.83	0.7	–	–	–
Granoc YT50–10S (JP)	6	–	490	4.1	0.8	–	–	–
Granoc YS50 ^e (JP)	7	2.09	490	3.73	0.8	–	–	–
Thornel P25 (US)	8.6–11.0	1.90	125–159	1.40	0.9–1.0	–	–	–
Diallead K321 (JP)	–	1.90	176	1.96	1.08	–	–	–

(continued)

Table 2.10 (continued)

Trade mark and grade ^b	<i>D</i> , μm	<i>d</i> , g cm ⁻³	<i>E</i> , GPa	<i>σ_b</i> , GPa	δ, %	λ, W m ⁻¹ K ⁻¹	α, 10 ⁻⁶ K ⁻¹	ρ, μΩ m
Dialead K223 (<i>JP</i>)	—	2.00	225	2.84	1.2	—	—	—
	6.0–11.0	1.90–2.20	125–965	1.4–4.1	0.25–1.2	120–1100	—	2–13
<i>Viscose rayon (cellulose) based carbon fibres</i>								
Thornel 25 (<i>US</i>)	—	—	170	1.25	—	—	—	—
Thornel 40 (<i>US</i>)	6.9	1.55	276	1.72	0.8	—	—	—
Thornel 50 (<i>US</i>)	6.6	1.63	340–350	1.97–2.00	0.8	—	—	—
Thornel 50S (<i>US</i>)	—	1.67	392	1.96	—	—	—	—
Thornel 60 (<i>US</i>)	6.1	1.69–1.70	400–420	2.20–2.27	—	—	—	—
Thornel 70 (<i>US</i>)	—	1.86	520	2.60	—	—	—	—
Thornel 75 (<i>US</i>)	—	1.86	517–525	2.45–2.59	—	—	—	—
Thornel 75S (<i>US</i>)	—	1.82	540	2.35	—	—	—	—
Thornel 100 (<i>US</i>)	9.4	1.95–2.00	690	3.45–3.95	—	—	—	—
Thornel 300 (<i>US</i>)	—	1.70	225	2.06	0.8	—	—	—
VMN-3 (<i>RU</i>)	7.0	—	250	1.45	—	—	—	—
VMN-4 (<i>RU</i>)	6.0	1.71–1.75	250–300	2.0–2.5	0.8	—	—	—
VMN-5 (<i>RU</i>)	—	1.75	330–500	2.5–3.0	—	—	—	—
Ural 24 (<i>RU</i>)	—	1.70–1.80	150–200	1.7–2.0	—	—	—	—
Modmor II (<i>UK</i>)	8.1	1.74–1.80	245–275	2.45–3.15	0.8–1.0	—	—	—
Thornel 400 (<i>US</i>)	—	1.78	206	2.75	1.0	—	—	—
Hitex 46H (<i>US</i>)	5.0	1.80	322	5.6	1.7	—	—	—
	5.0–9.4	1.55–2.00	170–690	1.25–5.6	0.8–1.7	—	—	—

^a Physical properties: *D*—mean single filament diameter, *d*—bulk density, *E*—Young's modulus, *σ_b*—tensile strength, δ—strain to failure (elongation), λ—thermal conductivity, α—coefficient of thermal expansion, ρ—specific electrical resistivity; properties are given in the longitudinal (axial) direction to the axis of fibre filament at room temperature

^b For trade marks or grades country of origin is given in brackets: *US*—United States of America, *RU*—Russia, *JP*—Japan, *UK*—United Kingdom, *GE*—Germany, *IN*—India, *KR*—Korea

^c Young's modulus and tensile strength values are based on the tow test

^d Based on petroleum pitch

^e Based on coal tar pitch

^f Transverse tensile modulus—15 GPa, axial shear modulus—20 GPa, torsional shear modulus—5 GPa, Poisson's ratios: transverse contraction with axial extension—0.25, transverse contraction with transverse extension—0.40, axial contraction with transverse extension—0.013

^g Thermal conductivity across the fiber—3 W m⁻¹ K⁻¹, specific heat—0.75 (23 °C), 0.99 (143 °C), 1.42 (380 °C) kJ kg⁻¹ K⁻¹

^h Transversal coefficient of thermal expansion—12 × 10⁻⁶ K⁻¹

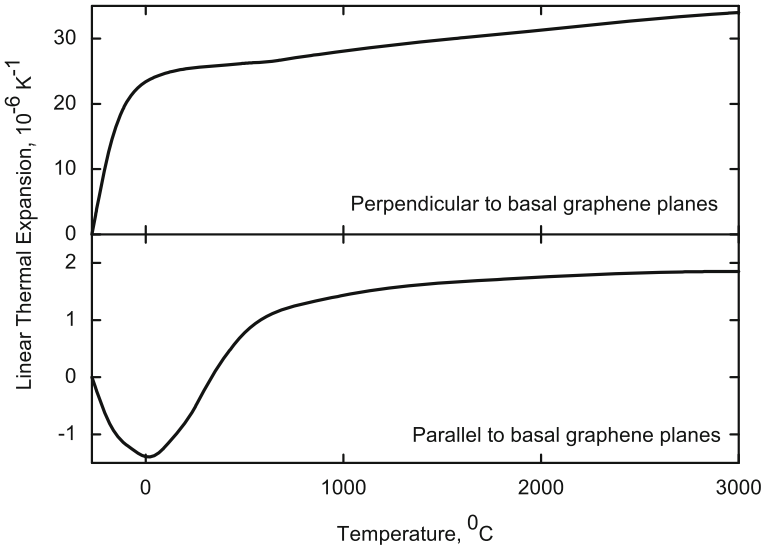


Fig. 2.4 Variations of linear thermal expansion coefficients in the different directions of graphite crystals with temperature [41–42, 209]

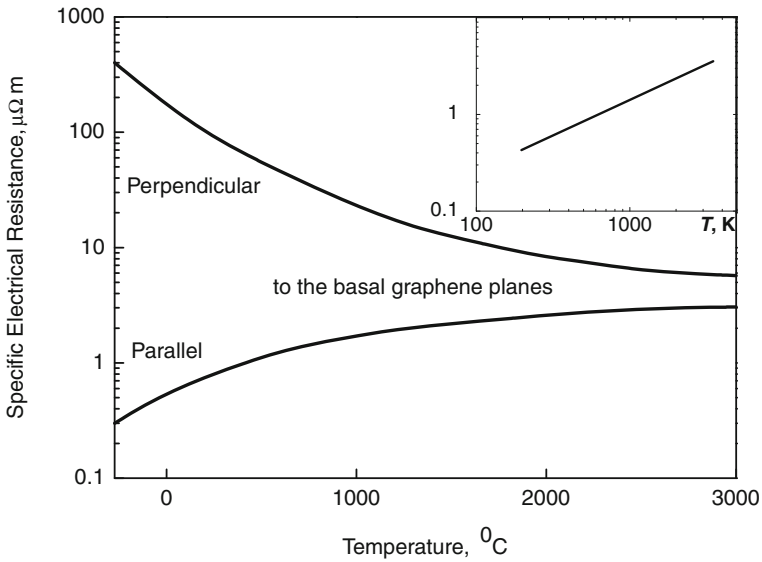


Fig. 2.5 Variations of specific electrical resistance in the different directions of graphite crystals with temperature (*Inset*—for the parallel direction to the basal planes in temperature (T , K) logarithm scale) [41, 209]

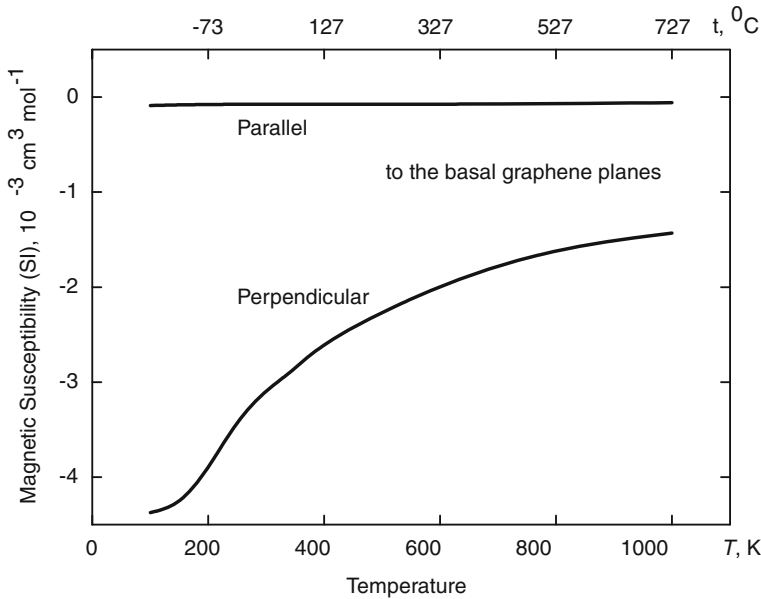


Fig. 2.6 Variations of molar magnetic susceptibility in the different directions of graphite crystals with temperature [539]

connected with certain difficulties because the hardness measurements have been made in practice by differing methods (Shore HS, Vickers HV, Rockwell HR, Brinell HB, Knoop HK, Mohs HM scales [192]). For the main types of carbon (graphite) materials approximate hardness values are following:

industrial structural and electrode graphitized (molded) products—HV 30–100 kgf mm^{-2} (0.3–1 GPa) [42], HM 1, HR 70–110 or HS 50–80 hardness numbers [192];

vitreous carbon (graphite)—HV 150–340 kgf mm^{-2} (1.5–3.4 GPa);

pyrolytic carbon (graphite)—HV 140–370 kgf mm^{-2} (1.4–3.7 GPa) [42, 136, 192].

At ambient temperatures, because of pores, flaws and microstructural defects concentrating the applied mechanical stresses, carbon (graphite) polycrystalline materials fails at much lower level than the theoretical strength of the graphite crystal, and mechanical failure occurs by absolutely brittle fracture. The flaws and defects are gradually annealed, stresses are relieved and plastic deformation becomes more probable with increasing temperature [42]. This evolution results in the general increase of the mechanical properties of graphite, so at the temperature range of about 2500 °C the strength of graphitized carbon materials is almost twice the value corresponding to room temperature. Theoretical predictions and experimental observations of tensile strength of graphitic nanostructured carbons are shown in Table 2.5. The values of strength characteristics of structural,

electrode and nuclear graphite materials for the different types of mechanical loading (tension, flexure and compression) are given in Table 2.6. Commonly, the physico-mechanical properties of graphitized materials, because of the preferential orientation of graphite grains (microcrystallites), vary with parallel and perpendicular directions to the axis of processing (extrusion, molding, pressing etc.). However, in spite of the fact that the individual crystals of graphite always perform super-high grade of anisotropy, special technological routes are elaborated for the industrial production of quasi-isotropic graphite materials [11]. The ratios between tensile σ_t , flexural (bending) σ_f and compressive σ_c strength characteristics for structural graphite materials

$$\sigma_f/\sigma_t \approx 2 \quad (2.4)$$

ranges from 1.5 to 2.1, and

$$\sigma_c/\sigma_f \approx 2 \quad (2.5)$$

ranges from 1.6 to 2.9 [194]. The various strength properties of pyrolytic carbon (graphite) materials are presented in Table 2.7. The flexural (bending) and compressive strengths of vitreous (glass-like) carbon materials are given in Table 2.8 and tensile strength of thermally expanded (exfoliated) graphite materials is included in Table 2.9. The tensile strength and strain to failure (elongation) of carbon (graphite) fibres are given in Table 2.10. Data on the fracture toughness (critical stress intensity factor) of some nuclear graphites are included in Table 2.6.

Although the strength of graphite rises with temperature increase, at the same time creep resistance of graphitized materials falls. Commonly, the creep characteristics of carbon (graphite) materials are higher in parallel direction to the preferential orientation of the normals to the basal planes of graphite grains (or in parallel direction to molding axis) than analogous characteristics in perpendicular directions. The strain rate of graphitized materials during steady-state stage of creep is defined by general relationship

$$\dot{\varepsilon} = C \left(\frac{\sigma}{\sigma_b} \right)^n \exp \left(-\frac{Q}{RT} \right) \quad (2.6)$$

where $\dot{\varepsilon} = \partial \varepsilon / \partial t = \partial l / l \partial t$ is the creep rate in s^{-1} , $C \approx 40$ is the constant independent of applied stress σ and temperature T in K, σ_b ultimate strength, $n \approx 4$ is the creep exponent constant, $Q \approx 210 \text{ kJ mol}^{-1}$ is the activation energy of creep and R is the gas constant [194, 908]. At the same temperature the creep rate of graphitized materials is higher in vacuum and reduces with inert gas pressure increase.

Quasi-single crystalline graphite (e.g. highly oriented pyrolytic graphite) is a typical transversely isotropic material, and most graphitic and graphite containing materials applied in practice possess the infinite order axis of symmetry as well. In the expression for the elastic constants of graphite crystals

$$\Sigma_i = c_{ij} \Xi_j (i, j = 1, 2, \dots, 6), \quad (2.7)$$

linking the stresses Σ_i and the strains Ξ_j in the low strain limit, only 12 parameters (stiffness coefficients or modules) c_{ij} are non-zero: $c_{11} = c_{22}$, $c_{12} = c_{21}$, $c_{13} = c_{31} = c_{23} = c_{32}$, c_{33} , $c_{44} = c_{55}$ and $c_{66} = (c_{11} - c_{12})/2$.

Thus, the elasticity tensor for single crystal graphite material is symmetrical, and the stress-strain relationship (representation of Hooke's law) expressed by the matrix notations is read [217, 229, 231]:

$$\begin{pmatrix} \sigma_{xx} \\ \sigma_{yy} \\ \sigma_{zz} \\ \sigma_{yz} \\ \sigma_{xz} \\ \sigma_{xy} \end{pmatrix} = \begin{pmatrix} c_{11} & c_{12} & c_{13} & 0 & 0 & 0 \\ c_{12} & c_{11} & c_{13} & 0 & 0 & 0 \\ c_{13} & c_{13} & c_{33} & 0 & 0 & 0 \\ 0 & 0 & 0 & c_{44} & 0 & 0 \\ 0 & 0 & 0 & 0 & c_{44} & 0 \\ 0 & 0 & 0 & 0 & 0 & \frac{1}{2}(c_{11} - c_{12}) \end{pmatrix} \begin{pmatrix} \varepsilon_{xx} \\ \varepsilon_{yy} \\ \varepsilon_{zz} \\ \varepsilon_{yz} \\ \varepsilon_{xz} \\ \varepsilon_{xy} \end{pmatrix} \quad (2.8)$$

or in the inverse form with compliances s_{ij} :

$$\begin{pmatrix} \varepsilon_{xx} \\ \varepsilon_{yy} \\ \varepsilon_{zz} \\ \varepsilon_{yz} \\ \varepsilon_{xz} \\ \varepsilon_{xy} \end{pmatrix} = \begin{pmatrix} s_{11} & s_{12} & s_{13} & 0 & 0 & 0 \\ s_{12} & s_{11} & s_{13} & 0 & 0 & 0 \\ s_{13} & s_{13} & s_{33} & 0 & 0 & 0 \\ 0 & 0 & 0 & s_{44} & 0 & 0 \\ 0 & 0 & 0 & 0 & s_{44} & 0 \\ 0 & 0 & 0 & 0 & 0 & 2(s_{11} - s_{12}) \end{pmatrix} \begin{pmatrix} \sigma_{xx} \\ \sigma_{yy} \\ \sigma_{zz} \\ \sigma_{yz} \\ \sigma_{xz} \\ \sigma_{xy} \end{pmatrix}. \quad (2.9)$$

The compliance coefficients are readily expressed in terms of the stiffness coefficients:

$$2s_{11} = \frac{c_{33}}{c^2} + \frac{1}{c_{11} - c_{12}}, \quad (2.10)$$

$$2s_{12} = \frac{c_{33}}{c^2} - \frac{1}{c_{11} - c_{12}}, \quad (2.11)$$

$$s_{13} = -\frac{c_{13}}{c^2}, \quad (2.12)$$

$$s_{33} = \frac{c_{11} + c_{12}}{c^2}, \quad (2.13)$$

$$s_{44} = \frac{1}{c_{44}}, \quad (2.14)$$

$$c^2 \equiv c_{33}(c_{11} + c_{12}) - 2c_{13}^2 = \frac{1}{s^2} > 0, \quad (2.15)$$

$$s^2 \equiv s_{33}(s_{11} + s_{12}) - 2s_{13}^2. \quad (2.16)$$

The reciprocal expressions of stiffness coefficients in terms of compliance coefficients have the same form if c^2 is replaced with s^2 .

In particular, there are seven elastic characteristics of graphitic materials, which can be defined and measured (various designations of them applied in the literature are given in brackets) [217, 226, 229, 231]:

E_1 (E , E_x , E_a or E_{11})—in-plane Young's modulus (for directions within the isotropic (isometric) plane, or in the parallel directions to the basal graphene planes; for carbon (graphite) high-modulus fiber filament—longitudinal modulus, commonly);

E_2 (E' , E_z , E_c or E_{33})—out-of-plane Young's modulus (for the direction perpendicular to the isotropic (isometric) plane, or in the perpendicular direction to the basal graphene planes; for carbon (graphite) high-modulus fiber filament—transversal modulus, commonly);

G_{12} (G or G_{xy})—Coulomb's (shear) modulus for the isotropic (isometric) plane, or in the parallel planes to the basal graphene planes;

G_{13} (G' or $G_{yz} = G_{zx}$)—Coulomb's (shear) modulus for planes normal to the isotropic (isometric) plane, or in the perpendicular planes to the basal graphene planes;

ν_{12} (ν or ν_{xy})—Poisson's ratio (major), which characterizes the contraction within the isotropic (isometric) plane due to forces applied within this plane;

ν_{13} (ν' or ν_{xz})—Poisson's ratio, which characterizes the contraction within the isotropic (isometric) plane due to forces applied in the direction perpendicular to it;

ν_{23} (ν'' or ν_{zx})—Poisson's ratio, which characterizes the contraction in the direction perpendicular to the isotropic (isometric) plane due to forces applied within this plane.

However, only five from seven characteristics mentioned above are independent. The equality $E_1\nu_{13} = E_2\nu_{23}$ exists because of the symmetry of the elasticity tensor.

Young's and Coulomb's (shear) moduli and Poisson's ratios are associated with the stiffness coefficients c_{ij} in the following forms:

$$\begin{pmatrix} 1/E_1 & -\nu_{12}/E_1 & -\nu_{13}/E_2 & 0 & 0 & 0 \\ -\nu_{12}/E_1 & 1/E_1 & -\nu_{13}/E_2 & 0 & 0 & 0 \\ -\nu_{13}/E_2 & -\nu_{13}/E_2 & 1/E_2 & 0 & 0 & 0 \\ 0 & 0 & 0 & 1/G_{13} & 0 & 0 \\ 0 & 0 & 0 & 0 & 1/G_{13} & 0 \\ 0 & 0 & 0 & 0 & 0 & 1/G_{12} \end{pmatrix}^{-1} = \begin{pmatrix} c_{11} & c_{12} & c_{13} & 0 & 0 & 0 \\ c_{12} & c_{11} & c_{13} & 0 & 0 & 0 \\ c_{13} & c_{13} & c_{33} & 0 & 0 & 0 \\ 0 & 0 & 0 & c_{44} & 0 & 0 \\ 0 & 0 & 0 & 0 & c_{44} & 0 \\ 0 & 0 & 0 & 0 & 0 & \frac{1}{2}(c_{11} - c_{12}) \end{pmatrix} \quad (2.17)$$

Table 2.11 Elastic properties of graphite crystals at room temperature

Property	Methods of determination			
	Ultrasonic, sonic resonance and static testing ^a [232]	Inelastic x-ray scattering [233]	Theoretical estimation [229, 235]	
			2H-graphite ^b	3R-graphite
c_{11} (E_x), GPa	1060 ± 20	1109 ± 16	1020	1020
c_{12} , GPa	180 ± 20	139 ± 36	–	–
c_{13} , GPa	15 ± 5	~ 0	–	–
c_{33} (E_z), GPa	36.5 ± 1.0	38.7 ± 0.7	36.1	36.4
c_{44} , (G_{zx}), GPa	$0.18\text{--}0.35^c$	5.0 ± 0.3	–	–
c_{66}^d (G_{xy}), GPa	440 ± 20	485 ± 10	–	–
ν_{12} (ν_{xy})	0.16	0.12	0.16	0.16
ν_{13} (ν_{xz})	0.012	~ 0	0.012	0.0065
ν_{23} (ν_{zx})	0.34	~ 0	0.34	0.18

^a Compliance coefficients $s_{ij} = \Xi_j/\Sigma_i$: $1/s_{11} = 1.02 \pm 0.03$ TPa, $s_{12} = 0.16 \pm 0.06$ TPa^{−1}, $s_{13} = 0.33 \pm 0.08$ TPa^{−1}, $1/s_{33} = 36.5 \pm 1.0$ GPa, $s_{66} = 2.3 \pm 0.2$ TPa^{−1} [232]

^b *Ab initio* calculations: $c_{11} + c_{12} = 1280$ GPa, $c_{13} = -0.5$ GPa, $c_{33} = 40.8$ GPa [236]

^c The spread in the value for c_{44} is due to the presence of dislocations and the value is ≥ 4.0 GPa for dislocation-free graphite [136, 234]

^d $c_{66} = (c_{11} - c_{12})/2$

The experimental estimates of the elastic properties of 2H-graphite crystals were based on rather indirect data on the ensembles of small pyrolytic graphite crystals with close orientations along the hexagonal axis of symmetry (axis c) and with a wide orientation scatter in perpendicular directions [232, 234]; later more direct experimental data on 2H-graphite single crystals were extracted using the method of inelastic x-ray scattering [233]. These experimental data together with some theoretical estimates for 2H- and 3R-graphites are shown in Table 2.11.

The condition for the isotropic character of media is

$$2c_{44}/(c_{11} - c_{12}) = 1, \quad (2.18)$$

so substituting the values for these elastic constants of graphite, this ratio becomes 0.0004 [136], which means that the Young's modulus varies appreciably with orientation and graphite materials are extremely anisotropic. The Young's modulus of graphite crystals as a function of angle θ with c axis (perpendicular to the basal graphene planes) is symmetric for 2H-graphite (or near-symmetric for 3R-graphite) reaching in both cases the highest values ($E > 1$ TPa) with sharp maximum at $\theta = \pi/2$ and the lowest values ($E < 5$ GPa) with low-grade minimum at $\theta \approx 0.2\pi$. For the analogous angular dependence of Poisson's ratio ν_{xy} , the asymmetry about $\theta = \pi/2$ for 3R-graphite is somewhat larger; ν_{xy} is limited by the value 0.16 reached in the neighborhood of $\theta = \pi/2$ and is rapidly reduced for both graphite polytypes. In the range of angles $\theta = (0.13\text{--}0.38)\pi$ Poisson's ratio ν_{xy} becomes negligible (less than 0.01) and even negative. In the transverse direction, orthogonal to the previous one, the behaviour of Poisson's ratio ν_{zx} is quite different, since its value can be higher than the upper limit of Poisson's ratio for a

elastic isotropic medium (its thermodynamic limits are $-1 < \nu < 0.5$) [229]. The values of Young's modules for graphitic nanostructured carbon forms are summarized in Table 2.5. For large stresses in reality, the stress-strain relationship for polycrystalline graphite materials is non-linear and approximated by the equation of Jenkins [237]

$$\varepsilon = A\sigma + B\sigma^2, \quad (2.19)$$

where A is equal to s_{33} for specimens cut off in parallel direction to the preferential orientation of the normals to the basal planes of graphite flake-like grains (against-grain specimens) or s_{11} for specimens cut off in perpendicular direction to the preferential orientation of the same normals (with-grain specimens), and in accordance to Jenkins' model

$$B = 2\varepsilon_0/\sigma_m^2, \quad (2.20)$$

where ε_0 is the longitudinal residual strain after the graphite has been subjected to a maximum stress σ_m . For various industrial graphitized carbon products (for specimens cut off in different directions), the values of A range from 0.044 to 0.207 GPa^{-1} and B range from 0.232 to 3.262 GPa^{-2} [237]. The elasticity of commercially available graphitic products is considerably different from those values of the ideal crystals since they are controlled by the preferential crystallite orientation, porosity and structural defects. The elastic properties of various industrial graphitized carbon materials, pyrolytic (pyrographite) and vitreous (glass-like) carbons and carbon (graphite) fibres are given in Tables 2.6–2.8 and 2.10. The temperature variation of Young's modulus and strength characteristics of averaged industrial graphitized materials is presented in Fig. 2.2.

For averaged highly oriented graphite and quasi-isotropic carbon (graphite), compared with other ultra-high temperature elements (refractory metals), the values of physico-mechanical (strength, elasticity) properties in the wide range of temperatures are summarized in Addendum.

2.5 Nuclear Physical Properties

The isotopes of carbon (standard atomic mass—12.0107 u) from ^8C to ^{22}C and their general characteristics are summarized in Table 2.12; the naturally occurring isotopes are listed in order of decreasing abundance, and unstable radioactive isotopes—in order of decreasing half-life period of decay.

Nuclear physical properties of carbon (isotopic mass range, total number of isotopes, thermal neutron macroscopic cross sections, moderating ability and capture resonance integral), compared with other ultra-high temperature elements (refractory metals), are given in Addendum.

Table 2.12 General characteristics of the isotopes of carbon [3, 6, 576–578]

Isotope	Mass, u	Abundance, %	Half-life period	Decay mode, excitation (radiation) energy, MeV
^{12}C	12.000000	98.93 ^a	–	–
^{13}C	13.003355	1.07 ^b	–	–
^{14}C	14.003242	$<10^{-10}$	5.70×10^3 y	β^- , 0.155
^{11}C	11.011434	–	20.33 min	β^+ , 0.99
^{10}C	10.016853	–	19.29 s	β^+ , 2.2; γ , 0.72, 1.05
^{15}C	15.010599	–	2.45 s	β^- , 4.3 (80 %), 9.8 (20 %)
^{16}C	16.014701	–	0.75 s	β^- , n (97.9 %), β^- (2.1 %)
^{17}C	17.022586	–	0.19 s	β^- (71.59 %), β^- , n (28.41 %)
^9C	9.0310367	–	0.127 s	β^+ (60 %); β^+ , p (23 %); β^+ , α (17 %)
^{18}C	18.02676	–	92 ms	β^- (68.5 %), β^- , n (31.5 %)
^{19}C	19.03481	–	46.2 ms	β^- , n (47.0 %), β^- (46.0 %), β^- , 2n (7.0 %)
^{20}C	20.04032	–	16 ms	β^- , n (72.0 %), β^- (28.0 %)
^{22}C	22.05720 (?)	–	6.2 ms	β^-
^{21}C	21.04934 (?)	–	<30 ns	n
^8C	8.037675	–	2.0×10^{-21} s	2p, 0.230

^a Range of natural variation—98.853–99.037 at. %^b Range of natural variation—0.963–1.147 at. %

2.6 Chemical Properties

The specific electron configuration of carbon atoms has been proved in the numberless variety of carbon containing compounds formed by the chemical interaction between carbon and other elements of the periodic table. Organic chemistry as a special discipline is devoted directly to the carbon compounds with hydrogen, oxygen and nitrogen and their multi-component derivatives, which are termed organic compounds and, correspondingly, differed from inorganic compounds. The various inorganic compounds of carbon are classified in the following types:

simple molecular compounds (with *p*-elements of groups 15–17: halogens (F, Cl, Br, I), chalcogens (O, S, Se) and pnictogens (N, P)), covalent bonded; salt-like carbides (or acetylenides, compounds with *s*-elements of groups 1–2: alkali metals (Li, Na, K, Rb, Cs) and alkaline earth metals (Be, Mg, Ca, Sr, Ba) and *d*-elements of groups 11–12: Cu, Ag, Au, Zn, Cd, Hg), mainly ionic or covalent-ionic (e.g. Be and Mg carbides) bonded; interstitial carbides (or metal-like carbides, compounds with *d*-elements of groups 4–6: Ti, Zr, Hf, V, Nb, Ta, Cr, Mo, W), mainly metallic bonded; intermediate carbides (compounds with *d*- and *f*-elements of group 3: Sc, Y, lanthanoides (La, Ce, Pr, Nd, Sm, Eu, Gd, Tb, Dy, Ho, Er, Tm, Yb, Lu) and actinoids (Th, Pa, U, Np, Pu, Am) and light *d*-elements of groups 7–10: Mn, Fe, Co, Ni), ionic-metallic or covalent-metallic bonding; covalent carbides (compounds with *p*-elements of groups 13–14: B, Al, Si), mainly covalent or covalent-ionic (e.g. Al carbides) bonded;

graphitic/graphene and fullerene compounds (or intercalation (lamellar) compounds, with some elements, ions and molecules), mainly molecular bonded; carbon containing complex compounds (ternary, quaternary and higher order compounds) with the combination of the different types of chemical bonding.

The comprehensive information on the chemical interaction of carbon with all the elements of the periodic table is given in Table 2.13. The carbon containing systems and corresponding binary compounds are considered there in accordance to the groups of elements from 1 to 17.

Table 2.13 Chemical interaction of carbon (graphite) with elements of the periodic table (binary systems in accordance to the groups of elements)^a

System	Type of phase diagram (constituent phases, temperatures and compositions of transformations)	Character of chemical interaction	References
<i>Group 1</i>			
C-H	H, variety of hydrocarbon compounds (e.g. CH ₄ , C ₂ H ₂ etc.), C	No interaction with H ₂ at normal conditions. At temp. ≤600–800 °C and $p \approx 0.1$ MPa, the interaction is extremely slow. Practically graphite is highly resistant to H ₂ at 800–2200 °C. With catalyst (Ni) at 900–1000 °C CH ₄ is formed, at temp. >1730 °C C ₂ H ₂ and other hydrocarbons are produced. The corrosion rate of commercial graphite in H ₂ gas flow ($56 \text{ kg m}^{-2} \text{ s}^{-1}$) at 1400 °C–0.13, 1580 °C–0.3 2230 °C–3.3 and 2730 °C–33 $\text{kg m}^{-2} \text{ s}^{-1}$.	[5, 138, 238]
C-Li	α -Li, β -Li, γ -Li, α -Li ₂ C ₂ (<~410–800 °C, invariable compos.), β -Li ₂ C ₂ (~410–440 °C, ?), γ -Li ₂ C ₂ (~440–560 °C, ?), δ -Li ₂ C ₂ (at least at 560 °C, ?), layered compounds (LiC _{6±x} , LiC _{12±x} , LiC _{18±x} , LiC _{24±x} , LiC _{36±x} , LiC _{72±x}), C Eutectic γ -Li– α -Li ₂ C ₂ (175 °C, <1 at. % C)	The solubility of C in liquid Li: at 200 °C–~ 2×10^{-4} at.% and at 735 °C–~0.4 at.%. The presence of ~0.26 wt.% N ₂ does not affect the solubility of C in Li at temp. >~350 °C, but at lower temp. it increases the solubility of C considerably. At 600 °C the corrosion resistance of graphite in liquid Li is low. The mixture of Li and C reacts at 800 °C with the formation of carbide (acetylenide) Li ₂ C ₂ . A number of C-rich lamellar or intercalate compounds are formed by the reaction of Li vapour with graphite. The wetting angle of molten pure Li: 115° (Ar, 200 °C), 110° (Ar, 400 °C).	[138, 238–241, 530, 905, 1004]

(continued)

Table 2.13 (continued)

System	Type of phase diagram (constituent phases, temperatures and compositions of transformations)	Character of chemical interaction	References
C–Na	α -Na, β -Na, NaC (?), α -Na ₂ C ₂ , β -Na ₂ C ₂ , layered compounds (NaC _{8±x} , NaC _{16±x} , NaC _{56±x} , NaC _{64±x}), intercalated fullerenes (Na ₂ (C ₆₀), Na ₃ (C ₆₀), Na ₄ (C ₆₀), Na ₆ (C ₆₀), Na _{9.7} (C ₆₀) and other), C No diagram plot	The solubility of C in liquid Na: with O = 0.004 wt.%, at 300 °C–0.90, 500 °C–1.22, 700 °C–1.44, and with O = 0.026 wt.%, at 300 °C–2.70, 500 °C–3.22, 700 °C–3.56, 10 ^{–2} at.%. At 300 °C the corrosion resistance of graphite in liquid Na is low. Na ₂ C ₂ is synthesized by the interaction of Na with C ₂ H ₂ at 300–400 °C.	[138, 238, 241, 290, 916–918, 920, 1003]
C–K	K, KC (?), K ₂ C ₂ , layered compounds (KC _{8±x} , KC _{16±x} , KC _{24±x} , KC _{36±x} , KC _{40±x} , KC _{48±x} , KC _{60±x} , KC _{72±x} and some other), intercalated fullerenes (α -K(C ₆₀), β -K(C ₆₀), γ -K(C ₆₀), δ -K(C ₆₀), K ₃ (C ₆₀), α -K ₄ (C ₆₀), β -K ₄ (C ₆₀), K ₆ (C ₆₀), K(C ₇₀), K ₄ (C ₇₀), K ₉ (C ₇₀), K(C ₇₂) and other), C No diagram plot	Binary compounds are synthesized by the interaction of K melt or vapour with graphite or C ₂ H ₂ at 300–400 °C.	[138, 238, 241, 290, 919–921, 923]
C–Rb	Rb, RbC (?), Rb ₂ C ₂ (?), layered compounds (RbC _{8±x} , RbC _{16±x} , α -RbC _{24±x} , β -RbC _{24±x} , RbC _{36±x} , RbC _{48±x} , RbC _{60±x} and some other), intercalated fullerenes (α -Rb(C ₆₀), β -Rb(C ₆₀), γ -Rb(C ₆₀), Rb ₃ (C ₆₀), Rb ₄ (C ₆₀), Rb ₆ (C ₆₀), Rb _{8.8} (C ₈₄) and other), C Order–disorder or structural transformations α -RbC _n → β -RbC _n (?) No diagram plot	Binary compounds are synthesized by the interaction of Rb melt or vapour with graphite or C ₂ H ₂ at 300–450 °C.	[138, 238, 241, 922–923, 925]
C–Cs	Cs, CsC (?), Cs ₂ C ₂ (?), layered compounds (CsC _{8±x} , CsC _{10±x} , CsC _{16±x} , α -CsC _{24±x} , β -CsC _{24±x} , CsC _{36±x} , CsC _{48±x} , CsC _{60±x} , CsC _{84±x} and some other), intercalated fullerenes (α -Cs(C ₆₀), β -Cs(C ₆₀), Cs ₃ (C ₆₀), α -Cs ₄ (C ₆₀), β -Cs ₄ (C ₆₀), Cs ₆ (C ₆₀) and other), C Order–disorder or structural transformations α -CsC _n → β -CsC _n (?) No diagram plot	Binary compounds are synthesized by the interaction of Cs melt or vapour with graphite or C ₂ H ₂ at 300–400 °C.	[138, 238, 241, 922, 924]
C–Fr	No data	–	–

(continued)

Table 2.13 (continued)

System	Type of phase diagram (constituent phases, temperatures and compositions of transformations)	Character of chemical interaction	References
<i>Group 2</i>			
C–Be	α -Be, β -Be, Be ₂ C ($< \sim 2100$ – 2200 °C), BeC ₂ , C No diagram plot	Be ₂ C is formed directly from the elements, BeC ₂ —by the interaction of Be with dry C ₂ H ₂ . The max. solid solubility of C in Be is < 0.1 at.% (?). For diffusion rate in the system at various temp. see Addendum.	[138, 238, 241–242]
C–Mg	Mg, MgC (< 2625 °C, invariable compos., ?), Mg ₂ C ₃ ($< \sim 600$ – 760 °C), MgC ₂ ($< \text{at least } \sim 2200$ °C, invariable compos., ?), C	Carbides are formed by the interaction of Mg with hydrocarbons at elevated temp. For diffusion rate in the system at various temp. see Addendum.	[138, 238, 241, 700, 926]
C–Ca	α -Ca, β -Ca, α -CaC ₂ ($< \sim 25$ °C, ?), β -CaC ₂ (~ 25 – 450 °C), γ -CaC ₂ (~ 350 – 435 °C), δ -CaC ₂ (from ~ 435 – 500 °C to ~ 2160 – 2980 °C, invariable compos.), layered compounds (CaC _{6\pmx} and other), intercalated fullerenes (Ca _{3\pmx} (C ₆₀), Ca ₅ (C ₆₀), Ca ₇ (C ₆₀) and other), C Eutectic δ -CaC ₂ –Ca (820 °C, 2 at.% C) Eutectic δ -CaC ₂ –C (2100 °C, 75 at.% C)	CaC ₂ is formed directly from the elements at 1250 °C in Ar atmosphere. For diffusion rate in the system at various temp. see Addendum.	[138, 238, 241–243, 701, 927–928]
C–Sr	α -Sr, β -Sr, α -SrC ₂ (< -30 °C, ?), β -SrC ₂ (from -30 °C to ~ 370 °C), γ -SrC ₂ (~ 370 – 1800 °C, invariable compos., ?), layered compounds (SrC _{6\pmx} , SrC _{12\pmx} , SrC _{18\pmx} , SrC _{24\pmx} , SrC _{30\pmx} , SrC _{36\pmx}), intercalated fullerenes (Sr _{2.08} (C ₆₀), Sr ₃ (C ₆₀), Sr ₆ (C ₆₀) and other), C Eutectic γ -SrC ₂ –C (?)	SrC ₂ is formed directly from the elements at 1250 °C in Ar atmosphere.	[138, 238, 241–243, 702, 929, 930]

(continued)

Table 2.13 (continued)

System	Type of phase diagram (constituent phases, temperatures and compositions of transformations)	Character of chemical interaction	References
C–Ba	Ba, α -BaC ₂ (< ~25 °C), β -BaC ₂ (~25–2000 °C, invariable compos., ?), layered compounds (BaC _{6±x} , BaC _{8±x} , BaC _{12±x} , BaC _{18±x} , BaC _{24±x} , BaC _{30±x} , BaC _{36±x}), inter- calated fullerenes (Ba ₆ (C ₆₀), Ba ₃ (C ₇₀) and other), C Eutectic β -BaC ₂ –Ba (?)	Carbides are synthesized directly from the elements at 575–700 °C in vacuum ($\sim 10^{-3}$ Pa).	[138, 238, 241–243, 703, 930, 937]
C–Ra	No data	–	–
<i>Group 3</i>			
C–Sc	α -Sc, β -Sc, ScC _{1–x} (or Sc _{2±x} C, < ~2255–2285 °C, congruent melt. point corresp. to ~ScC _{0.46} , homog. range— 21.5–38.5 at.% C at 1860–1865 °C and 23.5–34.5 at.% C at 20–30 °C), Sc ₃ C (?), α -Sc ₄ C ₃ (from ~950 °C to ~1500–1510 °C, invariable compos.), β -Sc ₄ C _{3+x} (or Sc ₁₃ C _{10±x} , from ~1500– 1510 °C to ~1860–1865 °C, incongruent melt. point, homog. range—42.8–48.5 at.% C), Sc ₃ C _{4–x} (or Sc ₁₅ C _{19±x} , < ~1790–1800 °C, incongruent melt. point, homog. range—54.1–55.9 at.% C), intercalated fullerenes (Sc ₂ (C ₈₄) and other), C Eutectic Sc ₃ C _{4–x} –C (~1720–1725 °C, 62 at.% C)	The presence of C increases the melt. point of Sc from 1541 °C to 1579 °C and temp. of polymorphic transformation α -Sc \rightarrow β -Sc from 1337 °C to 1543 °C. The max. solubility of C in α -Sc is ~4.5 at.% (at 1540–1545 °C) and in β -Sc is ~2.5 at.% (at 1575–1580 °C). The elemental Sc and C interact at 1800–2000 °C in vacuum (or reductive conditions) with the formation of ScC _{1–x} and Sc ₄ C _{3–x} . For diffusion rate in the system at various temp. see Addendum.	[138, 238, 241–245, 602, 931]

(continued)

Table 2.13 (continued)

System	Type of phase diagram (constituent phases, temperatures and compositions of transformations)	Character of chemical interaction	References
C–Y	α -Y, β -Y, Y_3C (or $YC_{0.25 \div 0.40}$, ?), $Y_{2 \pm x}C$ ($< \sim 905$ – 990 °C, homog. range— 28.5 – 36.0 at.% C at 900 °C, ?), $YC_{1 \pm x}$ (or $YC_{0.33}$, γ -phase, continuous solid solution with β - $YC_{2 \pm x}$, from ~ 905 – 1325 °C (?) to ~ 1805 – 2360 °C, with congruent melt. points corresp. to $\sim YC_{0.38 \div 0.43}$, at ~ 2000 – 2020 °C and $\sim YC_{1.94 \div 2.17}$ at ~ 2360 – 2415 °C and with min. melt. point corresp. to $\sim YC_{0.90 \div 1.17}$ at ~ 1805 – 1810 °C, homog. range—from ~ 61.5 to ~ 69 – 72 at.% C at 2020 °C, ~ 18.0 – 67.5 at.% C at 1660 °C, ~ 17 – 49.5 at.% C and ~ 63 – 67.5 at.% C at 1560 °C, ~ 17 – 42 at.% C at 1300 °C and ~ 18 – 37 at.% C at 1000 °C), α - Y_4C_5 ($< \sim 1305$ °C, invariable compos.), β - Y_4C_5 (~ 1305 – 1530 °C, invariable compos.), α - Y_3C_{4-x} (or α - $Y_{15}C_{19 \pm x}$, $< \sim 1185$ – 1325 °C, homog. range— ~ 54 – 59 at.% C, ?), β - Y_3C_{4-x} (or β - $Y_{15}C_{19 \pm x}$, from ~ 1185 – 1325 °C to ~ 1525 – 1655 °C, homog. range— ~ 54 – 59 at.% C, ?), α - Y_2C_{3-x} ($< \sim 1185$ °C, homog. range— ~ 58 – 60 at.% C, ?), β - Y_2C_{3-x} ($< \sim 1185$ – 1645 °C, homog. range— ~ 56 – 60 at.% C, ?), α - YC_2 ($< \sim 1320$ – 1325 °C, invariable compos.), β - $YC_{2 \pm x}$ (or γ -phase, continuous solid solution with $YC_{1 \pm x}$, see $YC_{1 \pm x}$ above), intercalated fullerenes ($Y(C_{82})$ and other), C	The presence of C increases the melt. point of Y from 1522 °C to 1560 °C and temp. of polymorphic transformation α -Y \rightarrow β -Y from 1478 °C to 1520 °C. The max. solubility of C in α -Y is 8.8 at.% (at 1520 °C) and in β -Y is ~ 7.0 at.% (at 1560 °C). Y carbides are formed directly from the elements at 1560 – 1600 °C in vacuum (or reductive conditions). For diffusion rate in the system at various temp. see Addendum.	[238, 241–242, 244, 246, 932–934]

(continued)

Table 2.13 (continued)

System	Type of phase diagram (constituent phases, temperatures and compositions of transformations)	Character of chemical interaction	References
	Continuous solid solution $YC_{1-x}-\beta-YC_{2+x}$ (or γ phase, see $YC_{1\pm x}$ above, miscibility gap: critical point— $\sim 57-58$ at.% C at $\sim 1645-1655$ °C, from $\sim 40-42$ to $\sim 66-67$ at.% C at 1325 °C) Eutectic $\beta-YC_{2\pm x}-C$ (2290 °C, 74 at.% C)		
<i>Lanthanides</i>			
C-La	α -La, β -La, γ -La, La_2C_{3-x} (<1415 °C, incongruent melt. point, homog. range— $\sim 54-60$ at.% C at 800 °C), $\alpha-LaC_2$ ($<\sim 1060-1080$ °C, invariable compos. at low temp. and restricted homog. range (~ 1 at.% C) at 1060 °C), $\beta-LaC_{2\pm x}$ (from $\sim 1060-1080$ °C to $\sim 2440-2360$ °C, congruent melt. point corresp. to $\sim LaC_{2.0}$, homog. range— $\sim 65.5-68$ at.% C at 2250 °C and $\sim 63-67$ at.% C at 1415 °C), $\epsilon-LaC_2$ (?), intercalated fullerenes ($La(C_{82})$ and other), C Eutectic $\beta-La-La_2C_{3-x}$ ($\sim 800-805$ °C, $\sim 20.6-20.8$ at.% C) Eutectic $\beta-LaC_{2\pm x}-C$ ($\sim 2235-2270$ °C, $\sim 69.5-71.5$ at.% C)	At $800-875$ °C the solubility of C in $\beta-La$ is $\sim 3.4-4.3$ at.% La carbides are formed directly from the elements at $920-1000$ °C in vacuum (or reductive conditions). For diffusion rate in the system at various temp. see Addendum.	[138, 241–242, 244, 247, 935]

(continued)

Table 2.13 (continued)

System	Type of phase diagram (constituent phases, temperatures and compositions of transformations)	Character of chemical interaction	References
C–Ce	α -Ce, β -Ce, γ -Ce, δ -Ce, Ce_2C (?), CeC (?), Ce_2C_3 ($< \sim 1535$ – 1900 °C, incongruent melt. point, invariable compos.), α - CeCe_2 ($< \sim 1050$ – 1110 °C with invariable compos. at low temp. and restricted homog. range (~ 1.5 at.% C) at 1050 – 1110 °C), β - $\text{CeCe}_{2\pm x}$ (from ~ 1050 – 1110 °C to ~ 2250 – 2340 °C, congruent melt. point corresp. to $\sim \text{CeC}_{2.0}$, homog. range width— ~ 1.5 – 2 at.% C), CeC_3 (?), intercalated fullerenes ($\text{Ce}(\text{C}_{82})$ and other), C Eutectic δ -Ce– Ce_2C_3 (~ 660 – 700 °C, ~ 19.5 – 20 at.% C) Eutectic β - $\text{CeCe}_{2\pm x}$ –C (~ 2220 – 2250 °C, ~ 69.0 – 69.5 at.% C)	The presence of C decreases the melt. point of Ce from 798 °C to ~ 700 – 705 °C and temp. of polymorphic γ -Ce \rightarrow δ -Ce transformation from 726 °C to 630 °C (corresp. to content ~ 6 at.% C). At elevated temp. the substantial solubility of C in δ -Ce and γ -Ce is observed. The max. solubility is ~ 10 at.% C at 650 – 700 °C. Ce carbides are formed directly from the elements at 800 – 900 °C in vacuum (or reductive conditions).	[138, 241–242, 244, 391, 936]
C–Pr	α -Pr, β -Pr, $\text{Pr}_2\text{C}_{3-x}$ ($< \sim 1540$ – 1555 °C, incongruent melt. point, homog. range ~ 55 – 60 at.% C at 800 °C), α - PrC_2 ($< \sim 1130$ – 1150 °C, invariable compos. at low temp. and restricted homog. range (~ 1 at.% C) at 1130 – 1150 °C), β - $\text{PrC}_{2\pm x}$ (from ~ 1130 – 1150 °C to 2320 °C, congruent melt. point, homog. range width— ~ 1.5 – 2 at.% C), C Eutectic β -Pr– $\text{Pr}_2\text{C}_{3-x}$ (~ 795 – 805 °C, ~ 15 at.% C) Eutectic β - $\text{PrC}_{2\pm x}$ –C (~ 2250 – 2260 °C, 71.5 at.% C)	The presence of C decreases the melt. point of Pr from 931 °C to ~ 795 – 805 °C and temp. of polymorphic α -Pr \rightarrow β -Pr transformation from 795 °C to ~ 670 – 680 °C. At elevated temp. the substantial solubility of C in β -Pr and α -Pr is observed. The max. solubility achieves ~ 8 at.% in β -Pr and ~ 5 at.% in α -Pr. Pr carbides are formed directly from the elements at 900 – 1000 °C in vacuum (or reductive conditions).	[238, 241–242, 244]

(continued)

Table 2.13 (continued)

System	Type of phase diagram (constituent phases, temperatures and compositions of transformations)	Character of chemical interaction	References
C–Nd	α -Nd, β -Nd, $\text{Nd}_2\text{C}_{3-x}$ ($< \sim 1570$ – 1670 °C, melt. point, homog. range— ~ 54 – 60 at.% C), α -NdC ₂ ($< \sim 1130$ – 1170 °C), β -NdC ₂ (from ~ 1130 – 1170 °C to ~ 2180 – 2340 °C, melt. point, ?), C Eutectic β -NdC ₂ –C (~ 2255 – 2295 °C) No diagram plot	No solubility of C in Nd at room temp. Nd carbides are formed directly from the elements at 1000–1100 °C in vacuum (or reductive conditions).	[238, 241– 242]
C–Pm	No data	—	—
C–Sm	α -Sm, β -Sm, γ -Sm, Sm_{3-x}C (or SmC_{1-x} , homog. range— ~ 25 – 33 at.% C), $\text{Sm}_2\text{C}_{3-x}$ ($< \text{at least } 1325$ °C, melt. point, homog. range— ~ 54 – 60 at.% C), α -SmC ₂ ($< \sim 1150$ – 1190 °C, invariable compos.), β -SmC ₂ ($< \sim 2200$ – 2300 °C, melt. point), layered compounds ($\text{SmC}_{6\pm x}$, $\text{SmC}_{12\pm x}$, $\text{SmC}_{18\pm x}$, $\text{SmC}_{24\pm x}$, $\text{SmC}_{30\pm x}$, $\text{SmC}_{36\pm x}$ and other), intercalated fullerenes ($\text{Sm}_3(\text{C}_{60})$, $\text{Sm}_6(\text{C}_{60})$, $\text{Sm}_3(\text{C}_{70})$ and other), C Eutectic β -SmC ₂ –C (~ 2210 – 2270 °C) No diagram plot	Sm carbides are formed directly from the elements at 1075–1150 °C in vacuum (or reductive conditions). For diffusion rate in the system at various temp. see Addendum.	[238, 241–242, 929, 937]
C–Eu	Eu, Eu_{3-x}C (or EuC_{1-x} , homog. range— ~ 25 – 33 at.% C), Eu_2C_3 , α -EuC ₂ ($< \sim 345$ – 375 °C, invariable compos.), β -EuC ₂ (from ~ 345 – 375 °C to at least 1700 °C, melt. point), layered compounds ($\text{EuC}_{6\pm x}$, $\text{EuC}_{12\pm x}$, $\text{EuC}_{18\pm x}$, $\text{EuC}_{24\pm x}$, $\text{EuC}_{30\pm x}$, $\text{EuC}_{36\pm x}$ and other), intercalated fullerenes ($\text{Eu}_{2.82}(\text{C}_{60})$, $\text{Eu}_6(\text{C}_{60})$, $\text{Eu}_3(\text{C}_{70})$, $\text{Eu}_9(\text{C}_{70})$ and other), C No diagram plot	Eu carbides are formed directly from the elements at 800–900 °C in vacuum (or reductive conditions).	[238, 241, 938–939]

(continued)

Table 2.13 (continued)

System	Type of phase diagram (constituent phases, temperatures and compositions of transformations)	Character of chemical interaction	References
C–Gd	α -Gd, β -Gd, β -Gd _{3-x} C (or GdC _{1-x} , homog. range— ~ 25–33 at.% C), α -Gd ₂ C, Gd ₄ C ₅ (?), Gd ₂ C _{3-x} (homog. range—~ 54–60 at.% C), α -GdC ₂ (<~ 1220–1290 °C, invariable compos.), β -GdC ₂ (from ~ 1220–1290 °C to ~ 2340–2400 °C, melt. point), GdC _{6±x} (layered compound, ?), C Eutectic β -GdC ₂ –C (~ 2280–2345 °C) No diagram plot	Gd carbides are formed directly from the elements at 1300–1400 °C in vacuum (or reductive conditions).	[238, 241, 616]
C–Tb	α' -Tb, α -Tb, β -Tb, Tb _{3-x} C (or TbC _{1-x} , homog. range— ~ 25–33 at.% C), α -Tb ₂ C (?), β -Tb ₂ C (?), Tb ₄ C ₅ (?), Tb ₁₅ C ₁₉ (?), Tb ₂ C _{3-x} (homog. range— ~ 54–60 at.% C), α -TbC ₂ (<~ 1100–1305 °C), β -TbC ₂ (from ~ 1100–1305 °C to ~ 2040–2280 °C, melt. point, ?), C Eutectic β -TbC ₂ –C (~ 2255–2295 °C) No diagram plot	Tb carbides are formed directly from the elements at 1350–1400 °C in vacuum (or reductive conditions).	[238, 241]
C–Dy	α' -Dy, α -Dy, β -Dy, Dy _{3-x} C (or DyC _{1-x} , homog. range— ~ 25–33 at.% C), α -Dy ₂ C, β -Dy ₂ C (?), Dy ₄ C ₅ (?), Dy ₁₅ C ₁₉ (?), Dy ₂ C _{3-x} (homog. range—~ 54–60 at.% C), α -DyC ₂ (<~ 1275–1315 °C), α' -DyC ₂ (?), β -DyC ₂ (from ~ 1275–1315 °C to at least 2250 °C, melt. point, ?), C Eutectic β -DyC ₂ –C (~ 2265–2315 °C) No diagram plot	Dy carbides are formed directly from the elements at 1400–1500 °C in vacuum (or reductive conditions).	[238, 241]

(continued)

Table 2.13 (continued)

System	Type of phase diagram (constituent phases, temperatures and compositions of transformations)	Character of chemical interaction	References
C–Ho	α -Ho, β -Ho, Ho_{3-x}C (or HoC_{1-x} , homog. range— ~ 25 – 33 at.% C), α - Ho_2C , β - Ho_2C (?), Ho_4C_5 (?), $\text{Ho}_{15}\text{C}_{19}$ (or Ho_5C_6 ?), Ho_3C_4 (?), Ho_4C_7 (?), $\text{Ho}_2\text{C}_{3-x}$ (homog. range— ~ 54 – 60 at.% C), α - HoC_2 ($< \sim 1280$ – 1330 °C), α' - HoC_2 (at least 1145 – 1165 °C, ?), β - HoC_2 (from ~ 1280 – 1330 °C to at least 2250 – 2290 °C, melt. point), C Eutectic β - HoC_2 –C (~ 2250 – 2290 °C) No diagram plot	The solubility of C in Ho at ~ 1300 °C is negligible. Ho carbides are formed directly from the elements at 1480 – 1550 °C in vacuum (or reductive conditions). For diffusion rate in the system at various temp. see Addendum.	[238, 241]
C–Er	α -Er, β -Er, Er_{3-x}C (or ErC_{1-x} , homog. range— ~ 25 – 33 at.% C), $\text{Er}_{15}\text{C}_{19}$, Er_3C_4 (?), Er_4C_7 (?), Er_2C_3 (metastable, ?), α - ErC_2 (< 1330 °C), α' - ErC_2 (at least at 1145 – 1165 °C, ?), β - ErC_2 (from 1330 °C to at least 2230 – 2280 °C, melt. point), C Eutectic β - ErC_2 –C (~ 2220 – 2290 °C) No diagram plot	Er carbides are formed directly from the elements at 1500 – 1600 °C in vacuum (or reductive conditions). For diffusion rate in the system at various temp. see Addendum.	[238, 241]
C–Tm	α -Tm, β -Tm, Tm_{3-x}C (or TmC_{1-x} , homog. range— ~ 25 – 33 at.% C), $\text{Tm}_{15}\text{C}_{19}$, Tm_3C_4 (?), Tm_4C_7 (?), Tm_2C_3 (metastable, ?), α - TmC_2 ($< \sim 1120$ – 1370 °C), α' - TmC_2 (?), β - TmC_2 (from ~ 1120 – 1370 °C to ~ 2130 – 2230 °C, melt. point, ?), TmC_3 , intercalated fullerenes ($\text{Tm}(\text{C}_{82})$ and other), C Eutectic β - TmC_2 –C (~ 2225 – 2265 °C) No diagram plot	Tm carbides are formed directly from the elements at 1550 – 1600 °C in vacuum (or reductive conditions).	[238, 241, 940]

(continued)

Table 2.13 (continued)

System	Type of phase diagram (constituent phases, temperatures and compositions of transformations)	Character of chemical interaction	References
C–Yb	α -Yb, β -Yb, γ -Yb, Yb_{3-x}C (YbC_{1-x} , homog. range— ~ 25–39 at.% C, at least <1500 °C, ?), $\text{YbC}_{0.95}$ (?), α - YbC_{1-x} (at least <1500 °C, ?), $\text{YbC}_{1.25+y}$ (homog. range— ~ 56.9–58.8 at.% C, ?), $\text{Yb}_{15}\text{C}_{19}$, $\text{Yb}_3\text{C}_{4\pm x}$ (at least <1500 °C), Yb_2C_3 (meta- stable, ?), α - YbC_2 (at least <1500 °C), β - YbC_2 (?), layered compounds ($\text{YbC}_{6\pm x}$, $\text{YbC}_{12\pm x}$ and other), intercalated fullerenes ($\text{Yb}_{2.75}(\text{C}_{60})$ and other), C Eutectic β - YbC_2 –C (~ 2175–2255 °C)	Yb carbides are formed directly from the elements at 800–900 °C in vacuum (or reductive conditions).	[238, 241, 938, 941–942]
C–Lu	α -Lu, β -Lu, Lu_{3-x}C (or LuC_{1-x} , ?), $\text{Lu}_{15}\text{C}_{19}$, Lu_3C_4 (?), Lu_4C_7 (?), Lu_2C_3 (metastable, ?), α - LuC_2 (<~ 1390–1520 °C), β - LuC_2 (from ~ 1390– 1520 °C to melt. point, ?), C Eutectic β - LuC_2 –C (~ 2210–2250 °C) No diagram plot	Lu carbides are formed directly from the elements at 1650–1750 °C in vacuum (or reductive conditions).	[238, 241]
<i>Actinides</i>			
C–Ac	No data	—	—

(continued)

Table 2.13 (continued)

System	Type of phase diagram (constituent phases, temperatures and compositions of transformations)	Character of chemical interaction	References
C–Th	<p>α-Th, β-Th, ThC_{1±x} (α-Th–ThC_{1±x} and ThC_{1±x}–γ-ThC_{2–x} continuous solid solutions (with miscibility gaps), <2500–2625 °C, congruent melt. point corresp. to \simThC_{1.0}, homog. ranges—\sim0–7 at.% C and \sim40–50 at.% C at 720–920 °C, \sim22–66 at.% C at 2000 °C), Th₂C₃ (metastable, ?), α-ThC_{2–x} (<1255–1440 °C, homog. range—\sim64–66 at.% C), β-ThC_{2–x} (from 1255–1440 °C up to 1470–1495 °C, homog. range—\sim62.5–66.0 at.% C at 1440–1450 °C), γ-ThC_{2–x} (from 1470–1495 °C up to \sim2550–2670 °C, congruent melt. point corresp. to \simThC_{1.9}), C</p> <p>Continuous solid solution α-Th–ThC_{1±x} (homog. range— from \sim8 at.% C up to \sim51 at.% C at 1570 °C; miscibility gap in the solid state: critical point— \sim1140–1570 °C at \sim30 at.% C, ranges from \sim6 at.% C to \sim40 at.% C at 900 °C)</p> <p>Continuous solid solution ThC_{1±x}–γ-ThC_{2–x} (min. melt point 2430 °C corresp. to \simThC_{1.2}, homog. range— from \sim15 at.% C up to \sim66 at.% C at 1800 °C, miscibility gap in the solid state: critical point— 1850 °C at \sim55 at.% C, ranges from \sim50 at.% C to \sim62 at.% C at 1470 °C)</p> <p>ThC_{1±x} + β-ThC_{2–x} miscibility gap in the solid state (1255–1470 °C, ranges from \sim50 at.% C to \sim63 at.% C at 1255 °C)</p> <p>ThC_{1±x} + α-ThC_{2–x} miscibility gap in the solid state (<1255 °C, ranges from \sim50 at.% C to \sim67 at.% C at 1000 °C)</p> <p>Eutectic γ-ThC_{2–x}–C (\sim2445–2500 °C, \sim70 at.% C)</p>	<p>Max. solid solubilities of C in Th are \sim66.0 at.% (α-Th) at 1500–2400 °C and \sim9.2 at.% (β-Th) at 1710 °C. Th carbides are formed directly from the elements at 1700–1900 °C in vacuum (or reductive conditions). For diffusion rate in the system at various temp. see Addendum.</p>	[138, 238, 241–244, 248, 492]

(continued)

Table 2.13 (continued)

System	Type of phase diagram (constituent phases, temperatures and compositions of transformations)	Character of chemical interaction	References
C–Pa	α -Pa, β -Pa, PaC, PaC ₂ , C No diagram plot	–	[241]
C–U	α -U, β -U, γ -U, UC _{1±x} (or δ -phase, <~2490–2590 °C, congruent melt. point corresp. to ~UC _{0.99} , invariable compos.—~50 at.% C at temp. <~1000 °C, homog. range—~47–56.5 at.% C at 2050 °C), ζ -U ₂ C ₃ (from ~860 °C (?) to ~1730–1825 °C, invariable compos.), α -UC _{2-x} (from ~1475–1515 °C to ~1760–1795 °C, homog. range—63.9–65.0 at.% C at 1755–1775 °C, max. C content corresp. to UC _{1.94}), β -UC _{2-x} (or δ -phase, <~2435–2585 °C, congruent melt. point corresp. to ~UC _{1.94±1.96} , represents the UC _{1±x} phase in equilibrium with graphite), C Continuous solid solution UC _{1±x} – β -UC _{2-x} (min. melt point ~2405 °C corresp. to ~UC _{1.5} , homog. range—from ~47 at.% C to 66.7 at.% C at 2200 °C; miscibility gap in the solid state: critical point—~2050–2105 °C at ~56.5 at.% C, ranges—from 52.8 at.% C to 62.3 at.% C at 1820 °C) Eutectic γ -U–UC _{1±x} (~1115–1120 °C, ~1 at.% C) Eutectic β -UC _{2-x} –C (~2400–2555 °C, ~67 at.% C)	The solubility of C in α -U at 660 °C is <0.006 at.%, in β -U at 770 °C–0.02 at.% and in γ -U at 1115–1120 °C–0.22–0.37 at.% C. The solubility of C in molten U is obeyed the rule: $\lg x$ (in at.% C) = 2.87–4000/T (in K). UC _{1±x} and UC _{2-x} are formed directly from the elements at 1700–1900 °C in vacuum (or reductive conditions). The UC _{1±x} – β -UC _{2-x} continuous solid solution alloys cannot be fixed by tempering, in the contrast to the U–UC _{1±x} solid solution alloys. At the temp. range of 1300–1600 °C molten U wets UC _{1±x} perfectly, the wetting contact angles in the U–UC _{1±x} are close to 40–60°. For diffusion rate in the system at various temp. see Addendum.	[138, 238, 241–244, 248, 492, 910]

(continued)

Table 2.13 (continued)

System	Type of phase diagram (constituent phases, temperatures and compositions of transformations)	Character of chemical interaction	References
C–Np	α -Np, β -Np, γ -Np, NpC_{1-x} (homog. range— ~ 45 – 49 at.% C at 950 °C), Np_2C_3 , NpC_2 , C No diagram plot	Np carbides are formed directly from the elements at 1700 – 1900 °C in vacuum (or reductive conditions).	[238, 241]
C–Pu	α -Pu, β -Pu, γ -Pu, δ -Pu, δ' -Pu, ε -Pu, Pu_3C_2 (<575 °C, incongruent melt. point, invariable compos.), PuC_{1-x} ($<\sim 1655$ °C, incongruent melt. point corresp. to $\text{PuC}_{0.89}$, homog. range— ~ 44.5 – 47.5 at.% C at 400 – 600 °C and— ~ 38 – 47.5 at.% C at 630 – 640 °C), $\text{Pu}_2\text{C}_{3-x}$ (<2020 – 2050 °C, incongruent melt. point, homog. range— 58.5 – 60 at.% C at 610 °C and ~ 57 – 61 at.% C at 1660 °C), α - PuC_2 ($<\sim 1660$ °C, invariable compos., metastable, ?), β - PuC_2 (from ~ 1660 °C to ~ 2200 – 2250 °C, incongruent melt. point, invariable compos.), C Eutectic (degenerative) ε -Pu– PuC_{1-x} (~ 634 °C, ?)	The presence of C decreases the melt. point of Pu from 640 °C to 634 °C, but slightly affects the temp. of polymorphic transitions. At 700 – 900 °C the solubility of C in molten Pu is obeyed the rule: $\lg x$ (in at.% C) = 2.5 – $2300/T$ (in K). Pu carbides are formed directly from the elements at 1500 – 1700 °C in vacuum (or reductive conditions).	[138, 238, 241–242, 244, 248, 492, 998]
C–Am	α -Am, β -Am, γ -Am, Am_2C_3 , AmC_2 , C No diagram plot	–	[241]
C–Cm	No data	–	–

(continued)

Table 2.13 (continued)

System	Type of phase diagram (constituent phases, temperatures and compositions of transformations)	Character of chemical interaction	References
<i>Group 4</i>			
C–Ti	α -Ti, β -Ti, $\text{Ti}_{2\pm x}\text{C}$ ($< \sim 1900$ °C, ?), $\text{Ti}_3\text{C}_{2\pm x}$ (?), $\text{Ti}_6\text{C}_{5\pm x}$ (?), TiC_{1-x} ($< \sim 3065$ – 3080 °C, congruent melt. point corresp. to $\sim \text{TiC}_{0.77 \div 0.80}$, homog. range— ~ 38 – 50 at.% C at 2780 °C, ~ 28.5 – 49.0 at.% C at 1650 °C and ~ 34.0 – 48.5 at.% C at 920 °C), C Order–disorder transformations (~ 590 – 785 °C (?), in TiC_{1-x} homog. range ~ 31.5 – 39.0 at.% C (?); $\text{Ti}_{2\pm x}\text{C}$, $\text{Ti}_3\text{C}_{2\pm x}$ and $\text{Ti}_6\text{C}_{5\pm x}$ —the ordered phases of TiC_{1-x} , ?) Eutectic β -Ti– TiC_{1-x} (~ 1640 – 1655 °C, ~ 1.5 – 4.4 at.% C) Eutectic TiC_{1-x} –C (~ 2775 – 2785 °C, ~ 63 at.% C)	The presence of C decreases the melt. point of Ti from 1670 °C to ~ 1640 – 1655 °C and increases the temp. of α -Ti \rightarrow β -Ti transition from 882 – 920 °C. At the β -Ti– TiC_{1-x} eutectic temp. the solubility of C in β -Ti is 0.55 at.% C. At 920 °C the solubility of C in β -Ti is 0.5 at.% C and in α -Ti– 2 at.% C. In the wide ranges of temp. the solubility of C is obeyed the rules: $\lg x$ (in at.% C) = 1.74 – $1800/T$ (in K) for α -Ti (600 – 900 °C) and $\lg x$ (in at.% C) = 1.40 – $2100/T$ (in K) for β -Ti (920 – 1645 °C). TiC_{1-x} is formed directly from the elements at 1700 – 2100 °C in vacuum (or reductive conditions). The reaction between C and Ti (in powdered mixtures) relates to the gasless combustion or solid flame phenomena, which are termed the self-propagating high temp. synthesis (SHS). The reaction is passing in the narrow layer called the combustion zone, which travels through the initial mixture by a wave spreading mechanism due to the great exothermic heat effect of the reaction and heat transfer of reagents. The reaction converts C and Ti to the carbide phase (products) after the only local initial ignition of the reaction.	[138, 238, 241–244, 248– 252, 411, 530, 579, 594, 600, 606, 904, 1018]

(continued)

Table 2.13 (continued)

System	Type of phase diagram (constituent phases, temperatures and compositions of transformations)	Character of chemical interaction	References
C–Zr	α -Zr, β -Zr, $Zr_{2\pm x}C$ (?), $Zr_3C_{2\pm x}$ (?), $Zr_6C_{5\pm x}$ (?), ZrC_{1-x} ($< \sim 3420$ – 3540 °C, congruent melt. point corresp. to $\sim ZrC_{0.80 \div 0.86}$, homog. range— ~ 38.5 – 49.0 at.% C at 2910 °C, ~ 36 – 50 at.% C at 1820 °C and ~ 37 – 50 at.% C at 870 °C), C Order–disorder transformations (max. temp. ~ 900 – 945 °C, in ZrC_{1-x} homog. range ~ 26 – 49 at.% C (?), $Zr_{2\pm x}C$, $Zr_3C_{2\pm x}$, $Zr_6C_{5\pm x}$ —the ordered phases of ZrC_{1-x} , ?) Eutectic β -Zr– ZrC_{1-x} (~ 1805 – 1835 °C, ~ 1.4 – 3.0 at.% C) Eutectic ZrC_{1-x} –C (~ 2850 – 2930 °C, ~ 64.5 – 65.0 at.% C)	<p>During the SHS extremely high temp. of heating are reached, so the necessary condition for its realisation is the high thermal stability of products. 2D-nano-sheets Ti_xC_y (graphene-like nanocrystals) is synthesized by the exfoliation of Ti_3AlC_2 in hydrofluoric acid. The wetting angle of molten pure Ti: 0° (vacuum, 1725 °C); for Ti containing alloys, see Table 2.16. For diffusion rate in the system at various temp. see Addendum.</p> <p>The presence of C decreases the melt. point of Zr from 1855 °C to ~ 1805–1835 °C and increases the temp. of α-Zr \rightarrow β-Zr transition from 863 °C to ~ 870–885 °C. At this temp. the solubility of C in α-Zr is ~ 3 at.%. At the β-Zr–ZrC_{1-x} eutectic temp. the solubility of C in β-Zr is ~ 1 at.% C. At lower temp. the solubility of C in β-Zr decreases to ~ 0.8 at.% at 1400 °C, ~ 0.5 at.% at 1330 °C and ~ 0.3 at.% at 1175 °C. At 1000–1800 °C the solubility of C in β-Zr is obeyed the rule: $\lg x$ (in at.% C) = $2.2 - 3800/T$ (in K) ZrC_{1-x} is formed directly from the elements at 1800–2200 °C in vacuum (or reductive conditions). The reaction between C and Zr (in powdered mixtures) relates to the SHS type (see special notes for the C–Ti system). The wetting angle of molten pure Zr: 0° (vacuum, 1900 °C). For diffusion rate in the system at various temp. see Addendum.</p>	<p>[138, 238, 241–244, 248–256, 530, 579, 1017]</p>

(continued)

Table 2.13 (continued)

System	Type of phase diagram (constituent phases, temperatures and compositions of transformations)	Character of chemical interaction	References
C–Hf	<p>α-Hf, β-Hf, $\text{Hf}_3\text{C}_{2\pm x}$ (?), $\text{Hf}_6\text{C}_{5\pm x}$ (?), HfC_{1-x} ($< \sim 3930$–3960 °C, congruent melt. point corresp. to $\sim \text{HfC}_{0.89 \pm 0.94}$, homog. range—$\sim 37.0$–$49.5$ at.% C at 3180 °C, ~ 34.0–49.5 at.% C at 2360 °C and ~ 38.0–49.5 at.% C at 1200 °C), C</p> <p>Order–disorder transformations (max. temp. ~ 505–535 °C, in HfC_{1-x} homog. range ~ 38–49 at.% C (?), $\text{Hf}_3\text{C}_{2\pm x}$, $\text{Hf}_6\text{C}_{5\pm x}$—the ordered phases of HfC_{1-x} ?)</p> <p>Eutectic α-Hf–β-Hf (~ 2180–2220 °C, ~ 1.5 at.% C)</p> <p>Peritectic α-Hf (~ 2240–2360 °C, ~ 14–15 at.% C)</p> <p>Eutectic HfC_{1-x}–C (~ 3150–3185 °C, ~ 65–68 at.% C)</p>	<p>The presence of C decreases the melt. point of Hf from 2231 °C to ~ 2180–2220 °C. C stabilizes α-Hf and increases the temp. of α-Hf \rightarrow β-Hf transition from 1743 °C to ~ 2240–2360 °C. In α-(Hf,C)–β-(Hf,C) eutectic alloy the solubility of C in β-Hf is ~ 0.6–1.0 at.% and in α-Hf—~ 2–3 at.%. The max. solid solubility of C in α-Hf is ~ 14–15 at.% (at 2240–2360 °C). HfC_{1-x} is formed directly from the elements at 1900–2300 °C in vacuum (or reductive conditions). The reaction between C and Hf (in powdered mixtures) relates to the SHS type (see special notes for the C–Ti system). For diffusion rate in the system at various temp. see Addendum.</p>	<p>[138, 238, 241–244, 248–252, 254, 257, 579, 1006]</p>
<i>Group 5</i>			
C–V	<p>V, V_{64}C (?), V_5C (?), α-V_{2+x}C ($< \sim 800$–850 °C, homog. range—~ 31–33 at.% C), β-V_{2+x}C (from ~ 800–850 °C to ~ 2185–2190 °C, incongruent melt. point, homog. range—~ 26.5–36.5 at.% C at 1650 °C), β'-V_{2+x}C ($< \sim 1500$–1610 °C, homog. range—27.5–32.0 at.% C), ζ-V_4C_{3-x} (or V_3C_2, or ξ-phase, $< \sim 1320$–1700 °C, ~ 37.7–42.8 at.% C), $\text{V}_6\text{C}_{5\pm x}$ ($< \sim 1180$–1260 °C, homog. range—~ 43–45.5 at.% C), $\text{V}_8\text{C}_{7\pm x}$ ($< \sim 1080$–1160 °C, homog. range—~ 46.3–48.1 at.% C), VC_{1-x} ($< \sim 2625$–2800 °C, congruent melt. point corresp. to $\sim \text{VC}_{0.75 \pm 0.86}$, homog. range—$\sim 42.5$–$46.0$ at.% C at 2650–2670 °C, ~ 37–47 at.% C at 2185 °C and ~ 40.5–48.0 at.% C at 1320 °C, max. C content corresp. to $\sim \text{VC}_{0.88 \pm 0.89}$), C</p>	<p>The solubility of C in V: 0.13 at.% at 700 °C, 0.5 at.% at 1100 °C and 2.3–2.6 at.% at 1600 °C. At 1500–1600 °C the solubility of C in V is obeyed the rule: $\lg x$ (in at.% C) = 7.4–$12,800/T$ (in K)</p> <p>The max. solubility of C in V is ~ 4.3–5.5 at.% (at V–β-V_{2+x}C eutectic temp.). V carbides are formed directly from the elements at 1100–1200 °C in vacuum (or reductive conditions). The reaction between C and V (in powdered mixtures) relates to the SHS type (see special notes for the C–Ti system). For diffusion rate in the system at various temp. see Addendum.</p>	<p>[241–244, 248–251, 258–260, 579, 720, 723, 1000, 1020]</p>

(continued)

Table 2.13 (continued)

System	Type of phase diagram (constituent phases, temperatures and compositions of transformations)	Character of chemical interaction	References
C–Nb	Eutectic V– β -V _{2±x} C (1650 °C, 15 at.% C) Eutectic VC _{1-x} -C (~2625–2670 °C, ~49.5–53.5 at.% C)		
	Nb, α -Nb ₂ C (<~1200–1230 °C, invariable compos.), β -Nb _{2+x} C (from ~1200–1230 °C to ~2450–2575 °C, homog. range—~28–33 at.% C at 2350 °C), γ -Nb _{2±x} C (from ~2450–2575 °C to ~3035–3090 °C, incongruent melt. point, homog. range— ~27–35 at.% C), ζ -Nb ₄ C _{3-x} (or Nb ₃ C _{2+x} , <~1575–1750 °C, homog. range—~40.0–41.5 at.% C), Nb ₆ C _{5±x} (ordered, <~1050–1320 °C, homog. range—~42–49 at.% C), NbC _{1-x} (<~3600–3615 °C, congruent melt. point corresp. to ~NbC _{0.79÷0.84} , homog. range—~38–49 at.% C at 3300 °C, 29.2–49.6 at.% C at 2600 °C, 37.6–49.8 at.% C at 2350 °C and ~41–50 at.% C at 1200 °C, max. C content corresp. to ~NbC _{0.99}), C Eutectic Nb– β -Nb _{2+x} C (~2335–2355 °C, ~10.5–10.7 at.% C) Eutectic NbC _{1-x} -C (~3250–3305 °C, ~58–60 at.% C)	The solubility of C in Nb: 0.1 at.% at 1200 °C, 0.26 at.% at 1500 °C and ~5.5–7.2 at.% at 2230–2350 °C. At 1500–2200 °C the solid solubility of C in Nb is obeyed the rule: $\lg x$ (in at.% C) = $3.65 - 7600/T$ (in K) The solubility of Nb in graphite is ≤0.001 at.% C. Nb carbides are formed directly from the elements at 1300–1400 °C in vacuum (or reductive conditions). The reaction between C and Nb (in powdered mixtures) relates to the SHS type (see special notes for the C–Ti system). The limiting wetting angle of molten pure Nb: 60° (vacuum, 2700 °C); for Nb containing alloys, see Table 2.16. For diffusion rate in the system at various temp. see Addendum.	[138, 241–244, 248–251, 254, 258, 260–262, 530, 579, 719– 720]

(continued)

Table 2.13 (continued)

System	Type of phase diagram (constituent phases, temperatures and compositions of transformations)	Character of chemical interaction	References
C-Ta	Ta, Ta ₆₄ C (?), α -Ta _{2+x} C ($< \sim 1930$ – 2270 °C, homog. range— ~ 31.0 – 32.5 at.% C at 1930 °C), β -Ta _{2+x} C (from ~ 1930 – 2270 °C to ~ 3330 – 3400 °C, incongruent melt. point, homog. range— ~ 26 – 35 at.% C at 2830 – 2850 °C), ϵ -Ta ₃ C _{2+x} (~ 2000 °C, invariable compos., ?), ζ -Ta ₄ C _{3-x} ($0.44 \leq x \leq 0.53$, or ζ -TaC _{1-x} , $< \sim 2170$ – 2800 °C, homog. range— ~ 38.0 – 42.8 at.% C), Ta ₆ C _{5+x} (ordered, < 1160 °C), TaC _{1-x} (< 3985 – 4000 °C, congruent melt. point corresp. to \sim TaC _{0.88-0.89} , homog. range— 37.9 – 49.9 at.% C at 3450 °C, 36.5 – 49.9 at.% C at 3340 °C, 39.6 – 49.9 at.% C at 2850 °C and 41.5 – 49.9 at.% C at 1930 °C, max. C content corresp. to \sim TaC _{0.99}), C Eutectic Ta– β -Ta _{2+x} C (~ 2800 – 2860 °C, ~ 12.0 – 12.3 at.% C) Eutectic TaC _{1-x} –C (~ 3400 – 3450 °C, ~ 61 at.% C)	The max. solubility of C in Ta is ~ 7.0 – 7.5 at.% (at Ta– β -Ta _{2+x} C eutectic temp.). The solid solu- bility of C in Ta is obeyed the rules: $\ln x$ (in at.% C) = $8.23 - 16,700/T$ (in K) at 1500 – 1950 °C and $\ln x$ (in at.% C) = $5.18 - 9900/T$ (in K) at 1950 – 2640 °C. Ta carbides are formed directly from the elements at 1300 – 1500 °C in vacuum (or reductive conditions). The reaction between C and Ta (in powdered mixtures) relates to the SHS type (see special notes for the C–Ti system). For diffusion rate in the system at various temp. see Addendum.	[138, 241–244, 248–251, 254, 260, 579, 720, 722–723]
<i>Group 6</i>			
C-Cr	Cr, Cr ₂₃ C _{6+x} ($< \sim 1575$ – 1610 °C, incongruent melt. point corresp. to CrC _{0.27} , homog. range— ~ 20 – 21 at.% C at 1530 °C, ~ 20 – 22 at.% C at 1200 °C), Cr ₃ C (metastable, ?), Cr ₇ C _{3+x} ($< \sim 1765$ – 1790 °C, congruent melt. point corresp. to CrC _{0.43} , homog. range— ~ 29.5 – 31.5 at.% C at 1730 °C and ~ 28.5 – 31 at.% C at 1575 °C), Cr ₂ C (?), Cr ₃ C _{2-x} (< 1810 – 1830 °C, incongruent melt. point corresp. to CrC _{0.67} ,	The max. solid solubility of C in Cr is ~ 0.3 – 1.9 at.% C (?) at 1530 – 1580 °C. Cr carbides are formed directly from the elements at 1400 – 1800 °C in vacuum (or reductive conditions). For diffusion rate in the system at various temp. see Addendum.	[138, 241–242, 244, 248–250, 394, 417, 579, 841]

(continued)

Table 2.13 (continued)

System	Type of phase diagram (constituent phases, temperatures and compositions of transformations)	Character of chemical interaction	References
C–Mo	<p>homog. range—~ 39.7–40.0 at.% C at 1730 °C and ~ 39.8–40.0 at.% C at 1400 °C), CrC (metastable, ?), C</p> <p>Eutectic $\text{Cr} - \text{Cr}_{23}\text{C}_{6\pm x}$ (~ 1530–1580 °C, ~ 14–14.5 at.% C)</p> <p>Eutectic $\text{Cr}_7\text{C}_{3\pm x} - \text{Cr}_3\text{C}_{2-x}$ (~ 1725–1740 °C, 32.6 at.% C)</p>	<p>The max. solid solubility of C in Cr is ~ 0.3–1.9 at.% C (?) at 1530–1580 °C. Cr carbides are formed directly from the elements at 1400–1800 °C in vacuum (or reductive conditions). For diffusion rate in the system at various temp. see Addendum.</p>	
	<p>Mo, $\alpha\text{-Mo}_{2+x}\text{C}$ (or $\beta'\text{-Mo}_{2+x}\text{C}$, <1430–1440 °C, homog. range—~ 31.3–33.3 at.% C at 1230 °C), $\alpha'\text{-Mo}_{2+x}\text{C}$ (or $\varepsilon\text{-Mo}_{2+x}\text{C}$, ordered), $\beta\text{-Mo}_{2\pm x}\text{C}$ (from ~ 1200–1650 °C to ~ 2520–2540 °C, congruent melt. point corresp. to $\text{MoC}_{0.52}$, homog. range—26.0–35.7 at.% C at 2205 °C, ~ 30.0–35.5 at.% C at 1655 °C and ~ 31–34 at.% C at 1430 °C), $\eta\text{-MoC}_{1-x}$ (or $\text{Mo}_3\text{C}_{2-x}$, from ~ 1650–1655 °C to ~ 2530–2560 °C, congruent melt. point corresp. to $\text{MoC}_{0.61}$, homog. range—36.5–39.2 at.% C at 2510 °C and ~ 38.5–39.5 at.% C at 1960 °C, invariable compos. ~ 39 at.% C at temp. <1800 °C), $\alpha\text{-MoC}_{1-x}$ (from ~ 1950–1960 °C to ~ 2530–2650 °C, congruent melt. point corresp. to $\text{MoC}_{0.72}$, homog. range—~ 41.0–43.1 at.% C at 2585 °C, ~ 39.6–43.0 at.% C at 2545 °C and ~ 39.8–42.2 at.% C at 2200 °C), $\gamma\text{-MoC}$ (<1200–1220 °C, invariable compos. ~ 50 at.% C), C</p> <p>Eutectic $\text{Mo} - \beta\text{-Mo}_{2\pm x}\text{C}$ (~ 2200–2205 °C, ~ 16.7–18.0 at.% C)</p> <p>Eutectic $\beta\text{-Mo}_{2\pm x}\text{C} - \eta\text{-MoC}_{1-x}$ (~ 2510 °C, ~ 36 at.% C, ?)</p> <p>Eutectic $\alpha\text{-MoC}_{1-x} - \text{C}$ (~ 2584–2589 °C, 45 at.% C)</p>	<p>The max. solubility of C in Mo is ~ 1.1–1.3 at.% C at 2200–2205 °C. At 1330–2205 °C the solubility of C in Mo is obeyed the rule:</p> $\ln x \text{ (in at.\% C)} = 3.97 - 21,000/T \text{ (in K)}$ <p>Mo carbides are formed directly from the elements at 1200–1400 °C in vacuum (or reductive conditions). Under specific pressure 5 MPa the diffusion welded joint between $\beta\text{-Mo}_{2\pm x}\text{C}$ and Mo is produced at 1600 °C (5–15 min exposure). For diffusion rate in the system at various temp. see Addendum.</p>	[138, 241–244, 248–250, 260, 579, 723]

(continued)

Table 2.13 (continued)

System	Type of phase diagram (constituent phases, temperatures and compositions of transformations)	Character of chemical interaction	References
C-W	<p>W, α-W_{2+x}C (or β'-W_{2+x}C, from 1250 °C to ~2100–2140 °C, homog. range—~30–33 at.% C), β-W_{2+x}C (or β'-W_{2+x}C, from ~2100–2140 °C to ~2320–2490 °C, homog. range—~29.6–33.4 at.% C), γ-W_{2+x}C (or β-W_{2+x}C, from ~2320–2490 °C to ~2775–2795 °C, congruent melt. point corresp. to WC_{0.43 ÷ 0.45}, homog. range—~27.5–35.5 at.% C at 2735 °C, ~26–35 at.% C at 2710 °C and ~28–34 at.% C at 2530 °C), γ-WC_{1-x} (or α-WC_{1-x}, β-WC_{1-x}, from ~2530–2535 °C to ~2745–2785 °C, congruent melt. point corresp. to WC_{0.64}, homog. range—~37.4–40.0 at.% C at 2720 °C), δ-WC_{1±x} (or α-WC_{1±x}, <~2745–2785 °C, incongruent melt. point corresp. to WC_{1.00 ÷ 1.01}, homog. range—~49.6–50.6 at.% C at 2720 °C, ~49.9–50.6 at.% C at 2530 °C and ~50.1–50.6 at.% C at 2000 °C, invariable compos. at temp. <2000 °C), C</p> <p>Eutectic W-γ-W_{2+x}C (~2710–2715 °C, ~22–25 at.% C)</p> <p>Eutectic γ-W_{2+x}C-γ-WC_{1-x} (~2735–2760 °C, ~36.0–36.5 at.% C)</p> <p>Eutectic γ-WC_{1-x}-δ-WC_{1±x} (~2720–2760 °C, ~36–41 at.% C)</p> <p>Phase diagram data available in literature are controversial</p>	<p>The max. solubility of C in W is <1 at.% C (at 2710–2715 °C). At 1400–2600 °C the solubility of C in W is obeyed the rule: $\ln x$ (in at.% C) = 4.67–15,000/T (in K)</p> <p>W carbides are formed directly from the elements at 1400–1600 °C in vacuum (or reductive conditions). For diffusion rate in the system at various temp. see Addendum.</p>	<p>[138, 241–242, 244, 248–250, 263, 419, 579, 603, 721, 1001, 1005]</p>

(continued)

Table 2.13 (continued)

System	Type of phase diagram (constituent phases, temperatures and compositions of transformations)	Character of chemical interaction	References
<i>Group 7</i>			
C–Mn	α -Mn, β -Mn, γ -Mn, δ -Mn, ε -Mn _{4±x} C (from ~ 990 °C to ~ 1305 – 1310 °C, incongruent melt. point corresp. to MnC _{0.32±0.39} , homog. range— ~ 13 – 28 at.% C), Mn ₂₃ C ₆ ($< \sim 1020$ – 1035 °C, invariable compos.), Mn ₁₅ C ₄ (or Mn ₁₁ C ₃ (?), from ~ 850 °C to 1020 °C, invariable compos. ~ 21.1 – 21.5 at.% C, ?), Mn ₃ C (from ~ 970 °C to ~ 1050 – 1060 °C, invariable compos.), Mn ₅ C ₂ (from ~ 425 °C (?) to ~ 1090 – 1170 °C, invariable compos. ~ 28.5 – 28.6 at.% C), Mn ₇ C ₃ ($< \sim 1330$ – 1340 °C, incongruent melt. point corresp. to MnC _{0.43} , invariable compos. ≤ 30 at.% C), C	The max. solid solubility of C in Mn modifications: α -Mn— ~ 6.5 – 7.0 at.% (at ~ 770 – 900 °C), β -Mn— ~ 1.0 – 2.5 at.% (at ~ 820 – 900 °C), γ -Mn— ~ 13 – 16 at.% (at ~ 990 – 1240 °C), and δ -Mn— ~ 1 – 2 at.% (at ~ 1220 – 1240 °C). Mn carbides are formed directly from the elements at 1200 – 1300 °C in non-oxidative conditions.	[138, 238, 241, 244, 264]
C–Tc	Tc, TcC _{1–x} (or Tc _{3±x} C, ?), C Eutectic TcC _{1–x} –C (~ 1650 – 1885 °C, ~ 25 – 33 at.% C, ?) Eutectic Tc–C (1660 °C, ~ 30 at.% C, ?) Phase diagram data available in literature are controversial	At 910 °C the solubility of C in Tc is ~ 1 at.% C.	[241, 391, 840, 943]
C–Re	Re, metastable carbides (?), C Eutectic Re–C (~ 2480 – 2505 °C, ~ 16.5 – 23 at.% C)	The max. solubility of C in Re is ~ 11 – 17 at.% C at the Re–C eutectic temp. The solubility decreases with temp. decline and amounts ~ 4.2 at.% C at 1800 °C. Metastable Re carbides are synthesized at ultra-high pressures (6 – 18 GPa).	[138, 241, 265–266]

(continued)

Table 2.13 (continued)

System	Type of phase diagram (constituent phases, temperatures and compositions of transformations)	Character of chemical interaction	References
<i>Group 8</i>			
C–Fe	α -Fe, γ -Fe, δ -Fe, metastable compounds Fe_4C , θ - Fe_3C ($< \sim 1207$ – 1252 °C), χ - Fe_5C_2 , α - Fe_7C_3 , β - Fe_7C_3 , η - Fe_2C , ε - Fe_2C and α - Fe_2C , C (see refs. for details) Eutectic γ -Fe–C (1153 °C, 17.1 at.% C) Metastable eutectic γ -Fe– Fe_3C (1147 °C, 17.3 at.% C)	The max. solid solubility of C in Fe modifications: α -Fe– ~ 0.090 – 0.096 at.% (at 727–740 °C), γ -Fe– ~ 8.9 – 9.1 at.% (at 1147–1153 °C) and δ -Fe– ~ 0.4 – 0.5 at.% (at 1493–1499 °C). The presence of various contaminations decreases the γ -Fe–C eutectic temp. (see refs. for details). Molten Fe dissolves considerable amounts of C; the solubility of C increases with increasing temp. linearly and reaches >24 at.% C at 2000 °C. Fe carbides are not formed directly from the elements. The limiting wetting angle of molten pure Fe is 60° (vacuum, 1425–1540 °C), 0° (vacuum, ≥ 1550 °C), 37° (H_2 , 1550 °C); for Fe–4.3 at.% C alloy: 90° (vacuum, 1540 °C); for Fe–5 at.% C alloy: 130° (vacuum, 1540 °C). For diffusion rate in the system at various temp. see Addendum.	[138, 238, 241, 244, 267–268, 530, 907]
C–Ru	Ru, metastable carbides (?), C Eutectic Ru–C (~ 1940 – 1965 °C, ~ 18 at.% C)	The max. solubility of C in solid Ru is ~ 3 – 4 at.% C (at eutectic temp.). At 1000 °C the solubility amounts ~ 0.4 at.% C. At 800–1200 °C the solubility of C in Ru is obeyed the rule: $\lg x$ (in at.% C) = $3.02 - 4438/T$ (in K) The solubility of C in liquid Ru at boil. point (4150 °C) is ~ 30 at.% C.	[238, 241, 244, 945]
C–Os	Os, metastable carbides (?), C Eutectic Os–C (~ 2730 °C, ~ 10 – 17 at.% C)	The max. solubility of C in solid Os is ~ 2 at.% C (~ 2730 °C); in liquid Os at boil. point (5010 °C) it is 39.1–39.7 at.% C.	[138, 238, 241, 244]

(continued)

Table 2.13 (continued)

System	Type of phase diagram (constituent phases, temperatures and compositions of transformations)	Character of chemical interaction	References
<i>Group 9</i>			
C–Co	ε -Co, α -Co, metastable compounds Co_3C and Co_2C , C Eutectic α -Co–C (~ 1310 – 1320 °C, ~ 11.2 – 12.5 at.% C) Metastable eutectic α -Co– Co_3C (~ 1190 °C, ~ 17.4 – 21.0 at.% C) Gas-eutectic Co–C (gas–liquid-graphite non-variant equilibrium, ~ 2415 °C, ~ 38 – 39 at.% C)	The presence of C decreases the ε -Co \rightarrow α -Co transition temp. up to ~ 400 – 420 °C and magnetic (paramagnetic-ferromagnetic) phase transition up to 1035 °C. The max. solubility of C is ~ 4.1 – 4.3 at.% (in α -Co at the α -Co–C eutectic temp.) At room temp. the solubility of C in ε -Co– 0.49 at.% C. Molten Co dissolves considerable amounts of C (from ~ 12 at.% at 1320 °C to ~ 28 at.% C at 2400 – 2415 °C). Practically, no solubility of Co in graphite. Co carbides are not formed directly from the elements. The limiting wetting angle of molten pure Co is 82° (vacuum, 1425 °C); for Co– 2.7 at.% C alloy: 130° (vacuum, 1495 °C). For diffusion rate in the system at various temp. see Addendum.	[138, 238, 241, 244, 269, 530, 1021]
C–Rh	Rh, metastable carbides (?), C Eutectic Rh–C (~ 1670 – 1700 °C, ~ 15 at.% C)	The max. solubility of C in solid Rh is ~ 1.5 – 4.0 at.% C (at eutectic temp.). At 1000 °C the solubility amounts ~ 0.2 at.% C. At 800 – 1250 °C the solubility of C in Rh is obeyed the rule: $\lg x$ (in at.% C) = $3.05 - 4013/T$ (in K). The solubility of C in liquid Rh at boil. point (3700 °C) is ~ 16 at.% C.	[238, 241, 244, 945]
C–Ir	Ir, metastable carbides (?), C Eutectic Ir–C (~ 2280 – 2310 °C, ~ 21 – 29 at.% C)	The solubility of C in solid Ir is ~ 3 at.% at the eutectic temp. and ~ 0.01 at.% C at 1000 °C. At 800 – 1250 °C the solubility of C in Ir is obeyed the rule: $\lg x$ (in at.% C) = $1.45 - 3244/T$ (in K). The solubility of C in liquid Ir at boil. point (4400 °C) is ~ 31.5 at.% C.	[138, 238, 241, 244]

(continued)

Table 2.13 (continued)

System	Type of phase diagram (constituent phases, temperatures and compositions of transformations)	Character of chemical interaction	References
<i>Group 10</i>			
C–Ni	Ni, Ni ₃ C (metastable), C Eutectic Ni–C (~ 1317–1327 °C, ~ 8.5–10 at.% C) Metastable eutectic Ni–Ni ₃ C (~ 1050–1120 °C, ~ 20–23 at.% C) Gas-eutectic Ni–C (gas–liquid- graphite non-variant equi- librium, ~ 2490 °C, ~ 33–34 at.% C)	The solubility of C in solid Ni– 2.5–2.7 at.% at the eutectic temp. and 0.2–0.4 at.% C at 700 °C. It is obeyed the rule: $\lg x \text{ (in at.\% C)} = 0.2 - 2600/T$ (in K) at the range of temp. from 500 °C to 1300 °C. The max. C content in Ni metastable solid solution reaches ~ 7.4 at.% C. Molten Ni dissolves considerable amounts of C (from 10.9 at.% at 1450 °C to 25 at.% C at 2490 °C). The solubility of C in liquid Ni is obeyed the rule: $\lg x \text{ (in at.\% C)} = 1.55 - 896/T$ (in K) at the range of temp. from 1400 °C to 1700 °C. Practically, no solubility of Ni in graphite. Ni carbide is not formed directly from the elements. The wetting angle of molten pure Ni: 50° (vacuum, 1455 °C), 68° (H ₂ , 1500 °C); Ni–2.3 at.% C alloy: 145° (vacuum, 1455 °C); for other Ni containing alloys, see Table 2.16. For diffusion rate in the system at various temp. see Addendum.	[138, 238, 241, 244, 269–271, 530, 848]
C–Pd	Pd, no binary compounds, C Eutectic Pd–C (~ 1505–1515 °C, ~ 8–19 at.% C, ?)	The max. solubility of C in solid Pd is ~ 7–9 at.% C (at eutectic temp.). At 900 °C the solubility amounts ~ 3 at.% C. At 900–1500 °C the solubility of C in Pd is obeyed the rule: $\lg x \text{ (in at.\% C)} = 3.58 - 1262/T$ (in K). The solubility of C in liquid Pd at boil. point (2965 °C) is ~ 16–18 at.% C.	[138, 238, 241, 244, 944, 1022]

(continued)

Table 2.13 (continued)

System	Type of phase diagram (constituent phases, temperatures and compositions of transformations)	Character of chemical interaction	References
C–Pt	Pt, metastable compounds Pt ₇ C (?) and Pt ₂ C, C Eutectic Pt–C (~1705–1740 °C, 16.8 at.% C)	The solubility of C in solid Pt is ~2.5–4.0 at.% at the eutectic temp., ~1.7 at.% C at 1245 °C and ~0.8 at.% C at 875 °C. At 870–1250 °C the solubility of C in Pt is obeyed the rule: $\lg x \text{ (in at.\% C)} = 1.4 - 1800/T$ (in K) The solubility of C in liquid Pt at boil. point (3800 °C) is ~19 at.% C.	[138, 238, 241, 244]
<i>Group 11</i>			
C–Cu	Cu, unstable compounds (e.g. Cu ₂ C ₂ and CuC ₂), C Peritectic Cu (~1100 °C, ~0.04 at.% C)	No interaction. At melt. point (1084.87 °C) the solubility of C in solid Cu is ~100 times higher than the similar value in liquid Cu: ~0.03 and ~0.0003 at.% C, respectively. The solubility of C in liquid Cu is very low (~0.0027 at.% at 1500 °C and ~0.016 at.% C at 1700 °C). Chemical compounds, e.g. Cu ₂ C ₂ and CuC ₂ , are unstable and formed only indirectly. The wetting angle of molten pure Cu: 120–150° (high vacuum, 1090–1100 °C), 139–145° (on vitreous carbon, high vacuum, 1090–1100 °C), 157° (vacuum, 1100 °C), 150° (H ₂ , 1100 °C), 170° (vacuum, 1200 °C); for Cu containing alloys, see Table 2.16.	[138, 238, 241, 244, 530, 910]

(continued)

Table 2.13 (continued)

System	Type of phase diagram (constituent phases, temperatures and compositions of transformations)	Character of chemical interaction	References
C–Ag	Ag, unstable compounds, C Peritectic Ag (962.23 °C, 0.036 at.% C)	No interaction. At melt. point (961.93 °C) the solubility of C in solid Ag is $>10^5$ times higher than the similar value in liquid Ag (>0.035 and $<\sim 10^{-7}$ at.% C, respectively). The solubility of C in liquid Ag is very low (~ 0.01 at.% at 1660 °C and ~ 0.02 at.% C at 1940 °C). Chemical compounds, e.g. Ag_2C_2 , are unstable and formed only indirectly. The wetting angle of molten pure Ag: 135–150° (high vacuum, 970–1100 °C), 167° (vacuum, 1000 °C); for Ag containing alloys, see Table 2.16.	[138, 238, 241, 530, 910]
C–Au	Au, unstable compounds (e.g. Au_2C_2), C Eutectic Au–C (~ 1040 – 1050 °C, ~ 4.7 at.% C, ?)	The max. solubility of C in solid Au is ~ 0.080 – 0.082 at.% C (at eutectic temp.). The solubility of C in liquid Au at boil. Point (2860 °C) is ~ 4.9 at.% C. Chemical compounds, e.g. Au_2C_2 , are unstable and formed only indirectly. The wetting angle of molten pure Au on graphite single crystal–119° (vacuum, 1100 °C) and vitreous carbon—135–138° (high vacuum, 1100 °C).	[138, 238, 241, 910]
<i>Group 12</i>			
C–Zn	Zn, unstable compounds (e.g. ZnC_2), C No diagram plot	No interaction. The solubility of C in liquid Zn at boil. point is negligible (traces). Zn carbide ZnC_2 is unstable and formed only indirectly. At 600–700 °C the corrosion resistance of graphite in liquid Zn is very high. For diffusion rate in the system at various temp. see Addendum.	[138, 238, 241]

(continued)

Table 2.13 (continued)

System	Type of phase diagram (constituent phases, temperatures and compositions of transformations)	Character of chemical interaction	References
C–Cd	Cd, unstable compounds, C No diagram plot	No interaction. The solubility of C in liquid Cd at boil. point is negligible (traces). For the range of temp. from melt. point (321.1 °C) to boil. point (767 °C), theoretical estimation gives the values of C solubility in molten Cd from 3×10^{-14} to 2×10^{-7} at.% C, respectively. Carbide CdC ₂ is unstable and formed only indirectly	[138, 238, 241]
C–Hg	Hg, unstable (e.g. Hg ₂ C ₂ , HgC ₂ ,) and lamellar (e.g. HgC ₁₆ , at least at 25–105 °C, ?) compounds, C No diagram plot	No interaction. The solubility of C in liquid Hg at boil. point is negligible (traces). C is the least soluble element in Hg. For the range of temp. from melt. point (–38.8 °C) to boil. point (356.6 °C), theoretical estimation gives the values of the C solubility in molten Hg from $\sim 10^{-40}$ to 2×10^{-15} at.% C, respectively. Carbides HgC ₂ and Hg ₂ C ₂ are metastable and formed only indirectly. At 300–600 °C the corrosion resistance of graphite in liquid Hg is very high (30 days exposure with circulating Hg). The contact wetting angle of molten pure Hg: 154° (air, 20 °C).	[138, 238, 241, 530, 913–914]

(continued)

Table 2.13 (continued)

System	Type of phase diagram (constituent phases, temperatures and compositions of transformations)	Character of chemical interaction	References
<i>Group 13</i>			
C-B	β -B, B ₅₁ C (or B ₅₀ C, <1280 °C, metastable, ?), B ₅₆ C ₂ (?), B ₅₀ C ₂ (or B ₂₅ C, C ₂ B ₂ B ₄₈ , <1100–1245 °C, metastable, ?), B ₄₉ C ₃ (?), B ₂₄ C (?), B ₈ C (?), B ₁₃ C _{2±x} (<2450 °C, congruent melt. point corresp. to ~B _{5.25} C, homog. range—~11.5–20.0 at.% C at 2350 °C, ~9.5–19.7 at.% C at 1980 °C and ~12.0–13.4 at.% C at 1400 °C, ?), B ₁₃ C _{3-x} (1200–1980 °C, homog. range—18.0–18.5 at.% C at 1850 °C, ?), B _{4±x} C (<~2450 °C, congruent melt. point corresp. to ~B _{3.95–4.45} C, homog. range—~10.0–24.3 at.% C at 2375–2245 °C, ~9.3–22.3 at.% C at 2080 °C and ~9.2–21.6 at.% C at 1800 °C, ?), B ₁₁ C ₄ (?), ~BC ₂ (?), ~BC ₃ (or B _n C _m , ?), C Peritectic β -B (~2080–2105 °C, ~1.0–1.4 at.% C, ?) Eutectic β -B–B _{4±x} C (~2075–2080 °C, <1 at.% C, ?) Eutectic B _{4±x} C–C (~2245–2390 °C, ~28.5–30.0 at.% C) Phase diagram data available in literature are controversial	The solubility of C in B is negligible. The max. solubility of B in graphite is 2.3 at.% at 2390 °C. It decreases with temp. decreasing and amounts ~1 at.% C at 1700 °C. B carbides are formed directly from the elements at elevated temp. For diffusion rate in the system at various temp. see Addendum.	[138, 238, 241, 244, 252, 272–279, 321, 359, 724, 1019]

(continued)

Table 2.13 (continued)

System	Type of phase diagram (constituent phases, temperatures and compositions of transformations)	Character of chemical interaction	References
C–Al	Al, Al ₃ C ₂ (<1730 °C, ?), Al ₄ C ₃ (<~1970–2250 °C (?), incongruent melt. point, invariable compos.), C Data on phase diagram available in literature are controversial.	Practically, no solubility of C in solid Al. The solubility of C in liquid Al is extremely low: 0.7 at.% at 1200 °C, 0.31 at.% at 1000 °C and 0.22 at.% at 800 °C. Al carbide is formed directly from the elements in H ₂ at 1200–1300 °C. The wetting angle of molten pure Al in vacuum is 123° at 830 °C (initially, before reaction), ~145–160° at 875–1000 °C, ~140° at 1100 °C, ~85° at 1200 °C (5 min exposure), ~50–70° at 1200 °C (long-term exposure), 139° at 830 °C (on vitreous carbon, before reaction); pure Al wets sintered Al ₄ C ₃ with a contact angle of 55° at 1100 °C; for Al containing alloys, see Table 2.16.	[138, 238, 241, 244, 277, 278–280, 307, 530, 661, 910, 946–947, 1016]
C–Ga	Ga, no binary compounds, C No diagram plot	No interaction. Ternary compounds are formed by the interaction of transition metal carbides with Ga. At 600 °C the corrosion resistance of graphite in liquid Ga is very high. The wetting angle of molten pure Ga on vitreous carbon: 138° (high vacuum, 30 °C), 125° (high vacuum, 900 °C).	[138, 238, 278, 681, 910]
C–In	In, no binary compounds, C	No interaction. Ternary compounds are formed by the interaction of transition metal carbides with In. The wetting angle of molten pure In on graphite or vitreous carbon: 135–150° (high vacuum, 200–800 °C).	[238, 278, 681, 704, 910]
C–Tl	α -Tl, β -Tl, TIC _x (metastable, ?), C No diagram plot	No solubility of C in liquid Tl. Ternary carbides are formed by the interaction of transition metal carbides with Tl. For the range of temp. from melt. point (304 °C) to boil. point (1473 °C), theoretical estimation gives the values of C solubility in molten Tl from 4×10^{-17} to 1×10^{-4} at.% C, respectively.	[238, 241, 278, 681]

(continued)

Table 2.13 (continued)

System	Type of phase diagram (constituent phases, temperatures and compositions of transformations)	Character of chemical interaction	References
<i>Group 14</i>			
C–Si	Si, Si ₅ C ₃ (?), α -SiC (variety of polytypes), β -SiC (<~2500–2830 °C, incongruent melt. point, invariable compos.), SiC ₂ (?), C Eutectic Si–SiC (~1400–1410 °C, ~0.03–1.25 at.% C, ?) Data available in literature on α -SiC \leftrightarrow β -SiC transformation are controversial.	The solubility of C at eutectic temp.: in liquid Si– 5×10^{-3} at.%, and in solid Si– $(7 \div 9) \times 10^{-4}$ at.% (?). At 1150–1350 °C the solubility of C in Si is obeyed the rule: $\lg x$ (in at.% C) = $3.2 - 10,400/T$ (in K) Si carbides are formed directly from the elements at elevated temp. At temp. >2000 °C in vacuum, SiC decomposes with the formation of graphite. Data available in literature on the solubility of C in Si are controversial. SiC is perfectly wetted by molten Si, the contact angle of Si on α -SiC is 30–40°. The wetting kinetics of Si on C is fast, the contact angle of 40–50° is reached in less than 40–60 s; on polycrystalline graphite the final contact angle is 10–30°. For diffusion rate in the system at various temp. see Addendum.	[138, 238, 241–244, 252, 278–282, 359, 705–708, 1015]
C–Ge	Ge, no binary compounds, C Eutectic (degenerative) Ge–C (~938 °C, ?)	No interaction. Ge ternary carbides are formed by the interaction of transition metal carbides with Ge. Practically, no solubility of C in solid Ge. Near the melt. point (938 °C) the solubility of C in liquid Ge is 0.23 at.%, but it increases near the boil. point (2834 °C) considerably. The wetting angle of molten pure Ge on graphite or vitreous carbon: 135–150° (high vacuum, 950–1100 °C).	[238, 241, 244, 681, 709, 910]

(continued)

Table 2.13 (continued)

System	Type of phase diagram (constituent phases, temperatures and compositions of transformations)	Character of chemical interaction	References
C–Sn	α -Sn, β -Sn, intercalated fullerenes (Sn(C ₆₀), Sn _x (C ₆₀) and other), C No diagram plot	For the range of temp. from melt. point (232 °C) to boil. point (2270 °C), theoretical estimation, in accordance to $\lg x$ (in at.% C) = $-1.685 - 13,800/T$ (in K), gives the values of C solubility in molten Sn from 1×10^{-25} to 8×10^{-4} at.% C, respectively. Sn ternary carbides are formed by the interaction of transition metal carbides with Sn. The corrosion resistance of graphite in liquid Sn is very high. The wetting angle of molten pure Sn on graphite or vitreous carbon: ~ 135 – 150° (high vacuum, 250–800 °C).	[138, 238, 241, 681, 910, 948]
C–Pb	Pb, PbC ₂ (metastable, ?), C	Practically, no solubility of C in solid Pb. The solubility of C in liquid Pb is: 0.41 at.% at 1170 °C, 0.79 at.% at 1415 °C and 1.6 at.% C at 1555 °C. Pb ternary carbides are formed by the interaction of transition metal carbides with Pb. Data on C solubility available in literature are controversial. At 300 °C the corrosion resistance of graphite in liquid Pb is very high. The wetting angle of molten pure Pb on vitreous carbon: 142° (high vacuum, ~ 330 °C).	[138, 238, 241, 681, 710, 910]
<i>Group 15</i>			
C–N	N, variety of compounds (e.g. C ₂ N ₂ , some polymorphs of C ₃ N ₄ , azafullerenes (C ₅₉ N) ₂ , C ₅₈ N ₂ , C ₅₇ N ₃ , C ₄₈ N ₁₁ , cyanofullerenes (C ₆₀ (CN) _{2n} , $n = 1 \div 9$), percyanoalkynes (-alkenes, -alkanes), perazidoalkynes (-alkenes, -alkanes), percyanoheterocycles, dicyanopolynes, aromatic cyanocarbons etc.), C	No direct interaction at high temp. without any special activation (e.g. microwave radiation, electrical discharge etc.), so N ₂ is recommended for graphite as a protective atmosphere at temp. ≤ 2500 – 3000 °C. At higher temp. gas cyanogen (dicyan) C ₂ N ₂ is formed. Several polymorphs of C nitride (C ₃ N ₄) and related structures are prepared in the form of films by employing special technological routes.	[5, 138, 238, 283–284, 359, 531, 711–717]

(continued)

Table 2.13 (continued)

System	Type of phase diagram (constituent phases, temperatures and compositions of transformations)	Character of chemical interaction	References
C–P	P, some unstable compounds (e.g. C_6P_6), intercalated fullerenes ($P_8(C_{60})$ and other), C	No direct interaction. C_6P_6 is formed by special reaction pathways. Ternary carbides are formed by the interaction of transition metal carbides with P.	[238, 681, 718, 949, 1024]
C–As	As, AsC_3 (?), C No diagram plot	The solubility of C in As near the boil. point is extremely low. As carbide has been prepared indirect methods; ternary carbides are formed by the interaction of transition metal carbides with As.	[138, 238, 241, 681]
C–Sb	Sb, no binary compounds, C No diagram plot	At 1300 °C the solubility of C in liquid Sb is ~ 1 at.%. At 600 °C the corrosion resistance of graphite in liquid Sb is very high.	[138, 238, 241]
C–Bi	Bi, no binary compounds, C No diagram plot	No interaction. The solubility of C in Bi near the boil. point (1565 °C) is very low. At 600 °C the corrosion resistance of graphite in liquid Bi is very high. The wetting angle of molten pure Bi on vitreous carbon: 142° (high vacuum, ~ 300 °C).	[138, 238, 241, 910]
<i>Group 16</i>			
C–O	O, CO_2 , CO, C_3O_2 (metastable), fullerene containing compounds (O_3) _x (C_{60}), (O_3) _x (C_{70}) and other, C	Graphite is in equilibrium with CO_2 (<400 °C), or CO + CO_2 (~ 400 –1000 °C), or CO (~ 1000 –3200 °C). In common conditions the oxidation of carbon in air initiates from 450–500 °C. The oxidation process is controlled by the mechanisms of the chemical reaction of gasification at 600–800 °C ($Q = 170$ –200 kJ mol^{-1}), or gas diffusion at 800–1000 °C ($Q = 20$ –45 kJ mol^{-1}). At temp. <600 °C the main product of oxidation is CO_2 , at higher temp.—CO. The average oxidation rate of pyrolytic carbon is ~ 0.12 (<900 °C) and ~ 1.2 (>2000 °C) $\text{kg m}^{-2} \text{s}^{-1}$. The oxidation rate of graphitized materials in air flow (150 cm^3 s^{-1}): at 350 °C–0.1, 400 °C–0.6, 500 °C–80 and 600 °C–800 $\text{kg m}^{-2} \text{s}^{-1}$.	[5, 136, 238, 285–289, 531, 664, 996, 1025]

(continued)

Table 2.13 (continued)

System	Type of phase diagram (constituent phases, temperatures and compositions of transformations)	Character of chemical interaction	References
C–S	α -S, β -S, $S_{12}CS_2$ (?), C_3S_8 (?), CS_2 , α - C_2S_3 (?), β - C_2S_3 (?), C_3S_4 (?), CS, C_3S_2 , C_2S (?), fullerene containing com- pounds ($S_8CS_2(C_{60})$, (S_8) $_2(C_{60})$, $S_{48}(C_{70})$, $S_{48}(C_{76})$ and other), C No complete diagram plot	C sulfides are formed directly from the elements at elevated temp. S ternary carbides are formed by the interaction of transition metal carbides with S.	[5, 238, 681, 950, 997]
C–Se	Se, CSe_2 , C No diagram plot	No direct interaction. CSe_2 is synthesized by special reaction pathways.	[5, 238, 241]
C–Te	Te, no binary compounds, C No diagram plot	No interaction	[238, 850]
C–Po	α -Po, β -Po, no binary compounds, C No diagram plot	No interaction with Po vapours at temp. ≤ 700 °C.	[241]
<i>Group 17</i>			
C–F	F, variety of compounds, including fullerene containing (e.g. $(C_{60})F_{18}$ and other), C	The intensive interaction of C with F_2 begins at 500–600 °C CF_4 , C_2F_6 and other fluoro-carbons are formed directly from the elements. At 450 °C CF_n ($n \leq 1$, variable compos. from CF to C_4F) intercalation (lamellar) compounds are synthesized.	[5, 238, 290, 953]
C–Cl	Cl, variety of compounds, including fullerene containing (e.g. $(C_{60})Cl_5$ and other), C	No direct interaction with Cl_2 at temp. < 2300 °C. C_8Cl and other lamellar (intercalate) compounds are synthesized by special reaction pathways.	[138, 238, 290, 952, 999]
C–Br	Br, CBr_4 , C_8Br , (or $C_{16}Br_2$, or $C_{56}Br \cdot 3Br_2$, lamellar com- pound), fullerene containing compounds ($(C_{60})Br$, α -(C_{60}) $Br_{24} \cdot Br_2$, β -(C_{60}) $Br_{24} \cdot Br_2$, (C_{70}) Br_{14} and some other), C No diagram plot	Intercalation (lamellar) and full- erene containing compounds are synthesized.	[5, 238, 290, 951]
C–I	I, CI_4 , C_2I_4 (?), C_2I_2 (?), fullerene containing com- pounds ($(C_{60})(I_2)$, $(C_{60})(I_2)_2$ and some other), C No diagram plot	–	[238, 954]
C–At	No data	–	–

^a The intervals of temperatures and compositions for the melting and invariant equilibria points, homogeneity ranges and thermal stability regions of constituent phases are given taking into account the minimal and maximal values (data spread) available in literature

The data on the selected ternary, quaternary, quasi-binary, quasi-ternary and multi-component carbon containing systems, which are the most important for the design, manufacture and application of ultra-high temperature materials, are summarized in Table 2.14. The composition and temperature stability regions for the main binary and ternary carbon containing high temperature phases are given in Tables 2.13, 2.14 taking into account the spread of numerical magnitudes available in literature currently.

Table 2.14 Chemical interaction of carbon (graphite) with elements and compounds at elevated, high and ultra-high temperatures (selected ternary, quaternary, quasi-binary, quasi-ternary and multi-component systems in alphabetical order)^a

System	Type of phase diagram (temperature and composition sections, constituent phases or phase fields) and/or character of interphase interaction and materials compatibility	References
C–Al–B	Plotted at 900, 1000 and 1400 °C: $\text{Al}_{2+x}\text{B}_{51}\text{C}_8$ ($x = 0.1$), $\text{AlB}_{40}\text{C}_4$ (eventually high-temp. phase of $\text{Al}_{2+x}\text{B}_{51}\text{C}_8$, ?), $\alpha\text{-Al}_3\text{B}_{48}\text{C}_2$ (<650 °C), $\beta\text{-Al}_3\text{B}_{48}\text{C}_2$ (or $\text{Al}_3\text{B}_{44}\text{C}_2$, >650 °C), Al_3BC_3 (or $\text{Al}_8\text{B}_4\text{C}_7$, $2\text{Al}_4\text{C}_3\cdot\text{B}_4\text{C}$, <1835 °C), Al_3BC (<1100 °C), Al_2B_3 ($\leq \sim 955$ °C, ?), AlB_2 ($\leq \sim 955\text{--}980$ °C), AlB_{10} (1660–1850 °C), $\alpha\text{-AlB}_{12}$ ($\leq \sim 1450\text{--}1550$ °C), $\beta\text{-AlB}_{12}$ ($\sim 1450\text{--}2150$ °C, ?), $\gamma\text{-AlB}_{12}$ ($\sim 1550\text{--}2150$ °C, ?), $\text{B}_{4\pm x}\text{C}$, Al_4C_3 , Al, $\beta\text{-B}$, C	[241–242, 244, 277, 291, 313]
C–Al–B–N	No diagram plot $\text{Al}_{1-x}\text{B}_{24}\text{C}_4\text{N}_{1+y}$ (or $\text{Al}_{0.185}\text{B}_6\text{CN}_{0.256}$) No interaction between $\text{B}_{4\pm x}\text{C}$ and AlN in powder mixtures at 1500–1850 °C (hot pressing in graphite dies without protective environment).	[892, 955]
C–Al–B–Si	$\text{Al}_4\text{C}_3\text{--B}_4\text{C}\text{--SiC}$ is plotted at 1800 °C: $\text{Al}_8\text{B}_4\text{C}_7$ (or $2\text{Al}_4\text{C}_3\cdot\text{B}_4\text{C}$), Al_4SiC_4 (or $\text{Al}_4\text{C}_3\cdot\text{SiC}$), $\text{Al}_4\text{Si}_2\text{C}_5$ (or $\text{Al}_4\text{C}_3\cdot 2\text{SiC}$), Al_4C_3 , $\text{B}_{4\pm x}\text{C}$, SiC	[292]
C–Al–Be–Si	$\text{Al}_4\text{C}_3\text{--Be}_2\text{C}\text{--SiC}$ is plotted at 1860 °C: $\text{Al}_{16}\text{Be}_2\text{SiC}_{14}$ (or $4\text{Al}_4\text{C}_3\cdot\text{Be}_2\text{C}\cdot\text{SiC}$), $\text{Al}_{24}\text{Be}_2\text{Si}_4\text{C}_{23}$ (or $6\text{Al}_4\text{C}_3\cdot\text{Be}_2\text{C}\cdot 4\text{SiC}$, ?), $\text{Al}_{16}\text{Be}_4\text{SiC}_{15}$ (or $4\text{Al}_4\text{C}_3\cdot 2\text{Be}_2\text{C}\cdot\text{SiC}$), $\text{Al}_8\text{Be}_2\text{SiC}_8$ (or $2\text{Al}_4\text{C}_3\cdot\text{Be}_2\text{C}\cdot\text{SiC}$), Al_6BeC_5 (or $3\text{Al}_4\text{C}_3\cdot\text{Be}_2\text{C}$), Al_2BeC_2 (or $\text{Al}_4\text{C}_3\cdot\text{Be}_2\text{C}$), $\text{Al}_2\text{Be}_3\text{C}_3$ (or $\text{Al}_4\text{C}_3\cdot 3\text{Be}_2\text{C}$), Al_4SiC_4 (or $\text{Al}_4\text{C}_3\cdot\text{SiC}$), Al_4C_3 , Be_2C , SiC	[295–297]
C–Al–Cr–Ti	No diagram plot $(\text{Ti,Cr})_2\text{AlC}$ ($\text{M}_{n+1}\text{AX}_n$ -phase solid solution)	[680–681, 860]
C–Al–Cr–V	No diagram plot $(\text{V,Cr})_3\text{AlC}$, $(\text{V,Cr})_3\text{AlC}_2$ ($\text{M}_{n+1}\text{AX}_n$ -phase solid solutions), $(\text{V,Cr})_5\text{Al}_2\text{C}_3$ ($\text{M}_{n+1}\text{AX}_n$ -phase solid solution, intergrown structure, ?)	[680–681, 744–745, 860]
C–Al–Hf	Plotted at 700 °C: $\text{Hf}_2\text{Al}_3\text{C}_4$, $\text{Hf}_3\text{Al}_3\text{C}_5$ (or $\text{HfAlC}_{1.67}$), $\text{Hf}_5\text{Al}_3\text{C}$, HfAl_3 (<1590 °C), HfAl_2 (<1650 °C), Hf_2Al_3 (<1640 °C), HfAl (<1800 °C), Hf_4Al_3 (<~ 1420 °C), Hf_3Al_2 (<~ 1595 °C), Hf_2Al (<~ 1145 °C), Al_4C_3 , HfC_{1-x} , $\alpha\text{-Hf}$, $\beta\text{-Hf}$, C Depending on compos., graphite is in equilibrium with $\text{Hf}_2\text{Al}_3\text{C}_4 + \text{HfC}_{1-x}$, or $\text{Hf}_2\text{Al}_3\text{C}_4 + \text{Al}_4\text{C}_3$. The interaction between HfC_{1-x} and Al at temp. >1250 °C leads to the formation of solid solutions (?).	[242, 896, 956, 965]

(continued)

Table 2.14 (continued)

System	Type of phase diagram (temperature and composition sections, constituent phases or phase fields) and/or character of interphase interaction and materials compatibility	References
C–Al–Ir	Plotted partially at 1100 °C: no ternary compounds (at least in the Ir rich part of the system), $\text{IrAl}_{1\pm x}$ (<2120 °C), $\text{Ir}_2\text{Al}_{5\pm x}$ (<~1615 °C), IrAl_3 (<1450 °C), $\text{Ir}_4\text{Al}_{13}$ (<1015 °C), Ir_2Al_9 (<900 °C), Al_4C_3 , Al, Ir, C In the wide compos. range graphite is in equilibrium with metal Ir based solid solution and $\text{IrAl}_{1\pm x}$.	[241, 244, 593, 995]
C–Al–Mn–Si	$\text{Mn}_5\text{Si}_3\text{C}_x$ – Mn_3AlC_x – $\text{Mn}_{15}\text{Si}_3\text{C}_2$ –C and $\text{Mn}_5\text{Si}_3\text{C}_x$ – Mn_3AlC_x – Al_4C_3 –C are plotted schematically.	[298–299]
C–Al–Mo	Plotted at 1000 and 1450 °C: $\text{Mo}_{3-x}\text{Al}_{2+x}\text{C}$ ($-0.12 \leq x \leq 0.24$, or $\text{Mo}_{0.46} \div 0.52\text{Al}_{0.31} \div 0.37\text{C}_{0.17}$), $(\text{Al},\text{Mo})_4\text{C}_3$ (solid solution based on Al_4C_3 ; ≤ 5 at.% Mo), MoAl_{12} (<~690 °C), MoAl_5 (<735 °C), MoAl_4 (or $\text{Mo}_4\text{Al}_{17}$, <1130 °C), $\text{Mo}_3\text{Al}_{8\pm x}$ (<~1550 °C), MoAl_{2-x} ($x = 0.3$, ~1490–1570 °C), $\text{MoAl}_{1\pm x}$ (~1470–1720 °C), $\text{Mo}_{3\pm x}\text{Al}$ (<2150 °C), α - Mo_{2+x}C , α' - Mo_{2+x}C , β - $\text{Mo}_{2\pm x}\text{C}$, η - MoC_{1-x} , α - MoC_{1-x} , γ - MoC , Al, Mo, C The interaction between β - $\text{Mo}_{2\pm x}\text{C}$ and Al at temp. >1250 °C leads to the formation of solid solutions (?).	[242, 896, 957]
C–Al–Mo–Ni	Plotted schematically and partially General consideration of the system.	[851]
C–Al–N–Si	Al_4C_3 – AlN – SiC is plotted at 1860 °C: $\text{Al}_{9+x}\text{Si}_{1-x}\text{N}_{1+x}\text{C}_{7-x}$ ($-0.04 \leq x \leq 0.04$), Al_5SiNC_4 (or Al_4C_3 · AlN · SiC), Al_8SiC_7 (or $2\text{Al}_4\text{C}_3$ · SiC), Al_4SiC_4 (or Al_4C_3 · SiC), $\text{Al}_4\text{Si}_2\text{C}_5$ (or Al_4C_3 · 2SiC , ?), Al_5NC_3 (or Al_4C_3 · AlN), Al_3NC (?), AlN (<2400–2450 °C), Al_4C_3 , SiC Si_3N_4 – AlN – SiC and Al_4C_3 – AlN – SiC are plotted at 1760 and 1860 °C, respectively: $\text{Al}_{5-x}\text{Si}_x\text{N}_{1-x}\text{C}_{3+x}$ ($0 < x \leq 0.4$), $\text{Al}_{5-x}\text{Si}_x\text{N}_{1-x}\text{C}_{3+x}$ ($x \approx 0.5$), $\text{Al}_{5-x}\text{Si}_x\text{N}_{1-x}\text{C}_{3+x}$ ($0.85 \leq x < 1$), Al_5SiNC_4 (or Al_4C_3 · AlN · SiC), Al_5NC_3 (or Al_4C_3 · AlN), Al_4SiC_4 (or Al_4C_3 · SiC), AlN (<2400–2450 °C), β - Si_3N_4 (<~1800–1900 °C), Al_4C_3 , SiC	[280, 297, 300–302]
C–Al–N–Ti	No diagram plot $\text{Ti}_2\text{AlC}_{x-y}\text{N}_y$ ($x = \sim 0.8$, $0 \leq y \leq \sim 0.8$), $\text{Ti}_3\text{Al}(\text{C},\text{N})_2$ ($\text{M}_{n+1}\text{AX}_n$ -phase solid solutions)	[680–681, 744–745, 860]
C–Al–Nb	Plotted at 700 and 800 °C: Nb_2AlC ($\text{M}_{n+1}\text{AX}_n$ -phase), α - Nb_4AlC_3 , β - Nb_4AlC_3 ($\text{M}_{n+1}\text{AX}_n$ -phases, ?), NbAl_{3-x} (<1680 °C), $\text{Nb}_{2\pm x}\text{Al}$ (<1940 °C), Nb_{3+x}Al (<2060 °C), Al_4C_3 , α - Nb_2C , β - Nb_{2+x}C , γ - $\text{Nb}_{2\pm x}\text{C}$, ζ - $\text{Nb}_4\text{C}_{3-x}$, $\text{Nb}_6\text{C}_{5\pm x}$, NbC_{1-x} , Al, Nb, C No solid solutions based on ternary and binary compounds.	[680–681, 744–745, 860, 896, 898, 958–959, 965]
C–Al–Nb–Ti	No diagram plot $(\text{Ti},\text{Nb})_2\text{AlC}$ ($\text{M}_{n+1}\text{AX}_n$ -phase solid solution)	[680–681, 860]
C–Al–Nb–V	No diagram plot $(\text{V},\text{Nb})_2\text{AlC}$ ($\text{M}_{n+1}\text{AX}_n$ -phase solid solution)	[680–681, 860]

(continued)

Table 2.14 (continued)

System	Type of phase diagram (temperature and composition sections, constituent phases or phase fields) and/or character of interphase interaction and materials compatibility	References
C–Al–Nb–Zr	No diagram plot (Nb,Zr) ₂ AlC ($M_{n+1}AX_n$ -phase solid solution)	[680–681, 860]
C–Al–O	Plotted at 1000–2400 °C: Al ₂ OC, Al ₄ O ₄ C, AlC ₉ O ₁₀ (at least at 2000–2050 °C), AlC ₂ O ₂ (at least at 2100 °C), Al ₄ C ₇ O ₉ (at least at 2100 °C), AlCO (at least at 2400 °C), Al ₂ O (?) , γ -Al ₂ O _{3-x} , α -Al ₂ O ₃ (<~2030–2055 °C), Al ₄ C ₃ , Al, O, C Al ₂ O ₃ –Al ₄ C ₃ is plotted: Al ₂ OC (1650–2000 °C), Al ₄ O ₄ C (<1890 °C), α -Al ₂ O ₃ , Al ₄ C ₃ In vacuum, the interaction between C and α -Al ₂ O ₃ initiates in powdered mixtures from ~1350 °C, on bulk materials contacts—from ~1800 °C, and is ruled by diffusion stage (parabolic law) with formation of Al ₄ C ₃ .	[138, 194, 303–304, 382, 960]
C–Al–O–Si	No diagram plot At 2000 °C in powdered mixtures, the interaction between SiC and Al ₂ O ₃ in air leads to the formation of elemental Al, Si and phases close to nonstoichiometric mullite $x\text{Al}_2\text{O}_3 \cdot y\text{SiO}_2$ (?).	[891]
C–Al–O–Ti	No diagram plot Ti ₂ Al(C,O) ($M_{n+1}AX_n$ -phase oxycarbide solid solution)	[744–745]
C–Al–O–U	No diagram plot At 1900 °C the interaction between β -UC _{2-x} and Al ₂ O ₃ is weak.	[242]
C–Al–Si	Plotted at <580, 2000 and 2150 °C: Al ₈ SiC ₇ (or 2Al ₄ C ₃ ·SiC), Al ₄ SiC ₄ (or Al ₄ C ₃ ·SiC), Al ₄ C ₃ , SiC, Al, Si, C Al ₄ C ₃ –SiC is plotted: Al ₈ SiC ₇ (<2085 °C, incongruent melt. point), α -Al ₄ SiC ₄ , β -Al ₄ SiC ₄ (<2080 °C, congruent melt. point), Al ₄ Si ₂ C ₅ (or Al ₄ C ₃ ·2SiC, ?), Al ₄ Si ₃ C ₆ (or Al ₄ C ₃ ·3SiC, ?), Al ₄ Si ₄ C ₇ (or Al ₄ C ₃ ·4SiC, ?), Al ₄ C ₃ , SiC The presence of Si in Al alloys results in the predominant formation of SiC and suppresses the formation of Al ₄ C ₃ during the contact interaction of the Al–Si alloys with graphite.	[242, 292–294, 661, 1002]
C–Al–Ta	Plotted at 700 and 1000 °C: Ta ₂ AlC, Ta ₃ AlC ₂ , Ta ₅ Al ₃ C _{1-x} , α -Ta ₄ AlC ₃ (<~1600 °C), β -Ta ₄ AlC ₃ ($M_{n+1}AX_n$ -phases), Ta ₃ Al ₂ C (?), TaAl ₃ (<1550–1630 °C, ?), TaAl ₂ (<~1595 °C, ?), α -Ta ₂ Al ₃ (<1225 °C, ?), β -Ta ₂ Al ₃ (<~1225–1550 °C, ?), TaAl (<1770 °C, ?), δ -Ta _{2±x} Al (<~2000–2100 °C), Ta ₃ Al (?), Al ₄ C ₃ , α -Ta _{2+x} C, β -Ta _{2±x} C, ζ -Ta ₄ C _{3-x} , Ta ₆ C _{5±x} , TaC _{1-x} , Al, Ta, C The interaction between TaC _{1-x} and Al at temp. ≥1250 °C leads to the formation of solid solutions (?).	[242, 680–681, 744–745, 860, 881, 896, 965]
C–Al–Ta–Ti	Plotted at 1100 °C (for 9.1 and 25 at.% C): (Ti,Ta) ₂ AlC ($M_{n+1}AX_n$ -phase solid solution), (Ta,Ti)C _{1-x} (TaC _{1-x} –TiC _{1-x} monocarbide continuous solid solution with the critical point of the miscibility gap calculated to be below 0 °C)	[680–681, 860, 881]

(continued)

Table 2.14 (continued)

System	Type of phase diagram (temperature and composition sections, constituent phases or phase fields) and/or character of interphase interaction and materials compatibility	References
C–Al–Ta–V	No diagram plot (V,Ta) ₂ AlC ($M_{n+1}AX_n$ -phase solid solution)	[680–681, 860]
C–Al–Ti	Plotted at 750–1300 °C: Ti_3AlC_{1-x} ($x = 0.5$, <1570–1590 °C), Ti_2AlC_{1-x} ($x = 0.2$, <1615–1635 °C, $M_{n+1}AX_n$ -phase), Ti_3AlC_{2-x} (at least at ~1300 °C, $M_{n+1}AX_n$ -phase), β -(Ti,Al) (ordered, ~1105–1425 °C), α_2 - $Ti_{3\pm x}Al$ (<~1180–1195 °C), α - $Ti_{2\pm x}Al$ (<~1500 °C, ?), γ - $TiAl_{1\pm x}$ (<~1455–1480 °C), $Ti_{1-x}Al_{1+x}$ (disordered, 1170–1480 °C), Ti_3Al_5 (<700–810 °C, ?), α - $TiAl_{2\pm x}$ (<~1225–1240 °C), β - $TiAl_{2\pm x}$ (?), ζ - Ti_5Al_{11} (from 990–995 °C to ~1415 °C, ?), ζ - $Ti_2Al_{5\pm x}$ (or δ - $Ti_2Al_{5\pm x}$, or Ti_9Al_{23} , from ~975–1150 °C to ~1385–1430 °C), α - $TiAl_3$ (<~600–930 °C), β - $TiAl_3$ (from ~600–930 to 1355–1395 °C), Al_4C_3 (no solubility for Ti), TiC_{1-x} , α -Ti, β -Ti, Al, C TiC_{1-x} - γ - $TiAl_{1\pm x}$ is partially plotted: Ti_2AlC_{1-x} , TiC_{1-x} , γ - $TiAl_{1\pm x}$; the max. solubility of TiC_{1-x} in γ - $TiAl_{1\pm x}$ at 1530 °C is 0.9 mol.% and it decreases to <0.7 mol.% as the temp. decreases to 600–1200 °C. Non-stoichiometric TiC_{1-x} ($0.09 < x < 0.18$) is resistant to corrosion in molten Al at temp. <1000–1100 °C; the interaction of near-stoichiometric TiC_{1-x} ($x < 0.09$) with Al leads to the formation of Al_4C_3 , whereas highly non-stoichiometric TiC_{1-x} ($x > 0.18$) interacts with the formation of β - $TiAl_3$. At 1250–1400 °C weak interaction between TiC_{1-x} and Al with the formation of Al_4C_3 is observed. At 1700 °C Al vapour penetrates into the porous structure of TiC_{1-x} without chemical interaction. The $M_{n+1}AX_n$ -phase of Ti_3AlC_2 exfoliated in hydrofluoric acid are employed for the fabrication of Ti_xC_y 2D-nanosheets (graphene-like nanocrystals).	[241–242, 244, 305–312, 605–606, 624, 680–681, 744–745, 830, 859–860, 881, 896, 903–904, 962]
C–Al–Ti–V	No diagram plot (Ti,V) ₂ AlC ($M_{n+1}AX_n$ -phase solid solution)	[680–681, 860]
C–Al–U	Plotted at 600 °C: UAl_5C_4 , α - UAl_3C_3 (?), β - UAl_3C_3 , $U_2Al_3C_4$ (?), α - UAl_{4+x} (<~645 °C), β - UAl_{4+x} (~645–730 °C), UAl_3 (<1350 °C), UAl_2 (<1620 °C), Al_4C_3 , $UC_{1\pm x}$, ζ - U_2C_3 , α - UC_{2-x} , β - UC_{2-x} , α -U, β -U, γ -U, Al, C $UC_{1\pm x}$ - UAl_2 is plotted: eutectic—1540 °C, ~10 mol.% $UC_{1\pm x}$ (~3.5 at.% C) No solid solutions based on ternary and binary compounds. The interactions between $UC_{1\pm x}$ and Al at temp. ≥ 500 °C, and between α - UC_{2-x} and Al at temp. ≥ 600 °C are active; and lead to the formation of C, UAl_3 and UAl_{4+x} .	[242, 961]

(continued)

Table 2.14 (continued)

System	Type of phase diagram (temperature and composition sections, constituent phases or phase fields) and/or character of interphase interaction and materials compatibility	References
C–Al–V	Plotted at 800 and 1000 °C: V_2AlC , V_3AlC_2 ($M_{n+1}AX_n$ -phases), V_4AlC_{3-x} ($x = 1/3$, $M_{n+1}AX_n$ -phase, ?), V_2Al_{21} ($< \sim 665$ °C), V_7Al_{45} ($< \sim 690$ °C), V_4Al_{23} ($< \sim 735$ °C), VAl_3 (< 1360 °C), V_5Al_8 (< 1670 °C), Al_4C_3 , α - $V_{2+x}C$, β - $V_{2+x}C$, β' - $V_{2+x}C$, ζ - V_4C_{3-x} , V_6C_{5+x} , V_8C_{7+x} , VC_{1-x} , V, Al, C No solid solutions based on ternary and binary compounds.	[680–681, 744–745, 748, 860, 896, 898, 962]
C–Al–W	Plotted at 900 °C: $WAlC_{2-x}$ ($x = 0 \div 1.0$, or ($W_{0.5}Al_{0.5}$) C_{1-y} with $y = 0 \div 0.5$, ?), $W_xAl_yC_z$ (ordered phase W_2AlC , ?), γ - WAl_{12} (< 697 °C), δ - WAl_{5-x} (< 870 – 871 °C), ϵ - $WAl_{4\pm x}$ ($< \sim 1325$ °C), ζ - $WAl_{3\pm x}$ (~ 1300 – 1345 °C), η - $W_3Al_{7\pm x}$ (~ 1325 – 1420 °C), θ - $WAl_{2\pm x}$ (~ 1335 – 1650 °C), Al_4C_3 , α - $W_{2+x}C$, β - $W_{2+x}C$, γ - $W_{2\pm x}C$, γ - WC_{1-x} , δ - $WC_{1\pm x}$, W, Al, C The interaction between δ - $WC_{1\pm x}$ and Al at temp. ≥ 1250 °C leads to the formation of solid solutions (?).	[242, 541, 644, 896, 963]
C–Al–Zr	Plotted at 600, 700 and 1000 °C: $Zr_3Al_3C_5$, $Zr_2Al_3C_5$, Zr_5Al_3C , $Zr_2Al_3C_4$ (?), $ZrAlC_{2-x}$ (?), $ZrAl_3$ (< 1580 °C), $ZrAl_2$ (< 1645 °C), Zr_2Al_3 (< 1595 °C), $ZrAl$ (< 1275 °C), Zr_5Al_4 (~ 1000 – 1530 °C), Zr_4Al_3 ($< \sim 1035$ °C), Zr_3Al_2 ($< \sim 1480$ °C), Zr_5Al_3 (~ 1000 – 1400 °C), Zr_2Al (< 1250 °C), Zr_3Al ($< \sim 990$ °C), Al_4C_3 , ZrC_{1-x} , α -Zr, β -Zr, Al, C The interaction between ZrC_{1-x} and Al at temp. ≥ 1250 °C leads to the formation of solid solutions (?).	[242, 744–745, 882–883, 896, 964–965]
C–As–Nb	No diagram plot Nb_2AsC ($M_{n+1}AX_n$ -phase)	[680–681, 744–745, 860]
C–As–V	Plotted at 1100 °C: V_2AsC ($M_{n+1}AX_n$ -phase), V_3AsC (wide homog. range), $V_5As_3C_{1-x}$ ($x \approx 0.3$), VAs_2 , VAs , α - V_4As_3 , β - V_4As_3 , V_3As_2 , α - V_5As_3 , β - V_5As_3 , γ - V_5As_3 , V_2As , V_3As , α - $V_{2+x}C$, β - $V_{2+x}C$, β' - $V_{2+x}C$, ζ - V_4C_{3-x} , V_6C_{5+x} , V_8C_{7+x} , VC_{1-x} , V, As, C	[680–681, 744–745, 860, 956–967]
C–Au–Th	No diagram plot At 850 °C, in vacuum the interaction between $ThC_{1\pm x}$ and Au leads to the formation of C and $Th_{14}Au_{51}$ (or $ThAu_3$).	[242]
C–Au–U	No diagram plot At 950–1100 °C, in vacuum the interaction between $UC_{1\pm x}$ and Au leads to the formation of C and $U_{14}Au_{51}$ (or UAu_3).	[242]
C–B–Be	No diagram plot BeB_2C (?), $BeB_{12}C$ (?) The interactions of C with Be_4B (or Be_5B) and BeB_2 at temp. ≥ 900 °C, with Be_2B at temp. ≥ 1000 °C and with BeB_4 at temp. ≥ 1200 °C lead to the formation of Be_2C .	[242]

(continued)

Table 2.14 (continued)

System	Type of phase diagram (temperature and composition sections, constituent phases or phase fields) and/or character of interphase interaction and materials compatibility	References
C–B–Ce	Plotted at 1730 °C: $\text{Ce}_5\text{B}_3\text{C}_{12}$, $\text{Ce}_5\text{B}_2\text{C}_{6+x}$ ($0 \leq x \leq 0.2$, ?), $\text{Ce}_5\text{B}_4\text{C}_5$ (?), $\alpha\text{-CeB}_2\text{C}_2$ (?), $\beta\text{-CeB}_2\text{C}_2$ (?), CeB_2C_4 (?), CeB_2C (?), $\text{Ce}_{10}\text{B}_9\text{C}_{12}$ (?), CeBC (?), CeB_4 ($< \sim 2380\text{--}2390$ °C), $\text{CeB}_{6\pm x}$ ($< \sim 2290\text{--}2550$ °C), Ce_2C_3 , $\alpha\text{-CeC}_2$, $\beta\text{-CeC}_{2\pm x}$, $\text{B}_{4\pm x}\text{C}$, $\alpha\text{-Ce}$, $\beta\text{-Ce}$, $\gamma\text{-Ce}$, $\beta\text{-B}$, C	[241, 244, 391, 690, 958]
C–B–Co	No equilibrium phase diagram plot $\text{Co}_{22}\text{B}_4\text{C}_2$ The interaction between $\text{B}_{4\pm x}\text{C}$ and Co leads to the formation of eutectic alloy and solid solutions.	[242, 727]
C–B–Cr	Plotted at 1100 and 1450 °C: $\text{Cr}_3(\text{B,C})\text{C}_{1-x}$ (or $\text{Cr}_3\text{B}_x\text{C}_{1-x}$, $\sim 1550\text{--}1710$ °C), $\text{Cr}_3(\text{B}_x\text{C}_{1-x})_2$ (or $\text{Cr}_3(\text{C,B})_{2-x}$, Cr_3BC , $< 1810\text{--}1830$ °C), $\text{Cr}_7(\text{B}_x\text{C}_{1-x})_{3\pm x}$ (or $\text{Cr}_7(\text{C,B})_{3\pm x}$, Cr_7BC_4 , $< 1765\text{--}1780$ °C), $\text{Cr}_{23}(\text{B}_x\text{C}_{1-x})_{6\pm x}$ (or $\text{Cr}_{23}(\text{C,B})_{6\pm x}$, $< 1575\text{--}1615$ °C), $\text{Cr}_{2\pm x}\text{B}$ ($< \sim 1870$ °C), $\text{Cr}_5\text{B}_{3\pm x}$ ($< \sim 1900$ °C), $\alpha\text{-CrB}_{1\pm x}$ (≤ 1000 °C, ?), $\beta\text{-CrB}_{1\pm x}$ ($\sim 1000\text{--}2150$ °C, ?), $\text{Cr}_3\text{B}_{4\pm x}$ ($< 2070\text{--}2075$ °C), Cr_2B_3 (at least at $\sim 1000\text{--}1500$ °C), $\text{CrB}_{2\pm x}$ ($< \sim 2150\text{--}2250$ °C), CrB_4 ($< \sim 1450\text{--}1500$ °C), $\text{B}_{4\pm x}\text{C}$, Cr, $\beta\text{-B}$, C $\text{CrB}_2\text{--B}_{4\pm x}\text{C}$ is plotted: eutectic— 2150 °C, ~ 40 mol.% $\text{B}_{4\pm x}\text{C}$ ($\sim 7\text{--}8$ at.% C) $\text{CrB}_2\text{--C}$ is plotted: eutectic— $\sim 1875\text{--}1980$ °C	[241–242, 244, 276, 314–317, 320, 322–323, 394, 690, 725–726]
C–B–Cr–N	No diagram plot At 1650 °C the interaction between $\alpha\text{-BN}$ and $\text{Cr}_3\text{C}_{2-x}$ leads to the formation of Cr and Cr_{2+x}N .	[242]
C–B–Cr–Si	SiC--CrB_2 is plotted: eutectic— 2030 °C, ~ 25 mol.% SiC (12.5 at.% C); the max. solid solubility of CrB_2 in SiC is ~ 2 mol.% and that of SiC in CrB_2 is ~ 2.5 mol.% (at the eutectic temp.)	[318, 566–567]
C–B–Dy	No diagram plot DyBC , DyB_2C , DyB_2C_2 , $\text{Dy}_5\text{B}_2\text{C}_5$, $\text{Dy}_2\text{B}_4\text{C}$, $\text{Dy}_5\text{B}_2\text{C}_6$, ?	[391, 690]
C–B–Eu	Plotted at 1500 °C: EuB_2C_2 , EuB_xC_y (or $\text{Eu}_2(\text{C,B})_3$), $\text{EuB}_{6-x}\text{C}_x$, ($0 \leq x \leq 0.25$, or $\text{Eu}(\text{C,B})_6$), $\text{EuB}_{6\pm x}$ ($< \sim 2580\text{--}2710$ °C), Eu_{3-x}C , Eu_2C_3 , $\alpha\text{-EuC}_2$, $\beta\text{-EuC}_2$, EuC_6 , $\text{B}_{4\pm x}\text{C}$, Eu, $\beta\text{-B}$, C	[241, 319, 690]
C–B–Er	No diagram plot ErB_2C , ErB_2C_2 , $\text{Er}_5\text{B}_2\text{C}_5$, $\text{Er}_2\text{B}_4\text{C}$, $\text{Er}_5\text{B}_2\text{C}_6$, $\text{ErB}_{28.5}\text{C}_4$, ?	[391, 690]
C–B–Gd	Plotted at $2000\text{--}3000$ °C: GdBC , GdB_2C_2 , GdB_2C_4 , $\text{Gd}_2\text{B}_2\text{C}$, $\text{Gd}_2\text{B}_3\text{C}_2$, $\text{Gd}_3\text{B}_2\text{C}_3$, $\text{Gd}_3\text{B}_4\text{C}_2$, $\text{Gd}_3\text{B}_4\text{C}_3$ (or $\text{Gd}_{0.3}\text{B}_{0.4}\text{C}_{0.3}$), $\text{Gd}_3\text{B}_5\text{C}_2$, $\text{Gd}_4\text{B}_3\text{C}_3$, $\text{Gd}_4\text{B}_3\text{C}_4$, $\text{Gd}_5\text{B}_2\text{C}_5$, $\text{Gd}_5\text{B}_2\text{C}_6$, $\text{Gd}_5\text{B}_8\text{C}_4$, $\text{Gd}_6\text{B}_9\text{C}_4$, $\text{Gd}_7\text{B}_4\text{C}_9$ (or $\text{Gd}_{0.35}\text{B}_{0.19}\text{C}_{0.46}$, ?), $\text{Gd}_7\text{B}_5\text{C}_4$ (or $\text{Gd}_{0.35}\text{B}_{0.45}\text{C}_{0.2}$, ?), $\text{Gd}_8\text{B}_7\text{C}_5$ (or $\text{Gd}_{0.4}\text{B}_{0.35}\text{C}_{0.25}$, ?), $\text{Gd}_8\text{B}_8\text{C}_9$, $\text{Gd}_8\text{B}_9\text{C}_7$, $\text{Gd}_9\text{B}_8\text{C}_5$ (or $\text{Gd}_{10}\text{B}_9\text{C}_5$), $\text{Gd}_9\text{B}_8\text{C}_7$, $\text{Gd}_9\text{B}_{10}\text{C}_6$, $\text{Gd}_{10}\text{B}_9\text{C}_6$, $\text{Gd}_{15}\text{B}_4\text{C}_{16}$, GdB_2 ($\sim 1280\text{--}2050$ °C), $\sim \text{Gd}_2\text{B}_5$ (< 2100 °C), GdB_4 ($< \sim 2650$ °C), $\text{GdB}_{6\pm x}$ (< 2510 °C), GdB_{66} (or GdB_{100} , < 2150 °C), Gd_{3+x}C , Gd_2C , GdC_{1-x} , $\text{Gd}_2\text{C}_{3-x}$, $\alpha\text{-GdC}_2$, $\beta\text{-GdC}_2$, GdC_6 , $\text{B}_{4\pm x}\text{C}$, Gd, $\beta\text{-B}$, C No solid solutions based on binary and ternary compounds.	[241, 391, 616–618, 690]

(continued)

Table 2.14 (continued)

System	Type of phase diagram (temperature and composition sections, constituent phases or phase fields) and/or character of interphase interaction and materials compatibility	References
C–B–Fe	Plotted at 700–1080 °C: $\text{Fe}_3(\text{B}_x\text{C}_{1-x})$ (or $\text{Fe}_3(\text{C},\text{B})$, $< \sim 1190$ – 1250 °C, $0.05 \leq x \leq 0.90$ at 1050 °C), $\text{Fe}_{23}(\text{B}_x\text{C}_{1-x})_6$ (or $\text{Fe}_{23}(\text{C},\text{B})_6$, $\text{Fe}_{23}\text{C}_3\text{B}_3$, < 800 – 965 °C), Fe_2B ($< \sim 1405$ °C), FeB ($< \sim 1590$ °C), Fe_3C , $\text{B}_{4\pm x}\text{C}$, α -Fe, γ -Fe, δ -Fe, β -B, C	[241–242, 244, 324–327, 391]
C–B–Fe–Ti	TiC_{1-x} – $\text{TiB}_{2\pm x}$ –Fe is plotted: eutectic— 1170 °C, 1 mol.% TiC_{1-x} , 7.5 mol.% $\text{TiB}_{2\pm x}$ (0.8 at.% C)	[834]
C–B–Hf	Plotted at 1400 – 3200 °C: $\text{HfB}_{1\pm x}$ (< 2100 °C), $\text{HfB}_{2\pm x}$ ($< \sim 3250$ – 3410 °C), HfC_{1-x} , $\text{B}_{4\pm x}\text{C}$, α -Hf, β -Hf, β -B, C Eutectic $\text{HfB}_{1\pm x}$ – α -Hf– β -Hf (1850 °C) Eutectic $\text{HfB}_{2\pm x}$ – $\text{B}_{4\pm x}\text{C}$ – β -B (1950 °C) Eutectic $\text{HfB}_{2\pm x}$ – $\text{B}_{4\pm x}\text{C}$ –C (~ 2260 – 2320 °C, ~ 6.5 – 9.0 at.% Hf, ~ 25.0 – 28.5 at.% C) Eutectic $\text{HfB}_{2\pm x}$ – HfC_{1-x} –C (~ 2480 – 2515 °C, ~ 21 – 24 at.% Hf, ~ 38.0 – 39.7 at.% C) $\text{HfB}_{2\pm x}$ – $\text{B}_{4\pm x}\text{C}$ is plotted: eutectic— ~ 2330 – 2410 °C, ~ 68 – 78 mol.% $\text{B}_{4\pm x}\text{C}$ (~ 15.0 – 15.8 at.% C); the max. solid solubility of $\text{HfB}_{2\pm x}$ in $\text{B}_{4\pm x}\text{C}$ is < 1 mol.% and that of $\text{B}_{4\pm x}\text{C}$ in $\text{HfB}_{2\pm x}$ is < 2 mol.% (at the eutectic temp.) $\text{HfB}_{2\pm x}$ – HfC_{1-x} is plotted: eutectic— ~ 3110 – 3140 °C, ~ 35 mol.% HfC_{1-x} (~ 16.0 – 16.3 at.% C); the max. solid solubility of $\text{HfB}_{2\pm x}$ in HfC_{1-x} is ~ 10 mol.% and that of HfC_{1-x} in $\text{HfB}_{2\pm x}$ is < 2 mol.% (at the eutectic temp.) $\text{HfB}_{2\pm x}$ –C is plotted: eutectic— ~ 2340 – 2515 °C, ~ 24 – 38 mol.% $\text{HfB}_{2\pm x}$ (~ 35 – 40 at.% C); the max. solubility of C in $\text{HfB}_{2\pm x}$ is < 3 at.% (at the eutectic temp.)	[138, 241–242, 244, 328–333, 573]
C–B–Hf–Si	No diagram plot The general consideration of $\text{HfB}_{2\pm x}$ –SiC phase relations.	[566–567, 653]
C–B–Hf–W	No diagram plot The general consideration of $\text{HfB}_{2\pm x}$ – α -WC phase relations.	[653]
C–B–Ho	Plotted at 1500 °C: HoBC , HoB_2C , HoB_2C_2 , $\text{Ho}_2\text{B}_2\text{C}_3$, $\text{Ho}_3\text{B}_2\text{C}_3$, $\text{Ho}_5\text{B}_2\text{C}_6$, $\text{Ho}_5\text{B}_2\text{C}_5$, $\text{Ho}_{15}\text{B}_2\text{C}_{17}$, HoB_2 (< 2200 °C), HoB_4 (< 2500 °C), $\text{HoB}_{6\pm x}$ (< 2180 °C), HoB_{12} (< 2100 °C), HoB_{66} (< 2025 °C), Ho_2C , Ho_5C_6 , Ho_2C_3 , HoC_2 , $\text{B}_{4\pm x}\text{C}$, α -Ho, β -Ho, β -B, C No solid solutions based on binary and ternary compounds.	[241, 334, 690]
C–B–Ir–Th	No diagram plot $\text{ThIr}_2\text{B}_2\text{C}$, ?	[976]

(continued)

Table 2.14 (continued)

System	Type of phase diagram (temperature and composition sections, constituent phases or phase fields) and/or character of interphase interaction and materials compatibility	References
C–B–La	No complete diagram plot LaBC, LaB ₂ C ₂ , LaB ₂ C ₄ , La ₅ B ₂ C ₆ , (?), La ₁₀ B ₉ C ₁₂ , (?), La ₁₅ B ₁₄ C ₁₉ , (?), La ₁₀ B _{5–y} C _{11–x} , (or La ₅ B _{2.1 ÷ 2.5} C _{5.1 ÷ 5.5} , ?), La ₅ B ₄ C _{5–x} , ($x \approx 0.15$, ?), LaB ₄ (<1800 °C), LaB _{6±x} (<~2500–2715 °C), La ₂ C _{3–x} , α -LaC ₂ , β -LaC _{2±x} , B _{4±x} C, α -La, β -La, γ -La, β -B, C LaB _{6±x} –B _{4±x} C is plotted: eutectic—~2220–2260 °C, ~70 mol.% B _{4±x} C (~12.5 at.% C); mutual solubilities of the components are very low	[241–242, 244, 370, 391, 690]
C–B–La–Mo	No diagram plot LaB _{6±x} and β -Mo _{2±x} C are stable and compatible with each other at 1800–2100 °C	[242]
C–B–La–Si	LaB _{6±x} –SiC is plotted: eutectic—~2090–2130 °C, ~75 mol.% SiC	[568]
C–B–La–Si–W	α -W ₂ B _{5–x} –LaB _{6±x} –SiC is plotted: triple eutectic—~1860–1900 °C, ~45 mol.% SiC, ~10 mol.% LaB _{6±x} ; virtually no mutual solubilities between the components	[570]
C–B–Lu	No diagram plot LuB ₂ C ₂ , Lu ₃ BC ₃ , LuB ₂ C, ?	[690]
C–B–Mn	Plotted at 800, 850 and 1000 °C: Mn ₇ BC ₂ (?), Mn ₂₃ B ₃ C ₃ (?), Mn ₂₃ (C,B) ₆ (extended solid solution based on Mn ₂₃ C ₆), Mn ₇ (C,B) ₃ (extended solid solution based on Mn ₇ C ₃), Mn ₅ (C,B) ₂ (extended solid solution based on Mn ₅ C ₂), MnB ₄ (<~1380 °C), MnB ₂ (~1100–1830 °C), Mn ₃ B ₄ (<~1825 °C), MnB (<~1890 °C), Mn ₂ B (<~1580 °C), Mn ₄ B (<~1120 °C), ϵ -Mn _{4±x} C, Mn ₁₅ C ₄ , Mn ₃ C, B _{4±x} C, α -Mn, β -Mn, γ -Mn, δ -Mn, β -B, C	[242, 391, 969–970]
C–B–Mo	Plotted at 1300 and 1800 °C: Mo ₂ BC _{1–x} (<2100–2300 °C), Mo _{2±x} B (<2280 °C), Mo ₃ B ₂ (1920–2070 °C), α -MoB _{1–x} (<2180 °C), β -MoB _{1±x} (~1800–2610 °C), MoB _{2–x} (~1515–2375 °C), Mo ₂ B _{5–x} (<2140 °C), MoB _{4–x} (or MoB _{3+x} , <~1805 °C), α -Mo _{2+x} C, α' -Mo _{2+x} C, β -Mo _{2±x} C, η -MoC _{1–x} , α -MoC _{1–x} , γ -MoC, B _{4±x} C, Mo, β -B, C Eutectic MoB _{2–x} –B _{4±x} C–C (~2250–2280 °C, ~22 at.% Mo, ~17 at.% C) Eutectic Mo ₂ BC _{1–x} – β -MoB _{1±x} –C (~2170–2215 °C, ~43 at.% Mo, ~30 at.% C) Eutectic Mo ₂ BC _{1–x} – α -MoC _{1–x} –C (~2115–2165 °C, ~48 at.% Mo, ~41 at.% C) Eutectic β -MoB _{1±x} – β -Mo _{2±x} C–Mo ₂ BC _{1–x} (~2260–2270 °C, ~56 at.% Mo, ~18 at.% C) Eutectic Mo _{2±x} B– β -Mo _{2±x} C–Mo (~2100–2155 °C, ~76 at.% Mo, ~10 at.% C) β -MoB _{1±x} –C is plotted: eutectic—~2300 °C, ~45 mol.% β -MoB _{1±x} (~36 at.% C)	[138, 241–242, 244, 320, 335–337, 394, 690, 853, 877]

(continued)

Table 2.14 (continued)

System	Type of phase diagram (temperature and composition sections, constituent phases or phase fields) and/or character of interphase interaction and materials compatibility	References
	<p>MoB_{2-x}-C is plotted: eutectic—2180 °C (?)</p> <p>Mo₂BC_{1-x}-C is plotted: eutectic—1825 °C (?)</p> <p>Mo₂B_{5-x}-C is plotted: eutectic—2175–2200 °C (?)</p> <p>MoB_{2-x}-B_{4±x}C is plotted: eutectic—~ 30–40 mol.% B_{4±x}C (?)</p>	
C–B–Mo–N	<p>No diagram plot</p> <p>In vacuum the interaction between metal Mo and composition of α-BN + 23 mol.% B_{4±x}C begins from 1600 °C (in powder mixtures—from 1500 °C) and leads to the formation of Mo_{2±x}B, α-MoB_{1-x} (frontal layers) and β-Mo_{2±x}C (inclusions); at temp. >1700 °C dense specimens weld together.</p>	[829]
C–B–Mo–Ni	<p>No diagram plot</p> <p>The intensive interaction between B_{4±x}C and Ni–Mo alloy is observed.</p>	[242]
C–B–Mo–Si	<p>No diagram plot</p> <p>The general consideration of MoB_{2-x}-SiC phase relations.</p>	[566–567]
C–B–N	<p>Plotted at 1530–4030 °C: B₃CN₃ (or B(CN)₃, <450 °C), α-BC_xN_y ($0 \leq x \leq \sim 2$, BN–C substitutional solid solution, graphene/graphite-like), β-BC_xN_y ($0 \leq x \leq \sim 1$, BN–C substitutional solid solution, diamond-like), variety of metastable phases—B₂CN₂, BCN, BC₂N, BC₃N, (BN)_xC_{1-x}, B_{1-x}C_xN, BC_{4-x}N, B₅₀(C_{1-x}N_x)₂ and others, α-BN (or h-BN, graphene/graphite-like, <2770–3170 °C), α'-BN (or r-BN, β-graphite-like), β-BN (or c-BN, diamond-like), γ-BN (lonsdaleite-like), B_{4±x}C, β-B, N, C</p> <p>α-BN–C is plotted: gas-eutectic B_{4±x}C–C (2385 °C, ~ 30 at.% C)</p> <p>The interaction between graphite materials and α-BN initiates from 1900 °C and leads to the formation of B_{4±x}C and some complex phases. The solubility limit of carbon in the α-BN is ~ 15 at.%. The chemical composition of nanotubular structures varies widely within the C–B–N system. The stacking of C-rich or BN-rich tubular shells in multiwalled structures can be varied as well.</p>	[241–242, 244, 338–346, 359, 571–572, 635–638, 735, 862, 867, 878–879, 886]
C–B–N–Nb	<p>No diagram plot</p> <p>In vacuum the interaction between metal Nb and composition of α-BN + 23 mol.% B_{4±x}C begins from 1600 °C and leads to the formation of NbB_{1±x} and NbB_{2±x}; at 1900 °C dense specimens weld together.</p>	[829]
C–B–N–Si	<p>Plotted at 1400 and 2000 °C: Si₃B₂₀C₂ (?), α-BN (or h-BN, graphene/graphite-like, <2770–3170 °C), SiB_{3±x} (<~ 1270 °C), SiB₆ (<1850 °C), SiB_n (<~ 2020–2035 °C), α-Si₃N₄ (metastable, ?), β-Si₃N₄ (<~ 1800–1900 °C), B_{4±x}C, α-SiC, β-SiC, Si, β-B, N, C</p>	[241, 244, 359, 571–572, 762]

(continued)

Table 2.14 (continued)

System	Type of phase diagram (temperature and composition sections, constituent phases or phase fields) and/or character of interphase interaction and materials compatibility	References
C–B–N–Ta	No diagram plot In vacuum the interaction between metal Ta and composition of α -BN + 23 mol.% $B_{4\pm x}C$ begins from 1600 °C and leads to the formation of $Ta_3B_{4\pm x}$ (traces of λ - $TaB_{1\pm x}$, $TaB_{2\pm x}$ and γ - $Ta_{2\pm x}N$).	[829]
C–B–N–Ti	Plotted schematically General consideration of the system.	[571]
C–B–N–W	No diagram plot In vacuum the interaction between metal W and composition of α -BN + 23 mol.% $B_{4\pm x}C$ begins from 1900 °C (in powder mixtures—from 1800 °C) and leads to the formation of $W_{2\pm x}B$ and α - $WB_{1\pm x}$ (at temp. >2100 °C).	[829]
C–B–Nb	Plotted at 1750 °C: Nb_3B_3C (<2970 °C), $Nb_4B_3C_2$ (?), $Nb_7B_6C_3$ (?), $Nb_7B_4C_4$ (?), Nb_3B_2 (<~1800–2230 °C), $NbB_{1\pm x}$ (<~2270–2915 °C), Nb_5B_6 (<~2295–2870 °C, ?), Nb_3B_4 (<~2700–2935 °C), $NbB_{2\pm x}$ (<~3000–3035 °C), α - Nb_2C , β - $Nb_{2+x}C$, γ - $Nb_{2\pm x}C$, ζ - Nb_4C_{3-x} , $Nb_6C_{5\pm x}$, NbC_{1-x} , $B_{4\pm x}C$, Nb, β -B, C Eutectic $NbB_{2\pm x}$ - Nb_3B_4 - Nb_3B_3C (2900 °C, ~43 at.% Nb, ~12.5 at.% C) Eutectic $NbB_{2\pm x}$ - NbC_{1-x} - Nb_3B_3C (2700 °C, ~41.5 at.% Nb, ~15.5 at.% C) Eutectic $NbB_{1\pm x}$ - Nb_5B_6 - NbC_{1-x} (2730 °C, ~49.5 at.% Nb, ~8 at.% C) Eutectic Nb_3B_4 - NbC_{1-x} - Nb_3B_3C (2340 °C, ~44.5 at.% Nb, ~12.5 at.% C) Eutectic Nb- $NbB_{1\pm x}$ - β - $Nb_{2+x}C$ (2060 °C, ~75 at.% Nb, ~7 at.% C) Eutectic $NbB_{2\pm x}$ - NbC_{1-x} -C (2570 °C, 28.5 at.% Nb, 31.5 at.% C) Eutectic $NbB_{2\pm x}$ - $B_{4\pm x}C$ -C (2245 °C, ~15 at.% Nb, ~22.5 at.% C) Nb_3B_4 - Nb_3B_3C is plotted: eutectic—2940 °C, ~12–13 mol.% Nb_3B_4 (~12.5 at.% C) $NbB_{2\pm x}$ - Nb_3B_3C is plotted: eutectic—2910 °C, ~16–17 mol.% $NbB_{2\pm x}$ (~13 at.% C) Nb_3B_3C - NbC_{1-x} is plotted: eutectic—2790 °C, ~3–5 mol.% NbC_{1-x} (~14.5 at.% C) $NbB_{1\pm x}$ - NbC_{1-x} is plotted: eutectic—~2800 °C, ~20 mol.% NbC_{1-x} (~8.5 at.% C) Nb_3B_4 - NbC_{1-x} is plotted: eutectic—2830 °C, ~50 mol.% NbC_{1-x} (~10 at.% C) $NbB_{2\pm x}$ - NbC_{1-x} is plotted: eutectic—~2600–2900 °C (?), ~43–47 mol.% NbC_{1-x} (~16–18 at.% C) $NbB_{2\pm x}$ - $B_{4\pm x}C$ is plotted: eutectic—~2220–2280 °C, ~60–65 mol.% $B_{4\pm x}C$ (~12–13 at.% C, ?); the max. solid solubility of $NbB_{2\pm x}$ in $B_{4\pm x}C$ is ~3 mol.% and that of	[138, 241–244, 336, 347–351, 394, 832, 877]

(continued)

Table 2.14 (continued)

System	Type of phase diagram (temperature and composition sections, constituent phases or phase fields) and/or character of interphase interaction and materials compatibility	References
	<p>$B_{4\pm x}C$ in $NbB_{2\pm x}$ is ~ 2 mol.% (at the eutectic temp.) $NbB_{2\pm x}-C$ is plotted: eutectic—~ 2360–2710 °C, ~ 32–40 mol.% $NbB_{2\pm x}$ (~ 29 at.% C) At 2200 °C in vacuum the interaction of graphite with $NbB_{1\pm x}$ results in the formation of $NbB_{2\pm x}$ and NbC_{1-x}. Some data on the system available in literature are controversial.</p>	
C–B–Nb–Si	No diagram plot The general consideration of $NbB_{2\pm x}$ –SiC phase relations.	[566–567]
C–B–Nd	No diagram plot NdB_2C_2 , $Nd_5B_2C_5$, Nd_2BC , $Nd_{10}B_9C_{12}$, $Nd_5B_2C_{7+x}$ ($x \approx 0.1$), $NdBC$, ?	[391, 690]
C–B–Ni	Plotted at 900 – 1300 °C: $Ni_xB_yC_z$ (or $Ni_2B_{1-x}C_x$, $Ni_{6.6}B_{2.7}C_{0.6}$, ?), Ni_3B ($< \sim 1155$ °C), Ni_2B (< 1125 °C), Ni_4B_{3-x} (or o - Ni_4B_3 , $x \approx 0.2$, < 1025 °C), Ni_4B_{3+x} (or m - Ni_4B_3 , $x \approx 0.1$, $< \sim 1030$ °C), NiB (< 1035 °C), $B_{4\pm x}C$, Ni, β -B, C The contact interaction between $B_{4\pm x}C$ and Ni results in the formation of multi-phase transition zone, including Ni_4B_3 phase.	[241–242, 244, 727–729]
C–B–Ni–Si	No diagram plot The intensive interaction between $B_{4\pm x}C$ and Ni–Si alloy is observed at 1450 – 1480 °C.	[242]
C–B–Ni–Y	Plotted at 1300 °C: $YNi_2B_{2-y}C_x$ ($x = 1$, $0 \leq y \leq 1$), $YNiB_{4-x}C_x$, $YNiBC$, $Ni_xB_yC_z$ (or $Ni_2B_{1-x}C_x$, $Ni_{6.6}B_{2.7}C_{0.6}$, ?), YNi_4B , $YNi_{12}B_6$, $YNiB_4$, $Y_2Ni_3B_6$, YNi_8B_3 , Y_4NiB_{13} , $Y_3Ni_7B_2$, YNi_2C_2 , $Y_5Ni_{29}C_3$, $YNiC_2$, YBC , YB_2C_2 , YB_2C , Y_2BC_2 , YB_2 ($< \sim 2100$ – 2320 °C), YB_4 ($< \sim 2610$ – 2800 °C), $YB_{6\pm x}$ ($< \sim 2600$ – 2780 °C), YB_{12} (< 2200 °C), YB_{66} (< 2100 °C), Ni_3B ($< \sim 1155$ °C), Ni_2B (< 1125 °C), Ni_4B_{3-x} ($x \approx 0.2$, or o - Ni_4B_3 , < 1025 °C), Ni_4B_{3+x} ($x \approx 0.1$, or m - Ni_4B_3 , $< \sim 1030$ °C), NiB (< 1035 °C), $Y_{2\pm x}C$, $YC_{1\pm x}$, α - Y_3C_{4-x} , β - Y_3C_{4-x} , α - Y_2C_{3-x} , β - Y_2C_{3-x} , α - YC_2 , β - $YC_{2\pm x}$, $B_{4\pm x}C$, α -Y, β -Y, Ni, β -B, C At 1300 °C the complex compounds $YNiB_{4-x}C_x$ and YB_2C_2 are stable in the presence of graphite.	[241–242, 244, 728, 730]
C–B–Os–Th	No diagram plot $ThOs_2B_2C$?	[976]
C–B–Pd	No diagram plot Pd_5BC_x ($x \approx 0.2$, ?) At 1480 – 1500 °C the interaction between $B_{4\pm x}C$ and Pd results in the formation of Pd borides.	[242]
C–B–Pr	No diagram plot PrB_2C_2 , $Pr_{10}B_9C_{12}$, Pr_2BC , $Pr_5B_2C_5$, $PrBC$, $Pr_{10}B_4C_{13-x}$ ($0 \leq x \leq 0.5$, or $Pr_5B_2C_{6.25 \div 6.50}$), ?	[391, 690]

(continued)

Table 2.14 (continued)

System	Type of phase diagram (temperature and composition sections, constituent phases or phase fields) and/or character of interphase interaction and materials compatibility	References
C–B–Pt	No diagram plot At 1480–1500 °C the interaction between $B_{4\pm x}C$ and Pt results in the formation of Pt borides.	[242]
C–B–Pt–Th	No diagram plot $ThPt_2B_2C$, ?	[983]
C–B–Sc	Plotted at 25 and 1700 °C: ScB_2C_2 , Sc_2BC_2 , Sc_4BC_4 (or $Sc_3B_{0.75}C_3$), $\sim Sc_2BC_3$ (or $Sc_{98}B_{54}C_{157}$, $Sc_2B_{1.1}C_{3.2}$), $\sim Sc_2B_{30}C_3$ (or $ScB_{15}C_{1.60}$, ?), $\sim Sc_4B_{68}C$ (or $ScB_{17}C_{0.25}$, ?), ScB_2C (?), $ScB_{13}C$ (?), ScB_2 (<2250 °C), ScB_{12} (<2040 °C), ScC_{1-x} , α - Sc_4C_3 , β - Sc_4C_{3+x} , Sc_3C_{4-x} , $B_{4\pm x}C$, α -Sc, β -Sc, β -B, C No solid solutions based on binary and ternary compounds.	[391, 690, 971–972]
C–B–Si	Plotted at 1130–2480 °C: SiB_nC_x ($n \approx 30$, $x = 0.35$), $\sim SiB_6C_9$ (?), $SiB_{3\pm x}$ (<~1270 °C), SiB_6 (<1850 °C), SiB_n (<~2020–2035 °C), $B_{4\pm x}C$, SiC, Si, β -B, C Eutectic SiC – $B_{4\pm x}C$ –C (~2245–2300 °C, ~62–70 mol.% $B_{4\pm x}C$, ~30 mol.% SiC, ?) Transition reaction: liquid + C (graphite) \leftrightarrow SiC + $B_{4\pm x}C$ (2295 °C, ?) SiC – $B_{4\pm x}C$ is plotted: eutectic—~2240–2300 °C (?)	[241–242, 244, 352–359, 571–572, 889–890]
C–B–Si–Ta	No diagram plot The general consideration of $TaB_{2\pm x}$ –SiC phase relations.	[566–567]
C–B–Si–Ti	Plotted schematically: $Ti_5Si_3(B,C)_{1-x}$ (Nowotny phase), $Ti_5Si_{3\pm y}C_x$ ($0 \leq x \leq 0.99$, solid solution based on $Ti_5Si_{3\pm x}$, <~2130–2335 °C), Ti_3SiC_2 (<2375 °C, narrow homog. range at lower temp., $M_{n+1}AX_n$ -phase), SiB_nC_x ($n \approx 30$, $x = 0.35$), $\sim SiB_6C_9$ (?), $SiB_{3\pm x}$ (<~1270 °C), SiB_6 (<1850 °C), SiB_n (<~2020–2035 °C), Ti_3Si (<1170 °C), Ti_5Si_4 (<1920 °C), $TiSi$ (<1570 °C), $TiSi_2$ (<1490–1500 °C), TiB_{1-x} (<~2180–2200 °C), Ti_3B_4 (<~2200–2205 °C), $TiB_{2\pm x}$ (<3200–3250 °C), TiC_{1-x} , $B_{4\pm x}C$, SiC, α -Ti, β -Ti, Si, β -B, C TiC_{1-x} –SiC– $TiB_{2\pm x}$ is plotted: eutectic—~2110–2190 °C, ~16–34 mol.% TiC_{1-x} , ~44–56 mol.% SiC (~32–35 at.% C) SiC – $B_{4\pm x}C$ – $TiB_{2\pm x}$ is plotted: eutectic—~2200–2250 °C, ~51 mol.% $B_{4\pm x}C$, ~41 mol.% SiC (~25 at.% C) SiC – $TiB_{2\pm x}$ is plotted: eutectic—~2150–2250 °C, ~64–68 mol.% SiC (~27 at.% C)	[241–242, 244, 419, 463, 487, 503, 506–509, 566–567, 571, 640–642, 654–659, 680–681, 691, 731–734, 860, 889]
C–B–Si–V	No diagram plot The general consideration of VB_2 –SiC phase relations	[566–567]

(continued)

Table 2.14 (continued)

System	Type of phase diagram (temperature and composition sections, constituent phases or phase fields) and/or character of interphase interaction and materials compatibility	References
C–B–Si–W	SiC– β -W ₂ B _{5-x} is plotted: eutectic— ~ 2030 – 2090 °C, ~ 40 mol.% SiC	[566–567, 569]
C–B–Si–Zr	SiC–ZrB _{2+x} is plotted: eutectic— 2270 °C, 23 mol.% ZrB _{2+x} ; the max. solid solubility of ZrB _{2+x} in SiC is ~ 2.7 mol.% and that of SiC in ZrB _{2+x} is ~ 3 mol.% (at the eutectic temp.) At 2000 °C SiC, ZrB _{2+x} and B _{4+x} C within the mol. ratios $\sim (20\text{--}45) : (30\text{--}70) : (10\text{--}25)$ are compatible with each other.	[360, 566–567, 590, 654]
C–B–Sm	No diagram plot α -SmB ₂ C ₂ , β -SmB ₂ C ₂ , Sm ₅ B ₂ C ₅ , Sm ₅ B ₂ C ₆ , SmBC, ?	[391, 690]
C–B–Ta	Plotted at 1750 °C: Ta _{2+x} B (~ 1900 – 2420 °C), Ta ₃ B _{2+x} (< 2180 °C), λ -TaB _{1+x} (< 3090 °C), Ta ₃ B _{4+x} (< 3030 °C), TaB _{2+x} ($< \sim 3040$ °C), α -Ta _{2+x} C, β -Ta _{2+x} C, ζ -Ta ₄ C _{3-x} , Ta ₆ C _{5+x} , TaC _{1-x} , B _{4+x} C, Ta, β -B, C Eutectic TaB _{2+x} –B _{4+x} C– β -B (~ 2000 °C, ?) Eutectic TaB _{2+x} –B _{4+x} C–C (~ 2150 °C) Eutectic TaB _{2+x} –TaC _{1-x} –C (2550 °C) TaB _{2+x} –B _{4+x} C is plotted: eutectic— ~ 2340 – 2400 °C, ~ 67 – 69 mol.% B _{4+x} C (~ 14.5 at.% C); the max. solid solubility of TaB _{2+x} in B _{4+x} C is < 1 mol.% and that of B _{4+x} C in TaB _{2+x} is ~ 1 mol.% (at the eutectic temp.) TaB _{2+x} –TaC _{1-x} is plotted: eutectic— ~ 2690 – 2770 °C, ~ 34 – 35 mol.% TaC _{1-x} (~ 12 at.% C); the max. solid solubility of TaB _{2+x} in TaC _{1-x} is ~ 7 mol.% (at the eutectic temp.), the components are virtually insoluble in each other at temp. ≤ 2100 °C TaB _{2+x} –C is plotted: eutectic— ~ 2390 – 2650 °C, ~ 32 mol.% TaB _{2+x} (~ 40 at.% C)	[138, 241–242, 244, 349, 351, 361–365, 723, 832]
C–B–Tb	No diagram plot TbB ₂ C, TbB ₂ C ₂ , Tb ₂ B ₄ C, Tb ₅ B ₂ C ₅ , Tb ₅ B ₂ C ₆ , ?	[391, 690]
C–B–Th	Plotted at 900 , 1300 and 1400 °C: ThB ₂ C, ThBC ₂ , Th ₂ BC ₂ , ThBC, Th ₃ BC ₃ , ThB ₄ (< 2475 °C), ThB _{6+x} (< 2450 °C), \sim ThB ₆₆₊₇₇ ($< \sim 2150$ °C), ThC _{1+x} , α -ThC _{2-x} , β -ThC _{2-x} , γ -ThC _{2-x} , B _{4+x} C, α -Th, β -Th, β -B, C No mutual solid solubility between Th carbides and borides.	[138, 238, 241, 244, 391]

(continued)

Table 2.14 (continued)

System	Type of phase diagram (temperature and composition sections, constituent phases or phase fields) and/or character of interphase interaction and materials compatibility	References
C–B–Ti	<p>Plotted at 1500–2900 °C: TiB_3C_y (?), TiB_{1-x} ($< \sim 2180$–2200 °C), Ti_3B_4 ($< \sim 2200$–2205 °C), $\text{TiB}_{2\pm x}$ (< 3200–3250 °C), $\text{B}_{4\pm x}\text{C}$, TiC_{1-x}, α-Ti, β-Ti, β-B, C</p> <p>Eutectic TiB_{1-x}–TiC_{1-x} ($x \approx 0.5$)–β-Ti (~ 1450–1535 °C, ~ 91–93 at.% Ti, ~ 2–3 at.% C)</p> <p>Eutectic $\text{TiB}_{2\pm x}$–$\text{B}_{4\pm x}\text{C}$ ($x \approx 4 \div 7$, $\sim \text{B}_{8 \div 11}\text{C}$)–$\beta$-B ($\sim 1990$–$2060$ °C, ~ 1.5–1.9 at.% Ti, ~ 0.2–1.5 at.% C)</p> <p>Eutectic $\text{TiB}_{2\pm x}$–$\text{B}_{4\pm x}\text{C}$ ($x \approx 0$)–C (~ 2110–2245 °C, ~ 7–10 at.% Ti, ~ 23–28 at.% C)</p> <p>Eutectic $\text{TiB}_{2\pm x}$–TiC_{1-x} ($x \approx 0$)–C (~ 2380–2400 °C, ~ 26–29 at.% Ti, 37.4–38.0 at.% C)</p> <p>$\text{TiB}_{2\pm x}$–$\text{B}_{4\pm x}\text{C}$ ($x \approx 0$) is plotted: eutectic—~ 1900–2240 °C, ~ 58–60 mol.% $\text{B}_{4\pm x}\text{C}$ (~ 14 at.% C); the max. solid solubility of $\text{TiB}_{2\pm x}$ in $\text{B}_{4\pm x}\text{C}$ is ~ 2 mol.% and that of $\text{B}_{4\pm x}\text{C}$ in $\text{TiB}_{2\pm x}$ is ~ 0.5 mol.% (at the eutectic temp.)</p> <p>$\text{TiB}_{2\pm x}$–$\text{B}_{4\pm x}\text{C}$ ($x \approx 0.5 \div 2.0$, $\sim \text{B}_{4.5 \div 6.0}\text{C}$) is plotted: eutectic—$\sim 2160$–$2380$ °C, ~ 70–75 mol.% $\text{B}_{4\pm x}\text{C}$ (~ 11–16 at.% C); the max. solid solubility of $\text{TiB}_{2\pm x}$ in $\text{B}_{4\pm x}\text{C}$ is ~ 2.4–4.0 mol.% and that of $\text{B}_{4\pm x}\text{C}$ in $\text{TiB}_{2\pm x}$ is ~ 1.0–1.5 mol.% (at the eutectic temp.)</p> <p>$\text{TiB}_{2\pm x}$ ($x \approx 0$)–TiC_{1-x} ($x = 0.05$) is plotted: eutectic—~ 2480–2700 °C, ~ 54–70 mol.% TiC_{1-x} (~ 21–29 at.% C); the max. solid solubility of $\text{TiB}_{2\pm x}$ in TiC_{1-x} is ~ 2–3.5 mol.% and that of TiC_{1-x} in $\text{TiB}_{2\pm x}$ is < 2 mol.% (at the eutectic temp.)</p> <p>$\text{TiB}_{2\pm x}$ ($x \approx 0$)–TiC_{1-x} ($x = 0.08$) is plotted: eutectic—~ 2600–2685 °C, ~ 67–70 mol.% TiC_{1-x} (~ 27–29 at.% C); the max. solid solubility of $\text{TiB}_{2\pm x}$ in TiC_{1-x} is ~ 2–5 mol.% and that of TiC_{1-x} in $\text{TiB}_{2\pm x}$ is ~ 2–3 mol.% (at the eutectic temp.)</p> <p>$\text{TiB}_{2\pm x}$ ($x \approx 0$)–TiC_{1-x} ($x = 0.20$) is plotted: eutectic—~ 2450–2690 °C, ~ 62–71 mol.% TiC_{1-x} (~ 22–26.5 at.% C); the max. solid solubility of $\text{TiB}_{2\pm x}$ in TiC_{1-x} is ~ 3–5 mol.% and that of TiC_{1-x} in $\text{TiB}_{2\pm x}$ is ~ 1–5 mol.% (at the eutectic temp.)</p> <p>$\text{TiB}_{2\pm x}$ ($x \approx 0$)–TiC_{1-x} ($x = 0.32$) is plotted: eutectic—~ 2380–2675 °C, ~ 76 mol.% TiC_{1-x} (~ 28–29 at.% C); the max. solid solubility of $\text{TiB}_{2\pm x}$ in TiC_{1-x} is ~ 5–7 mol.% and that of TiC_{1-x} in $\text{TiB}_{2\pm x}$ is ~ 5 mol.% (at the eutectic temp.)</p> <p>$\text{TiB}_{2\pm x}$–C is plotted: eutectic—~ 2490–2555 °C, ~ 39–42 mol.% $\text{TiB}_{2\pm x}$ (~ 32–34.5 at.% C); the max. solid solubility of C in $\text{TiB}_{2\pm x}$ is ~ 2–5 mol.% (at the eutectic temp.)</p>	[138, 241–242, 244, 252, 330, 364–366, 391, 567, 571, 573, 596–599, 627, 691, 838, 889, 985]

(continued)

Table 2.14 (continued)

System	Type of phase diagram (temperature and composition sections, constituent phases or phase fields) and/or character of interphase interaction and materials compatibility	References
	At 1600 °C TiB_{1-x} is in equilibrium with TiC_{1-x} ($\text{TiC}_{0.4 \div 0.65}$), $\text{TiB}_{2 \pm x}$ —with TiC_{1-x} ($\text{TiC}_{0.65 \div 1.0}$) and Ti_3B_4 —with $\text{TiC}_{0.65}$. In the $\text{TiB}_{2 \pm x}$ – TiC_{1-x} system, with increasing C content in TiC_{1-x} from $\text{TiC}_{0.6}$ to $\text{TiC}_{0.8}$, the eutectic temp. increases; and further increase in C content from $\text{TiC}_{0.8}$ to $\text{TiC}_{1.0}$ leads to the decrease of the eutectic temp. With increasing C content in TiC_{1-x} , the solubility of $\text{TiB}_{2 \pm x}$ in TiC_{1-x} declines. In the wide temp. ranges, depend. on compos., graphite is in equilibrium with $\text{TiB}_{2 \pm x} + \text{TiC}_{1-x}$ or $\text{TiB}_{2 \pm x} + \text{B}_{4 \pm x}\text{C}$.	
C–B–Tm	No diagram plot	[690]
	TmB_2C_2 , TmB_2C , $\text{Tm}_5\text{B}_2\text{C}_6$, $\text{Tm}_5\text{B}_2\text{C}_5$, $\text{Tm}_2\text{B}_{57}\text{C}_8$, ?	
C–B–U	Plotted at 1300–1600 °C: $\text{UB}_{1-x}\text{C}_{1+x}$ (<2145 °C), UB_2C (<2280 °C), $\sim \text{U}_5\text{B}_2\text{C}_7$, $\text{UB}_{2 \pm x}$ (<2385 °C), UB_4 (<2495 °C), UB_{12} (<2145 – 2235 °C), $\text{UC}_{1 \pm x}$, ζ - U_2C_3 , α - UC_2 , β - UC_{2-x} , $\text{B}_{4 \pm x}\text{C}$, U, β -B, C	[138, 241, 244, 367–368, 391, 690]
C–B–V	Plotted at 1450, 1600 and 2000 °C: $\text{V}_{1-x}\text{B}_{24}\text{C}$ ($\text{V}_{1-x}\text{B}_{25-x}\text{B}_{25}\text{C}$ solid solution, metastable, ?), V_3B_2 (or $\text{V}_3(\text{B}_{1-x}\text{C}_x)_2$, $<\sim 1900$ – 1915 °C), VB ($<\sim 2550$ – 2570 °C), V_5B_6 ($<\sim 1725$ – 2560 °C), V_3B_4 ($<\sim 2600$ – 2615 °C), V_2B_3 ($<\sim 2610$ – 2665 °C), $\text{VB}_{2 \pm x}$ (<2700 – 2750 °C), α - V_{2+x}C , β - V_{2+x}C , β' - V_{2+x}C , ζ - V_4C_{3-x} , $\text{V}_6\text{C}_{5 \pm x}$, $\text{V}_8\text{C}_{7 \pm x}$, VC_{1-x} , $\text{B}_{4 \pm x}\text{C}$, V, β -B, C $\text{VB}_{2 \pm x}$ – $\text{B}_{4 \pm x}\text{C}$ is plotted: eutectic— ~ 2140 – 2200 °C, ~ 52 – 55 mol.% $\text{B}_{4 \pm x}\text{C}$ (~ 13 at.% C); the max. solid solubility of $\text{VB}_{2 \pm x}$ in $\text{B}_{4 \pm x}\text{C}$ is <1.5 mol.% and that of $\text{B}_{4 \pm x}\text{C}$ in $\text{VB}_{2 \pm x}$ is ~ 2 mol.% (at the eutectic temp.) $\text{VB}_{2 \pm x}$ – VC_{1-x} ($x = 0.12$) is plotted: eutectic— ~ 2100 – 2140 °C, ~ 54 mol.% VC_{1-x} (~ 20 at.% C); the max. solid solubility of $\text{VB}_{2 \pm x}$ in VC_{1-x} is ~ 8.5 – 10.0 mol.% and that of VC_{1-x} in $\text{VB}_{2 \pm x}$ is <2 mol.% (at the eutectic temp.) $\text{VB}_{2 \pm x}$ –C is plotted: eutectic— 2450 °C, ~ 30 – 32 mol.% $\text{VB}_{2 \pm x}$ (~ 44 at.% C); the solubility of C in $\text{VB}_{2 \pm x}$ is low Some data on the system available in literature are controversial.	[138, 241–242, 244, 349, 362, 364–365, 369, 371, 832]

(continued)

Table 2.14 (continued)

System	Type of phase diagram (temperature and composition sections, constituent phases or phase fields) and/or character of interphase interaction and materials compatibility	References
C-B-W	<p>Plotted at 1500–2800 °C: $W_{2\pm x}B$ (<2670 °C), $\alpha-WB_{1\pm x}$ (<2110–2170 °C), $\beta-WB_{1\pm x}$ (from 2110–2170 °C to 2665 °C), $\beta-W_2B_{5-x}$ (~900–2365 °C), WB_{4+x} (<2020 °C), $\alpha-W_{2+x}C$, $\beta-W_{2+x}C$, $\gamma-W_{2+x}C$, $\beta-WC_{1-x}$, $\delta-WC_{1\pm x}$, $B_{4\pm x}C$, W, $\beta-B$, C</p> <p>Eutectic $WB_{4+x}-B_{4\pm x}C-\beta-B$ (1950 °C)</p> <p>Eutectic $W_{2\pm x}B-\gamma-W_{2\pm x}C-W$ (~2355–2385 °C, ~70.7–71.0 at.% W, ~11–12 at.% C)</p> <p>Eutectic $W_{2\pm x}B-\beta-WB_{1\pm x}-\gamma-W_{2\pm x}C$ (~2305–2325 °C, ~60–62 at.% W, ~14 at.% C)</p> <p>Eutectic $\beta-WB_{1\pm x}-\gamma-W_{2\pm x}C-\delta-WC_{1\pm x}$ (~2300–2325 °C, ~55–58 at.% W, ~16–19 at.% C)</p> <p>Eutectic $\beta-WB_{1\pm x}-\alpha-W_2B_{5-x}-C$ (~2240–2260 °C, ~32–35 at.% W, ~7.4–7.9 at.% C)</p> <p>Eutectic $\alpha-W_2B_{5-x}-B_{4\pm x}C-C$ (2180 °C, ~18–20 at.% W, ~8–11 at.% C)</p> <p>$W_{2\pm x}B-\gamma-W_{2\pm x}C$ is plotted: eutectic—~2370–2390 °C, ~41 mol.% $\gamma-W_{2\pm x}C$ (~12.0–12.5 at.% C); the max. solid solubility of $W_{2\pm x}B$ in $\gamma-W_{2\pm x}C$ is ~7 mol.% and that of $\gamma-W_{2\pm x}C$ in $W_{2\pm x}B$ is ~3 mol.% (at the eutectic temp.)</p> <p>$W_{2\pm x}B-\delta-WC_{1\pm x}$ is plotted: eutectic—2290 °C</p> <p>$\beta-WB_{1\pm x}-\gamma-W_{2\pm x}C$ is plotted: eutectic—~2325–2330 °C, ~38 mol.% $\gamma-W_{2\pm x}C$ (~15 at.% C); the max. solid solubility of $\beta-WB_{1\pm x}$ in $\gamma-W_{2\pm x}C$ is ~5 mol.% and that of $\gamma-W_{2\pm x}C$ in $\beta-WB_{1\pm x}$ is ~5.5 mol.% (at the eutectic temp.)</p> <p>$\alpha-W_2B_{5-x}-B_{4\pm x}C$ is plotted: eutectic—~2130–2220 °C, ~76 mol.% W_2B_{5-x} (~6.0–7.2 at.% C); the max. solid solubility of $\alpha-W_2B_{5-x}$ in $B_{4\pm x}C$ is ~1.5 mol.% and that of $B_{4\pm x}C$ in $\alpha-W_2B_{5-x}$ is ~3 mol.% (at the eutectic temp.)</p> <p>$\beta-WB_{1\pm x}-C$ is plotted: eutectic—~2270–2400 °C, ~77 mol.% $\beta-WB_{1\pm x}$ (~13–14 at.% C); the max. solubility of C in $\beta-WB_{1\pm x}$ is 2–3 at.% (at the eutectic temp.)</p> <p>$\alpha-W_2B_{5-x}-C$ is plotted: eutectic—~2190–2285 °C, ~63–65 mol.% $\alpha-W_2B_{5-x}$ (~7.0–7.6 at.% C); the max. solubility of C in $\alpha-W_2B_{5-x}$ is 2.0–2.5 at.% (at the eutectic temp.)</p> <p>At 2000 °C the interaction of graphite with $W_{2\pm x}B$ results in the formation of $\alpha-WB_{1\pm x}$ and $\delta-WC_{1\pm x}$. At 1100–1600 °C $B_{4\pm x}C$ reacts with metal W with the formation of $W_{2\pm x}B$ and $\alpha-WB_{1\pm x}$.</p>	[138, 241–242, 244, 320, 372–377, 394, 564–565, 912]

(continued)

Table 2.14 (continued)

System	Type of phase diagram (temperature and composition sections, constituent phases or phase fields) and/or character of interphase interaction and materials compatibility	References
C–B–Y	Plotted schematically: YBC, YB ₂ C ₂ , YB ₂ C, Y ₂ BC ₂ , YB ₂ (<~ 2100–2320 °C), YB ₄ (<~ 2610–2800 °C), YB _{6±x} (<~ 2600–2780 °C), YB ₁₂ (<2200 °C), YB ₆₆ (<2100 °C), Y _{2±x} C, YC _{1±x} , α-Y ₃ C _{4-x} , β-Y ₃ C _{4-x} , α-Y ₂ C _{3-x} , β-Y ₂ C _{3-x} , α-YC ₂ , β-YC _{2±x} , B _{4±x} C, α-Y, β-Y, β-B, C	[241, 244, 391, 690, 728]
C–B–Yb	No diagram plot YbB ₂ C, YbB ₂ C ₂ , ?	[391, 690]
C–B–Zr	Plotted at 1400–3000 °C: ZrB _{2±x} (<3220–3265 °C), ZrB _{12-x} (~ 1695–2290 °C), ZrC _{1-x} , B _{4±x} C, α-Zr, β-Zr, β-B, C Eutectic ZrB _{2±x} –ZrC _{1-x} –β-Zr (~ 1615–1650 °C, ~ 86–88 at.% Zr, ~ 1.4–2.0 at.% C) Eutectic ZrB _{12-x} –B _{4±x} C–β-B (~ 1990 °C) Eutectic ZrB _{2±x} –B _{4±x} C–C (~ 2165–2190 °C, ~ 11 at.% Zr, ~ 23–25 at.% C) Eutectic ZrB _{2±x} –ZrC _{1-x} –C (2360 °C) ZrB _{2±x} –B _{4±x} C is plotted: eutectic—~ 2200–2300 °C, ~ 65–75 mol.% B _{4±x} C (~ 13–16 at.% C); the max. solid solubility of ZrB _{2±x} in B _{4±x} C is ~ 1 mol.% and B _{4±x} C in ZrB _{2±x} is ~ 1.5 mol.% (at the eutectic temp.) ZrB _{2±x} (x ≈ 0)–ZrC _{1-x} (x = 0.03 ÷ 0.12) is plotted: eutectic—~ 2620–2850 °C, ~ 42–43 mol.% ZrC _{1-x} (~ 19–20 at.% C); the max. solid solubility of ZrB _{2±x} in ZrC _{1-x} is ~ 1–5 mol.% and that of ZrC _{1-x} in ZrB _{2±x} is <2 mol.% (at the eutectic temp.); some data on this quasibinary system available in literature are controversial ZrB _{2±x} –C is plotted: eutectic—~ 2230–2390 °C, ~ 40 mol.% ZrB _{2±x} (~ 33 at.% C); the max. solubility of C in ZrB _{2±x} is ≤ 2 at.% C (at the eutectic temp.)	[138, 241–242, 244, 252, 330, 364–365, 378–381, 391, 394, 567, 573–574]
C–Be–O	No diagram plot In vacuum (~ 10 ⁻² –10 ⁻⁴ Pa), the interaction in powdered mixtures between C and BeO with the formation of Be ₂ C initiates from 1300–1315 °C and that on bulk materials contacts—from 2000–2300 °C. In air, heating the powdered mixture BeO + C at 1800–1900 °C results in the reduction of BeO with the subsequent secondary oxidation of Be ₂ C and Be vapour.	[138, 194, 382]
C–Be–O–Th	No diagram plot At temp. ≥ 1100 °C BeO and ThC _{1±x} interact with the formation of ThO _{2-x} .	[242]
C–Be–O–Ti	No diagram plot At 1500–2200 °C BeO and TiC _{1-x} interact with the formation of Be ₂ C.	[242]
C–Be–O–U	No diagram plot At 1600–2000 °C BeO and UC _{1±x} interact with the formation of Be ₂ C and intermetallic compounds.	[592]

(continued)

Table 2.14 (continued)

System	Type of phase diagram (temperature and composition sections, constituent phases or phase fields) and/or character of interphase interaction and materials compatibility	References
C–Be–Si	Plotted schematically at 1000 °C: Be ₂ C, α -SiC, Be, Si, C Graphite is in equilibrium with Be ₂ C + SiC. In vacuum at 1000–1150 °C SiC interacts with Be negligibly; at higher temp. the interaction leads to the formation of Be ₂ C and Si.	[242, 814]
C–Be–Ta	No diagram plot Be _x TaC _{0.76} , ? At 1400–2800 °C the addition of Be (1 %) does not affect the densification process of TaC _{1-x} powder by hot pressing.	[138]
C–Be–Th	Plotted at 1000 °C: no ternary compounds, ThBe ₁₃ (<~1930 °C), ThC _{1±x} , α -ThC _{2-x} , β -ThC _{2-x} , γ -ThC _{2-x} , Be ₂ C, BeC ₂ , α -Th, β -Th, α -Be, β -Be, C No solid solutions based on binary compounds.	[244, 973]
C–Be–U	Plotted at 1000 °C: no ternary compounds, UBe ₁₃ (<~1980 °C), UC _{1±x} , ζ -U ₂ C ₃ , α -UC _{2-x} , β -UC _{2-x} , Be ₂ C, BeC ₂ , α -U, β -U, γ -U, α -Be, β -Be, C No solid solutions based on binary compounds. α -UC _{2-x} -UC _{1±x} -Be ₂ C is plotted at 1700 °C: UC _{1±x} (solid solution), ζ -U ₂ C ₃ , α -UC _{2-x} (solid solution), Be ₂ C	[242, 244, 383, 973]
C–Bi–Pb	No diagram plot The corrosion resistance of graphite in liquid eutectic alloy Bi–Pb in the wide range of temp. is very high: no corrosion/erosion in dynamic conditions (4 m/s) testing at 1095 °C for 24 h.	[138]
C–Ca–O	Plotted at 25 °C: CaCO ₃ , CaO (<2565–2585 °C), α -CaC ₂ , β -CaC ₂ , γ -CaC ₂ , δ -CaC ₂ , CaC _{6±x} , α -Ca, β -Ca, O, C The interaction between C and CaO in powdered mixtures initiates in vacuum from 1300 °C and under atmospheric pressure—from 2130 °C.	[194, 382, 974]
C–Ca–O–U	No diagram plot At 1900 °C the interaction between β -UC _{2-x} and CaO is weak.	[242]
C–Cd–Ti	No diagram plot Ti ₂ CdC (M _{n+1} AX _n -phase)	[680–681, 744–745, 860]
C–Ce–Ir	Plotted partially at 1100–1400 °C: Ce ₄ Ir (<710 °C), Ce ₃ Ir (<~880–950 °C), Ce ₇ Ir ₃ (<950 °C), Ce ₂ Ir (or Ce ₃ Ir ₂ (?), <1100 °C), Ce ₅ Ir ₃ (<1100 °C), Ce ₅ Ir ₄ (or Ce ₁₅ Ir ₁₃ (?), <1180 °C), CeIr _{2±x} (<2250 °C), CeIr ₃ (<2105–2120 °C), Ce ₂ Ir ₇ (<2000 °C), CeIr ₅ (<1955–1960 °C), Ce ₂ C ₃ , α -CeC ₂ , β -CeC _{2±x} , α -Ce, β -Ce, γ -Ce, δ -Ce, Ir, C Depend. on compos., graphite is in equilibrium with CeIr ₅ + Ir, or CeIr ₅ + CeIr _{2±x} , or CeIr _{2±x} + β -CeC _{2±x} .	[990]
C–Ce–Mo	Plotted at 1600 °C: Ce ₂ C ₃ , β -CeC _{2±x} , β -Mo _{2±x} C, α -Ce, β -Ce, γ -Ce, δ -Ce, Mo, C No solubility between Ce and Mo carbides	[391]

(continued)

Table 2.14 (continued)

System	Type of phase diagram (temperature and composition sections, constituent phases or phase fields) and/or character of interphase interaction and materials compatibility	References
C–Ce–N–Th	No diagram plot ThC _{1±x} –CeN _{1±x} carbonitride continuous solid solution	[391]
C–Ce–N–U	No diagram plot UC _{1±x} –CeN _{1±x} carbonitride continuous solid solution	[391]
C–Ce–Si	Plotted at 400 °C: Ce ₃ SiC, Ce ₃ Si ₂ C ₂ (?), (Ce ₃ Si ₂)C _x (interstitial solid solution based on Ce ₃ Si ₂ —up to ~12–14.5 at.% C, <~1390 °C), CeSi _{2–x} (<1620 °C), Ce ₃ Si ₅ (<~1560 °C), CeSi (<1470 °C), Ce ₅ Si ₄ (<~1440 °C), Ce ₅ Si ₃ (<~1400 °C), CeC, Ce ₂ C ₃ , α-CeC ₂ , β-CeC _{2±x} , β-SiC, α-Ce, β-Ce, γ-Ce, δ-Ce, Si, C No solid solutions based on binary and ternary compounds apart from Ce ₃ Si ₂ .	[628]
C–Ce–Th	Plotted at 1600 °C: (Th,Ce)C _{1–x} (monocarbide solid solution based on ThC _{1–x} —up to 40 mol.% ‘CeC’), (Ce,Th) ₂ C ₃ (solid solution based on Ce ₂ C ₃), (Th,Ce)C _{2±x} (γ-ThC _{2–x} –β-CeC _{2±x} dicarbide continuous solid solution), α-Ce, β-Ce, γ-Ce, δ-Ce, α-Th, β-Th, C	[391]
C–Ce–U	Plotted at 1600 °C: (U,Ce)C _{1±x} (monocarbide solid solution based on UC _{1±x} —up to 15 mol.% ‘CeC’), ζ-U ₂ C ₃ , Ce ₂ C ₃ , (U,Ce)C _{2±x} (α-UC _{2–x} –β-CeC _{2±x} dicarbide continuous solid solution), α-Ce, β-Ce, γ-Ce, δ-Ce, α-U, β-U, γ-U, C	[391]
C–Ce–U–Zr	No diagram plot The solubility of ‘CeC’ in (U,Zr,Ce)C _{1–x} decreases sharply with increasing concentration of Zr	[391]
C–Ce–Zr	Plotted at 1600 °C: ZrC _{1–x} , Ce ₂ C ₃ , α-CeC ₂ , β-CeC _{2±x} , α-Ce, β-Ce, γ-Ce, δ-Ce, α-Zr, β-Zr, C No solubility between Ce and Zr carbides.	[391]
C–Co–Fe–Ni–W	Plotted partially General consideration of the system	[757]
C–Co–Hf	Plotted at 1100 °C: Hf _{2+x} Co (<1315 °C), HfCo _{1±x} (<1640 °C), HfCo _{2±x} (<1670 °C), Hf ₂ Co ₇ (or HfCo ₄ , <1350 °C), Hf ₆ Co ₂₃ (~950–1280 °C), HfCo ₇ (~1050–1250 °C), HfC _{1–x} , α-Hf, β-Hf, α-Co, C HfC _{1–x} –Co is plotted: eutectic—1370 °C, ~3 mol.% HfC _{1–x} HfC _{1–x} is in equilibrium with Co and series of Co-Hf intermetallides.	[242, 244, 391, 417]
C–Co–Hf–Nb	HfC _{1–x} (x = 0.06)–NbC _{1–x} (x = 0.18)–Co is plotted The eutectic equilibrium between two solid solutions based on HfC _{1–x} –NbC _{1–x} monocarbide continuous solid solution and metal Co at 1360–1435 °C.	[621]
C–Co–Hf–Ta	HfC _{1–x} (x = 0.06)–TaC _{1–x} (x = 0.08)–Co is plotted The eutectic equilibrium between two solid solutions based on HfC _{1–x} –TaC _{1–x} monocarbide continuous solid solution and metal Co at 1420–1445 °C.	[621]

(continued)

Table 2.14 (continued)

System	Type of phase diagram (temperature and composition sections, constituent phases or phase fields) and/or character of interphase interaction and materials compatibility	References
C–Co–Hf–Ti	HfC _{1-x} ($x = 0.06$)–TiC _{1-x} ($x = 0.20$)–Co is plotted There are three binary and one ternary (1370 °C, 3.5 mol.% HfC _{1-x} , 5.5 mol.% TiC _{1-x}) eutectics in the system.	[622]
C–Co–Hf–V	HfC _{1-x} ($x = 0.06$)–VC _{1-x} ($x = 0.17$)–Co is plotted There are three binary and one ternary (1320 °C, 3.5 mol.% HfC _{1-x} , 10.0 mol.% VC _{1-x}) eutectics in the system.	[622]
C–Co–Hf–Zr	HfC _{1-x} ($x = 0.06$)–ZrC _{1-x} ($x = 0.19$)–Co is plotted The eutectic equilibrium between two solid solutions based on HfC _{1-x} –ZrC _{1-x} monocarbide continuous solid solution and metal Co at 1380–1435 °C.	[621]
C–Co–Mo	Plotted at 1000 °C: $\sim \text{Mo}_{3 \div 4}\text{Co}_{2 \div 3}\text{C}$ (or η_2 , η_1 -Mo ₃ Co ₃ C), η_1 -Mo ₆ Co ₆ C, σ -Mo ₃ Co _{2-x} (~ 1000 –1620 °C), μ -Mo ₆ Co _{7 \pm x} (or μ -MoCo _{1+x} , ε -MoCo _{1+x} , $< \sim 1510$ °C), κ -MoCo _{3 \pm x} (< 1025 °C), θ -Mo ₂ Co _{9-x} (~ 1015 –1200 °C), α -Mo _{2+x} C, Mo, α -Co, C	[242, 244, 391, 417]
C–Co–Nb	Plotted at 1100 °C: η -Co ₂ Nb ₄ C, Co ₃ Nb ₃ C (?), μ -CoNb _{1 \pm x} (or μ -Co ₇ Nb _{6 \pm x} , $< \sim 1400$ –1480 °C), λ_1 -Co ₅ Nb _{3-x} (1200–1420 °C), $\lambda_2(\beta)$ -Co _{2 \pm x} Nb ($< \sim 1480$ –1520 °C), λ_3 -Co ₃ Nb (from 1030 °C to 1240–1250 °C), χ -Co ₇ Nb _{2 \pm x} (< 1050 °C), α -Nb ₂ C, β -Nb _{2+x} C, NbC _{1-x} , Nb, α -Co, ε -Co, C NbC _{1-x} –Co is plotted: eutectic— ~ 1360 –1380 °C, ~ 5 mol.% NbC _{1-x} ; the max. solubility of NbC _{1-x} in Co is ~ 1.5 mol.% and that of Co in NbC _{1-x} is 8 mol.% (at the eutectic temp.)	[242, 244, 384–385, 391, 417]
C–Co–Nb–Ta	NbC _{1-x} ($x = 0.18$)–TaC _{1-x} ($x = 0.18$)–Co is plotted The eutectic equilibrium between two solid solutions based on NbC _{1-x} –TaC _{1-x} monocarbide continuous solid solution and metal Co at 1410–1445 °C.	[621]
C–Co–Nb–Ta–Ti–W	General consideration of the system.	[1023]
C–Co–Nb–Ti	NbC _{1-x} ($x = 0.10$)–TiC _{1-x} ($x = 0.14$)–Co is plotted The eutectic equilibrium between two solid solutions based on NbC _{1-x} –TiC _{1-x} monocarbide continuous solid solution and metal Co at 1390–1410 °C.	[621]
C–Co–Nb–V	NbC _{1-x} –VC _{1-x} –Co is plotted schematically and partially at 1100 °C: (Nb,V)C _{1-x} (monocarbide solid solution based on NbC _{1-x}), (V,Nb)C _{1-x} (monocarbide solid solution based on VC _{1-x}), Co Eutectic (Nb,V)C _{1-x} –(V,Nb)C _{1-x} –Co (~ 1310 –1350 °C, 2 mol.% NbC _{1-x} , 11 mol.% VC _{1-x}) NbC _{1-x} ($x = 0.18$)–VC _{1-x} ($x = 0.12$)–Co is plotted: eutectic—1330 °C, 3.0 mol.% NbC _{1-x} , 10.5 mol.% VC _{1-x} In total, there are three binary and one ternary eutectics in the system.	[385–386, 622]

(continued)

Table 2.14 (continued)

System	Type of phase diagram (temperature and composition sections, constituent phases or phase fields) and/or character of interphase interaction and materials compatibility	References
C–Co–Nb–W	General consideration of the system.	[1023]
C–Co–Nb–Zr	NbC _{1-x} ($x = 0.18$)–ZrC _{1-x} ($x = 0.19$)–Co is plotted The eutectic equilibrium between two solid solutions based on NbC _{1-x} –ZrC _{1-x} monocarbide continuous solid solution and metal Co at 1380–1410 °C.	[621]
C–Co–Ni–W	No diagram plot Some phase fields are considered.	[755, 848]
C–Co–Os–W	No diagram plot Os promotes α -Co \rightarrow ε -Co transformation in the WC–Co system.	[856]
C–Co–Re–W	No diagram plot Re promotes α -Co \rightarrow ε -Co transformation in the WC–Co system.	[856]
C–Co–Ru–W	No diagram plot Ru promotes α -Co \rightarrow ε -Co transformation in the WC–Co system.	[856]
C–Co–Si	Plotted at 1000, 1100 and 1500 °C: Co ₃ Si (~ 1170 – 1215 °C), α -Co _{2\pmx} Si (< 1320 °C), β -Co _{2-x} Si (~ 1240 – 1335 °C), CoSi _{1\pmx} (< 1460 °C), CoSi ₂ ($< \sim 1325$ °C), SiC, ε -Co, α -Co, Si, C In vacuum, the contact melting between SiC and Co is observed at 1150–1160 °C. At 1500 °C CoSi ₂ reacts with C to form CoSi _{1\pmx} and SiC. CoSi _{1\pmx} and β -Co _{2-x} Si are more stable in equilibrium with C.	[242, 244, 417, 503, 645]
C–Co–Ta	Plotted at 1100 °C: η -Ta ₄ Co ₂ C, λ_3 -Co _{3-x} Ta (or Co _{2.7} Ta, Co _{2.2} Ta _{0.8} , < 1450 °C), λ_2 -Co _{2\pmx} Ta (< 1595 – 1650 °C), λ_1 -Co ₃ Ta _{2-x} (from 1110–1150 °C to 1540 °C), μ -CoTa _{1\pmx} (or μ -Co ₇ Ta _{6\pmx} , < 1700 °C), CoTa ₂ (< 1800 °C), α -Ta _{2+x} C, β -Ta _{2\pmx} C, ζ -Ta ₄ C _{3-x} , Ta ₆ C _{5\pmx} , TaC _{1-x} , Ta, α -Co, C TaC _{1-x} –Co is plotted: eutectic— ~ 1340 – 1370 °C, ~ 3 mol.% TaC _{1-x} TaC _{1-x} is in equilibrium with Co and λ_2 -Co _{2\pmx} Ta.	[242, 244, 391, 417]
C–Co–Ta–Ti	TaC _{1-x} ($x = 0.18$)–TiC _{1-x} ($x = 0.20$)–Co is plotted The eutectic equilibrium between two solid solutions based on TaC _{1-x} –TiC _{1-x} monocarbide continuous solid solution and metal Co at 1390–1445 °C.	[621]
C–Co–Ta–V	TaC _{1-x} ($x = 0.18$)–VC _{1-x} ($x = 0.17$)–Co is plotted There are three binary and one ternary (1320 °C, 4.0 mol.% TaC _{1-x} , 7.0 mol.% VC _{1-x}) eutectics in the system.	[622]
C–Co–Ta–W	General consideration of the system.	[1023]

(continued)

Table 2.14 (continued)

System	Type of phase diagram (temperature and composition sections, constituent phases or phase fields) and/or character of interphase interaction and materials compatibility	References
C–Co–Ta–Zr	TaC _{1-x} ($x = 0.18$)–ZrC _{1-x} ($x = 0.19$)–Co is plotted There are three binary and one ternary (1250 °C, 3.0 mol.% TaC _{1-x} , 5.0 mol.% ZrC _{1-x}) eutectics in the system.	[622]
C–Co–Ti	Plotted at 1000 and 1100 °C: Ti _{2±x} Co (<~1060 °C), TiCo _{1±x} (<1325 °C), α -TiCo _{2±x} (or c -TiCo _{2±x} , <1235 °C), β -TiCo _{2+x} (or h -TiCo _{2+x} , <~1210–1220 °C), TiCo _{3±x} (<1190 °C), TiC _{1-x} , β -Ti, α -Co, C TiC _{1-x} –Co is plotted: eutectic—~1360–1400 °C, ~6 mol.% TiC _{1-x} At 1230–1360 °C the solubility of TiC _{1-x} in Co is ~1 mol.%; TiC _{1-x} is in equilibrium with Co, TiCo _{1±x} , α -TiCo _{2±x} and Ti–Co melt.	[242, 244, 391, 417, 609, 1009]
C–Co–Ti–V	TiC _{1-x} ($x = 0.20$)–VC _{1-x} ($x = 0.17$)–Co is plotted The eutectic equilibrium between two solid solutions based on TiC _{1-x} –VC _{1-x} monocarbide continuous solid solution and metal Co at 1330–1390 °C.	[621]
C–Co–Ti–W	No diagram plot Some phase fields are considered.	[848, 1023]
C–Co–Ti–Zr	TiC _{1-x} ($x = 0.20$)–ZrC _{1-x} ($x = 0.19$)–Co is plotted There are three binary and one ternary (1320 °C, 5.0 mol.% TiC _{1-x} , 5.0 mol.% ZrC _{1-x}) eutectics in the system.	[622]
C–Co–U	No diagram plot UCoC ₂ , ?	[391]
C–Co–V	Plotted at 1100 °C: η -V ₄ Co ₂ C, V ₃ Co (<~1025 °C), σ -VCo _{1±x} (<~1420 °C), VCo _{3±x} (<~1070 °C), α -V _{2+x} C, β -V _{2±x} C, β' -V _{2+x} C, ζ -V ₄ C _{3-x} , V ₆ C _{5±x} , V ₈ C _{7±x} , VC _{1-x} , α -(Co,V), (V,Co), C VC _{1-x} –Co is plotted: eutectic—~1320–1360 °C, ~14–16 mol.% VC _{1-x} ; the max. solubility of VC _{1-x} in Co is ~5–11 mol.% and that of Co in VC _{1-x} is 3 mol.% (at the eutectic temp.) VC _{1-x} is in equilibrium with α -(Co,V) and σ -VCo _{1±x} .	[242, 244, 385–386, 391, 417]
C–Co–V–Zr	ZrC _{1-x} ($x = 0.19$)–VC _{1-x} ($x = 0.17$)–Co is plotted There are three binary and one ternary (1300 °C, 4.0 mol.% ZrC _{1-x} , 9.0 mol.% VC _{1-x}) eutectics in the system.	[622]

(continued)

Table 2.14 (continued)

System	Type of phase diagram (temperature and composition sections, constituent phases or phase fields) and/or character of interphase interaction and materials compatibility	References
C–Co–W	Plotted at 1000–1500 °C: η_1 -(Co,W) ₁₂ C, (or Co _{6-x} W _{6+x} C, $x \approx 0 \div 0.1$, $< \sim 1730$ °C), η_2 -(Co,W) ₆ C (or Co _{2+x} W _{4-x} C, Co _{3+x} W _{3-x} C, $x \approx 0 \div 0.2$, $< \sim 1965$ °C), κ -(Co,W) ₄ C (or CoW ₃ C, or Co ₃ W ₉ C ₄ , metastable), κ -Co _{3±x} W ($< \sim 1090$ – 1100 °C), μ -Co ₇ W _{6±x} ($< \sim 1690$ °C), α -W _{2+x} C, β -W _{2+x} C, γ -W _{2+x} C, γ -WC _{1-x} , δ -WC _{1±x} , α -Co, W, C Eutectic δ -WC _{1±x} – α -Co–C (~ 1300 °C, 4.6 at.% W, 11.5 at.% C) Eutectic δ -WC _{1±x} – α -Co–Co _{2+x} W _{4-x} C (1325 °C) δ -WC _{1±x} –Co is plotted: eutectic— ~ 1290 – 1340 °C, ~ 19.5 mol.% δ -WC _{1±x} ; the max. solid solubility of δ -WC _{1±x} in Co is 7–10 mol.% (at the eutectic temp.); the solubility of Co in δ -WC _{1±x} is very low.	[242, 244, 387–391, 417, 513, 755, 786, 796–800]
C–Co–Zr	Plotted at 800, 1200 and 1400 °C: Zr _{3±x} Co ($< \sim 980$ °C), η -Zr ₂ Co ($< \sim 1090$ – 1100 °C), ζ -ZrCo ($< \sim 1370$ – 1400 °C), ε -ZrCo _{2±x} (or λ_2 -ZrCo _{2±x} , $< \sim 1560$ – 1590 °C), δ -ZrCo ₄ (or Zr ₆ Co ₂₃ , $< \sim 1350$ – 1450 °C), γ -Zr ₂ Co ₁₁ (or Zr ₅ Co ₂₈ , $< \sim 1270$ °C), ZrC _{1-x} , β -Zr, α -Co, C ZrC _{1-x} –Co is plotted: eutectic— 1360 °C, ~ 4 – 5 mol.% ZrC _{1-x} The mutual solubilities between the components of the system are low; ZrC _{1-x} is in equilibrium with Co and series of Co–Zr intermetallides.	[138, 242, 244, 391, 417, 547]
C–Cr–Fe–Mo	Plotted partially at 1000 °C	[842]
C–Cr–Fe–Ti	No diagram plot TiC interacts with Fe–Cr alloy intensively.	[242]
C–Cr–Fe–V	Plotted partially at 700 – 1150 °C	[841, 843]
C–Cr–Fe–W	Plotted partially at 700 , 1000 and 1150 °C	[841]
C–Cr–Hf	Plotted at 1350 °C: λ_2 -HfCr _{2±x} ($< \sim 1335$ – 1420 °C), λ_1 -HfCr _{2±x} (from ~ 1335 – 1420 °C to 1825 °C), Cr ₂₃ C _{6±x} , Cr ₇ C _{3±x} , Cr ₃ C _{2-x} , HfC _{1-x} , α -Hf, β -Hf, Cr, C HfC _{1-x} –Cr is plotted: eutectic— 1810 °C, ~ 13 mol.% HfC _{1-x} The max. solubility of Cr in HfC _{1-x} is corresp. to compos. (Hf _{0.91} Cr _{0.09})C _{1-x} . The mutual solubilities of other constituent binary phases in the system are low too.	[242, 244, 391, 417, 583, 603]
C–Cr–Ir	No diagram plot \sim Cr ₂ Ir ₂ C (at least at ~ 1500 °C)	[391, 583]

(continued)

Table 2.14 (continued)

System	Type of phase diagram (temperature and composition sections, constituent phases or phase fields) and/or character of interphase interaction and materials compatibility	References
C–Cr–Mo	<p>Plotted at 1000–1800 °C: ζ-(Mo,Cr)₂C_{3–x} ($y/z \approx 3$, at least at 1650–2290 °C, ?), β-(Mo,Cr)_{2±x}C (semicarbide extended solid solution based on β-Mo_{2±x}C with max. solubility of “imaginary” phase ‘Cr_{2±x}C’—up to ~60–90 mol.%), (Cr,Mo)₂₃C_{6±x} (extended solid solution based on Cr₂₃C_{6±x} with max. solubility of “imaginary” phase ‘Mo₂₃C_{6±x}’—up to ~20 mol.%), α-(Mo,Cr)C_{1–x} (extended solid solution based on α-MoC_{1–x}—up to ~ (Mo_{0.3}Cr_{0.7})C_{1–x}) at higher temp.), η-(Mo,Cr)C_{1–x} (extended solid solution based on η-MoC_{1–x} with max. solubility of Cr—up to 30 at.% at 2005–2035 °C), Cr₇C_{3±x} (max. solubility of Mo–5.0 at.% at 1350 °C and 6.3 at.% at 1515 °C), Cr₃C_{2–x} (no solubility of Mo at 1350 °C and max. solubility of Mo–10.4 at.% at 1810 °C), (Mo,Cr), C</p> <p>Eutectic β-(Mo,Cr)_{2±x}C–Cr₇C_{3±x} (~1740 °C, 62 at.% Cr, 31 at.% C)</p> <p>Eutectic β-(Mo,Cr)_{2±x}C–Cr₇C_{3±x}–Cr₃C_{2–x} (~1685–1710 °C, 63 at.% Cr, 32.5 at.% C)</p> <p>Eutectic β-(Mo,Cr)_{2±x}C–(Mo,Cr)–(Cr,Mo)₂₃C_{6±x} (~1500–1515 °C, 55.5 at.% Cr, 19 at.% C)</p> <p>Eutectic β-(Mo,Cr)_{2±x}C–α-(Mo,Cr)C_{1–x}–η-(Mo,Cr)C_{1–x} (~2020 °C)</p> <p>Eutectic β-(Mo,Cr)_{2±x}C–α-(Mo,Cr)C_{1–x}–Cr₃C_{2–x} (~1800 °C)</p> <p>Eutectic β-(Mo,Cr)_{2±x}C–(Cr,Mo)₂₃C_{6±x}–Cr₇C_{3±x} (~1540 °C)</p> <p>Eutectic α-(Mo,Cr)C_{1–x}–Cr₃C_{2–x}–C (~1840 °C)</p> <p>Depend. on compos., graphite is in equilibrium: at 1300 °C—with β-(Mo,Cr)_{2±x}C, β-(Mo,Cr)_{2±x}C + Cr₃C_{2–x} and Cr₃C_{2–x}; at 1800 °C—with η-(Mo,Cr)C_{1–x}, η-(Mo,Cr)C_{1–x} + α-(Mo,Cr)C_{1–x}, α-(Mo,Cr)C_{1–x}, α-(Mo,Cr)C_{1–x} + ζ-(Mo_yCr_z)₄C_{3–x} and Cr₃C_{2–x}.</p> <p>Practically, at 1800–2000 °C Mo is compatible with Cr₇C_{3±x}.</p>	[138, 242, 244, 391, 402–403, 417, 580–583, 603, 794–795, 837, 842]
C–Cr–Mo–	No diagram plot	[852]
Re–Ti	General consideration of the system	
C–Cr–Mo–Ti	Plotted partially	[852]
	Eutectic (Mo,Cr)–TiC _{1–x} (~1630 °C, ~4–8 at.% Mo)	

(continued)

Table 2.14 (continued)

System	Type of phase diagram (temperature and composition sections, constituent phases or phase fields) and/or character of interphase interaction and materials compatibility	References
C–Cr–Nb	<p>Plotted at 1050–1750 °C: (Nb,Cr)C_{1–x} (monocarbide extended solid solution based on NbC_{1–x}—up to (Nb_{0.72}÷0.74Cr_{0.26}÷0.28)C_{1–x}), λ_2-NbCr_{2±x} (<1585–1625 °C), λ_1-NbCr_{2±x} (from 1585–1625 °C to ~1670–1820 °C), Cr₂₃C_{6±x}, Cr₇C_{3±x}, Cr₃C_{2–x}, α-Nb₂C, β-Nb_{2+x}C (solubility of C at 1050 °C is 6 at.% Cr), γ-Nb_{2+x}C, ζ-Nb₄C_{3–x}, Nb₆C_{5±x}, Nb, Cr, C</p> <p>Eutectic β-Nb_{2+x}C–λ_1-NbCr_{2±x}–Nb (~1660–1665 °C)</p> <p>Eutectic (Nb,Cr)C_{1–x}–β-Nb_{2+x}C–λ_1-NbCr_{2±x} (~1670–1690 °C)</p> <p>Eutectic (Nb,Cr)C_{1–x}–λ_1-NbCr_{2±x}–Cr (~1610–1630 °C)</p> <p>Eutectic (Nb,Cr)C_{1–x}–Cr₂₃C_{6±x}–Cr (~1540–1560 °C)</p> <p>Eutectic (Nb,Cr)C_{1–x}–Cr₇C_{3±x}–Cr₂₃C_{6±x} (~1565–1595 °C)</p> <p>Eutectic (Nb,Cr)C_{1–x}–Cr₃C_{2–x}–Cr₇C_{3±x} (~1650–1680 °C)</p> <p>Eutectic (Nb,Cr)C_{1–x}–Cr₃C_{2–x}–C (~1740 °C)</p> <p>NbC_{1–x}–Cr is plotted: eutectic—1640 °C; the solubility of Cr in NbC_{1–x} is ~3–9 mol.% and that of NbC_{1–x} in Cr is ~2 mol.%</p> <p>NbC_{1–x}–(Cr_yNb_z) is plotted ($x \approx 0.1 \div 0.2$, $y \approx 0.98$, $z \approx 0.02$): eutectic—≥ 1640 °C, ~12 mol.% NbC_{1–x} (12.2 at.% Nb, 8.3 at.% C)</p> <p>NbC_{1–x}–λ_1-NbCr_{2±x} is plotted: eutectic—~1690–1695 °C; the max. solubility of λ_1-NbCr_{2±x} in NbC_{1–x} is corresp. to compos. (Nb_{0.98}Cr_{0.02})C_{1–x} and that of NbC_{1–x} in λ_1-NbCr_{2±x} is corresp. to ~0.8 at.% C</p> <p>NbC_{1–x}–Cr₇C_{3±x} is plotted: eutectic—~1685 °C; the max. solubility of Cr₇C_{3±x} in NbC_{1–x} is corresp. to compos. (Nb_{0.90}Cr_{0.10})C_{1–x} and that of NbC_{1–x} in Cr₇C_{3±x}—to compos. (Cr_{0.99}Nb_{0.01})₇C_{3±x}</p> <p>The solubility of Nb in Cr carbides is low. Depend. on compos., graphite is in equilibrium with one (Nb,Cr)C_{1–x}, or two carbide (Nb,Cr)C_{1–x} + Cr₃C_{2–x} phases.</p> <p>Some data on the mutual solubilities of the compounds available in literature are controversial.</p>	[242, 244, 391, 417, 581–583, 603, 663, 784, 837, 858]
C–Cr–O–W	<p>No diagram plot.</p> <p>At 1300 °C, in vacuum δ-WC_{1±x} interacts with Cr₂O₃ in powder mixtures intensively; W–Cr alloy is formed (100 % reduction time–30 min.).</p>	[242, 808]
C–Cr–O–Zr	<p>No diagram plot</p> <p>At 1300–1800 °C, in vacuum the interaction between Cr₃C_{2–x} and ZrO_{2–x} led to the formation of Cr₇C_{3±x} and ZrC_xO_y.</p>	[242]

(continued)

Table 2.14 (continued)

System	Type of phase diagram (temperature and composition sections, constituent phases or phase fields) and/or character of interphase interaction and materials compatibility	References
C–Cr–Re	<p>Plotted at 1300–1800 °C: (Re,Cr)_{2±x}C (extended solid solution based on Re; at 1700 °C the combined max. solid solubilities of Cr and C in Re are 53 and 36 at.%, respectively, and corresp. to compos. \sim(Cr_{0.8}Re_{0.2})_{2±x}C), σ-Cr₂Re_{3±x}, Cr₂₃C_{6±x}, Cr₇C_{3±x}, Cr₃C_{2-x}, Re, Cr, C</p> <p>Eutectic (Re,Cr)_{2±x}C–Cr₂₃C_{6±x}–Cr (\sim1650–1665 °C)</p> <p>Eutectic (Re,Cr)_{2±x}C–Cr₂₃C_{6±x}–σ-Cr₂Re_{3±x} (\sim1665–1680 °C)</p> <p>Eutectic (Re,Cr)_{2±x}C–Cr₇C_{3±x}–Cr₃C_{2-x} (\sim1705–1730 °C)</p> <p>Eutectic (Re,Cr)_{2±x}C–Cr₇C_{3±x}–Cr₂₃C_{6±x} (\sim1625–1640 °C)</p> <p>Eutectic (Re,Cr)_{2±x}C–Cr₃C_{2-x}–C (\sim1750–1780 °C)</p> <p>(Re,Cr)_{2±x}C–Cr₂₃C_{6±x} is plotted: eutectic—\sim1675 °C; the max. solubility of Cr₂₃C_{6±x} in (Re,Cr)_{2±x}C is corresp. to compos. (Re_{0.4}Cr_{0.6})_{2±x}C and that of (Re,Cr)_{2±x}C in Cr₂₃C_{6±x}—to compos. (Cr_{0.76}Re_{0.24})₂₃C_{6±x}</p> <p>At 1665 °C the max. solubility of Re in Cr₂₃C_{6±x} is corresp. to compos. (Cr_{0.80}Re_{0.20})₂₃C_{6±x} and in Cr₇C_{3±x}—to compos. (Cr_{0.92}Re_{0.08})₇C_{3±x}; at 1300 °C the max. solubility of Re in Cr₂₃C_{6±x} (\sim10 at.%) is also higher than in Cr₇C_{3±x} and Cr₃C_{2-x}. Depend. on compos., graphite is in equilibrium with (Re,Cr)_{2±x}C, or (Re,Cr)_{2±x}C + Cr₃C_{2-x}, or Cr₃C_{2-x}.</p>	[244, 391, 417, 580, 583, 603, 837]
C–Cr–Re–Ti	<p>No diagram plot</p> <p>General consideration of the system</p>	[852]
C–Cr–Si	<p>Plotted at 1000, 1400 and 1600 °C: Cr₅Si₃C_x ($x \approx 0.8 \div 1.0$, or Cr_{5-x}Si_{3-z}C_{x+z} ($0.25 \leq x + z \leq 1.05$), or Cr₅Si_{3-x}C_x, at least <1400 °C), Cr_{3±x}Si (<1770 °C), α-Cr₅Si_{3±x} (<1505 °C), β-Cr₅Si_{3±x} (1505–1680 °C), CrSi (<\sim1415 °C), CrSi₂ (<1490 °C), Cr₂₃C_{6±x}, Cr₇C_{3±x}, Cr₃C_{2-x}, SiC, Si, Cr, C</p> <p>The max. solubility of C in Cr₅Si₃C_x, Cr_{3±x}Si, CrSi and CrSi₂ is about 11, <4, 1 and 0.06 mol.% C, respectively; no Si solubility—in Cr₇C_{3±x} and Cr₃C_{2-x}. Graphite is in equilibrium with SiC + Cr₃C_{2-x}. SiC—with Cr₃C_{2-x}, Cr₅Si₃C_x, CrSi and CrSi₂, and Cr_{3±x}Si—with Cr₂₃C_{6±x}, Cr₇C_{3±x}, and Cr₅Si₃C_x. At 1000–1200 °C the sequence of reaction layers observed in the diffusion couples is following: Cr/Cr₂₃C_{6±x}/Cr₇C_{3±x}/Cr₇C_{3±x} + Cr_{3±x}Si/Cr_{3±x}Si/Cr₅Si₃C_x/SiC. In inert gas or H₂ atmosphere the interaction in powder Cr–SiC mixtures initiates at temp. \geq1000–1100 °C; at 1450–1650 °C, depend. on compos., the formation of solid solution of C and Si in Cr, Cr₂₃C_{6±x}, Cr₇C_{3±x}, Cr₃C_{2-x}, Cr_{3±x}Si and Cr₅Si₃C_x is observed.</p>	[242, 244, 267, 392–394, 417, 503, 623, 792–793, 854]

(continued)

Table 2.14 (continued)

System	Type of phase diagram (temperature and composition sections, constituent phases or phase fields) and/or character of interphase interaction and materials compatibility	References
C–Cr–Ta	<p>Plotted at 1000–2000 °C: (Ta,Cr)C_{1–x} (monocarbide extended solid solution based on TaC_{1–x}—up to \sim (Ta_{0.64}÷0.73Cr_{0.27}÷0.36)C_{1–x}), λ_2-TaCr_{2±x} (<1660–1695 °C), λ_1-TaCr_{2±x} (from 1660–1695 °C to \sim 2010–2040 °C), Cr₂₃C_{6±x}, Cr₇C_{3±x}, Cr₃C_{2–x}, α-Ta_{2±x}C (solubility of Cr is <2 at.%), β-Ta_{2±x}C, ζ-Ta₄C_{3–x}, Ta₆C_{5±x}, Ta, Cr, C</p> <p>Eutectic β-Ta_{2±x}C–λ_1-TaCr_{2±x}–Ta (\sim 1935–1950 °C)</p> <p>Eutectic (Ta,Cr)C_{1–x}–β-Ta_{2±x}C–λ_1-TaCr_{2±x} (\sim 1945–1960 °C)</p> <p>Eutectic (Ta,Cr)C_{1–x}–λ_1-TaCr_{2±x}–Cr (\sim 1665–1685 °C)</p> <p>Eutectic (Ta,Cr)C_{1–x}–Cr₂₃C_{6±x}–Cr (\sim 1540–1545 °C)</p> <p>Eutectic (Ta,Cr)C_{1–x}–Cr₇C_{3±x}–Cr₂₃C_{6±x} (\sim 1560–1590 °C)</p> <p>Eutectic (Ta,Cr)C_{1–x}–Cr₃C_{2–x}–Cr₇C_{3±x} (\sim 1700–1710 °C)</p> <p>Eutectic (Ta,Cr)C_{1–x}–Cr₃C_{2–x}–C (\sim 1745–1755 °C)</p> <p>(Ta,Cr)C_{1–x} ($x = 0.21$)–(Cr_yTa_z) ($y = 0.991$, $z = 0.009$) is plotted: eutectic—\sim 1695 °C, \sim 10–11 mol.% (Ta,Cr)C_{1–x}</p> <p>TaC_{1–x}–Cr is plotted: eutectic—\sim 1675–1695 °C; the max. solubility of Cr in TaC_{1–x} is \sim 3.4 mol.% and that of TaC_{1–x} in Cr is \sim 2 mol.%</p> <p>TaC_{1–x}–λ_1-TaCr_{2±x} is plotted: eutectic—\sim 1990 °C; the max. solubility of λ_1-TaCr_{2±x} in TaC_{1–x} is corresp. to compos. (Ta_{0.98}Cr_{0.02})C_{1–x} and that of TaC_{1–x} in λ_1-TaCr_{2±x} is 1 at.% C</p> <p>TaC_{1–x}–Cr₇C_{3±x} is plotted: eutectic—\sim 1720 °C; the max. solubility of Cr₇C_{3±x} in TaC_{1–x} is corresp. to compos. \sim (Ta_{0.9}Cr_{0.1})C_{1–x} and that of TaC_{1–x} in Cr₇C_{3±x}—to compos. \sim (Cr_{0.99}Ta_{0.01})₇C_{3±x}</p> <p>β-Ta_{2±x}C–λ_1-TaCr_{2±x} is plotted: eutectic—\sim 1960 °C</p> <p>Depend. on compos., graphite is in equilibrium with one (Ta,Cr)C_{1–x}, or two (Ta,Cr)C_{1–x} + Cr₃C_{2–x} carbide phases.</p>	[242, 244, 391, 417, 581–583, 603, 784, 837, 865, 876]
C–Cr–Tc	Plotted schematically	[583, 840]
C–Cr–Ti	<p>Plotted at 800–2800 °C: (Ti,Cr)C_{1–x} (monocarbide extended solid solution based on TiC_{1–x}—up to (Ti_{0.32}Cr_{0.68})C_{1–x}), λ_2-TiCr_{2–x} (<1220 °C), λ_1'-TiCr_{2–x} (800–1270 °C), λ_1''-TiCr_{2–x} (1270–1370 °C), Cr₂₃C_{6±x}, Cr₇C_{3±x}, Cr₃C_{2–x}, (β-Ti,Cr), C</p> <p>Eutectic (Ti,Cr)C_{1–x}–Cr₃C_{2–x}–Cr₇C_{3±x} (1695 °C)</p> <p>Eutectic (Ti,Cr)C_{1–x}–Cr₂₃C_{6±x}–Cr (1540 °C)</p> <p>(Ti,Cr)C_{1–x}–Cr₇C_{3±x} (TiC_{0.98}–CrC_{0.40}) is plotted: eutectic—1725 °C, \sim 65 mol.% Cr₇C_{3±x} (\sim 5 at.% Ti, \sim 31 at.% C)</p> <p>(Ti,Cr)C_{1–x}–Cr₃C_{2–x} is plotted: eutectic—\sim 1700 °C, \sim 90 mol.% Cr₃C_{2–x}; the max. solubility of Cr₃C_{2–x} in (Ti,Cr)C_{1–x} is \sim 25 mol.%</p> <p>(Ti,Cr)C_{1–x} ($x = 0.04$)–(Cr_yTi_z) ($y \approx 1.0$, $z \approx 0$) is plotted: eutectic—\sim 1100–1130 °C, \sim 10 mol.%</p>	[242, 244, 391, 395–396, 417, 581–583, 603, 788–791, 837]

(continued)

Table 2.14 (continued)

System	Type of phase diagram (temperature and composition sections, constituent phases or phase fields) and/or character of interphase interaction and materials compatibility	References
	<p>(Ti,Cr)C_{1-x} (~9 at.% Ti, ~8.5 at.% C); at 1100 °C the max. solubility of TiC_{0.96} in Cr is ~3 mol.% and that of Cr in TiC_{0.96} is ~4 mol.%</p> <p>(Ti,Cr)C_{1-x}-(Cr_yTi_z) is plotted ($x = 0.20$, $y = 0.95$, $z = 0.05$): eutectic—1685 °C, ~15 mol.% (Ti,Cr)C_{1-x} (~14 at.% Ti, ~8 at.% C)</p> <p>(Ti,Cr)C_{1-x}-(Cr_yTi_z) is plotted ($x = 0.33$, $y = 0.40$, $z = 0.60$): eutectic—1360 °C, ~5 mol.% (Ti,Cr)C_{1-x} (~60 at.% Ti, ~2 at.% C)</p>	
C–Cr–U	<p>Plotted at 1200 °C: UCrC₂, U₂Cr₉C₉, UCr₂C_{3+x}, U₃Cr₄C₂, UC_{1±x}, ζ-U₂C₃, Cr₂₃C_{6±x}, Cr₇C_{3±x}, Cr₃C_{2-x}, U, Cr, C</p> <p>UC_{1±x}–Cr is plotted: eutectic—~1430 °C, ~28 mol.% UC_{1±x}</p> <p>UC_{1±x} is in equilibrium with Cr and Cr carbides. The max. solubility of “imaginary” phase ‘CrC’ in hypostoichiometric (U,Cr)C_{1-x} is ~20 mol.%.</p>	[242, 244, 391, 417, 612]
C–Cr–V	<p>Plotted at 1000 and 1350 °C: VCr₂C_{2-x} (ordered phase (V,Cr)₃C_{2-x}, $x \approx 0.5$, or V₂₀₊₂₅Cr₃₈₊₄₃C₃₇, ≤1750 °C), (V,Cr)C_{1-x} (extended monocarbide solid solution based on VC_{1-x}—up to ~ (V_{0.43+0.58}Cr_{0.42+0.57})C_{1-x} at 1000–1350 °C, ?), β-(V,Cr)_{2±x}C (extended semicarbide solid solution based on β-V_{2±x}C—up to ~ (V_{0.5}Cr_{0.5})_{2±x}C at 1000 °C and ~ (V_{0.4}Cr_{0.6})_{2±x}C at 1350 °C), (Cr,V)₂₃C_{6±x} (solid solution based on Cr₂₃C_{6±x}—up to ~ (Cr_{0.91}V_{0.09})₂₃C_{6±x} at 1000 °C and ~ (Cr_{0.82}V_{0.18})₂₃C_{6±x} at 1350 °C), (Cr,V)₇C_{3±x} (solid solution based on Cr₇C_{3±x}—up to ~ (Cr_{0.9}V_{0.1})₇C_{3±x} at 1000 °C and ~ (Cr_{0.8}V_{0.2})₂₃C_{6±x} at 1350 °C), Cr₃C_{2-x}, α-V_{2+x}C, β'-V_{2+x}C, ζ-V₄C_{3-x}, V₆C_{5±x}, V₈C_{7±x}, (V,Cr), C</p> <p>Eutectic β-(V,Cr)_{2±x}C–(Cr,V)₂₃C_{6±x}–(V,Cr) (~1490 °C)</p> <p>Eutectic β-(V,Cr)_{2±x}C–(Cr,V)₂₃C_{6±x}–(Cr,V)₇C_{3±x} (~1520 °C)</p> <p>In general, V carbides dissolve a large amount of Cr, in comparison with it the solubility of V in Cr carbides is low.</p>	[242, 391, 417, 583, 603, 782–787, 837, 843]
C–Cr–W	<p>Plotted at 1300–1600 °C: WCr₆C₃, W₃Cr₂C₄, WCr₅C₃ (?), α-(W,Cr)_{2+x}C (extended semicarbide solid solution based on α-W_{2+x}C—up to compos. (W_{0.1}Cr_{0.9})_{2+x}C), γ-(W,Cr)C_{1-x} (extended monocarbide solid solution based on γ-WC_{1-x}—up to ~ (W_{0.3}Cr_{0.7})C_{1-x} at higher temp.), (Cr,W)₂₃C_{6±x} (extended solid solution based on Cr₂₃C_{6±x}—up to compos. ~ (Cr_{0.8}W_{0.2})₂₃C_{6±x}), (Cr,W)₃C_{2-x} (extended solid solution based on Cr₃C_{2-x}—up to ~ (Cr_{0.85}W_{0.15})₃C_{2-x} at 1350 °C), (Cr,W)₇C_{3±x} (solid solution based on Cr₇C_{3±x}—up to ~ (Cr_{0.95}W_{0.05})₇C_{3±x} at 1350 °C), δ-WC_{1±x}, (W,Cr), (Cr,W), C</p> <p>The max. solubility of “imaginary” phase ‘W₂₃C_{6±x}’ in (Cr,W)₂₃C_{6±x} is ~20 mol.% at 1300 °C, ~13 mol.% at 1350 °C and ~10 mol.% at 1400 °C.</p>	[242, 244, 391, 397–399, 404, 417, 580–583, 603, 780, 781, 837]

(continued)

Table 2.14 (continued)

System	Type of phase diagram (temperature and composition sections, constituent phases or phase fields) and/or character of interphase interaction and materials compatibility	References
C–Cr–Zr	<p>Plotted at 1300–1800 °C: λ_2-ZrCr_{2-x} (<~ 1530–1590 °C), λ_1'-ZrCr_{2-x} (from ~ 1530–1590 °C to 1620 °C), λ_1''-ZrCr_{2-x} (1620–1675 °C), Cr₂₃C_{6±x}, Cr₇C_{3±x}, Cr₃C_{2-x}, ZrC_{1-x}, β-Zr, Cr, C</p> <p>Eutectic ZrC_{1-x}-Cr₃C_{2-x}-Cr₇C_{3±x} (1730 °C)</p> <p>Eutectic ZrC_{1-x}-Cr₂₃C_{6±x}-Cr (1575 °C)</p> <p>Eutectic ZrC_{1-x}-λ_1'-ZrCr_{2-x}-Cr (1595 °C)</p> <p>Eutectic ZrC_{1-x}-λ_2-ZrCr_{2-x}-Zr (1330 °C)</p> <p>ZrC_{1-x}-Cr₇C_{3±x} is plotted: eutectic—1750 °C</p> <p>ZrC_{1-x}-λ_1''-ZrCr_{2-x} is plotted: eutectic—1630 °C</p> <p>ZrC_{1-x}-Cr_yZr_z ($x = 0.28$, $y = 0.998$, $z = 0.002$) is plotted: eutectic—~ 1760–1775 °C, ~ 5.0–5.6 mol.% ZrC_{1-x} (~ 91 at.% Cr, ~ 3.7 at.% C)</p> <p>ZrC_{1-x}-Cr ($x = 0.095$) is plotted: eutectic—~ 1730–1805 °C (?), ~ 4–5 mol.% ZrC_{1-x} (~ 91 at.% Cr, ~ 4.3 at.% C); max. solubility of ZrC_{1-x} in Cr is 1.3 mol.% (at eutectic temp.)</p> <p>ZrC_{1-x}-Cr ($x = 0.03$) is plotted: eutectic—1120–1140 °C (?), ~ 3.5–6.4 mol.% ZrC_{1-x} (~ 93.5 at.% Cr, ~ 3.2 at.% C); max. Cr solubility in ZrC_{1-x} is ~ 2.3–8.5 mol.% (?) and that of ZrC_{1-x} in Cr is ≤ 0.1 mol.%</p> <p>The max. solubility of Cr in ZrC_{1-x} is ~ 1.5–3.0 mol.% and corresp. to compos. ~ (Zr_{0.97}Cr_{0.03})C_{1-x}; the solubility of Zr in Cr carbides is very low.</p> <p>Data on the system available in literature are very controversial.</p>	[242, 244, 391, 395, 400, 417, 581–583, 603, 775–779, 837]
C–Cs–Zr	<p>No diagram plot</p> <p>The solubility of Cs in ZrC_{1-x} decreases with increasing temp. from 1.5×10^{-2} mol.% at 1210 °C to 0.4×10^{-4} mol.% at 1210 °C.</p>	[833]
C–Cu–Si	<p>No diagram plot</p> <p>At 1100–1600 °C, in the reducing atmosphere the interaction between SiC and Cu results in the formation of C and Cu silicides, which dissociate at higher temp., forming secondary SiC.</p>	[242]
C–Cu–Zr	<p>No diagram plot</p> <p>Zr_xCu_yC_z (?)</p>	[902]
C–Dy–U	<p>No diagram plot</p> <p>UC_{1±x}-DyC_{1-x} monocarbide continuous solid solution or extended solid solution based on UC_{1±x} (?).</p>	[391]
C–Er–Ir	<p>Plotted partially at 1100–1400 °C: Er₃Ir, Er₅Ir₂, α-Er₅Ir_{3±x} (?), β-Er₅Ir_{3±x}, Er₃Ir₂, ErIr, ErIr_{2±x}, Er_{3-x}C, Er₁₅C₁₉, α-ErC₂, β-ErC₂, α-Er, β-Er, Ir, C</p> <p>Depend. on compos., graphite is in equilibrium with ErIr_{2±x} + Ir, or ErIr_{2±x} + α-ErC₂.</p>	[990]
C–Er–N–Th	<p>No diagram plot</p> <p>ThC_{1±x}-ErN_{1±x} continuous solid solution</p>	[391]

(continued)

Table 2.14 (continued)

System	Type of phase diagram (temperature and composition sections, constituent phases or phase fields) and/or character of interphase interaction and materials compatibility	References
C–Er–U	No diagram plot UC _{1±x} –ErC _{1–x} monocarbide continuous solid solution or extended solid solution based on UC _{1±x} .	[391]
C–Eu–U	No diagram plot UC _{1±x} –EuC _{1–x} monocarbide continuous solid solution or extended solid solution based on UC _{1±x} .	[391]
C–Fe–Hf	Plotted at 1100 °C: Hf _{2±x} Fe (<1260 °C), α -HfFe _{2±x} (<~ 1200 °C), β -HfFe _{2±x} (~ 1200–1640 °C), λ -Hf ₃ Fe _{7±x} (<~ 1820 °C), Fe ₃ C, HfC _{1–x} , α -Fe, γ -Fe, δ -Fe, α -Hf, β -Hf, C HfC _{1–x} –Fe is plotted: eutectic—~ 1410–1490 °C, ~ 2–4 mol.% HfC _{1–x} ; at the eutectic temp. the solubility of HfC _{1–x} in Fe is ≤ 0.3 mol.% HfC _{1–x} is in equilibrium with Fe and Fe–Hf intermetallics.	[242, 244, 391, 417]
C–Fe–Mo	Plotted at 550–1800 °C: η_1 –(Mo _{1–x} Fe _x) ₆ C (or Mo ₃ Fe ₃ C, Mo ₂ Fe ₄ C, <2065 °C), ξ –(Fe _{1–x} Mo _x) ₃ C (or MoFe ₂ C, Mo ₁₂ Fe ₂₂ C ₁₀ , 655–1085 °C), (Fe,Mo) ₂₃ C ₆ (or Mo ₂ Fe ₂₁ C ₆ , metastable, ?) and other metastable ternary phases, λ -Fe ₂ Mo (<~ 900–1000 °C), ρ -Fe ₃ Mo _{2–x} (or Fe ₆₂ Mo ₃₈ , R-phase, from ~ 1190–1210 °C to ~ 1490 °C), μ -Fe ₇ Mo _{6–x} (<1370 °C), σ -FeMo _{1±x} (from ~ 1540–1610 °C to 1215–1255 °C), Fe ₃ C, α -Mo _{2+x} C, α' -Mo _{2+x} C, β -Mo _{2±x} C, η -MoC _{1–x} , α -MoC _{1–x} , γ -MoC, α -Fe, γ -Fe, δ -Fe, Mo, C Eutectic ξ –(Fe _{1–x} Mo _x) ₃ C–(Fe _{1–x} Mo _x) ₃ C– γ -Fe (1065 °C, 7.7 at.% Mo, 18 at.% C) At 1000 °C β -Mo _{2±x} C is in equilibrium with steel phase containing 2 at.% Mo and 4 at.% C.	[138, 242, 244, 391, 417, 542–545, 610, 846, 900]
C–Fe–N–Nb	No diagram plot General consideration of the system	[869]
C–Fe–N–Nb–Ti	NbC _{1–x} –TiC _{1–x} –TiN _{1±x} –Fe and NbC _{1–x} – δ -NbN _{1–x} –TiN _{1±x} –Fe are plotted schematically at 1200 °C	[870–871]
C–Fe–N–Nb–Ti–V	NbC _{1–x} –VC _{1–x} – δ -NbN _{1–x} –TiN _{1±x} – δ -VN _{1–x} –Fe is plotted schematically at 1000 °C	[871]
C–Fe–N–Ti	No diagram plot General consideration of the system	[872]
C–Fe–Nb	Plotted at 800–2000 °C: ε -Fe _{2±x} Nb (or λ -Fe _{2±x} Nb <~ 1625–1665 °C), μ -FeNb _{1±x} (or μ -Fe ₇ Nb _{6+x} , or Fe ₂₁ Nb _{19±x} , <~ 1600–1700 °C), Fe ₃ C, α -Nb ₂ C, β -Nb _{2+x} C, γ -Nb _{2±x} C, ζ -Nb ₄ C _{3–x} , Nb ₆ C _{5±x} , NbC _{1–x} , α -Fe, γ -Fe, δ -Fe, Nb, C Eutectic μ -FeNb _{1±x} – ε -Fe _{2±x} Nb– β -Nb _{2+x} C (1595 °C) Eutectic μ -FeNb _{1±x} – β -Nb _{2+x} C–Nb (~ 1400 °C) Eutectic ε -Fe _{2±x} Nb–NbC _{1–x} – δ -Fe (~ 1370 °C) Eutectic NbC _{1–x} – γ -Fe–C (~ 1150 °C) NbC _{1–x} –Fe is plotted: eutectic—1420 °C, ~ 3–5 mol.% NbC _{1–x} ; at 1250 °C the max. solubility of NbC _{1–x} in Fe is ~ 2 mol.% The solubility of C in ε -Fe _{2±x} Nb and μ -FeNb _{1±x} is negligible. NbC _{1–x} is in equilibrium with Fe and ε -Fe _{2±x} Nb.	[138, 242, 244, 391, 417, 546–548, 868]

(continued)

Table 2.14 (continued)

System	Type of phase diagram (temperature and composition sections, constituent phases or phase fields) and/or character of interphase interaction and materials compatibility	References
C–Fe–Nb–V	NbC _{1-x} –VC _{1-x} –Fe is plotted schematically at 1000 °C	[871]
C–Fe–Ni–Ti	No diagram plot At 1500 °C TiC _{1-x} interacts with Fe–Ni alloy intensively.	[242]
C–Fe–Ni–W	No diagram plot Some phase fields are considered.	[755, 848]
C–Fe–Si	Plotted at 800–1450 °C: Fe ₆ SiC, Fe ₅ SiC (?), Fe ₈ Si ₂ C (?), Fe ₉ SiC ₂ (?), α ₂ –Fe _{3+x} Si (< ~1300 °C), α ₁ –Fe _{3±x} Si (< ~1155 °C), α ₁ '–Fe _{3±x} Si (or Fe ₃ Si _{2±x} , 965–1250 °C), β–Fe _{2±x} Si (1040–1210 °C), η–Fe ₅ Si ₃ (~825–1100 °C), ε–FeSi _{1±x} (<1410 °C), ζ ₁ –FeSi ₂ (~935–1220 °C), ζ ₂ –FeSi ₂ (<980 °C), Fe ₃ Si _{7±x} (or FeSi _{2+x} , x ≈ 0.3, 935–1220 °C), Fe ₃ C, SiC, α–Fe, γ–Fe, δ–Fe, Si, C Eutectic Fe ₆ SiC–γ–Fe–Fe ₃ C (1030 °C, 8.8 at.% Si, 15.2 at.% C) Eutectic α,δ–Fe–γ–Fe–C (1156 °C, 15.0 at.% Si, 7.6 at.% C) Eutectic α,δ–Fe–ε–FeSi _{1±x} –C (1182 °C, 31.9 at.% Si, 0.6 at.% C) At 1100 °C in H ₂ the interaction between SiC and Fe results in the formation of η–Fe ₅ Si ₃ ; in vacuum the contact melting is observed at 1165 °C.	[242, 244, 267, 393, 401, 417, 503, 505, 549–550]
C–Fe–Si–Ti	No diagram plot At 1500 °C TiC _{1-x} interacts with Fe–Si alloy intensively.	[242]
C–Fe–Si–V	Plotted partially and schematically. Eutectic VC _{1-x} –Fe ₃ C–γ–Fe–C (1150 °C)	[608]
C–Fe–Ta	Plotted at 1100 °C: ε–Fe _{2±x} Ta (< ~1775 °C), μ–FeTa _{1±x} (or μ–Fe ₇ Ta _{6±x} , < ~1800–1900 °C), Fe ₃ C, α–Ta _{2+x} C, β–Ta _{2±x} C, ζ–Ta ₄ C _{3-x} , Ta ₆ C _{5±x} , TaC _{1-x} , α–Fe, γ–Fe, δ–Fe, Ta, C TaC _{1-x} –Fe is plotted: eutectic—1440 °C, ~2–3 mol.% TaC _{1-x} α–Ta _{2+x} C is in equilibrium with ε–Fe _{2±x} Ta and μ–FeTa _{1±x} , TaC _{1-x} (x > 0.15)—with ε–Fe _{2±x} Ta and TaC _{1-x} (0.01 ≤ x ≤ 0.15)—with Fe.	[242, 244, 391, 417]
C–Fe–Ti	Plotted at 25–1600 °C: TiFe _{1±x} (< ~1315 °C), TiFe _{2±x} (< ~1425 °C), Fe ₃ C, TiC _{1-x} , α–Fe, γ–Fe, δ–Fe, β–Ti, α–Ti, C Eutectic TiFe _{2±x} –TiC _{1-x} (~1425 °C, 33.4 at.% Ti, 0.5 at.% C) Eutectic TiFe _{1±x} –TiC _{1-x} –β–Ti (~1070 °C, 71.8 at.% Ti, 0.1 at.% C) Eutectic TiFe _{2±x} –TiC _{1-x} –δ–Fe (~1290 °C, 16.4 at.% Ti, 0.2 at.% C) Eutectic TiC _{1-x} –γ–Fe–C (1150 °C, 0.9 at.% Ti, 17.6 at.% C) TiC _{1-x} –Fe is plotted: eutectic—~1380–1475 °C, ~6–10 mol.% TiC _{1-x} At 1250–1260 °C the solubility of TiC _{1-x} in γ–Fe is ≤0.6 ÷ 0.7 mol.%; depend. on temp., TiC _{1-x} is in equilibrium with γ–Fe or α–Fe and Fe–Ti intermetallides.	[242, 244, 391, 405–406, 417, 551–556, 611]

(continued)

Table 2.14 (continued)

System	Type of phase diagram (temperature and composition sections, constituent phases or phase fields) and/or character of interphase interaction and materials compatibility	References
C-Fe-U	Plotted at 1000–1400 °C: UFeC_2 (<1615 °C), $\sim \text{U}_3\text{Fe}_2\text{C}_5$ (<1500 °C), $\sim \text{U}_3\text{FeC}_6$ (at least ≥ 1150 –1400 °C), $\text{U}_{11}\text{Fe}_{12}\text{C}_{18}$ (<1200 °C), U_6Fe (<795–805 °C), UFe_{2-x} (<1230 °C), Fe_3C , $\text{UC}_{1\pm x}$, ζ - U_2C_3 , α - UC_{2-x} , β - UC_{2-x} , δ -Fe, γ -Fe, α -Fe, γ -U, β -U, α -U, C Eutectic $\text{UC}_{1\pm x}$ - UFe_{2-x} - γ -Fe (1040 °C); no mutual solid solubilities between the components Eutectic $\text{UC}_{1\pm x}$ - UFe_{2-x} - U_6Fe (720 °C); no mutual solid solubilities between the components $\text{UC}_{1\pm x}$ - UFe_{2-x} is plotted: eutectic— ~ 1040 –1200 °C, ~ 11 mol.% $\text{UC}_{1\pm x}$ (~ 3.8 at.% C); no mutual solid solubilities between the components $\text{UC}_{1\pm x}$ - γ -Fe is plotted: eutectic— ~ 1120 –1205 °C, ~ 17 mol.% $\text{UC}_{1\pm x}$ (~ 15 at.% C); no mutual solid solubilities between the components UFeC_2 - γ -Fe is plotted: eutectic—1160 °C, ~ 14 mol.% UFeC_2 (~ 20 at.% C); no mutual solid solubilities between the components	[242, 244, 391, 452]
C-Fe-V	Plotted at 500–1150 °C: η - $\text{V}_3\text{Fe}_3\text{C}$ (?), σ - $\text{VFe}_{1\pm x}$ (from ~ 100 –650 to ~ 1200 –1250 °C), Fe_3C , α - V_{2+x}C , β - V_{2+x}C , β' - V_{2+x}C , ζ - V_4C_{3-x} , $\text{V}_6\text{C}_{5\pm x}$, $\text{V}_8\text{C}_{7\pm x}$, VC_{1-x} , δ -Fe, γ -Fe, α -Fe, V, C Eutectic Fe_3C - ζ - V_4C_{3-x} (~ 1150 °C, 10.2 at.% V, 27.7 at.% C) Eutectic β - V_{2+x}C - VC_{1-x} - α -Fe (~ 1390 °C, ~ 36 at.% V, ~ 4.5 at.% C) Eutectic Fe_3C - VC_{1-x} - γ -Fe (~ 1120 °C, 2.75 at.% V, 17.1 at.% C) VC_{1-x} -Fe is plotted: eutectic— ~ 1390 –1415 °C, ~ 7 –8 mol.% VC_{1-x} VC_{1-x} is in equilibrium with α -(Fe,V) and γ -Fe, β - V_{2+x}C —with α -(Fe,V), σ - $\text{VFe}_{1\pm x}$ and (V,Fe)	[242, 244, 391, 417, 557–558, 843, 845, 873]
C-Fe-W	Plotted at 600–1500 °C: κ - W_3FeC ($\leq \sim 1600$ °C), η_1 - $\text{W}_3\text{Fe}_3\text{C}$ ($< \sim 1670$ °C), η_1 - $\text{W}_6\text{Fe}_6\text{C}$ ($\leq \sim 1400$ °C), $\text{W}_2\text{Fe}_{21}\text{C}_6$ (metastable), WFeC (metastable, ?), λ - Fe_2W ($\leq \sim 1060$ °C), μ - $\text{Fe}_7\text{W}_{6-x}$ (or Fe_3W_2 , ~ 1190 –1635 °C), δ - $\text{FeW}_{1\pm x}$ (~ 400 –1215 °C), Fe_3C , α - W_{2+x}C , β - W_{2+x}C , γ - W_{2+x}C , γ - WC_{1-x} , δ - $\text{WC}_{1\pm x}$, δ -Fe, γ -Fe, α -Fe, W, C Eutectic δ - $\text{WC}_{1\pm x}$ - γ -Fe-C (~ 1145 °C, 1.3 at.% W, 17.5 at.% C)	[242, 244, 391, 417, 559–562, 604, 662, 755–847]
C-Fe-Zr	Plotted at 1100 °C: $\text{Zr}_3\text{Fe}_3\text{C}$ (?), $\text{Zr}_{3\pm x}\text{Fe}$ ($< \sim 885$ °C), Zr_{2+x}Fe (~ 775 –975 °C), ZrFe_{2+x} ($< \sim 1675$ °C), ZrFe_3 ($< \sim 1480$ °C), Fe_3C , ZrC_{1-x} , γ -Fe, β -Zr, C ZrC_{1-x} -Fe is plotted: eutectic— ~ 1400 –1475 °C, ~ 3 –4 mol.% ZrC_{1-x} The solubility of ZrC_{1-x} in γ -Fe is ≤ 0.5 mol.%; ZrC_{1-x} is in equilibrium with Fe and Fe-Zr intermetallics.	[241–242, 244, 391, 417]

(continued)

Table 2.14 (continued)

System	Type of phase diagram (temperature and composition sections, constituent phases or phase fields) and/or character of interphase interaction and materials compatibility	References
C–Ga–Mo	No diagram plot Mo ₂ GaC ($M_{n+1}AX_n$ -phase)	[680–681, 744–745, 860]
C–Ga–Nb	Plotted partially at 800 °C: Nb ₂ GaC ($M_{n+1}AX_n$ -phase), NbGa _{3–x} (<1235 °C), Nb ₄ Ga ₅ (<1300 °C), Nb ₅ Ga ₄ (<1540 °C), Nb ₅ Ga _{3±x} (<1950 °C), Nb _{3–x} Ga (<1860 °C), α -Nb ₂ C, β -Nb _{2+x} C, γ -Nb _{2±x} C, ζ -Nb ₄ C _{3–x} , Nb ₆ C _{5±x} , NbC _{1–x} , Nb, Ga, C	[244, 680–681, 744–745, 860, 975]
C–Ga–Ta	No diagram plot Ta ₂ GaC ($M_{n+1}AX_n$ -phase)	[680–681, 744–745, 860]
C–Ga–Ti	No diagram plot Ti ₂ GaC, Ti ₄ GaC ₃ ($M_{n+1}AX_n$ -phases)	[680–681, 744–745, 859–860]
C–Ga–V	Plotted partially at 800 °C: V ₂ GaC ($M_{n+1}AX_n$ -phase), V ₈ Ga ₄₁ (<495 °C), V ₂ Ga ₅ (<1050 °C), V ₆ Ga _{7±x} (~995–1155 °C), V ₆ Ga _{5±x} (<1095 °C), V _{3±x} Ga (<1300 °C), α -V _{2+x} C, β -V _{2±x} C, β' -V _{2+x} C, ζ -V ₄ C _{3–x} , V ₆ C _{5±x} , V ₈ C _{7±x} , VC _{1–x} , V, Ga, C	[244, 680–681, 744–745, 860, 975]
C–Gd–U	Plotted at 1000–1500 °C: (U,Gd)C _{1±x} (UC _{1±x} - β -GdC _{1–x} (or β -Gd _{3–x} C) monocarbide continuous solid solution), α -Gd ₂ C, (Gd,U) ₂ C _{3–x} (solid solution based on Gd ₂ C _{3–x}), ζ -(U,Gd) ₂ C ₃ (solid solution based on ζ -U ₂ C ₃), β -(Gd,U)C _{2–x} (solid solution based on β -GdC ₂), γ -U, β -U, α -U, α -Gd, β -Gd, C α -UC _{2–x} - α -GdC ₂ and β -UC _{2–x} - β -GdC ₂ series of dicarbide continuous solid solutions are also formed. At temp. <1000 °C UC _{1±x} - β -GdC _{1–x} (or β -Gd _{3–x} C) monocarbide continuous solid solution has a miscibility gap.	[241, 391]
C–Gd–N–Th	No diagram plot ThC _{1±x} -GdN _{1–x} continuous solid solution	[391]
C–Ge–Si–Ti	No diagram plot Ti ₃ Si _x Ge _{1–x} C ₂ ($0 \leq x \leq 1$, $M_{n+1}AX_n$ -phase solid solution)	[680–681, 860]
C–Ge–Ti	Plotted at 1200 °C: Ti ₂ GeC, Ti ₃ GeC ₂ ($M_{n+1}AX_n$ -phases), Ti ₄ GeC ₃ ($M_{n+1}AX_n$ -phase, metastable, ?), Ti ₅ Ge ₃ (<1980 °C), Ti ₆ Ge ₅ (<1650 °C), TiGe ₂ (<1075 °C), TiC _{1–x} , α -Ti, β -Ti, Ge, C	[244, 633, 680–681, 744–745, 860]
C–Ge–V	Plotted partially at 800 °C: V ₂ GeC ($M_{n+1}AX_n$ -phase), V ₃ GeC (?), V ₁₇ Ge ₃₁ (<955–965 °C), V ₁₁ Ge ₈ (<1565–1585 °C), V ₅ Ge _{3–x} (~1930 °C), V _{3±x} Ge (<1690 °C), α -V _{2+x} C, β -V _{2±x} C, β' -V _{2+x} C, ζ -V ₄ C _{3–x} , V ₆ C _{5±x} , V ₈ C _{7±x} , VC _{1–x} , V, Ge, C	[680–681, 744–745, 748, 860]

(continued)

Table 2.14 (continued)

System	Type of phase diagram (temperature and composition sections, constituent phases or phase fields) and/or character of interphase interaction and materials compatibility	References
C–H–Hf	No diagram plot HfC_xH_y ($x = 0.55 \div 0.58$, $y = 0.42 \div 0.43$, or $\text{Hf}_2\text{C}_{1+x}\text{H}_{1-y}$ ($\text{HfC}_{1+x} \cdot \text{HfH}_{1-y}$), $x = 0.1$, $y = 0.14$)	[825]
C–H–La	No diagram plot LaC_xH_y (or La_2CH_z , $\text{LaC} \cdot \text{LaH}_z$)	[825]
C–H–Nb	No diagram plot NbC_xH_y ($0.71 \leq x \leq 0.81$, $0 \leq y \leq 0.30$, ?)	[825, 888]
C–H–O–Zr	No diagram plot $\text{ZrO}_{0.6}\text{C}_{0.2}\text{H}_x$	[825]
C–H–Th	No diagram plot Th_2CH_2 (or $\text{ThC} \cdot \text{ThH}_2$), Th_3CH_4 (or $\text{ThC} \cdot 2\text{ThH}_2$)	[825]
C–H–Ti	No diagram plot TiC_xH_y ($x = 0.460 \div 0.675$, $y = 0.158 \div 0.625$, or Ti_2CH_x ($\text{TiC} \cdot \text{TiH}_x$), $x = 0.46 \div 0.60$), TiC_xH_z ($x = 0.4$, $z = 1.2$)	[825]
C–H–V	No diagram plot VC_xH_y ($x = 0.75$, $y = 0.25$), V_2CH_x ($x = 0.3$)	[825]
C–H–Y	No diagram plot YC_xH_y (or Y_2CH_z , $\text{YC} \cdot \text{YH}_z$, $z = 2.55$)	[825]
C–H–Zr	No diagram plot ZrC_xH_y ($x = 0.30 \div 0.65$, $y = 0.30 \div 1.25$, or Zr_2CH_x , $\text{Zr}_2\text{C}_{1 \pm x}\text{H}_{1 \pm y}$, $\text{ZrC}_{1 \pm x} \cdot \text{ZrH}_{1 \pm y}$, or Zr_3CH_x , $\text{Zr}_3\text{C}_{1 \pm x}\text{H}_{1 \pm y}$, $\text{ZrC}_{1 \pm x} \cdot 2\text{ZrH}_{1 \pm y}$)	[825–826, 866]
C–Hf–In	No diagram plot Hf_2InC ($\text{M}_{n+1}\text{AX}_n$ -phase)	[680–681, 744–745, 860]
C–Hf–In–Ti	No diagram plot $(\text{Ti}, \text{Hf})_2\text{InC}$ ($\text{M}_{n+1}\text{AX}_n$ -phase solid solution)	[680–681, 860]
C–Hf–Ir	Plotted at 1500 °C: Hf_{2+x}Ir ($< \sim 1720\text{--}1775$ °C), Hf_3Ir_2 (or Hf_5Ir_3 , $< \sim 1930\text{--}1970$ °C), HfIr_{1+x} (or $\text{Hf}_{47}\text{Ir}_{53}$, $< \sim 2410\text{--}2440$ °C), HfIr_{3+x} ($< \sim 2460\text{--}2470$ °C), HfC_{1-x} , $\alpha\text{-Hf}$, $\beta\text{-Hf}$, Ir, C Depend. on compos., graphite is in equilibrium with $\text{HfIr}_{3+x} + \text{HfC}_{1-x}$ or $\text{HfIr}_{3+x} + (\text{Ir}, \text{Hf})$.	[244, 391, 417]
C–Hf–Mn	No diagram plot The interaction between HfC_{1-x} and Mn leads to the formation of eutectic alloy and solid solutions.	[242]

(continued)

Table 2.14 (continued)

System	Type of phase diagram (temperature and composition sections, constituent phases or phase fields) and/or character of interphase interaction and materials compatibility	References
C–Hf–Mo	<p>Plotted at 1250–2100 °C: (Hf,Mo)C_{1-x} (HfC_{1-x}–α-MoC_{1-x} monocarbide continuous solid solution at temp. > ~ 1700–2000 °C, or extended solid solution based on HfC_{1-x} with homog. range from HfC_{0.56} \div 0.99 to (Hf_{0.15}Mo_{0.85})C_{0.72} \div 0.77 at 1400 °C, from HfC_{0.54} \div 0.99 to (Hf_{0.11}Mo_{0.89})C_{0.72} \div 0.77 at 1700 °C, from HfC_{0.54} \div 0.99 to MoC_{0.64} \div 0.71 at 2000 °C; the C content of the mixed monocarbide phase increases as Hf substitutes for Mo), β-(Mo,Hf)_{2\pmx}C (semicarbide solid solution based on β-Mo_{2\pmx}C with homog. range from MoC_{0.4} \div 0.55 to (Mo_{0.9}Hf_{0.1})C_{0.475} \div 0.50 at 1400–2000 °C), α-(Mo,Hf)C_{1-x} (extended monocarbide solid solution based on α-MoC_{1-x} with homog. range from MoC_{0.65} \div 0.70 to (Mo_{0.93} \div 0.95Hf_{0.05} \div 0.07)C_{0.65} \div 0.70 at 1400–1700 °C; α-MoC_{1-x}–HfC_{1-x} monocarbide continuous solid solution at temp. > ~ 1700–2000 °C), η-(Mo,Hf)C_{1-x} (solid solution based on η-MoC_{1-x} with max. solubility of Hf—up to 3 at.% at 1700 °C), α-HfMo_{2\pmx} (< ~ 1770–1875 °C), β-HfMo_{2-x} (from ~ 1770–1875 °C to ~ 2130–2210 °C), α-Hf, β-(Hf,Mo), Mo, C</p> <p>Eutectic (Hf,Mo)C_{1-x}–Mo–β-(Mo,Hf)_{2\pmx}C (~ 2100–2140 °C, 6 at.% Hf, 20 at.% C)</p> <p>Eutectic (Hf,Mo)C_{1-x}–β-(Hf,Mo)–α-Hf (~ 1740–1780 °C, 83 at.% Hf, 2.5 at.% C)</p> <p>Eutectic (Hf,Mo)C_{1-x}–β-(Hf,Mo)–β-HfMo_{2-x} (~ 1850 °C)</p> <p>Eutectic (Hf,Mo)C_{1-x}–η-(Mo,Hf)C_{1-x}–β-(Mo,Hf)_{2\pmx}C (~ 2470 °C)</p> <p>HfC_{1-x}–Mo is plotted: eutectic—~ 2310–2370 °C, ~ 11–15 mol.% HfC_{1-x} (~ 11.5 at.% C); at eutectic temp. the max. solid solubility of Mo in HfC_{1-x} is \geq 15 mol.% and that of HfC_{1-x} in Mo is ~ 1.6 mol.%, the latter one decreases with decreasing temp. up to—0.4 mol.% at 2100 °C and 0.25 mol.% at 1250 °C</p> <p>Additions of Hf affect the solid solubility of C in Mo; at higher Hf content, the solubility of C decreases obviously. The presence of Hf stabilizes α-MoC_{1-x}. The interaction between HfC_{1-x} and Mo initiates from 1500–1800 °C (5 h exposure) and becomes noticeable at 2000–2200 °C (2 h exposure).</p> <p>Some data available on the system in literature are controversial.</p>	[138, 242, 391, 407, 409–410, 579, 614, 772–774, 827–828, 832, 835, 837]
C–Hf–Mo–Ni	<p>HfC_{1-x}–β-Mo_{2\pmx}C–Ni is plotted at 1220 °C: eutectic—~ 1200–1240 °C, ~ 7 mol.% β-Mo_{2\pmx}C, ~ 4 mol.% HfC_{1-x}; the max. mutual solubilities of the components at eutectic temp. are: in HfC_{1-x}—9 mol.% β-Mo_{2\pmx}C and 15.5 mol.% Ni, in β-Mo_{2\pmx}C—3 mol.% HfC_{1-x} and 20 mol.% Ni and in Ni—1 mol.% HfC_{1-x} and 4 mol.% β-Mo_{2\pmx}C.</p>	[408]

(continued)

Table 2.14 (continued)

System	Type of phase diagram (temperature and composition sections, constituent phases or phase fields) and/or character of interphase interaction and materials compatibility	References
C–Hf–Mo–Si	No diagram plot. At 1900–1950 °C in Ar atmosphere or low vacuum (~ 100 Pa) the interaction in $\text{HfC}_{1-x}\text{–MoSi}_2$ powder mixtures leads to the formation of SiC and $(\text{Mo,Hf})_5\text{Si}_{3\pm x}$.	[894, 899]
C–Hf–Mo–Ti	HfC_{1-x} ($x = 0.02$)– TiC_{1-x} ($x = 0.03$)–‘MoC’ is plotted at 1500–1650 °C: a small miscibility gap forms at temp. < 1630 °C at compos. $\text{Hf}_{0.45}\text{Mo}_{0.55}\text{C}_{1.0}$; at lower temp. a large miscibility gap connects the $\text{TiC}_{1-x}\text{–HfC}_{1-x}$ and $\text{HfC}_{1-x}\text{–‘MoC’}$ boundary systems; addition of ‘MoC’ to the $\text{TiC}_{1-x}\text{–HfC}_{1-x}$ solid solution decreases the critical miscibility temp., while addition of TiC_{1-x} to $\text{HfC}_{1-x}\text{–‘MoC’}$ raises the critical temp.; no max. type ternary critical point.	[409]
C–Hf–Mo–V	HfC_{1-x} ($x = 0.02$)– VC_{1-x} ($x = 0.12$)–‘MoC’ is plotted at 1500–2750 °C: addition of VC_{1-x} to the $\text{HfC}_{1-x}\text{–‘MoC’}$ monocarbide solid solution increases the critical miscibility temp.; phase equilibria are dominated by a large miscibility gap at 1500 °C.	[410]
C–Hf–N	$\text{HfC}_{1-x}\text{–HfN}_{1\pm x}\text{–Hf}$ is plotted at 1150 and ~ 2000 °C: HfC_xN_z ($0.6 \leq x + z \leq 1$, $\text{HfC}_{1-x}\text{–HfN}_{1\pm x}$ carbonitride continuous solid solution, homog. range at 1150 °C: $\sim \text{HfC}_{0.60}\text{–HfN}_{0.72}\text{–HfN}_{1.0}\text{–HfC}_{0.98}$), $\beta\text{–Hf}$	[138, 242, 391, 411, 454]
C–Hf–N–O	$\text{HfC}_{1-x}\text{–HfN}_{1\pm x}\text{–‘HfO’}$ is plotted at 1600 and 2000 °C: homog. limits of $\text{HfC}_{1-x}\text{–HfN}_{1\pm x}$ continuous solid solution ($\text{HfC}_x\text{N}_y\text{O}_z$) are $\text{HfC}_{0.75}\text{O}_{0.25}$ and $\text{HfN}_{0.80}\text{O}_{0.20}$ (1600 °C) and $\text{HfC}_{0.70}\text{O}_{0.30}$ and $\text{HfN}_{0.75}\text{O}_{0.25}$ (2000 °C)	[411–412]
C–Hf–Nb	Plotted at 1200–2050 °C: $(\text{Hf,Nb})\text{C}_{1-x}$ ($\text{HfC}_{1-x}\text{–NbC}_{1-x}$ monocarbide continuous solid solution), $\beta\text{–Nb}_{2+x}\text{C}$ (max. solubility of Hf is ~ 5 at.%), $\gamma\text{–Nb}_{2\pm x}\text{C}$, $\zeta\text{–Nb}_4\text{C}_{3-x}$, $\text{Nb}_6\text{C}_{5\pm x}$, $\beta\text{–(Hf,Nb)}$, C Graphite is in equilibrium with $(\text{Hf,Nb})\text{C}_{1-x}$.	[138, 242, 391, 413, 813, 824, 837, 844]
C–Hf–Nb–U	$\text{HfC}_{1-x}\text{–NbC}_{1-x}\text{–UC}_{1\pm x}$ is plotted at 2050 °C: $(\text{Hf,Nb,U})\text{C}$ (based on $\text{HfC}_{1-x}\text{–NbC}_{1-x}$ and $\text{NbC}_{1-x}\text{–UC}_{1\pm x}$ monocarbide continuous solid solutions with homog. range depend. on temp.), 2 monocarbide solid solutions region (or miscibility gap, limited by compos. $\sim (\text{Hf}_{0.4}\text{U}_{0.6})\text{C}_{1-x}$ $\sim (\text{Hf}_{0.75}\text{U}_{0.25})\text{C}_{1-x}$ $\sim (\text{Hf}_{0.5}\text{Nb}_{0.2}\text{U}_{0.3})\text{C}_{1-x}$)	[391]
C–Hf–Nb–V	$\text{HfC}_{1-x}\text{–NbC}_{1-x}\text{–VC}_{1-x}$ is plotted at 2050 °C: $(\text{Hf,Nb,V})\text{C}_{1-x}$ (based on $\text{HfC}_{1-x}\text{–NbC}_{1-x}$ and $\text{VC}_{1-x}\text{–NbC}_{1-x}$ monocarbide continuous solid solutions, with homog. range depend. on temp.), 2 monocarbide solid solutions region (or miscibility gap, limited by compos. $\sim (\text{Hf}_{0.98}\text{V}_{0.02})\text{C}_{1-x}$ $\sim (\text{Hf}_{0.03}\text{V}_{0.97})\text{C}_{1-x}$ $\sim (\text{Hf}_{0.2+0.3}\text{Nb}_{0.51+0.52}\text{V}_{0.2+0.3})\text{C}_{1-x}$)	[413]

(continued)

Table 2.14 (continued)

System	Type of phase diagram (temperature and composition sections, constituent phases or phase fields) and/or character of interphase interaction and materials compatibility	References
C–Hf–Ni	Plotted at 1100 °C: Hf ₂ Ni (<~1195–1200 °C), α -HfNi (<1170 °C), β -HfNi (1170–1530 °C), Hf ₉ Ni ₁₁ (<1335–1340 °C), Hf ₇ Ni ₁₀ (or Hf ₂ Ni ₃ , <1290–1295 °C), Hf ₃ Ni ₇ (or Hf ₂ Ni ₅ , from ~1015–1020 °C to 1250 °C), Hf ₈ Ni ₂₁ (from ~1175–1180 °C to 1300 °C), α -HfNi ₃ (<1200 °C), β -HfNi ₃ (from 1200 °C to ~1300–1340 °C), Hf ₂ Ni ₇ (<1480 °C), HfNi ₅ (<1240 °C), HfC _{1-x} , Ni, α -Hf, β -Hf, C HfC _{1-x} –Ni is plotted: eutectic—~1320–1330 °C, ~3–5.6 mol.% HfC _{1-x} ; at the eutectic temp. the solubility of HfC _{1-x} in Ni is $\leq 0.7 \div 1.0$ mol.% and that of Ni in HfC _{1-x} ~ 7.5 mol.% HfC _{1-x} is in equilibrium with Ni and Ni-Hf intermetallics	[242, 244, 391, 414–415, 417, 839]
C–Hf–Ni–Ti	HfC _{1-x} –TiC _{1-x} –Ni is plotted at 1225 °C: eutectic—~1205–1235 °C, ~1.0–1.2 mol.% HfC _{1-x} , ~5–6 mol.% TiC _{1-x}	[414]
C–Hf–Ni–W	HfC _{1-x} – δ -WC _{1-x} –Ni is plotted at 1000 °C: eutectic—15 mol.% HfC _{1-x} , 15 mol.% δ -WC _{1-x} ; regions of solid solutions based on the individual components are not large (6–7 mol.%)	[415]
C–Hf–Ni–Zr	HfC _{1-x} ($x = 0.02$)–ZrC _{1-x} ($x = 0.17$)–Ni is plotted partially: HfC _{1-x} –ZrC _{1-x} monocarbide continuous solid solution forms in the presence of Ni; minimum on the line of eutectic solidification (Hf,Zr)C _{1-x} –Ni is lower by 100–150 °C than eutectic temp. in the HfC _{1-x} –Ni and ZrC _{1-x} –Ni systems and corresp. to compos. 4 mol.% HfC _{1-x} , 4 mol.% ZrC _{1-x} and 92 mol.% Ni	[839]
C–Hf–O	C–Hf– β -HfO _{2-x} is partially plotted at 1900 °C: homog. limits of HfC _x O _y (HfC _{1-x} –‘HfO’ oxycarbide solid solution) are ~HfC _{0.75} O _{0.25} –HfC _{0.55} –HfC _{0.99} The equilibrium pressure of CO over graphite in the mixture with α -HfO _{2-x} and HfC _{1-x} is ~0.1 MPa at 1640 °C, ~0.05 MPa at 1600 °C, ~0.02 MPa at 1500 °C and ~0.01 MPa at 1400 °C.	[411, 416]
C–Hf–O–Ti	No diagram plot. At 1500–2200 °C the interaction between TiC _{1-x} and HfO _{2-x} leads to the formation of TiC _x O _y .	[242]
C–Hf–Os	Plotted at 1500 °C: θ -Hf _{3+x} Os (<1640–1680 °C), ε -Hf _{2+x} Os (<1860–1900 °C), η -Hf _{2+x} Os (<2040–2080 °C), δ -HfOs _{1+x} (<2500–2540 °C), λ -HfOs _{2+x} (<~2700 °C), HfC _{1-x} , α -Hf, β -Hf, Os, C Graphite is in equilibrium with (Os,Hf) + HfC _{1-x} . The solubility of Hf in Os (with the presence of C) and solubility of Os in HfC _{1-x} are low.	[391, 417]
C–Hf–Pb	No diagram plot Hf ₂ PbC (M _{n+1} AX _n -phase)	[680–681, 744–745, 860]

(continued)

Table 2.14 (continued)

System	Type of phase diagram (temperature and composition sections, constituent phases or phase fields) and/or character of interphase interaction and materials compatibility	References
C–Hf–Pd	Plotted at 1300 °C: Hf ₂ Pd (<1405–1425 °C), HfPd (<1600–1620 °C), Hf ₃ Pd ₄ (<1550–1570 °C), HfPd ₂ (from 1350–1390 °C to 2075 °C), HfPd ₃ (<1955–1975 °C), HfC _{1–x} , α -Hf, β -Hf, Pd, C Depend. on compos., graphite is in equilibrium with (Pd,Hf) alloy, or HfPd ₃ , or HfPd ₃ + HfC _{1–x} .	[244, 391, 417]
C–Hf–Pt	Plotted at 1500 °C: Hf ₂ Pt (<1620 °C), HfPt (<2100 °C), Hf ₉ Pt ₁₁ (<1550 °C), Hf ₂ Pt ₃ (1400–1670 °C), HfPt ₂ (1630–1960 °C), HfPt _{3±x} (<2150 °C), HfC _{1–x} , α -Hf, β -Hf, Pt, C Depend. on compos., graphite is in equilibrium with (Pt,Hf) alloy + HfPt _{3±x} or HfPt _{3±x} + HfC _{1–x} .	[391, 417]
C–Hf–Re	Plotted at 1500 °C: HfRe _{1±x} (or Hf ₁₁ Re ₉ , or Hf ₃ Re ₂ , <~2280–2445 °C), λ -HfRe _{2±x} (<~2850–3160 °C), χ -Hf ₅ Re _{24±x} (or HfRe ₇ , <~2800–3100 °C), HfC _{1–x} , α -Hf, β -Hf, Re, C HfC _{1–x} –Re is plotted: eutectic—2720 °C, ~20–30 mol.% HfC _{1–x} ; the mutual solubilities of the components are low Graphite is in equilibrium with Re + HfC _{1–x} .	[242, 244, 391, 417, 835, 837]
C–Hf–Rh	Plotted at 1500 °C: HfRh ₃ C _x ($x \approx 0.4$), γ -Hf _{2±x} Rh (<~1450–1520 °C), δ -HfRh _{1±x} (<~2180–2290 °C), Hf ₃ Rh _{5±x} (or Hf ₃ Rh _{3+3x} , <2040 °C), HfRh _{3±x} (<2130 °C), HfC _{1–x} , α -Hf, β -Hf, Rh, C The solubility of C in HfRh _{3±x} is ~5–10 at.%; no solubility of Rh in HfC _{1–x} . Depend. on compos., graphite is in equilibrium with Rh + HfRh ₃ C _x or HfRh ₃ C _x + HfC _{1–x} .	[244, 391, 417]
C–Hf–Ru	Plotted at 1500 °C: HfRu ₃ C _{1–x} ($x \approx 0.3$), HfRu _{1±x} (<~2350–2400 °C), HfRu ₂ (<~1900–1950 °C), HfC _{1–x} , α -Hf, β -Hf, Ru, C HfC _{1–x} –Ru is plotted: eutectic—~2000 °C Graphite is in equilibrium with Ru + HfC _{1–x} .	[391, 417]
C–Hf–S	No diagram plot Hf ₂ SC ($M_{n+1}AX_n$ -phase)	[680–681, 744–745, 860]
C–Hf–Si	Plotted at 1300 °C: Hf ₅ Si ₃ C _{1+x} ($x = 0.09$), Hf ₂ Si (<~2070–2095 °C), Hf ₃ Si ₂ (<2460–2500 °C), Hf ₅ Si ₄ (or Hf ₅ Si ₃ , <2305–2335 °C), HfSi (<~2125–2155 °C), HfSi ₂ (<~1535–1550 °C), HfC _{1–x} , SiC, α -Hf, Si, C Graphite is in equilibrium with SiC + HfC _{1–x} .	[242, 417–419, 503, 771]
C–Hf–Sn	No diagram plot Hf ₂ SnC ($M_{n+1}AX_n$ -phase)	[680–681, 744–745, 860]

(continued)

Table 2.14 (continued)

System	Type of phase diagram (temperature and composition sections, constituent phases or phase fields) and/or character of interphase interaction and materials compatibility	References
C–Hf–Ta	Plotted at 1000–3950 °C: (Hf,Ta) C_{1-x} (Hf C_{1-x} –Ta C_{1-x} monocarbide continuous solid solution), α –(Ta,Hf) $_{2+x}C$ (extended semicarbide solid solution based on α –Ta $_{2+x}C$, ~1000–2230 °C, max. solubility of Hf, depend. on temp.—~1.5–10.7 at.%), β –(Ta,Hf) $_{2\pm x}C$ (extended semicarbide solid solution based on β –Ta $_{2\pm x}C$, ~2000–3200 °C, max. solubility of Hf, depend. on temp.—~1.5–18.5 at.%), ζ –Ta $_4C_{3-x}$, Ta $_6C_{5\pm x}$, α –Hf, β –Hf, Ta, C Hf C_{1-x} –Ta C_{1-x} is plotted: miscibility gap in the solid state (critical point—890 °C, at compos. ~Hf $_{0.5\div 0.6}$ Ta $_{0.4\div 0.5}C_{1-x}$) The data on the higher melting points of (Hf,Ta) C_{1-x} in comparison with individual Hf C_{1-x} and Ta C_{1-x} are not confirmed. Graphite is in equilibrium with (Hf,Ta) C_{1-x} .	[138, 242, 391, 419–423, 723, 813, 837, 885]
C–Hf–Ta–U	Hf C_{1-x} –Ta C_{1-x} –UC $_{1\pm x}$ is plotted at 2050 °C: (Hf,Ta,U) $C_{1\pm x}$ (based on Hf C_{1-x} –Ta C_{1-x} and Ta C_{1-x} –UC $_{1\pm x}$ monocarbide continuous solid solutions with homog. range depend. on temp.), 2 monocarbide solid solutions region (or miscibility gap, limited by compos. ~ (Hf $_{0.4}U_{0.6}$) C_{1-x} —~ (Hf $_{0.75}U_{0.25}$) C_{1-x} —~ (Hf $_{0.55}Ta_{0.15}U_{0.3}$) C_{1-x})	[391]
C–Hf–Tc	Plotted schematically	[840]
C–Hf–Th	No diagram plot Hf C_{1-x} –Th $C_{1\pm x}$ extended monocarbide solid solutions (terminal solubility).	[138]
C–Hf–Ti	Plotted at 800, 1500 and 2000 °C: (Hf,Ti) C_{1-x} (Hf C_{1-x} –Ti C_{1-x} monocarbide continuous solid solution at higher temp. with miscibility gap at lower temp.), two monocarbide extended solid solutions region (Hf,Ti) C_{1-x} (based on Hf C_{1-x}) + (Ti,Hf) C_{1-x} (based on Ti C_{1-x}), α –Hf, β –Hf, α –Ti, β –Ti, C Hf C_{1-x} –Ti C_{1-x} is plotted: miscibility gap in the solid state (critical point—~1765–2050 °C (?), at ~Hf $_{0.40\div 0.45}$ Ti $_{0.55\div 0.60}C_{1-x}$, gap width at 1500 °C—from ~Hf $_{0.1\div 0.2}$ Ti $_{0.8\div 0.9}C_{1-x}$ to ~Hf $_{0.50\div 0.75}$ Ti $_{0.25\div 0.50}C_{1-x}$) Graphite is in equilibrium with (Hf,Ti) C_{1-x} or (Hf,Ti) C_{1-x} + (Ti,Hf) C_{1-x} .	[138, 242, 391, 414, 424–426, 625, 813, 816]
C–Hf–Ti–V	Hf C_{1-x} –Ti C_{1-x} –VC $_{1-x}$ is plotted at 2050 °C: (Hf,Ti,V) C_{1-x} (based on Hf C_{1-x} –Ti C_{1-x} and VC $_{1-x}$ –Ti C_{1-x} monocarbide continuous solid solutions with homog. range depend. on temp.), 2 monocarbide solid solutions region (or miscibility gap, limited by compos. ~ (Hf $_{0.98}V_{0.02}$) C_{1-x} —~ (Hf $_{0.03}V_{0.97}$) C_{1-x} —~ (Hf $_{0.14\div 0.17}$ Ti $_{0.73\div 0.74}V_{0.09\div 0.12}$) C_{1-x})	[413]

(continued)

Table 2.14 (continued)

System	Type of phase diagram (temperature and composition sections, constituent phases or phase fields) and/or character of interphase interaction and materials compatibility	References
C–Hf–Ti–W	HfC _{1-x} –TiC _{1-x} – δ -WC _{1±x} is plotted at 1500–3100 °C: (Hf,Ti,W)C _{1-x} (monocarbide solid solution based on HfC _{1-x}), (Ti,Hf,W)C _{1-x} (monocarbide solid solution based on TiC _{1-x}), (Hf,Ti,W)C _{1-x} + (Ti,Hf,W)C _{1-x} , (Hf,Ti,W)C _{1-x} (monocarbide solid solution based on (Hf,Ti)C _{1-x}) + δ -(W,Hf,Ti)C _{1±x} (monocarbide solid solution based on δ -WC _{1±x}) (Hf,W)C _{1-x} –(Ti,W)C _{1-x} miscibility gap in the solid state: limited by compos. Hf _{0.64} Ti _{0.36} C _{1-x} –Hf _{0.22} Ti _{0.78} C _{1-x} –Hf _{0.41} Ti _{0.27} W _{0.32} C _{1±x} (at 1540 °C)	[426]
C–Hf–Ti	No diagram plot Hf ₂ TiC (M _{n+1} AX _n -phase)	[680–681, 744–745, 860]
C–Hf–U	Plotted at 1800 and 2000 °C: (Hf,U)C _{1-x} (HfC _{1-x} –UC _{1±x} monocarbide continuous solid solution, or extended monocarbide solid solutions based on HfC _{1-x} and UC _{1±x} at lower temp.), α -UC _{2-x} , α -Hf, β -Hf, U, C HfC _{1-x} –UC _{1±x} is plotted: miscibility gap in the solid state (critical point—~1730 °C, ?) At higher temp., depend. on compos., graphite is in equilibrium with (Hf,U)C _{1-x} or (Hf,U)C _{1-x} + UC _{2-x} ; the compos. of (Hf,U)C _{1-x} in equilibrium with C + UC _{2-x} is corresp. to ~ (Hf _{0.9} U _{0.1})C _{1-x} (at 2200 °C) and shifts to lower U concentrations with temp. increase.	[138, 391]
C–Hf–U–Zr	HfC _{1-x} –ZrC _{1-x} –UC _{1±x} is plotted at 2050 °C: (Hf,Zr,U)C _{1±x} (based on HfC _{1-x} –ZrC _{1-x} and ZrC _{1-x} –UC _{1±x} monocarbide continuous solid solutions with homog. range depend. on temp.), 2 monocarbide solid solutions region (or miscibility gap, limited by compos. ~ (Hf _{0.4} U _{0.6})C _{1±x} –~ (Hf _{0.75} U _{0.25})C _{1±x} –~ (Hf _{0.45} Zr _{0.10} U _{0.45})C _{1±x})	[391]
C–Hf–V	Plotted at 1000 °C: HfV _{2±x} (<1550 °C), α -V _{2+x} C, β -V _{2±x} C, β' -V _{2+x} C, ζ -V ₄ C _{3-x} , V ₆ C _{5±x} , V ₈ C _{7±x} , VC _{1-x} , HfC _{1-x} , α -Hf, V, C HfC _{1-x} –VC _{1-x} is plotted: eutectic—~2580–2650 °C, ~70–75 mol.% VC _{1-x} ; the mutual solubilities of HfC _{1-x} and VC _{1-x} in each other are ~15 vol.% (at eutectic temp.) The mutual solubilities of other components are lower.	[391, 427, 813, 837]
C–Hf–V–W	HfC _{1-x} –VC _{1-x} – δ -WC _{1±x} is plotted at 1750–2970 °C: (Hf,V,W)C _{1-x} (monocarbide solid solution based on (Hf,V)C _{1-x}), (Hf,V,W)C _{1-x} (monocarbide solid solution based on HfC _{1-x}), (V,Hf,W)C _{1-x} (monocarbide solid solution based on VC _{1-x}) (Hf,W)C _{1-x} –(V,W)C _{1-x} miscibility gap in the solid state: limited by compos. ~ (Hf _{0.9} V _{0.1})C _{1-x} –~ (Hf _{0.1} V _{0.9})C _{1-x} –~ (Hf _{0.40+0.45} V _{0.40+0.45} W _{0.15})C _{1±x} (at 2580 °C) Addition of δ -WC _{1±x} decreases the critical temp. of miscibility gap.	[427]

(continued)

Table 2.14 (continued)

System	Type of phase diagram (temperature and composition sections, constituent phases or phase fields) and/or character of interphase interaction and materials compatibility	References
C–Hf–W	Plotted at 1500–2660 °C: (Hf,W)C _{1–x} (HfC _{1–x} – γ -WC _{1–x} monocarbide continuous solid solution at higher temp.), HfW _{2±x} (< ~2495–2530 °C), α -W _{2+x} C, β -W _{2+x} C, γ -W _{2+x} C, γ -WC _{1–x} , δ -WC _{1±x} , α -Hf, β -Hf, W, C Eutectic (Hf,W)C _{1–x} – γ -W _{2±x} C–W (2660 °C, 8 at.% Hf, 22 at.% C); at the eutectic temp. the monocarbide solid solution compos. is (Hf _{0.83} W _{0.17})C _{0.89} and semicarbide solid solution compos. is (W _{0.94} Hf _{0.06}) ₂ C _{0.99} (with max. solubility of Hf in γ -W _{2±x} C); the max. solid solubilities of C and Hf in metal W are ~1 at.% HfC _{1–x} –W is plotted: eutectic—~2790–2930 °C, ~20–25 mol.% HfC _{1–x} (~20 at.% C); the solubility of W in HfC _{1–x} is 6 mol.% (at eutectic temp.) The presence of Hf stabilizes γ -WC _{1–x}	[242, 244, 391, 415, 417, 428–430, 773, 827, 835, 837]
C–Hf–Zr	Plotted at 1600–3900 °C: (Hf,Zr)C _{1–x} (HfC _{1–x} –ZrC _{1–x} monocarbide continuous solid solution), α -(Hf,Zr), β -(Hf,Zr), C Eutectic (Hf,Zr)C _{1–x} – β -(Zr,Hf)– α -(Hf,Zr) (2030 °C) HfC _{1–x} –ZrC _{1–x} is plotted: continuous solid solution Graphite is in equilibrium with (Hf,Zr)C _{1–x} .	[138, 391, 424–425, 634, 813, 1006]
C–Ho–U	No diagram plot UC _{1±x} –HoC _{1–x} monocarbide continuous solid solution or extended solid solution based on UC _{1±x} .	[391]
C–In–Nb	No diagram plot Nb ₂ InC (M _{n+1} AX _n -phase)	[680–681, 744–745, 860]
C–In–Ti	Plotted partially at 1300 °C: Ti ₂ InC (M _{n+1} AX _n -phase), Ti ₃ InC, Ti ₃ In ₄ (< ~795 °C), TiC _{1–x} (solubility of In ≤ 5 at.%), α -Ti, β -Ti, In, C The extension of homog. range for both ternary compounds in the system is ~2–4 at.%.	[587, 680–681, 744–745, 859–860]
C–In–Zr	No diagram plot Zr ₂ InC (M _{n+1} AX _n -phase)	[680–681, 744–745, 860]
C–Ir–Mo	Plotted at 1500 °C: ~Mo ₂ Ir ₂ C (stable at least at temp. <1500 °C, ?), Ir _{3–x} Mo (<2300 °C), ε -IrMo _{1±x} (from 1400–1620 °C to 2270 °C), IrMo _{1±x} (<1600–1620 °C), σ -Ir ₃ Mo _{7+x} (from ~1970–1980 °C to ~2080–2110 °C), IrMo _{3+x} (<2100–2120 °C), β -Mo _{2±x} C, Mo, Ir, C	[244, 391, 431]
C–Ir–Nb	Plotted at 1500 °C: Ir _{3±x} Nb (<2435–2440 °C), α_2 -IrNb _{1–x} (< ~1985 °C), α_1 -IrNb _{1–x} (< ~1900 °C), σ -IrNb _{2–x} (< ~2060 °C), IrNb _{3±x} (<2125–2130 °C), β -Nb _{2+x} C, ζ -Nb ₄ C _{3–x} , NbC _{1–x} , Nb, Ir, C Depend. on compos., graphite is in equilibrium with Ir _{3±x} Nb + NbC _{1–x} or Ir _{3±x} Nb + (Ir,Nb).	[244, 391, 431]
C–Ir–Rh	No diagram plot Eutectic (50 % Ir + 50 % Rh)–C (1930 °C)	[138]

(continued)

Table 2.14 (continued)

System	Type of phase diagram (temperature and composition sections, constituent phases or phase fields) and/or character of interphase interaction and materials compatibility	References
C–Ir–Sc	No digram plot ScIr ₃ C, α -Sc ₃ IrC ₄ , β -Sc ₃ IrC ₄	[986–988]
C–Ir–Si	Plotted at 1340 °C: IrSi ₃ (at least at ~ 1400 – 1500 °C), IrSi ₂ (at least at ~ 1400 – 1500 °C), Ir ₂ Si ₃ (or IrSi _{~ 1.5} , at least at ~ 1250 – 1400 °C), IrSi (at least at ~ 1500 °C), Ir ₃ Si ₂ (or Ir _{1.5} Si, at least from ~ 500 – 700 °C to ~ 1500 °C), Ir ₂ Si (at least at ~ 1500 °C), Ir ₃ Si (at least at ~ 1500 °C), SiC, Si, Ir, C	[431, 503–504]
C–Ir–Ta	Plotted at 1500 °C: β -Ir _{3$\pm x$} Ta (< 2450 – 2455 °C), γ -Ir ₃ Ta _{2+x} (or α_2 -Ir ₃ Ta _{2+x} , < 1860 – 1865 °C), δ -IrTa _{1–x} (or α_1 -IrTa _{1–x} , $< \sim 2120$ – 2125 °C), σ -IrTa _{3$\pm x$} (< 2475 – 2480 °C), α -Ta _{2+x} C, β -Ta _{2$\pm x$} C, ζ -Ta ₄ C _{3–x} , Ta ₆ C _{5$\pm x$} , TaC _{1–x} , Ta, Ir, C Depend. on compos., graphite is in equilibrium with β -Ir _{3$\pm x$} Ta + TaC _{1–x} or β -Ir _{3$\pm x$} Ta + (Ir,Ta).	[244, 391, 431]
C–Ir–Th	No diagram plot Th _{x} Ir _{y} C _{z} (?)	[391]
C–Ir–Ti	Plotted at 1500 °C: Ti _{3–x} Ir (< 1515 °C), α -TiIr _{1$\pm x$} ($< \sim 1745$ °C), β -TiIr _{1$\pm x$} ($< \sim 2130$ °C), TiIr _{3$\pm x$} ($< \sim 2115$ – 2125 °C), TiC _{1–x} , β -Ti, Ir, C Depend. on compos., graphite is in equilibrium with TiIr _{3$\pm x$} + TiC _{1–x} or TiIr _{3$\pm x$} + (Ir,Ti).	[244, 391, 431]
C–Ir–U	Plotted at 1300 °C: U ₂ IrC ₂ , U ₃ Ir (~ 750 – 945 °C), U ₂ Ir ($< \sim 775$ °C), α -U ₃ Ir ₂ ($< \sim 900$ °C), β -U ₃ Ir ₂ (~ 900 – 1120 °C), UIr (< 1470 °C), UIr ₂ ($< \sim 1850$ – 1875 °C), UIr ₃ ($< \sim 2000$ – 2005 °C), UC _{1$\pm x$} , ζ -U ₂ C ₃ , U, Ir, C	[242, 244, 391, 431, 693]
C–Ir–V	Plotted at 1500 °C: V _{3$\pm x$} Ir ($< \sim 1900$ – 1960 °C), VIr _{1+x} ($\leq \sim$ at least 1880 °C), V _{1–x} Ir _{1+x} (or (V _{1–x} Ir) _{x})Ir, $0.04 < x < 0.19$, \leq at least 1900 °C), VIr _{3$\pm x$} (\leq at least 2000 °C), β -V _{2$\pm x$} C, β' -V _{2+x} C, ζ -V ₄ C _{3–x} , V ₆ C _{5$\pm x$} , V ₈ C _{7$\pm x$} , VC _{1–x} , V, Ir, C Depend. on compos., graphite is in equilibrium with VIr _{3$\pm x$} + VC _{1–x} or VIr _{3$\pm x$} + (Ir,V).	[391, 431]
C–Ir–W	Plotted at 2000 °C: \sim W ₂ Ir ₂ C (?), δ -Ir _{3–x} W (?), β -Ir ₃ W _{2$\pm x$} ($< \sim 2500$ °C), ε -IrW _{1$\pm x$} (?), σ -IrW _{3$\pm x$} (from 1795 – 1850 °C to 2520 – 2570 °C), α -W _{2+x} C, β -W _{2+x} C, γ -W _{2$\pm x$} C, γ -WC _{1–x} , δ -WC _{1$\pm x$} , W, Ir, C	[244, 391, 431]
C–Ir–Y	Plotted partially at 1100 – 1500 °C: Y ₃ Ir (< 1425 °C), Y ₅ Ir ₂ (< 1525 °C), Y ₆₄ Ir ₃₇ (?), α' -Y ₅ Ir _{3$\pm x$} (?), α -Y ₅ Ir _{3$\pm x$} (?), β -Y ₅ Ir _{3$\pm x$} (< 1600 °C), Y ₃ Ir ₂ (< 1725 °C), YIr (< 2150 °C), YIr _{2$\pm x$} (< 2400 °C), YIr ₃ (< 2100 °C), Y _{2$\pm x$} C, YC _{1$\pm x$} , α -Y ₄ C ₅ , β -Y ₄ C ₅ , α -Y ₃ C _{4–x} , β -Y ₃ C _{4–x} , α -Y ₂ C _{3–x} , β -Y ₂ C _{3–x} , α -YC ₂ , β -YC _{2$\pm x$} , α -Y, β -Y, Ir, C Depend. on compos., graphite is in equilibrium with YIr _{2$\pm x$} + Ir, or YIr _{2$\pm x$} + α -YC ₂ .	[990]

(continued)

Table 2.14 (continued)

System	Type of phase diagram (temperature and composition sections, constituent phases or phase fields) and/or character of interphase interaction and materials compatibility	References
C–Ir–Zr	Plotted at 1500 °C: Zr_3Ir (<1305 °C), Zr_2Ir (<1340 °C), Zr_5Ir_3 (<1730 °C), α - $ZrIr_{1-x}$ (<900–950 °C), β - $ZrIr_{1\pm x}$ (from 900–950 °C to 2050 °C), $ZrIr_2$ (<2085 °C), $ZrIr_{3\pm x}$ (<2280 °C), ZrC_{1-x} , α -Zr, β -Zr, Ir, C Depend. on compos., graphite is in equilibrium with $ZrIr_{3\pm x} + ZrC_{1-x}$, or $ZrIr_{3\pm x} + (Ir, Zr)$.	[244, 391, 431]
C–La–N–Th	No diagram plot $ThC_{1\pm x}$ – $LaN_{1\pm x}$ carbonitride continuous solid solution	[391]
C–La–U	Plotted at 1500 °C: β -(La,U) $C_{2\pm x}$ (extended dicarbide solid solution based on β - $LaC_{2\pm x}$), $UC_{1\pm x}$, ζ - U_2C_3 , La_2C_{3-x} , U, La, C The solubilities of ‘LaC’ in $UC_{1\pm x}$ and La_2C_{3-x} in ζ - U_2C_3 are <1 mol.%.	[244, 391]
C–Lu–U	No diagram plot $UC_{1\pm x}$ – LuC_{1-x} (or $Lu_{3-x}C$) monocarbide continuous solid solution or extended solid solution based on $UC_{1\pm x}$.	[391]
C–Mg–Mo–O	No diagram plot At 1800–2300 °C the interaction between MgO and β - $Mo_{2\pm x}C$ is weak.	[242]
C–Mg–Nb–O	No diagram plot At 1800–2300 °C, in vacuum MgO and NbC_{1-x} interact with the formation of Nb and NbC_xO_y .	[242]
C–Mg–O	No diagram plot $MgCO_3$, MgC_2O_4 In vacuum (0.01–0.05 Pa), the interaction between C and MgO is ruled by chemical boundary reaction stage (linear law) and initiates in powdered mixtures from ~1350 °C and on bulk materials contacts—from ~1800 °C.	[138, 194]
C–Mg–O–Si	No diagram plot At 1600 °C MgO and SiC interact intensively.	[242]
C–Mg–O–Ta	No diagram plot In vacuum, the interaction between MgO and TaC_{1-x} initiates at temp. >2200–2300 °C.	[138, 242]
C–Mg–O–Ti	No diagram plot At 1600–1900 °C, in He MgO and TiC_{1-x} interact with the formation of Mg_2TiO_4 , $TiO_{1\pm x}$ and CO; at 1800–2300 °C, in vacuum—with the formation of C, Mg and TiC_xO_y .	[242]
C–Mg–O–W	No diagram plot At 1800–2300 °C the interaction between MgO and δ - $WC_{1\pm x}$ is weak.	[242]
C–Mg–O–Zr	No diagram plot At 2000–2300 °C in vacuum MgO and ZrC_{1-x} interact with the formation of C, Mg and ZrC_xO_y .	[242]

(continued)

Table 2.14 (continued)

System	Type of phase diagram (temperature and composition sections, constituent phases or phase fields) and/or character of interphase interaction and materials compatibility	References
C–Mn–Nb	No diagram plot At 1350 °C the interaction between NbC _{1–x} and Mn leads to the formation of eutectic alloy and solid solutions.	[242]
C–Mn–Mo	Plotted at 800 °C: η -Mo ₃ Mn ₃ C, Mo ₂ Mn ₄ C, α -(Mo,Mn) _{2+x} C (extended solid solution based on α -Mo _{2+x} C), σ -Mn ₅ Mo _{3–x} (from 1075–1105 °C to 1300–1500 °C), μ -Mn ₅ Mo _{4±x} (<1400–1600 °C), ε -Mn _{4±x} C, Mn ₂₃ C ₆ , Mn ₁₅ C ₄ , Mn ₃ C, Mn ₅ C ₂ , Mn ₇ C ₃ , α' -Mo _{2+x} C, γ -MoC, α -Mn, β -Mn, γ -Mn, Mo, C Depend. on compos., graphite is in equilibrium with α -(Mo,Mn) _{2+x} C, or α -(Mo,Mn) _{2+x} C + Mn ₇ C ₃ , or Mn ₇ C ₃ .	[391]
C–Mn–Si	Plotted at 1000 and 1130 °C: Mn ₅ SiC (Nowotny phase), Mn ₈ Si ₂ C, Mn ₅ Si ₃ C _x (<1285–1300 °C, solid solution based on Mn ₅ Si ₃), Mn _{6±x} Si (<880 °C), ν -Mn ₉ Si _{2±x} (<1060 °C), α -Mn _{3–x} Si (<~675 °C), β -Mn _{3±x} Si (from ~675 °C to 1070–1075 °C), Mn ₅ Si ₂ (<850 °C), MnSi _{1–x} (<1270–1275 °C), Mn ₁₁ Si _{19±x} (or MnSi _{1.75–x} , <1150–1155 °C), θ -MnSi ₂ (or θ -Mn ₁₅ Si ₂₆ , ?), ε -Mn _{4±x} C, Mn ₂₃ C ₆ , Mn ₁₅ C ₄ , Mn ₃ C, Mn ₅ C ₂ , Mn ₇ C ₃ , SiC, β -Mn, γ -Mn, δ -Mn, Si, C The solubility of Mn in SiC is very low (~2×10 ^{–4} at.% at 1850 °C and ~2×10 ^{–2} at.% at 1950 °C).	[244, 299, 393, 431, 503, 769–770]
C–Mn–U	No diagram plot UMn ₂	[391]
C–Mn–W	Plotted at 800 °C: η -W ₃ Mn ₃ C, κ -W ₃ MnC _{1–x} , (Mn,W) ₂ C (or ~Mn ₇ W _{0.5÷1} C _{2÷2.5}), ε -Mn _{4±x} C, Mn ₂₃ C ₆ , Mn ₁₅ C ₄ , Mn ₃ C, Mn ₅ C ₂ , Mn ₇ C ₃ , δ -WC _{1±x} , α -Mn, β -Mn, W, C Depend. on compos., graphite is in equilibrium with δ -WC _{1±x} + Mn ₇ C ₃ or Mn ₇ C ₃ .	[391]
C–Mn–Zr	No diagram plot At 1300 °C the interaction between ZrC _{1–x} and Mn leads to the formation of eutectic alloy and solid solutions.	[242]
C–Mo–N	Plotted at 1100 °C: δ -Mo(C,N) _{1±x} (extended solid solution based on δ -MoN or δ -MoN–‘MoC’ carbonitride continuous solid solution at higher temp.), α -Mo _{2+x} (C,N) (extended solid solution based on α -Mo _{2+x} C with max. solubility of γ -Mo _{2±x} N–65 mol.%), γ -Mo _{2±x} N, Mo, N, C	[391, 431, 476, 853]
C–Mo–N–Ti	TiC _{1–x} –TiN _{1±x} – α -MoC _{1–x} – δ -MoN is plotted at 1450 °C ($p_{N_2} \leq 0.2$ MPa) and 1600–1650 °C ($p_{N_2} \leq 0.3$ MPa): (Ti,Mo)(C,N) _{1±x} (extended solid solution based on TiC _{1–x} –TiN _{1±x} carbonitride continuous solid solution) TiC _{1–x} –TiN _{1±x} – α -MoC _{1–x} is partially plotted at 1600 °C: (Ti,Mo)(C,N) _{1–x} (extended solid solution based on TiC _{1–x}) (Ti,Mo)(C,N) phase separates into two phases, of which one is richer in Ti and N than another; the two-phase field becomes smaller at higher temp.	[432, 584, 588]

(continued)

Table 2.14 (continued)

System	Type of phase diagram (temperature and composition sections, constituent phases or phase fields) and/or character of interphase interaction and materials compatibility	References
C–Mo–Nb	Plotted at 1400–3000 °C: (Nb,Mo)C _{1-x} (extended solid solution based on NbC _{1-x} , or NbC _{1-x} -α-MoC _{1-x} monocarbide continuous solid solution at 2000–2600 °C), β-(Mo,Nb) _{2±x} C (extended solid solution based on β-Mo _{2±x} C with max. Nb solubility corresp. to ~ (Mo _{0.6} Nb _{0.4}) ₂ C), β-(Nb,Mo) _{2±x} C (solid solution based on β-Nb _{2±x} C with max. Mo solubility—~ 3 at.%), η-MoC _{1-x} , (Nb,Mo), C The interaction between NbC _{1-x} and Mo initiates from 1700–1800 °C (5 h exposure) and becomes noticeable at 2000–2200 °C (2 h exposure). Under specific pressure 5 MPa the diffusion welded joint between NbC _{1-x} and Mo is produced at 1600 °C (5–15 min exposure).	[138, 242, 391, 433–434, 773, 827, 837, 853]
C–Mo–Nb–Ta	β-Mo _{2±x} C–β-Nb _{2±x} C–α-Ta _{2±x} C is plotted at 1650 and 2000 °C: (Ta,Nb,Mo) _{2±x} C (based on β-Nb _{2±x} C–α-Ta _{2±x} C semicarbide continuous solid solution), β-(Mo,Ta,Nb) _{2±x} C (solid solution based on β-Mo _{2±x} C), (Ta,Nb,Mo) _{2±x} C + (Ta,Nb,Mo)C _{1-x} + (Mo,Nb,Ta), (Ta,Nb,Mo)C _{1-x} + (Mo,Nb,Ta), β-(Mo,Ta,Nb) _{2±x} C + (Ta,Nb,Mo)C _{1-x} + (Mo,Nb,Ta)	[435]
C–Mo–Nb–U	α-MoC _{1-x} –NbC _{1-x} –UC _{1±x} is plotted at 2000 °C: (U,Nb,Mo)C _{1-x} (based on NbC _{1-x} –UC _{1±x} monocarbide continuous solid solution), UMoC ₂ , α-(Mo,Nb,U)C _{1-x} (based on α-MoC _{1-x})	[436]
C–Mo–Nb–Zr	α-MoC _{1-x} –NbC _{1-x} –ZrC _{1-x} is plotted at 2000 °C: (Zr,Nb,Mo)C _{1-x} (based on NbC _{1-x} –ZrC _{1-x} continuous solid solution), α-(Mo,Zr,Nb)C _{1-x} (based on α-MoC _{1-x})	[436]
C–Mo–Ni	Plotted at 1000 °C: η ₁ -Mo ₆ Ni ₆ C, η _{1,2} -Mo _{3÷4} Ni _{2÷3} C, β-Ni _{4±x} Mo (<865–875 °C), γ-Ni _{3±x} Mo (<905–915 °C), δ-NiMo _{1±x} (or μ-MoNi _{1±x} , <~ 1360–1365 °C), α-Mo _{2±x} C, α'-Mo _{2±x} C, Mo, Ni, C β-Mo _{2±x} C–Ni is plotted: eutectic—1265 °C, ~ 9 mol.% β-Mo _{2±x} C; the solubility of β-Mo _{2±x} C in Ni is ~ 2.5 mol.% (at eutectic temp.) and ~ 1.5 mol.% (at 950 °C), and that of Ni in β-Mo _{2±x} C is ~ 21 mol.% (at eutectic temp.) and ~ 10–11 mol.% (at 950 °C)	[242, 244, 391, 408]
C–Mo–O	Plotted partially at 930 and 1530 °C: β-MoO _{2±x} (<2125–2325 °C), α-Mo _{2±x} C, α'-Mo _{2±x} C, β-Mo _{2±x} C, Mo, O, C	[431, 575, 853]
C–Mo–O–Zr	No diagram plot At 1500–2000 °C the interaction between β-Mo _{2±x} C and ZrO _{2-x} results in the formation of ZrC _x O _y and Mo.	[242]
C–Mo–Os	Plotted at 1500 °C: ~ Mo ₃ Os ₃ C ₂ (<1500–1530 °C), β-Mo _{3±x} Os (<2210 °C), σ-Mo _{2±x} Os (<2420–2440 °C), β-Mo _{2±x} C, Mo, Os, C The mutual solubilities of all the constituent binary phases are low. Depend. on compos., graphite is in equilibrium with (Os,Mo) or (Os,Mo) + β-Mo _{2±x} C.	[244, 391, 431]

(continued)

Table 2.14 (continued)

System	Type of phase diagram (temperature and composition sections, constituent phases or phase fields) and/or character of interphase interaction and materials compatibility	References
C–Mo–Pt	Plotted at 1100 and 1500 °C: $\sim\text{Mo}_{5.6}\text{Pt}_{4.5}\text{C}_{1-1.1}$ (at least $> 1230\text{--}1260$ °C), $\eta\text{-Pt}_{2\pm x}\text{Mo}$ ($< \sim 1780\text{--}1820$ °C), $\delta\text{-PtMo}_{1\pm x}$ ($< 1280\text{--}1320$ °C), $\varepsilon'\text{-PtMo}_{3-x}$ ($< \sim 1455\text{--}1910$ °C), $\varepsilon\text{-PtMo}_{3-x}$ (from $1455\text{--}1495$ °C to $\sim 2155\text{--}2195$ °C), $\beta\text{-PtMo}_{6-x}$ (from $1270\text{--}1290$ °C to $1760\text{--}1800$ °C), $\alpha\text{-Mo}_{2\pm x}\text{C}$, $\alpha'\text{-Mo}_{2+x}\text{C}$, $\beta\text{-Mo}_{2\pm x}\text{C}$, Mo, Pt, C	[244, 391, 431]
C–Mo–Pu	Plotted at 20, 900 and 1000 °C: $\alpha\text{-PuMoC}_2$ (< 1680 °C), $\beta\text{-PuMoC}_2$ (from 1680 °C to $2130\text{--}2170$ °C, congruent melt. point), $\eta\text{-Pu}_4\text{Mo}_3\text{C}_3$ (or Pu_2MoC_2 , $< \sim 1900$ °C, congruent melt. point, ?), PuC_{1-x} , $\text{Pu}_2\text{C}_{3-x}$, $\alpha\text{-Mo}_{2+x}\text{C}$, $\alpha'\text{-Mo}_{2+x}\text{C}$, $\beta\text{-Mo}_{2\pm x}\text{C}$, $\eta\text{-MoC}_{1-x}$, $\alpha\text{-Pu}$, $\beta\text{-Pu}$, $\gamma\text{-Pu}$, $\delta\text{-Pu}$, $\delta'\text{-Pu}$, $\varepsilon\text{-Pu}$, Mo, C Eutectic $\eta\text{-Pu}_4\text{Mo}_3\text{C}_3\text{--PuC}_{1-x}\text{--}\varepsilon\text{-Pu}$ ($\sim 610\text{--}630$ °C) Depending on compos., graphite is in equilibrium with $\text{PuMoC}_2 + \text{Pu}_2\text{C}_{3-x}$ or $\text{PuMoC}_2 + \alpha\text{-Mo}_{2+x}\text{C}$.	[242, 391, 906]
C–Mo–Pu–U	No diagram plot (U,Pu)MoC ₂ (PuMoC ₂ –UmoC ₂ dicarbide continuous solid solution), (U,Pu)MoC _{2-x} (or (U,Pu)MoC _{1.7} , solid solution based on UMoC _{2-x} , or UMoC _{1.7})	[391]
C–Mo–Re	Plotted at 1400 and 1500 °C: $\pi\text{-Mo}_3\text{Re}_2\text{C}$ (at least at 1400 °C, ?), $\sim\text{MoReC}_{1-x}$ ($x \approx 0.2$ at least at $\sim 1400\text{--}1500$ °C, ?), $\beta\text{-(Mo,Re)}_{2\pm x}\text{C}$ ($\beta\text{-Mo}_{2\pm x}\text{C}\text{--Re}$ continuous solid solution), $\alpha\text{-(Mo,Re)C}_{1-x}$ (extended solid solution based on $\alpha\text{-MoC}_{1-x}$ with the max. solubility of Re corresp. to compos. $\sim(\text{Mo}_{0.2}\text{Re}_{0.8})\text{C}_{1-x}$), $\sigma\text{-Mo}_2\text{Re}_{3\pm x}$ (from $1100\text{--}1150$ to $2620\text{--}2670$ °C), $\chi\text{-MoRe}_{3+x}$ ($< 1970\text{--}2030$ °C), Mo, Re, C The presence of Re stabilizes $\alpha\text{-MoC}_{1-x}$.	[138, 244, 391, 431, 581–583, 603, 811]
C–Mo–Rh	Plotted at 1100 and 1500 °C: $\sim\text{Mo}_2\text{Rh}_2\text{C}$ (at least $> \sim 1360$ °C), $\text{Rh}_{3\pm x}\text{Mo}$ ($< 1180\text{--}1220$ °C), $\varepsilon\text{-Rh}_{2\pm x}\text{Mo}$ (from $\sim 1000\text{--}1200$ to $2065\text{--}2085$ °C), $\varepsilon'\text{-RhMo}_{1\pm x}$ ($< 975\text{--}1125$ °C), $\beta\text{-Mo}_{2\pm x}\text{C}$, Mo, Rh, C	[244, 391, 431]
C–Mo–Ru	Plotted at 1100 and 1500 °C: $\sim\text{Mo}_3\text{Ru}_3\text{C}_2$ (at least $> \sim 1300$ °C), $\sigma\text{-Ru}_3\text{Mo}_{5\pm x}$ (from ~ 1145 °C to $1915\text{--}1920$ °C), $\alpha\text{-Mo}_{2+x}\text{C}$, $\alpha'\text{-Mo}_{2+x}\text{C}$, $\beta\text{-Mo}_{2\pm x}\text{C}$, Mo, Ru, C	[244, 391, 431, 853]
C–Mo–Sc	Partially plotted at 1200 °C: (Sc,Mo)C _{1-x} ($\alpha\text{-MoC}_{1-x}\text{--ScC}_{1-x}$ monocarbide continuous solid solution), $\alpha\text{-Sc}_4\text{C}_3$, $\beta\text{-Sc}_4\text{C}_{3+x}$, $\text{Sc}_3\text{C}_{4-x}$ (or $\text{Sc}_{15}\text{C}_{19\pm x}$), $\alpha\text{-Mo}_{2+x}\text{C}$, $\alpha'\text{-Mo}_{2+x}\text{C}$, $\beta\text{-Mo}_{2\pm x}\text{C}$, $\eta\text{-MoC}_{1-x}$, $\gamma\text{-MoC}$, Mo, $\alpha\text{-Sc}$, $\beta\text{-Sc}$, C	[244–245, 431]

(continued)

Table 2.14 (continued)

System	Type of phase diagram (temperature and composition sections, constituent phases or phase fields) and/or character of interphase interaction and materials compatibility	References
C–Mo–Si	Plotted at 1100–1730 °C: $\text{Mo}_{5-y}\text{Si}_3\text{C}_x$ ($x \approx 0.6 \div 1.0$, $y \approx 0.2 \div 1.0$, or $\text{Mo}_3(\text{Si}_x\text{Mo}_{1-x})_2(\text{C}_y\text{Si}_{1-x})_3$, $x = 0.10 \div 0.55$, $y = 0.15 \div 0.40$, or $\text{Mo}_9\text{Si}_7\text{C}_4$, $\text{Mo}_8\text{Si}_5\text{C}$, $\text{Mo}_4\text{Si}_3\text{C}$, at least at 1200–1700 °C, Nowotny phase), $\alpha\text{-MoSi}_2$ (<1900 °C), $\beta\text{-MoSi}_2$ (from 1850–1900 °C to 2020 °C), $\text{Mo}_5\text{Si}_{3\pm x}$ (<2170–2180 °C), Mo_3Si (<2025–2065 °C), $\alpha\text{-Mo}_{2+x}\text{C}$, $\alpha'\text{-Mo}_{2+x}\text{C}$, $\beta\text{-Mo}_{2\pm x}\text{C}$, $\eta\text{-MoC}_{1-x}$, $\alpha\text{-MoC}_{1-x}$, $\gamma\text{-MoC}$, SiC , Mo , Si , C SiC–Mo is plotted: $\text{Mo}_{5-y}\text{Si}_3\text{C}_x$, Mo_3Si , $\text{Mo}_5\text{Si}_{3\pm x}$, $\beta\text{-Mo}_{2\pm x}\text{C}$, $\alpha\text{-MoC}_{1-x}$, SiC , Mo At 1600 °C, depend. On compos., graphite is in equilibrium with $\text{Mo}_{5-y}\text{Si}_3\text{C}_x$, $\text{Mo}_{5-y}\text{Si}_3\text{C}_x + \text{SiC}$, or $\text{Mo}_{5-y}\text{Si}_3\text{C}_x + \beta\text{-Mo}_{2\pm x}\text{C}$. In vacuum, the reaction between graphite and $\alpha\text{-MoSi}_2$ begins at ~ 1500 °C (2 h contact exposure) and leads to the formation of $\text{Mo}_{5-y}\text{Si}_3\text{C}_x$ and SiC .	[138, 242, 244, 431, 437, 503, 630–632, 665, 736–738, 819]
C–Mo–Si–Ta	No diagram plot. At 1900–1950 °C in Ar atmosphere or low vacuum (~ 100 Pa) the interaction in TaC_{1-x} – MoSi_2 powder mixtures leads to the formation of SiC and $(\text{Mo,Ta})_5\text{Si}_{3\pm x}$.	[894, 899]
C–Mo–Si–Zr	No diagram plot. At 1950 °C in Ar atmosphere the interaction in ZrC_{1-x} – MoSi_2 powder mixtures leads to the formation of SiC and $(\text{Mo,Zr})_5\text{Si}_{3\pm x}$.	[894]
C–Mo–Ta	Plotted at 1400–3500 °C: $(\text{Ta,Mo})\text{C}_{1-x}$ (extended solid solution based on TaC_{1-x} , or TaC_{1-x} – $\alpha\text{-MoC}_{1-x}$ monocarbide continuous solid solution at 2000–2600 °C), $\beta\text{-(Mo,Ta)}_2\text{C}$ (extended solid solution based on $\beta\text{-Mo}_{2\pm x}\text{C}$ or $\beta\text{-Mo}_{2\pm x}\text{C}$ – $\beta\text{-Ta}_{2\pm x}\text{C}$ semicarbide continuous solid solution at 2300–2500 °C), $\alpha\text{-Ta}_{2+x}\text{C}$, $\zeta\text{-Ta}_4\text{C}_{3-x}$, (stabilized by Mo), $\text{Ta}_6\text{C}_{5\pm x}$, $\eta\text{-MoC}_{1-x}$, (Mo,Ta) , C At higher temp. graphite is in equilibrium with single solid phase $(\text{Ta,Mo})\text{C}_{1-x}$. In vacuum the interaction between TaC_{1-x} and Mo initiates from 2000 °C (5 h exposure). Under specific pressure 5 MPa the diffusion welded joint between TaC_{1-x} and Mo is produced at 1400 °C (5–15 min exposure).	[138, 242, 391, 419, 438–439, 723, 773, 827, 837]
C–Mo–Ta–V	$\beta\text{-Mo}_{2\pm x}\text{C}$ – $\beta\text{-V}_{2\pm x}\text{C}$ – $\alpha\text{-Ta}_{2+x}\text{C}$ is plotted at 1650 and 2000 °C: $(\text{Ta,V,Mo})_{2\pm x}\text{C}$ (based on $\beta\text{-V}_{2\pm x}\text{C}$ – $\alpha\text{-Ta}_{2+x}\text{C}$ and $\beta\text{-V}_{2\pm x}\text{C}$ – $\beta\text{-Mo}_{2\pm x}\text{C}$ semicarbide continuous solid solutions), $(\text{Ta,V,Mo})_{2\pm x}\text{C} + (\text{Ta,V,Mo})\text{C}_{1-x} + (\text{Ta,V,Mo})$, $(\text{Ta,V,Mo})\text{C}_{1-x} + (\text{Ta,V,Mo})$	[435]
C–Mo–Tc	Plotted schematically	[840]
C–Mo–Th	Plotted at 1500 °C: $\text{Th}_x\text{Mo}_y\text{C}_z$ (?), $\eta\text{-(Mo,Th)}\text{C}_{1-x}$, $\beta\text{-Mo}_{2\pm x}\text{C}$, $\text{ThC}_{1\pm x}$ ($\gamma\text{-ThC}_{2-x}$), $\beta\text{-Th}$, Mo , C	[138, 391]

(continued)

Table 2.14 (continued)

System	Type of phase diagram (temperature and composition sections, constituent phases or phase fields) and/or character of interphase interaction and materials compatibility	References
C–Mo–Ti	<p>Plotted at 1200–2750 °C: (Ti,Mo)C_{1-x} (TiC_{1-x}–α-MoC_{1-x} monocarbide continuous solid solution at 1900–2600 °C, or extended solid solution based on TiC_{1-x} with the max. solubility of Mo corresp. to compos. \sim Ti_{0.1}Mo_{0.9}C_{0.8} at 1500 °C and \sim Ti_{0.05}Mo_{0.95}C_{0.8} at 1750 °C), β-Mo_{2\pmx}C, η-MoC_{1-x}, β-Ti, Mo, C</p> <p>Eutectic (Ti,Mo)C_{1-x}–β-Mo_{2\pmx}C–(β-Ti,Mo) (2160 °C)</p> <p>Eutectic (Ti,Mo)C_{1-x}–(β-Ti,Mo) (2240 °C)</p> <p>TiC_{1-x}–Mo is plotted: eutectic—\sim2160–2310 °C, \sim20 mol.% TiC_{1-x}; the solubility of Mo in TiC_{1-x} is \sim35 mol.% and that of TiC_{1-x} in Mo is \sim4–6 mol.% (at eutectic temp.)</p> <p>At higher temp. graphite is in equilibrium with single solid phase (Ti,Mo)C_{1-x}. In vacuum the interaction between TiC_{1-x} and Mo initiates at temp. >2000 °C (5 h exposure). Under specific pressure 5 MPa the diffusion welded joint between TiC_{1-x} and Mo is produced at 1600 °C (5–15 min exposure).</p>	[138, 242, 391, 419, 440, 579, 767–768, 773, 821, 823, 827, 837, 1013]
C–Mo–U	<p>Plotted at 550–2000 °C: UMoC_{2-x} ($x \approx 0.3$, a low C form of UMoC₂), UMoC₂ (<2230–2350 °C (?), congruent melt. point), ω-UMo₂C₂ (metastable, ?), χ-UMoC (metastable, ?), UMo₂C (?), MoU_{2\pmx} (<595–630 °C), UC_{1\pmx}, ζ-U₂C₃, α-UC_{2-x}, β-UC_{2-x}, α-Mo_{2\pmx}C, α'-Mo_{2\pmx}C, β-Mo_{2\pmx}C, η-MoC_{1-x}, α-MoC_{1-x}, γ-MoC, α-U, β-U, γ-U, Mo, C</p> <p>UC_{1\pmx}–Mo is plotted: eutectic—\sim1700–1800 °C</p> <p>UMoC_{2-x}–UC_{1\pmx} is plotted: eutectic—2160 °C</p> <p>UMoC_{2-x}–β-Mo_{2\pmx}C is plotted: eutectic—2270 °C</p> <p>UMoC_{2-x}–Mo is plotted: eutectic—\sim2000 °C</p> <p>UMoC_{2-x}–C is plotted: eutectic—2200 °C</p> <p>UC_{1\pmx} and Mo are compatible with each other at temp. \leq1000–1100 °C; at 1000 °C (500 h exposure) the dimension of reaction zone between them reaches 10 μm.</p> <p>At 1200 °C the reaction results in the formation of β-Mo_{2\pmx}C and metal U. At 1000–1200 °C the performance of UC_{2-x} in the contact with Mo is very similar.</p>	[138, 242, 244, 391, 431, 441, 453, 612, 620, 812]
C–Mo–U–Zr	<p>α-MoC_{1-x}–ZrC_{1-x}–UC_{1\pmx} is plotted at 2000 °C: (U,Zr,Mo)C_{1\pmx} (based on ZrC_{1-x}–UC_{1\pmx} monocarbide continuous solid solution), UMoC₂, α-(Mo,Zr,U)C_{1-x} (solid solution based on α-MoC_{1-x})</p> <p>At \sim2000 °C (U_{0.5}Zr_{0.5})C_{1\pmx} reacts vigorously with metal Mo.</p>	[436, 812]
C–Mo–V	<p>Plotted at 1500–2000 °C: (V,Mo)C_{1-x} (extended solid solution based on VC_{1-x} or VC_{1-x}–α-MoC_{1-x} monocarbide continuous solid solution at higher temp.), β-(V,Mo)_{2\pmx}C (β-V_{2\pmx}C–β-Mo_{2\pmx}C semicarbide continuous solid solution), η-MoC_{1-x}, α-MoC_{1-x}, (V,Mo), C</p>	[242, 391, 442, 773, 827, 837]

(continued)

Table 2.14 (continued)

System	Type of phase diagram (temperature and composition sections, constituent phases or phase fields) and/or character of interphase interaction and materials compatibility	References
C–Mo–W	Plotted at 1000–2500 °C: (W,Mo)C (γ -MoC– δ -WC _{1±x} monocarbide continuous solid solution at temp. <1100–1200 °C, or extended solid solution based on δ -WC _{1±x} at higher temp.), α -(Mo,W)C _{1-x} (α -MoC _{1-x} – γ -WC _{1-x} continuous solid solution at ~2550–2650 °C, or extended high temp. solid solution based on α -MoC _{1-x} with the max. solubility of W corresp. to compos. ~ (Mo _{0.75} W _{0.25})C _{0.65} at 2000 °C, ~ (Mo _{0.67} W _{0.33})C _{0.65} at 2100 °C, ~ (Mo _{0.33} W _{0.67})C _{0.65} at 2230 °C and ~ (Mo _{0.03} W _{0.97})C _{0.62} at 2500 °C), η -(Mo,W)C _{1-x} (extended solid solution based on η -MoC _{1-x} with max. solubility of W corresp. to compos. ~ (Mo _{0.75} W _{0.25})C _{0.64} at 1850–2000 °C, ~ (Mo _{0.67} W _{0.33})C _{0.64} at 2100 °C and ~ (Mo _{0.5} W _{0.5})C _{0.64} at 2200–2500 °C), β -(Mo,W) _{2±x} C (β -Mo _{2±x} C– α / β -W _{2±x} C semicarbide continuous solid solution or extended solid solution based on β -Mo _{2±x} C at lower temp.), (W,Mo), C At 1800–2000 °C Mo is compatible with δ -WC _{1±x} . Under specific pressure 5 MPa the diffusion welded joint between δ -WC _{1±x} and Mo is produced at 1600 °C (5–15 min exposure).	[138, 241–242, 244, 391, 443, 764–766, 827, 837, 853]
C–Mo–W–Zr	ZrC _{1-x} –Mo–W is plotted partially at 1200, 1600 and 2000 °C: solubility of ZrC _{1-x} in the Mo–W solid solution decreases with fall in temp.; homog. range of the solid solution steadily decreases with rise in W content	[831]
C–Mo–Zr	Plotted at 1400–2100 °C: (Zr,Mo)C _{1-x} (extended solid solution based on ZrC _{1-x} , or ZrC _{1-x} – α -MoC _{1-x} monocarbide continuous solid solution at higher temp.), β -Mo _{2±x} C, η -MoC _{1-x} , α -MoC _{1-x} , σ -ZrMo _{2±x} (<~1880–2000 °C), Zr, Mo, C ZrC _{1-x} –Mo is plotted: eutectic—~2240–2280 °C, ~20–30 mol.% ZrC _{1-x} ; the solubility of Mo in ZrC _{1-x} is >10 mol.% and that of ZrC _{1-x} in Mo is <20 mol.% (at eutectic temp.) At higher temp. graphite is in equilibrium with single solid phase (Zr,Mo)C _{1-x} . At 2000–2200 °C Mo is compatible with ZrC _{1-x} (2–5 h exposure). In vacuum the interaction between ZrC _{1-x} and Mo initiates from 1900 °C (5 h exposure). Under specific pressure 5 MPa the diffusion welded joint between ZrC _{1-x} and Mo is produced at 1300 °C (5–15 min exposure).	[138, 242, 244, 391, 431, 579, 773, 827, 835, 837]
C–N–Nb	NbC _{1-x} – δ -NbN _{1-x} –Nb is plotted at 1250–1450 °C: Nb(C,N) _{1-x} (or NbC _y N _z , NbC _{1-x} – δ -NbN _{1-x} monocarbonitride continuous solid solution), β -Nb _{2±x} (C,N) (or Nb ₂ C _y N _z , β -Nb _{2±x} C– β -Nb _{2±x} N semicarbonitride continuous solid solution), Nb	[242, 391, 444, 662, 863]
C–N–Nb–W	General consideration of the system	[915, 1023]

(continued)

Table 2.14 (continued)

System	Type of phase diagram (temperature and composition sections, constituent phases or phase fields) and/or character of interphase interaction and materials compatibility	References
C–N–Nd–Th	No diagram plot ThC _{1±x} –NdN _{1±x} carbonitride continuous solid solution	[391]
C–N–O–Pu–U	See C–N–Pu–U in this table.	
C–N–O–Si	Plotted schematically at 1430–1840 °C: Si ₂ ON ₂ (<~1860 °C), SiO ₂ (<~1700 °C), β-Si ₃ N ₄ (<~1800–1900 °C), SiC, Si, O, N, C Si ₃ N ₄ –SiO ₂ –C is plotted at 1480–1850 °C: Si ₂ ON ₂ , SiO ₂ , β-Si ₃ N ₄ , SiC, C Si ₃ N ₄ –SiC–SiO ₂ is plotted at 1810–1850 °C: Si ₂ ON ₂ , SiO ₂ , β-Si ₃ N ₄ , SiC, Si Si ₂ ON ₂ –SiC is plotted: gas eutectic—~1840 °C, ~25 mol.% SiC Si ₂ ON ₂ –C is plotted: graphite is in equilibrium with SiC + Si ₂ ON ₂ at ~1490 °C and ~37 mol.% C	[244, 445–446]
C–N–O–Ti	No diagram plot Ti(C,N,O) _{1±x} (or TiC _x N _y O _z , oxycarbonitride phase, TiC _{1-x} –TiO _{1±x} oxycarbide, TiC _{1-x} –δ-TiN _{1±x} carbonitride and δ-TiN _{1±x} –TiO _{1±x} oxynitride continuous solid solutions)	[411]
C–N–O–Zr	ZrC _{1-x} –ZrN _{1±x} –‘ZrO’ is plotted at 1600 and 2000 °C: homog. range limits of ZrC _{1-x} –ZrN _{1±x} carbonitride continuous solid solution (ZrC _x N _y O _z , oxycarbonitride phase) are ~ZrC _{0.45} O _{0.55} and ~ZrN _{0.65} O _{0.35} (1600 °C) and ~ZrC _{0.25} O _{0.75} and ~ZrN _{0.45} O _{0.55} (2000 °C)	[411–412]
C–N–Pr–Th	No diagram plot ThC _{1±x} –PrN _{1±x} carbonitride continuous solid solution	[391]
C–N–Pu–U	(U,Pu)–C–N is plotted at 1480 °C (taking into account the presence of O): (U _{1-x} Pu _x)C _{1-y-z} N _y O _z ((U _{1-x} Pu _x)C _{1±u} –(U _{1-x} Pu _x)N _{1-u} carbonitride continuous solid solution contaminated with O, z = 0 ÷ 0.15), (U _{1-x} Pu _x) ₂ C _{3-x} , α-(U _{1-x} Pu _x)C ₂ , α-U ₂ N _{3+x} (<~1130 °C), β-U ₂ N _{3-x} (from ~940–1100 °C to ~1350 °C), (U,Pu), N, C (U,Pu) _{0.49} N _{0.49} C _{0.02} –(U,Pu) _{0.49} N _{0.51} –(U,Pu) _{0.51} N _{0.49} is plotted at 730 °C and 1230 °C (O concentration—500 and 2000 ppm): (U _{1-x} Pu _x)C _{1-y-z} N _y O _z , (U,Pu)O _{2±x} (<~2370–2860 °C), α-U ₂ N _{3+x} , β-U ₂ N _{3-x} , (U,Pu), N, C Graphite is in equilibrium with (U _{1-x} Pu _x)C _{1-y-z} N _y O _z , or α-U ₂ N _{3+x} (β-U ₂ N _{3-x}) and (U _{1-x} Pu _x)C _{1-y-z} N _y O _z .	[447–448, 595]

(continued)

Table 2.14 (continued)

System	Type of phase diagram (temperature and composition sections, constituent phases or phase fields) and/or character of interphase interaction and materials compatibility	References
C–N–Si	Plotted at 1415–2700 °C (total pressure—0.1 MPa): α -SiC ₂ N ₄ (?), β -SiC ₂ N ₄ (<900 °C), α -Si ₂ CN ₄ (?), β -Si ₂ CN ₄ (<1000 °C), SiC _x N _y (?), α -Si ₃ N ₄ (metastable, ?), β -Si ₃ N ₄ (<~1800–1900 °C), SiC, Si, N, C Si ₃ N ₄ –SiC is plotted: Si ₃ N ₄ , SiC, Si At 1780 °C the solubility limit of SiC in β -Si ₃ N ₄ is ~2 mol.%. At temp. <1500 °C the nitridation of C–Si mixtures leads to the formation of β -Si ₃ N ₄ and β -SiC. The polytype stability and the structural failures in SiC are affected by N ₂ pressure.	[138, 359, 445, 571–572, 760–763, 887]
C–N–Si–Ti	Plotted at 1650 °C: TiC _x N _z (TiC _{1–x} – δ -TiN _{1±x} carbonitride continuous solid solution), β -Si ₃ N ₄ (<~1800–1900 °C), SiC, Ti, Si, N, C Graphite is in equilibrium with TiC _{1–x} N _x (0 < x < 0.66) and TiC _{0.34} N _{0.66} + SiC, SiC—with TiC _{1–x} N _x (0.66 < x < 0.87) and TiC _{0.13} N _{0.87} + β -Si ₃ N ₄ and β -Si ₃ N ₄ + Si, β -Si ₃ N ₄ —with TiC _{1–x} N _x (0.87 < x < 1.0) and δ -TiN _{1±x} + N ₂ . Thin film Ti ₃ Si(C,N) ₂ (M _{n+1} AX _n -phase carbonitride solid solution) were synthesized.	[571, 642, 744–745]
C–N–Sm–Th	No diagram plot ThC _{1±x} –SmN _{1±x} carbonitride continuous solid solution	[391]
C–N–Ta	TaC _{1–x} – δ -TaN _{1–x} –Ta is plotted at 1250, 1450 and 1900 °C: Ta(C,N) _{1–x} (or TaC _y N _z , TaC _{1–x} – δ -TaN _{1–x} monocarbonitride continuous solid solution), Ta _{2±x} (C,N) (or Ta ₂ C _y N _z , α -Ta _{2+x} C– γ -Ta _{2±x} N semicarbonitride continuous solid solution at higher temp., or extended solid solutions based on α -Ta _{2+x} C and γ -Ta _{2±x} N at lower temp.), ϵ -Ta ₂ N, ζ -Ta ₄ C _{3–x} , Ta At 1150–2370 °C the interaction between C and δ -TaN _{1–x} converts the nitride phase into carbonitride or carbide phases.	[138, 242, 244, 391, 431, 662]
C–N–Ta–U	No diagram plot At 1400 °C (66 h exposure) small reaction zone was found on the contact surface between metal Ta with UC _{0.7} N _{0.3} and UC _{0.4} N _{0.6} , at 1800 °C (3 h exposure)—the interaction is noticeable.	[822]
C–N–Ta–W	General consideration of the system	[803, 1023]
C–N–Th	Plotted at 1500–2200 °C: ThCN, Th(C,N) _{1–x} (or ThC _y N _z , ThC _{1±x} –ThN _{1±x} and ThC _{1±x} – α -Th continuous solid solutions with miscibility gaps), Th ₃ N _{4±x} , γ -ThC _{2–x} , α -Th, β -Th, N, C	[391, 449]

(continued)

Table 2.14 (continued)

System	Type of phase diagram (temperature and composition sections, constituent phases or phase fields) and/or character of interphase interaction and materials compatibility	References
C–N–Ti	TiC _{1-x} – δ -TiN _{1±x} –Ti is plotted at 500–2000 °C: Ti(C,N) _{1-x} (or TiC _x N _z , 0.33 ≤ x + z ≤ 1.04, TiC _{1-x} – δ -TiN _{1±x} carbonitride continuous solid solution with homog. range: TiC _{0.48} –TiC _{0.95} –TiN _{0.43} –TiN _{1.0} at 1650 °C and TiC _{0.75} –TiC _{1.0} –TiN _{0.69} –TiN _{1.0} at 500 °C), ζ -Ti ₄ N _{3-x} (at least at ~ 1000–1200 °C, ?), η -Ti ₃ N _{2-x} (at least at ~ 1000 °C, ?), δ' -Ti ₅ N _{3±x} (<800 °C), ε -Ti _{2±x} N (<~ 1100 °C), α -Ti, β -Ti TiC _{1-x} (x = 0.05)– δ -TiN _{1±x} (TiN _{1.0}) is plotted at pressure N ₂ 0.1 MPa	[138, 242, 391, 411, 454, 571, 584, 643, 977–979, 1010]
C–N–Ti–V	No diagram plot	[241, 244, 391, 431]
C–N–Ti–W	TiC _{1-x} – δ -WC _{1±x} – δ -TiN _{1±x} – δ -WN _{1-x} is plotted at 1425 °C: (Ti,W)(C,N) _{1±x} (extended solid solution based on TiC _{1-x} – δ -TiN _{1±x} carbonitride continuous solid solution), δ -W(C,N) _{1±x} , C Upon increasing C concentration, graphite and δ -W(C,N) _{1±x} are formed together with two (Ti,W)(C,N) phases, of which one is richer in Ti and N than another. The addition of N to (Ti,W)C _{1-x} at 1750 °C also results in partitioning of the mixed carbonitride phase in a W-rich carbide with low N content (W,Ti)(C,N) _{1±x} and W-poor Ti carbonitride (Ti,W)(C,N) _{1±x} .	[563, 584–586, 880, 1013]
C–N–U	Plotted at 800–2100 °C: U ₅ C ₈ N ₂ (?), U ₆ C ₁₃ N (?), U(C,N) _{1±x} (or UC _x N _z , UC _{1±x} –UN _{1-x} monocarbonitride continuous solid solution with wider homog. range (x + z ≠ 1) in the UC _{1±x} -rich area; in UC _x N _z + C equilibrium index z in compos. is affected by the pressure of N ₂ and structural form of C), α -U ₂ N _{3+x} (<~ 1130 °C), β -U ₂ N _{3-x} (from ~ 940–1100 °C to ~ 1350–1550 °C at N ₂ pressure 0.1 MPa), ζ -U ₂ C ₃ , α -UC _{2-x} , β -UC _{2-x} , U, N, C UC _{1±x} –UN _{1-x} is plotted: continuous solid solution, max. melt. point 2910 °C is corresp. to ~ UC _{0.3} N _{0.7} Essentially no solid solubility of N in ζ -U ₂ C ₃ , α -UC _{2-x} , β -UC _{2-x} or that of C in β -U ₂ N _{3-x} . At N ₂ pressure 0.1 MPa, the U nitrides are more stable than the U carbides up to 1800 °C, but at 2000 °C, the U carbides β -UC _{2-x} and U(C,N) _{1±x} become more stable. In vacuum or Ar graphite is in equilibrium with U(C,N) _{1±x} + β -UC _{2-x} . For diffusion rate in the system at various temp. see Addendum.	[138, 244, 391, 450–451, 740–743, 759]
C–N–U–V	No diagram plot At 1000 °C (66 h exposure) the carburization or nitridation of metal V is occurred on the contact surface with UC _{0.7} N _{0.3} and UC _{0.4} N _{0.6} , at 1400 °C (66 h exposure)—the interaction is significant.	[822]

(continued)

Table 2.14 (continued)

System	Type of phase diagram (temperature and composition sections, constituent phases or phase fields) and/or character of interphase interaction and materials compatibility	References
C–N–U–Zr	No diagram plot. At 1000 °C (66 h exposure) no appreciable reaction was occurred on the contact surface of metal Zr with $\text{UC}_{0.7}\text{N}_{0.3}$ and $\text{UC}_{0.4}\text{N}_{0.6}$, at 1400 °C (66 h exposure)—small reaction zone was found.	[822]
C–N–V	$\text{VC}_{1-x}-\delta\text{-VN}_{1-x}-\text{V}$ is plotted at 1400 °C: $\text{V}(\text{C},\text{N})_{1-x}$ (or VC_yN_z , $\text{VC}_{1-x}-\delta\text{-VN}_{1-x}$ continuous solid solution, ordering at low temp.), $\text{V}_{2\pm x}(\text{C},\text{N})$ (or $\text{V}_2\text{C}_y\text{N}_z$, $\beta\text{-V}_{2\pm x}\text{C}-\beta\text{-V}_{2\pm x}\text{N}$ continuous solid solution), V The ordering of VC_yN_z leads to the formation of a $\text{V}_6\text{C}_{5\pm x}$ - or $\text{V}_8\text{C}_{7\pm x}$ -type superstructure, depend. on compos.	[138, 391, 411, 643, 884]
C–N–W	No diagram plot. $\text{WC}_{1\pm x}\text{N}_y$ (extended solid solution based on $\delta\text{-WC}_{1\pm x}$?)	[391, 541]
C–N–Zr	$\text{ZrC}_{1-x}-\text{ZrN}_{1\pm x}-\text{Zr}$ is plotted at 1120–2000 °C: $\text{Zr}(\text{C},\text{N})_{1\pm x}$ (or ZrC_xN_z , $0.54 \leq x + z \leq 1.04$, $\text{ZrC}_{1-x}-\text{ZrN}_{1\pm x}$ continuous solid solution with homog. range: $\text{ZrC}_{0.59}-\text{ZrC}_{0.95}-\text{ZrN}_{0.56}-\text{ZrN}_{1.0}$ at 1150 °C), $\alpha\text{-Zr}$, $\beta\text{-Zr}$ ZrC_{1-x} ($x = 0.07$)– $\text{ZrN}_{1\pm x}$ ($\text{ZrN}_{0.81}$) is plotted Plotted at 1100 °C: $\eta\text{-Nb}_4\text{Ni}_2\text{C}$, $\text{Nb}_3\text{Ni}_3\text{C}$ (?), $\text{Nb}_6\text{Ni}_6\text{C}$ (?), Ni_8Nb (<535 °C), $\text{Ni}_{3\pm x}\text{Nb}$ (<~1400 °C), $\mu\text{-Ni}_6\text{Nb}_{7-x}$ (or $\mu\text{-NiNb}_{1+x}$, <1290 °C), $\alpha\text{-Nb}_2\text{C}$, $\beta\text{-Nb}_{2+x}\text{C}$, NbC_{1-x} , Ni , Nb , C $\text{NbC}_{1-x}-\text{Ni}$ is plotted: eutectic—~1320–1345 °C, ~5–6 mol.% NbC_{1-x} ; at the eutectic temp. the solubility of NbC_{1-x} in Ni is ~2–3 mol.% and that of Ni in NbC_{1-x} ~9 mol.%	[138, 242, 244, 391, 411, 454, 584, 980]
C–Nb–Ni	$\text{NbC}_{1-x}-\text{Ni}$ is plotted: eutectic—~1320–1345 °C, ~5–6 mol.% NbC_{1-x} ; at the eutectic temp. the solubility of NbC_{1-x} in Ni is ~2–3 mol.% and that of Ni in NbC_{1-x} ~9 mol.%	[242, 244, 391, 431, 455–458]
C–Nb–Ni–Ta	NbC_{1-x} ($x = 0.2$)– TaC_{1-x} ($x = 0.1$)– Ni is plotted schematically: eutectic—from 1330 °C ($\text{NbC}_{1-x}-\text{Ni}$) to 1350 °C ($\text{TaC}_{1-x}-\text{Ni}$), ~5–6 mol.% $(\text{Nb},\text{Ta})\text{C}_{1-x}$ ($\text{NbC}_{1-x}-\text{TaC}_{1-x}$ monocarbide continuous solid solution); at the eutectic temp. the solubility of $(\text{Nb},\text{Ta})\text{C}_{1-x}$ in Ni is ~3.0–3.5 mol.%	[459]
C–Nb–Ni–V	NbC_{1-x} ($x = 0.1$)– VC_{1-x} ($x \approx 0.1$)– Ni is plotted: eutectic—~1285–1315 °C, 3 mol.% $(\text{Nb},\text{V})\text{C}_{1-x}$, 6 mol.% $(\text{V},\text{Nb})\text{C}_{1-x}$; at the eutectic temp. the max. solubility of NbC_{1-x} in VC_{1-x} is ~15 mol.%, in Ni is ~3 mol.% and that of VC_{1-x} in NbC_{1-x} is ~20 mol.%, in Ni is ~3 mol.% and that of Ni in NbC_{1-x} is ~9 mol.%, in VC_{1-x} is ~4 mol.%	[458]
C–Nb–Ni–Zr	$\text{NbC}_{1-x}-\text{ZrC}_{1-x}-\text{Ni}$ is plotted: eutectic—from 1290 °C ($\text{ZrC}_{1-x}-\text{Ni}$) to 1330 °C ($\text{NbC}_{1-x}-\text{Ni}$), ~5–6 mol.% $(\text{Nb},\text{Zr})\text{C}_{1-x}$ ($\text{NbC}_{1-x}-\text{ZrC}_{1-x}$ monocarbide continuous solid solution); at the eutectic temp. the solubility of $(\text{Nb},\text{Zr})\text{C}_{1-x}$ in Ni is 2–3 mol.% and that of Ni in $(\text{Nb},\text{Zr})\text{C}_{1-x}$ is ~6 mol.%	[460]

(continued)

Table 2.14 (continued)

System	Type of phase diagram (temperature and composition sections, constituent phases or phase fields) and/or character of interphase interaction and materials compatibility	References
C–Nb–O	Plotted at 1300–2000 °C: Nb(C,O) _{1–x} (or NbC _x O _y , extended solid solution based on NbC _{1–x} with homog. limits: NbC _{0.7} –Nb(C _{0.5} O _{0.15})–Nb(C _{0.35} O _{0.45})–Nb(C _{0.35} O _{0.65})–NbC _{0.99}), β-Nb _{2±x} (C,O) (or Nb ₂ C _x O _y , extended solid solution based on β-Nb _{2+x} C with homogeneity limits: Nb ₂ C _{0.8} –Nb ₂ (C _{0.3} O _{0.3})–Nb ₂ (C _{0.15} O _{0.7})–Nb ₂ (C _{0.35} O _{0.8})–Nb ₂ C _{1.0}), NbO (<1945 °C), γ-NbO _{2±x} (from ~900 °C to ~1910–1920 °C), β-Nb ₂ O ₅ (<1495–1510 °C), Nb, O, C	[242, 244, 411, 431, 461]
C–Nb–O–Si	No diagram plot At 1100 °C (4 h exposure, C and O contamination from the vacuum system during annealing) in the reaction zone formed between SiC and Nb the following layer sequence is observed: SiC → Nb ₅ Si ₄ C (or NbC _{1–x}) → α-Nb ₅ Si _{3+x} → β-Nb _{2+x} C → NbO → Nb.	[607]
C–Nb–O–W	No diagram plot At 1300–1400 °C, in vacuum the interaction between δ-WC _{1±x} and β-Nb ₂ O ₅ in powder mixtures results in the formation of W–Nb alloy.	[242, 808]
C–Nb–O–Zr	No diagram plot At 1300–2400 °C the interaction between NbC _{1–x} and ZrO _{2–x} results in the formation of mixed (complex) oxides and carbides.	[242]
C–Nb–Os	Plotted at 1500 °C: β-Nb _{3–x} Os (<1975 °C), σ-Nb ₃ Os _{2±x} (<2200 °C), χ-Nb ₂ Os _{3±x} (<2270 °C), β-Nb _{2+x} C, NbC _{1–x} , Nb, Os, C Graphite is in equilibrium with (Os,Nb) + NbC _{1–x} . The solubility of Nb in Os (with the presence of C) and that of Os in NbC _{1–x} are low.	[244, 391, 431]
C–Nb–P	No diagram plot Nb ₂ PC (M _{n+1} AX _n -phase)	[680–681, 744–745, 860]
C–Nb–Pd	Plotted at 1300 °C: β-Pd _{3±x} Nb (<~1610 °C), Pd _{2±x} Nb (<~1610 °C), α-Pd _{1±x} Nb (1255–1565 °C), β-Nb _{2+x} C, NbC _{1–x} , Nb, Pd, C Depend. on compos., graphite is in equilibrium with (Pd _x Nb _{1–x}) alloy or (Pd _{0.85} Nb _{0.15}) alloy + NbC _{1–x} .	[242, 244, 391, 431]
C–Nb–Pt	Plotted at 1500 °C: α-Pt _{3±x} Nb (<2040 °C), β-Pt _{3±x} Nb (?), Pt _{2±x} Nb (<1990 °C), α'-PtNb _{1–x} (or α'-Pt, 1670–1780 °C), Pt _{1+x} Nb _{1–x} (<1750 °C), σ-PtNb _{2±x} (<1800 °C), PtNb _{3±x} (<2040 °C), β-Nb _{2+x} C, NbC _{1–x} , Nb, Pt, C Depend. on compos., graphite is in equilibrium with (Pt,Nb) alloy + α-Pt _{3±x} Nb or α-Pt _{3±x} Nb + NbC _{1–x} .	[242, 244, 391, 431]
C–Nb–Pu	Plotted at 1600 °C: (Nb,Pu)C _{1–x} (NbC _{1–x} –PuC _{1–x} monocarbide continuous solid solution, ?), Pu ₂ C _{3–x} , α-PuC ₂ , β-PuC ₂ , β-Nb _{2+x} C, Nb, Pu, C	[138, 242, 244, 391]

(continued)

Table 2.14 (continued)

System	Type of phase diagram (temperature and composition sections, constituent phases or phase fields) and/or character of interphase interaction and materials compatibility	References
C–Nb–Re	Plotted at 1800 and 2000 °C: σ -Nb ₂ Re _{3–x} (from 2160–2300 °C to 2400–2565 °C), χ -NbRe _{3±x} (<2520–2745 °C), β -Nb _{2+x} C, NbC _{1–x} , Nb, Re, C NbC _{1–x} –Re is plotted: eutectic—2225 °C, ~30 mol.% NbC _{1–x} ; the mutual solid solubilities of the components are low Graphite is in equilibrium with Re + NbC _{1–x} .	[244, 391, 431, 818]
C–Nb–Rh	Plotted at 1500 °C: Rh _{3±x} Nb (<1950 °C), η -Rh _{2±x} Nb (<~1900 °C), ζ -Rh _{3±x} Nb ₂ (<~1625 °C), ε -RhNb _{1–x} (from ~1335–1420 °C to ~1580–1600 °C), β -RhNb _{1±x} (from ~1335–1420 to ~1550–1580 °C), δ -RhNb _{1–x} (<~1420 °C), γ -RhNb _{1–x} (<~1350 °C), σ -RhNb _{2±x} (<1660 °C), RhNb _{3±x} (<1220 °C), β -Nb _{2+x} C, NbC _{1–x} , Nb, Rh, C The solubility of C in Rh _{3±x} Nb is low.	[391, 431]
C–Nb–Ru	Plotted at 1600 °C: NbRu ₃ C _{1–x} ($x \approx 0.6$, stable in the limited range of temp.), Ru _{3±x} Nb (<1540 °C), β -Nb _{2+x} C, NbC _{1–x} , Nb, C Graphite is in equilibrium with Ru + NbC _{1–x} .	[391, 431, 897]
C–Nb–S	No diagram plot Nb ₂ SC _{1–x} ($x = 0.6$, M _{n+1} AX _n -phase), α -Nb ₂ CS ₂ , β -Nb ₂ CS ₂ , ?	[680–681, 744–745, 860]
C–Nb–Si	Plotted at 800, 1300 and 1730 °C: α -Nb ₅ Si ₃ C _x ($x = 0.04$), β -Nb ₅ Si ₃ C _x ($0.04 < x < 0.33$), γ -Nb ₅ Si ₃ C _x ($0.33 \leq x \leq 0.50$, ?), Nb ₃ (Si _{1–x} C _x) ($x = 0.1$), Nb ₂ SiC, Nb ₃ SiC ₂ , α -Nb ₄ SiC ₃ , β -Nb ₄ SiC ₃ (M _{n+1} AX _n -phases, ?), Nb ₅ Si ₄ C, NbSi ₃ C (?), Nb ₁₂ Si ₇ C (?), Nb ₁₅ Si ₄ C (?), NbSi ₂ (<~1920–1960 °C), α -Nb ₅ Si _{3+x} (<~1635–1960 °C), β -Nb ₅ Si _{3+x} (from ~1635 to 1960 °C to ~2490–2545 °C), Nb ₃ Si (~1655–2000 °C), α -Nb ₂ C, β -Nb _{2+x} C, NbC _{1–x} , SiC, Si, Nb, C NbC _{1–x} –NbSi ₂ is plotted: eutectic (degenerated)—~1880–1920 °C, ~1 mol.% NbC _{1–x} ; no mutual solubility Graphite is in equilibrium with SiC + NbC _{1–x} . In vacuum the reaction between graphite and NbSi ₂ begins at ~1500 °C (2 h contact exposure) and leads to the formation of SiC and NbC _{1–x} .	[138, 242, 419, 431, 462–463, 503, 739, 744–745, 819, 836, 898, 901]
C–Nb–Sn	Plotted at 1300 °C: Nb _{2±x} Sn _{1±y} C _{1–z} (from Nb _{2.20} Sn _{0.80} C _{0.93} to Nb _{1.92} Sn _{1.08} C _{0.91} , M _{n+1} AX _n -phase), Nb _{3±x} SnC _y (extended solid solution based on Nb _{3±x} Sn with C content—up to 5 at.%, 775–2130 °C), β -Nb _{2+x} C, NbC _{1–x} , Sn, Nb, C The solubility of Sn in β -Nb _{2+x} C and NbC _{1–x} is extremely low. Graphite is in equilibrium with NbC _{1–x} + Sn	[678–681, 744–745, 860]

(continued)

Table 2.14 (continued)

System	Type of phase diagram (temperature and composition sections, constituent phases or phase fields) and/or character of interphase interaction and materials compatibility	References
C–Nb–Ta	Plotted at 1500–3800 °C: (Nb,Ta)C _{1–x} (NbC _{1–x} –TaC _{1–x} monocarbide continuous solid solution), (Nb,Ta) _{2±x} C (β -Nb _{2+x} C– α -Ta _{2+x} C, β -Nb _{2+x} C– β -Ta _{2±x} C and γ -Nb _{2±x} C– β -Ta _{2±x} C (?) semicarbide continuous solid solutions with probable miscibility gaps (extended solid solutions) at 2200–2600 °C), (Nb,Ta), C Graphite is in equilibrium with (Nb,Ta)C _{1–x} .	[138, 242, 391, 419, 464, 813]
C–Nb–Ta–Ti	No diagram plot (Nb,Ta,Ti)C _{1–x} (NbC _{1–x} –TaC _{1–x} –TiC _{1–x} monocarbide continuous solid solution)	[138]
C–Nb–Ta–W	β -Nb _{2+x} C– α -Ta _{2+x} C– γ -W _{2±x} C is plotted at 1650 and 2000 °C: (Nb,Ta,W) _{2±x} C (based on β -Nb _{2+x} C– α -Ta _{2+x} C semicarbide continuous solid solution), (W,Nb,Ta) _{2±x} C (based on γ -W _{2±x} C), (Nb,Ta,W) _{2±x} C + (Nb,Ta,W)C _{1–x} + (Nb,Ta,W), (Nb,Ta,W)C _{1–x} + (Nb,Ta,W), (W,Nb,Ta) _{2±x} C + (Nb,Ta,W)C _{1–x} + (Nb,Ta,W) At 1650–2000 °C the max. solubilities of γ -W _{2±x} C in (Nb,Ta,W) _{2±x} C (based on β -Nb _{2+x} C– α -Ta _{2+x} C semicarbide continuous solid solution) reach ~3.5–14.0 mol.% (depend. on (Nb,Ta) _{2+x} C compos.). At 1450 °C the max. solubility of δ -WC _{1±x} in (Nb,Ta,W)C _{1–x} (based on NbC _{1–x} –TaC _{1–x} monocarbide continuous solid solution) is ~9 mol.%.	[419, 435, 465–466]
C–Nb–Tc	Plotted schematically	[840]
C–Nb–Th	Plotted at 1500 °C: β -Nb _{2+x} C, NbC _{1–x} , ThC _{1±x} , (γ -ThC _{2–x}), β -Th, Nb, C The mutual solid solubilities of the components are low.	[391]
C–Nb–Ti	Plotted at 1500–3100 °C: (Nb,Ti)C _{1–x} (NbC _{1–x} –TiC _{1–x} monocarbide continuous solid solution), β -(Nb,Ti) _{2+x} C (semicarbide extended solid solution based on β -Nb _{2+x} C at temp. ≤2280 °C, the max. solubility of Ti varies from ~5 to ~9 at.%), γ -Nb _{2±x} C (at 2600 °C the max. solubility of Ti is ~1 at.%, ?), (β -Ti,Nb), C The (Nb,Ti)C _{1–x} monocarbide continuous solid solution miscibility gap (critical point—~50 °C at ~Nb _{0.4} Ti _{0.6} C _{1–x} , at 0 °C ranges from ~Nb _{0.15} Ti _{0.85} C _{1–x} to ~Nb _{0.7} Ti _{0.3} C _{1–x} , calculated). Graphite is in equilibrium with (Nb,Ti)C _{1–x} . For diffusion rate in the system at various temp. see Addendum.	[138, 242, 391, 419, 440, 467–468, 813, 837, 1007]
C–Nb–Ti–U	NbC _{1–x} –TiC _{1–x} –UC _{1±x} is plotted at 2000–2050 °C: (Nb,Ti,U)C _{1–x} (extended solid solution based on NbC _{1–x} –TiC _{1–x} and NbC _{1–x} –UC _{1±x} monocarbide continuous solid solutions with great miscibility gap because of low mutual solubilities in the pair TiC _{1–x} –UC _{1±x})	[391]

(continued)

Table 2.14 (continued)

System	Type of phase diagram (temperature and composition sections, constituent phases or phase fields) and/or character of interphase interaction and materials compatibility	References
C–Nb–Ti–V	NbC _{1-x} –TiC _{1-x} –VC _{1-x} is plotted schematically at 1000 °C	[871]
C–Nb–Ti–W	NbC _{1-x} –TiC _{1-x} – δ -WC _{1±x} is plotted at 1450 °C: (Nb,Ti,W)C _{1-x} (extended solid solution based on NbC _{1-x} –TiC _{1-x} monocarbide continuous solid solution) The max. solubilities of δ -WC _{1±x} in NbC _{1-x} and TiC _{1-x} are ~10 and ~35 mol.%, respectively; the solubilities of NbC _{1-x} and TiC _{1-x} in δ -WC _{1±x} are low.	[419, 465]
C–Nb–U	Plotted at 1200 and 1700 °C: (Nb,U)C _{1-x} (NbC _{1-x} –UC _{1±x} monocarbide continuous solid solution), β -Nb _{2+x} C, ζ -U ₂ C ₃ , α -UC _{2-x} , β -UC _{2-x} , U, Nb, C At higher temp., depend. on compos. graphite is in equilibrium with (Nb,U)C _{1-x} or (Nb,U)C _{1-x} + UC _{2-x} ; the compos. of (Nb,U)C _{1-x} in equilibrium with C + UC _{2-x} is corresp. to (Nb _{0.75÷0.77} U _{0.23÷0.25})C _{1-x} (at 2200 °C) and shifts to lower U concentrations with temp. increase.	[138, 242, 391, 436, 812]
C–Nb–U–V	NbC _{1-x} –VC _{1-x} –UC _{1±x} is plotted at 2000–2050 °C: (Nb,V,U)C _{1-x} (extended solid solution based on NbC _{1-x} –VC _{1-x} and NbC _{1-x} –UC _{1±x} monocarbide continuous solid solutions with great miscibility gap because of low mutual solubilities in the pair VC _{1-x} –UC _{1±x})	[391]
C–Nb–U–Zr	NbC _{1-x} –ZrC _{1-x} –UC _{1±x} is plotted at 2050 °C: (Nb,Zr,U)C _{1-x} (NbC _{1-x} –ZrC _{1-x} –UC _{1±x} monocarbide continuous solid solution) At ~2000 °C (U _{0.5} Zr _{0.5})C _{1±x} reacts vigorously with metal Nb.	[391, 436, 812]
C–Nb–V	Plotted at 1400–3310 °C: (Nb,V)C _{1-x} (NbC _{1-x} –VC _{1-x} monocarbide continuous solid solution), (Nb,V) _{2±x} C (β -Nb _{2+x} C– β -V _{2±x} C semicarbide continuous solid solution at temp. <2200 °C, extended solid solution based on β -Nb _{2+x} C at temp. 2200–2445 °C and extended solid solution based on γ -Nb _{2±x} C at temp. 1780–2650 °C with miscibility gaps (two solid solution phases regions) at temp. 1780–2445 °C), β -(V,Nb) _{2±x} C (extended solid solution based on β -V _{2±x} C), (Nb,V), C NbC _{1-x} –VC _{1-x} is plotted: miscibility gap (critical point—~1400–1480 °C at compos. ~Nb _{0.4÷0.5} V _{0.5÷0.6} C _{1-x} , at 1300 °C ranges from ~Nb _{0.8} V _{0.2} C _{1-x} to ~Nb _{0.15} V _{0.85} C _{1-x}). Graphite is in equilibrium with (Nb,V)C _{1-x} .	[138, 242, 391, 419, 458, 469, 813, 871]

(continued)

Table 2.14 (continued)

System	Type of phase diagram (temperature and composition sections, constituent phases or phase fields) and/or character of interphase interaction and materials compatibility	References
C–Nb–W	Plotted at 1700–2860 °C: (Nb,W)C _{1-x} (monocarbide extended solid solution based on NbC _{1-x} at temp. ≤ ~ 2500 °C and ≥ ~ 2700–2850 °C, or NbC _{1-x} –β-WC _{1-x} monocarbide continuous solid solution at temp. ~ 2500–2850 °C), β-(Nb,W) _{2+x} C (semicarbide extended solid solution based on β-Nb _{2+x} C at temp. < ~ 2500 °C with the max. solubility of W—up to ~ 8 at.% at 2000 °C), γ-(Nb,W) _{2+x} C (semicarbide solid solution based on γ-Nb _{2+x} C at temp. ~ 2500–3000 °C with the max. solubility of W—up to ~ 8 at.% at 2500 °C and ~ 2 at.% at 2690 °C), α-(W,Nb) _{2+x} C (semicarbide extended solid solution based on α-W _{2+x} C at temp. < ~ 2000 °C with the max. solubility of Nb—up to ~ 20 at.% at 1700 °C and ~ 12 at.% at 2000 °C), γ-(W,Nb) _{2+x} C (semicarbide extended solid solution based on γ-W _{2+x} C at temp. ~ 2500–2800 °C with the max. solubility of Nb—up to ~ 15 at.% at 2500 °C and ~ 25 at.% at 2690 °C), δ-WC _{1±x} , (Nb,W), C In the wide range of temp. the solid solubility of Nb in δ-WC _{1±x} is low. Depend. on compos., graphite is in equilibrium with δ-WC _{1±x} + (Nb,W)C _{1-x} or (Nb,W)C _{1-x} .	[138, 242, 391, 419, 470, 758, 773, 827, 837]
C–Nb–Zr	Plotted at 1500 and 1800 °C: (Nb,Zr)C _{1-x} (NbC _{1-x} –ZrC _{1-x} monocarbide continuous solid solution), β-Nb _{2+x} C, (β-Zr,Nb), C NbC _{1-x} –ZrC _{1-x} is plotted: miscibility gap (critical point—~ 410 °C at ~ Nb _{0.55} ÷0.65Zr _{0.35} ÷0.45C _{1-x} , at 300 °C ranges from ~ Nb _{0.3} Zr _{0.7} C _{1-x} to ~ Nb _{0.9} Zr _{0.1} C _{1-x}). The solid solubility of Zr in β-Nb _{2+x} C is low. Graphite is in equilibrium with (Nb,Zr)C _{1-x} . For diffusion rate in the system at various temp. see Addendum.	[138, 242, 391, 419, 421, 436, 468, 813, 837, 844, 864, 874–875]
C–Nd–U	Plotted at 1500 °C: (Nd,U)C ₂ (dicarbide solid solution based on β-NdC ₂), Nd ₂ C _{3-x} , UC _{1±x} , ζ-U ₂ C ₃ , U, Nd, C The max. solubility of “imaginary” phase ‘NdC’ in UC _{1±x} varies from ~ 4 mol.% (~ 1300 °C) to ~ 6 mol.% (~ 1500 °C) and that of Nd ₂ C _{3-x} in ζ-U ₂ C ₃ is ~ 2.5 mol.%	[241, 391]
C–Ni–Si	Plotted at 850 and 1150 °C: β ₁ -Ni _{3+x} Si (<1035 °C), β ₂ -Ni _{3+x} Si (990–1115 °C), β ₃ -Ni _{3+x} Si (1115–1170 °C), γ-Ni ₅ Si _{2-x} (or Ni ₃₁ Si ₁₂ , <~ 1240 °C), δ-Ni ₂ Si (<1255 °C), θ-Ni ₃ Si _{2-x} (~ 825–1305 °C), ε-Ni ₃ Si _{2±x} (<830 °C), ε'-Ni ₃ Si _{2±x} (800–845 °C), NiSi (<~ 990 °C), α-NiSi ₂ (<~ 980 °C), β-NiSi ₂ (~ 980–995 °C), SiC, Ni, Si, C In vacuum, the contact melting between SiC and Ni is observed at 1130–1140 °C.	[242, 244, 431, 503]

(continued)

Table 2.14 (continued)

System	Type of phase diagram (temperature and composition sections, constituent phases or phase fields) and/or character of interphase interaction and materials compatibility	References
C–Ni–Ta	Plotted at 1100 °C: η -Ta ₄ Ni ₂ C, ζ -Ni _{8\pmx} Ta (<1330 °C), κ -Ni _{3\pmx} Ta (<1550 °C), Ni _{2\pmx} Ta (<1405 °C), μ -NiTa _{1+x} (or μ -Ni ₇ Ta _{6+x} <1570 °C), NiTa _{2+x} (<~1790 °C), α -Ta _{2+x} C, β -Ta _{2+x} C, ζ -Ta ₄ C _{3-x} , Ta ₆ C _{5\pmx} , TaC _{1-x} , Ta, Ni, C TaC _{1-x} –Ni is plotted: eutectic—~1340–1370 °C, ~3–7 mol.% TaC _{1-x} ; at the eutectic temp. the max. solubility of TaC _{1-x} in Ni is ~2–4 mol.% TaC _{1-x} is in equilibrium with Ni and Ni-Ta intermetallics.	[242, 244, 391, 431, 459, 613]
C–Ni–Th	Plotted at 1000 °C: Th ₂ Ni ₃ C ₂ , Th ₂ Ni ₃ C ₅ , Th _x Ni _y C _z (?), Th ₇ Ni ₃ (<~1040–1110 °C), ThNi (<~1185–1190 °C), Th ₄ Ni ₇ (<1075 °C), ThNi _{2-x} (<~1050–1060 °C), α -Th ₂ Ni _{7\div8} (or α -ThNi ₄ , <~1195 °C), β -Th ₂ Ni _{7\div8} (or β -ThNi ₄ , from 1195 °C to ~1210–1245 °C), ThNi _{5\div6} (<~1510–1530 °C), Th ₂ Ni _{17\div19} (<~1310–1355 °C), ThC _{1\pmx} , α -ThC _{2-x} , α -Th, Ni, C	[244, 391, 431]
C–Ni–Ti	Plotted at 870, 1100 and 1600 °C: Ti _{2\pmx} Ni (<~985 °C), TiNi _{1\pmx} (<1310 °C), TiNi ₃ (<1380 °C), TiC _{1-x} , α -Ti, β -Ti, Ni, C Eutectic TiC _{1-x} –TiNi–TiNi ₃ (1120 °C) Eutectic TiC _{1-x} –Ni–TiNi ₃ (1295 °C) Eutectic TiC _{1-x} –Ni–C (1270 °C) TiC _{1-x} –Ni is plotted: eutectic—~1280–1310 °C, ~9–10 mol.% TiC _{1-x} (~83 at.% Ni, ~4 at.% C); at the eutectic temp. the max. solubility of TiC _{1-x} in Ni is ~5–6 mol.% (~5 mol.% at 1260 °C) and that of Ni in TiC _{1-x} is ~2.5 mol.%	[242, 244, 391, 406, 414, 431, 471, 1011]
C–Ni–U	Plotted at 1000 °C: UNiC ₂ (<1400 °C), UNiC ₃ (<1800 °C), U ₆ Ni (<790 °C), U ₇ Ni ₉ (<785 °C), U ₅ Ni _{7\pmx} (<820 °C), UNi _{2\pmx} (<985 °C), δ -UNi _{3+x} (<1260 °C), ε -UNi _{4-x} (<1290 °C), UNi _{5\pmx} (<1305 °C), UC _{1\pmx} , ζ -U ₂ C ₃ , γ -U, Ni, C	[242, 391, 431]
C–Ni–V	Plotted at 1100 °C: η ₂ -V ₄ Ni ₂ C, Ni _{8\pmx} V (<405 °C), Ni _{3\pmx} V (<1045 °C), Ni _{2\pmx} V (<~920 °C), σ -NiV _{2\pmx} (<~655–790 °C), σ' -NiV _{2\pmx} (from ~655–790 °C to 1280 °C), NiV _{3+x} (<900 °C), β -V _{2\pmx} C, β' -V _{2+x} C, ζ -V ₄ C _{3-x} , V ₆ C _{5\pmx} , V ₈ C _{7\pmx} , VC _{1-x} , V, C VC _{1-x} –Ni is plotted: eutectic—1310 °C, ~9–10 mol.% VC _{1-x} ; at the eutectic temp. the max. solubilities of VC _{1-x} in Ni and that of Ni in VC _{1-x} equal ~3 mol.%	[242, 244, 391, 431, 458]
C–Ni–W	Plotted at 700–1500 °C: κ -(Ni,W) ₄ C (or NiW ₃ C, Ni ₃ W ₁₆ C ₆), η ₁ -(Ni,W) ₁₂ C (or η ₆₆ -Ni ₆ W ₆ C, Ni ₅ W ₆ C), η ₂ -(Ni,W) ₆ C (or η ₂₄ -Ni ₂ W ₄ C), W ₁₆ Ni ₃ C ₆ (?), β -Ni _{4+x} W (<970 °C), δ -NiW _{1-x} (<~1060 °C), γ -NiW ₂ (<~1025 °C), α -W _{2+x} C, δ -WC _{1\pmx} , Ni, W, C δ -WC _{1\pmx} –Ni is plotted: eutectic—1300 °C, ~12 mol.% δ -WC _{1\pmx} ; at 1000 °C the max. solubilities of δ -WC _{1\pmx} in Ni and that of Ni in δ -WC _{1\pmx} equal to ~7 mol.%	[242, 244, 270, 391, 415, 431, 662, 754–756]

(continued)

Table 2.14 (continued)

System	Type of phase diagram (temperature and composition sections, constituent phases or phase fields) and/or character of interphase interaction and materials compatibility	References
C–Ni–W–Zr	ZrC _{1-x} – δ -WC _{1±x} –Ni is plotted at 1000 °C: eutectic—15 mol.% ZrC _{1-x} , 15 mol.% δ -WC _{1±x} ; regions of solid solutions based on the individual components are not large (~6–8 mol.%)	[415]
C–Ni–Zr	Plotted at 1100 °C: Zr ₂ Ni (<1120 °C), ZrNi (<1260 °C), Zr ₉ Ni ₁₁ (~980–1170 °C), Zr ₇ Ni _{10±x} (<~1165 °C), Zr ₂ Ni ₅ (or Zr ₈ Ni ₂₁ , <1180 °C), ZrNi _{3±x} (<920 °C), Zr ₂ Ni ₇ (<1440 °C), ZrNi _{5±x} (<1300 °C), ZrC _{1-x} , β -Zr, Ni, C ZrC _{1-x} –Ni is plotted: eutectic—~1230–1290 °C, ~5–6 mol.% ZrC _{1-x} (?); at the eutectic temp. the max. solid solubility of ZrC _{1-x} in Ni is ~3.5 mol.% (~1 mol.% at 1100 °C) and that of Ni in ZrC _{1-x} is ~5 mol.%	[242, 244, 391, 415, 431, 460]
C–Np–Th	No diagram plot ThC _{1±x} –NpC _{1-x} monocarbide continuous solid solution	[391]
C–O–Pu–U	Plotted partially The interaction between C and UO _{2+x} –Pu ₂ O _{3±x} solid solution at 1527 °C with formation of (U,Pu) ₂ C _{3-x} is analyzed in relationship with CO pressure.	[472]
C–O–Si	Plotted at 1525–1825 °C: SiO ₂ (<~1700 °C), SiC, Si, O, C SiO ₂ –SiC is plotted SiO ₂ –C is plotted In vacuum (0.01–0.05 Pa), the interaction between C and SiO ₂ initiates in powdered mixtures from ~1250 °C. In CO–N ₂ atmosphere (0.1 MPa), at 1800–1900 °C the reaction rate in SiO ₂ –SiC powder mixtures is limited by C diffusion from the bulk SiC to the interface SiC/SiO ₂ .	[194, 242, 445, 473–475, 857, 1012]
C–O–Si–Sr	No diagram plot At 1000 °C the interaction between SiC and SrO leads to the formation of SrO·SiO ₂ and CO ₂ (in air), or 2SrO·SiO ₂ , SrC ₂ and Sr (in vacuum or Ar).	[242]
C–O–Si–Ti	No diagram plot Ti ₃ Si(C,O) ₂ (M _{n+1} AX _n -phase oxycarbide solid solution)	[744–745, 895]
C–O–Si–Zr	No diagram plot At 1600 °C the interaction between SiC and ZrO _{2-x} leads to the formation of ZrC _x O _y oxycarbide phase.	[242]
C–O–Ta	Plotted partly at 1300–1700 °C: Ta(C,O) _{1-x} (or TaC _x O _y , extended solid solution based on TaC _{1-x} with homogeneity limits: TaC _{0.7} –Ta(C _{0.7} O _{<0.05})–Ta(C _{0.95} O _{<0.05})–TaC _{0.99}), Ta _{2+x} (C,O) (or Ta ₂ C _x O _y , extended solid solution based on α -Ta _{2+x} C with homogeneity limits: Ta ₂ C _{0.8} –Ta ₂ (C _{0.6} O _{0.2})–Ta ₂ (C _{0.4} O _{0.3})–Ta ₂ (C _{0.5} O _{0.4})–Ta ₂ C _{1.0}), β -Ta ₂ O ₅ (<~1200–1360 °C), α -Ta ₂ O ₅ (from ~1200–1360 °C to ~1620–1900 °C), Ta, O, C	[242, 411, 579, 629, 639]

(continued)

Table 2.14 (continued)

System	Type of phase diagram (temperature and composition sections, constituent phases or phase fields) and/or character of interphase interaction and materials compatibility	References
C–O–Ta–U	No diagram plot At 1400 °C (66 h exposure) small reaction zone was found on the contact surface between metal Ta and $\text{UC}_{0.89}\text{O}_{0.06}$, at 1800 °C (3 h exposure)—the interaction was noticeable.	[822]
C–O–Ta–W	No diagram plot At 1300–1400 °C, in vacuum the interaction between $\delta\text{-WC}_{1\pm x}$ and Ta_2O_5 in powder mixtures results in the formation of W–Ta alloy.	[242, 808]
C–O–Ta–Zr	No diagram plot At 2000–2300 °C the interaction between TaC_{1-x} and ZrO_{2-x} results in the formation of new phases.	[242]
C–O–Th	No diagram plot In vacuum (0.01–0.05 Pa), the interaction between C and ThO_{2-x} is ruled by diffusion stage (parabolic law) and initiates in powdered mixtures from ~ 1400 °C and on bulk materials contacts—from ~ 2000 °C.	[138, 194, 382]
C–O–Th–Ti	No diagram plot At 1500–2000 °C the interaction between TiC_{1-x} and ThO_{2-x} leads to the formation of metal oxycarbides.	[242]
C–O–Ti	Plotted partly at 800–1500 °C: $\text{Ti}(\text{C},\text{O})_{1-x}$ (or TiC_xO_y , $\text{TiC}_{1-x}\text{-TiO}_{1\pm x}$ oxycarbide continuous solid solution with homog. limits: $\text{TiC}_{0.4}\text{-TiC}_{0.99}\text{-TiO}_{1.2}\text{-TiO}_{0.8}$), Ti_3O_2 (< 920 °C), $\beta\text{-Ti}_2\text{O}_3$ ($< \sim 1840$ °C), $\text{Ti}_n\text{O}_{2n-1}$ ($4 \leq n \leq 10$, $< \sim 1600$ °C, Magneli phases), TiO_2 (< 1870 °C), $\alpha\text{-(Ti,C,O)}$, $\beta\text{-(Ti,C,O)}$, O, C C-doped titania nanotubes of the $\text{TiO}_{2-x}\text{C}_x$ type were synthesized.	[242, 244, 411, 431, 477, 482, 893]
C–O–Ti–W	No diagram plot. At 1300–1400 °C in powder mixtures $\delta\text{-WC}_{1\pm x}$ interacts with TiO_2 with the formation of W–Ti alloy very intensively.	[242, 808]
C–O–Ti–Zr	No diagram plot. At 1400–2400 °C, in vacuum the interaction between TiC_{1-x} and ZrO_{2-x} leads to the formation of CO and TiC_xO_y oxycarbide phase.	[242]

(continued)

Table 2.14 (continued)

System	Type of phase diagram (temperature and composition sections, constituent phases or phase fields) and/or character of interphase interaction and materials compatibility	References
C–O–U	<p>Plotted at 1000–2000 °C: $U(C,O)_{1\pm x}$ (or $UC_{1-x}O_x$, extended solid solution based on $UC_{1\pm x}$ with max. O solubility corresp. to $UC_{0.12}O_{0.88}$ at <1100 °C and $UC_{0.63\div 0.68}O_{0.32\div 0.37}$ at ~1300–1800 °C), $\alpha-U(C,O)_{2-x}$ (or $\alpha-UC_{2-x}O_x$, extended solid solution based on $\alpha-UC_{2-x}$), $\zeta-U_2C_3$, UO_{2+x} (<~2780–2860 °C), U_4O_{9-x} (<~1140 °C), $\alpha-U_3O_{8-x}$ (~350–770 °C), $\beta-U_3O_{8-x}$ (~770–940 °C), $\gamma-U_3O_{8-x}$ (~940–1700 °C), $\alpha-UO_3$ (?), $\beta-UO_3$ (<~1900 °C), $\alpha-U$, $\beta-U$, $\gamma-U$, O, C</p> <p>UO_{2+x} ($x \approx 0$)–$UC_{1\pm x}$ ($x \approx 0$) is plotted: eutectic—~2250 °C, ~33 mol.% $UC_{1\pm x}$</p> <p>Depend. on temp. and compos., graphite is in equilibrium: at <1100 °C—with UO_{2+x}, or $UO_{2+x} + UC_{0.2}O_{0.8}$ (?), or $UC_{1-x}O_x$ ($0.1 \leq x \leq 0.8$, ?), or $\alpha-UC_{2-x}O_x + UC_{0.9}O_{0.1}$ (?), or $\alpha-UC_{2-x}O_x$; at 1300 °C—with UO_{2+x}, or $UO_{2+x} + \alpha-UC_{2-x}O_x$ ($x = 0.08$), or $\alpha-UC_{2-x}O_x$ ($x \leq 0.08$, ?); at ~1400–1500 °C—with U_3O_{8-x}, or $U_3O_{8-x} + UO_{2+x}$, or UO_{2+x}, or $UO_{2+x} + \alpha-UC_{2-x}O_x$, or $\alpha-UC_{2-x}O_x$; at 1700 °C—with UO_{2+x}, or $UO_{2+x} + \alpha-UC_{2-x}O_x$, or $\alpha-UC_{2-x}O_x$.</p> <p>The interaction between C and UO_{2+x} in vacuum leads to the elimination of excess oxygen (at 1000 °C) and then to the formation of carbides (at 1200–1530 °C).</p>	[138, 242, 244, 431, 472, 478–481, 751–753]
C–O–U–V	<p>No diagram plot.</p> <p>At 1000 °C (66 h exposure) the carburization of metal V was occurred on the contact surface with $UC_{0.89}O_{0.06}$, at 1400 °C (66 h exposure)—the interaction was significant.</p>	[822]
C–O–U–Zr	<p>No diagram plot.</p> <p>At 1900 °C the interaction between U carbides and ZrO_{2-x} is weak. At 1000 °C (66 h exposure) no appreciable reaction was occurred on the contact surface between metal Zr and $UC_{0.89}O_{0.06}$, at 1400 °C (66 h exposure)—small reaction zone was found.</p>	[242, 822]
C–O–V	<p>Plotted partly at 1000–1700 °C: $V(C,O)_{1-x}$ (or VC_xO_y, $VC_{1-x}-\delta-VO_{1\pm x}$ continuous solid solution with homog. limits: $VC_{0.67}-VC_{0.88}-VO_{1.25}-VO_{0.85}$, <~1185–2800 °C), $V_{2\pm x}(C,O)$ (or $V_2C_xO_y$, extended solid solution based on $\beta-V_{2\pm x}C$), $\alpha'-V_{8\pm x}O$ (<~520 °C), $\beta-V_{4\pm x}O$ (from ~320 to 520 °C to 1665 °C), $\beta'-V_{4\pm x}O$ (or $V_{16}O_{3\pm x}$, <400 °C), $\gamma-V_{2\pm x}O$ (or $V_{14}O_{6\pm x}$, <1185 °C), $\delta'-VO_{1+x}$ (or $V_{52}O_{64\pm x}$, <810 °C), $\alpha-V_2O_{3+x}$ (?), $\beta-V_2O_{3+x}$ (<~1955 °C), $\alpha-V_3O_5$ (?), $\beta-V_3O_5$ (<~1600 °C), V_4O_7 (<~1600 °C), V_5O_9 (<~1600 °C), V_6O_{11} (<~1600 °C), V_7O_{13} (<~1600 °C), V_8O_{15} (<~1600 °C), $\alpha-VO_2$ (?), $\beta-VO_2$ (<~1540 °C), $\alpha-V_6O_{13}$ (?), $\beta-V_6O_{13}$ (<700 °C), V_3O_7 (<~670 °C), V_2O_5 (<~680 °C), $\beta'-V_{2+x}C$, $\zeta-V_4C_{3-x}$, $V_6C_{5\pm x}$, $V_8C_{7\pm x}$, V, O, C</p>	[242, 411, 431, 483]

(continued)

Table 2.14 (continued)

System	Type of phase diagram (temperature and composition sections, constituent phases or phase fields) and/or character of interphase interaction and materials compatibility	References
C–O–V–W	No diagram plot. δ -WC _{1±x} interacts in powder mixtures with β -V ₂ O _{3+x} (at 1300–1400 °C) and V ₂ O ₅ (at 900–1400 °C) intensively with the formation of W–V alloy.	[242, 808]
C–O–V–Zr	No diagram plot At 1500–2000 °C the interaction between VC _{1-x} and ZrO _{2-x} leads to the formation of ZrC _x O _y oxycarbide phase and β -V _{2±x} C (at 1600–1700 °C) or metal V (at 1700–2000 °C).	[242]
C–O–W	No diagram plot δ -WC _{1-x} O _x (solid solution based on δ -WC _{1±x} , ?), WO _{3-x} C _x (solid solution based on WO _{3-x} , ?)	[541, 660, 981]
C–O–W–Zr	No diagram plot At 1400–2000 °C the interaction between δ -WC _{1±x} and ZrO _{2-x} results in the formation ZrC _x O _y oxycarbide phase, α -W _{2+x} C and W–Zr alloy.	[242, 808]
C–O–Zr	Plotted partially at 1555, 1600 and 1700 °C: Zr(C,O) _{1-x} (or ZrC _x O _y , extended solid solution based on ZrC _{1-x} with the homog. limits: ZrC _{0.6} –ZrC _{0.5} O _{0.2} –ZrC _{0.4+0.6} O _{0.3+0.55} –ZrC _{0.8} O _{0.2} –ZrC _{0.99}), α -ZrO _{2-x} (<1205 °C), β -ZrO _{2-x} (~1205–2375 °C), γ -ZrO _{2-x} ($x \leq 0.44$, ~1525–2710 °C), γ -ZrO _{2-x} C _z ($z \approx 0.06$, metastable, ?), α -(Zr,C,O) (metal solid solution with the solubility limits: ZrC _{0.02+0.03} and ZrO _{0.41+0.54}), β -(Zr,C,O), O, C In vacuum (0.01–0.05 Pa), the interaction between C and ZrO _{2-x} initiates in powdered mixtures from ~1300 °C and on bulk materials contacts—from ~1600 to 1900 °C.	[138, 194, 241–242, 382, 411–412, 431, 484, 861]
C–Os–Sc	No diagram plot Sc ₃ OsC ₄	[988–989]
C–Os–Si	Plotted at 1350 °C: OsSi ₂ (or OsSi _{1.8} , <1620–1660 °C), Os ₂ Si ₃ (<1820–1860 °C), OsSi _{1±x} (<1720–1740 °C), SiC, Si, Os, C	[244, 431, 503–504]
C–Os–Ta	Plotted at 1500 °C: σ -Ta ₃ Os _{2±x} (<~2500 °C), γ -Ta ₂ Os _{3±x} (<~2420 °C), α -Ta _{2+x} C, TaC _{1-x} , Ta, Os, C Graphite is in equilibrium with (Os,Ta) + TaC _{1-x} . The solubility of Ta in Os (with the presence of C) and that of Os in TaC _{1-x} are low.	[391, 431]
C–Os–Th	No diagram plot Th _x Os _y C _z (?)	[391]
C–Os–Ti	Plotted at 1500 °C: δ -TiOs _{1±x} (<2160–2180 °C), TiC _{1-x} , α -Ti, β -Ti, Os, C Graphite is in equilibrium with (Os, Ti) + TiC _{1-x} . The solubility of Ti in Os (with the presence of C) and that of Os in TiC _{1-x} are low.	[244, 391, 431]

(continued)

Table 2.14 (continued)

System	Type of phase diagram (temperature and composition sections, constituent phases or phase fields) and/or character of interphase interaction and materials compatibility	References
C–Os–U	Plotted at 1500 °C: U_2OsC_2 , U_3Os (<1030 °C), U_2Os (<920 °C), U_5Os_4 (<1280 °C), $UOs_{2\pm x}$ (<2280 °C), $UC_{1\pm x}$, ζ - U_2C_3 , α - UC_{2-x} , β - UC_{2-x} , α -U, β -U, γ -U, Os, C The mutual solubilities of all constituent phases in the system are low.	[244, 391, 431]
C–Os–V	Plotted at 1500 °C: $V_3Os_{2\pm x}$ (<2140 °C), VOs_{1-x} (?), α - $V_{2+x}C$, β - $V_{2\pm x}C$, β' - $V_{2+x}C$, ζ - V_4C_{3-x} , $V_6C_{5\pm x}$, $V_8C_{7\pm x}$, VC_{1-x} , V, Os, C Graphite is in equilibrium with $(Os,V) + VC_{1-x}$. The solubility of V in Os (with the presence of C) and that of Os in VC_{1-x} are low.	[244, 391, 431]
C–Os–W	Plotted at 2000 °C: $\sim W_3Os_3C_2$ (<2000–2030 °C), σ - $OsW_{3\pm x}$ (<2945 °C), α - $W_{2+x}C$, δ - $WC_{1\pm x}$, W, Os, C The mutual solubilities of all constituent binary phases are low. Depend. on compos., graphite is in equilibrium with (Os,W) or $(Os,W) + \delta$ - $WC_{1\pm x}$.	[244, 391, 431]
C–Os–Y	No diagram plot Y_2OsC_2 , $Y_{12}Os_5C_{15}$	[991–992]
C–Os–Zr	Plotted at 1500 °C: $Zr_{11}Os_4$ (<1350 °C), $ZrOs$ (<2040 °C), λ_1 - $ZrOs_{2\pm x}$ (<2660 °C), ZrC_{1-x} , α -Zr, β -Zr, Os, C The solubility of Zr in Os (with the presence of C) and that of Os in ZrC_{1-x} are low. Graphite is in equilibrium with $(Os,Zr) + ZrC_{1-x}$.	[244, 391, 431]
C–P–V	Plotted partially at 1000 °C: V_2PC ($M_{n+1}AX_n$ -phase), V_3PC , V_4P_2C , $V_{11}P_5C$ (or $V_{32}P_{15}C_3$), $V_{20}P_{11}C_2$ (or $V_5P_{2.83}C_{0.5}$), VP_4 , VP_2 , VP , V_4P_3 , $V_{12}P_7$, V_2P , V_3P , α - $V_{2+x}C$, β - $V_{2\pm x}C$, β' - $V_{2+x}C$, ζ - V_4C_{3-x} , $V_6C_{5\pm x}$, $V_8C_{7\pm x}$, VC_{1-x} , V, P, C The homog. range extension of non-stoichiometric V_3PC and $V_{20}P_{11}C_2$ is ~ 3 –5 at.%. [680–681, 744–745, 860, 982]	[680–681, 744–745, 860, 982]
C–Pb–Ti	No diagram plot Ti_2PbC ($M_{n+1}AX_n$ -phase)	[680–681, 744–745, 860]
C–Pb–Zr	No diagram plot Zr_2PbC ($M_{n+1}AX_n$ -phase)	[680–681, 744–745, 860]
C–Pd–Si	Plotted at 825 and 1600 °C: Pd_5Si (from ~ 725 °C to ~ 815 – 835 °C), Pd_4Si (or Pd_9Si_2 , ~ 725 – 830 °C), Pd_3Si (<1070 °C), $Pd_{2\pm x}Si$ (<1395 °C), $PdSi$ (~ 825 – 900 °C), SiC, Si, Pd, C	[244, 431, 503–504]
C–Pd–Ta	Plotted at 1300 °C: $Pd_{3\pm x}Ta$ (<1770–1945 °C, ?), $Pd_{2\pm x}Ta$ (<1670–1800 °C, ?), $PdTa$ (< ~ 1720 – 2000 °C, ?), α - $Pd_{1\pm x}Ta$ (<1410 °C, ?), β - $Pd_{1\pm x}Ta$ (1550–1720 °C, ?), σ - $PdTa_{3\pm x}$ (<2550 °C or 1575–2350 °C, ?), α - $Ta_{2+x}C$, TaC_{1-x} , Ta, Pd, C Depend. on compos., graphite is in equilibrium with (Pd,Ta) alloy or $(Pd_{0.84}Ta_{0.16})$ alloy + TaC_{1-x} .	[242, 244, 391, 431]

(continued)

Table 2.14 (continued)

System	Type of phase diagram (temperature and composition sections, constituent phases or phase fields) and/or character of interphase interaction and materials compatibility	References
C–Pd–Th	Plotted at 1100 °C: δ -Th ₃ Pd _{13±x} (<1215 °C), ε -ThPd _{4-x} (<1340 °C), ThPd _{3+x} (<~ 1560–1575 °C), Th ₃ Pd ₅ (<~ 1385 °C), Th ₃ Pd ₄ (<1325 °C), ThPd (<~ 1410 °C), Th ₂ Pd (<~ 1160 °C), ThC _{1±x} , α -ThC _{2-x} , β -ThC _{2-x} , γ -ThC _{2-x} α -Th, β -Th, Pd, C	[244, 391, 431, 485]
C–Pd–Ti	Plotted at 1300 °C: Ti ₄ Pd (<~ 580 °C), Ti ₂ Pd (<960 °C), α -TiPd _{1±x} (<~ 440–510 °C), β -TiPd _{1±x} (~ 440–1400 °C), Ti ₂ Pd ₃ (<1330 °C), Ti ₃ Pd ₅ (?), α -TiPd _{2-x} (<1280 °C), β -TiPd _{2-x} (~ 1280–1400 °C), TiPd ₃ (<1530 °C), γ -TiPd _{4±x} (<~ 1485 °C, ?), TiC _{1-x} , α -Ti, β -Ti, Pd, C Depend. on compos., graphite is in equilibrium with (Pd,Ti) alloy, or TiPd ₃ , or TiPd ₃ + TiC _{1-x} .	[244, 391, 431]
C–Pd–U	Plotted at 1300 °C: UPd _{1+x} (970–1050 °C), U ₅ Pd _{6+x} (980–1110 °C), UPd _{3-x} (<1640 °C), UPd _{4±x} (<1525–1585 °C), UPd _{5±x} (<1445 °C, ?), U ₂ Pd ₁₁ (<1015 °C), UPd ₈ (or U ₂ Pd ₁₇ , <800 °C, ?), UC _{1±x} , ζ -U ₂ C ₃ , α -UC _{2-x} , β -UC _{2-x} , U, Pd, C	[244, 391, 431, 486]
C–Pd–V	Plotted at 1300 °C: V _{3±x} Pd (<840 °C), VPd _{2±x} (<905 °C), VPd _{3±x} (<815 °C), β -V _{2±x} C, β' -V _{2+x} C, ζ -V ₄ C _{3-x} , V ₆ C _{5±x} , V ₈ C _{7±x} , VC _{1-x} , V, Pd, C Depend. on compos., graphite is in equilibrium with (Pd,V) alloy or (Pd _{0.8} V _{0.2}) alloy + VC _{1-x} .	[244, 391, 431]
C–Pd–W	No diagram plot At 1200–1500 °C δ -WC _{1±x} interacts with Pd intensively (W–Pd solid solution is formed, ?).	[242]
C–Pd–Zr	Plotted at 1300 °C: Zr ₂ Pd (<1085 °C), ZrPd (<~ 1600 °C), ZrPd ₂ (<1600 °C), ZrPd ₃ (<1780 °C), ZrC _{1-x} , α -Zr, β -Zr, Pd, C Depend. on compos., graphite is in equilibrium with (Pd,Zr) alloy, or ZrPd ₃ , or ZrPd ₃ + ZrC _{1-x} .	[244, 391, 431]
C–Pt–Si	Plotted at 800 and 1600 °C: α -Pt ₃ Si (<360 °C), β -Pt ₃ Si (from 360 °C to ~ 775–880 °C), γ -Pt ₃ Si (~ 775–870 °C, ?), α -Pt ₇ Si ₃ (or α -Pt ₁₂ Si ₅ , <280 °C), β -Pt ₇ Si ₃ (or β -Pt ₁₂ Si ₅ , ~ 280–985 °C), α -Pt ₂ Si (<695 °C), β -Pt ₂ Si (695–1100 °C), Pt ₆ Si ₅ (<975 °C), PtSi (<~ 1230 °C), SiC, Si, Pt, C	[244, 487, 503–504]
C–Pt–Ta	Plotted at 1500 °C: Pt _{3±x} Ta (<2065–2085 °C), Pt _{2±x} Ta (<2245 °C), Pt _{1±x} Ta (1635–1795 °C), σ -PtTa _{2+x} (<2470 °C), PtTa _{3+x} (<1725 °C), α -Ta _{2+x} C, TaC _{1-x} , Ta, Pt, C Depend. on compos., graphite is in equilibrium with (Pt,Ta) alloy + Pt _{3±x} Ta or Pt _{3±x} Ta + TaC _{1-x} .	[242, 391, 487]
C–Pt–Th	No diagram plot Th _x Pt _y C _z , ?	[391]

(continued)

Table 2.14 (continued)

System	Type of phase diagram (temperature and composition sections, constituent phases or phase fields) and/or character of interphase interaction and materials compatibility	References
C–Pt–Ti	Plotted at 1500 °C: $\text{Ti}_{3\pm x}\text{Pt}$ (<1370 °C), $\alpha\text{-TiPt}_{1\pm x}$ (<~960–1025 °C), $\beta\text{-TiPt}_{1\pm x}$ (from ~960–1025 °C to 1830 °C), Ti_3Pt_5 (from ~1000 °C to ~1880–1900 °C), TiPt_{3-x} (<~1900 °C), $\gamma\text{-TiPt}_{3\pm x}$ (<1950 °C), TiPt_8 (<1080 °C), TiC_{1-x} , $\alpha\text{-Ti}$, $\beta\text{-Ti}$, Pt, C Depend. on compos., graphite is in equilibrium with (Pt,Hf) alloy + $\gamma\text{-TiPt}_{3\pm x}$ or $\gamma\text{-TiPt}_{3\pm x} + \text{TiC}_{1-x}$.	[244, 391, 487]
C–Pt–U	Plotted at 1300 °C: U_2PtC_2 (<~1700 °C), UPt (<~960 °C), UPt_2 (<1370 °C), UPt_3 (<1700 °C), UPt_5 (<1460 °C), $\text{UC}_{1\pm x}$, $\zeta\text{-U}_2\text{C}_3$, $\alpha\text{-UC}_{2-x}$, $\beta\text{-UC}_{2-x}$, U, Pt, C The mutual solubilities of all the constituent binary phases are low.	[244, 391, 487]
C–Pt–V	Plotted at 1500 °C: $\text{VPt}_{3\pm x}$ (<~1015 °C), $\text{VPt}_{2\pm x}$ (<~1100 °C), $\text{VPt}_{1\pm x}$ (<~1500 °C), $\text{V}_{3\pm x}\text{Pt}$ (<~1800 °C), $\beta\text{-V}_{2\pm x}\text{C}$, $\beta'\text{-V}_{2+x}\text{C}$, $\zeta\text{-V}_4\text{C}_{3-x}$, $\text{V}_6\text{C}_{5\pm x}$, $\text{V}_8\text{C}_{7\pm x}$, VC_{1-x} , V, Pt, C Depend. on compos., graphite is in equilibrium with (Pt,V) alloy + $\text{VPt}_{3\pm x}$ or $\text{VPt}_{3\pm x} + \text{VC}_{1-x}$.	[244, 391, 487]
C–Pt–W	Plotted at 2000 °C: $\text{W}_5\text{Pt}_5\text{C}_x$ ($x \approx 1$ at 2000 °C), $\gamma\text{-Pt}_2\text{W}$ (~1400 °C, ?), $\varepsilon\text{-PtW}$ (~1400 °C, ?), $\alpha\text{-W}_{2+x}\text{C}$, $\beta\text{-W}_{2+x}\text{C}$, $\gamma\text{-W}_{2\pm x}\text{C}$, $\gamma\text{-WC}_{1-x}$, $\delta\text{-WC}_{1\pm x}$, W, Pt, C	[242, 391, 487]
C–Pt–Zr	Plotted at 1500 °C: $\text{Zr}_{5+x}\text{Pt}_3$ (<~1725 °C), ZrPt (<~2100–2105 °C), $\text{Zr}_9\text{Pt}_{11}$ (?), $\text{Zr}_7\text{Pt}_{10}$ (?), $\text{ZrPt}_{3\pm x}$ (<~2120–2155 °C, ?), ZrC_{1-x} , $\alpha\text{-Zr}$, $\beta\text{-Zr}$, Pt, C Depend. on compos., graphite is in equilibrium with (Pt,Zr) alloy + $\text{ZrPt}_{3\pm x}$ or $\text{ZrPt}_{3\pm x} + \text{ZrC}_{1-x}$.	[244, 391, 487]
C–Pu–Si	Plotted at 20–1000 °C: Pu_5Si_3 (<~1375 °C), Pu_3Si_2 (<~1440 °C), PuSi (<~1575 °C), $\text{Pu}_3\text{Si}_{5\pm x}$ (<~1645 °C), $\text{PuSi}_{2\pm x}$ (<~1640 °C), Pu_3C_2 , PuC_{1-x} , $\text{Pu}_2\text{C}_{3-x}$, $\beta\text{-PuC}_2$, SiC, $\alpha\text{-Pu}$, $\beta\text{-Pu}$, $\gamma\text{-Pu}$, $\delta\text{-Pu}$, $\delta'\text{-Pu}$, $\varepsilon\text{-Pu}$, Si, C The solubilities of Pu silicides in Pu carbides is very low (<1 mol.%). At temp. <~1600–1750 °C graphite is in equilibrium with $\text{Pu}_2\text{C}_{3-x}$ and SiC.	[906]
C–Pu–Ta	No diagram plot At temp. ≥ 1050 °C the interaction between PuC_{1-x} and Ta leads to the formation of $\alpha\text{-(Ta,Pu)}_{2+x}\text{C}$.	[242]
C–Pu–Th	Plotted at 1050–1600 °C: $(\text{Th,Pu})\text{C}_{1\pm x}$ (or $\text{Th}_y\text{Pu}_{1-y}\text{C}_{1-x}$, $\alpha\text{-Th-ThC}_{1\pm x}\text{-PuC}_{1-x}$ monocarbide continuous solid solution; at 1050 °C: for $x = 0$, $0.68 \leq y \leq 1.0$ and for $x = 0.18$, $0 \leq y \leq 1$), $(\text{Pu,Th})_2\text{C}_{3-x}$ (or $(\text{Pu}_y\text{Th}_{1-y})_2\text{C}_{3-x}$, sesquicarbide extended solid solution based on $\text{Pu}_2\text{C}_{3-x}$; $0.7 \leq y \leq 1$ at ~1200 °C), $(\text{Th,Pu})\text{C}_{2-x}$ (or $\text{Th}_y\text{Pu}_{1-y}\text{C}_{2-x}$, dicarbide continuous or extended solid solutions based on $\alpha\text{-ThC}_{2-x}$, $\beta\text{-ThC}_{2-x}$ and $\gamma\text{-ThC}_{2-x}$; at ~1100 °C—for $\alpha\text{-Th}_y\text{Pu}_{1-y}\text{C}_{2-x}$, $0.45 \leq y \leq 1$; at ~1200 °C—for $\gamma\text{-Th}_y\text{Pu}_{1-y}\text{C}_{2-x}$, $0 \leq y \leq 1$; at ~1150–1410 °C $\beta\text{-Th}_y\text{Pu}_{1-y}\text{C}_{2-x}$ exists only as a ternary solution), $\alpha\text{-Th}$, $\beta\text{-(Th,Pu)}$, Pu, C	[138, 391, 906]

(continued)

Table 2.14 (continued)

System	Type of phase diagram (temperature and composition sections, constituent phases or phase fields) and/or character of interphase interaction and materials compatibility	References
C–Pu–Ti	Plotted at 1600 °C: PuC_{1-x} , $\text{Pu}_2\text{C}_{3-x}$, TiC_{1-x} , $\beta\text{-Ti}$, Pu, C The mutual solid solubilities of all the constituent binary phases are low. Graphite is in equilibrium with $\text{Pu}_2\text{C}_{3-x}$ + TiC_{1-x} .	[391]
C–Pu–U	Plotted at 400–2000 °C: $(\text{U,Pu})\text{C}_{1-x}$ (or $\text{U}_{1-y}\text{Pu}_y\text{C}_{1-x}$, $\text{UC}_{1\pm x}$ – PuC_{1-x} monocarbide continuous solid solution, or extended solid solutions based on $\text{UC}_{1\pm x}$ (at temp. >melt. point of PuC_{1-x}); stoichiometric compos. ($x = 0$) are observed at $0 \leq y \leq 0.7$, so for Pu-rich solutions the miscibility occurs only in hypostoichiometric regions), $\zeta\text{-(U,Pu)}_2\text{C}_{3-x}$ (or $\zeta\text{-(U}_{1-y}\text{Pu}_y)_2\text{C}_{3-x}$, sesquicarbide continuous solid solution; at higher temp. $\zeta\text{-U}_2\text{C}_3$ is stabilized by Pu), $\alpha\text{-(U,Pu)}\text{C}_{2-x}$ (or $\alpha\text{-U}_{1-y}\text{Pu}_y\text{C}_{2-x}$, dicarbide continuous solid solution, or extended solid solutions based on $\alpha\text{-UC}_{2-x}$, metastable at higher Pu concentrations, ?), $\beta\text{-(U,Pu)}\text{C}_{2-x}$ (or $\beta\text{-U}_{1-y}\text{Pu}_y\text{C}_{2-x}$, dicarbide continuous solid solution (at 1800–2200 °C, ?), or extended solid solutions based on $\beta\text{-UC}_{2-x}$), $\text{Pu}_3\text{C}_{2-x}$, $\eta\text{-(Pu}_{1-x}\text{U}_x)$ (from ~280 to 700–705 °C), $\zeta\text{-PuU}_{1-x}$ (<~590–630 °C), $\alpha\text{-U}$, $\beta\text{-U}$, ($\epsilon\text{-Pu}$, $\gamma\text{-U}$), $\gamma\text{-Pu}$, $\delta\text{-Pu}$, $\delta'\text{-Pu}$, C	[238, 244, 391, 488–493]
C–Pu–U–W	$(\text{U}_{0.8}\text{Pu}_{0.2})\text{-W-C}$ is plotted at 1700 °C: $(\text{U}_{0.8}\text{Pu}_{0.2})\text{WC}_2$, $(\text{U}_{0.8}\text{Pu}_{0.2})_4\text{W}_4\text{C}_7$, $(\text{U}_{0.8}\text{Pu}_{0.2})\text{C}_{1\pm x}$ (terminal solubility of W is low), $\zeta\text{-(U}_{0.8}\text{Pu}_{0.2})_2\text{C}_{3-x}$, $\beta\text{-W}_{2+x}\text{C}$, $\gamma\text{-W}_{2\pm x}\text{C}$, $\gamma\text{-WC}_{1-x}$, $\delta\text{-WC}_{1\pm x}$ ($\text{U}_{0.8}\text{Pu}_{0.2}$), W, C	[489]
C–Pu–U–Zr	No diagram plot $(\text{U}_{1-z-y}\text{Pu}_z\text{Zr}_y)\text{C}_{1-x}$ ($\text{UC}_{1\pm x}$ – PuC_{1-x} – ZrC_{1-x} monocarbide continuous solid solution in the regions with low values of z)	[391]
C–Pu–W	Plotted at 1400 °C: PuWC_2 , $\text{Pu}_4\text{W}_4\text{C}_7$, PuC_{1-x} , $\text{Pu}_2\text{C}_{3-x}$, $\alpha\text{-W}_{2+x}\text{C}$, $\delta\text{-WC}_{1\pm x}$, Pu, W, C The mutual solid solubilities of all the constituent binary phases are low. Depend. on compos., graphite is in equilibrium with $\text{Pu}_2\text{C}_{3-x}$ + PuWC_2 , or $\delta\text{-WC}_{1\pm x}$ + PuWC_2 . At temp. ≥ 1050 °C the interaction between PuC_{1-x} and W leads to the formation of $\alpha\text{-(W,Pu)}_{2+x}\text{C}$.	[242, 391]
C–Pu–Zr	Plotted at 1250–1600 °C: $(\text{Pu,Zr})\text{C}_{1-x}$ (monocarbide extended solid solution based on PuC_{1-x} with max. terminal solubility of ZrC_{1-x} ~25 mol.%), $\text{Pu}_2\text{C}_{3-x}$ (terminal solubility of Zr is low), $(\text{Zr,Pu})\text{C}_{1-x}$ (monocarbide extended solid solution based on ZrC_{1-x} with max. terminal solubility of PuC_{1-x} ~25 mol.%), Pu, $\beta\text{-Zr}$, C Graphite is in equilibrium with $\text{Pu}_2\text{C}_{3-x}$ + $(\text{Zr,Pu})\text{C}_{1-x}$.	[391, 494–495]

(continued)

Table 2.14 (continued)

System	Type of phase diagram (temperature and composition sections, constituent phases or phase fields) and/or character of interphase interaction and materials compatibility	References
C–Re–Si	Plotted at 1000 and 1600 °C: ReSi_2 (or $\text{ReSi}_{1.8}$, $< \sim 1930$ – 1980 °C), ReSi (from 1650 °C to ~ 1820 – 1880 °C, ?), Re_5Si_3 (< 1020 °C, ?), Re_2Si (or $\text{Re}_{17}\text{Si}_9$, $< \sim 1810$ – 1960 °C), SiC , Re , Si , C	[244, 487, 503–504]
C–Re–Ta	Plotted at 1800 and 2100 °C: $\sigma\text{-Ta}_2\text{Re}_{3-x}$ (from 2200 – 2460 °C to 2680 – 2740 °C), $\chi\text{-TaRe}_{3\pm x}$ (< 2790 – 2830 °C), $\alpha\text{-Ta}_{2+x}\text{C}$, TaC_{1-x} , Ta , Re , C TaC_{1-x} – Re is plotted: eutectic— 2420 °C, ~ 30 mol.% TaC_{1-x} ; the mutual solid solubilities of the components are low Graphite is in equilibrium with $\text{Re} + \text{TaC}_{1-x}$.	[242, 391, 487, 818]
C–Re–Tc	Plotted schematically	[840]
C–Re–Th	No diagram plot $\text{Th}_3\text{Re}_5\text{C}_z$	[391]
C–Re–Ti	TiC_{1-x} – Re is plotted: eutectic— 2540 °C, ~ 44 – 50 mol.% TiC_{1-x} ; the mutual solid solubilities of the components are low Graphite is in equilibrium with $\text{Re} + \text{TiC}_{1-x}$.	[242, 391, 581–583, 835]
C–Re–U	Plotted at 1500 and 2110 °C: UReC_2 ($< \sim 2000$ °C), $\sim \text{U}_4\text{Re}_4\text{C}_{7-x}$ ($< \sim 2000$ °C), $\text{U}_5\text{Re}_3\text{C}_{8-x}$ (?), $\alpha\text{-URe}_2$ (< 180 °C), $\beta\text{-URe}_2$ (180 – 2200 °C), $\text{UC}_{1\pm x}$, $\zeta\text{-U}_2\text{C}_3$, $\alpha\text{-UC}_{2-x}$, $\beta\text{-UC}_{2-x}$, U , Re , C $\text{UC}_{1\pm x}$ – Re is plotted: eutectic— 1860 °C, ~ 40 mol.% $\text{UC}_{1\pm x}$	[138, 242, 244, 391, 487, 612, 812]
C–Re–U–Zr	No diagram plot At ~ 2100 °C ($\text{U}_{0.5}\text{Zr}_{0.5}$) $\text{C}_{1\pm x}$ is compatible for periods of up to 35 min. with metal Re .	[812]
C–Re–V	Plotted at 1950 °C: $\beta\text{-(V,Re)}_{2\pm x}\text{C}$ ($\beta\text{-V}_{2\pm x}\text{C}$ – Re semicarbide continuous solid solution or extended solid solution based on $\beta\text{-V}_{2\pm x}\text{C}$, ?), $(\text{V,Re})\text{C}_{1-x}$ (monocarbide extended solid solution based on VC_{1-x} with max. terminal solubility of $\text{Re} \sim 65$ at.%, ?), $\delta\text{-VRe}_{2+x}$ (from 1470 °C to 1950 – 2310 °C), $\sigma\text{-VRe}_{3+x}$ (from 1950 – 1990 °C to 2440 – 2630 °C), V , Re , C VC_{1-x} – Re is plotted: eutectic— 2050 °C, ~ 60 mol.% Re ; the mutual solid solubilities of the components are low (?) Data available on the system in literature are very controversial.	[244, 391, 487, 496, 581–583, 603, 837]
C–Re–W	Plotted at 1500 and 2000 °C: $\pi\text{-W}_3\text{Re}_2\text{C}$, $(\text{W,Re})\text{C}_{1-x}$ (metastable, ?), $\beta\text{-(W,Re)}_{2+x}\text{C}$ ($\beta\text{-W}_{2+x}\text{C}$ – Re(W,C) continuous solid solution), $\sigma\text{-W}_2\text{Re}_{3\pm x}$ ($< \sim 2890$ – 3005 °C), $\chi\text{-WRe}_{3-x}$ (< 2125 – 2130 °C), $\delta\text{-WC}_{1\pm x}$, W , Re , C Graphite is in equilibrium with $\delta\text{-WC}_{1\pm x}$, $\beta\text{-(W,Re)}_{2+x}\text{C} + \delta\text{-WC}_{1\pm x}$ and $\beta\text{-(W,Re)}_{2+x}\text{C}$	[138, 242, 244, 391, 487, 581–582, 591, 809, 837]

(continued)

Table 2.14 (continued)

System	Type of phase diagram (temperature and composition sections, constituent phases or phase fields) and/or character of interphase interaction and materials compatibility	References
C–Re–Y	No diagram plot Y_2ReC_2 , $Y_{12}Re_5C_{15}$	[993–994]
C–Re–Zr	Plotted at 1900 and 2000 °C: σ -Zr ₂ Re (<~ 1640–1900 °C, ?), Zr ₂₁ Re ₂₅ (?), λ -ZrRe _{2-x} (<2450–2750 °C, ?), χ -Zr ₅ Re _{24+x} (<2500 °C), ZrC _{1-x} , Zr, Re, C ZrC _{1-x} –Re is plotted: eutectic—~ 2540–2670 °C, ~ 20–35 mol.% ZrC _{1-x} (?); at 1900 °C the solubility of Re in ZrC _{1-x} is ~ 3 mol.% and that of ZrC _{1-x} in Re is <0.5 mol.%; data available in literature on this quasibinary system are controversial Graphite is in equilibrium with Re + ZrC _{1-x} .	[242, 244, 391, 487, 820, 835, 837]
C–Rh–Si	Plotted at 1170 °C: Rh ₂ Si (<1650 °C), Rh ₅ Si ₃ (<1470 °C), Rh ₃ Si ₂ (<820 °C), Rh ₂₀ Si ₁₃ (or RhSi _{0.7} , 1050–1225 °C), α -RhSi _{1±x} (<1030–1080 °C), β -RhSi _{1+x} (from 1030–1080 °C to 1450 °C), Rh ₄ Si ₅ (<1030 °C), Rh ₃ Si ₄ (<1040 °C), SiC, Si, Rh, C	[244, 487, 503–504]
C–Rh–Ta	Plotted at 1500 °C: Rh _{3±x} Ta (<~ 2125 °C), α -Rh _{2±x} Ta (or α_2 -Rh _{2±x} Ta, <~ 1890 °C), α_1 -Rh _{3±x} Ta ₂ (<~ 1860 °C), α_3 -RhTa _{1-x} (from 1355–1395 °C to ~ 1840 °C), σ -RhTa _{2±x} (<~ 2080–2140 °C), α -Ta _{2+x} C, TaC _{1-x} , Ta, Rh, C The solubility of C in Rh _{3±x} Ta is low.	[244, 391, 487]
C–Rh–Th	Plotted at 1200 °C: ~ ThRh ₃ C _x ($x \approx 0.3$, ?), Th ₇ Rh ₃ (<1350–1375 °C), ThRh (<at least ~ 1500 °C), Th ₃ Rh ₄ (<~ 1475–1500 °C), Th ₃ Rh ₅ (<~ 1440–1460 °C), α -ThRh ₂ (<~ 1250 °C), β -ThRh ₂ (at least from ~ 1250 °C to 1500 °C), ThRh ₃ (<at least ~ 1500 °C), ThRh ₅ (<at least ~ 1500 °C), ThC _{1±x} , α -ThC _{2-x} , β -ThC _{2-x} , α -Th, β -Th, Rh, C	[391, 487, 497]
C–Rh–Ti	Plotted at 1500 °C: TiRh ₃ C _x ($x \approx 0.25$, ?), Ti _{2±x} Rh (<790 °C), α -TiRh _{1±x} (?), β -TiRh _{1±x} (<1940 °C), Ti ₃ Rh ₅ (<~ 1765 °C, ?), TiRh _{3±x} (<1750 °C), TiRh ₅ (<1100 °C, ?), TiC _{1-x} , α -Ti, β -Ti, Rh, C The solubility of C in TiRh _{3±x} is ~ 5 at.%; no solubility of Rh in TiC _{1-x} . Depend. on compos., graphite is in equilibrium with Rh + TiRh ₃ C _x or TiRh ₃ C _x + TiC _{1-x} .	[244, 391, 487]
C–Rh–U	Plotted at 700 and 1300 °C: U ₂ RhC ₂ (≤ 1715 °C), URh ₃ C (?), α -U ₄ Rh ₃ (<720 °C), β -U ₄ Rh ₃ (720–1155 °C), U ₃ Rh ₄ (<1450 °C), U ₃ Rh ₅ (<1550 °C), URh ₃ (<1700 °C), UC _{1±x} , ζ -U ₂ C ₃ , α -U, β -U, γ -U, Rh, C	[242, 244, 391, 487, 498]
C–Rh–V	Plotted at 1500 °C: β -V _{2±x} Rh (or V _{3±x} Rh, <1730 °C), α_1 -VRh _{1-x} (~ 1320–1535 °C, ?), α_2 -VRh _{1+x} (<1560 °C), α_3 -VRh _{1±x} (<~ 1400–1405 °C), ε -V ₂ Rh _{3+x} (or V ₃ Rh _{5±x} <1615 °C), γ -VRh _{3±x} (<1740 °C), β -V _{2±x} C, β' -V _{2+x} C, ζ -V ₄ C _{3-x} , V ₆ C _{5±x} , V ₈ C _{7±x} , VC _{1-x} , V, Rh, C The solubility of C in γ -VRh _{3±x} is very low.	[244, 391, 487]

(continued)

Table 2.14 (continued)

System	Type of phase diagram (temperature and composition sections, constituent phases or phase fields) and/or character of interphase interaction and materials compatibility	References
C–Rh–W	Plotted at 1500 and 2000 °C: $(\text{W,Rh})_4\text{C}_{1-x}$ ($0 < x < 0.2$, ~ 1700 – 2000 °C), Rh_3W (from ~ 1200 °C to ?), $\varepsilon\text{-Rh}_{2\pm x}\text{W}$ ($< \sim 2250$ – 2255 °C), $\alpha\text{-W}_{2+x}\text{C}$, $\beta\text{-W}_{2+x}\text{C}$, $\delta\text{-WC}_{1\pm x}$, W, Rh, C	[244, 391, 487]
C–Rh–Zr	Plotted at 1500 °C: ZrRh_3C_x ($x \approx 0.5$, ?), Zr_2Rh (< 1170 – 1180 °C), $\alpha\text{-ZrRh}_{1+x}$ ($< \sim 200$ – 670 °C), $\beta\text{-ZrRh}_{1+x}$ (from ~ 200 – 670 °C to 1935 °C), $\text{Zr}_3\text{Rh}_{4\pm x}$ (< 1660 °C), $\text{Zr}_3\text{Rh}_{5\pm x}$ (< 1790 °C), $\text{ZrRh}_{3\pm x}$ (< 1920 °C), ZrC_{1-x} , $\beta\text{-Zr}$, Rh, C The solubility of C in $\text{ZrRh}_{3\pm x}$ is ~ 10 at.%; no solubility of Rh in ZrC_{1-x} . Depend. on compos., graphite is in equilibrium with Rh + ZrRh_3C_x or ZrRh_3C_x + ZrC_{1-x} .	[391, 487]
C–Ru–Si	Plotted at 1340 °C: Ru_2Si ($< \sim 1225$ – 1545 °C), Ru_5Si_3 (~ 1330 – 1550 °C), Ru_4Si_3 (or $\text{RuSi}_{0.9}$, < 1695 °C), RuSi ($< \sim 1800$ °C), Ru_2Si_3 (or $\text{RuSi}_{1.8}$, $< \sim 1710$ °C), SiC , Si, Ru, C	[487, 503–504]
C–Ru–Ta	Plotted at 1600 °C: $\text{TaRu}_3\text{C}_{1-x}$ ($x \approx 0.6$, stable in the limited range of temp.), $\gamma\text{-Ru}_3\text{Ta}_{2-x}$ ($< \sim 1665$ °C), $\mu\text{-RuTa}_{1\pm x}$ ($< \sim 2080$ °C), $\mu'\text{-RuTa}_{1\pm x}$ ($< \sim 1400$ °C), $\mu''\text{-RuTa}_{1\pm x}$ ($< \sim 800$ °C), $\alpha\text{-Ta}_{2+x}\text{C}$, TaC_{1-x} , Ta, C Graphite is in equilibrium with Ru + TaC_{1-x} .	[391, 487, 897]
C–Ru–Th	Plotted at 900 and 1200 °C: $\sim \text{Th}_{11}\text{Ru}_{12}\text{C}_{18}$ (or $\text{Th}_{3+x}\text{Ru}_{4-x}\text{C}_5$, $x \approx 0.3$, ?), $\sim \text{Th}_2\text{Ru}_6\text{C}_5$ (or $\text{ThRu}_3\text{C}_{1.5}$, ?), $\sim \text{ThRu}_3\text{C}_{1-x}$ ($0 < x < 0.1$, ?), Th_7Ru_3 ($< \sim 1410$ °C), Th_3Ru_2 (< 1425 °C), ThRu ($< \sim 1460$ °C), ThRu_2 ($< \text{at least } 1550$ °C), $\text{ThC}_{1\pm x}$, $\alpha\text{-ThC}_{2-x}$, $\beta\text{-ThC}_{2-x}$, $\alpha\text{-Th}$, $\beta\text{-Th}$, Ru, C	[391, 487, 499–500]
C–Ru–Ti	Plotted at 1500 °C: $\text{TiRu}_3\text{C}_{1-x}$ (?), $\text{TiRu}_{1\pm x}$ (or TiRu_{1+x} $< \sim 2130$ – 2150 °C), TiC_{1-x} , $\beta\text{-Ti}$, Ru, C TiC_{1-x} –Ru is plotted: eutectic— ~ 1700 – 1840 °C Graphite is in equilibrium with Ru + TiC_{1-x} .	[244, 391, 487]
C–Ru–U	Plotted at 1000 and 1300 °C: U_2RuC_2 ($< \sim 1700$ °C), URu_3C_x ($0 \leq x \leq 0.7$ at 1300 °C, extended solid solution based on URu_3 , < 1850 °C), U_2Ru ($< \sim 935$ °C), $\alpha\text{-URu}$ (< 795 °C), $\beta\text{-URu}$ (~ 795 – 1160 °C), U_3Ru_4 ($< \sim 1165$ °C), U_3Ru_5 ($< \sim 1180$ °C), $\text{UC}_{1\pm x}$, $\zeta\text{-U}_2\text{C}_3$, $\gamma\text{-U}$, $\beta\text{-U}$, $\alpha\text{-U}$, Ru, C	[244, 391, 487, 495, 501–502, 619]
C–Ru–V	Plotted at 1600 °C: $\text{VRu}_3\text{C}_{1-x}$ ($x \approx 0.6$, stable in the limited range of temp.), V_3Ru (at least < 1500 °C, ?), $\text{VRu}_{1\pm x}$ (< 1925 – 1975 °C), $\beta\text{-V}_{2\pm x}\text{C}$, $\beta'\text{-V}_{2+x}\text{C}$, $\zeta\text{-V}_4\text{C}_{3-x}$, $\text{V}_6\text{C}_{5\pm x}$, $\text{V}_8\text{C}_{7\pm x}$, VC_{1-x} , V, Ru, C Graphite is in equilibrium with Ru + VC_{1-x} .	[244, 391, 487, 897]
C–Ru–W	Plotted at 1500 and 2000 °C: $(\text{W,Ru})_3\text{C}_{1-x}$ (~ 2000 °C), $\sigma\text{-Ru}_2\text{W}_{3\pm x}$ (from ~ 1665 – 1670 °C to 2300 °C), $\alpha\text{-W}_{2+x}\text{C}$, $\beta\text{-W}_{2+x}\text{C}$, $\delta\text{-WC}_{1\pm x}$, W, Ru, C	[244, 391, 487]

(continued)

Table 2.14 (continued)

System	Type of phase diagram (temperature and composition sections, constituent phases or phase fields) and/or character of interphase interaction and materials compatibility	References
C–Ru–Zr	Plotted at 1500 °C: $\text{ZrRu}_3\text{C}_{1-x}$ ($x \approx 0.3$), $\delta\text{-ZrRu}_{1\pm x}$ (<2130 °C), $\lambda_1\text{-ZrRu}_2$ (1285–1825 °C), ZrC_{1-x} , $\beta\text{-Zr}$, Ru, C ZrC_{1-x} –Ru is plotted: eutectic—~1800 °C Graphite is in equilibrium with Ru + ZrC_{1-x} .	[244, 391, 487]
C–S–Ta	No diagram plot $\text{Ta}_2\text{S}_2\text{C}$ (2 polytypes; C in carbosulfides is related to graphene sheets on (111) surfaces of TaC_{1-x})	[855]
C–S–Ti	No diagram plot Ti_2SC ($\text{M}_{n+1}\text{AX}_n$ -phase)	[680–681, 744–745, 860]
C–S–Ti–V	No diagram plot $(\text{Ti,V})_2\text{SC}$ ($\text{M}_{n+1}\text{AX}_n$ -phase solid solution)	[680–681, 860]
C–S–Zr	No diagram plot Zr_2SC ($\text{M}_{n+1}\text{AX}_n$ -phase)	[680–681, 744–745, 860]
C–Sc–Tc	Plotted schematically	[840]
C–Sc–Ti	Plotted at 1300–1800 °C: $(\text{Sc,Ti})\text{C}_{1-x}$ (ScC_{1-x} – TiC_{1-x} monocarbide continuous solid solution), $\alpha\text{-Sc}_4\text{C}_3$, $\beta\text{-Sc}_4\text{C}_{3+x}$, $\text{Sc}_3\text{C}_{4-x}$ (or $\text{Sc}_{15}\text{C}_{19\pm x}$), $\alpha\text{-Sc}$, $\alpha\text{-Ti}$, $\beta\text{-(Sc,Ti)}$, C Graphite is in equilibrium with $(\text{Sc,Ti})\text{C}_{1-x}$ + $\text{Sc}_3\text{C}_{4-x}$ (or $\text{Sc}_{15}\text{C}_{19\pm x}$).	[138, 244, 391, 601]
C–Sc–Zr	Plotted at 1500–1900 °C: $(\text{Sc,Zr})\text{C}_{1-x}$ (ScC_{1-x} – ZrC_{1-x} monocarbide continuous solid solution), $\alpha\text{-Sc}_4\text{C}_3$, $\beta\text{-Sc}_4\text{C}_{3+x}$, $\text{Sc}_3\text{C}_{4-x}$ (or $\text{Sc}_{15}\text{C}_{19\pm x}$), $\alpha\text{-(Sc,Zr)}$, $\beta\text{-(Sc,Zr)}$, C Graphite is in equilibrium with $(\text{Sc,Zr})\text{C}_{1-x}$ + $\text{Sc}_3\text{C}_{4-x}$ (or $\text{Sc}_{15}\text{C}_{19\pm x}$).	[244, 602]
C–Si–Ta	Plotted at 800–1820 °C: $\text{Ta}_5\text{Si}_3\text{C}_{1-x}$ (at least at ~1000–1820 °C), $\alpha\text{-Ta}_4\text{SiC}_3$, $\beta\text{-Ta}_4\text{SiC}_3$ ($\text{M}_{n+1}\text{AX}_n$ -phases, ?), Ta_3Si (or $\text{Ta}_{4.5}\text{Si}$, <~2340–2520 °C), Ta_2Si (<2440–2460 °C), $\alpha\text{-Ta}_5\text{Si}_3$ (<~1700–2160 °C), $\beta\text{-Ta}_5\text{Si}_3$ (from ~1700–2160 °C to 2500–2550 °C), TaSi_2 (<~2040–2300 °C), $\alpha\text{-Ta}_{2+x}\text{C}$, TaC_{1-x} , SiC, Ta, Si, C Graphite is in equilibrium with SiC + TaC_{1-x} .	[138, 242, 244, 487, 503, 639, 898]
C–Si–Ti	Plotted at 1100–2875 °C: $\alpha\text{-Ti}_3\text{SiC}_2$, $\beta\text{-Ti}_3\text{SiC}_2$ (<2375 °C, small homog. range at lower temp., $\text{M}_{n+1}\text{AX}_n$ -phases), Ti_2SiC ($\text{M}_{n+1}\text{AX}_n$ -phase, ?), Ti_4SiC_3 , Ti_5SiC_4 ($\text{M}_{n+1}\text{AX}_n$ -phases, metastable, ?), $\text{Ti}_5\text{Si}_2\text{C}_3$, $\text{Ti}_7\text{Si}_2\text{C}_5$ (intergrown structures, $\text{M}_{n+1}\text{AX}_n$ -phases, ?), $\text{Ti}_5\text{Si}_{3\pm y}\text{C}_x$ ($0 \leq x \leq 0.99$, solid solution based on $\text{Ti}_5\text{Si}_3\pm x$, <~2130–2335 °C), Ti_3Si (<1170 °C), Ti_5Si_4 (<1920 °C), TiSi (<1570 °C), TiSi_2 (<1490–1500 °C), TiC_{1-x} , SiC, $\beta\text{-Ti}$, Si, C Carbon stabilizes the structure of $\text{Ti}_5\text{Si}_{3\pm x}$. Graphite is in equilibrium with SiC + TiC_{1-x} . In vacuum, the interaction between graphite and TiSi_2 begins at ~1300 °C (2 h contact exposure) and leads to the formation of SiC and $\text{Ti}_5\text{Si}_{3\pm y}\text{C}_x$. At 900–1300 °C, in vacuum the interaction between SiC and Ti results in the formation of $\text{Ti}_5\text{Si}_{3\pm y}\text{C}_x$ and TiC_{1-x} .	[242, 244, 419, 463, 487, 503, 506–509, 640–642, 680–681, 744–746, 819, 860]

(continued)

Table 2.14 (continued)

System	Type of phase diagram (temperature and composition sections, constituent phases or phase fields) and/or character of interphase interaction and materials compatibility	References
C–Si–U	Plotted at 675–1500 °C: $U_3Si_2C_2$ (or $U_3Si_2C_3$, <1750 °C), $U_3Si_2C_{1-x}$ (?), $U_5Si_4C_{1-x}$ ($x = 0.25$, or $U_{20}Si_{16}C_3$, <1600 °C), U_3SiC_3 (?), USi_3 (<1510 °C), USi_2 (<450 °C, metastable, ?), $\alpha-USi_{2-x}$ (?), $\beta-USi_{2-x}$ ($x = 0.12$, <1710 °C), $\alpha-U_3Si_5$ (?), $\beta-U_3Si_5$ (?), $\gamma-U_3Si_5$ (<1770 °C), USi (<1580 °C), U_3Si_2 (<1665 °C), $\alpha-U_3Si$ (<–150 °C), $\beta-U_3Si$ (~–150–760 °C), $\gamma-U_3Si$ (~760–930 °C), $UC_{1\pm x}$, $\zeta-U_2C_3$, $\alpha-UC_{2-x}$, $\beta-UC_{2-x}$, SiC , $\gamma-U$, $\beta-U$, $\alpha-U$, Si , C Eutectic $UC_{1\pm x}-U_3Si_2-\gamma-U$ (~950–980 °C) Eutectic $\alpha-UC_{2-x}-\beta-USi_{2-x}-U_3Si_2C_2$ (~1600 °C, ?) $UC_{1\pm x}-U_3Si_2$ is plotted: eutectic—~1660 °C Mutual solid solubilities between $UC_{1\pm x}$ and SiC are negligible. At 1000 °C the interaction between $UC_{1\pm x}$ and Si leads to the formation of USi_{2-x} .	[138, 242, 244, 533–534, 692, 849]
C–Si–V	Plotted at 800 and 1000 °C: V_2SiC , V_2SiC_2 (predicted $M_{n+1}AX_n$ -phases, ?), $V_5Si_3C_{1-x}$ (extended solid solution based on V_5Si_3 , <2010 °C, ?), $V_{3+x}Si$ (<1925 °C), V_6Si_5 (1160–1670 °C), VSi_2 (<~1675 °C), $\alpha-V_{2+x}C$, $\beta-V_{2+x}C$, $\beta'-V_{2+x}C$, $\zeta-V_4C_{3-x}$, $V_6C_{5\pm x}$, $V_8C_{7\pm x}$, VC_{1-x} , SiC , Si , V , C $SiC-VC_{1-x}$ ($x = 0.17$) is plotted: eutectic—~2220 °C, ~38 mol.% SiC ; no mutual solubilities between the components At 800 °C the solubility of C in $V_{3+x}Si$ and that of Si in $\alpha-V_{2+x}C$ are ~2 at.%. Graphite is in equilibrium with $SiC + VC_{1-x}$.	[244, 267, 393–394, 503, 744–745, 748–750]
C–Si–W	Plotted at 1800 °C: $W_xSi_yC_z$ (or $W_{5-x}Si_{3-y}C_{x+y}$, ?), W_5Si_{3+x} (<2095–2320 °C), WSi_2 (<2020–2160 °C), $\beta-W_{2+x}C$, $\delta-WC_{1\pm x}$, SiC , W , Si , C Graphite is in equilibrium with $SiC + \delta-WC_{1\pm x}$. In vacuum the interaction between graphite and WSi_2 begins at ~1500 °C (2 h contact exposure) and results in the formation of SiC and $W_xSi_yC_z$. At 1100–1900 °C the interaction between SiC and metal W results in the formation of $\delta-WC_{1\pm x}$, W_5Si_{3+x} and WSi_2 .	[138, 242, 419, 463, 487, 503, 819, 912]
C–Si–Zr	Plotted at 1000–1700 °C: $Zr_5Si_3C_x$ ($0 < x \leq \sim 0.4$ (1200 °C) and $0 < x \leq \sim 0.7$ (1700 °C), solid solution based on Zr_5Si_3 , at least at 1745–2180 °C, ?), Zr_3Si (<1650 °C), Zr_2Si (<1925 °C), Zr_3Si_2 (<2215–2220 °C), $\alpha-Zr_5Si_4$ (<1860 °C), $\beta-Zr_5Si_4$ (1860–2250 °C), $\alpha-ZrSi$ (<1460 °C), $\beta-ZrSi$ (1460–2210 °C), $ZrSi_2$ (<1620 °C), ZrC_{1-x} , SiC , $\alpha-Zr$, $\beta-Zr$, Si , C C stabilizes the structure of Zr_5Si_3 at low temp.; the solubility of C in other Zr silicides is low. Graphite is in equilibrium with $SiC + ZrC_{1-x}$.	[242, 244, 418–419, 487, 503, 510–512, 689]

(continued)

Table 2.14 (continued)

System	Type of phase diagram (temperature and composition sections, constituent phases or phase fields) and/or character of interphase interaction and materials compatibility	References
C–Sm–U	No diagram plot UC _{1±x} –SmC _{1–x} monocarbide continuous solid solution or extended solid solution based on UC _{1±x} .	[391]
C–Sn–Ti	Plotted partially at 1600 °C: Ti ₂ SnC, Ti ₃ SnC ₂ (M _{n+1} AX _n -phases), α-Ti ₆ Sn ₅ (<790 °C), β-Ti ₆ Sn ₅ (790–1490 °C), Ti ₅ Sn ₃ (<1505 °C), Ti _{2–x} Sn (<1550 °C), Ti _{3+x} Sn (<1670 °C), TiC _{1–x} , α-Ti, β-Ti, α-Sn, β-Sn, C	[680–681, 744–745, 860, 984]
C–Sn–Zr	No diagram plot Zr ₂ SnC (M _{n+1} AX _n -phase), Zr ₅ Sn ₃ C, ?	[680–681, 744–745, 860]
C–Ta–Tc	Plotted schematically	[840]
C–Ta–Th	Plotted at 1500 °C: ThC _{1±x} , γ-ThC _{2–x} , α-Ta _{2+x} C, TaC _{1–x} , α-Th, β-Th, Ta, C The mutual solid solubilities in the pairs of metals and their carbides are very low. Graphite is in equilibrium with γ-ThC _{2–x} + TaC _{1–x} .	[244, 391]
C–Ta–Ti	Plotted at 1500–3200 °C: (Ta,Ti)C _{1–x} (TaC _{1–x} –TiC _{1–x} monocarbide continuous solid solution with the critical point of the miscibility gap calculated to be <0 °C), α-(Ta,Ti) _{2+x} C (low temp. semicarbide extended solid solution based on α-Ta _{2+x} C, the solubility of Ti varies: from ~6 to ~28 at.% at 1500–1800 °C and ~2–30 at.% at 2000 °C), β-(Ta,Ti) _{2±x} C (high temp. semicarbide extended solid solution based on β-Ta _{2±x} C, the solubility of Ti varies: ~0–30 at.% at 2400–2600 °C, ~0–20 at.% at 3000 °C and ~0–10 at.% at 3200 °C), (β-Ti, Ta), C Graphite is in equilibrium with (Ta,Ti)C _{1–x} .	[138, 242, 391, 419, 440, 468, 513, 662, 747, 813, 837, 881]
C–Ta–Ti–U	TaC _{1–x} –TiC _{1–x} –UC _{1±x} is plotted at 2000–2050 °C: (Ta,Ti,U)C _{1–x} (TaC _{1–x} –TiC _{1–x} –UC _{1±x} extended solid solution based on TaC _{1–x} –TiC _{1–x} and TaC _{1–x} –UC _{1±x} monocarbide continuous solid solutions with great miscibility gap because of low mutual solubilities in the TiC _{1–x} –UC _{1±x} system)	[391]
C–Ta–Ti–W	TaC _{1–x} –TiC _{1–x} –δ-WC _{1±x} is plotted at 1450, 2200 and 2500 °C: (Ta,Ti,W)C _{1–x} (TaC _{1–x} –TiC _{1–x} –δ-WC _{1±x} extended solid solution based on TaC _{1–x} –TiC _{1–x} monocarbide continuous solid solution) The solubilities of δ-WC _{1±x} in TaC _{1–x} and TiC _{1–x} are ~10 and ~35 mol.%, respectively; the solubilities of TaC _{1–x} and TiC _{1–x} in δ-WC _{1±x} are low.	[250, 419, 465, 589]

(continued)

Table 2.14 (continued)

System	Type of phase diagram (temperature and composition sections, constituent phases or phase fields) and/or character of interphase interaction and materials compatibility	References
C-Ta-U	Plotted at 1200 and 1700 °C: (Ta,U)C _{1-x} (TaC _{1-x} -UC _{1±x} monocarbide continuous solid solution), α-Ta _{2+x} C, ζ-U ₂ C ₃ , α-UC _{2-x} , β-UC _{2-x} , U, Ta, C Depend. on compos., graphite is in equilibrium with (Ta,U)C _{1-x} or (Ta,U)C _{1-x} + UC _{2-x} ; the compos. of (Ta,U)C _{1-x} in equilibrium with C + UC _{2-x} is corresp. to (Ta _{0.78} U _{0.22})C _{0.99} (at 1700 °C) and (Ta _{0.85} U _{0.15})C _{1-x} (at 2200 °C), and shifts to lower U concentrations with temp. increase. At 1400 °C (66 h exposure) no appreciable reaction is occurred on the contact surface between metal Ta and UC _{1.06} , at 1800 °C (3 h exposure)—the interaction is noticeable.	[138, 242, 391, 812, 822]
C-Ta-U-V	TaC _{1-x} -VC _{1-x} -UC _{1±x} is plotted at 2000–2050 °C: (Ta,V,U)C _{1-x} (TaC _{1-x} -VC _{1-x} -UC _{1±x} extended solid solution based on TaC _{1-x} -VC _{1-x} and TaC _{1-x} -UC _{1±x} monocarbide continuous solid solutions with great miscibility gap because of low mutual solubilities in the pair VC _{1-x} -UC _{1±x})	[391]
C-Ta-U-Zr	TaC _{1-x} -ZrC _{1-x} -UC _{1±x} is plotted at 2050 °C: (Ta,Zr,U)C _{1-x} (TaC _{1-x} -ZrC _{1-x} -UC _{1±x} monocarbide continuous solid solution) At ~2100 °C (U _{0.5} Zr _{0.5})C _{1±x} is compatible for periods of up to 35 min. with metal Ta.	[391, 812]
C-Ta-V	Plotted at 1400 °C: Ta _{2±y} VC _{2-x} (Ta _{1.80±2.04} V _{1.0±0.96} C _{1.74±1.80} at 1650 °C), (Ta,V)C _{1-x} (TaC _{1-x} -VC _{1-x} monocarbide continuous solid solution), (Ta,V) _{2±x} C (α-Ta _{2+x} C-β-V _{2±x} C semicarbide continuous solid solution), (Ta,V), C TaC _{1-x} -VC _{1-x} is plotted: miscibility gap (critical point—~1300 °C at ~Ta _{0.4} V _{0.6} C _{1-x} , at 1000 °C ranges from ~Ta _{0.85} V _{0.15} C _{1-x} to ~Ta _{0.05} V _{0.95} C _{1-x}). Graphite is in equilibrium with (Ta,V)C _{1-x} .	[391, 723, 813, 837]
C-Ta-V-W	α-Ta _{2+x} C-β-V _{2±x} C-α-W _{2+x} C is plotted at 1650 and 2000 °C: (Ta,V,W) _{2±x} C (extended solid solution based on α-Ta _{2+x} C-β-V _{2±x} C and β-V _{2±x} C-α-W _{2+x} C semicarbide continuous solid solutions), (Ta,V,W) _{2±x} C + (Ta,V,W)C _{1-x} + (Ta,V,W), (Ta,V,W)C _{1-x} + (Ta,V,W)	[435]

(continued)

Table 2.14 (continued)

System	Type of phase diagram (temperature and composition sections, constituent phases or phase fields) and/or character of interphase interaction and materials compatibility	References
C-Ta-W	Plotted at 1500–3500 °C: $(\text{Ta,W})\text{C}_{1-x}$ (TaC_{1-x} – γ - WC_{1-x} monocarbide continuous solid solution at temp. ~ 2500 – 2750 °C, or monocarbide extended solid solution based on TaC_{1-x} at temp. $\leq \sim 2500$ °C and $\geq \sim 2750$ °C with the max solubility of W corresp. to compos.: $\sim (\text{Ta}_{0.9}\text{W}_{0.1})\text{C}_{1-x}$ at 1500 °C, $\sim (\text{Ta}_{0.8}\text{W}_{0.2})\text{C}_{1-x}$ at 1800 °C and $\sim (\text{Ta}_{0.7}\text{W}_{0.3})\text{C}_{1-x}$ at 2000 °C), $(\text{Ta,W})_{2\pm x}\text{C}$ (β - $\text{Ta}_{2\pm x}\text{C}$ – γ - $\text{W}_{2\pm x}\text{C}$ semicarbide continuous solid solution in the limited range of temp. ~ 2460 – 2790 °C), α -($\text{Ta,W})_{2\pm x}\text{C}$ (semicarbide extended solid solution based on α - $\text{Ta}_{2\pm x}\text{C}$ at temp. $\leq \sim 1950$ – 2200 °C), β -($\text{Ta,W})_{2\pm x}\text{C}$ (semicarbide extended solid solution based on β - $\text{Ta}_{2\pm x}\text{C}$ at ~ 1950 – 2450 °C and ~ 2750 – 3400 °C), α -($\text{W,Ta})_{2\pm x}\text{C}$ (semicarbide extended solid solution based on α - $\text{W}_{2\pm x}\text{C}$ at temp. ~ 1250 – 2100 °C), β -($\text{W,Ta})_{2\pm x}\text{C}$ (semicarbide extended solid solution based on β - $\text{W}_{2\pm x}\text{C}$ at temp. ~ 2100 – 2450 °C), γ -($\text{W,Ta})_{2\pm x}\text{C}$ (semicarbide extended solid solution based on γ - $\text{W}_{2\pm x}\text{C}$ at temp. ~ 2300 – 2450 °C), δ - $\text{WC}_{1\pm x}$ (max. solubility of Ta is ~ 4 at.% at 2760 °C), ζ - $\text{Ta}_4\text{C}_{3-x}$, $\text{Ta}_6\text{C}_{5\pm x}$, (Ta,W), C Eutectic β -($\text{Ta,W})_{2\pm x}\text{C}$ –(Ta,W) (2860 °C, ~ 25 at.% W, ~ 11 at.% C) Depend. on compos., graphite is in equilibrium with δ - $\text{WC}_{1\pm x}$ + ($\text{Ta,W})\text{C}_{1-x}$ or ($\text{Ta,W})\text{C}_{1-x}$.	[138, 242, 391, 419, 514, 591, 723, 773, 801–804, 827, 837]
C-Ta-Zr	Plotted at 1000–3900 °C: $(\text{Ta,Zr})\text{C}_{1-x}$ (TaC_{1-x} – ZrC_{1-x} monocarbide continuous solid solution at temp. ~ 940 – 3400 °C), α -($\text{Ta,Zr})_{2\pm x}\text{C}$ (semicarbide extended solid solution based on α - $\text{Ta}_{2\pm x}\text{C}$ at temp. $\leq \sim 2100$ °C with the solid solubility of Zr—up to ~ 12 at.% at temp. 1775 – 1820 °C), β -($\text{Ta,Zr})_{2\pm x}\text{C}$ (semicarbide extended solid solution based on β - $\text{Ta}_{2\pm x}\text{C}$ at 1930 – 3300 °C with the solid solubility of Zr—up to ~ 14 at.% at 2500 °C), (Ta,β -Zr), C Eutectic $(\text{Ta,Zr})\text{C}_{1-x}$ –(Ta,β -Zr) (~ 1800 °C) TaC_{1-x} – ZrC_{1-x} is plotted: miscibility gap (critical point— ~ 940 °C at $\sim \text{Ta}_{0.65}\text{Zr}_{0.35}\text{C}_{1-x}$ to $\sim \text{Ta}_{0.95}\text{Zr}_{0.05}\text{C}_{1-x}$). Graphite is in equilibrium with $(\text{Ta,Zr})\text{C}_{1-x}$.	[138, 242, 391, 419, 421, 423, 468, 515, 622, 805–807, 813, 837]
C-Tb-U	No diagram plot $\text{UC}_{1\pm x}$ – TbC_{1-x} monocarbide continuous solid solution, or extended solid solution based on $\text{UC}_{1\pm x}$ (?).	[391]
C-Tc-Ti	Plotted schematically	[840]
C-Tc-U	Plotted at 1500 °C: UTcC_2 (<1800 °C), $\text{UTc}_3\text{C}_{1-x}$ ($0.55 \leq x \leq 0.65$, ?), $\text{UTc}_3\text{C}_{1+x}$ (?), UTc_2 , TcC_{1-x} (or $\text{Tc}_{3\pm x}\text{C}$, ?), $\text{UC}_{1\pm x}$, ζ - U_2C_3 , α - UC_{2-x} , β - UC_{2-x} , α -U, β -U, γ -U, Tc, C	[391]

(continued)

Table 2.14 (continued)

System	Type of phase diagram (temperature and composition sections, constituent phases or phase fields) and/or character of interphase interaction and materials compatibility	References
C–Tc–V	Plotted schematically	[840]
C–Tc–W	Plotted schematically	[840]
C–Tc–Zr	Plotted schematically	[840]
C–Th–Ti	Plotted at 1500 °C: ThC _{1±x} , α-ThC _{2–x} , β-ThC _{2–x} , γ-ThC _{2–x} , TiC _{1–x} , α-Ti, β-Ti, α-Th, β-Th, C The solid solubilities of metal Th and Th carbides in TiC _{1–x} and those of TiC _{1–x} in metal Th and Th carbides are low.	[391]
C–Th–U	Plotted at 1000–1800 °C: (U,Th)C _{1±x} (UC _{1±x} –ThC _{1±x} monocarbide continuous solid solution based on UC _{1±x} –β-UC _{2–x} , α-Th–ThC _{1±x} and ThC _{1±x} –γ-ThC _{2–x} continuous solid solutions with specific miscibility gaps, homog. range (limits) at 1800 °C: ~UC _{0.9} –UC _{1.9} –ThC _{1.9} –ThC _{0.2} with two miscibility gaps (two-phase regions) UC _{1.1} –(U _{0.9} Th _{0.1})C _{1.4} –UC _{1.7} and ThC _{1.1} –(U _{0.15} Th _{0.85})C _{1.2} –ThC _{1.3}), at temp. <1700 °C—separated regions based on UC _{1±x} , γ-ThC _{2–x} , ThC _{1±x} and α-Th solid solutions), α-(U,Th)C _{2–x} (dicarbide extended solid solution based on α-UC _{2–x}), β-(Th,U)C _{2–x} (dicarbide extended solid solution based on β-ThC _{2–x}), α-(Th,U)C _{2–x} (dicarbide extended solid solution based on α-ThC _{2–x}), ζ-U ₂ C ₃ , α-Th, β-Th, γ-U, C UC _{1±x} (x = 0)–ThC _{1±x} (x = 0) is plotted: no mutual solubilities at 500 °C, the critical point of the miscibility gap—~1600 °C, (U _{0.5} Th _{0.5})C _{1.0} (the compos. corresp. to the min. melt. point of the (U,Th)C _{1±x} phase (x = 0)—2200 °C).	[138, 242, 391, 516–517]
C–Th–U–Zr	UC _{1±x} –ThC _{1±x} –ZrC _{1–x} is plotted at 2000 °C: (U,Th,Zr)C _{1±x} (UC _{1±x} –ThC _{1±x} –ZrC _{1–x} extended solid solution based on UC _{1±x} –ThC _{1±x} and UC _{1±x} –ZrC _{1–x} continuous solid solutions with great miscibility gap because of very low mutual solubilities in the pair ThC _{1±x} –ZrC _{1–x})	[391]
C–Th–W	Plotted at 1500 °C: ThC _{1±x} , γ-ThC _{2–x} , α-W _{2+x} C, δ-WC _{1±x} , β-Th, W, C The solubilities of Th carbides in W carbides and those of W carbides in Th carbides are low.	[138, 391]
C–Th–Y	Plotted at 1600 °C: (Th,Y)C _{1–x} (ThC _{1±x} –YC _{1±x} monocarbide continuous solid solution), (Th,Y)C _{2±x} (γ-ThC _{2–x} –β-YC _{2±x} dicarbide continuous solid solution), β-Y ₂ C _{3–x} , β-Th, β-Y, C Graphite is in equilibrium with (Th,Y)C _{2±x} .	[391]
C–Th–Zr	Plotted at 1100 and 1500 °C: ThC _{1±x} , α-ThC _{2–x} , β-ThC _{2–x} , γ-ThC _{2–x} , ZrC _{1–x} , α-Th, β-Th, α-Zr, β-Zr, C The solid solubilities of metal Th and Th carbides in ZrC _{1–x} and those of ZrC _{1–x} in metal Th and Th carbides are low. Graphite is in equilibrium with γ-ThC _{2–x} + ZrC _{1–x} .	[391, 518–520]

(continued)

Table 2.14 (continued)

System	Type of phase diagram (temperature and composition sections, constituent phases or phase fields) and/or character of interphase interaction and materials compatibility	References
C–Ti–Ti	No diagram plot Ti_2TiC ($\text{M}_{n+1}\text{AX}_n$ -phase), Ti_3TiC , ?	[680–681, 744–745, 860]
C–Ti–U	Plotted at 1500 °C: $\text{UC}_{1\pm x}$, $\zeta\text{-U}_2\text{C}_3$, $\alpha\text{-UC}_{2-x}$, $\beta\text{-UC}_{2-x}$, TiC_{1-x} , $\alpha\text{-Ti}$, $\beta\text{-Ti}$, $\alpha\text{-U}$, $\beta\text{-U}$, $\gamma\text{-U}$, C The max. solid solubilities of U carbides in TiC_{1-x} and those of TiC_{1-x} in U carbides are low. Graphite is in equilibrium with $\zeta\text{-U}_2\text{C}_3 + \text{TiC}_{1-x}$.	[242, 391]
C–Ti–U–Zr	$\text{UC}_{1\pm x}\text{-TiC}_{1-x}\text{-ZrC}_{1-x}$ is plotted at 2000–2050 °C: $(\text{U,Ti,Zr})\text{C}_{1\pm x}$ ($\text{UC}_{1\pm x}\text{-TiC}_{1-x}\text{-ZrC}_{1-x}$ extended solid solution based on $\text{TiC}_{1-x}\text{-ZrC}_{1-x}$ and $\text{UC}_{1\pm x}\text{-ZrC}_{1-x}$ monocarbide continuous solid solutions with great miscibility gap because of low mutual solubilities in the pair $\text{UC}_{1\pm x}\text{-TiC}_{1-x}$)	[391]
C–Ti–V	Plotted at 1000–2700 °C: $(\text{V,Ti})\text{C}_{1-x}$ ($\text{VC}_{1-x}\text{-TiC}_{1-x}$ monocarbide continuous solid solution at temp. ≤ 2625 °C; the compos. of the phase at the min. melt point— $\sim (\text{V}_{0.9}\text{Ti}_{0.1})\text{C}_{0.8}$), $\beta\text{-(V,Ti)}_{2\pm x}\text{C}$ (semicarbide extended solid solution based on $\beta\text{-V}_{2\pm x}\text{C}$ at temp. ≤ 2000 °C; the max. solubility of Ti corresp. to compos. $(\text{V}_{0.82\pm 0.93}\text{Ti}_{0.07\pm 0.18})_{2\pm x}\text{C}$), $\beta'\text{-V}_{2+x}\text{C}$, $\zeta\text{-V}_4\text{C}_{3-x}$, $\text{V}_6\text{C}_{5\pm x}$, $\text{V}_8\text{C}_{7\pm x}$, $(\beta\text{-Ti, V})$, C VC_{1-x} ($x = 0.12$)– TiC_{1-x} ($x \approx 0$) is plotted: completely soluble in each other Graphite is in equilibrium with $(\text{V,Ti})\text{C}_{1-x}$.	[138, 242, 391, 419, 425, 521, 615, 810, 813, 815, 837, 1008]
C–Ti–W	Plotted at 1500–3100 °C: $\text{Ti}_2\text{W}_4\text{C}_{3-x}$ ($0 < x < 1$, at least at 1100 °C, ?), $(\text{Ti,W})\text{C}_{1-x}$ (extended solid solution based on TiC_{1-x} at temp. < 2530 °C with the max. solubility of W corresp. to compos. $(\text{Ti}_{0.7}\text{W}_{0.3})\text{C}_{1-x}$ at 1500 °C, $(\text{Ti}_{0.45}\text{W}_{0.55})\text{C}_{1-x}$ at 2000 °C and $(\text{Ti}_{0.3}\text{W}_{0.7})\text{C}_{1-x}$ at 2400 °C, or $\text{TiC}_{1-x}\text{-}\gamma\text{-WC}_{1-x}$ monocarbide continuous solid solution at temp. $\sim 2530\text{--}2780$ °C with max. melt. point 3130 °C corresp. to $(\text{Ti}_{0.55}\text{W}_{0.45})\text{C}_{0.75}$), $\alpha\text{-W}_{2+x}\text{C}$, $\beta\text{-W}_{2+x}\text{C}$, $\gamma\text{-W}_{2\pm x}\text{C}$, $\delta\text{-WC}_{1\pm x}$, $(\beta\text{-Ti,W})$, C Eutectic $(\text{Ti,W})\text{C}_{1-x}\text{-}\gamma\text{-W}_{2\pm x}\text{C-W}$ (2680 °C, 13 at.% Ti, 23 at.% C) $\text{TiC}_{1-x}\text{-W}$ is plotted: eutectic— $\sim 2650\text{--}2700$ °C, $\sim 24\text{--}28$ mol.% TiC_{1-x} ($\sim 19\text{--}22$ at.% C) $(\text{Ti}_{0.5}\text{W}_{0.5})\text{C}_{1-x}\text{-C}$ is plotted: eutectic—3030 °C, ~ 56 at.% C	[138, 242, 391, 522, 662, 773, 827, 835, 837, 848, 1014]

(continued)

Table 2.14 (continued)

System	Type of phase diagram (temperature and composition sections, constituent phases or phase fields) and/or character of interphase interaction and materials compatibility	References
C–Ti–Zr	Plotted at 600, 1500 and 2100 °C: (Ti,Zr)C _{1-x} (TiC _{1-x} –ZrC _{1-x} monocarbide continuous solid solution at higher temp., or monocarbide extended solid solutions based on TiC _{1-x} and ZrC _{1-x} at lower temp.), (β-Ti,β-Zr), C ZrC _{1-x} –TiC _{1-x} is plotted: miscibility gap in the solid state (critical point—~2000 °C, at ~Zr _{0.2 ÷ 0.4} Ti _{0.6 ÷ 0.8} C _{1-x} , gap width at 1500 °C—from Zr _{0.1 ÷ 0.2} Ti _{0.8 ÷ 0.9} C _{1-x} to Zr _{0.8} Ti _{0.2} C _{1-x}) Depend. on temp., graphite is in equilibrium with (Zr,Ti)C _{1-x} or (Zr,Ti)C _{1-x} + (Ti,Zr)C _{1-x} .	[138, 242, 391, 424–425, 626, 813, 816, 817]
C–Ti–Zr	No diagram plot Zr ₂ TiC (M _{n+1} AX _n -phase)	[680–681, 744–745, 860]
C–Tm–U	No diagram plot UC _{1±x} –TmC _{1-x} monocarbide continuous solid solution or extended solid solution based on UC _{1±x}	[391]
C–U–V	Plotted at 1600 °C: UVC ₂ (<1800 °C), α-V _{2+x} C, β-V _{2±x} C, β'-V _{2+x} C, ζ-V ₄ C _{3-x} , V ₆ C _{5±x} , V ₈ C _{7±x} , VC _{1-x} , UC _{1±x} , ζ-U ₂ C ₃ , α-UC _{2-x} , β-UC _{2-x} , α-U, β-U, γ-U, V, C The solubilities of U carbides in V carbides and those of V carbides in U carbides are low. Graphite is in equilibrium with α-UC _{2-x} + VC _{1-x} . At 1000 °C (66 h exposure) the carburization of metal V is occurred on the contact surface with UC _{1.06} , at 1400 °C (66 h exposure)—the interaction is significant.	[242, 391, 822]
C–U–W	Plotted at 1700 and 2200 °C: η-UWC _{2-x} (x ≈ 0.3, from 2150 °C to ~2570–2580 °C, a low C form of UWC ₂), UWC ₂ (<2570–2580 °C, ?), U ₄ W ₄ C ₇ (or UWC _{1.75} , ≤ ~2300 °C), α-W _{2+x} C, δ-WC _{1±x} , UC _{1±x} , ζ-U ₂ C ₃ , α-UC _{2-x} , β-UC _{2-x} , U, W, C The homog. ranges of ternary phases are very small. The solubilities of U carbides in W carbides and those of W carbides in U carbides are low. Depend. on compos., graphite is in equilibrium with α-UC _{2-x} + UWC _{2-x} , or δ-WC _{1±x} + UWC _{2-x} .	[138, 242, 391, 612, 620, 812]
C–U–W–Zr	No diagram plot At ~2100 °C (U _{0.5} Zr _{0.5})C _{1±x} is compatible for periods of up to 35 min. with metal W.	[812]
C–U–Y	Plotted at 1600 °C: (U,Y)C _{1±x} (UC _{1±x} –YC _{1±x} monocarbide continuous solid solution), β-(Y,U)C _{2±x} (dicarbide extended solid solutions based on β-UC _{2-x} and β-YC _{2±x} at temp. <~1800 °C, or β-UC _{2-x} –β-YC _{2±x} continuous solid solution at higher temp.), ζ-U ₂ C ₃ , β-Y ₂ C _{3-x} , α-U, β-U, γ-U, α-Y, β-Y, C	[138, 391]

(continued)

Table 2.14 (continued)

System	Type of phase diagram (temperature and composition sections, constituent phases or phase fields) and/or character of interphase interaction and materials compatibility	References
C–U–Yb	No diagram plot UC _{1±x} –YbC _{1–x} monocarbide continuous solid solution or extended solid solution based on UC _{1±x} .	[391]
C–U–Zr	Plotted at 1700–3420 °C: (U,Zr)C _{1–x} (UC _{1±x} –ZrC _{1–x} monocarbide continuous solid solution), ζ–U ₂ C ₃ , α–UC _{2–x} , β–UC _{2–x} , α–U, β–U, γ–U, α–Zr, β–Zr, C UC _{1±x} (x = 0)–ZrC _{1–x} (x = 0.19) is plotted: completely soluble in each other α–UC _{2–x} (β–UC _{2–x})–ZrC _{1–x} (x ≈ 0) is plotted: quasi-eutectic—2410 °C, ~80 mol.% β–UC _{2–x} , (~12 at.% Zr, ~63 at.% C); at β–(U,Zr)C _{2–x} –(Zr,U)C _{1–x} –(γC) quasi-eutectic temp., max. solubility of Zr in β–(U,Zr)C _{2–x} ~ 2–4 at.% (corresp. to ~ (U _{0.94} Zr _{0.06})C _{1.94} compos.) and in (Zr,U)C _{1–x} ~ 40 at.% (corresp. to ~ 80–90 mol.% (Zr _{0.8÷0.9} U _{0.1÷0.2})C _{1.0} + ~10–20 mol.% C) At 1700–2200 °C graphite is in equilibrium with (Zr,U)C _{1–x} or (Zr,U)C _{1–x} + UC _{2–x} . At higher temp. the compos. of (Zr,U)C _{1–x} , which is in equilibrium with C + UC _{2–x} , shifts to lower U concentrations from ~ (Zr _{0.6÷0.65} U _{0.35÷0.4})C _{1–x} (at 1700 °C) to ~ (Zr _{0.7÷0.8} U _{0.2÷0.3})C _{1–x} (at 2000–2200 °C). At 1000 °C (66 h exposure) no appreciable reaction was occurred on the contact surface of metal Zr with UC _{1.06} , at 1400 °C (66 h exposure)—small reaction zone was found.	[138, 242, 391, 436, 520, 523–527, 822]
C–V–W	Plotted at 1500–2600 °C: (V,W)C _{1–x} (monocarbide extended solid solution based on VC _{1–x} at temp. < ~ 2600 °C, VC _{1–x} –WC _{1–x} monocarbide continuous solid solution at temp. ~ 2600–2700 °C), β–(V,W) _{2±x} C (β–V _{2±x} C–β–W _{2±x} C semicarbide continuous solid solution), δ–WC _{1±x} , (V,W), C Depend. on compos., graphite is in equilibrium with δ–WC _{1±x} + (V,W)C _{1–x} , or (V,W)C _{1–x} .	[138, 242, 391, 528, 773, 827, 837]
C–V–Zr	Plotted at 1000 °C: ZrV _{2–x} (<1280–1300 °C), ZrC _{1–x} , α–V _{2+x} C, β–V _{2+x} C, β'–V _{2+x} C, ζ–V ₄ C _{3–x} , V ₆ C _{5±x} , V ₈ C _{7±x} , VC _{1–x} , α–Zr, β–Zr, V, C VC _{1–x} (x = 0.12)–ZrC _{1–x} (x ≈ 0) is plotted: eutectic—~ 2460–2530 °C, ~ 23–34 mol.% ZrC _{1–x} ; at the eutectic temp. the solubility of ZrC _{1–x} in VC _{1–x} is ~ 2.5–5.0 mol.% and that of VC _{1–x} in ZrC _{1–x} is ~ 8.0–8.5 mol.%.	[244, 391, 425, 487, 813]

(continued)

Table 2.14 (continued)

System	Type of phase diagram (temperature and composition sections, constituent phases or phase fields) and/or character of interphase interaction and materials compatibility	References
C–W–Zr	Plotted at 1100–2600 °C: (Zr,W)C _{1-x} (ZrC _{1-x} –γ-WC _{1-x} monocarbide continuous solid solution at temp. >2500 °C, or extended solid solution based on ZrC _{1-x}), ZrW ₂ (<~2160–2210 °C), α-W _{2+x} C, β-W _{2+x} C, γ-W _{2+x} C, δ-WC _{1±x} , α-Zr, β-Zr, W, C Eutectic (Zr,W)C _{1-x} –γ-W _{2+x} C–W (2620 °C, 65 at.% W, 26.4 at.% C) Eutectic (Zr,W)C _{1-x} –ZrW ₂ –β-Zr (≤1740 °C, 7 at.% W, 3.5 at.% C) ZrC _{1-x} –W is plotted: eutectic—2800 °C, ~30 mol.% ZrC _{1-x} ; the solubility of W in ZrC _{1-x} is ~7 mol.% The solubility of Zr in γ-W _{2+x} C is 3.5 mol.%. At higher temp. graphite is in equilibrium with single solid phase (Zr,W)C _{1-x} .	[242, 391, 429–430, 529, 591, 647–648, 773, 827, 837]

^a See notes to Table 2.13

The results obtained by Wang et al. [646] indicate that at room temperature surface energy of graphene, graphene oxide and natural graphite flakes are 47, 62 and 55 mJ m⁻², respectively. Before, a 150 mJ m⁻² value for the surface energy of the basal plane of graphite was measured at room temperature by wetting experiments [910]. The formation of a surface-orientated perpendicular to the basal plane needs the rupture of C–C chemical bonds. The surface energy for this orientation has not been determined experimentally, but is expected to be an order of magnitude higher than that of the basal plane. In the case of vitreous carbon, the value was measured and found to be 32 mJ m⁻² [910]. This is five times lower than that of the graphite basal plane and may be explained by the low density of vitreous carbon. The average static contact angles of graphene/graphite with some liquids, which were measured by the droplet on the film surface at room temperature, are listed in Table 2.15 [646, 909]. The quantitative characteristics of the

Table 2.15 Average static contact angles (in degrees) of graphite, graphene oxide and graphene with some liquids measured by the droplet on the film surface at room temperature [646]^a

Materials	Water	Formamide	Diiodometane	Ethylene glycol	Glycerol
Graphite	98	45	22	56	67
Graphene oxide	67	19	39	22	50
Graphene	127	80	43	76	111

^a For water, formamide and glycerol the contact angles on de-ashed natural graphite (in degrees) were 71.5–86.6, 46.5–60.7 and 61.3–77.8, respectively, with measured surface tensions at 20.0 ± 0.5 °C: water—72.6, formamide—58.7, ethylene glycol—47.6 and glycerol—63.7, 10⁻³ N m⁻¹ [909]

Table 2.16 Wettability of graphite materials by some non-ferrous metal alloys (melts) in vacuum [530, 661, 910]

Alloy composition	Wetting contact angle, degree	Temperature, °C
Ag–0.1 at.% Ti	85	1000
Ag–1.0 at.% Ti	7	1000
Al–1.7–2.0 at.% Ti	142–145	1000
	140	1100
	75	1200
Al–12 at.% Si	145–150	1000
	140–142	1150
	97	1200
	30	1300
Cu–0.01 at.% Cr	140	1150
Cu–0.1 at.% Cr	90	1150
Cu–0.6 at.% Cr	84	1150
Cu–1.0 at.% Cr	45 ^b	1130
	20–30 ^c	1500
Cu–6.1 at.% Cr	40	1150
Cu–12.0 at.% Cr	23	1150
Cu–1.25 at.% V	118	1150
	110	1200
	75	1250
Cu–3.75 at.% V	90	1150
	75	1200
Cu–6.2 at.% V	130	1150
	60	1200
	40	1250
Cu–2.9 at.% Sn–2.7 at.% Ti	28	1150
Cu–2.9 at.% Sn–4 at.% Ti	21	1150
Cu–5.6 at.% Sn	135	1150
Cu–5.6 at.% Sn–1.4 at.% Ti	48	1150
Cu–5.6 at.% Sn–3.95 at.% Ti	21	1150
Cu–5.6 at.% Sn–4.1 at.% Ti	10	1150
Cu–11.5 at.% Sn	135	1150
Cu–11.5 at.% Sn–0.75 at.% Ti	70	1150
Cu–11.5 at.% Sn–1.45 at.% Ti	22	1150
Cu–11.5 at.% Sn–2.9 at.% Ti	14	1150
Cu–20 at.% Sn	160	1150
Cu–50 at.% Sn	147	1150
Cu–5.0 at.% Ni	140	1300
Cu–9.3 at.% Ni	140	1300
Cu–9.3 at.% Ni–0.7 at.% Nb	150	1200
	140	1250
	120	1300
Cu–9.3 at.% Ni–1.4 at.% Nb	150	1200
	95	1250
	50	1300

(continued)

Table 2.16 (continued)

Alloy composition	Wetting contact angle, degree	Temperature, °C
Cu–9.3 at.% Ni–2.05 at.% Nb	5	1300
Cu–9.3 at.% Ni–3.45 at.% Nb	35	1250
Cu–9.3 at.% Ni–7.05 at.% Nb	40	1200
Cu–9.3 at.% Ni–1.25 at.% V	110	1150
	67	1200
	55	1250
Cu–9.3 at.% Ni–3.75 at.% V	115	1150
Cu–9.3 at.% Ni–6.2 at.% V	70	1150
	30	1200
Cu–21.0 at.% Ni	134	1500
Cu–25.0 at.% Ni	128	1500
Cu–25.0 at.% Ni–8.0 at.% Sn–6.0 at.% W	115	1300
Cu–28.0 at.% Ni–4.0 at.% Sn–6.0 at.% W	90	1300
Cu–30.0 at.% Ni	120	1500
Cu–35.0 at.% Ni	115	1500
Cu–35.0 at.% Ni–3.0 at.% Sn–9.0 at.% W	85	1300
Cu–36.0 at.% Ni–7.0 at.% Sn–9.0 at.% W	61	1420
Cu–5.0 at.% Co	138	1300
Cu–10.2 at.% Ti	0	1150
Cu–24.0 at.% Mn	70	1200
Ni–45.4 at.% Pd	137	1240
Sn–0.9 at.% Ti	76	1150
Sn–7.1 at.% Ti	5	1150
Sn–25.0 at.% Ni	143	1500

^a For the same alloy on vitreous carbon in high vacuum, contact angle values (in degrees) are 37–45 at 1100 °C and ~40 at 1150 °C [910]

^b In Ar atmosphere

^c In Ar–5 % H₂ gas medium

Table 2.17 Wetting contact angles (in degrees) of pure molten halides MeX (Me = Li, Na, K, Rb; X = F, Cl, Br) on graphite in dry inert gas atmosphere at 1000 °C [910]

Halides	LiX	NaX	KX	RbX
Fluoride	143	139	81	—
Chloride	134	127	73	46
Bromide	—	120	73	—

wettability of graphite materials by some non-ferrous metal alloys (melts) at elevated and high temperatures are shown in Table 2.16 [530, 661, 910], and wetting characteristics in alkali metal halide–graphite systems are given in Table 2.17 [910].

The character of chemical interaction and general reactions of carbon (graphite) with common chemicals (solids, aqueous solutions) and complex gases are summarized in Table 2.18.

Table 2.18 The interaction of carbon (graphite) with some chemicals and complex gases [5, 82, 238, 531–532]

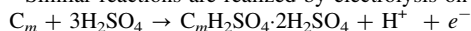
Reagent, formula	Character of chemical interaction, general reactions
Air, $N_2 + O_2$	In air the oxidation of C initiates from 450 to 500 °C and leads to the formation of gaseous oxides: $2C + O_2 \leftrightarrow 2CO$ $C + O_2 \leftrightarrow CO_2$
Water, H_2O	At ambient temp. C adsorbs water vapour from atmosphere intensively. The interaction between C and water vapour initiates from 650 to 800 °C: $C + H_2O \leftrightarrow CO + H_2$
Phosphine, PH_3	The interaction with PH_3 is initiated by electrical discharge between C electrodes: $C + PH_3 \rightarrow HCP + H_2$
Potassium hydroxide, KOH	No interaction
Potassium carbonate, K_2CO_3	During heating in ammonia containing media, the interaction results in the formation of potassium cyanide: $C + K_2CO_3 + 2NH_3 \rightarrow 2KCN + 3H_2O$
Calcium cyanamide with soda, $CaCN_2 + Na_2CO_3$	The interaction between C and calcium cyanamide—soda melt results in the formation of sodium cyanide: $C + CaCN_2 + Na_2CO_3 \rightarrow CaCO_3 + 2NaCN$
Nitric acid, HNO_3	The interaction with hot concentrated nitric acid results in the oxidation of C and formation of mellitic (also called graphitic or benzenhexacarboxylic) acid: $33C + 18HNO_3 \rightarrow 2C_6(COOH)_6 + 9CO_2 + 9N_2O + 3H_2O$
Sulphuric acid, H_2SO_4	No interaction
Hydrochloric acid, HCl	No interaction
Hydrofluoric acid, HF	No interaction
Chromic acid, $H_2CrO_4 + H_2SO_4$, or $K_2Cr_2O_7 + H_2SO_4$	The interaction results in the oxidation of C: $3C + 4H_2CrO_4 + 6H_2SO_4 \rightarrow 2Cr_2(SO_4)_3 + 3CO_2 + 10H_2O$, $3C + 2K_2Cr_2O_7 + 8H_2SO_4 \rightarrow 2Cr_2(SO_4)_3 + 2K_2SO_4 + 3CO_2 + 8H_2O$
Potassium chlorate with nitric acid, $KClO_3 + HNO_3$	The interaction results in the oxidation of C and formation of mellitic (also called graphitic or benzenhexacarboxylic) acid: $15C + 6KClO_3 + 6HNO_3 \rightarrow C_6(COOH)_6 + 3CO_2 + 3Cl_2 + 6KNO_3$
Sulphuric acid with nitric acid, $H_2SO_4 + HNO_3$	During heating, the interaction results in the formation of graphite bisulphate: $192C + 24H_2SO_4 + 2HNO_3 \rightarrow 8C_{24}HSO_4 \cdot 2H_2SO_4 + N_2O + 5H_2O^a$
Sulphuric acid with chromium trioxide, $H_2SO_4 + CrO_3$	During heating, the interaction results in the formation of graphite bisulphate: $144C + 21H_2SO_4 + 2CrO_3 \rightarrow 6C_{24}HSO_4 \cdot 2H_2SO_4 + Cr_2(SO_4)_3 + 6H_2O^a$
Sulphuric acid with potassium permanganate,	During heating, the interaction results in the formation of graphite bisulphate:

(continued)

Table 2.18 (continued)

Reagent, formula	Character of chemical interaction, general reactions
$\text{H}_2\text{SO}_4 + \text{KMnO}_4$	$240\text{C} + 33\text{H}_2\text{SO}_4 + 2\text{KMnO}_4 \rightarrow 10[\text{C}_{24}\text{HSO}_4 \cdot 2\text{H}_2\text{SO}_4] + 2\text{MnSO}_4 + \text{K}_2\text{SO}_4 + 8\text{H}_2\text{O}^a$
Aluminium chloride, AlCl_3	During heating, the interaction results in the formation of intercalation compound: $9\text{C} + \text{AlCl}_3 \rightarrow \text{C}_9 \cdot \text{AlCl}_3$
Iron (III) chloride, FeCl_3	During heating, the interaction results in the formation of intercalation compounds: $n\text{C} + \text{FeCl}_3 \rightarrow \text{C}_n \cdot \text{FeCl}_3$
Sodium amide, NaNH_2	During heating to 500–600 °C, the interaction results in the formation of sodium cyanide and molecular hydrogen: $\text{C} + \text{NaNH}_2 \leftrightarrow \text{NaCN} + \text{H}_2$
Lithium amide, LiNH_2	The interaction results in the formation of lithium cyanamide and molecular hydrogen: $\text{C} + 2\text{LiNH}_2 \leftrightarrow \text{Li}_2\text{NCN} + 2\text{H}_2$
Nitrogen–hydrogen gas mixture, $\text{N}_2 + \text{H}_2$	At higher temp. the interaction results in the formation of hydrogen cyanide: $2\text{C} + \text{N}_2 + \text{H}_2 \rightarrow 2\text{HCN}$
Fluorine–fluorine hydride mixture, $\text{F}_2 + \text{HF}$	The interaction results in the formation of carbon fluorides C_4F and CF : $2\text{C} + \text{F}_2 \rightarrow 2\text{CF}$, $8\text{C} + \text{F}_2 \rightarrow 2\text{C}_4\text{F}$

^a Similar reactions are realized by electrolysis on a graphite anode:



The self-diffusion characteristics of carbon atoms, diffusion characteristics in the carbon—element and carbon—chemical compound systems in the wide range of temperatures, and summarized data on the physico-chemical interaction of carbon with the elements of periodic table are given in Addendum.

References

1. Mendeleev DI (1947) *Osnovy khimii* (Foundations of chemistry), Vol. 1. Goskhimizdat, Moscow, Leningrad (in Russian)
2. Rao CNR (2010) *Understanding chemistry*. World Scientific, New Jersey, London
3. Lide DR, ed (2010) *CRC handbook of chemistry and physics*, 90th ed. CRC Press, Boca Raton, New York
4. Speight JG, ed (2005) *Lange's handbook of chemistry*, 16th ed. McGraw-Hill, New York
5. Nekrasov BV (1973) *Osnovy obschei khimii* (Foundations of general chemistry), 3rd ed., Vol. 1. Khimiya, Moscow (in Russian)
6. Samsonov GV, ed (1976) *Svoistva elementov* (Properties of elements), 2nd ed., Vol. 1. Metallurgiya, Moscow (in Russian)
7. Rabinovich VA, Khavin ZYa (1978) *Kratkii khimicheskii spravochnik* (Concise handbook of chemistry), 2nd ed. Khimiya, Leningrad (in Russian)

8. Bushuev YuG, Persin MI, Sokolov VA (1994) Uglerod-uglerodnye kompozitsionnye materialy (Carbon-carbon composite materials). Metallurgiya, Moscow (in Russian)
9. McEnaney B (1999) Structure and bonding in carbon materials. In: Burchell TD (ed) Carbon materials for advanced technologies, pp. 1–33. Pergamon, Elsevier, Amsterdam
10. Heimann RB, Evsyukov SE, Koga Y (1997) Carbon allotropes: a suggested classification scheme based on valence orbital hybridization. Carbon 35:1654–1658
11. Inagaki M (2000) New carbons. Elsevier, Amsterdam
12. Belenkov EA (2003) Classification of carbon structures. In: Veziroglu TN, Zaginichenko SYu, Schur DV et al (eds) Proc. 8th Int. conf. on hydrogen materials science and chemistry of carbon nanomaterials (ICHMS-2003), Sudak, Ukraine, 14–20 Sep 2003, pp. 730–733. IHSE, Kyiv
13. Shenderova OA, Barnard AS, Gruen DM (2006) Carbon family at the nanoscale. In: Shenderova OA, Gruen DM (eds) Ultrananocrystalline diamond, pp. 3–22. William Andrew, Norwich, New York
14. Falcao EHL, Wudl F (2007) Carbon allotropes: beyond graphite and diamond. J Chem Technol Biotechnol 82:524–531
15. Korshak VV, Kasatochkin VI, Sladkov AM, Kudryavtsev YuP, Usenbayev K (1961) O sinteze i svoistvakh poliatsetilena (On synthesis and properties of polyacetylene). Doklady AN SSSR 136(6):1342–1344 (in Russian)
16. Sladkov AM (2003) Karbin – tretya allotropnaya forma ugleroda (Carbyne – the third allotropic form of carbon). Nauka, Moscow (in Russian)
17. Chalifoux WA, Tykwinski RR (2010) Synthesis of polyynes to model the *sp*-carbon allotrope carbyne. Nature Chem 2:967–971
18. Tanuma S, Palnichenko A (1995) Synthesis of low density carbon crystal “carbolite” by quenching of carbon gas. J Mater Res 10(5):1120–1125
19. Belenkov EA, Shabiev FK (2007) Structure of new carbon phases from carbyne nanorings. Crystallogr Rep 52(2):343–348
20. Belenkov EA, Mavrinsky VV (2008) Crystal structure of a perfect carbyne. Crystallogr Rep 53(1):83–87
21. Belenkov EA, Ivanovskii AL, Ul'yanov SN, Shabiev FK (2005) New framework nanostructures of carbon atoms in sp^2 and sp^3 hybridized states. J Struct Chem 46(6):961–967
22. Baughman RH, Eckhardt H, Kertesz M (1987) Structure-property predictions for new planar forms of carbon: layered phases containing sp^2 and sp atoms. J Chem Phys 87(11):6687–6699
23. Haley MM, Brand SC, Pak JJ (1997) Carbon networks based on dehydrobenzoannulenes: synthesis of graphdiyne substructures. Angew Chem 36:835–838
24. Narita N, Nagai S, Suzuki S, Nakao K (1998) Optimized geometries and electronic structures of graphyne and its family. Phys Rev B 58(16):11009–11014
25. Enyashin AN, Sofronov AA, Makurin YN, Ivanovskii AL (2004) Structural and electronic properties of new α -graphyne-based carbon fullerenes. J Molec Struct 684(1):29–33
26. Zhao X, Ando Y, Liu Y, Jinno M, Suzuki T (2003) Carbon nanowire made of a long linear carbon chain inserted inside a multiwalled carbon nanotube. Phys Rev Lett 90(18):187401
27. Coluci VR, Braga SF, Legoas SB, Galvao DS, Baughman RH (2004) New families of carbon nanotubes based on graphyne motifs. Nanotechnol 15:S142–S149
28. Whittaker AG (1978) Carbon: a new view of its high-temperature behaviour. Science 200:763–764
29. Whittaker AG, Kintner PL (1985) Carbon: analysis of spherules and splats formed from the liquid state and of the forms produced by quenching gas and solid. Carbon 23(3):255–262
30. Pisula W, Feng X, Mullen K (2010) Self-organization of nanographenes. In: Guldi DM, Martin N (eds) Carbon nanotubes and related structures, pp. 405–453. Wiley-VCH, Weinheim

31. Novoselov KS, Geim AK, Morozov SV, Jiang D, Zhang Y, Dubonos SV, Grigorieva IV, Firsov AA (2004) Electric field effect in atomically thin carbon films. *Science* 306:666–669
32. Novoselov KS, Jiang D, Schedin F, Booth TJ, Khotkevich VV, Morozov SV, Geim AK (2005) Two-dimensional atomic crystals. *Proc Nat Acad Sci USA* 102(30):10451–10453
33. Neto AC, Guinea F, Peres NM (2006) Drawing conclusions from graphene. *Phys World* 11:1–5
34. Ishigami M, Chen JH, Cullen WG, Fuhrer MS, Williams ED (2007) Atomic structure of graphene on SiO₂. *Nano Lett* 7(6):1643–1648
35. Geim AK, MacDonald AH (2007) Graphene: exploring carbon flatland. *Phys Today* 8:35–41
36. Geim AK, Novoselov KS (2007) The rise of graphene. *Nature Mater* 6(3):183–191
37. Meyer JC, Geim AK, Katsnelson MI, Novoselov KS, Booth TJ, Roth S (2007) The structure of suspended graphene sheets. *Nature* 446(3):60–63
38. Geim AK (2009) Graphene: status and prospects. *Science* 324:1530–1534
39. Liu Z, Suenaga K, Harris PJF, Iijima S (2009) Open and closed edges of graphene layers. *Phys Rev Lett* 102(1):015501
40. Biswas S, Drzal LT (2010) Multilayered nano-architecture of variable sized graphene nanosheets for enhanced supercapacitor electrode performance. *ACS Appl Mater Interfaces* 2(8):2293–2300
41. Kelly BT (1981) *Physics of graphite*. Applied Science, London
42. Pierson HO (1993) *Handbook of carbon, graphite, diamond and fullerenes*. Noyes, New Jersey
43. Shulepov SV (1990) *Fizika uglegrafitovykh materialov* (Physics of carbon materials). Metallurgiya, Chelyabinsk (in Russian)
44. Shmakova ES, Lebedev YuN, Nagornyi VG (1979) Temperatur'naya ustoychivost' romboedricheskoi fazy grafita (Temperature stability of the rhombohedral graphite phase). *Izv AN SSSR Neorg Mater* 15(12):2134–2137 (in Russian)
45. Kroto HW, Heath JR, O'Brien SC, Curl RF, Smalley RE (1985) C₆₀: buckminsterfullerene. *Nature* 318:162–163
46. Radushkevich LV, Luk'yanovich VM (1952) O structure ugleroda, obrazuyuschegosya pri termicheskom razlozhenii okisi ugleroda na zheleznom kontakte (On carbon structure formed during the thermal decomposition of carbon oxide on iron contact). *Zh Fiz Khim* 26:88–95 (in Russian)
47. Osawa E (1970) Chohokozoku (Superaromaticity). *Kagaku* 25:854–863 (in Japanese)
48. Fowler PW (1993) Systematics of fullerenes and related clusters. In: Kroto HW, Walton DRM (eds) *The fullerenes*, pp. 39–51. Cambridge University Press
49. Iijima S (1991) Helical microtubules of graphitic carbon. *Nature* 354:56–58
50. Dresselhaus MS, Dresselhaus G, Eklund PC (1996) *Science of fullerenes and carbon nanotubes*. Academic Press, Elsevier, San Diego
51. Lu X, Chen Z (2005) Curved pi-conjugation, aromaticity, and the related chemistry of small fullerenes (<C₆₀) and single-walled carbon nanotubes. *Chem Rev* 105:3643–3696
52. Trefilov VI, Schur DV, Tarasov BP, Shulga YuM, Chernogorenko AV, Pishuk VK, Zaginaichenko SYu (2001) Fullereny – osnova materialov buduschego (Fullerenes as the basis of future materials). ADEF-Ukraine, Kyiv (in Russian)
53. Pokropivny VV, Ivanovskii AL (2008) New nanoforms of carbon and boron nitride. *Russ Chem Rev* 77(10):837–873
54. Yudasaka M, Iijima S (2010) Carbon nanohorn. In: Guldi DM, Martin N (eds) *Carbon nanotubes and related structures*, pp. 385–404. Wiley-VCH, Weinheim
55. Giacalone F, Martin N, Wudl F (2009) Fullerene-containing polymers: an overview. In: Martin N, Giacalone F (eds) *Fullerene polymers*, pp. 1–14. Wiley-VCH, Weinheim
56. Rettenbacher AS, Elliot B, Hudson JS, Amirkhanian A, Echegoyen L (2006) Preparation and functionalization of multilayer fullerenes (carbon nano-onions). *Chem Eur J* 12:376–387

57. Shames AI, Katz EA, Panich AM, Mogilyansky D, Mogilko E, Grinblat J, Belousov VP, Belousova IM, Ponomarev AN (2009) Structural and magnetic resonance study of astralen nanoparticles. *Diamond Relat Mater* 18:505–510
58. Krueger A (2010) Carbon materials and nanotechnology. Wiley-VCH, Weinheim
59. Wang X, Li Q, Xie J, Jin Z, Wang J, Li Y, Jiang K, Fan S (2009) Fabrication of ultralong and electrically uniform single-walled carbon nanotubes on clean substrates. *Nano Lett* 9(9):3137–3141
60. Savoskin MV, Mochalin VN, Yaroshenko AP, Lazareva NI, Konstantinova TE, Barsukov IV, Prokofiev IG (2007) Carbon nanoscrolls produced from acceptor-type graphite intercalation compounds. *Carbon* 45:2797–2800
61. Nasibulin AG, Anisimov AS, Pikhitsa PV, Jiang H, Brown P, Choi M, Kauppinen EI (2007) Investigations of nanobud formation. *Chem Phys Lett* 446:109–114
62. Okada S, Otani M, Oshiyama A (2003) Energetics and electronic structure of C₇₀-peapods and one-dimensional chains of C₇₀. *New J Phys* 5:122.1–122.11
63. Imaizumi Y, Kushida M, Arakawa Y, Arai F, Fukuda T (2006) TEM observation of the giant carbon nanotube construction using Langmuir-Blodgett films. In: Proc. 6th IEEE conf. on nanotechnology (IEEE-NANO 2006), Cincinnati, 17–20 June 2006, Vol. 2, pp. 628–631
64. Blinc R, Arcon D, Umek P, Apih T, Milia F, Rode AV (2007) Carbon nanofoam as a potential hydrogen storage material. *Phys Stat Sol B* 244(11):4308–4310
65. Mileeva ZhA, Shabalin IL, Ross DK, Bogolepov VA, Zaginaichenko SYu, Schur DV, Begenev VA, Matysina ZA (2011) Carbon nano/microstructures for hybrid hydrogen storage based on specially treated carbon fibers. In: Zaginaichenko SYu, Schur DV, Skorokhod VV, Veziroglu A, Ibrahimoglu B (eds) Carbon nanomaterials in clean-energy hydrogen systems – II, pp. 107–114. Springer, Dordrecht
66. Zhang S, Koziol KKK, Kinloch IA, Windle AH (2008) Macroscopic fibers of well-aligned carbon nanotubes by wet spinning. *Small* 4(8):1217–1222
67. Herranz MA, Martin N (2009) Polymers based on carbon nanotubes. In: Martin N, Giacalone F (eds) Fullerene polymers, pp. 271–303. Wiley-VCH, Weinheim
68. Schur DV, Shul'ga YuM, Zaginaichenko SYu (2008) Nanostrukturnye modifikatsii ugleroda (Nanostructured carbon modifications). In: Gnesin GG, Skorokhod VV (eds) Neorganicheskoe materialovedenie (Inorganic materials science), Vol. 1. Naukova Dumka, Kyiv, pp. 437–458 (in Russian)
69. Marsh H, Rodriguez-Reinoso F (2006) Activated carbon. Elsevier, Amsterdam
70. Al-Muhtaseb SA, Ritter JA (2003) Preparation and properties of resorcinol-formaldehyde organic and carbon gels. *Adv Mater* 15(2):101–114
71. Yushin G, Nikitin A, Gogotsi Y (2006) Carbide-derived carbon. In: Gogotsi Y (ed) Carbon nanomaterials, pp. 211–254. CRC Press, Taylor & Francis, Boca Raton, London
72. Shenderova OA, McGuire G (2006) Types of nanocrystalline diamond. In: Shenderova OA, Gruen DM (eds) Ultrananocrystalline diamond, pp. 79–114. William Andrew, Norwich, New York
73. Kroto H (2010) Carbyne and other myths about carbon. RSC Chemistry World. <http://www.rsc.org/chemistryworld/Issues/2010/November/CarbyneOtherMythsAboutCarbon.asp>. Accessed 20 January 2011.
74. Nakada K, Fujita M, Dresselhaus G, Dresselhaus MS (1996) Edge state in graphene ribbons: nanometer size effect and edge shape dependence. *Phys Rev B* 54(24):17954–17961
75. Braga S, Coluci VR, Legoas SB, Giro R, Galvao DS, Baughman RH (2004) Structure and dynamics of carbon nanoscrolls. *Nano Lett* 4(5):881–884
76. Trucano P, Chen R (1975) Structure of graphite by neutron diffraction. *Nature* 258:136–137
77. Lipson H, Stokes AR (1942) The structure of graphite. *Proc Royal Soc London A* 181:101–105

78. Shenderova OA, Zhirnov VV, Brenner DW (2002) Carbon nanostructures. *Crit Rev Solid State Mater Sci* 27(3/4):227–356
79. Lueking AD, Pan L, Narayanan DL, Clifford EB (2005) Effect of expanded graphite lattice in exfoliated graphite nanofiber on hydrogen storage. *J Phys Chem B* 109:12710–12717
80. Schniepp HC, Li J-L, McAllister MJ, Sai H, Herrera-Alonso M, Adamson DH, Prud'homme RK, Car R, Saville DA, Aksay IA (2006) Functionalized single graphene sheets derived from splitting graphite oxide. *J Phys Chem B* 110(17):8535–8539
81. Kim H, Macosko CW (2008) Morphology and properties of polyester / exfoliated graphite nanocomposites. *Macromol* 41:3317–3327
82. Ubbelohde AR, Lewis FA (1960) Graphite and its crystal compounds. Oxford University Press, London
83. Fialkov AS (1997) Uglerod, mezhsluevye soedineniya i kompozity na ego osnove (Carbon, intercalation compounds and composites on its basis). Aspekt-Press, Moscow (in Russian)
84. Chung DDL (1994) Carbon fibre composites. Butterworth-Heinemann, Boston
85. Edie DD, Stoner EG (1993) Effect of microstructure and shape on carbon fiber properties. In: Buckley JD, Edie DD (eds) Carbon-carbon materials and composites. Noyes, New Jersey
86. Eletskii AV, Smirnov BM (1993) Fullereny (Fullerenes). *Usp Fiz Nauk* 163(2):33–60 (in Russian)
87. Haddon RC (1993) The fullerenes: powerful carbon-based electron acceptors. In: Kroto HW, Walton DRM (eds) The fullerenes, pp. 53–61. Cambridge University Press
88. Rao CNR, Seshadri R, Govindaraj A, Sen R (1995) Fullerenes, nanotubes, onions and related carbon structures. *Mater Sci Eng R* 15(95):209–262
89. Mitchell DR, Brown RM Jr, Spires TL, Romanovicz DK, Lagow RJ (2001) The synthesis of megatubes: new dimensions in carbon materials. *Inorg Chem* 40:2751–2755
90. Rahmani A, Chadli H (2011) Structure and vibrations in C_{60} carbon peapods. In: Sattler KD (ed) Handbook of nanophysics – 2. Clusters and fullerenes, pp. 46–1–46–29. CRC Press, Taylor & Francis, Boca Raton, London
91. Schur DV, Shulga YuM, Zaginichenko SYu (2008) Uglerodnye nanostrukturnye materialy (Carbon nanostructured materials). In: Gnesin GG, Skorokhod VV (eds) Neorganicheskoe materialovedenie (Inorganic materials science), Vol. 2, Part 2, Naukova Dumka, Kyiv, pp. 530–553 (in Russian)
92. David WIF, Ibberson RM, Mathewman JC, Prassides K, Dennis TJS, Hare JP, Kroto HW, Taylor R, Walton DRM (1991) Crystal structure and bonding of ordered C_{60} . *Nature* 353:147–149
93. Buerger HB, Restori R, Schwarzenbach D (1993) Structure of C_{60} : partial orientational order in the room-temperature modification of C_{60} . *Acta Crystallogr B* 49:832–838
94. Dorset DL, McCourt MP (1994) Disorder and the molecular packing of C_{60} buckminsterfullerene: a direct electron-crystallographic analysis. *Acta Crystallogr A* 50:344–351
95. Okada S, Saito S (1999) Electronic structure and energetics of pressure-induced two-dimensional C_{60} polymers. *Phys Rev B* 59:1930–1936
96. Chen X, Yamanaka S (2002) Single-crystal X-ray structural refinement of the “tetragonal” C_{60} polymer. *Chem Phys Lett* 360:501–508
97. Chen X, Yamanaka S, Sako K, Inoue Y, Yasukawa M (2002) First single-crystal X-ray structural refinement of the rhombohedral C_{60} polymer. *Chem Phys Lett* 356:291–297
98. Narymbetov BZh, Agafonov V, Davydov VA, Kashevarova LS, Rakhmanina AV, Dzyabchenko AV, Kulakov VI, Ceolin R (2003) The crystal structure of the 2D polymerized tetragonal phase of C_{60} . *Chem Phys Lett* 367:157–162
99. Van Smaalen S, Petricek V, De Boer JL, Dusek M, Verheijen MA, Meijer G (1994) Low-temperature structure of solid C_{70} . *Chem Phys Lett* 223:323–328

100. Soldatov AV, Roth G, Dzyabchenko A, Johnels D, Lebedkin S, Meingast C, Sundqvist B, Haluska M, Kuzmany H (2001) Topochemical polymerization of C_{70} controlled by monomer crystal packing. *Science* 293:680–683
101. Seifert G, Enyashin AN, Heine T (2011) Solid-state structures of small fullerenes. In: Sattler KD (ed) *Handbook of nanophysics – 2. Clusters and fullerenes*, pp. 30–1–30–13. CRC Press, Taylor & Francis, Boca Raton, London
102. Nakamura M (2011) Clusters of fullerenes. In: Sattler KD (ed) *Handbook of nanophysics – 2. Clusters and fullerenes*, pp. 37–1–30–15. CRC Press, Taylor & Francis, Boca Raton, London
103. Zhao X, Liu Y, Inoue S, Suzuki T, Jones RO, Ando Y (2004) Smallest carbon nanotube is 3 angstroms in diameter. *Phys Rev Lett* 92:125502
104. Harris PJF (1999) *Carbon nanotube and related structures*. Cambridge University Press
105. Harris PJF (2009) *Carbon nanotube science*. Cambridge University Press
106. Li Y, Huang Y, Du S, Liu R (2001) Structures and stabilities of C_{60} -rings. *Chem Phys Lett* 335:524–532
107. Hayashi T, Kim YA, Matoba T, Esaka M, Nishimura K, Tsukada T, Endo M, Dresselhaus MS (2003) Smallest freestanding single-walled carbon nanotube. *Nano Lett* 3:887–889
108. Hornbostel B, Haluska M, Cech J, Dettlaff U, Roth S (2006) Arc discharge and laser ablation synthesis of single-walled carbon nanotubes. In: Popov VN, Lambin P (eds) *Carbon nanotubes*, pp. 1–18. Springer, Dordrecht
109. Salvétat J-P, Desarmot G, Gauthier C, Poulin P (2006) Mechanical properties of individual nanotubes and composites. In: Loiseau A, Launois P, Petit P, Roche S, Salvétat J-P (eds) *Understanding carbon nanotubes*, pp. 439–493. Springer, Berlin, Heidelberg
110. Fischer JE (2006) Carbon nanotubes: structure and properties. In: Gogotsi Y (ed) *Nanotubes and nanofibers*, pp. 1–35. CRC Press, Taylor & Francis, Boca Raton, London
111. Han J (2005) Structures and properties of carbon nanotubes. In: Meyyappan M (ed) *Carbon nanotubes*, pp. 2–24. CRC Press, Taylor & Francis, Boca Raton, London
112. Rich RL (2003) Fullerenes, endohedral fullerenes and the prediction of high boiling points. *Phys Chem Chem Phys* 5:2053–55
113. Iijima S, Yudasaka M, Yamada R, Bandow S, Suenaga K, Kokai F, Takahashi K (1999) Nano-aggregates of single-walled graphitic carbon nanohorns. *Chem Phys Lett* 309:165–170
114. Singh P, Da Ros T, Kostarelos K, Prato M, Bianco A (2010) Carbon-based nanomaterial applications in biomedicine. In: Guldi DM, Martin N (eds) *Carbon nanotubes and related structures*, pp. 199–232. Wiley-VCH, Weinheim
115. Ge M, Sattler K (1994) Observation of fullerene cones. *Chem Phys Lett* 220(3–5):192–196
116. Balaban A, Klein D, Liu X (1994) Graphitic cones. *Carbon* 32:357–359
117. Krishnan A, Dujardin E, Treacy MMJ, Hugdahl J, Lynum S, Ebbesen TW (1997) Graphitic cones and the nucleation of curved carbon surfaces. *Nature* 388:451–454
118. Naess SN, Elgsaeter A, Helgesen G, Knudsen KD (2009) Carbon nanocones: wall structure and morphology. *Sci Technol Adv Mater* 10:065002
119. Ihara S, Itoh S, Kitakami J (1993) Toroidal forms of graphitic carbon. *Phys Rev B* 47(19):12908–12911
120. Itoh S, Ihara S (1993) Toroidal forms of graphitic carbon. II. Elongated tori. *Phys Rev B* 48(11):8323–8328
121. Martel R, Shea HR, Avouris P (1999) Rings of single-walled carbon nanotubes. *Nature* 398:299
122. Rode AV, Hyde ST, Gamaly EG, Elliman RG, McKenzie DR, Bulcock S (1999) Structural analysis of a carbon foam formed by high pulse-rate laser ablation. *Appl Phys A Mater Sci Process* 69(7): S755–S758
123. Bacon R (1960) Growth, structure and properties of graphite whiskers. *J Appl Phys* 31:283–290
124. Lavin JG, Subramoney S, Ruoff RS, Berber S, Tomanek D (2002) Scrolls and nested tubes in multiwall carbon nanotubes. *Carbon* 40:1123–1130

125. Ihara S Itoh S, Kitakami J (1993) Helically coiled cage forms of graphitic carbon. *Phys Rev B* 48(8):5643–5647
126. Terrones H, Terrones M (2003) Curved nanostructured materials. *New J Phys* 5:126.1–126.37
127. Dresselhaus MS, Dresselhaus G, Sugihara K, Spain IL, Goldberg HA (1988) Graphite fibers and filaments. Springer, New York
128. Chang Y-H, Chiu H-T, Wang L-S, Wan C-Y, Peng C-W, Lee C-Y (2003) Synthesis of sp^2 carbon nano- and microrods with novel structure and morphology. *J Mater Chem* 13:981–982
129. Ozkan T, Naraghi M, Chasiotis I (2010) Mechanical properties of vapour grown carbon nanofibers. *Carbon* 48:239–244
130. Arshad SN, Naraghi M, Chasiotis I (2011) Strong nanofibers from electrospun polyacrylonitrile. *Carbon* 49:1710–1719
131. Melechko AV, Merkulov VI, McKnight TE, Guillom MA, Klein KL, Lowndes DH, Simpson ML (2005) Vertically aligned carbon nanofibers and related structures: controlled synthesis and directly assembly. *J Appl Phys* 97:041301
132. Retterer ST, Melechko A, Hensley DK, Simpson ML, Doktycz MJ (2008) Positional control of catalyst nanoparticles for the synthesis of high density carbon nanofiber arrays. *Carbon* 46:1378–1383
133. Yoon S-H, Lim S, Hong S, Mochida I, An B, Yokogawa K (2004) Carbon nano-rod as a structural unit of carbon nanofibers. *Carbon* 42:3087–3095
134. Zheng G-B, Sano H, Uchiyama Y (2003) New structure of carbon nanofiber after high-temperature heat-treatment. *Carbon* 41:853–856
135. Li J, Vergne MJ, Mowles ED, Zhong W-H, Hercules DM, Lukehart CM (2005) Surface functionalization and characterization of graphitic carbon nanofibers (GCNFs). *Carbon* 43:2883–2893
136. Morgan P (2005) Carbon fiber and their composites. CRC Press, Taylor & Francis, Boca Raton, London
137. Simamura S, Sindo A, Kotsuka K, Tsutiyama N, Sato T, Ito Y, Ikegami K, Yamada K, Sakamoto A, Vatanabe Y, Takeda H, Isikawa T, Sasaki V, Abe Y (1984) Carbon fibre. Omsya, Tokyo (in Japanese)
138. Kotelnikov RB, Bashlykov SN, Galiakbarov ZG, Kashtanov AI (1968) Osobo tugoplavkie elementy i soedineniya (Extra refractory elements and compounds). *Metallurgiya*, Moscow (in Russian)
139. Albers PW, Rotgerink HL, Bosing S, Ross DK, Parker SF (2002) Inelastic neutron scattering study on the influence of after-treatments on different technical cokes of varying impurity level and their sp^2/sp^3 character. *Carbon* 40(9):1549–1558
140. Harris PJF, Liu Z, Suenaga K (2008) Imaging the atomic structure of activated carbon. *J Phys Condens Matter* 20:362201
141. Kiyono M, Williams PJ, Koros WJ (2010) Effect of pyrolysis atmosphere on separation performance of carbon molecular sieve membranes. *J Membr Sci*:359:2–10
142. Tin PS, Xiao Y, Chung T-S (2006) Polyimide-carbonized membranes for gas separation: structural, composition and morphological control of precursors. *Separation & Purification Rev* 35:285–318
143. Koresh JE, Soffer A (1980) Study of molecular sieve carbons. I – Pore structure, gradual pore opening and mechanism of molecular sieving. *J Chem Soc Faraday Trans I* 76:2457–2471
144. Jenkins GM, Kawamura K (1976) Polymeric carbons – carbon fiber, glass and char. Cambridge University Press, London
145. Liu M, Cowley JM (1994) Structures of the helical carbon nanotubes. *Carbon* 32:393–403
146. Charlier J-C, Lambin P, Ebbesen TW (1997) Electronic properties of carbon nanotubes with polygonal cross sections. *Phys Rev B* 54(12):8377–8380
147. Chuvilin AL, Kuznetsov VL, Obratsov AN (2009) Chiral carbon nanoscrolls with polygonal cross-section. *Carbon* 47:3099–3105

148. Gavalda S, Kaneko K, Thomson KT, Gubbins KE (2001) Molecular modeling of carbon aerogels. *Colloid Surf A* 187–188:531–538
149. Gavalda S, Gubbins KE, Hanzawa Y, Kaneko K, Thompson KT (2002) Nitrogen adsorption in carbon aerogels: a molecular simulation study. *Langmuir* 18(6):2141–2151
150. Job N, Pirard R, Marien J, Pirard J-P (2004) Porous carbon xerogels with textures tailored by pH control during sol-sol process. *Carbon* 42(3):619–628.
151. Fitzer E, Schafer W (1970) The effect of crosslinking on the formation of glasslike carbons from thermosetting resins. *Carbon* 8:353–364
152. Mildner DFR, Carpenter JM (1982) On the short range atomic structure of non-crystalline carbon. *J Non-Crystalline Solids* 47:391–402
153. Pesin LA, Baitinger EM (2002) A new structural model of glass-like carbon. *Carbon* 40:295–306
154. Brooks JD, Taylor GH (1965) The formation of graphitizing carbons from the liquid phase. *Carbon* 3:185–193
155. Yamada Y, Imamura T, Kakiyama H, Honda H, Oi S, Fukuda K (1974) Characteristics of meso-carbon microbeads separated from pitch. *Carbon* 12:307–319
156. Auguie D, Oberlin M, Oberlin A, Hyvernat P (1980) Microtexture of mesophase spheres as studied by high resolution conventional transmission electron microscopy (CTEM). *Carbon* 18: 337–346
157. Fedorov NF, Ivakhnyuk GK, Tetenov VV, Matyukhin GV (1981) Carbon adsorbents based on silicon carbide. *J Appl Chem USSR* 54:1239–1242
158. Fedorov NF, Ivakhnyuk GK, Samonin VV (1981) Mesoporous carbon adsorbents from calcium carbide. *J Appl Chem USSR* 54:2253–2255
159. Fedorov NF, Ivakhnyuk GK, Gavrilo DN (1982) Poristaya struktura uglerodnykh adsorbentov iz karbida titana (Porous structure of carbon adsorbents from titanium carbide). *Zh Prikladnoi Khimii* 55:46–50 (in Russian)
160. Kusunoki M, Rokkaku M, Suzuki T (1997) Epitaxial carbon nanotube film self-organized by decomposition of silicon carbide. *Appl Phys Lett* 71:2620–2622
161. Gogotsi Y, Nikitin A, Ye H, Zhou W, Fischer JE, Yi B, Foley HC, Barsoum MW (2003) Nanoporous carbide-derived carbon with tunable pore size. *Nature Mater* 2:591–594
162. Dash RK, Yushin G, Gogotsi Y (2005) Synthesis, structure and porosity analysis of microporous and mesoporous carbon derived from zirconium carbide. *Microporous Mesoporous Mater* 86:50–57
163. Yushin G, Hoffman E, Nikitin A, Ye H, Barsoum MW, Gogotsi Y (2005) Synthesis of nanoporous carbide-derived carbon by chlorination of titanium silicon carbide. *Carbon* 43:2075–2082
164. Dash RK, Nikitin A, Gogotsi Y (2004) Nanoporous carbon derived from boron carbide. *Microporous Mesoporous Mater* 72:203–208
165. Seredych M, Portet C, Gogotsi Y, Bandosz TJ (2009) Nitrogen modified carbide-derived carbons as adsorbents of hydrogen sulphide. *J Colloid Interface Sci* 330:60–66
166. Fayos J (1999) Possible 3D carbon structures as progressive intermediates in graphite to diamond phase transition. *J Solid State Chem* 148:278–285
167. Wen B, Zhao J, Li T, Dong C (2006) n-diamond: an intermediate state between rhombohedral graphite and diamond. *New J Phys* 8:1–10
168. Irifune T, Kurio A, Sakamoto S, Inoue T, Sumiya H (2003) Materials: ultrahard polycrystalline diamond from graphite. *Nature* 421:599–600
169. Dubrovinskaia N, Dubrovinsky L, Crichton W, Langenhorst F, Richter A (2005) Aggregated diamond nanorods, the densest and least compressible form of carbon. *Appl Phys Lett* 87:083106
170. Gogotsi Y, Weltz S, Ersoy DA, McNallan MJ (2001) Conversion of silicon carbide to crystalline diamond-structured carbon at ambient pressure. *Nature* 411:283–287
171. Gogotsi YG, Kofstad P, Yoshimura M, Nickel KG (1996) Formation of sp^3 -bonded carbon upon hydrothermal treatment of SiC. *Diamond Relat Mater* 5:151–162

172. Ownby PD, Yang X, Liu J (1992) Calculated x-ray diffraction for diamond polytypes. *J Am Ceram Soc* 75:1876–1883
173. Johnston RL, Hoffmann R (1989) Superdense carbon C₈: supercubane or analogue of gamma-Si. *J Am Chem Soc* 111:810–815
174. Liu P, Cui H, Yang GW (2008) Synthesis of body-centred cubic carbon nanocrystals. *Crystal Growth Design* 8:581–586
175. Liu P, Cao YI, Wang CX, Chen XY, Yang GW (2008). Micro- and nanocubes of carbon with C8-like and blue luminescence. *Nano Lett* 8(8):2570–2575
176. Natyushenko NN, Strelnitsky VE, Gusev VA (1981) An electron-diffraction investigation of the structure of the crystalline phase of carbon C₈. *Sov Phys Crystallography* 26:274–276
177. Openov LA, Elesin VF (1998) Prismane C8: A new form of carbon. *JETP Lett* 68:726–731
178. Zazula JM (1997) On graphite transformations at high temperature and pressure induced by absorption of the LHC beam. LHC Project Note 78/97, CERN-SL/BT(TA)
179. Asinovskii EI, Kirillin AV, Kostanovskii AV (2002) Experimental investigation of the thermal properties of carbon at high temperatures and moderate pressures. *Phys Usp* 45(8):869–882
180. Savvatimskiy AI (2005) Measurements of the melting point of graphite and the properties of liquid carbon (a review for 1963–2003). *Carbon* 43:1115–1142
181. Savvatimskii AI (2003) Melting point of graphite and liquid carbon. *Phys Usp* 173(12):1295–303
182. Asinovskii EI, Kirillin AV, Kostanovskii AV (2003) Esche raz ob eksperimentalnom issledovanii termicheskikh svoistv ugleroda (Once more on experimental investigation of the thermal properties of carbon). *Usp Fiz Nauk* 173(12):1380–1381 (in Russian)
183. Asinovskii EI, Kirillin AV, Kostanovskii AV (1997) The phase diagram of carbon in the vicinity of the solid–liquid–vapour triple point. *High Temp* 35(5):704–709
184. Sheindlin MA (1998) About the paper by EI Asinovskii, AV Kirillin, and AV.Kostanovskii on “The phase diagram of carbon in the vicinity of the solid–liquid–vapour triple point”. *High Temp* 36(4):663–664
185. Asinovskii EI, Kirillin AV, Kostanovskii AV (1998) Melting parameters of carbon. *High Temp* 36(5):716–721
186. Basharin AY, Dozhdikov VS, Kirilin AV, Turchaninov MA, Fokin LR (2010) Phase diagram with a region of liquid carbon – diamond metastable states. *Tech Phys Lett* 36(6):559–562
187. Basharin AY, Dozhdikov VS, Dubinchuk VT, Kirilin AV, Lysenko IYu, Turchaninov MA, (2010) Phases formed during rapid quenching of liquid carbon. *Tech Phys Lett* 35(5):428–431
188. Son LD, Rusakov GM, Katkov NN (2006) The phase diagram of carbon in the vicinity of graphite-diamond transition. *Dokl Phys* 51(2):56–59
189. Correa AA, Bonev SA, Galli G (2006) Carbon under extreme conditions: phase boundaries and electronic properties from first-principles theory. *Proc Nat Acad Sci USA* 103(5):1204–1208
190. Ghiringhelli LM, Los JH, Meijer EJ, Fasolino A, Frenkel D (2005) Modeling the phase diagram of carbon. *Phys Rev Lett* 94:145701
191. Balandin AA, Ghosh S, Bao W, Calizo I, Teweldebrhan D, Miao F, Lau CN (2008) Superior thermal conductivity of single-layer graphene. *Nano Lett* 8(3):902–907
192. Cardarelli F (2008) *Materials handbook*, 2nd ed. Springer, London
193. Virgilev YuS, Seleznev AN, Sviridov AA, Kalyagina IP (2006) Reaktornyi grafit: razrabotka, proizvodstvo i svoistva (Nuclear graphite: development, production and properties). *Ros Khim Zh* 50(1):4–12 (in Russian)
194. Marmer EN, Gurvich OS, Maltseva LF (1967) *Vysokotemperaturnye materialy* (High-temperature materials). Metallurgiya, Moscow (in Russian)
195. Pop E, Mann D, Wang Q, Goodson K, Dai HJ (2006) Thermal conductance of an individual single-wall carbon nanotube above room temperature. *Nano Lett* 6(1):96–100

196. Sinha S, Barjami S, Iannacchione G, Schwab A, Muench G (2005) Off-axis thermal properties of carbon nanotube films. *J Nanoparticle Res* 7(6):651–657
197. Lee C, Wei X, Kysar JW, Hone J (2008) Measurement of the elastic properties and intrinsic strength of monolayer graphene. *Science* 321:385–388
198. Tsai J-L, Tu J-F (2010) Characterizing mechanical properties of graphite using molecular dynamics simulation. *Mater Design* 31:194–199
199. Chen J-H, Jang C, Xiao S, Ishigami M, Fuhrer MS (2008) Intrinsic and extrinsic performance limits of graphene devices on SiO₂. *Nature Nanotechnol* 3(4):206–209
200. Akturk A, Goldsman N (2008) Electron transport and full-band electron-phonon interactions in graphene. *J Appl Phys* 103:053702
201. Belluci S (2005) Carbon nanotubes: physics and applications. *Phys Status Solid C* 2(1):34–47
202. Chae HG, Kumar S (2006) Rigid rod polymeric fibers. *J Appl Polym Sci* 100(1):791–802
203. Meo M, Rossi M (2006) Prediction of Young's modulus of single wall carbon nanotubes by molecular-mechanics-based finite element modelling. *Compos Sci Technol* 66(11–12):1597–1605
204. Sinnott SB, Andrews R (2001) Carbon nanotubes: synthesis, properties and applications. *Crit Rev Solid State Mater Sci* 26(3):145–249
205. Yu M-F, Lourie O, Dyer MJ, Moloni K, Kelly TF, Ruoff RS (2000) Strength and breaking mechanism of multiwalled carbon nanotubes under tensile load. *Science* 287:637–640
206. Demczyk BG, Wang YM, Cumings J, Hetman M, Han W, Zettl A., Ritchie RO (2002) Direct mechanical measurement of the tensile strength and elastic modulus of multiwalled carbon nanotubes. *Mater Sci Eng A* 334(1–2):173–178
207. Schurik AG (2006) *Iskusstvennye uglirodnye materialy* (Artificial carbon materials). Ural Scientific Research Institute of Composite Materials, Perm (in Russian)
208. Meleshko AI, Polovnikov SP (2007) *Uglerod, uglerodnye volokna, uglerodnye kompozity* (Carbon, carbon fibre, carbon composites). Science-Press, Moscow (in Russian)
209. Ostrovskii VS, Virgilev YuS, Kostikov VI, Shipkov NN (1986) *Iskusstvennyi grafit* (Artificial graphite). Metallurgiya, Moscow (in Russian)
210. Burchell TD (1999) Fission reactor applications of carbon. In: Burchell TD (ed) *Carbon materials for advanced technologies*, pp. 429–484. Pergamon, Elsevier, Amsterdam
211. Nonishneva NT, Bukharova AA, Zheleznyak AYU, Podkopaev SA, Sviridov AA, Seleznev AN, Gnedin YuF (2006) Application of new dual-purpose graphite. *Refract Indust Ceram* 47(6):348–350
212. Sementsov YuI, Pyatkovskii ML (2008) *Termorasshirenniy grafit* (Thermal expanded graphite). In: Gnesin GG, Skorokhod VV (eds) *Neorganicheskoe materialovedenie* (Inorganic materials science), Vol. 2, Part 2, Naukova Dumka, Kyiv, pp. 410–425 (in Russian)
213. Celzard A, Mareche JF, Furdin G (2005) Modelling of exfoliated graphite. *Prog Mater Sci* 50:93–179
214. Kostikov VI, Samoilov VM, Beilina NYu, Ostronov BG (2004) *Novye vysokoprochnye uglerodnye materialy dlya traditsionnykh tekhnologii* (New high-strength carbon materials for conventional technologies). *Ros Khim Zh* 48(5):64–75 (in Russian)
215. Zheleznyak AYU, Seleznev AN, Bukharova AA, Sviridov AA, Gnedin YuF, Podkopaev SA, Nonishneva NP (2004) *Promyshlennoe osvoenie tekhnologii proizvodstva perspektivnykh marok grafitov s povyshennoi plotnost'yu* (Industrial developing production technologies of high-density advanced graphite grades). *Ros Khim Zh* 48(5):76–81 (in Russian)
216. SGL Carbon Group (2003) **Sigraflex foil – flexible graphite foil manufactured from expanded graphite* (Technical information brochure). Expanded Graphite SGL Technologies GmbH, Meitingen, Germany
217. Vishnyakov LR, Grudina TV, Kadyrov VKh, Karpinos DM, Oleynik VI, Sapozhnikova AB, Tuchinskii LI (1985) *Kompozitsionnye materialy* (Composite materials). Naukova Dumka, Kyiv (in Russian)

218. Kostikov VI, Varenkov AN (2003) *Sverkhvysokotemperaturnye kompozitsionnye materialy* (Ultra-high temperature composite materials). Internet Engineering, Moscow (in Russian)
219. Fitzer E, Manocha LM (1998) *Carbon reinforcements and carbon/carbon composites*. Springer, Berlin
220. Thomas CR (1993) Overview – what are carbon-carbon composites and what do they offer. In: Thomas CR (ed) *Essentials of carbon-carbon composites*, p. 1–36, Royal Society of Chemistry, Cambridge
221. Walker EJ (1993) The importance of fibre type and fibre surface in controlling composite properties. In: Thomas CR (ed) *Essentials of carbon-carbon composites*, p. 37–66, Royal Society of Chemistry, Cambridge
222. Kostikov VI, Varenkov AN (2008) *Uglerodnye i uglegrafitovye materialy* (Carbon and graphite materials). In: Gnesin GG, Skorokhod VV (eds) *Neorganicheskoe materialovedenie* (Inorganic materials science), Vol. 2, Part 2, Naukova Dumka, Kyiv, pp. 553–559 (in Russian)
223. Groupe Carbone Lorraine (2010) *Sintering – specialty graphite material for advanced ceramics* (Technical information brochure). Carbone Lorraine Composants, Gennevilliers, France
224. Groupe Carbone Lorraine (2010) *Purified graphite, silicon carbide, graphite enhancement – innovative solutions for the semiconductor industry* (Technical information brochure). Carbone Lorraine Composants, Gennevilliers, France
225. Groupe Carbone Lorraine (2010) *Graphite grade 2333* (Technical information brochure). Carbone Lorraine Composants, Gennevilliers, France
226. Ambartsumyan SA (1970) *Theory of anisotropic plates*. Technomic, Stamford
227. Zefirov AP (ed), Veryatin UD, Mashirev VP, Ryabtsev NG, Tarasov VI, Rogozkin BD, Korobov IV (1965) *Termodinamicheskie svoystva neorganicheskikh veshchestv* (Thermodynamic properties of inorganic substances). Atomizdat, Moscow (in Russian)
228. SGL Group, The Carbon Company (2007) *®Ringsdorff – specialty graphite grades for continuous casting* (Technical information brochure). Graphite Specialties, SGL Carbon GmbH, Germany
229. Goldstein RV, Gorodtsov VA, Lisovenko DS (2009) Mesomechanics of multiwall carbon nanotubes and nanowhiskers. *Phys Mesomechanics* 12(1–2):38–53
230. Nakhodchi S, Flewitt PEJ, Smith DJ (2011) A method of measuring through-thickness internal strains and stresses in graphite. *Strain* 47:37–48
231. Wang LF, Zheng QS (2007) Extreme anisotropy of graphite and single-walled carbon nanotube bundles. *Appl Phys Lett* 90:153113
232. Blakslee OL, Proctor DG, Seldin EJ, Spence GB, Weng T (1970) Elastic constants of compression-annealed pyrolytic graphite. *J Appl Phys* 41(8):3373–3382
233. Bosak A, Krisch M, Mohr M, Maultzsch J, Thomsen C (2007) Elasticity of single-crystalline graphite: inelastic x-ray scattering study. *Phys Rev B* 75:153408
234. Seldin EJ, Nezbeda CW (1970) Elastic constants and electron-microscope observation of neutron-irradiated compression-annealed pyrolytic and single-crystal graphite. *J Appl Phys* 41(8):3389–3400
235. Cousins CSG (2003) Elasticity of carbon allotropes. IV. Rhombohedral graphite: zone-center optic modes and phase transformation using transferred Keating parameters. *Phys Rev B* 67:024110
236. Boettger JC (1997) All-electron full-potential calculation of the electronic band structure, elastic constants and equation of state for graphite. *Phys Rev B* 55:11202–11211
237. Seldin EJ (1966) Stress-strain properties of polycrystalline graphites in tension and compression at room temperature. *Carbon* 4:177–191
238. Samsonov GV, ed (1976) *Svoystva elementov* (Properties of elements), 2nd ed., Vol. 2. Metallurgiya, Moscow (in Russian)
239. DiVincenzo DP, Koch TC (1984) Theoretical phase diagram for Li-intercalated graphite. *Phys Rev B* 30(12):7092–7096

240. Okamoto H (1989) The C-Li (carbon-lithium) system. *Bull Alloy Phase Diagrams* 10(1):69–72
241. Lyakishev NP, ed (1996) *Diagrammy sostoyaniya dvoynykh metallicheskih sistem* (Phase diagrams of binary metallic systems), Vol. 1. Mashinostroenie, Moscow (in Russian)
242. Kosolapova TYa, ed (1990) *Handbook of high-temperature compounds: properties, production and applications*. Hemisphere, New York
243. Andrievskii RA, Spivak II (1989) *Prochnost tugoplavkikh soedinenii i materialov na ikh osnove* (Strength of refractory compounds and materials based on them). Metallurgiya, Chelyabinsk (in Russian)
244. Massalski TB, Subramanian PR, Okamoto H, Kacprzak L, eds (1990) *Binary alloy phase diagrams*, 2nd ed. ASM International, Metals Park, Ohio
245. Velikanova TYa, Eremenko VN, Artyukh LV, Bondar AA, Gordiichuk OV (1989) Phase diagrams of Sc-M(IV-VII)-C systems. *Powder Metall Met Ceram* 28(9):711–718
246. Gschneidner KA, Jr, Calderwood FW (1986) The C-Y (carbon-yttrium) system. *Bull Alloy Phase Diagrams* 7(6):564–568
247. Gschneidner KA, Jr, Calderwood FW (1986) The C-La (carbon-lanthanum) system. *Bull Alloy Phase Diagrams* 7(5):446–449
248. Storms EK (1967) *The refractory carbides*. Academic Press, New York and London
249. Toth LE (1971) *Transition metal carbides and nitrides*. Academic Press, New York, London
250. Kieffer R, Schwarzkopf P (1953) *Hartstoffe und Hartmetalle* (Refractory hard metals). Springer, Vienna (in German)
251. Merzhanov AG (2004) The chemistry of self-propagating high-temperature synthesis. *J Mater Chem* 14:1779–1786
252. Shabalin IL, Luchka MV, Shabalin LI (2007) Vacuum SHS in systems with group IV transition metals for production of ceramic compositions. *Phys Chem Solid State* 8(1):159–175
253. Fernandez Guillermet A (1995) Analysis of thermochemical properties and phase stability in the zirconium-carbon system. *J Alloys Compd* 217(1):69–89
254. Gusev AI, Rempel AA (1994) Calculation of phase diagrams of interstitial compounds. *J Phys Chem Solids* 55(3):299–304
255. Gusev AI, Rempel AA (1997) Phase diagrams of metal-carbon and metal-nitrogen systems and ordering in strongly nonstoichiometric carbides and nitrides. *Phys Stat Sol A* 163:273–304
256. Gusev AI, Rempel AA (1999) Atomic ordering and phase equilibria in strongly nonstoichiometric carbides and nitrides. In: Gogotsi YG, Andrievskii RA (eds) *Materials science of carbides, nitrides and borides*, pp. 47–64. Kluwer Academic, Dordrecht
257. Okamoto H (1990) The C-Hf (carbon-hafnium) system. Assessed diagram. *Bull Alloy Phase Diagrams* 11(4):396–403
258. Rudy E, Windisch S, Brukl CE (1968) Revision of the vanadium-carbon and niobium-carbon systems. *Planseeber Pulvermet* 16(1):3–33
259. Carlson ON, Ghaneya AH, Smith JF (1985) The C-V (carbon-vanadium) system. *J Phase Equilib* 6(2):115–124
260. Storms EK (1989) Special report to the phase equilibria program. American Ceramic Society, Westerville, Ohio
261. Rudy E, Brukl CE (1967) Lower-temperature modifications of Nb₂C and V₂C. *J Am Ceram Soc* 50(5):265–268
262. Smith JF, Carlson ON, De Avillez RR (1987) The niobium-carbon system. *J Nucl Mater* 148(1):1–16
263. Rudy E, Hoffman JR (1967) *Phasengleichgewichte im Bereich der kubischen Karbidphase im System Wolfram-Kohlenstoff* (Phase equilibria in the cubic carbide phase in the system tungsten-carbon). *Planseeber Pulvermet* 15(3):174–178 (in German)
264. Benz R, Elliot JF, Chipman J (1973) Solid phases of the Mn-C system. *Metall Trans* 4(6):1449–1452

265. Kharkova AM, Velikanova TYa (1987) Structure of alloys of the system rhenium-carbon in the region rich with rhenium. *Powder Metall Met Ceram* 26(12):994–997
266. Popova SV, Boiko LG (1971) A new rhenium carbide formed by high-pressure treatment. *High Temp High Press* 3(2):237–238
267. Goldschmidt HJ (1967) *Interstitial alloys*. Butterworths, London, New York
268. Kubaschewski O (1982) *Iron binary phase diagrams*. Springer, Berlin
269. Gabriel A, Chatillon C, Ansara I (1988) Thermochemical and phase diagram analysis of the Ni-C, Co-C and Co-Ni-C systems. *High Temp Sci* 25(1):17–54
270. Gustafson P, Gabriel A, Ansara I (1987) Thermodynamic evaluation of the C-Ni-W system. *Z Metallkd* 78(2):151–156
271. Singleton MF, Nash P (1989) The C-Ni (carbon-nickel) system. *Bull Alloy Phase Diagrams* 10(2):121–126
272. Beauvy M (1983) Stoichiometric limits of carbon-rich boron carbide phases. *J Less-Common Met* 90(2):169–175
273. Jansson U, Carlsson J-O (1985) Chemical vapour deposition of boron carbides in the temperature range 1300–1500 K and at a reduced pressure. *Thin Solid Films* 124(2):101–107
274. Lartigue S, Male G (1988) Contribution to the study of tetragonal compounds in the boron carbon system. *J Mater Sci Lett* 7(2):153–156
275. Ekbohm LB, Amundin CO (1981) Microstructural evaluation of sintered boron carbides with different compositions. *Sci Ceram* 11:237–243
276. Rogl P (2009) Boron – carbon – chromium system. In: Effenberg G, Ilyenko S (eds) *Ternary alloy systems*. Subvol. E, Part 1, pp. 261–281. Springer, Berlin, Heidelberg
277. Grytsiv A, Rogl P (2009) Aluminium – boron – carbon system. In: Effenberg G, Ilyenko S (eds) *Ternary alloy systems*. Subvol. E, Part 1, pp. 1–23. Springer, Berlin, Heidelberg
278. Kosolapova TYa (1968) *Karbidy (Carbides)*. Metallurgiya, Moscow (in Russian)
279. Kosolapova TYa, Andreeva TV, Bartnitskaya TB, Gnesin GG, Makarenko GN, Osipova II, Prilutskii ÉV (1985) *Nemetallicheskie tugoplavkie soedineniya (Non-metallic refractory compounds)*. Metallurgiya, Moscow (in Russian)
280. Oden LL, McCune RA (1987) Phase equilibria in the Al-Si-C system. *Metall Trans A* 18(12):2005–2014
281. Olesinski RW, Abbaschian GJ (1984) The C-Si (carbon-silicon) system. *Bull Alloy Phase Diagrams* 5(5):486–489
282. Gnesin GG (1977) *Karbidokremnievye materialy (Silicon carbide materials)*. Metallurgiya, Moscow (in Russian)
283. Wang EG (1997) Research on carbon nitrides. *Prog Mater Sci* 41:241–298
284. Wang EG (2002) Carbon nitride – related nanomaterials from chemical vapor deposition: structure and properties. *J Am Ceram Soc* 85(1):105–108
285. Cascarini de Torre LE, Llanos LE, Bottani EJ (1991) Graphite oxidation in air at different temperatures. *Carbon* 29(7):1051–1052
286. Gozzi D, Guzzardi G, Salleo A (1996) High temperature reactivity of different forms of carbon at low oxygen fugacity. *Solid State Ionics* 83(3–4):177–189
287. Luo X, Robin J-C, Yu S (2004) Effect of temperature on graphite oxidation behaviour. *Nucl Eng Des* 227(3):273–280
288. Thomas JM (1965) Microscopic study of graphite oxidation. In: Walker PL, Jr (ed) *Chemistry and physics of carbon*, Vol. 1, pp. 135–168. Marcel Dekker, New York
289. Shabalin IL, Roach DL, Shabalin LI (2008) Oxidation of titanium carbide – graphite hetero-modulus ceramics with low carbon content. II. Physico-chemical interpretation of the ridge effect. *J Eur Ceram Soc* 28:3177–3188
290. Ubbelohde AR, Lewis FA (1960) *Graphite and its crystal compounds*, Oxford University Press
291. Inoue Z, Tanaka H, Inomata Y (1980) Synthesis and x-ray crystallography of aluminium boron carbide. *J Mater Sci* 15:3036–3040

292. Inomata Y, Tanaka H, Inoue Z, Kawabata H (1980) Phase relation in SiC-Al₄C₃-B₄C system at 1800°C. *Yogyo-Kyokaiishi-Shi* 88(6):353–355
293. Oskroft RJ, Korgul P, Thompson DP (1989) Crystal structure and microstructure of some new silicon aluminum carbonitrides. *Br Ceram Proc* 42:33–47
294. Kidwell BL, Oden LL, McCune RA (1984) 2Al₄C₃-SiC: a new intermediate phase in the Al – Si – C system. *J Appl Crystallogr* 17(6):481–482
295. Schneider G, Gauckler LJ, Petzow G, Zangvil A (1979) Phase equilibria in the system Al₄C₃ – Be₂C – SiC. *J Am Ceram Soc* 62(11–12):574–576
296. Zangvil A, Gauckler LJ, Schneider G, Ruehle M (1979) TEM studies on Al₄C₃·3Be₂C. *J Mater Sci* 14(11):2741–2746
297. Schneider G, Gauckler LJ, Petzow G (1979) Phase equilibria in the Si, Al, Be / C, N system. *Ceramurgia Int* 5(3):101–104
298. Gasik MI, Myachin VG, Polyakov OI, Kurasov AN (1990) Fazovy sostav kompleksnykh splavov na osnove silikomargantsa, soderzhashchikh aluminii i titan (The phase composition of complex alloys on the base of silicon manganese containing aluminium and titanium). *Izv Vyssh Uchebn Zaved Chern Metall* (9):63–67 (in Russian)
299. Gasik MI, Lysenko BF (1977) Metallofizicheskie issledovaniya fazovogo sostava sinteticheskikh i promyshlennykh splavov sistemy Mn-Fe-Si-C (Metal physics studies of the phase composition of synthetic and industrial alloys of the Mn-Fe-Si-C system). In: Gasik MI, Rostovtsev ST (eds) *Vostanovitelnye protsessy v proizvodstve ferrosplavov* (Reduction processes in ferroalloy production). Nauka, Moscow, pp. 12–15 (in Russian)
300. Oden LL, McCune RA (1990) Contribution to the phase diagram Al₄C₃ – AlN – SiC. *J Am Ceram Soc* 73(6):1529–1533
301. Oskroft RJ, Thompson DP (1991) Comment on “Contribution to the phase diagram Al₄C₃ – AlN – SiC”. *J Am Ceram Soc* 74(9):2327–2328
302. Oden LL (1991) Reply to “Comment on “Contribution to the phase diagram Al₄C₃ – AlN – SiC”. *J Am Ceram Soc* 74(9):2329
303. Larrere Y, Willer B, Lihmann JM, Daire M (1984) Diagrammes d'équilibre stable et métastable dans le système Al₂O₃ - Al₄C₃ (Stable and metastable phase equilibrium diagrams in the Al₂O₃-Al₄C₃ binary system). *Rev Int Hautes Temp Refract* 21(1):3–18 (in French)
304. Foster LM, Long G, Hunter MS (1956) Reactions between aluminum oxide and carbon. The Al₂O₃ – Al₄C₃ phase diagram. *J Am Ceram Soc* 39(1):1–11
305. Cornish L, Cacciamani G, Cupid DM, De Keyser J (2009) Aluminium – carbon – titanium system. In: Effenberg G, Ilyenko S (eds) *Ternary alloy systems*. Subvol. E, Part 1, pp. 41–71. Springer, Berlin, Heidelberg
306. Ge Z, Chen K, Guo J, Zhou H, Ferreira JMF (2003) Combustion synthesis of ternary carbide Ti₃AlC₂ in Ti-Al-C system. *J Eur Ceram Soc* 23(3):567–574
307. Pietzka MA, Schuster JC (1994) Summary of constitutional data on the aluminium-carbon-titanium system. *J Phase Equilib* 15(4):392–400
308. Zhang MX, Chang YA (1994) Phase diagrams of Ti-Al-C, Ti-Y-O, Nb-Y-O and Nb-Al-O at 1100 °C. *J Phase Equilib* 15(5):470–472
309. Bandyopadhyay D, Sharma RC, Chakraborti N (2000) The Ti-Al-C (titanium-aluminium-carbon) system. *J Phase Equilib* 21(2):195–198
310. Cam G, Flower HM, West DRF (1991) Constitution of Ti-Al-C alloys in the temperature range 1250–750 °C. *Mater Sci Technol* 7:505–511
311. Riaz S, Flower HM, West DRF (2000) Phase relationships involving TiC and Ti₃AlC (P phase) in Ti-Al-C system. *Mater Sci Technol* 16:984–992
312. Viala JC, Vincent C, Vincent H, Bouix J (1990) Approche thermodynamique de l'interaction chimique entre l'aluminium et le carbure de titane (Thermodynamic approach of the chemical interaction between aluminium and titanium carbide). *Mater Res Bull* 25:457–464 (in French)
313. Viala JC, Bouix J, Gonzalez G, Esnouf C (1997) Chemical reactivity of aluminium with boron carbide. *J Mater Sci* 32:4559–4573

314. Pradelli G (1974) La ricerca sulle on Cr borocarbides (Research on Cr borocarbides). *Metall Ital* 66(10):551–556 (in Italian)
315. Pradelli G (1978) La ricerca sulle on Cr borocarbides (Research on Cr borocarbides). *Metall Ital* 70(5):223–226 (in Italian)
316. Papesch G, Nowotny H, Benesovsky F (1973) Untersuchung in den Systemen Cr-B-C, Mn-B-C and Mn-Ge-C (Studies in the systems Cr-B-C, Mn-B-C and Mn-Ge-C). *Monatsh Chem* 104:933–942 (in German)
317. Lange D, Holleck H (1985) Verschleissfeste Werkstoffe auf Borcarbidgebasis (Wear resistant materials based on boron carbide). In: Bildstein H (ed) *Proc. 11th Int. Plansee seminar*, Vol. 2, pp. 747–759. Plansee GmbH, Reutte (in German)
318. Ordanyan SS, Dmitriev AI, Kapitonova IM (1991) Vzaimodeistvie SiC s CrB₂ (The interaction of SiC with CrB₂). *Izv AN SSSR Neorg Mater* 27(1):157–159 (in Russian)
319. Schwetz KA, Hoerle M, Bauer J (1979) Contribution to the system europium-boron-carbon. *Ceramurgia Int* 5:105–109
320. Levinskii YuV, Salibekov SE, Levinskaya MKh (1965) Reaction of chromium, molybdenum and tungsten borides with carbon. *Powder Metall Met Ceram* 4(12):1004–1009
321. Lowell CE (1967) Solid solution of boron in graphite. *J Am Ceram Soc* 50:142–144
322. Markovskii LY, Vekshina NV, Bezruk ET (1969) Vzaimodeistvie boridov s uglerodom i karbidami (Reaction of borides with carbon and carbides). In: Samsonov GV (ed) *Khimicheskie svoistva i metody analiza tugoplavkikh soedinenii* (The chemical properties and analysis methods of refractory compounds). Ukrainian SSR Academy of Sciences, Institute for Problems of Materials Science, Kyiv, pp. 143–148 (in Russian)
323. Ordanyan SS, Dmitriev AI (1989) Reaction in the B₄C-CrB₂ system. *Inorg Mater* 25(4):593–595
324. Borlera ML, Pradelli G (1967) Solid equilibri dello stato nel sistema Fe-B-C (Solid state equilibria in the system Fe-B-C). *Metall Ital* 59:907–912 (in Italian)
325. Schürmann E, Li S-X (1985) Untersuchung der Schmelzgleichgewichte im der ternären System Eisen-Kohlenstoff-Bor (Investigation of the liquid equilibria in the ternary system iron-boron-carbon). *Giessereiforschung* 37(4):121–129 (in German)
326. Fomichev OI, Katkov VF, Kushnereva AK, Brekharya GP (1976) Study of the ternary phase in the system Fe-B-C. *Inorg Mater* 12(1):111–112
327. Rogl P (2008) Boron – carbon – iron system. In: Effenberg G, Ilyenko S (eds) *Ternary alloy systems*. Subvol. D, Part 1, pp. 279–301. Springer, Berlin, Heidelberg
328. Rogl P (2009) Boron – carbon – hafnium system. In: Effenberg G, Ilyenko S (eds) *Ternary alloy systems*. Subvol. E, Part 1, pp. 282–305. Springer, Berlin, Heidelberg
329. Levinskii YuV, Salibekov SE (1965) Interaction of titanium, zirconium and hafnium diborides with carbon. *Russ J Inorg Chem* 10(3):319–320
330. Rudy E, Windisch S (1966) Phase diagrams of the systems Ti-B-C, Zr-B-C and Hf-B-C. In: *Ternary phase equilibria in transition metal - boron - carbon - silicon systems*. Report AFML-TR-65-2, Contract USAF 33(615)-1249, Part 2, Vol. 13, pp. 1–212. Air Force Materials Laboratory, Wright Patterson Air Force Base, Ohio
331. Ordanyan SS, Unrod VI, Lutsenko AE (1977) Reaction in the system HfC-HfB₂. *Inorg Mater* 13:451–453
332. Ordanyan SS, Dmitriev AI (1989) Interaction in the B₄C-HfB₂ system. *Powder Metall Met Ceram* 28(5):424–426
333. Bittermann H, Rogl P (1998) The system boron – carbon – hafnium. In: Effenberg G (ed) *Phase diagrams of ternary metal-boron-carbon systems*, pp. 102–141. ASM International, Materials Park, Ohio
334. Bauer J, Vennegues P, Vergneau JL (1985) The ternary system holmium-boron-carbon; isothermal section at 1500 °C. *J Less-Common Met* 110:295–298
335. Rogl P, Korniyenko K, Velikanova T (2009) Boron – carbon – molybdenum system. In: Effenberg G, Ilyenko S (eds) *Ternary alloy systems*. Subvol. E, Part 1, pp. 306–322. Springer, Berlin, Heidelberg

336. Paderno V, Paderno Yu, Filippov V, Liashchenko A (2004) Directional crystallization of B_4C - NbB_2 and B_4C - MoB_2 eutectic compositions. *J Solid State Chem* 117:523–528
337. Salibekov SE, Levinskii YuV, Lobankov VU (1970) Synthesis and properties of molybdenum borocarbide. *Inorg Mater* 6(9):1430–1432
338. Tomashik V (2009) Boron – carbon – nitrogen system. In: Effenberg G, Ilyenko S (eds) Ternary alloy systems. Subvol. E, Part 1, pp. 323–346. Springer, Berlin, Heidelberg
339. Ruh R, Kearns M, Zangvil A, Xu Y (1992) Phase and property studies of boron carbide – boron nitride composites. *J Am Ceram Soc* 75(4):864–872
340. Lundström T, Andreev YG (1996) Superhard boron-rich borides and studies of the B-C-N system. *Mater Sci Eng A* 209(1–2):16–22
341. Grigoriev ON, Lyashenko VI, Timofeeva II, Rogozinskaya AA, Tomila TV, Dubovik TV, Panashenko VM (2005) Study of the synthesis of the ternary compound B-N-C. *Powder Metall Met Ceram* 44(9–10):415–419
342. Pan Z, Sun H, Chen C (2006) Ab initio structural identification of high density cubic BC_2N . *Phys Rev B* 73(21):214111
343. Nicolich JP, Hofer F, Brey G, Riedel R (2001) Synthesis and structure of three-dimensionally ordered graphite like BC_2N ternary crystals. *J Am Ceram Soc* 84(2):279–282
344. Gago R, Jimenez I, Agullo-Rueda F, Albella JM, Czigany ZS, Hultman L (2002) Transition from amorphous boron carbide to hexagonal boron carbon nitride thin films induced by nitrogen ion assistance. *J Appl Phys* 92(9):5177–5182
345. Williams D, Pleune B, Kouvetakis J, Williams MD, Andersen RA (2000) Synthesis of $LiBC_4N_4$, BC_3N_3 and related C-N compounds of boron: new precursors to light element ceramics. *J Am Chem Soc* 122:7735–7741
346. Huang J, Zhu YT, Mori H (2001) Structure and phase characteristics of amorphous boron-carbon-nitrogen under high pressure and high temperature. *J Mater Res* 16(4):1178–1184
347. Rogl P, Korniyenko K, Velikanova T (2009) Boron – carbon – niobium system. In: Effenberg G, Ilyenko S (eds) Ternary alloy systems. Subvol. E, Part 1, pp. 347–366. Springer, Berlin, Heidelberg
348. Ordanyan SS, Stepanenko EK, Unrod VI (1977) Reactions in the system NbC - NbB_2 . *Inorg Mater* 13(2):312–314
349. Ordanyan SS, Dmitriev AI, Bizhev KT, Stepanenko EK (1987) Interaction in B_4C – Me^VB_2 systems. *Powder Metall Met Ceram* 26(10):834–836
350. Rogl P (1998) The system boron – carbon – niobium. In: Effenberg G (ed) Phase diagrams of ternary metal-boron-carbon systems, pp. 197–213. ASM International, Materials Park, Ohio
351. Levinskii YuV, Salibekov SE, Levinskaya MKh (1965) The reaction of vanadium, niobium and tantalum diborides of with carbon. *Powder Metall Met Ceram* 4(11):923–926
352. Korniyenko K (2009) Boron – carbon – silicon system. In: Effenberg G, Ilyenko S (eds) Ternary alloy systems. Subvol. E, Part 1, pp. 367–394. Springer, Berlin, Heidelberg
353. Lihua Z, Lijun W, Qizhong H, Qiaoqin Y, Shaoli L (1996) Structure of C- B_4C -SiC composites with silicon additive. *J Mater Sci Lett* 15(4):353–356
354. Lijun W, Qizhong H, Qiaoqin Y, Lihua Z, Zhongyu X (1996) Effect of sintering temperature on structure of C- B_4C -SiC composites with silicon additive. *Scr Mater* 35(1): 123–127
355. Roger J, Babizhetskyy V, Halet J-F, Guerin R (2004) Boron-silicon solid solution: synthesis and crystal structure of a carbon-doped boron-rich SiB_n ($n \sim 30$) compound. *J Solid State Chem* 177(11):4167–4174
356. Secríst DR (1964) Phase equilibria in the system boron carbide – silicon carbide. *J Am Ceram Soc* 47(3):127–130
357. Shaffer PTB (1969) The SiC phase in the system SiC - B_4C -C. *Mater Res Bull* 4(3):213–220
358. Kieffer R, Gugel E, Leimer G, Ettmayer P (1971) Untersuchungen im System B-C-Si (Investigations in the system B-C-Si). *Berich Deut Keram Gesel* 49(2):41–72 (in German)

359. Seifert HJ, Aldinger F (2002) Phase equilibria in the Si-B-C-N system. In: Jansen M (ed) High performance non-oxide ceramics. Vol. 1, pp. 1–58. Springer, Berlin, Heidelberg
360. Ordanyan SS, Dmitriev AI, Moroshkina FS (1989) Reaction of SiC with ZrB₂. *Inorg Mater* 28(10):1487–1489
361. Rogl P (2009) Boron – carbon – tantalum system. In: Effenberg G, Ilyenko S (eds) Ternary alloy systems. Subvol. E, Part 1, pp. 395–407. Springer, Berlin, Heidelberg
362. Rudy E, Benesovsky F, Toth LE (1963) Untersuchungen der ternären Systeme der Gruppe Va und VIa Metalle mit Bor und Kohlenstoff (Studies of the ternary systems of the group Va and VIa metals with boron and carbon). *Z Metallkd* 54(6):345–353 (in German)
363. Ordanyan SS, Unrod VI, Polishchuk VS, Storonkina NM (1976) Reactions in the system TaC-TaB₂. *Powder Metall Met Ceram* 15(9):692–695
364. Ordanyan SS (1980) Laws of interaction in the systems M^{IV,V}C – M^{IV,V}B₂. *Inorg Mater* 16(8):961–965
365. Ordanyan SS (1993) O zakonornostyakh vzaimodeistviya v sistemakh B₄C – Me^{IV}–Me^{VI}B₂ (On regularities of interaction in the systems B₄C – Me^{IV}–Me^{VI}B₂). *Ogneupory*, (1):15–17 (in Russian)
366. Ordanyan SS, Unrod VI, Avgustinik AI (1975) Reactions in the system TiC_x – TiB₂. *Powder Metall Met Ceram* 14(9):729–731
367. Toth LE, Benesovsky F, Nowotny H, Rudy E (1961) Der Dreistoff: Thorium-Bor-Kohlenstoff (The ternary system thorium-boron-carbon). *Monatsh Chem* 92(5):956–960 (in German)
368. Rogl P, Bauer J, Debuigne J (1989) The ternary system uranium-boron-carbon. *J Nucl Mater* 165(1):74–82
369. Rogl P (2009) Boron – carbon – vanadium system. In: Effenberg G, Ilyenko S (eds) Ternary alloy systems. Subvol. E, Part 1, pp. 408–426. Springer, Berlin, Heidelberg
370. Ordanyan SS, Yurchenko OV, Vikhman SV (2005) Polythermic section B₄C-LaB₆ in the ternary system La-B-C. *Rus J Appl Chem* 78(2):333–335
371. Ordanyan SS, Topchii LA, Khoroshilova IK, Chupov VD (1982) Reactions in the VC_{0.88} – VB₂ system. *Powder Metall Met Ceram* 21(2):122–124
372. Rogl P (2009) Boron – carbon – tungsten system. In: Effenberg G, Ilyenko S (eds) Ternary alloy systems. Subvol. E, Part 1, pp. 427–449. Springer, Berlin, Heidelberg
373. Rudy E (1970) The phase diagram W-B-C. In: Experimental phase equilibria of selected binary, ternary and higher order systems. Report AFML-TR-69–117, Contract USAF 33(615)-67-C-1513, Part 5, pp. 1–51. Air Force Materials Laboratory, Wright-Patterson Air Force Base, Ohio
374. Kiparisov SS, Nikiforov OA, Borisova NV (1968) Pseudobinary razrez sistemy volfram – bor – uglerod (Pseudobinary section of the tungsten – boron – carbon ternary system). *Sb Mosk Inst Stali Splavov* 45:128–131 (in Russian)
375. Paderno Y, Paderno V, Liashchenko A, Filipov V, Evdokimova A, Martynenko A (2006) The directional crystallization of W-B-C d-transition metal alloys. *J Solid State Chem* 179:2939–2943
376. Rogl P, Bittermann H (1999) Ternary metal boron carbides – constitution, thermodynamics, compound formation and structural chemistry. In: Gogotsi YG, Andrievskii RA (eds) Materials science of carbides, nitrides and borides, pp. 29–46. Kluwer Academic, Dordrecht
377. Epicier T, Dubois J, Esnouf C, Fantozzi G, Convert P (1988) Neutron powder diffraction studies of transition metal hemicarbides M₂C_{1-x}. II. In situ high temperature study on W₂C_{1-x} and Mo₂C_{1-x}. *Acta Metall* 36:1903–1921
378. Rogl P (2009) Boron – carbon – zirconium system. In: Effenberg G, Ilyenko S (eds) Ternary alloy systems. Subvol. E, Part 1, pp. 450–475. Springer, Berlin, Heidelberg
379. Ordanyan SS, Unrod VI (1975) Reactions in the system ZrC-ZrB₂. *Powder Metall Met Ceram* 14(5):393–395
380. Ordanyan SS, Dmitriev AI, Bizhev KT, Stepanenko EK (1988) Interaction in the system B₄C-ZrB₂. *Powder Metall Met Ceram* 27(1):38–40

381. Kovalev AV, Dubnik EM, Grigoriev ON, Shaposhnikova TI, Martsynyuk IS (2000) Directionally solidified eutectic of the B_4C - ZrB_2 system. *Powder Metall Met Ceram* 39(1-2):63–66
382. Samsonov GV, ed (1978) *Fiziko-khimicheskie svoistva okislov* (Physico-chemical properties of oxides), 2nd ed. Metallurgiya, Moscow (in Russian)
383. Burdick MD, Parker HS, Roth RS, McGandy EL (1955) An x-ray study of the system uranium monocarbide – uranium dicarbide – beryllium carbide. *J Res Natl Bur Stand* 54(4):217–229
384. Lemkey FD, Thompson ER (1971) Nickel and cobalt eutectic alloys reinforced by refractory metal carbides. *Metall Trans* 2(6):1537–1544
385. Dmitrieva GP, Krasnokutskaya ZB, Belyavina NN, Shurin AK (1989) Phase diagram of the Co-VC-NbC system. *Powder Metall Met Ceram* 28(3):233–238
386. Samsonov GV, Upadhyaya GS, Neshpor VS (1974) *Fizicheskoe materialovedenie karbidov* (Physical materials science of carbides). Naukova Dumka, Kyiv (in Russian)
387. Panov VS, Chuvilin AM (2001) *Tekhnologiya i svoistva spechennykh tverdykh splavov i izdeliy iz nikh* (Technology and properties of sintered hard alloys and their components). MISIS, Moscow (in Russian)
388. Pollock CB, Stadelmaier HH (1970) The η carbides in the Fe-W-C and Co-W-C systems. *Metall Trans* 1(4):767–770
389. Johansson T, Uhrenius B (1978) Phase equilibria, isothermal reactions and a thermodynamic study in the Co-W-C system at 1150°C. *Met Sci* 12(2):83–94
390. Fernandez Guillermet A. (1989) Thermodynamic properties of the Co-W-C system. *Metall Trans A* 20(5):935–956
391. Holleck H (1984) Binäre und ternäre Carbide- und Nitridsysteme der Übergangsmetalle (Binary and ternary carbide and nitride systems of the transition metals). Gebrüder Bornträger, Berlin, Stuttgart (in German)
392. Pellegrini PW, Giessen BC, Feldman JM (1972) A survey of the Cr-rich area of the Cr-Si-C phase diagram. *J Electrochem Soc* 119(4):535–537
393. Gasik MI, Em PA (1978) O vzaimodeistvii komponentov v sistemakh 3d-M – kremnii – uglirod (On the interaction of components in the systems 3d-Me-silicon-carbon). In: Ageev NV (ed) *Struktura faz i protsessy vosstanovleniya elementov v tverdykh i zhidkikh sistemakh* (Phase structures and reduction processes of elements in solid and liquid systems), pp. 54–58. USSR Academy of Sciences, Institute of Metallurgy, Moscow (in Russian)
394. Dergunova VS, Levinskii YuV, Shurshakov AN, Kravetskii GA (1974) *Vzaimodeistvie ugleroda s tugoplavkimi metallami* (Interaction of carbon with refractory metals). Metallurgiya, Moscow (in Russian)
395. Guha JP, Kolar D (1973) The systems TiC-Cr and ZrC-Cr. *J Less-Common Met* 31(3):337–343
396. Eremenko VN, Velikanova TYa, Sleptsov SV, Bondar AA (1990) Fazovye ravnovesiya pri kristallizatsii splavov sistemy Cr – Ti – C (Phase equilibria in the crystallization of the Cr – Ti – C system alloys). *Dopov Akad Nauk Ukr RSR Ser A Fiz Mat Tekh Nauki* 52(4):75–77 (in Russian)
397. Stecher P, Benesovsky F, Nowotny H (1964) Investigations of the chromium-tungsten-carbon system. *Planseeber Pulvermet* 12(2):89–95
398. Gladyshevskii EI, Telegus VS, Fedorov TF, Kuzma YuB (1967) Troinaya sistema W-Cr-C (The W-Cr-C ternary system). *Izv AN SSSR Metally* (1):190–193 (in Russian)
399. Gustafson P (1988) A thermodynamic evaluation of the C – Cr – Fe – W system. *Metall Trans A* 19(10):2547–2554
400. Eremenko VN, Velikanova TYa, Sleptsov SV, Bondar AA (1990) Diagramma plavkosti sistemy Cr – Zr – C (The meltability diagram of the Cr – Zr – C system). *Dopov Akad Nauk Ukr RSR Ser A Fiz Mat Tekh Nauki* 52(1):70–72 (in Russian)
401. Bunin KP, Malinochka YaN, Taran YuN (1969) *Osnovy metallovedeniya chuguna* (Principles of metallography of cast iron). Metallurgiya, Moscow (in Russian)

402. Kuzma YuB, Fedorov TF (1965) Phase equilibria in the system molybdenum-chromium-carbon. *Powder Metall Met Ceram* 4(11):920–922
403. Eremenko VN, Velikanova TYa, Bondar AA (1987) The phase diagram of the Cr-Mo-C system. II. Phase equilibria in the partial system Mo_2C - Cr_7C_3 -C. *Powder Metall Met Ceram* 26(6):506–511
404. Eremenko VN, Velikanova TYa, Bondar AA (1986) Diagramma sostoyaniya sistemy Cr-W-C pri vysokikh temperaturakh (The constitution diagram of the Cr-W-C system at high temperatures). *Dopov Akad Nauk Ukr RSR Ser A Fiz Mat Tekh Nauki* 48(11):74–78 (in Russian)
405. Andrievskii RA, Umanskii YaS (1977) *Fazy vnedreniya* (Interstitial phases). Nauka, Moscow (in Russian)
406. Frage NR, Gurevich YuG, Sokolova EV, Chumanov VI (1989) Stability of titanium carbide in molten iron and nickel. *Russ Metall* (3):30–34
407. Eremenko VN, Shabanova SV, Velikanova TYa, Petrenko LA (1975) Structure of alloys and the phase equilibrium diagram of the system Hf-Mo-C. II. *Powder Metall Met Ceram* 14(8):643–648
408. Dmitrieva GP, Razumova NA, Shurin AK (1984) Phase equilibria in alloys of the Ni-HfC- Mo_2C system. *Powder Metall Met Ceram* 23(9):714–718
409. Rogl P, Naik SK, Rudy E (1977) A constitutional diagram of the system TiC-HfC-MoC. *Monatsh Chem* 108(6):1325–1337
410. Rogl P, Naik SK, Rudy E (1977) A constitutional diagram of the system $\text{VC}_{0.88}$ - $\text{HfC}_{0.98}$ -(MoC). *Monatsh Chem* 108(6):1339–1352
411. Alyamovskii SI, Zainulin YuG, Shveikin GP (1981) Oksikarbidy i oksinitridy metallov IVA i VA podgrupp (Oxycarbides and oxynitrides of IVA and VA subgroups metals). Nauka, Moscow
412. Constant K, Kieffer R, Ettmayer P. (1975) Über das pseudoternäre System “ZrO”-ZrN-ZrC (On pseudoternary system “ZrO”-ZrN-ZrC). *Monatsh Chem* 106(4):823–832 (in German)
413. Rudy E, Nowotny H, Benesovsky F, Kieffer R, Neckel A (1960) Über Hafniumkarbid enthaltende Karbidsysteme (On hafnium carbide containing carbide system). *Monatsh Chem* 91(1):176–187 (in German)
414. Dmitrieva GP, Razumova NA, Shurin AK (1984) Phase equilibrium diagram of the Ni-TiC-HfC system. *Powder Metall Met Ceram* 23(2):159–162
415. Raevskaya MV, Tatarkina AL, Kulova LK (1981) Fazovye ravnovesiya v kvazi-troinykh sistemakh nikel – karbid volframa (WC) – karbid tsirkoniya (ZrC) i nikel – karbid volframa (WC) – karbid gafniya (HfC) (Phase equilibria in the nickel – tungsten carbide (WC) – zirconium carbide (ZrC) and nickel – tungsten carbide (WC) – hafnium carbide (HfC) quasiternary systems). In: Drits ME (ed) *Fazovye ravnovesiya v metallicheskih splavakh* (Phase equilibria in metallic alloys), pp. 273–276. Nauka, Moscow (in Russian)
416. Achour M, Pialoux A, Dode M (1975) Etude de la carboreduction progressive du dioxyde de hafnium. 2. Determination de la pression de l’équilibre monovariant: $\alpha\text{-HfO}_2 + 3\text{C} \leftrightarrow \text{HfC} + 2\text{CO}$, entre 1300 °C et 1650 °C. Isothermes de carboreduction de l’ $\alpha\text{-HfO}_2$ en presence d’un excès de carbone (Study of progressive reduction of hafnium dioxide by carbon. 2. Determination of the monovariant equilibrium pressure: $\alpha\text{-HfO}_2 + 3\text{C} \leftrightarrow \text{HfC} + 2\text{CO}$ between 1300 °C and 1650 °C. Isotherms of $\alpha\text{-HfO}_2$ reduction by carbon in the presence of carbon excess). *Rev Int Hautes Temp Refract* 12(3):281–287 (in French)
417. Lyakishev NP, ed (1997) *Diagrammy sostoyaniya dvoynykh metallicheskih sistem* (Phase diagrams of binary metallic systems), Vol. 2. Mashinostroenie, Moscow (in Russian)
418. Brukl CE (1966) The Zr-Si-C, Hf-Si-C, Zr-Si-B, and Hf-Si-B systems. In: *Ternary phase equilibria in transition metal-boron-carbon-silicon systems*. Report AFML-TR-65-2, Contract USAF 33(615)-1249, Part 2, Vol. 10, pp. 1–95. Air Force Materials Laboratory, Wright-Patterson Air Force Base, Ohio

419. Rudy E (1969) Compendium of phase diagram data. In: Ternary phase equilibria in transition metal-boron-carbon-silicon systems. Report AFML-TR-65-2, Contracts USAF 33(615)-1249 and USAF 33(615)-67-C-1513, Part 5, pp. 1–689. Air Force Materials Laboratory, Wright-Patterson Air Force Base, Ohio
420. Rudy E (1965) Ta-Hf-C system. In: Ternary phase equilibria in transition metal-boron-carbon-silicon systems. Report AFML-TR-65-2, Contract USAF 33(615)-1249, Part 2, Vol. 1, pp. 1–84. Air Force Materials Laboratory, Wright-Patterson Air Force Base, Ohio
421. Gusev AI (1985) Prognoz i raschety fazovykh diagramm psevdobinarykh system na osnove tugoplavkikh soedinenii perekhodnykh metallov. (The prediction and calculation of phase diagrams of pseudobinary systems based on high-melting transition metal compounds). In: Ageev NV (ed) Raschety i eksperimentalnye metody postroyeniya diagramm sostoyaniya (Calculation and experimental methods of plotting phase diagrams). Nauka, Moscow, pp. 42–47 (in Russian)
422. Fischer JJ (1964) Hot-pressing mixed carbides of Ta, Hf and Zr. *Am Ceram Soc Bull* 43(3):183–185
423. Andrievskii RA, Strelnikova NS, Poltaratskii NI, Kharkhardin ED, Smirnov VS (1967) Melting point in systems ZrC – HfC, TaC – ZrC, TaC – HfC. *Powder Metall Met Ceram* 6(1):65–67
424. Brukl CE, Harmon DP (1966) The Ti-Zr-C, Ti-Hf-C and Zr-Hf-C systems. In: Ternary phase equilibria in transition metal-boron-carbon-silicon systems. Report AFML-TR-65-2, Contract USAF 33(615)-1249, Part 2, Vol. 4, pp. 1–78. Air Force Materials Laboratory, Wright-Patterson Air Force Base, Ohio
425. Gusev AI (1984) Raschet diagram sostoyaniya psevdobinarykh system na osnove tugoplavkikh karbidov titana, tsirkoniya, gafniya i vanadiya (The calculation of the constitution diagrams of pseudo-binary systems based on titanium, zirconium, hafnium and vanadium carbides). *Izv AN SSSR Neorg Mater* 20(7):1132–1137 (in Russian)
426. Rogl P, Naik SK, Rudy E (1977) A constitutional diagram of the system TiC–HfC–WC. *Monatsh Chem* 108(5):1189–1211
427. Rogl P, Naik SK, Rudy E (1977) A constitutional diagram of the system VC_{0.88}–HfC_{0.98}–WC. *Monatsh Chem* 108(5):1213–1234
428. Eremenko VN, Velikanova TYa, Artyukh LV, Vishnevskii AS (1975) Phase diagram of ternary system hafnium-tungsten-carbon. Solidus surface projection. *Rev Int Hautes Temp Refract* 12(3):209–213
429. Eremenko VN, Velikanova TYa, Artyukh LV, Akselrod GM, Vishnevskii AS (1976) Issledovanie splavov troinykh sistem W-HfC-C i W-ZrC-C pri subsolidusnykh temperaturakh (A study of ternary systems W-HfC-C and W-ZrC-C alloys at subsolidus temperatures). *Dopov Akad Nauk Ukr RSR Ser A Fiz Mat Tekh Nauki* 38(1):83–89 (in Russian)
430. Zakharov AM, Naumkin OP, Kurganov GV (1974) Troinye sistemy W-Zr-C i W-Hf-C v oblasti, bogatyykh volframom (The W-Zr-C and W-Hf-C ternary systems in the tungsten-rich areas). *Izv AN SSSR Metall* (1):224–228 (in Russian)
431. Lyakishev NP, ed (2001) Diagrammy sostoyaniya dvoynykh metallicheskiykh sistem (Phase diagrams of binary metallic systems), Vol. 3, Part 1. Mashinostroenie, Moscow (in Russian)
432. Rudy E (1973) Boundary phase stability and critical phenomena in higher order solid solution systems. *J Less-Common Met* 33(1):43–70
433. Rudy E, Benesovsky F, Sedlatschek K (1961) Untersuchungen im System Niob-Molybdän-Kohlenstoff (Investigations in the system niobium-molybdenum-carbon). *Monatsh Chem* 92(4):841–855 (in German)
434. Rudy E, Brukl CE, Windisch S (1967) Constitution of niobium (columbium) – molybdenum – carbon alloys. *Trans Metall Soc AIME* 239(11):1796–1808
435. Brukl CE, (1972) Der Einfluß von Vanadin und Niob auf feste Subcarbiddösungen in den Systemen Tantal-Wolfram-Kohlenstoff und Tantal-Molybdän-Kohlenstoff (The influence

- of vanadium and niobium in solid subcarbide solutions in the systems tantalum-tungsten-carbon and tantalum-molybdenum-carbon). *Monatsh Chem* 103(3):820–830 (in German)
436. Funke VF, Pshenichnyi IV, Pliner LA, Loktionov YuD (1983) Phase fields and initial melting diagrams of the pseudoquaternary system UC-MoC_{1-x}-ZrC-NbC. *Powder Metall Met Ceram* 22(2):110–116
 437. Samsonov GV, Portnoy KI (1961) *Splavy na osnove tugoplavkikh soedineniy* (Alloys based on refractory compounds). Oborongiz, Moscow (in Russian)
 438. Rudy E, Brukl CE, Windisch S (1968) Constitution of ternary Ta-Mo-C alloys. *J Am Ceram Soc* 51(5):239–250
 439. Rudy E, Windisch S, Brukl CE (1967) Constitution of ternary Ta-Mo-C alloys. In: *Ternary phase equilibria in transition metal-boron-carbide-silicon systems*. Report AFML-TR-65-2, Contract USAF 33(615)-1249, Part 2, Vol. 17, pp. 1–71. Air Force Materials Laboratory, Wright-Patterson Air Force Base, Ohio
 440. Rudy E (1970) The phase diagram of the systems Ti-Nb-C, Ti-Ta-C and Ti-Mo-C. In: *Phase equilibria investigations of binary, ternary and higher order systems*. Report AFML-TR-69-117, Contract USAF 33(615)-67-C-1513, Part 1, pp. 1–132. Air Force Materials Laboratory, Wright-Patterson Air Force Base, Ohio
 441. Alekseeva ZM (1984) Phase equilibria in the solid state in the U-Mo-UC concentration range of the U-Mo-C system. *J Less-Common Met* 96:63–68
 442. Rudy E, Benesovsky F (1962) Study of the system vanadium-molybdenum-carbon. Stabilization of cubic molybdenum carbides. *Planseeber Pulvermet* 10:42–64
 443. Throop GJ, Rogl P, Rudy E (1978) Calculation of phase equilibria in ternary alloy systems: line compounds. *High Temp High Press* 10(5):553–559
 444. Sudarikov MV, Zhikharev VM (1988) Issledovanie *p-T-x*-diagrammy karbid – nitrid niobiya (A study of niobium carbide – nitride *p-T-x*-diagram). *Izv AN SSSR Neorg Mater* 24(2):239–242 (in Russian)
 445. Weiss J, Lukas HL, Lorenz J, Petzow G, Krieg H (1981) Calculation of heterogeneous phase equilibria in oxide-nitride systems : I. The Quaternary System C – Si – N – O. *Calphad* 5(2):125–140
 446. Ekelund M, Forslund B, Eriksson G, Johansson T (1988) Si-C-O-N high pressure equilibria and ΔG_f° for Si₂ON₂. *J Am Ceram Soc* 71(11):956–960
 447. Srivastava D, Garg SP, Goswami GL (1989) Thermodynamic analysis of mixed carbide, carbonitride and nitride fuels for fast breeder reactors. *J Nucl Mater* 161(1):44–56
 448. Potter PE (1976) Some phase relationships and equilibria for the uranium-plutonium monocarbonitrides including the effects of oxygen on some equilibria. In: Blank H, Lindner R (eds) *Plutonium and other actinides*, pp. 211–232. Elsevier, New York / North-Holland, Amsterdam
 449. Benz R, Troxel JE (1971) Phase diagram carbon-nitrogen-thorium at 1400 to 2200 °C. *High Temp Sci* 3(5):422–432
 450. Potter PE, Spear KE (1980) Advanced fuels for fast breeder reactors. A critical assessment of some phase equilibria. In: *Thermodynamics of nuclear materials*, Vol. 2, pp. 195–227. IAEA, Vienna
 451. Udovskij AL, Ivanov OS (1980) Thermodynamic calculation of the phase diagram of the UC-UN system. In: *Thermodynamics of nuclear materials*, Vol. 2, pp. 229–246. IAEA, Vienna
 452. Kuznetsov V (2007) Carbon – iron – uranium system. In: Effenberg G, Ilyenko S (eds) *Ternary alloy systems*. Subvol. C, Part 4, pp. 80–89. Springer, Berlin, Heidelberg
 453. Korniyenko K (2007) Carbon – molybdenum – uranium system. In: Effenberg G, Ilyenko S (eds) *Ternary alloy systems*. Subvol. C, Part 4, pp. 90–114. Springer, Berlin, Heidelberg
 454. Binder S, Lengauer W, Ettmayer P, Bauer J, Debuigne J, Bohn M (1995) Phase equilibria in the systems Ti – C – N, Zr – C – N and Hf – C – N. *J Alloys Compd* 217(1):128–136
 455. Stadelmaier HH, Fiedler ML (1975) The ternary system nickel-niobium-carbon. *Z Metallkd* 66(4):224–225

456. Gridnev VN, Barabash OM, Legkaya TN (1985) Termodinamicheskii rascheti eksperimentalnoe issledovanie poverkhnostei likvidusa i solidusa v troinoi sisteme nikel-niobii-uglerod (Thermodynamic calculation and experimental study of liquidus and solidus surfaces in the nickel-niobium-carbon ternary system). In: Ageev NV (ed) Raschety i eksperimentalnye metody postroeniya diagramm sostoyaniya (Calculation and experimental methods of plotting phase diagrams), pp. 130–133. Nauka, Moscow (in Russian)
457. Gridnev VN, Barabash OM, Legkaya TN (1985) Phase equilibria and structure of directionally crystallized alloys of the Ni-Nb-C system. Russ Metall (6):199–204
458. Shurin AK, Dmitrieva GP, Razumova NA, Khandros EL (1987) The phase diagram of the Ni-VC-NbC system. Powder Metall Met Ceram 26(8):658–660
459. Shurin AK, Razumova NA, Dmitrieva GP, Khandros EL (1987) Diagramma sostoyaniya sistemy Ni – NbC_{0.8} – TaC_{0.9} (The constitution diagram of the Ni – NbC_{0.8} – TaC_{0.9} system). Dopov Akad Nauk Ukr RSR Ser A Fiz Mat Tekh Nauki 49(6):81–83 (in Ukrainian)
460. Shurin AK, Dmitrieva GP, Razumova NA, Khandros E L (1987) State diagram of Ni-ZrC-NbC. Russ Metall (6):205–207
461. Ueda Y, Ono K, Moriyama J (1980) Thermodynamic study of the Nb-C-O solid solutions at 2073–2273 K. Nippon Kinzoku Gakkaishi 44(9):1069–1075 (in Japanese)
462. Savitskii EM, Efimov YuV, Bodak OI, Kharchenko OI, Myasnikova EA (1981) The niobium-silicon-carbon system. Inorg Mater 17(12):1649–1652
463. Brukl CE (1965) The Ti-Si-C, Nb-Si-C, and W-Si-C systems. In: Ternary phase equilibria in transition metal-boron-carbon-silicon systems. Report AFML-TR-65-2, Contract USAF 33(615)-1249, Part 2, Vol. 7, pp. 1–57. Air Force Materials Laboratory, Wright-Patterson Air Force Base, Ohio
464. Booker PH, Rudy E (1970) Phase equilibria studies in the Nb-Ta-C system. In: Phase equilibria investigations of binary, ternary and higher order systems. Report AFML-TR-69-117, Contract USAF 33(615)-67-C-1513, Part 3, pp. 1–56. Air Force Materials Laboratory, Wright-Patterson Air Force Base, Ohio
465. Chatfield C (1986) The γ -WC solubility boundary in the quaternary TiC-NbC-TaC-WC system at 1723 K. J Mater Sci 21(2):577–582
466. Brukl CE (1969) The effect of molybdenum and tungsten on the subcarbide solutions in the vanadium-tantalum-carbon and niobium-tantalum-carbon systems. In: Phase equilibria investigation of binary, ternary and higher order systems. Report AFML-TR-69-117, Contract USAF 33(615)-67-C-1513, Part 4, pp. 1–44. Air Force Materials Laboratory, Wright-Patterson Air Force Base, Ohio
467. Ono K, Moriyama J (1981) The phase relationships in the Nb-Ti-C system. J Less-Common Met 79(2):255–260
468. Gusev AI (1985) Phase diagrams of the pseudo-binary TiC – NbC, TiC – TaC, ZrC – NbC, ZrC – TaC and HfC – TaC carbide systems. Russ J Phys Chem 59(3):336–340
469. Chang YA (1967) V-Nb-C system. In: Ternary phase equilibria in transition metal-boron-carbon-silicon systems. Report AFML-TR-65-2, Contract USAF 33(615)-1249, Part 2, Vol. 16, pp. 1–54. Air Force Materials Laboratory, Wright-Patterson Air Force Base, Ohio
470. Rudy E (1966) Constitution of niobium-tungsten-carbon alloys. In: Ternary phase equilibria in transition metal-boron-carbon-silicon systems. Report AFML-TR-65-2, Contract USAF 33(615)-1249, Part 2, Vol. 18, pp. 1–61. Air Force Materials Laboratory, Wright-Patterson Air Force Base, Ohio
471. Stover ER, Wulff J (1959) The nickel-titanium-carbon system. Trans Metall Soc AIME 215:127–136
472. Potter PE (1972) The uranium-plutonium-carbon-oxygen systems: The ternary systems uranium-carbon-oxygen and plutonium-carbon-oxygen and the quaternary system uranium-plutonium-carbon-oxygen. J Nucl Mater 42(1):1–22

473. Goldshleger UI, Merzhanov AG (1983) Termodinamicheskii analiz vosstanovleniya okislov kremniya ugleterodom (Thermodynamic analysis of reduction of silicon oxides by carbon). Doklady AN SSSR 269(5):1107–1111 (in Russian)
474. Yakushevich NF, Berdnikov VI (1984) Diagramma fazovo-khimicheskikh ravovesiy sistemy Si-O-C (The diagram of the phase chemical equilibria of the Si-O-C system). Izv Vyssh Uchebn Zaved Chern Metall (10):4–7 (in Russian)
475. Berdnikov VI, Mizin VG, Karteleva MI (1982) Fazovoe ravnesie sistemy Si-O-C (The phase equilibrium of the Si-O-C system). Izv Vyssh Uchebn Zaved Chern Metall (12):31–34 (in Russian)
476. Arkharov VI, Konev VN, Timofeeva NF (1960) Issledovanie reaktsionnoy diffuzii v sistemakh metal – slozhnyi gaz. IV. Sistema molibden – azot – ugleterod (Study of reaction diffusion in the metal – complex gas systems. IV. Molybdenum – nitrogen – carbon system). Fiz Met Metalloved 9(5):695–700 (in Russian)
477. Stone L, Margolin H (1953) Titanium-rich portion of the Ti-C-N, Ti-C-O and Ti-N-O phase diagrams. J Met 5(11):1498–1502
478. Steele BCH, Javed NA, Alcock CB (1970) Measurement of the equilibrium oxygen, carbon and uranium activities associated with the uranium oxycarbide phase. J Nucl Mater 35(1):1–13
479. Javed NA (1970) Phase relations in the uranium-carbon-oxygen system at 1573 K. J Nucl Mater 37(3):353–354
480. Larin AA, Vlasov VG (1974) Effect of oxygen content on the structural characteristics of uranium oxycarbides. Powder Metall Met Ceram 13(9):761–763
481. Khromov YuF, Lyutikov RA (1980) Thermodynamic analysis of the interaction of UO_{2+x} with carbon. At Energ 49(1):28–30
482. Shabalin IL, Vishnyakov VM, Bull DJ, Keens SG, Yamshchikov LF, Shabalin LI (2009) Initial stages of oxidation of near-stoichiometric titanium carbide at low oxygen pressures. J Alloys Compd 472:373–377
483. Koyama K, Hashimoto Y, Hata H (1979) Phase relationship in the V-C-O ternary system. Trans Jpn Inst Met 20(7):371–376
484. Ouensanga AH, Dode M (1976) Etude thermodynamique et structurale a haute temperature du systeme Zr-C-O. Diagramme de phases a 1555 °C. (Thermodynamic and structural study of the system Zr-C-O at high temperatures. The phase diagram at 1555 °C.) J Nucl Mater 59(1):49–60 (in French)
485. Watson A, Cornish L (2007) Carbon – palladium – thorium system. In: Effenberg G, Ilyenko S (eds) Ternary alloy systems. Subvol. C, Part 4, pp. 120–122. Springer, Berlin, Heidelberg
486. Ivanchenko V, Pryadko T (2007) Carbon – palladium – uranium system. In: Effenberg G, Ilyenko S (eds) Ternary alloy systems. Subvol. C, Part 4, pp. 123–127. Springer, Berlin, Heidelberg
487. Lyakishev NP, ed (2000) Diagrammy sostoyaniya dvoynykh metallicheskh sistem (Phase diagrams of binary metallic systems), Vol. 3, Part 2. Mashinostroenie, Moscow (in Russian)
488. Rosen S, Nevitt MV, Barker JJ (1963) The U-Pu-C ternary phase diagram below 50 atomic percent carbon. J Nucl Mater 9(2):128–136
489. Rosen S, Nevitt MV, Mitchell AW (1963) The uranium monocarbide – plutonium monocarbide system. J Nucl Mater 9(2):137–142
490. Reavis JG, Shupe MW, Bjorklund CW, Leary JA (1967) Phase relations in the high-carbon portion of the U-Pu-C system”, Trans Amer Nucl Soc 10:111–112
491. Ugajin M, Abe J, Suzuki Y, Takahashi I, Kurihara M (1976) Phase equilibria in system U-Pu-W-C. J Nucl Sci Technol 13(1):36–39
492. Kotelnikov RB, Bashlykov SN, Kashtanov AI, Menshikova TS (1978) Vysokotemperaturnoe yadernoe toplivo (High-temperature nuclear fuel). Atomizdat, Moscow (in Russian)

493. Korniyenko K, Lebrun N (2007) Carbon – plutonium – uranium system. In: Effenberg G, Ilyenko S (eds) Ternary alloy systems. Subvol. C, Part 4, pp. 138–159. Springer, Berlin, Heidelberg
494. Korniyenko K (2007) Carbon – plutonium – zirconium system. In: Effenberg G, Ilyenko S (eds) Ternary alloy systems. Subvol. C, Part 4, pp. 160–167. Springer, Berlin, Heidelberg
495. Haines HR, Potter PE (1970) Constitutional studies in uranium and plutonium carbide – fission product systems. I. Uranium and plutonium-transition metal-carbon systems. UK Atomic Energy Authority, Report AERE-R 6512, pp. 1–15. Harwell Laboratory, Oxfordshire
496. Eremenko VN, Kharkova AM, Velikanova TYa (1984) Isotermicheskoe sechenie sistemy vanadii – renii – uglerod pri 1950 °C (The isothermal section of the vanadium – rhenium – carbon system at 1950 °C). Dopov Akad Nauk Ukr RSR Ser A Fiz Mat Tekh Nauki 46(5):84–86 (in Russian)
497. Korniyenko K (2007) Carbon – rhodium – thorium system. In: Effenberg G, Ilyenko S (eds) Ternary alloy systems. Subvol. C, Part 4, pp. 168–173. Springer, Berlin, Heidelberg
498. Korniyenko K (2007) Carbon – rhodium – uranium system. In: Effenberg G, Ilyenko S (eds) Ternary alloy systems. Subvol. C, Part 4, pp. 174–183. Springer, Berlin, Heidelberg
499. Korniyenko K (2007) Carbon – ruthenium – thorium system. In: Effenberg G, Ilyenko S (eds) Ternary alloy systems. Subvol. C, Part 4, pp. 184–190. Springer, Berlin, Heidelberg
500. Wachtmann KH, Moss MA, Hoffmann R-D, Jeitschko W (1995) Crystal structures of several ternary lanthanoid and actinoid ruthenium carbides. *J Alloys Compd* 219:279–284
501. Korniyenko K (2007) Carbon – ruthenium – uranium system. In: Effenberg G, Ilyenko S (eds) Ternary alloy systems. Subvol. C, Part 4, pp. 191–202. Springer, Berlin, Heidelberg
502. Alekseeva ZM (1991) Phase equilibria in the U-Ru-C system. *Russ Metall* (1):219–224
503. Schuster JC (1993–1994) Silicon carbide and transition metals: a critical evaluation of existing phase diagram data supplemented by new experimental results. *Int J Refract Met Hard Mater* 12(4):173–177
504. Searcy AW, Finnie LN (1962) Stability of solid phases in the ternary systems of silicon and carbon with rhenium and the six platinum metals. *J Amer Ceram Soc* 45(6):268–273
505. Schiepers RCJ, Van Loo FJJ, De With G (1988) Reactions between α -silicon carbide ceramic and nickel or iron. *J Amer Ceram Soc* 71(6):C284–C287
506. Sambasivan S, Petuskey WT (1992) Phase relationship in the Ti-Si-C system at high pressures. *J Mater Res* 7(6):1473–1479
507. Wakelkamp WJJ, Van Loo FJJ, Metselaar R (1991) Phase relations in the Ti-Si-C system. *J Eur Ceram Soc* 8(3):135–139
508. Goto T, Hirai T (1987) Chemically vapour deposited Ti_3SiC_2 . *Mater Res Bull* 22(9):1195–1201
509. Du Y, Schuster JC, Seifert HJ, Aldinger F (2000) Experimental investigation and thermodynamic calculations of the titanium-silicon-carbon system. *J Am Ceram Soc* 83(1):197–203
510. Brewer L, Krikorian OH (1956) Reactions of refractory silicides with carbon and nitrogen. *J Electrochem Soc* 103:38–51
511. Rother M, Holleck H (1993) The constitution of multicomponent high-tech ceramic systems. *J Chim Phys Phys-Chim Biol* 90(2):333–339
512. Wang YZ, Carim AH (1995) Ternary phase equilibria in the Zr-Si-C system. *J Am Ceram Soc* 78(3):662–666
513. Brukl CE, Harmon DP (1965) Ti-Ta-C system. In: Ternary phase equilibria in transition metal-boron-carbon-silicon systems. Report AFML-TR-65–2, Contract USAF 33(615)-1249, Part 2, Vol. 2, pp. 1–67. Air Force Materials Laboratory, Wright-Patterson Air Force Base, Ohio
514. Rudy E (1965) Ta-W-C system. In: Ternary phase equilibria in transition metal-boron-carbon-silicon systems. Report AFML-TR-65–2, Contract USAF 33(615)-1249, Part 2, Vol. 8, pp. 1–141. Air Force Materials Laboratory, Wright-Patterson Air Force Base, Ohio

515. Harmon DP, Brukl CE (1965) Zr-Ta-C system. In: Ternary phase equilibria in transition metal-boron-carbon-silicon systems. Report AFML-TR-65-2, Contract USAF 33(615)-1249, Part 2, Vol. 3, pp. 1–72. Air Force Materials Laboratory, Wright-Patterson Air Force Base, Ohio
516. Henney J, Jones JWS (1966) High-temperature phase equilibria in the Th-U-C system in the presence of free carbon. *Trans Brit Ceram Soc* 65:613–626
517. Korniyenko K, Lebrun N (2007) Carbon – thorium – uranium system. In: Effenberg G, Ilyenko S (eds) Ternary alloy systems. Subvol. C, Part 4, pp. 203–215. Springer, Berlin, Heidelberg
518. Perrot P (2007) Carbon – thorium – zirconium system. In: Effenberg G, Ilyenko S (eds) Ternary alloy systems. Subvol. C, Part 4, pp. 216–219. Springer, Berlin, Heidelberg
519. Rudy E, Benesovsky F (1962) Untersuchungen im System Th-Zr-C (Investigations of the system Th-Zr-C). *Monatsh Chem* 93:1279–1283 (in German)
520. Alekseeva ZM (1968) Fazovyi sostav splavov UC-Zr i Zr-ThC i odnositelnoe srodstvo C k Zr, Th i U (The phase composition of UC-Zr and Zr-ThC alloys and the relative affinity of C for Zr, Th and U). In: Ivanov OS (ed) *Fiziko-khimiya splavov i tugoplavkikh soedineniy* (Physico-chemistry of alloys and refractory compounds). Nauka, Moscow, pp. 136–145 (in Russian)
521. Rudy E (1970) The phase diagram Ti-V-C. In: Experimental phase equilibria of selected binary, ternary and higher order systems. Report AFML-TR-69-117, Contract USAF 33(615)-67-C-1513, Part 7, pp. 1–64. Air Force Materials Laboratory, Wright-Patterson Air Force Base, Ohio
522. Rudy E (1973) Constitution of ternary titanium-tungsten-carbon alloys. *J Less-Common Met* 33(2):245–273
523. Benesovsky F, Rudy E (1961) Auf der Systeme U – Zr (Hf, Nb, Ta) – C (On the systems U – Zr (Hf, Nb, Ta) – C). *Planseeber Pulvermet* 9:65–76 (in German)
524. Nickel H, Inanc Oe, Lücke K (1968) Auf das Wissen der U-Zr-C System (On the knowledge of the U-Zr-C system). *J Nucl Mater* 28:79–92 (in German)
525. Storms EK, Griffin J (1973) Thermodynamics and phase relationships of the zirconium-uranium-carbon system. *High Temp Sci* 5:423–437
526. Butt DP, Wallace TC (1993) The U-Zr-C ternary phase diagram above 2473 K. *J Am Ceram Soc* 76(6):1409–1419
527. Perrot P (2007) Carbon – uranium – zirconium system. In: Effenberg G, Ilyenko S (eds) Ternary alloy systems. Subvol. C, Part 4, pp. 220–229. Springer, Berlin, Heidelberg
528. Rudy E, Benesovsky F, Rudy EI (1962) Untersuchungen im System Vanadin-Wolfram-Kohlenstoff (Investigations of vanadium-tungsten-carbon system). *Monatsh Chem* 93(3):693–707 (in German)
529. Kuzma YuB, Fedorov TF, Shvets EA (1965) Phase equilibria in the system Zr-W-C. *Powder Metall Met Ceram* 4(2):106–109
530. Naidich YuV, Kolesnichenko GA (1967) Vzaimodeistvie metallicheskih rasplavov s poverkhnostyu almaza i grafita (The interaction of metallic melts with the surface of diamond and graphite). *Naukova Dumka*, Kyiv (in Russian)
531. Cotton FA, Wilkinson G (1965) Advanced inorganic chemistry. Wiley, New York, London
532. Alapati SV, Johnson JK, Sholl DS (2008) Large-scale screening of metal hydride mixtures for high-capacity hydrogen storage from first principles calculations. *J Phys Chem C* 112(14):5258–5262
533. Rogl P, Noël H (1995) The C-Si-U system (carbon – silicon – uranium). *J Phase Equilib* 16(1):66–72
534. Pottgen R, Kaczorowski D, Jeitschko W (1993) Crystal structure, magnetic susceptibility and electrical conductivity of the uranium silicide carbides $U_3Si_2C_2$ and $U_{20}Si_{16}C_3$. *J Mater Chem* 3:253–258
535. Whittaker AG (1978) The controversial carbon solid-liquid-vapour triple point. *Nature* 276:695–696

536. Gustafson P (1986) An evaluation of the thermodynamic properties and the (p , T) phase diagram of carbon. *Carbon* 24:169–176
537. Bundy FP (1989) Pressure-temperature phase diagram of elemental carbons. *Physica A* 156:169–178
538. Bundy FP, Bassett WA, Weathers MS, Hemley RJ, Mao HK, Goncharov AF (1996) The pressure-temperature phase and transformation diagram for carbon; updated through 1994. *Carbon* 34(2):141–153
539. Nagornyi VG, Kotosonov AS, Ostrovskii VS, Dymov BK, Lutkov AI, Anufriev YuP, Barabanov VN, Belogorskii VD, Kuteynikov AF, Virgilev YuS, Sokker GA (1975) *Svoistva konstruktsionnykh materialov na osnove ugleroda* (Properties of structural materials based on carbon). Metallurgiya, Moscow (in Russian)
540. Martienssen W (2005) The elements. In: Martienssen W, Warlimont H (eds) *Springer handbook of condensed matter and materials data*, pp. 45–158. Springer, Berlin, Heidelberg
541. Suetin DV, Shein IR, Ivanovskii AL (2010) Tungsten carbides and nitrides and ternary systems based on them: the electronic structure, chemical bonding and properties. *Russ Chem Rev* 79(7):611–634
542. Velikanova T, Turchanin M, Dobatkina T, Velikanova T (2008) Carbon – iron – molybdenum system. In: Effenberg G, Ilyenko S (eds) *Ternary alloy systems. Subvol. D, Part 2*, pp. 124–172. Springer, Berlin, Heidelberg
543. Savitskii EM, Zakharov AM, Burkhanov GS, Kataev RS (1970) Troinaya sistema molibden – zhelezo – uglerod (The ternary system molybdenum – iron – carbon). *Izv Vyssh Uchebn Zaved Tsvetn Metall* 13(6):113–115 (in Russian)
544. Anderson J-O (1988) A thermodynamic evaluation of the Fe-Mo-C system. *Calphad* 12(1):9–23
545. Giron G, Durand-Charre M (1995) High temperature phase equilibria in the system Fe-Mo-C. *Z Metallkd* 86(1):15–21
546. Cornish L, Watson A (2008) Carbon – iron – niobium system. In: Effenberg G, Ilyenko S (eds) *Ternary alloy systems. Subvol. D, Part 2*, pp. 184–199. Springer, Berlin, Heidelberg
547. Fedorov TF, Kuzma YuB, Skolozdra RV, Popova NM (1965) Phase equilibria in the ternary systems Zr-Co-C and Nb-Fe-C. *Powder Metall Met Ceram* 4(12):1010–1014
548. Das RC, Jha R, Mukherjee T (1986) The carbon – iron – niobium system. *J Alloy Phase Diagrams* 2(2):131–140
549. Lebrun N (2008) Carbon – iron – silicon system. In: Effenberg G, Ilyenko S (eds) *Ternary alloy systems. Subvol. D, Part 2*, pp. 240–286. Springer, Berlin, Heidelberg
550. Raghavan V (1992) Phase diagrams of ternary iron alloys. Part 6A, Indian Institute of Metals, Calcutta
551. Lebrun N, Perrot P (2008) Carbon – iron – titanium system. In: Effenberg G, Ilyenko S (eds) *Ternary alloy systems. Subvol. D, Part 2*, pp. 287–316. Springer, Berlin, Heidelberg
552. Sare IR (1980) Splat-cooled iron-titanium-carbon alloys. *Met Sci* 14:177–183
553. Ramaekers PPI, Van Loo FJJ, Bastin GF (1985) Phase relations, diffusion paths and kinetics in the system C-Fe-Ti at 1273 K. *Z Metallkd* 76(4):245–248 (Erratum – *Z Metallkd* (1985) 76(9):639)
554. Frage N (1999) Interaction between nonstoichiometric titanium carbide and Fe-C alloys. *Metall Mater Trans B* 30:857–663
555. Liu C-S, Huang J-H, Sheng Y (2002) Thermodynamic analysis of C-Fe-Ti system. *J Inorg Mat* 17(2):288–292 (in Chinese)
556. Raghavan V (2003) The C-Fe-Ti (carbon-iron-titanium) system. *J Phase Equilib* 24(1):62–66
557. Ivanchenko V, Pryadko T (2008) Carbon – iron – vanadium system. In: Effenberg G, Ilyenko S (eds) *Ternary alloy systems. Subvol. D, Part 2*, pp. 327–356. Springer, Berlin, Heidelberg
558. Huang W (1991) Thermodynamic evaluation of the C-Fe-V system. *Z Metallkd* 82(5):391–401

559. Korniyenko K (2008) Carbon – iron – tungsten system. In: Effenberg G, Ilyenko S (eds) Ternary alloy systems. Subvol. D, Part 2, pp. 327–356. Springer, Berlin, Heidelberg
560. Bergstroem M (1977) The η -carbides in the ternary system Fe-W-C at 1250 °C. *Mater Sci Eng* 27:257–269
561. Uhrenius B (1980) Calculation of phase equilibria in the Fe-W-C system. *Calphad* 4(3):173–191
562. Gustafson P (1987) A thermodynamic evaluation of the C-Fe-W system. *Metall Trans A* 18(2):175–188
563. Rynemark M (1991) Investigation of equilibria in the Ti-W-C-N system at 1750 °C. *Refract Met Hard Mater* 10:185–193
564. Ordanyan SS, Boldin AA, Prilutskii EV (2000) Interaction in the B_4C - W_2B_5 . *Rus J Appl Chem* 73(12):2128–2130
565. Ordanyan SS, Vikhman SV, Kuznetsov MN (2004) $T - x$ fazovaya diagramma linii B_4C - W_2B_5 v sisteme B-C-Si-W ($T - x$ phase diagram of the B_4C - W_2B_5 join in the B-C-Si-W system). *Ogneupory Tekh Keram* (12):2–4 (in Russian)
566. Ordanyan SS (1993) Obschie aspekty fazovykh otnosheniy v sistemakh $SiC - Me^{IV-VI}B_2$ (Common aspects of phase relations in $SiC - Me^{IV-VI}B_2$ systems). *Zh Prikl Khim* 66(11):2439–2444 (in Russian)
567. Ordanyan SS, Unrod VI (2005) Eutectics and their models, sintered composites in the systems of refractory materials. *Refract Industrial Ceram* 46(4):276–281
568. Ordanyan SS, Yurchenko OV, Vikhman SV (2004) Phase relations in the $SiC - LaB_6$ system. *Inorg Mater* 40(6):693–696
569. Ordanyan SS, Vikhman SV, Kuznetsov MN (2004) Stroenie politermicheskogo razreza $SiC - W_2B_5$ sistemy B-C-Si-W (Structure of the polythermal $SiC - W_2B_5$ section of the B-C-Si-W system). *Ogneupory Tekh Keram* (12):2–4 (in Russian)
570. Ordanyan SS, Nesmelov DD, Vikhman SV (2009) The system $SiC - W_2B_5 - LaB_6$. *Refract Industrial Ceram* 50(5):391–393
571. Seifert HJ (2004) Refractory and hard materials in the Ti-Si-B-C-N system – phase equilibria, phase reactions and thermal stabilities. Technical Report, pp. 1–8. University of Florida, Gainesville
572. Seifert HJ, Peng J, Golczewski J, Aldinger F (2001) Phase equilibria of precursor-derived Si-(B-)C-N ceramics. *Appl Organomet Chem* 15(10):794–808
573. Johnson WB, Nagelberg AS (1995) Application of phase diagrams to the production of advanced composites. In: Alper AM (ed) *Phase diagrams in advanced ceramics*, pp. 85–126, Academic Press, San Diego, New York
574. Duschaneck H, Rogl P (1998) The system boron – carbon – zirconium. In: Effenberg G (ed) *Phase diagrams of ternary metal-boron-carbon systems*. ASM International, Materials Park, Ohio, pp. 445–485
575. Young WS (1973) Molybdenum sintering and the molybdenum-oxygen-carbon system. *J Less-Common Met* 32:321–330
576. Audi G, Wapstra AH, Thibault C, Blachot J, Bersillon O (2003) The NUBASE evaluation of nuclear and decay properties. *Nucl Phys A* 729:3–128
577. De Laeter JR, Böhlke JK, De Bièvre P, Hidaka H, Peiser HS, Rosman KJR, Taylor PDP (2003) Atomic weights of the elements. Review 2000 (IUPAC Technical report). *Pure Appl Chem* 75(6):683–800
578. Wieser ME (2006) Atomic weights of the elements 2005. (IUPAC Technical report). *Pure Appl Chem* 78(11):2051–2066
579. Savitskii EM, Burkhanov GS (1971) Metallovedenie spлавov tugoplavkikh i redkih metallov (Metallography of refractory and less-common metal alloys), 2nd ed. Nauka, Moscow (in Russian)
580. Grytsiv AV, Bondar AA, Velikanova TYa (1997) Rhenium solid solution in the Cr – Re – C ternary system at solidus temperature. *J Alloys Compd* 262–263:402–405

581. Eremenko VN, ed (1981) Diagrammy sostoyaniya sistem sodержaschikh karbidy i nitridy (Alloy phase diagrams of systems containing carbides and nitrides). Naukova Dumka, Kyiv (in Russian)
582. Eremenko VN, ed (1988) Fizicheskaya khimiya neorganicheskikh materialov (Physical chemistry of inorganic materials), Vol. 1. Naukova Dumka, Kyiv (in Russian)
583. Bondar AA, Velikanova TYa (1996) Aspects of construction diagrams of ternary systems formed by chromium with carbon and *d*-transition metals. Powder Metall Met Ceram 35(7–8):484–496
584. Lengauer W (2000) Transition metal carbides, nitrides and carbonitrides. In: Riedel R (ed) Handbook of ceramic hard materials, pp. 202–252. Wiley-VCH, Weinheim
585. Jonsson S (1996) Assessment of the Ti-W-C system and calculations in the Ti-W-C-N system. Z Metallkd 87(10):788–795
586. Doi A, Nomura T, Tobioka M-A, Takahashi K, Hara A (1986) Thermodynamic evaluation of equilibrium nitrogen pressure and WC separation in Ti-W-C-N system carbonitride. High Temp High Press 18(4):443–452
587. Ganguly A, Barsoum MW, Schuster J (2005) The 1300 °C isothermal section in the Ti-In-C ternary phase diagram. J Am Ceram Soc 88:1290–1296
588. Chung H-J, Shim J-H, Lee DN (1999) Thermodynamic evaluation and calculation of phase equilibria of the Ti-Mo-C-N quaternary system. J Alloys Compd 282(1–2):142–148
589. Chatfield Ch (1983) Redetermination of the γ - α solubility line in the TiC-TaC-WC system at 1723 K. Powder Metall Int 15(1):18–19
590. Fahrenholtz WG, Neuman EW, Brown-Shaklee HJ, Hilmas E (2010) Superhard boride – carbide particulate composites. J Am Ceram Soc 93(11):3580–3583
591. Savitsky EM, Povarova KB, Makarov PV (1982) Physikalisch-chemische Grundlagen des Legierens von warmfesten Wolframlegierungen (Physical and chemical principles underlying alloying of heat-resistant tungsten alloys). Z Metallkd 73(2):92–97 (in German)
592. Shabalin IL (1973) Razrabotka tekhnologii polucheniya teplovdyelayushchikh elementov na osnove kompozitsii karbid urana – okis berilliya dlya yadernykh reaktorov aerokosmicheskoi tekhniki (Development of manufacturing technology of nuclear fuel ceramic elements based on uranium carbide – beryllium oxide composites for aerospace application). MSc Thesis, Ural Polytechnic Institute, Sverdlovsk (in Russian)
593. Kimura Y, Iida K, Wei F-G, Mishima Y (2006) Phase equilibria in the T – Al – C (T: Co, Ni, Rh, Ir) and T – Al – B (T: Rh, Ir) systems for the design of E2₁-Co₃AlC based heat resistant alloys. Intermetallics 14:508–514
594. Frisk K (2003) A revised thermodynamic description of the Ti-C system. Calphad 27:367–373
595. Sood DD, Agarwal R, Venugopal V (1997) Phase diagram calculations of U-Pu-N system with carbon and oxygen impurities. J Nucl Mater 247:293–300
596. Telle R, Brook RJ, Petzow G (1991) Phase relations in ceramic systems. J Hard Mater 2:79–114
597. Duschaneck H, Rogl P, Lukas HL (1995) A critical assessment and thermodynamic calculation of the boron-carbon-titanium (B-C-Ti) ternary system. J Phase Equilib 16(1):46–60
598. Gusev AI (1997) Phase equilibria in the ternary system titanium – boron – carbon: the sections TiC_y – TiB₂ and B₄C_y – TiB₂. J Solid State Chem 133:205–210
599. Brodtkin D, Barsoum MW (1996) Isothermal section of Ti-B-C phase diagram at 1600 °C. J Am Ceram Soc 79(3):785–787
600. Dumitrescu L, Hillert M, Sundman B (1999) Reassessment of Ti-C-N based on a critical review of available assessments of Ti-N and Ti-C. Z Metallkd 90(7):534–541
601. Artyukh LV, Ilyenko SM, Velikanova TYa (1996) The scandium – titanium – carbon phase diagram. J Phase Equilib 17(5):403–413
602. Artyukh LV, Velikanova TYa, Ilyenko SM (1998) Phase equilibria in the Sc-Zr-C system. J Alloys Compd 269:193–200

603. Velikanova TYa, Bondar AA, Grytsiv AV, Dovbenko OI (2001) Metallochemistry of chromium with *d*-metals and carbon. *J Alloys Compd* 320:341–352
604. Rivlin VG (1985) Critical review of constitution of carbon – iron – tungsten system. *Int Met Rev* 30(6):259–274
605. Zakharov AM, Lashkova LA, Semeryakova SG (1987) Polythermal section γ -TiAl – TiC of the Ti-Al-C system. *Russ Metall* (4):197–198
606. Naguib M, Kurtoglu M, Presser V, Lu J, Niu J, Heon M, Hultman L, Gogotsi Y, Barsoum MW (2011) Two-dimensional nanocrystals produced by exfoliation of Ti_3AlC_2 . *Adv Mater* 23(37):4207–4212
607. Yaney DL, Joshi A (1990) Reaction between niobium and silicon carbide at 1373 K. *J Mater Res* 5(10):2197–2208
608. Silman GO (1995) Diagramma sostoyaniya sistemy Fe-C-V-Si i splavy na ee osnove. 1. Postroenie i analiz chastei diagrammy. (State diagram of Fe-C-V-Si system and alloys on its base. 1. Construction and analysis of diagram sections.) *Metallovedenie Termicheskaya Obrabotka Metallov* (11):11–13 (in Russian)
609. Ramaekers PPJ, Bastin GF, Van Loo FJJ (1984) Phase relations and diffusion paths in the system Co-Ti-C at 1273 K. *Z Metallkd* 75(8):639–642
610. Rivlin VG (1985) Phase equilibria in iron alloys. 17. Critical review of constitution of carbon – iron – molybdenum system. *Int Met Rev* 30(3):109–124
611. Ramaekers PPJ, Van Loo FJJ, Bastin GF (1985) Phase relations, diffusion paths and kinetics in the system Fe-Ti-C at 1273 K. *Z Metallkd* 76(4):245–248
612. Alekseeva ZM, Ivanov OS (1974) Some new data from the experimental investigation of the phase structure of alloys and the phase diagrams of the U-C-Mo, -W, -Cr, -Re systems. *Thermodynamics of nuclear materials. Proc Symp Pap Discuss STI/PUB/380*, International Atomic Energy Agency, Vienna
613. Jackson MR (1977) Composites of γ + TaC in the Ni-Ta-C ternary system. *Metall Trans A* 8(6):905–913
614. Eremenko VN, Shabanova SV, Velikanova TYa (1977) Structure of alloys and the phase equilibrium diagram of the system Hf-Mo-C. VI. Isothermal section of the Hf-Mo-C system at 1400 °C. *Powder Metall Met Ceram* 16(10):772–777
615. Enomoto M (1996) The C-Ti-V system (carbon-titanium-vanadium). *J Phase Equilib* 17(3):237–247
616. Wiitkar P, Halet J-F, Saillard J-Y, Rogl P, Bauer J (1994) Crystal and electronic structure of the novel layered rare earth metal boride carbide $\text{Gd}_2\text{B}_3\text{C}_2$. *Inorg Chem* 33(7):1297–1305
617. Bidaud E, Hiebl K, Hoffman R-D, Pöttgen R, Jardin C, Bauer J, Gautier R, Gougeon P, Saillard J-Y, Halet J-F (2000) Structural, electronic and magnetic properties of ternary rare-earth metal borocarbides $R_5\text{B}_2\text{C}_5$ ($R = \text{Y, Ce-Tm}$) containing BC_2 “molecules”. *J Solid State Chem* 154(1):286–295
618. Ruiz D, Garland MT, Saillard J-Y, Halet J-F, Bohn M, Bauer J (2002) Electron probe microanalysis in the ternary Gd-B-C system. *Solid State Sci* 4:1173–1178
619. Holleck H, Kleykamp H (1970) Zur Konstitution und Thermodynamik im System Uran – Ruthenium – Kohlenstoff (Towards the constitution and thermodynamics in the system uranium – ruthenium – carbon). *J Nucl Mater* 35:158–166 (in German)
620. Ugajin M, Takahashi I (1970) The phase reaction in the UC-W system. *J Nucl Mater* 35:303–313
621. Shurin AK, Dmitrieva GP, Cherepova TS (1996) Phase equilibria in Co – Me'C – Me''C alloys. 1. Systems with three-phase eutectic equilibria. *Powder Metall Met Ceram* 35(11–12):615–620
622. Shurin AK, Dmitrieva GP, Cherepova TS (1997) Phase equilibria in Co – Me'C – Me''C alloys. 2. Systems with four-phase eutectic equilibrium. *Powder Metall Met Ceram* 36(3–4):193–196
623. Bhanumurthy K, Schmid-Fetzer R (1996) Solid state phase equilibria and reactive diffusion in the Cr-Si-C system. *Z Metallkd* 87(1):61–71

624. Frage N, Frumin N, Levin L, Polak M, Dariel MP (1998) High-temperature phase equilibria in the Al-rich corner of the Al-Ti-C. *Metall Mater Trans A* 29(4):1341–1345
625. Bandyopadhyay D, Sharma RC, Chakraborti N (2000) The C-Hf-Ti (carbon-hafnium-titanium) system. *J Phase Equilib* 21(6):535–538
626. Bandyopadhyay D, Sharma RC, Chakraborti N (2001) The C-Ti-Zr (carbon-titanium-zirconium) system. *J Phase Equilib* 22(1):61–64
627. Halverson DC, Munir ZA (1986) Boron carbide reactive metal cermets: I, Thermodynamic considerations in boron carbide titanium cermets. *Ceram Eng Sci Proc* 7(7/8):1000–1010
628. Stetskiv AO, Pavlyuk VV (2002) Issledovanie troinykh sistem Ce-Ge-C i Ce-Si-C pri 670 K (Investigation of Ce-Ge-C and Ce-Si-C ternary systems at 670 K). *Ukr Khim Zh* 68(7–8):80–82 (in Russian)
629. Laurila T, Zeng K, Molarius J, Riekkinen T, Suni I, Kivilahti JK (2002) Effect of oxygen on the reactions in Si/Ta/Cu and Si/TaC/Cu systems. *Microelect Eng* 64:279–287
630. Van Loo FJJ, Smet FM, Rieck GD, Verspui G (1982) Phase relations and diffusion paths in the Mo-Si-C system at 1200 °C. *High Temp High Press* 14(1):25–31
631. Costa Silva A, Kaufman MJ (1994) Phase relations in the Mo-Si-C system relevant to the processing of MoSi₂-SiC composites. *Metall Mater Trans A* 25(1):5–15
632. Gan G, Sun J, Chen J, Chen Y, Yan J (2002) Stabilized chemical potential diagrams for Mo-Si-C ternary system. *Kuei Suan Jen Hsueh Pao (J Chin Ceram Soc)* 30(2):193–197 (in Chinese)
633. Kephart JS, Carim AH (1998) Ternary compounds and phase equilibria in Ti-Ge-C and Ti-Ge-B. *J Electrochem Soc* 145(9):3253–3258
634. Bittermann H, Rogl P (2002) Critical assessment and thermodynamic calculation of ternary system C-Hf-Zr (carbon-hafnium-zirconium). *J Phase Equilib* 23(3):218–235
635. Golberg D, Bando Y, Dorozhkin P, Dong Z-C (2004) Synthesis, analysis and electrical property measurements of compound nanotubes in the B-C-N ceramic system. *MRS Bull* 29(1):38–42
636. Lee CH, Kayastha VK, Wang J, Yap YK (2009) Introduction to B-C-N materials. In: Yap YK (ed) *B-C-N nanotubes and related nanostructures*, pp. 1–22. Springer, Dordrecht, Heidelberg
637. Arenal R, Loiseau A (2009) Heteroatomic single-wall nanotubes made of boron, carbon and nitrogen. In: Yap YK (ed) *B-C-N nanotubes and related nanostructures*, pp. 45–82. Springer, Dordrecht, Heidelberg
638. Yu J, Wang EG (2009) Carbon nitride and boron carbon nitride nanostructures. In: Yap YK (ed) *B-C-N nanotubes and related nanostructures*, pp. 195–222. Springer, Dordrecht, Heidelberg
639. Laurila T, Molarius J, Kivilahti JK (2004) Interfacial reactions in the Si/TaC/Cu systems. *Microelect Eng* 71:301–309
640. Bandyopadhyay D (2004) The Ti-Si-C (titanium-silicon-carbon) system. *J Phase Equilib Diffus* 25(5):415–420
641. Choi SK, Chandrasekaran M, Brabers MJ (1990) Interaction between titanium and SiC. *J Mater Sci* 25(4):1957–1964
642. Seifert HJ (1993) Thermodynamic and phase optimization in the system Ti-Si-C-N. PhD Thesis, Max Plank Institut für Metallforschung, Institut für Metallkunde der Universität Stuttgart
643. Ohtani H, Hillert M (1993) Calculation of V-C-N and Ti-C-N phase diagrams. *Calphad* 17(1):93–99
644. Yan J, Ma X, Zhao W, Tang H, Zhu C, Cai S (2005) Crystal structure and carbon vacancy hardening of (W_{0.5}Al_{0.5})C_{1-x} prepared by a solid-state reaction. *Chem Phys Chem* 6:2099–2103
645. Guo Y, Yuan W, Song B, Xu Y (2008) Chemical reaction in the Co-Si-C system. *Powd Diffraction* 23(4):329–333
646. Wang S, Zhang Y, Abidi N, Cabrales L (2009) Wettability and surface free energy of graphene films. *Langmuir* 25(18):11078–11081

647. Xiong W, Du Y, Zhang W, Xu H (2010) Carbon – tungsten – zirconium system. In: Effenberg G, Ilyenko S (eds) Ternary alloy systems. Subvol. E, Part 3, pp. 31–47. Springer, Berlin, Heidelberg
648. Savitsky EM, Povarova KB, Makarov PV, Zavarzina YaK (1977) Phase-Zusammensetzung, Struktur und Eigenschaften von vakuumgeschmolzenem W-C-(Zr, Hf, Nb, Ta, Re) Legierung (Phase composition, structure and properties of vacuum-melted W-C-(Zr, Hf, Nb, Ta, Re) alloys). *Planseeber Pulvermet* 25(3):168–185 (in German)
649. Miyazawa K, Obayashi A, Kuwabara M (2001) C_{60} nanowhiskers in a mixture of lead zirconate titanate sol – C_{60} toluene solution. *J Am Ceram Soc* 84(12):3037–3039
650. Miyazawa K (2002) C_{70} nanowhiskers fabricated by forming liquid/liquid interfaces in the systems of toluene solution of C_{70} and isopropyl alcohol. *J Am Ceram Soc* 85(5):1297–1299
651. Liu H, Li Y, Jiang L, Luo H, Xiao S, Fang H, Li H, Zhu D, Yu D, Xu J, Xiang B (2002) Imaging as-grown [60]-fullerene nanotubes by template technique. *J Am Chem Soc* 124:13370–13371
652. Miyazawa K (2010) Synthesis and functions of fullerene nanotubes. In: Kijima T (ed) *Inorganic and metallic nanotubular materials*, pp. 201–214. Springer, Berlin, Heidelberg
653. Carney CM, Parthasarathy TA, Cinibulk MK (2011) Oxidation resistance of hafnium diboride ceramics with additions of silicon carbide and tungsten boride or tungsten carbide. *J Am Ceram Soc* 94(8):2600–2607
654. Grigoriev ON, Gogotsi GA, Gogotsi YG, Subbotin VI, Brodnikovskii NP (2000) Synthesis and properties of ceramics in the $SiC-B_4C-MeB_2$ system. *Powder Metall Met Ceram* 39(5–6):239–250
655. Ordanyan SS, Dmitriev AI, Stepanenko EK, Aulova NYu, Semenov NE (1987) $SiC-TiB_2$ system – a base of high-hardness wear-resistant materials. *Powder Metall Met Ceram* 26(5):375–377
656. Udalov YP, Valova EE, Ordanyan SS (1995) Preparation and abrasive properties of eutectic compositions in the system $B_4C-SiC-TiB_2$. *Refractories* 36(7–8):233–234
657. Ordanyan SS, Vikhman SV (1997) Some properties of composite materials in the system $SiC-TiB_2$. *Refract Indust Ceram* 38(7–8):251–252
658. Ordanyan SS, Vikhman SV, Prilutskii EV (2002) Investigation of the structure and properties of materials in the $SiC-TiB_2$ system. *Powder Metall Met Ceram* 41(1–2):42–46
659. Danilovich DP, Rumyantsev VI, Ordanyan SS (2009) Sistema $SiC-TiC-TiB_2$ kak osnova keramomatrixnykh kompozitsionnykh materialov (The $SiC-TiC-TiB_2$ system as a base of ceramic matrix composite materials). *Voprosy Materialovedeniya* (4):42–47 (in Russian)
660. Suetin DV, Shein IR, Ivanovskii AL (2011) Structural, electronic and magnetic properties of tungsten oxycarbides $WC_{1-x}O_x$ and $WO_{3-x}C_x$ from first principles calculations. *Phys Status Solidi B* 248(12):2884–2892
661. Pastukhov EA, Chentsov VP, Kiselev AV, Bodrova LE, Dolmatov AV, Popova EA, Petrova SA, Zakharov RG (2006) Wetting of graphite surface by the aluminium alloys melts. In: Proc. 4th Int. Conf. “Mathematical modeling and computer simulation in materials technologies”, Vol. 1, pp. 1–178 – 1–181. Ariel, Israel
662. English JJ (1961) Binary and ternary phase diagrams of columbium, molybdenum, tantalum and tungsten. Report DMIC-152, Contract AF-33(616)-7747, pp. 1–226. Defence Metals Information Center, Battelle Memorial Institute, Columbus, Ohio
663. Velikanova TYa, Bondar AA, Dovbenko OI (2002) Melting diagram for the Cr – Nb – C system in the (Cr) – (Nb) – (NbC) region. *Powder Metall Met Ceram* 41(11–12):620–626
664. FactSage (2011) Data from Tdnucl – Thermodata nuclear database. Collection of phase diagrams. http://www.crct.polymtl.ca/fact/phase_diagram.php?file=C-O.jpg&dir=TDnucl. Accessed 18 May 2011
665. Boettinger WJ, Peperczko JH, Frankwicz PS (1992) Application of ternary phase diagrams to the development of $MoSi_2$ -based materials. *Mater Sci Eng A* 155(1):33–44
666. Diudea MV (2010) Diamond D_5 , a novel allotrope of carbon. *Studia Universitatis Babes-Bolyai Chemia* (4):11–17

667. Diudea MV, Nagy CL, Ilic A (2011) Diamond D₅, a novel class of carbon allotropes. In: Putz MV (ed) Carbon bonding and structures: advances in physics and chemistry, pp. 273–289. Springer, Dordrecht, Heidelberg
668. Wang Z, Zhao Y, Tait K, Liao X, Schiferl D, Zha C, Downs RT, Qian J, Zhu Y, Shen T (2004) A quenchable superhard carbon phase synthesized by cold compression of carbon nanotubes. *Proc Nat Acad Sci USA* 101(38):13699–13702
669. Karfunkel HR, Dressler T (1992) New hypothetical carbon allotropes of remarkable stability estimated by modified neglect of diatomic overlap solid-state self-consistent field computations. *J Am Chem Soc* 114(7):2285–2288
670. Bucknum MJ, Castro EA (2006) Hexagonite: a hypothetical organic zeolite. *J Math Chem* 39(3–4):611–628
671. Bucknum MJ, Castro EA (2011) High pressure synthesis of the carbon allotrope hexagonite with carbon nanotubes in a diamond anvil cell. In: Putz MV (ed) Carbon bonding and structures: advances in physics and chemistry, pp. 79–93. Springer, Dordrecht, Heidelberg
672. Balaban AT, Klein DJ, Folden CA (1994) Diamond-graphite hybrids. *Chem Phys Lett* 217(3):266–270
673. Bucknum MJ, Hoffmann R (1994) A hypothetical dense 3,4-connected carbon net and related B₂C and CN₂ nets built from 1,4-cyclohexadienoid units. *J Am Chem Soc* 116(25):11456–11464
674. Bucknum MJ, Stamatin I, Castro EA (2005) A chemically intuitive proposal for the structure of n-diamond. *Mol Phys* 103(20):2707–2715
675. Bucknum MJ, Pickard CJ, Stamatin I, Castro EA (2006) On the structure of i-carbon. *J Theoret Comput Chem* 5(2):175–185
676. Seifert G, Kuc A, Heine T (2010) Hexagon preserving carbon nanofoams. In: Colombo L, Fasolino A (eds) Computer-based modeling of novel carbon systems and their properties, pp. 57–77. Springer, Dordrecht, Heidelberg
677. Dahl JE, Liu SG, Carlson RMK (2003) Isolation and structure of higher diamondoids, nanometer-sized diamond molecules. *Science* 299:96–99
678. Jeitschko W, Nowotny H, Benesovsky F (1964) Die H-phasen Ti₂TiC, Ti₂PbC, Nb₂InC, Nb₂SnC und Ta₂GaC (The H-phases Ti₂TiC, Ti₂PbC, Nb₂InC, Nb₂SnC and Ta₂GaC). *Monatsh Chem* 95(2):431–435 (in German)
679. Barsoum MW, Ganguly A, Seifert HJ, Aldinger F (2002) The 1300 °C isothermal section in the Nb-Sn-C ternary phase diagram. *J Alloys Compd* 337:202–207
680. Barsoum MW (2000) The M_{N+1}AX_N phases: a new class of solids. *Prog Solid St Chem* 28:201–281
681. Barsoum MW (2010) The M_{n+1}AX_n phases and their properties. In: Riedel R, Chen I-W (eds) *Ceramics science and technology*, Vol. 2 – Properties, pp. 299–347. Wiley-VCH, Weinheim
682. Yamada K, Sawaoka AB (1994) Very small spherical crystals of distorted diamond found in a detonation product of explosive/graphite mixtures and their formation mechanism. *Carbon* 32(4):665–673
683. Vora H, Moraec TJ (1981) Structural investigation of thin films of diamondlike carbon. *J Appl Phys* 52(10):6151–6157
684. Bursill LA, Fullerton AL, Bourgeois LN (2001) Size and surface structure of diamond nano-crystals. *Int J Modern Phys B* 15(31):4087–4102
685. Holland L, Ojha SM (1979) The growth of carbon films with random atomic structure from ion impact damage in a hydrocarbon plasma. *Thin Solid Films* 58(1):107–116
686. Konyashin I, Zern A, Mayer J, Aldinger F, Babaev V, Khvostov V, Guseva M (2001) A new carbon modification: ‘n-diamond’ or face-centred cubic carbon. *Diamond Relat Mater* 10(1):99–102
687. Palatnik LS, Guseva MB, Babaev VG, Savchenko NF, Falko II (1984) γ carbon. *Sov Phys JETP* 60:520–522

688. Hirai H, Kondo K-I (1991) Modified phases of diamond formed under shock compression and rapid quenching. *Science* 253:772–774
689. Farr JD (1968) Phase diagrams of selected refractory compounds. In: Hausner HH, Bowman MG (eds) *Fundamentals of refractory compounds*, pp. 33–48. Plenum Press, New York
690. Nowotny H, Rogl P (1977) Ternary metal borides. In: Matkovich VI (ed) *Boron and refractory borides*, pp. 413–438. Springer, Berlin, Heidelberg, New York
691. Ma X, Li C, Du Z, Zhang W (2004) Thermodynamic assessment of the Ti-B system. *J Alloys Compd* 370:149–158
692. Remschnig K, Le Bihan T, Noel H, Rogl P (1992) Structural chemistry and magnetic behaviour of binary uranium silicides. *J Solid State Chem* 97:391–399
693. Bowman AL, Arnold GP, Krikorian NH, Zachariasen WH (1971) The crystal structure of U_2IrC_2 . *Acta Crystallogr B* 27:1067–1068
694. Enyashin AN, Ivanovskii AL (2011) Graphene allotropes. *Phys Status Solidi B* 248(8):1879–1883
695. Appelhans DJ, Lin Z, Lusk MT (2010) Two-dimensional carbon semiconductor: density functional theory calculations. *Phys Rev B* 82(7):073410
696. Appelhans DJ, Carr LD, Lusk MT (2010) Embedded ribbons of graphene allotropes: an extended defect perspective. *New J Phys* 12:1250006
697. Enyashin AN, Ivanovskii AL (2007) New self-intercalated C_{28} , $Ti@C_{28}$ and $Zn@C_{28}$ hyperdiamonds: crystal structure and elastic and electronic properties. *JETP Letters* 86(8):537–542
698. Miura K, Tsuda D, Itamura N, Sasaki N (2007) Superlubricity of fullerene intercalated graphite composite. *Japan J Appl Phys* 46(8A):5269–5274
699. Skrzypek M, Gburski Z (2002) Fullerene cluster between graphite walls – computer simulation. *Europhys Lett* 59(2):305–310
700. FactSage (2012) Data from Tdnucl – Thermodata nuclear database. Collection of phase diagrams. http://www.crct.polymtl.ca/fact/phase_diagram.php?file=C-Mg.jpg&dir=TDnucl. Accessed 28 August 2012
701. FactSage (2012) Data from Tdnucl – Thermodata nuclear database. Collection of phase diagrams. http://www.crct.polymtl.ca/fact/phase_diagram.php?file=C-Ca.jpg&dir=TDnucl. Accessed 28 August 2012
702. FactSage (2012) Data from Tdnucl – Thermodata nuclear database. Collection of phase diagrams. http://www.crct.polymtl.ca/fact/phase_diagram.php?file=C-Sr.jpg&dir=TDnucl. Accessed 28 August 2012
703. FactSage (2012) Data from Tdnucl – Thermodata nuclear database. Collection of phase diagrams. http://www.crct.polymtl.ca/fact/phase_diagram.php?file=Ba-C.jpg&dir=TDnucl. Accessed 28 August 2012
704. FactSage (2012) Data from Tdnucl – Thermodata nuclear database. Collection of phase diagrams. http://www.crct.polymtl.ca/fact/phase_diagram.php?file=C-In.jpg&dir=TDnucl. Accessed 9 November 2012
705. Khaenko BV, Prilutskii EV, Mikhaliuk AA, Karpets MV (1995) Formation of a new phase upon heating of the products of interaction of SiC with SiO_2 . *Powder Metall Met Ceram* 34(9–10):513–514
706. Guo LB, Wang YL, Song F, He F, Huang Y, Yan LH, Wan YZ (2007) Formation and characterization of Si_5C_3 type silicon carbide by carbon ion implantation with a MEVVA ion source. *Mater Lett* 61(19–20):4083–4085
707. Bucknum MJ, Ienco A, Castro EA (2005) Electronic structure and bulk modulus of silicon dicarbide: a glitter phase. *J Molec Struct* 716:73–78
708. Andrew RC, Braun M, Chetty N (2012) A theoretical investigation of the stability of crystalline silicon dicarbide. *Comput Mater Sci* 55:186–191
709. Olesinski RW, Abbaschian GJ (1984) The C-Ge (carbon-germanium) system. *Bull Alloy Phase Diagrams* 5(5):484–486

710. Fromm E, Gebhardt, E (1976) Gase und Kohlenstoff in Metallen (Gases and carbon in metals). Springer, Berlin (in German)
711. FactSage (2007) Data from SGTE 2007 alloy database. Collection of phase diagrams. http://www.crct.polymtl.ca/fact/phase_diagram.php?file=C-N.jpg&dir=SGTE2007. Accessed 24 November 2012
712. Thomas A, Fischer A, Goettmann F, Antonietti M, Muller J-O, Schlogl R, Carlsson JM (2008) Graphitic carbon nitride materials: variation of structure and morphology and their use as metal-free catalysts. *J Mater Chem* 18(41):4893–4908
713. Dante RC, Martin-Ramos P, Correa-Guimaraes A, Martin-Gil J (2011) Synthesis of graphitic carbon nitride by reaction of melamine and uric acid. *Mater Chem Phys* 130(3):1094–1102
714. Niu C, Lu YZ, Lieber CM (1993) Experimental realization of the covalent solid carbon nitride. *Science* 261(5119):334–337
715. Yin LW, Li MS, Liu YX, Sui JL, Wang JM (2003) Synthesis of beta carbon nitride nanosized crystal through mechanochemical reaction. *J Phys Condens Matter* 15(2):309–314
716. Yin LW, Bando Y, Li MS, Liu YX, Qi YX (2003) Unique single-crystalline beta carbon nitride nanorods. *Adv Mater* 15(21):1840–1844
717. Hummelen JC, Knight B, Pavlovich J, Gonzales R, Wudl F (1995) Isolation of the heterofullerene $C_{59}N$ as its dimer $(C_{59}N)_2$. *Science* 269(5230):1554–1556
718. FactSage (2007) Data from SGTE 2007 alloy database. Collection of phase diagrams. http://www.crct.polymtl.ca/fact/phase_diagram.php?file=C-P.jpg&dir=SGTE2007. Accessed 24 November 2012
719. De Avillez RR, Grujicic M, Furtado HS (1989) A computer calculation of the niobium-carbon phase diagram. *Calphad* 13(1):45–51
720. Wiesenberger H, Lengauer W, Ettmayer P (1998) Reactive diffusion and phase equilibria in the V-C, Nb-C, Ta-C and Ta-N systems. *Acta Mater* 46(2):651–666
721. Kublii VZ, Velikanova TYa (2004) Ordering in the carbide W_2C and phase equilibria in the tungsten-carbon system in the region of its existence. *Powder Metall Met Ceram* 43(11–12):630–644
722. Morris RA, Wang B, Matson LE, Thompson GB (2012) Microstructural formations and phase transformation pathways in hot isostatically pressed tantalum carbides. *Acta Mater* 60:139–148
723. Demyashev GM (2010) Review: transition metal-based nanolamellar phases. *Prog Mater Sci* 55:629–674
724. Andrievski RA (2012) Micro- and nanosized boron carbide: synthesis, structure and properties. *Russ Chem Rev* 81(6):549–559
725. Samsonov GV, Serebryakova TI, Neronov VA (1975) Boridy (Borides). Atomizdat, Moscow (in Russian)
726. Rogl P, Schuster JC (1992) Phase diagrams of ternary boron nitride and silicon nitride systems. ASM International, Materials Park, Ohio
727. Markovskii LYa, Bezruk NT, Berkova GE (1971) Ob ustoychivosti boridov nikelya i kobalta po otnosheniyu k uglerodu (On the stability of nickel and cobalt borides with respect to carbon). *Izv AN SSSR Neorg Mater* 7(1):56–58 (in Russian)
728. Szillat H, Majewski P, Aldinger F (1997) Phase equilibria in the system Y-Ni-B-C. *J Alloys Compd* 261(1–2):242–249
729. Kudin VG, Makara VA (2004) On the thermodynamic properties of melts and phase equilibria in the Ni-B-C system. *Russ Metall* (5):436–439
730. Mazumdar C, Nagarajan R (2005) Quaternary borocarbides – a new class of superconductors and materials. *Current Sci* 88(1):83–95
731. Li W-J, Tu R, Goto T (2005) Preparation of TiB_2 -SiC eutectic composite by an arc-melted method and its characterization. *Mater Trans* 46(11):2504–2508
732. Li W-J, Tu R, Goto T (2005) Preparation of B_4C - TiB_2 -SiC ternary eutectic composites by a floating zone method and their properties. *Mater Trans* 46(9):2067–2072

733. Li W-J, Tu R, Goto T (2006) Preparation of TiC-TiB₂-SiC ternary eutectic composites by an arc-melting and their characterizations. *Mater Trans* 47(4):1193–1197
734. Zakaryan DA, Kartuzov VV, Khachatryan (2009) Pseudopotential method for calculating the eutectic temperature and concentration of the components of the B₄C-TiB₂, TiB₂-SiC and B₄C-SiC systems. *Powder Metall Met Ceram* 48(9–10):588–594
735. Saikia N, Deka RC (2012) First principles study on the boron-nitrogen domains segregated within (5,5) and (8,0) single-wall carbon nanotubes: formation energy, electronic structure and reactivity. *Comput Theoret Chem* 996:11–20
736. Parthe E, Jeitschko W, Sadagopan V (1965) A neutron diffraction study of the Nowotny phase Mo_{4.8}Si₃C_{0.6}. *Acta Crystallogr* 19:1031–1037
737. Guiot JM (1966) Contribution a l'étude des cermets a base de SiC. Etude du système Mo-SiC. (Contribution to the study of SiC cermets. Study of SiC-Mo system.) *Silic Ind* 31:363–367 (in French)
738. Rokhlin L, Lysova E (2010) Carbon – molybdenum – silicon system. In: Effenberg G, Ilyenko S (eds) Ternary alloy systems. Subvol. E, Part 2, pp. 444–462. Springer, Berlin, Heidelberg
739. Cacciamani G, Riani P (2010) Carbon – niobium – silicon system. In: Effenberg G, Ilyenko S (eds) Ternary alloy systems. Subvol. E, Part 2, pp. 560–566. Springer, Berlin, Heidelberg
740. Katsura M, Sano T (1966) The uranium-carbon-nitrogen system. *J Nucl Sci Technol* 3(5):194–199
741. Cordfunke EHP, Ouweltjes W (1979) Investigations on uranium carbonitrides. II. Phase relationships. *J Nucl Mater* 79(2):271–276
742. Perrot P (2010) Carbon – nitrogen – uranium system. In: Effenberg G, Ilyenko S (eds) Ternary alloy systems. Subvol. E, Part 2, pp. 551–559. Springer, Berlin, Heidelberg
743. Besmann TM, Shin D, Lindemer TB (2012) Uranium nitride as LWR TRISO fuel: thermodynamic modelling of U-C-N. *J Nucl Mater* 427:162–168
744. Eklund P, Beckers M, Jansson U, Hogberg H, Hultman L (2010) The M_{n+1}AX_n phases: materials science and thin-film processing. *Thin Solid Films* 518:1851–1878
745. Sun ZM (2011) Progress in research and development on MAX phases: a family of layered ternary compounds. *Int Mater Rev* 56(3):143–166
746. Lin ZJ, Li MS, Zhou YC (2008) High-temperature corrosion mechanism of layered ternary ceramics. In: Gao W, Li Z (eds) Developments in high-temperature corrosion and protection of materials. pp. 255–289, Woodhead, CRC Press, Boca Raton, Boston
747. Lukas HL (2010) Carbon – tantalum – titanium system. In: Effenberg G, Ilyenko S (eds) Ternary alloy systems. Subvol. E, Part 2, pp. 619–631. Springer, Berlin, Heidelberg
748. Savitsky EM, Efimov YV, Mikhailov BP, Moroz EA (1979) Vzaimodeistvie silitsidov, germanidov i drugikh faz struktury A15 s uglerodom (Reaction of silicides, germanides and other phases of the A15 structure type with carbon). *Izv AN SSSR Neorg Mater* 15(4):658–662 (in Russian)
749. Ordanyan SS, Vikhman SV, Unrod VI (2000) On the interaction in SiC-M'(IV-V)C systems. *Russ J Appl Chem* 73(12):2009–2012
750. Rokhlin LL, Dobatkina TV (2010) Carbon – silicon – vanadium system. In: Effenberg G, Ilyenko S (eds) Ternary alloy systems. Subvol. E, Part 2, pp. 606–618. Springer, Berlin, Heidelberg
751. Besson J, Blum PL, Morlevat JP (1965) Le diagramme ternaire U-UO₂-UOC (The ternary diagram U-UO₂-UOC). *Compt Rend Acad Sci Paris* 260:3390–3392 (in French)
752. Blum PL, Morlevat JP (1966) Le diagramme ternaire U-C-O (The ternary diagram U-C-O). *Rev Hautes Temp Refract* 3:253–254 (in French)
753. Perrot P (2010) Carbon – oxygen – uranium system. In: Effenberg G, Ilyenko S (eds) Ternary alloy systems. Subvol. E, Part 2, pp. 595–605. Springer, Berlin, Heidelberg
754. Fiedler M-L, Stadelmaier HH (1975) The ternary system Ni-W-C. *Z Metallkd* 66(9):402–404

755. Gabriel A, Pastor H, Deo DM, Basu S, Allibert CH (1986) New experimental data in the C-Fe-W, C-Co-W, C-Ni-W, C-Fe-Ni-W and C-Co-Ni-W cemented carbides systems and their application to sintering conditions. *Int J Refract Met Hard Mater* 5(4):215–221
756. Bochvar N, Rokhlin L (2010) Carbon – nickel – tungsten system. In: Effenberg G, Ilyenko S (eds) Ternary alloy systems. Subvol. E, Part 2, pp. 579–594. Springer, Berlin, Heidelberg
757. Raghavan V (2007) The C-Co-Fe-Ni-W (carbon-cobalt-iron-nickel-tungsten) system. *J Phase Equilib Diffus* 28(3):284–285
758. Perrot P, Lebrun N (2010) Carbon – niobium – tungsten system. In: Effenberg G, Ilyenko S (eds) Ternary alloy systems. Subvol. E, Part 2, pp. 567–578. Springer, Berlin, Heidelberg
759. Austin AE, Gerds AF (1958) The uranium-nitrogen-carbon system. Report BMI-1272-UC-25 (TIDD-4500), Contract No. W-7405-eng-92, pp. 1–18. Battelle Memorial Institute, Columbus, Ohio
760. Kandori T, Kamiya N, Kamigato O (1975) Solid solubility of SiC in β -Si₃N₄. *Jpn J Appl Phys* 14(1):137–138
761. Seifert HJ, Peng J, Lukas HL, Aldinger F (2001) Phase equilibria and thermal analysis of Si-C-N ceramics. *J Alloys Compd* 320(2):251–261
762. Seifert HJ, Aldinger F (2002) Phase equilibria in the Si-B-C-N System. *Struct Bonding* 101:1–58
763. Tomashik V (2010) Carbon – nitrogen – silicon system. In: Effenberg G, Ilyenko S (eds) Ternary alloy systems. Subvol. E, Part 2, pp. 531–550. Springer, Berlin, Heidelberg
764. Gorshkova LV, Telegus VS, Shamrai FI, Kuzma YB (1973) System molybdenum-tungsten-carbon. *Powder Metall Met Ceram* 12(3):237–239
765. Gustafson P (1988) Thermodynamic evaluation of the C-Mo-W system. *Z Metallkd* 79(7):397–402
766. Rokhlin L, Dobatkina T (2010) Carbon – molybdenum – tungsten system. In: Effenberg G, Ilyenko S (eds) Ternary alloy systems. Subvol. E, Part 2, pp. 516–530. Springer, Berlin, Heidelberg
767. Zakharov AM, Novikov II, Parshikov VG (1970) Troinaya sistema Mo-Ti-C (The Mo-Ti-C ternary system). *Izv Vyssh Uchebn Zaved Tsvetn Metall* 13(6):106–112 (in Russian)
768. Kroupa A, Watson A (2010) Carbon – molybdenum – titanium system. In: Effenberg G, Ilyenko S (eds) Ternary alloy systems. Subvol. E, Part 2, pp. 463–490. Springer, Berlin, Heidelberg
769. Lyakishev NP, Gasik MI, Polyakov OI (1991) Thermodynamic investigation of the interparticle interactions in the Me(Ti,V,Cr,Mn,Fe,Co,Ni)-Si-C systems as theoretical prerequisites for improving the technology of smelting bulk silicon ferroalloys. *Russ Metall* (1):1–9
770. Lebrun N, Perrot P (2010) Carbon – manganese – silicon system. In: Effenberg G, Ilyenko S (eds) Ternary alloy systems. Subvol. E, Part 2, pp. 433–443. Springer, Berlin, Heidelberg
771. Cacciamani G, Riani P (2010) Carbon – hafnium – silicon system. In: Effenberg G, Ilyenko S (eds) Ternary alloy systems. Subvol. E, Part 2, pp. 429–432. Springer, Berlin, Heidelberg
772. Ordanyan SS, Kraskovskaya AA, Avgustinnik AI (1966) Fazovaya diagramma sistemy HfC-Mo (Phase diagram of the HfC-Mo). *Izv AN SSSR Neorg Mater* 2 (2):299–302 (in Russian)
773. Eremenko VN, Velikanova TY, Shabanova SV, Artyukh LV (1973) Continuous series of solid solutions of carbides with NaCl structure in the ternary systems Mo(W)-Me^{IV,V}-C. *Powder Metall Met Ceram* 12(11):909–912
774. Rokhlin L, Kolchugina N, Dobatkina T, Semenova E (2010) Carbon – hafnium – molybdenum system. In: Effenberg G, Ilyenko S (eds) Ternary alloy systems. Subvol. E, Part 2, pp. 409–428. Springer, Berlin, Heidelberg

775. Fedorov TF, Kuzma YuB (1965) Phase equilibria in the system zirconium-chromium-carbon. *Powder Metall Met Ceram* 4(3):234–237
776. Eremenko VN, Velikanova TYa, Sleptsov SV, Bondar AA (1992) Fazovye ravnovesiya pri subsolidusnykh temperaturakh i skhema kristallizatsii splavov sistema Cr-Zr-C (Phase equilibria at subsolidus temperatures and solidification behaviour of Cr-Zr-C alloys). *Izv AN SSSR Metall* (5):144–150 (in Russian)
777. Ivanchenko VG, Pogorelaya VV (2001) Structure formation in eutectic alloys of chromium with carbide Cr_{23}C_6 and with carbides of IVA-group metals. *Met Phys Adv Techn* 19(3):869–874
778. Ivanchenko VG (2001) Phase equilibria and formation of structure and properties in the chromium alloys with interstitial phases. *Met Phys Adv Techn* 19(3):669–710
779. Ivanchenko V, Pryadko T (2010) Carbon – chromium – zirconium system. In: Effenberg G, Ilyenko S (eds) Ternary alloy systems. Subvol. E, Part 2, pp. 397–408. Springer, Berlin, Heidelberg
780. Velikanova TYa, Eremenko VN (1988) Relationships governing phase equilibria in refractory carbide-bearing systems of transition metals. *Powder Metall Met Ceram* 27(2):145–149
781. Watson A, Kroupa A (2010) Carbon – chromium – tungsten system. In: Effenberg G, Ilyenko S (eds) Ternary alloy systems. Subvol. E, Part 2, pp. 379–396. Springer, Berlin, Heidelberg
782. Rassaerts H, Kieffer R, Nowotny H (1965) Die V-Cr-C Dreistoffsystem (The V-Cr-C ternary system). *Monatsh Chem* 96:1536–1542 (in German)
783. Kieffer R, Rassaerts H (1966) Am System V-Cr-C und Verwendung von Vanadium und Chromcarbid in Hartmetallen. I (On system V-Cr-C and use of vanadium and chromium carbides in hard metals. I) *Metall* 20(7):691–695 (in German)
784. Fedorov TF, Popova NM, Gorshkova LV, Skolozdra RV, Kuzma YuB (1968) Phase equilibria in the systems V-Cr-C, Nb-Cr-C and Ta-Cr-C. *Powder Metall Met Ceram* 7(3):193–197
785. Steurer W, Rogl P, Boller H (1980) A neutron powder diffraction study of $(\text{V,Cr})_3\text{C}_{2-x}$. *J Less-Common Met* 76:145–151
786. Nowotny H, Rogl P, Schuster JC (1982) Structural chemistry of complex carbides and related compounds. *J Solid State Chem* 44:126–133
787. Velikanova T, Turchanin M, Pavlyuchkov D, Tomashuk V (2010) Carbon – chromium – vanadium system. In: Effenberg G, Ilyenko S (eds) Ternary alloy systems. Subvol. E, Part 2, pp. 369–378. Springer, Berlin, Heidelberg
788. Booker PH, Kunrath AO, Hepworth MT (1997) Experimental determination of the ternary diagram of the Ti-Cr-C system. *Acta Mater* 45(4):1625–1632
789. Bandyopadhyay D, Sharma RC, Chakraborti N (1999) The Ti-Cr-C (titanium-chromium-carbon) system. *J Phase Equilib* 20(3):325–331
790. Schuster JC, Du Y (1999) Thermodynamic description of the system Ti-Cr-C. *Calphad* 23(3–4):393–408
791. Ivanchenko V, Pryadko T (2010) Carbon – chromium – titanium system. In: Effenberg G, Ilyenko S (eds) Ternary alloy systems. Subvol. E, Part 2, pp. 348–368. Springer, Berlin, Heidelberg
792. Borisova AL, Borisov YuS, Shvedova LK, Kocherzhinskii YuA, Nechiporenko VI, Vasilev MA, Kostyuchenko VG (1979) Reactions in the Cr-SiC system under conditions of ordinary and plasma heating. *Powder Metall Met Ceram* 18(10):722–728
793. Lebrun N, Perrot N, Serbruyns A, Tedenac J-C (2010) Carbon – chromium – silicon system. In: Effenberg G, Ilyenko S (eds) Ternary alloy systems. Subvol. E, Part 2, pp. 330–347. Springer, Berlin, Heidelberg
794. Eremenko VN, Velikanova TYa, Bondar AA (1990) Zakonomernosti fazovykh ravnovesii v troinykh sistemakh metallov VI gruppy s uglerodom (Regularities of phase equilibria in the ternary systems of the VI group metals with carbon) In: Eremenko VN (ed) Fazovye

- ravnovesiya, struktura i svoistva splavov (The phase equilibria, structure and properties of alloys). Naukova Dumka, Kyiv pp. 4–17 (in Russian)
795. Bondar A, Dovbenko O, Ivanchenko V, Kozlov A (2010) Carbon – chromium – molybdenum system. In: Effenberg G, Ilyenko S (eds) Ternary alloy systems. Subvol. E, Part 2, pp. 290–307. Springer, Berlin, Heidelberg
 796. Uhrenius B, Carlsson B, Franzen T (1976) A study of the Co-W-C system at liquidus temperatures. *Scand J Met* 5(2):49–56
 797. Uhrenius B (1991) Contribution to the knowledge of phase equilibria in tungsten-carbon based system. *Scand J Met* 20(1):93–98
 798. Kruse O, Jansson B, Frisk K (2001) Experimental study of invariant equilibria in the Co-W-C and Co-W-C-Me (Me = Ti, Ta, Nb) systems. *J Phase Equilib* 22:552–555
 799. Markstrom A, Sundman B, Frisk K (2005) A revised thermodynamic description of the Co-W-C system. *J Phase Equilib Diffus* 26(2):152–160
 800. Bondar A, Bochvar N, Dobatkina T, Krendelsberger N (2010) Carbon – cobalt – tungsten system. In: Effenberg G, Ilyenko S (eds) Ternary alloy systems. Subvol. E, Part 2, pp. 249–289. Springer, Berlin, Heidelberg
 801. Hachisuka T (1968) Preparation of TaC-WC solid solutions and their properties. *J Jpn Soc Powder Metall* 15:110–117 (in Japanese)
 802. Eremenko VN, Velikanova TYa (1973) Stroenie diagramm sostoyaniya troinykh sistem (Mo, W) – (Ti, Zr, Hf, V, Nb, Ta) – C (Structure of phase diagrams of the (Mo, W) – (Ti, Zr, Hf, V, Nb, Ta) – C ternary systems). In: Ageev VN (ed) *Obshchie zakonomernosti stroeniya diagramm sostoyaniya metallicheskih sistem* (The general regularities of the phase diagrams structures of metal systems). Nauka, Moscow, pp. 49–52 (in Russian)
 803. Frisk K (1999) A thermodynamic analysis of the Ta-W-C and the Ta-W-C-N systems. *Z Metallkd* 90(9):704–711
 804. Bochvar N, Rokhlin L, Lysova E (2010) Carbon – tantalum – tungsten system. In: Effenberg G, Ilyenko S (eds) Ternary alloy systems. Subvol. E, Part 3, pp. 1–17. Springer, Berlin, Heidelberg
 805. Ogorodnikov VV, Ogorodnikova AA (1982) Calculation of the phase diagrams for pseudo-binary systems of cubic transition metal monocarbides. *Russ J Phys Chem* 56(11):1749–1751
 806. Gusev AI (2000) Order-disorder transformations and phase equilibria in strongly nonstoichiometric compounds. *Phys Uspekhi* 43(1):1–37
 807. Dobatkina T, Bochvar N (2010) Carbon – tantalum – zirconium system. In: Effenberg G, Ilyenko S (eds) Ternary alloy systems. Subvol. E, Part 3, pp. 18–30. Springer, Berlin, Heidelberg
 808. Shveikin GP (1962) Reaction of tungsten carbide with oxides of refractory metals in a vacuum. *Powder Metall Met Ceram* 1(6):454–457
 809. Kuzma YuB, Lakh VI, Markiv Vya, Stadnyk BI, Gladyshevskii EI (1963) X-ray diffraction study of the system tungsten-rhenium-carbon. *Powder Metall Met Ceram* 2(4):286–272
 810. Eremenko VN, Tretyachenko LA (1964) The isothermal section of the system Ti-V-C. *Powder Metall Met Ceram* 3(6):464–469
 811. Borusevich LK, Gladyshevskii EI (1964) X-ray diffraction study of alloys in the system Mo-Re-C. *Powder Metall Met Ceram* 3(6):460–463
 812. Allinson JD, Riviere JC (1965) High temperature short-term compatibility of some refractory metals with the thermoionic fuel UC-ZrC. *J Nucl Mater* 17:97–110
 813. Fedorov TF, Gladyshevskii EI (1965) Phase equilibria in ternary systems of transition metals of groups IV and V and carbon. *Powder Metall Met Ceram* 4(1):27–29
 814. Matyushenko NN, Rozen AA, Pugachev NS (1966) Triangulation of the system C-Si-Be. *Powder Metall Met Ceram* 5(4):310–312
 815. Tretyachenko LA, Eremenko VN (1966) Structure and certain properties of alloys of sections TiC-VC_{0.90}, TiC-V₂C, TiC-V and in the region TiC-VC_{0.90}-C of the ternary system Ti-V-C. *Powder Metall Met Ceram* 5(7):581–584

816. Voroshilov YuV, Gorshkova LV, Popova AM, Fedorov TF (1967) Ternary systems Ti-Zr-C and Ti-Hf-C. *Powder Metall Met Ceram* 6(5):403–405
817. Voroshilov YuV (1968) Concerning ternary systems of titanium-zirconium-carbon and titanium-hafnium-carbon. *Powder Metall Met Ceram* 7(8):669
818. Gorshkova LV, Fedorov TF, Kuzma YuB (1967) Ternary systems niobium-rhenium-carbon and tantalum-rhenium-carbon. *Powder Metall Met Ceram* 6(4):287–290
819. Evtushok TM, Burykina AL (1969) Interaction of graphite and pyrographite with titanium, niobium, molybdenum and tungsten disilicides. *Powder Metall Met Ceram* 8(7):581–586
820. Gorshkova LV, Voroshilov YuV, Fedorov TF (1969) Study of the ternary system zirconium-rhenium-carbon. *Powder Metall Met Ceram* 8(2):146–148
821. Eremenko VN, Velikanova TYa (1969) Phase equilibria in the Mo – TiC – Ti region of the ternary system Mo – Ti – C. Character of solidification of alloys and projection of the solidus surface. Part I. *Powder Metall Met Ceram* 8(11):931–936
822. Kuroda Y, Tanaka K, Suzuki M, Akimoto Y (1970) Compatibility of U(N,C) with potential cladding materials. *J Nucl Mater* 34:174–181
823. Eremenko VN, Velikanova TYa (1970) Phase equilibria in the Mo – TiC – Ti region of the ternary system Mo – Ti – C. Part II. *Powder Metall Met Ceram* 9(9):744–747
824. Williams AJ, Briggs DC (1970) Ageing in niobium-rich niobium-hafnium-carbon alloys. *J Less-Common Met* 21:255–273
825. Samsonov GV, Antonova MM, Morozov VV (1970) Ternary systems Me-C-H and Me-N-H. *Powder Metall Met Ceram* 9(4):318–327
826. Khodosov EF, Andrievskii RA (1967) Studying nuclear magnetic resonance spectra of zirconium and yttrium hydrides. *Powder Metall Met Ceram* 6(8):649–653
827. Velikanova TYa, Eremenko VN (1974) Phase equilibria in the ternary systems formed by molybdenum and tungsten with the groups IV and V transition metals and carbon. *Powder Metall Met Ceram* 13(4):293–297
828. Eremenko VN, Shabanova SV, Velikanova TYa, Petrenko LA (1975) Structure of alloys and phase equilibria of the system Hf-Mo-C. I. Projection of the solidus surface of the partial system Mo-HfC-Hf. *Powder Metall Met Ceram* 14(7):555–561
829. Borisova AL, Martsenyuk IS (1975) Reactions of boron and aluminum nitrides and materials based on them with refractory metals. *Powder Metall Met Ceram* 14(10):822–826
830. Ivchenko VI, Lesnaya MI, Nemchenko VF, Kosolapova TYa (1976) Some physical properties of ternary compounds in the system Ti – Al – C. *Powder Metall Met Ceram* 15(5):367–369
831. Gorshkova LV (1976) Joint solubility of carbon and zirconium in molybdenum-tungsten solid solutions. *Powder Metall Met Ceram* 15(3):215–216
832. Eremenko VN, Shabanova SV, Velikanova TYa (1977) Structure of alloys and the phase equilibrium diagram of the system Hf-Mo-C. V. Isothermal section of the system Hf-Mo-C at 1700 °C. *Powder Metall Met Ceram* 16(9):712–717
833. Stark WA, Jr (1978) Cesium solubility, diffusion and permeation in zirconium carbide. *J Nucl Mater* 73:169–179
834. Shurin AK, Razumova NA (1979) Quasiternary system Fe-TiC-TiB₂. *Powder Metall Met Ceram* 18(12):903–905
835. Kosterova NV, Ordanyan SS, Neshpor VS, Ostrovskii EK (1980) Thermoionic properties of cermets of eutectic compositions in Me(IV) – (C,B) – (Mo,Re,W) systems. *Powder Metall Met Ceram* 19(1):61–66
836. Stepanenko EK, Dogadaeva IM, Ordanyan SS (1982) Reactions in the NbC-NbSi₂ and NbB₂-NbSi₂ systems. *Powder Metall Met Ceram* 21(7):568–570
837. Eremenko VN, Velikanova TYa (1983) Use of the phase diagrams of ternary transition metal systems containing carbides in the development of heat-resisting hard alloys. *Powder Metall Met Ceram* 22(12):1010–1021
838. Ordanyan SS, Stepanenko EK, Dmitriev AI, Shchemeleva MV (1986) Interaction in the B₄C-TiB₂ system. *Sov J Superhard Mater* 8(5):34–37

839. Shurin AK, Dmitrieva GP, Razumova NA, Khandros EL (1987) Phase diagram of the Ni-ZrC-HfC. *Powder Metall Met Ceram* 26(9):754–757
840. Eremenko VN, Velikanova TYa, Bondar AA (1989) Phase equilibria at the solidus surface of the equilibrium diagram of ternary systems of technetium with carbon and d-transition metals of groups III-VII. *Powder Metall Met Ceram* 28(11):868–873
841. Lee B-J (1992) On the stability of Cr carbides. *Calphad* 16(2):121–149
842. Hillert M, Qiu C (1992) A reassessment of the Fe-Cr-Mo-C system. *J Phase Equilib* 13(5):512–521
843. Lee B-J, Lee DN (1992) A thermodynamic evaluation of the Fe-Cr-V-C system. *J Phase Equilib* 13(4):349–364
844. Sheftel EN, Bannykh OA (1993–1994) Niobium-base alloys. *Int J Refract Met Hard Mater* 12:303–314
845. Raghavan V (1993) The C-Fe-V (carbon-iron-vanadium) system. *J Phase Equilib* 14(5):622–623
846. Raghavan V (1994) The C-Fe-Mo (carbon-iron-molybdenum) system. *J Phase Equilib* 15(4):425–427
847. Raghavan V (1994) The C-Fe-W (carbon-iron-tungsten) system. *J Phase Equilib* 15(4):429–430
848. Uhrenius B, Forsen K, Haglund B-O, Andersson I (1995) Phase equilibria and phase diagrams in carbide systems. *J Phase Equilib* 16(5):430–440
849. Alekseeva ZM (1992) Phase equilibria in the U-Si-C system. *J Nucl Mater* 186:294–298
850. Itkin VP (1996) The C-Te (carbon-tellurium) system. *J Phase Equilib* 17(2):131
851. Barabash OM, Legkaya TN, Petrushin NV, Cherkasova EV (1997) Effect of aluminum on the parameters of eutectic transformation $L \leftrightarrow \gamma + \text{Mo}_2\text{C}$ in the Ni-Mo-Al-C quaternary system. *Powder Metall Met Ceram* 36(11–12):664–667
852. Artyukh LV, Belous OA, Bondar AA, Burka MP, Velikanova TYa, Tsyganenko NI (1997) Structure and properties of multicomponent eutectic alloys based on chromium and titanium carbide. *Powder Metall Met Ceram* 36(1–2):15–23
853. Hugosson HW, Nordstrom L, Jansson U, Johansson B, Eriksson O (1999) Theoretical studies of substitutional impurities in molybdenum carbide. *Phys Rev B* 60(22):15123–15130
854. Shvedova LK (1999) Contact reaction, structure and phase formation in the chromium – silicon carbide system. *Powder Metall Met Ceram* 38(9–10):477–481
855. Walter J, Boonchuduang W, Hara S (2000) XPS study on pristine and intercalated tantalum carbosulfide. *J Alloys Compd* 305:259–263
856. Lisovskii AF (2000) Cemented carbides alloyed with ruthenium, osmium and rhenium. *Powder Metall Met Ceram* 39(9–10):428–433
857. Khrushchev MS (2000) Kinetics and mechanism of reaction between silicon carbide and silica. *Inorg Mater* 36(5):462–464
858. Dovbenko OI, Bondar AA, Velikanova TYa, Sleptsov SV (2000) The (Cr) + (NbC) quasibinary eutectic in the Cr-Nb-C system. *Powder Metall Met Ceram* 39(5–6):256–261
859. Ivanovskii AL, Sabiryanov RF, Skazkin AN, Zhukovskii VM, Shveikin GP (2000) Electronic structure and bonding configuration of the *H*-phases Ti_2MC and Ti_2MN ($\text{M} = \text{Al, Ga, In}$). *Inorg Mater* 36(1):28–31
860. Ivanovskii AL, Gusev AI, Shveikin GP (1996) *Kvantovaya khimiya v materialovedenii: troinye karbidy i nitridy perekhodnykh metallov i elementov IIIb, IVb podgrupp* (Quantum chemistry in materials science: ternary carbides and nitrides of transition metals and subgroup IIIa, IVa elements). *Uralskoe Otdelenie Rossiiskoi Akademii Nauk, Yekaterinburg* (in Russian)
861. Ivanovskii AL, Okatov SV, Shveikin GP (2000) Electronic structure of high-temperature ZrO_2C_x . *Inorg Mater* 36(11):1121–1124
862. Kurdyumov AV, Solozhenko VL, Gubachek M, Borimchuk NI, Zelyavskii VB, Ostrovskaya NF, Yarosh VV (2000) Shock synthesis of ternary diamond-like phases in the B-C-N system. *Powder Metall Met Ceram* 39(9–10):467–473

863. Sudarikov MV, Zhikharev VM, Lykasov AA (2001) Gibbs energy of formation of cubic NbC_xN_y . *Inorg Mater* 37(3):243–247
864. Rempel SV, Gusev AI (2001) ZrC segregation to the surface of dilute solid solutions of zirconium carbide in niobium carbide. *Inorg Mater* 37(10):1024–1029
865. Velikanova TYa, Bondar AA, Dovbenko OI (2002) The Cr-Ta-C melting diagram in the (Cr)-(Ta)-(TaC) region. *Powder Metall Met Ceram* 41(7–8):400–406
866. Iekhsanyan AG, Aghajanyan NN, Dolukhanyan SK, Mnatsakanyan NL, Harutyunyan KhS, Hayrapetyan VS (2002) Thermal-radiation synthesis of zirconium hydridonitrides and carbohydrides. *J Alloys Compd* 330–332:559–563
867. Golubenko AN, Kosinova ML, Titov AA, Kuznetsov FA (2003) Thermodynamic modelling of BC_xN_y chemical vapour deposition in the B-C-N-H system. *Inorg Mater* 39(4):362–365
868. Raghavan V (2003) The C-Fe-Nb (carbon-iron-niobium) system. *J Phase Equilib* 24(1):57–61
869. Raghavan V (2003) The C-Fe-N-Nb (carbon-iron-nitrogen-niobium) system. *J Phase Equilib* 24(1):73–74
870. Raghavan V (2003) The C-Fe-N-Nb-Ti (carbon-iron-nitrogen-niobium-titanium) system. *J Phase Equilib* 24(1):77–78
871. Raghavan V (2003) The C-Fe-N-Nb-Ti-V (carbon-iron-nitrogen-niobium-titanium-vanadium) system. *J Phase Equilib* 24(1):79–81
872. Raghavan V (2003) The C-Fe-N-Ti (carbon-iron-nitrogen-titanium) system. *J Phase Equilib* 24(1):75–76
873. Raghavan V (2003) The C-Fe-V (carbon-iron-vanadium) system. *J Phase Equilib* 24(1):67
874. Tan Y, Ma CL, Kasama A, Tanaka R, Mishima Y, Hanada S, Yang J-M (2003) Effect of alloy composition on microstructure and high temperature properties of Nb-Zr-C ternary alloys. *Mater Sci Eng A* 341:282–288
875. Gusev AI, Rempel SV (2003) X-ray diffraction study of the nanostructure resulting from decomposition of $(\text{ZrC})_{1-x}(\text{NbC})_x$ solid solutions. *Inorg Mater* 39(1):43–46
876. Dovbenko OI, Bondar AA, Velikanova TYa, Bilous OO, Burka MP, Martseniuk PS, Shapoval TO, Tsyganyenko NI (2003) Quasi-binary metal-carbide eutectic of Cr-Ta-C system. *Mater Lett* 57:2866–2871
877. Paderno V, Paderno Y, Filippov V, Liashchenko A (2004) Directional crystallization of $\text{B}_4\text{C-NbB}_2$ and $\text{B}_4\text{C-MoB}_2$ eutectic compositions. *J Solid State Chem* 177:523–528
878. Grigorev ON, Bega ND, Lyashenko VI, Dubovik TV, Panashenko VM, Shcherbina OD (2005) Dependence of the structure of sintered boron carbonitride on the defect level in the starting BN powder. *Powder Metall Met Ceram* 44(5–6):287–293
879. Enyashin AN, Seifert G, Ivanovskii AL (2005) Calculation of the electronic and thermal properties of C/BN nanotubular heterostructures. *Inorg Mater* 41(6):595–603
880. Pantelev IB, Vladimirova MA, Ordanyan SS (2005) Synthesis of complex carbonitrides $\text{Ti}_{1-x}\text{W}_xC_{1-x}\text{N}_y$. *Powder Metall Met Ceram* 44(11–12):573–577
881. Raghavan V (2006) The Al-C-Ta-Ti (aluminum-carbon-tantalum-titanium) system. *J Phase Equilib* 27(2):169–170
882. Lin ZJ, Zhuo MJ, He LF, Zhou YC, Li MS, Wang JY (2006) Atomic-scale microstructures of $\text{Zr}_2\text{Al}_3\text{C}_4$ and $\text{Zr}_3\text{Al}_3\text{C}_5$. *Acta Mater* 54:3843–3851
883. Leela-Adisorn U, Choi SM, Matsunaga T, Hashimoto S, Honda S, Hayakawa K, Awaji H, Yamaguchi A (2006) AlZrC_2 synthesis. *Ceram Int* 32:431–439
884. Lipatnikov VN, Gusev AI (2007) Crystal structure and microstructure of disordered and ordered vanadium carbonitrides. *Inorg Mater* 43(8):827–833
885. Li J, Han J, Meng S, Zhang X, Liang J (2008) Valence bond structure and properties of $4\text{TaC}+\text{HfC}$ solid solutions. *Xiyou Jinshu Cailiao Yu Gongcheng* 37(5):840–843 (in Chinese)
886. Filonenko VP, Khabashesku VN, Davydov VA, Zibrov IP, Agafonov VN (2008) Synthesis of a new cubic phase in the B-C-N system. *Inorg Mater* 44(4):395–400

887. Du HJ, Li DC, He JL, Yu DL, Xu B, Liu ZY, Wang H-T, Tian YJ (2009) Hardness of α - and β - $\text{Si}_{3-n}\text{C}_n\text{N}_4$ ($n = 0, 1, 2, 3$) crystals. *Diamond Relat Mater* 18:72–75
888. Skripov AV, Wu H, Udovic TJ, Huang Q, Hempelmann R, Solonin AV, Rempel AA, Gusev AI (2009) Hydrogen in nonstoichiometric cubic niobium carbides: neutron vibrational spectroscopy and neutron diffraction studies. *J Alloys Compd* 478:68–74
889. Zakaryan DA, Kartuzov VV, Khachatryan AV (2009) Pseudopotential method for calculating the eutectic temperature and concentration of the components of the B_4C - TiB_2 , TiB_2 - SiC and B_4C - SiC systems. *Powder Metall Met Ceram* 48(9–10):588–594
890. Hong JD, Spear KE, Stubican VS (1979) Directional solidification of SiC - B_4C eutectic: growth and some properties. *Mater Res Bull* 14(6):775–783
891. Gadzyra NF, Davidchuk NK, Gnesin GG (2009) Structurization of composite ceramics based on stoichiometric silicon carbide during free sintering and hot pressing. *Powder Metall Met Ceram* 48(5–6):311–315
892. Grigorev ON, Kotenko VA, Shcherbina OD, Bega ND, Dubovik TV, Subbotin VI, Mosina TV, Lychko VV, Berezhinskii IL (2010) Production and properties of impact-resistant composites based on boron carbide and aluminium nitride. *Powder Metall Met Ceram* 49(3–4):193–200
893. Kar P (2010) Effect of anodization voltage on the formation of phase pure anatase nanotubes with doped carbon. *Inorg Mater* 46(4):377–382
894. Silvestroni L, Sciti D (2010) Sintering behaviour, microstructure and mechanical properties: a comparison among pressureless sintered ultra-refractory carbides. *Adv Mater Sci Eng* ID835018:1–11 (doi:10.1155/2010/835018)
895. Medvedeva NI, Novikov DL, Ivanovsky AL, Kuznetsov MV, Freeman AJ (1998) Electronic properties of Ti_3SiC_2 -based solid solutions. *Phys Rev B* 58(24):16042–16050
896. He X, Bai Y, Zhu C, Sun Y, Li M, Barsoum MW (2010) General trends in the structural, electronic and elastic properties of the M_3AlC_2 phases (M = transition metal): a first-principle study. *Comput Mater Sci* 49:691–698
897. Haddadi K, Bouhemadou A, Louail L, Maamache M (2011) Density functional study of the structural, electronic, elastic and thermodynamic properties of ACRu_3 ($\text{A} = \text{V}, \text{Nb}$ and Ta) compounds. *Intermetallics* 19:476–485
898. Islam MS, Islam AKMA (2011) Structural, elastic, electronic and optical properties of a new layered-ternary Ta_4SiC_3 compound. *Phys B* 406:275–279
899. Silvestroni L, Bellosi A, Melandri C, Sciti D, Liu JX, Zhang GJ (2011) Microstructure and properties of HfC and TaC-based ceramics obtained by ultrafine powder. *J Eur Ceram Soc* 31:619–627
900. Velikanova TA, Karpets MV, Agraval PG, Turchanin MA (2011) Phase states of Fe-Mo-C spinning alloys at high temperatures. *Powder Metall Met Ceram* 49(9–10):606–615
901. Ghebouli MA, Ghebouli B, Bouhemadou A, Fatmi M (2011) Theoretical study of the structural, elastic, electronic and thermal properties of the MAX phase Nb_2SiC . *Solid State Comm* 151:382–387
902. Zhao Y-W, Wang Y-J, Zhou Y, Peng H-X, Song G-M (2011) Ternary phase $\text{Zr}_x\text{Cu}_y\text{C}_z$ in reactively infiltrated ZrC/W composite. *J Am Ceram Soc* 94(10):3178–3180
903. Shein IR, Ivanovskii AL (2012) Planar nano-block structures $\text{Ti}_{n+1}\text{Al}_{0.5}\text{C}_n$ and $\text{Ti}_{n+1}\text{C}_n$ ($n = 1$ and 2) from MAX phases: structural, electronic properties and relative stability from first principles calculations. *Superlattices and microstructures* 52:147–157
904. Shein IR, Ivanovskii AL (2012) Graphene-like titanium carbides and nitrides $\text{Ti}_{n+1}\text{C}_n$, $\text{Ti}_{n+1}\text{N}_n$ ($n = 1, 2$ and 3) from de-intercalated MAX phases: first-principles probing of their structural, electronic properties and relative stability. *Comput Mater Sci* 65:104–114
905. Yonco RM, Homa MI (1986) The solubility of carbon in low-nitrogen liquid lithium. *J Nucl Mater* 138:117–122
906. Dalton JT, Potter PE, Shaw JL (1967) Constitutional studies on the ternary system plutonium-molybdenum-carbon, plutonium-silicon-carbon and plutonium-thorium-carbon. In: Kay AE, Waldron HB (eds) *Plutonium 1965. Proc. 3rd Int. Conf. on plutonium*, London, 1965, pp. 775–805. Institute of Metals, Chapman & Hall, London

907. Okamoto H (1992) The C-Fe (carbon-iron) system. *J Phase Equilib* 13(5):543–565
908. Shabalin IL, Tomkinson DM, Shabalin LI (2007) High-temperature hot-pressing of titanium carbide – graphite hetero-modulus ceramics. *J Eur Ceram Soc* 27(5):2171–2181
909. Eissler RL, Van Holde KE (1962) Wettability of coal, graphite and naphthalene as measured by contact angles. Circular 333. Illinois State Geological Survey, Urbana
910. Eustathopoulos N, Nicholas MG, Drevet B (1999) Wettability at high temperatures. Elsevier Science, Oxford
911. Leider HR, Krikorian OH, Young DA (1973) Thermodynamic properties of carbon up to the critical point. *Carbon* 11:555–563
912. Lassner E, Schubert W-D (1999) Tungsten. Kluwer Academic / Plenum Publishers, New York
913. Guminski C (1993) The C-Hg (carbon-mercury) system. *J Phase Equilib* 14(2):219–220
914. Guminski C (1989) Selected properties of simple amalgams. *J Mater Sci* 24:2661–2676
915. Huang W (1997) Thermodynamic properties of the Nb-W-C-N system. *Z Metallkd* 84:63–68
916. Rosseinsky MJ, Murphy DW, Fleming RM, Tycko R, Ramirez AP, Siegrist T, Dabbagh G, Barrett SE (1992) Structural and electronic properties of sodium-intercalated C_{60} . *Nature* (London) 356:416–418
917. Yildirim T, Zhou O, Fischer JE, Bykovetz N, Strongin RA, Cichy MA, Smith AB, Lin CL, Jelinek R (1992) Intercalation of sodium hetero-clusters into the C_{60} lattice. *Nature* (London) 360:568–571
918. Klöss KH, Hinz Hübner D, Ruschewitz U (2002) On a new modification of Na_2C_2 . *Z Anorg Allg Chem* 628:2701–2704
919. Fleming RM, Rosseinsky MJ, Ramirez AP, Murphy DW, Tully JC, Haddon RC, Siegrist T, Tycko R, Glarum SH, Marsh P, Dabbagh G, Zahurak SM, Makhija AV, Hampton C (1991) Preparation and structure of the alkali-metal fulleride A_4C_{60} . *Nature* (London) 352:701–703
920. Hemmersbach S, Zibrowius B, Ruschewitz U (1999) Na_2C_2 and K_2C_2 : synthesis, crystal structure and spectroscopic properties”, *Z Anorg Allg Chem* 625:1440–1446
921. Kobayashi M, Akahama Y, Kawamura H, Shinohara H, Sato H, Saito Y (1993) Structure sequence and possible superconductivity in potassium-doped fullerene $C_{70}K_x$. *Phys Rev B* 48:16877–16880
922. Ruschewitz U, Müller P, Kockelmann W (2001) On the crystal Structure of Rb_2C_2 and Cs_2C_2 . *Z Anorg Allg Chem* 627:513–522
923. Stephens PW, Bortel G, Falgel G, Tegze M, Janossy A, Pekker S, Oszlanyi G, Forro L (1994) Polymeric fullerene chains in RbC_{60} and KC_{60} . *Nature* (London) 370:636–639
924. Zhou O, Fischer JE, Coustel N, Kycia S, Zhu Q, McGhie AR, Romanow WJ, McCauley JP Jr, Smith AB, Cox DE (1991) Structure and bonding in alkali-metal-doped C_{60} . *Nature* (London) 351:462–464
925. Rikiishi Y, Kashino Y, Kusai H, Takabayashi Y, Kuwahara E, Kubozono Y, Kambe T, Takenobu T, Iwasa Y, Mizorogi N, Nagase S, Okada S (2005) Metallic phase in the metal-intercalated higher fullerene $Rb_{8.8(7)}C_{84}$. *Phys Rev B* 71:224118(1–6)
926. Ignateva IY, Barabash OM, Legkaya TN (1990) Evolution of the phase diagram for the magnesium-carbon system as a function of pressure on the basis of thermodynamic calculations. *Sverkhtrverd Mater* 12:1–5
927. Schürmann E, Jacke H (1987) Schmelzgleichgewichte im System Fe-C-Ca (Melting equilibria in the system Fe-C-Ca). *Steel Res* 58:399–405
928. Claridge JB, Kubozono Y, Rosseinsky MJ (2003) A complex fulleride superstructure – decoupling cation vacancy and anion orientational ordering in $Ca_{3+x}C_{60}$ with maximum entropy data analysis. *Chem Mater* 15:1830–1839
929. Guérard D, Hérol A (1975) Chimie Macromoléculaire. Synthèse directe de composés d’insertion du strontium dans le graphite (Macromolecular Chemistry. Direct synthesis of strontium intercalation in graphite compounds). *C R Seances Acad Sci Ser C* 280:729–730 (in French)

930. Saito S, Oshiyama A (1993) Sr_6C_{60} and Ba_6C_{60} : Semimetallic fullerides. *Phys Rev Lett* 71:121–124
931. Beyers R, Klang C, Johnson RD, Salem JR, De Vrles MS, Yannoni CS, Bethune DS, Dorn HC, Burbank P, Harich K, Stevenson S (1994) Preparation and structure of crystals of the metallofullerene Sc_2C_{84} . *Nature (London)* 370:196–199
932. Okamoto H (1996) The C-Y (carbon-yttrium) system. *J Phase Equilib* 17:548
933. Gröbner J, Lukas HL, Aldinger F (1995) Thermodynamic calculations in the Y-Al-C system. *J Alloys Compd* 220:8–14
934. Takata M, Umeda B, Nishibori E, Sakata M, Saito Y, Ohno M, Shinohara H (1995) Confirmation by x-ray diffraction of the endohedral nature of the metallofullerene $\text{Y}@\text{C}_{82}$. *Nature (London)* 377:46–49
935. Kessler B, Bringer A, Cramm S, Schlebusch C, Eberhardt W, Suzuki S, Achiba Y, Esch F, Barnaba M, Cocco D (1997) Evidence for incomplete charge transfer and La-derived states in the valence bands of endohedrally doped $\text{La}@\text{C}_{82}$. *Phys Rev Lett* 79:2289–2292
936. Rikiishi Y, Kubozono Y, Hosokawa T, Shibata K, Haruyama Y, Takabayashi A, Fujiwara A, Kobayashi S, Mori S, Iwasa Y (2004) Structural and electronic characterizations of two isomers of $\text{Ce}@\text{C}_{82}$. *J Phys Chem B* 108:7580–7585
937. Chen XH, Chi DH, Sun Z, Takenobu T, Liu ZS, Iwasa Y (2000) Synthesis, structure, and transport properties of novel fullerides A_3C_{70} (A = Ba and Sm). *J Am Chem Soc* 122:5729–5732
938. Molodtsov SL, Laubschat C, Richter M, Gantz T, Shikin AM (1996) Electronic structure of Eu and Yb graphite intercalation compounds. *Phys Rev B* 53:16621–16630
939. Takenobu T, Chi DH, Margadonna S, Prassides K, Kubozono Y, Fitch AN, Kato KI, Iwasa Y (2003) Synthesis, structure, and magnetic properties of the fullerene-based ferromagnets Eu_3C_{70} and Eu_6C_{70} . *J Am Chem Soc* 125:1897–1904
940. Pichler T, Golden MS, Knupfer M, Fink J, Kirbach U, Kuran P, Dunsch L (1997) Monometallofullerene $\text{Tm}@\text{C}_{82}$: proof of an encapsulated divalent Tm ion by high-energy spectroscopy. *Phys Rev Lett* 79:3026–3029
941. Haschke JM, Eick HA (1970) A phase investigation of the ytterbium-carbon system. *J Am Chem Soc* 92:1526–1530
942. Margadonna S, Arvanitidis J, Papagelis K, Prassides K (2005) Negative thermal expansion in the mixed valence ytterbium fulleride $\text{Yb}_{2.75}\text{C}_{60}$. *Chem Mater* 17:4474–4478
943. Burylev BP (1985) Phase diagram and activity of the components in the Tc-C system. *Russ Metall* (3):219–221
944. Du Z, Guo C, Yang X, Liu T (2006) A thermodynamic description of the Pd-Si-C system. *Intermetallics* 14:560–569
945. Savitskii EM, Polyakova VP (1975) Physico-chemical research in noble metals. *J Less-Common Met* 43:169–177
946. Ohtani H, Yamano M, Hasebe M (2004) Thermodynamic analysis of the Co-Al-C and Ni-Al-C systems by incorporating ab initio energetic calculations into the CALPHAD approach. *Calphad* 28:177–190
947. Okamoto H (1992) The Al-C (aluminum-carbon) system. *J Phase Equilib* 13:97–98
948. Baran LV (2006) Spontaneous growth of single crystals of various shapes in tin-fullerite films. *Crystallogr Rep* 51:690–695
949. Locke IW, Darwish AD, Kroto HW, Prassides K, Taylor R, Walton DRM (1994) Phosphorus/buckminsterfullerene intercalation compound $\text{C}_{60}(\text{P}_4)_2$. *Chem Phys Lett* 225:186–190
950. Roth G, Adelmann P, Knitter R (1993) Preparation and crystal structure of $\text{C}_{60}\text{S}_8\text{CS}_2$, a new fullerene-containing heteromolecular solid. *Mater Lett* 16:357–363
951. Tebbe FN, Harlow RL, Chase DB, Thorn DL, Campbell GC Jr, Calabrese JC, Herron N, Young RJ Jr, Wasserman E (1992) Synthesis and single-crystal x-ray structure of a highly symmetrical C_{60} derivative, $\text{C}_{60}\text{Br}_{24}$. *Science (Washington DC)* 256:822–825
952. Troyanov SI, Kemnitz E (2007) Singly-bonded fullerene dimers: neutral $(\text{C}_{60}\text{Cl}_5)_2$ and cationic $(\text{C}_{70})^{2+}$. *Chem Commun (Cambridge)* 2707–2709

953. Goldt IV, Boltalina OV, Sidorov LN, Kemnitz E, Troyanov SI (2002) Preparation and crystal structure of solvent free $C_{60}F_{18}$. *Solid State Sci* 4:1395–1401
954. Zhu Q, Cox DE, Fischer JE, Kniaz K, McGhie AR, Zhou O (1992) Intercalation of solid C_{60} with iodine. *Nature (London)* 355:712–714
955. Rizzoli C, Salamakha PS, Sologub OL, Bocelli G (2002) X-ray investigation of the Al-B-N ternary system: isothermal section at 1500 °C: crystal structure of the $Al_{0.185}B_6CN_{0.256}$ compound. *J Alloys Compd* 343:135–141
956. Kubaschewski O (1990) The Al-C-Hf (aluminium-carbon-hafnium) system. *Ternary Alloys VCH* 3:494–496
957. Velikanova TY (1990) The Al-C-Mo (aluminium-carbon-molybdenum) system. *Ternary Alloys VCH* 3:507–513
958. Monteiro WA (1990) The Al-C-Nb (aluminium-carbon-niobium) system. *Ternary Alloys VCH* 3:515–517
959. Savitskii EM, Efimov YV, Myasnikova EA, Bodak OI, Ryabtsev LA (1981) The niobium-aluminium-carbon system and the critical temperatures of the alloys (summary). *Sov Non-Ferrous Met Res* 9:342–343
960. Aponchuk AV, Karpov IK, Katkov OM (1987) On the dependence of triangulation of composition paragenesis diagram for the system Al-O-C on the temperature. *Dokl Akad Nauk SSSR* 294:1200–1202
961. Alexeeva ZM (1990) The Al-C-U (aluminium-carbon-uranium) system. *Ternary Alloys VCH* 3:568–574
962. Schuster JC, Nowotny H, Vaccaro C (1980) The ternary systems: Cr-Al-C, V-Al-C, and Ti-Al-C and the behavior of H-Phases (M_2AlC). *J Solid State Chem* 32:213–219
963. Schuster JC (1990) The Al-C-W (aluminium-carbon-tungsten) system *Ternary Alloys VCH* 3:575–577
964. Schuster JC (1990) The Al-C-Zr (aluminium-carbon-zirconium) system *Ternary Alloys VCH* 3:582–586
965. Schuster JC, Nowotny H (1980) Investigations of the ternary systems (Zr,Hf,Nb,Ta)-Al-C and studies on complex carbides. *Z Metallkd* 71:341–346
966. Schuster JC (1994) The As-C-V (arsenic-carbon-vanadium) system *Ternary Alloys VCH* 9:277–278
967. Boller H, Nowotny H (1967) Zum Dreistoff: Vanadin-Arsen-Kohlenstoff (On ternary system: vanadium-arsenic-carbon). *Monatsh Chem* 98:2127–2132
968. Brewer L, Haraldsen H (1955) The thermodynamic stability of refractory borides. *J Electrochem Soc* 102:399–406
969. Stadelmaier HH, Ballance JB (1967) Das Mischungsverhalten der τ -Boride (The mixing behavior of the τ -borides). *Z Metallkd* 58:449–451 (in German)
970. Lucco-Borlera M, Pradelli G (1971) Equilibri allo stato solido nel sistema manganese-carbonio-boro (Equilibria in the carbon-manganese-boron system in the solid state). *Atti Accad Naz Lincei Mem Cl Sci Fis Mat Nat Ser 2a* 10:69–89 (in Italian)
971. Shi Y, Leithe-Jasper A, Tanaka T (1999) New ternary compounds $Sc_3B_{0.75}C_3$, $Sc_2B_{1.1}C_{3.2}$, $ScB_{15}C_{1.60}$ and subsolidus phase relations in the Sc-B-C System at 1700 °C. *J Solid State Chem* 148:250–259
972. Tanaka T (1998) A new scandium borocarbide: $ScB_{17}C_{0.25}$. *J Alloys Compd* 270:132–135
973. Brisi C, Abbattista F (1961) Equilibri allo stato solido nei sistemi uranio-berillio-carbinio e torio-berillio-carbinio (Equilibria of uranium-beryllium-carbon and thorium-beryllium-carbon solid-state systems). *Ann Chim (Rome)* 51:1404–1408 (in Italian)
974. Zimin SS, Zalishchak BL (1986) A new model of the formation of carbonatites and ores associated with them. *Dokl Akad Nauk SSSR* 289:700–702
975. Savitskii EM, Efimov YV, Myasnikova EA, Bodak OI, Kharchenko OI (1984) Phase equilibria in Nb(V)-Ga-C systems. *Inorg Mater* 20:350–352
976. Gupta LC, Nagarajan R, Godart C, Dhar SK, Mazumdar C, Hossain Z, Lévy-Clement C, Padalia BD, Vijayaraghavan PR (1994) The new class of superconducting quaternary R-T-B-C systems (R= rare earth, T = Ni, Pd)”, *Physica C* 235–240:150–153

977. Frisk K, Zackrisson J, Jansson B, Makrström A (2004) Experimental investigation of the equilibrium composition of titanium carbonitride and analysis using thermodynamic modelling. *Z Metallkd* 95:987–992
978. Teyssandier F, Ducarroir M, Bernard C (1984) Thermodynamic study of the titanium-carbon-nitrogen phase diagram at high temperature. *Calphad* 8:233–242
979. Arbuzov MP, Golub SY, Khaenko BV (1978) Phases of the system Ti-TiC-TiN. *Inorg Mater* 14:1126–1128
980. Danisina IN, Vilk YN, Avarbé RG, Omelchenko YA, Ryzhkova TP (1968) Phase diagram of the system zirconium – zirconium nitride – zirconium carbide. *J Appl Chem USSR* 41:478–485
981. Babad-Zakhryapin AA, Gert LM, Valyavko LR (1968) Possibility of forming tungsten oxycarbide with a fcc lattice. *Inorg Mater* 4:1200–1201
982. Boller H (1973) Röntgenographische Untersuchungen im Dreistoff V-P-C (X-ray studies in the V-P-C ternary system). *Monatsh Chem* 104:48–56 (in German)
983. Jeng FS, You YB, Ku HC, Ho JC (1996) Superconducting and calorimetric properties of $\text{ThPt}_2\text{B}_2\text{C}$ and the anomalous T_c variation for non-magnetic $\text{RPt}_2\text{B}_2\text{C}$ systems ($\text{R} = \text{Y, Th, La}$). *Phys Rev B* 53:3492–3496
984. Kerans RJ, Mazdiasni KS, Ruh R, Lipsitt HA (1984) Solubility of metals in substoichiometric TiC_{1-x} . *J Am Ceram Soc* 67:34–38
985. Pakholkov VV, Brettser-Portnov IV, Grigorov IG, Alyamovskii SI, Zainulin YG (1991) Phase formation in the TiB-TiC system. *Russ J Inorg Chem* 36:912–915
986. Vogt C, Hoffmann RD, Pöttgen R (2005) The superstructure of Sc_3RhC_4 and Sc_3IrC_4 . *Solid State Sci* 7:1003–1009
987. Holleck H (1977) Carbon- and boron-stabilized ordered phases of scandium. *J Less-Common Met* 52:167–172
988. Hoffmann RD, Pöttgen R, Jeitschko W (1992) Scandium transition metal carbides Sc_3TC_4 with $\text{T} = \text{Fe, Co, Ni, Ru, Rh, Os, Ir}$. *J Solid State Chem* 99:134–139
989. Vogt C, Hoffmann RD, Rodewald UC, Pöttgen R, Bohrmoser B, Scherer W, Zhang L, Eckert H (2006) Überstruktur, experimentelle Elektronendichte und spektroskopische Eigenschaften der Carbide Sc_3TC_4 ($\text{T} = \text{Fe, Co, Ni, Ru, Rh, Os, Ir}$) (On the structure, experimental electron density and spectroscopic properties of the carbides Sc_3TC_4 ($\text{T} = \text{Fe, Co, Ni, Ru, Rh, Os, Ir}$)). *Z Anorg Allg Chem* 632(12–13):2116 (in German)
990. Krikorian NH (1971) The reaction of selected lanthanide carbides with platinum and iridium. *J Less-Common Met* 23(3):271–279
991. Gerdes MH, Jeitschko W, Wachtmann KH, Danebrock ME (1997) Gd_2OsC_2 , a soft ferromagnet with a surprisingly high Curie temperature and other rare-earth osmium and rhenium carbides with Pr_2ReC_2 type structure. *J Mater Chem* 7(12):2427–2431
992. Hüfken T, Wachtmann KH, Jeitschko W (1998) Preparation and crystal structure of the ternary carbides $\text{R}_{12}\text{Os}_5\text{C}_{15}$ with $\text{R} = \text{Y, Pr, Nd, Sm, Gd-Tm}$. *J Alloys Compd* 281(2):233–236
993. Jeitschko W, Block G, Kahnert GE, Behrens RK (1990) Pr_2ReC_2 and other ternary rare earth metal rhenium carbides with filled PbCl_2 (Co_2Si) structure. *J Solid State Chem* 89(1):191–201
994. Pöttgen R, Block G, Jeitschko W, Behrens RK (1994) Preparation and crystal structure of the carbides $\text{Ln}_{15}\text{Re}_5\text{C}_{15}$ ($\text{Ln} = \text{Y, La-Nd, Gd-Er}$). *Z Naturforsch B* 49:1081–1088
995. Raghavan V (2008) The Al-C-Ir (aluminum-carbon-iridium) system. *J Phase Equilib Diffus* 29(1):51
996. Okamoto H (2012) The C-O (carbon-oxygen) system. *J Phase Equilib Diffus* 33(3):244
997. Okamoto H (2012) The C-S (carbon-sulfur) system. *J Phase Equilib Diffus* 33(3):245
998. Okamoto H (2011) The C-Pu (carbon-plutonium) system. *J Phase Equilib Diffus* 32(4):389–390
999. Okamoto H (2010) The C-Cl (carbon-chlorine) system. *J Phase Equilib Diffus* 31(5):496
1000. Okamoto H (2010) The C-V (carbon-vanadium) system. *J Phase Equilib Diffus* 31(1):91–92

1001. Okamoto H (2008) The C-W (carbon-tungsten) system. *J Phase Equilib Diffus* 29(6):543–544
1002. Raghavan V (2008) The Al-C-Si (aluminium-carbon-silicon) system. *J Phase Equilib Diffus* 29(4):365–366
1003. Sangster J (2007) The C-Na (carbon-sodium) system. *J Phase Equilib Diffus* 28(6):571–579
1004. Sangster J (2007) The C-Li (carbon-lithium) system. *J Phase Equilib Diffus* 28(6):561–570
1005. Demetriou MD, Ghoniem NM, Lavine AS (2002) Computation of metastable phases in tungsten-carbon system. *J Phase Equilib* 23(4):305–309
1006. Bittermann H, Rogl P (1997) Critical assessment and thermodynamic calculation of the binary system hafnium-carbon (Hf-C). *J Phase Equilib* 18(4):344–356
1007. Bandyopadhyay D, Sharma RC, Chakraborti N (2000) The C-Nb-Ti (carbon-niobium-titanium) system. *J Phase Equilib* 21(1):102–104
1008. Bandyopadhyay D, Sharma RC, Chakraborti N (2000) The Ti-V-C (titanium-vanadium-carbon) system. *J Phase Equilib* 21(1):199–202
1009. Bandyopadhyay D, Sharma RC, Chakraborti N (2000) The Ti-Co-C (titanium-cobalt-carbon) system. *J Phase Equilib* 21(2):179–185
1010. Bandyopadhyay D, Sharma RC, Chakraborti N (2000) The Ti-N-C (titanium-nitrogen-carbon) system. *J Phase Equilib* 21(2):192–194
1011. Bandyopadhyay D, Sharma RC, Chakraborti N (2000) The Ti-Ni-C (titanium-nickel-carbon) system. *J Phase Equilib* 21(2):186–189
1012. Durand F, Duby JC (2000) Solid-liquid equilibria in the silicon-rich corner of the Si-O-C system. *J Phase Equilib* 21(2):130–135
1013. Bandyopadhyay D, Halder B, Sharma RC, Chakraborti N (1999) The Ti-Mo-C (titanium-molybdenum-carbon) system. *J Phase Equilib* 20(3):332–336
1014. Halder B, Bandyopadhyay D, Sharma RC, Chakraborti N (1999) The Ti-W-C (titanium-tungsten-carbon) system. *J Phase Equilib* 20(3):337–343
1015. Durand F, Duby JC (1999) Carbon solubility in solid and liquid silicon – a review with reference to eutectic equilibrium. *J Phase Equilib* 20(1):61–63
1016. Goksen NA, Oden LL (1998) Phase equilibria in aluminium-carbon system at high temperatures. *J Phase Equilib* 19(5):409–411
1017. Okamoto H (1996) The C-Zr (carbon-zirconium) system. *J Phase Equilib* 17(2):162
1018. Okamoto H (1995) Comment on C-Ti (carbon-titanium) system. *J Phase Equilib* 16(6):532–533
1019. Okamoto H (1992) The B-C (boron-carbon) system. *J Phase Equilib* 13(4):436
1020. Okamoto H (1991) The C-V (carbon-vanadium) system. *J Phase Equilib* 12(6):699
1021. Ishida K, Nishizawa T (1991) The C-Co (carbon-cobalt) system. *J Phase Equilib* 12(4):417–424
1022. Okamoto H (2007) The C-Pd (carbon-palladium) system. *J Phase Equilib Diffus* 28(3):313
1023. Frisk K, Dumitrescu L, Ekroth M, Jansson B, Kruse O, Sundman B (2001) Development of a database for cemented carbides: thermodynamic modelling and experiments. *Phase Equilib* 22(6):645–655
1024. Claeysens F, Fuge GM, Allan NL, May PW, Ashfold MNR (2004) Phosphorus carbides: theory and experiment. *Dalton Trans* (19):3085–3092
1025. Cataldo F (2002) Polymeric fullerene oxide (fullerene ozopolymers) produced by prolonged ozonation of C₆₀ and C₇₀ fullerenes. *Carbon* 40(9):1457–1467
1026. Tkachenko YuG, Ordanyan SS, Yulyugin VK, Yurchenko DZ, Unrod VI, Evdokimova NI (1977) High-temperature friction and wear of eutectic carboride alloys of group V metals. *Powder Metall Met Ceram* 16(10):781–784

Ultra-High Temperature Materials I

Carbon (Graphene/Graphite) and Refractory Metals

Shabalov, I.L.

2014, XVII, 794 p. 30 illus., 1 illus. in color., Hardcover

ISBN: 978-94-007-7586-2